Development of Design Procedures for Fiber Reinforced Concrete (FRC) & Ultra-High-Performance Concrete (UHPC) Based on Experimental Evaluations

By

Farrokh Kianmofrad

A Thesis Presented in Partial Fulfillment
of the Requirements for the Degree
Master of Science

Approved November 2018 by the
Graduate Supervisory Committee:

Barzin Mobasher, Chair
Subramaniam Dharma Rajan
Christian Hoover

ARIZONA STATE UNIVERSITY

December 2018

ABSTRACT

A comprehensive study was performed on non-proprietary ultra-high-performance concrete (UHPC) material and several design methods were suggested based on numerous experimental results. Several sets of compression tests, direct tensile tests, and flexural tests were performed on UHPC to provide a better understanding of the mechanisms involved in the mechanical behavior of the fiber reinforced material. In addition to compressive tests, flexural tests, based on ASTM C1609 and EN 14651, were performed. The effect of the strain rate on the UHPC material was also investigated through the high-speed tensile tests at different strain rates. Alongside the usual measurement tools such as linear variable differential transformers (LVDT) and clip gages, digital image correlation (DIC) method was also used to capture the full-range deformations in the samples and localized crack propagations. Analytical approaches were suggested, based on the experimental results of the current research and other research groups, to provide design solutions for different applications and design approaches for UHPC and hybrid reinforced concrete (HRC) sections. The suggested methods can be used both in the ultimate limit state (ULS) and the serviceability limit state (SLS) design methods. Closed form relationships, based on the non-linear design of reinforced concrete, were used in the calculation of the load-deflection response of UHPC. The procedures were used in obtaining material properties from the flexural data using procedures that are based on back calculation of material properties from the experimental results. Model simulations were compared with other results available in the literature. Performance of flexural reinforced UHPC concrete beam sections tested under different types of loading was addressed using a combination of fibers and rebars. The

same analytical approach was suggested for the fiber reinforced concrete (FRC) sections strengthened (rehabilitated) by fiber reinforced polymers (FRP) and textile reinforced concrete (TRC). The objective is to validate the proper design procedures for flexural members as well as connection elements. The proposed solutions can be used to reduce total reinforcement by means of increasing the ductility of the FRC, HRC, and UHPC members in order to meet the required flexural reinforcement, which in some cases leads to total elimination of rebars.

TABLE OF CONTENTS

Page

CHAPTER Page

CHAPTER Page

LIST OF TABLES

Table Page

Table Page

Table Page

LIST OF FIGURES

Figure Page

Figure Page

Figure Page

Figure Page

Figure Page

Figure Page

Figure Page

Figure Page

Figure Page

Figure Page

Figure Page

Figure Page

INTRODUCTION

Concrete is one of the constructional materials which has been used for thousands of years and still is the most ubiquitous man-made material in the word [1]. However, regarding the new challenges in civil engineering and the construction industry, such as economical construction, climate changes and the necessity to reduce the carbon footprint, many research groups, governmental sections, and industrial companies have been trying to develop innovative methods to make stronger constructional materials with a lower amount of raw materials. Fiber reinforced concrete (FRC), high and ultra-high-performance concrete (UHPC), textile reinforced concrete (TRC), and self-healing concrete (SHC) are some of the modern approaches to reduce the amount of concrete and simultaneously increase its strength capacity against the applied loads.

Concrete is weak in tension and has a brittle behavior. The concept of using fibers to improve the properties of construction materials (i.e., composite materials) is not a modern solution. The addition of straw to mud bricks, horse hair to reinforce plaster, and asbestos to reinforce pottery are some of the old but effective means of composite reinforcements. Use of continuous reinforcement in concrete (reinforced concrete) increases strength and ductility but is expensive and requires labor skill. Alternatively, the use of short fibers in discrete form in plain or reinforced concrete may deliver a better result. The modern development of (FRC) started in the early sixties [2] by applying chopped fibers into the concrete mixture. When concrete cracks, the randomly oriented fibers arrest crack propagation and improve strength and ductility. The failure modes of FRC are either bond failure between fiber and matrix or material failure[2].

Despite the fact that FRC has been employed in the construction industry for more than five decades, applications are still limited, and this is primarily due to the lack of standard guidelines for design practices [3]. The *fib* Model Code 2010 [4] has introduced an appropriate classification of fiber-reinforced material based on post-cracking residual strengths measured by a three-point bending (3PB) test on notched prisms according to EN 14651 [5]. This model encourages a performance-based design approach in the FRC sections. ACI 544.4R is another guide for design with FRC material. This guide discusses the type and dosage of fibers, material properties and available test methods for the characterization of FRC [6]. It provides an overview of the design concepts and existing guidelines for FRC, including constitutive laws, design for flexure, shear, and crack-width control.

Although FRC has been used for decades, there is no established design guideline in North America for some of its applications [6]. Numerous groups around the world are developing new ideas to analyze and design the FRC structural (and non-structural) elements, and more research needs to be done to develop well-established design approaches for FRC materials. The main goal of this research is to provide a better understanding of the mechanisms involved in the mechanical behavior of the FRC and UHPC, by analyzing the experimental results obtained from compression tests, direct tensile tests, and flexural tests. For this purpose, a number of analytical solutions are suggested, based on a constitutive analytical approach [3], [7], [8], which will be discussed in detail in section 2. The suggested analytical solutions are a part of a more comprehensive study on the design approaches, based on ACI committees 544 and 239

recommendations, and were submitted to the Arizona Department of Transportation (ADOT) as the main funder of this research.

This research is divided into four major parts. In the first section, the mechanical properties of FRC and UHPC materials are investigated. Numerous sets of non-proprietary UHPC samples were tested and their properties were scrutinized through comparative graphs and tables. In addition to compressive tests, several sets of flexural tests, based on ASTM C1609 and EN 14651, were performed on prismatic samples with different dimensions, at different fiber contents and mix designs. The effect of the strain rate on the UHPC material was also investigated through the high-speed tensile tests at different strain rates. During these sets of tests, alongside the usual measurement tools such as linear variable differential transformers (LVDT) and clip gages, digital image correlation (DIC) method was also used to capture the full-range deformations in the samples and localized crack propagations.

In the second chapter, several analytical approaches are suggested, based on the experimental results of the current research and also other research groups, to provide design solutions for different applications and different design approaches. The suggested methods can be used both in the ultimate limit state (ULS) and the serviceability limit state (SLS) design methods. This section addresses the methods employed in the analysis of flexural UHPC members. Closed form relationships based on the non-linear design of reinforced concrete are used in the calculation of the load-deflection response of UHPC [3], [7], [8]. Procedures to calibrate the test methods to obtain material properties from

experiments are discussed as well. Equations that relate the material properties to the structural design and analysis procedures of UHPC are also discussed.

The developed procedures are used in obtaining material properties from the flexural data using procedures that are based on back-calculation of material properties from the experimental results. Model simulations are compared with other results available in the literature. Performance of flexural reinforced UHPC concrete beam sections tested under different types of loading is addressed using a combination of fibers and rebars. The objective is to validate the proper design procedures for UHPC flexural members as well as connection elements used with UHPC. The proposed solutions can be used to reduce total reinforcement by means of increasing the ductility of the UHPC mixtures in order to meet the required flexural reinforcement. In addition, the cracking and ductility response can be analyzed as well as the serviceability deflection level estimated from moment-curvature expressions for homogenized UHPC Concrete.

The third section investigates the reinforcement and strengthening aspects of the FRC members. The flexural response of the FRC sections rehabilitated using fiber reinforced polymer (FRP) plates is analyzed and a constitutive analytical approach is suggested for these types of sections. The suggested method can be used in the flexural analysis and design of the FRC beams and slabs rehabilitated using FRP strips. The suggested analytical simulation is validated based on the previous experimental results on FRC sections strengthened using FRP plates. Several parametric studies were performed to investigate the effect of reinforcement and material properties of the FRP strips on the flexural response of the rehabilitated sections as well.

In the fourth and the last section, the application of the constitutive analytical approach on the hybrid reinforced concrete (HRC) sections (i.e., FRC sections reinforced with rebars) is studied. This approach is specifically used for analyzing the flexural behavior of the full-scale tunnel segments. Several analytical simulations have been done on the full-scale tunnel segments, then the simulation results were compared to the experimental results from different research or industrial groups. In the end, a number of parametric studies were performed to capture the effect of several parameters, such as the dimension of the tunnel segments, fiber content, reinforcement ratio, and so forth. Regarding the size of the tunnel segments (that in some cases is as long as 12 ft and a width of 6 ft), the mechanical testing of these segments is very cumbersome, time-consuming and expensive. Therefore, a reliable simulation method can be very effective for the initial estimations and design process and saves a lot of time and efforts in casting and testing these huge segments.

1 MECHANICAL PROPERTIES OF NON-PROPRIETARY ULTRA-HIGH-PERFORMANCE CONCRETE

Ultra-High-Performance Concrete (UHPC) is a special type of concrete designed to demonstrate exceptional strength, ductility, and durability properties. The high compressive strength of UHPC enables a reduction in cross section and self-weight of reinforced concrete structures. UHPC is constituted by employing a well-defined size distribution of particles (both fine particles including cement replacement materials such as silica fume, and fine and coarse aggregates), fibers, and a very low water-to-binder ratio (w/b) (0.2-to-0.3). The very low w/b demands the use of higher-than-normal amounts of chemical admixtures including high range water reducers and viscosity modifiers. This complex mixture formulation, which is often proprietary in nature, leads to a significant increase in the cost of production of UHPC. Development of economical, yet optimally performing UHPC mixtures is a major challenge for many users including State Departments of Transportation. In the remainder of this section, answers to some of the commonly encountered questions relating to UHPC are provided to contextualize the discussions describe later in this document.

While the 28-day compressive strength of conventional concrete ranges from 4000-7000 psi and that of high-performance concrete lies between 7000 psi and 14000 psi, the compressive strength of UHPC is in the order of 20000-24000 psi. The significantly higher tensile strength (1000-1500 psi) and bending strength also set UHPC apart from conventional concrete and even traditional high-performance concrete. In addition, the use of a high dosage rate (of the order of 1%-3% equivalent steel fibers) of fibers in UHPC increases the ductility of the member, in addition to allowing to

withstand tension and bending loads without any passive or active reinforcement. The use of a low w/b, coupled with optimal particle packing, significantly increases the durability properties of UHPC by resisting the ingress of moisture and other deleterious ions such as chlorides and sulfates. These special properties of UHPC have been utilized for the construction of several transportation structures as well as the connections for precast elements in the U.S and Canada.

Accelerated Bridge Construction (ABC) using Prefabricated Bridge Elements and Systems (PBES) is being widely implemented to ensure that construction and maintenance activities pose as little impediment to traffic. Prefabricated elements ensure reduced onsite construction time and minimal traffic interruption, which allows state DOTs to build and maintain economic and durable bridges with increased safety. However, transverse connections between the precast elements using normal or high strength/performance concrete suffer from cracking and construction-related deficiencies, detrimentally influencing their service-lives. This makes UHPC a material of choice in ABC to ensure superior structural performance and the long-term durability [9], [10].

Figure 1 shows the first UHPC bridge in the U.S. which was built in Iowa and the casting of longitudinal connections between precast bridge girders in the state of New York.

Figure 1: (a) The first UHPC bridge constructed in the U.S (in Wapello County, IA), (b) casting of longitudinal connections between deck-bulb-tee girders (Route 31 Bridge, Lyons NY)[11].

Use of innovative technologies such as UHPC enables construction of infrastructural components at lower life-cycle costs. UHPC can also be used in applications such as high-performance decks and slabs, and environmental applications such as buried structures, bridge piers, foundations, box culverts, and tunnel segments [12], [13]. UHPC can also be used in beams, closure pours, and approach slabs as well as areas where excessive congestion of reinforcement or high demand for ductility are required.

Many of the advantages of using UHPC in structural applications, related to material and structural performance, were detailed earlier. Other major advantages are (i) reduction in labor and construction time, (ii) reduction in the use of heavy equipment facilitated by a reduction in the use of continuous reinforcement, (iii). significant ductility and reductions in structural weight provided by the employment of an elasto-plastic design approach, (iv) improved safety through the optimization of physical and labor-intensive tasks in the job site, and (v) improved mobility and safety of personnel because of the absence of layers of rebars.

However, since the intrinsic brittleness of concrete, the ultimate state of the structural member is usually not dominated by its compressive strength. Post-crack tensile and flexural strength, as well as the strain and deflection, are significant the performance in ultimate limit state and serviceability state design. The high compressive strength of 22 ksi (150 MPa) may not be necessary for many applications. Consequently, there is a need to develop high-performance concrete mixtures that satisfy the strength

and durability requirements yet remain economically feasible. Textile reinforced concrete (TRC) and hybrid reinforced concrete (HRC) which contains steel rebars and fibers, for example, may outperform the tensile and flexural properties of UHPC achieved by researchers[14]. Similar to the performance exhibited by the high dose of fibers used in UHPC, continuous fibers or hybrid reinforcement provides tensile capacity across cracks, resulting in high shear capacity in bending members, hence it can result in reducing the amount of shear reinforcement. This means that the increased ductility and crack resistance reduces the near for excessive shear reinforcement, and some of the complexities in the reinforcement placement can be avoided (see Figure 2). Note that the tensile cracks are a pathway for the intrusion of chlorides and harmful ions into the concrete. They are also quite compatible with post-tensioned sections and can be used to reduce the congestion of reinforcement in the anchor zones.

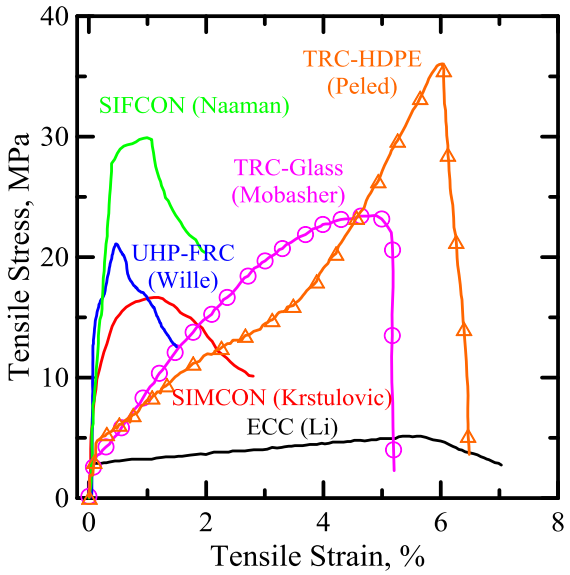

Figure 2. Comparison of the tensile responses of several different FRC systems exhibiting strain-hardening behavior [15].

TRC materials are about an order of magnitude higher in strength and two orders of magnitude higher in ductility than fiber reinforced concrete (FRC). A fiber content of

0.75% without stirrups is considered sufficient to achieve the equivalent ultimate resistance of a conventional RC flexural member with stirrups, however, it greatly depends on the depth of the beam as well [16]. Naaman and Reinhardt [17] compared the tensile performance of different strain-hardening FRC materials and illustrated the trade-off between strength and ductility. As shown in Figure 2, in order to achieve a high post-crack tensile strength of 20-30 MPa, the peak strains are limited to about 1.5%, compared to the 6% strain shown by more ductile but low strength ECC. Nevertheless, the concrete reinforced by textile (glass, HDPE) exhibits the post-crack tensile strength up to of about 35 MPa while maintaining very high ductility (6% peak strain). Addition of short fibers in a hybrid manner reduces the congestion of rebars in reinforced concrete, fibers in self-consolidated concrete to increase the cost-effectiveness, and labor efficiency of structures such as water and wastewater structures with improved durability and minimized need of maintenance and repair operations during the lifetime.

This study addresses a potential direction for ultimate and serviceability-based design for ultra high tensile and flexural strength, and high ductility concrete based on experimental evaluations on UHPC, TRC, and FRP reinforced sections. As shown in Figure 3, the high ductility and energy absorption are essentially attributed to the interfacial behavior characterized by effective pullout resistance and length. Hardening effects after the first crack are referred to as tension stiffening that is accompanied by multiple cracking mechanisms. Deflection hardening is subsequently observed in the flexural behavior where the cracks are bridged and mitigated by the distributed or continuous fibers, which enables the reduction of web and shear reinforcements. The structural members made of these systems include tension, flexural and shear resistance

member (beam), shrinkage control (slab on grade), axial and bending combined loading (column). Design procedures integrate serviceability with the ultimate strength approach for practical structural members. Both stress-crack width and smeared stress-strain approaches are used in the modeling procedure. Indirect measurement of the localized zone using digital image correlation (DIC) method enables the birding from σ-ω to σ-ε.

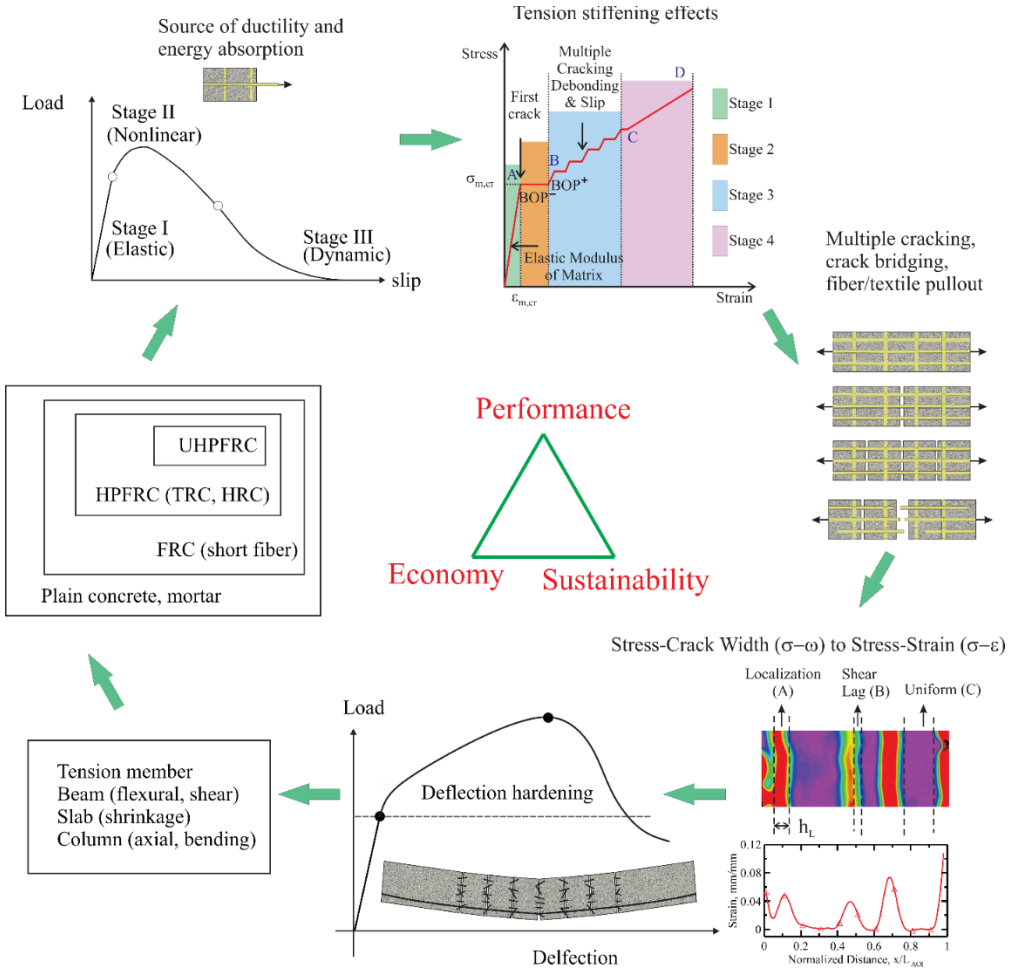

Figure 3. Mechanisms and performance of ultra-high-performance concrete and textile reinforced concrete materials [15].

The major objectives of this project are outlined below:

1) Experimentally evaluate the mechanical properties (strength, elastic modulus, toughness) of the selected proposed systems using multiple techniques.
2) Investigate the effect of fibers on toughening and mechanisms of crack growth in UHPC.
3) Inspect the effect of mix design, mixing method, size of the member, duration of the curing period, and the fiber content on the strength parameters
4) Develop and propose design procedures for practical applications such as beam flexure, joint slabs (bridge connections), TRC and FRP reinforced sections and tunnel segments.

1.1 Distributed Cracking and Tension Stiffening

One of the most important mechanical properties of UHPC is its resistance to cracking due to enhanced tensile strength and ductility. This enhanced response is attributed to the strength of the matrix phase as well as the toughening mechanism due to fiber reinforcement. Flexural testing is commonly used as an indirect method in lieu of tensile testing because the complexities of specimen preparation and gripping make it difficult to conduct a tensile test. Tension tests are also associated with various challenges such as localization of failure after the first crack, the effect of fixed versus rotating free supports (which may lead to sample rotation or asymmetric crack growth), and potential for growth of multiple cracks [18]. Unlike a compression test or tensile test, a flexure test does not measure fundamental material properties. When a specimen is placed under flexural loading all three fundamental stresses − tension, compression, and shear stresses

− are present. Therefore, the flexural properties are due to the combined effect of all three stresses.

A comprehensive discussion of the effect of fibers on the toughening in concrete materials is presented in an earlier report AZ633 [19]. Concrete materials produced with short, randomly distributed fibers may be superior to forms of reinforced concrete using welded wire mesh or rebars. Both the tensile strength and the toughness, especially the post-crack strength, are improved [20]. It has been shown that due to the reduced specific spacing, fibers strengthen the composite at the micro level by bridging the microcracks before they reach the critical flaw size [21]. The small diameter of the individual fibers ensures a better and more uniform distribution of reinforcement. In addition, the high surface area offers significant bond capability. Since the bond strength of glass, steel, or even polymeric fibers is far superior to reinforcing bars, this increases the efficiency of reinforcement so that there is limited crack opening due to the debonding and pullout of reinforcement. The fibers are distributed randomly, offering efficiency in load transfer by the fiber phase. Finally, because the fibers that bridge the matrix cracks are resilient and highly compliant, they can orient to carry the load across the crack faces. This factor is expected to increase the durability of concrete substantially since the crack width control affects long-term durability.

1.2 Fundamentals of Toughening Cement Composites by Controlling the Crack Growth Mechanisms

One of the main problems observed with HPC and UHPC is that the high strength and stiffness result in a brittle behavior of the material. The cracks, which initiate due to the concentration of stresses, may extend with a minimal amount of energy and lead to

fracture. This low strength post-cracking response is concerning and limits many potential applications. The addition of sufficient fibers would help bridge the potential microcracks and lead to the toughening of the fiber-matrix composite, due to processes such as fiber bridging and crack deflection; it would also carry the load post-peak after the matrix failure. The high cost of fibers is always a deterrent that inhibits the use of extremely high percentage of fibers. Therefore, the fiber volume percent in UHPC needs to be optimized to utilize their strength, stiffness, and bond capacity in reinforcing the brittle matrix. The efficiency of fibers also depends on their volume percent, stiffness, type, and aspect ratio.

Toughening is affected by the interaction of the fiber, the matrix, and the interface. In the presence of fibers, the propagation of a matrix crack results in fiber debonding, and as the pullout force on the fiber increases, cracks are closed and fail to propagate easily as a decrease in the stress intensity at the crack tip is observed. Further growth of the matrix crack depends on the extent of fiber debonding, which itself dissipates energy. Two mechanisms play a key role in toughening in the case of UHPC. First, the particle packing results in a densified mixture using particles with different size distribution achieving a maximum packing efficiency, as shown in Figure 4 (a). Second, the use of fibers aids in bridging the cracks, and therefore significantly increases the potential for toughening (see Figure 4(b)).

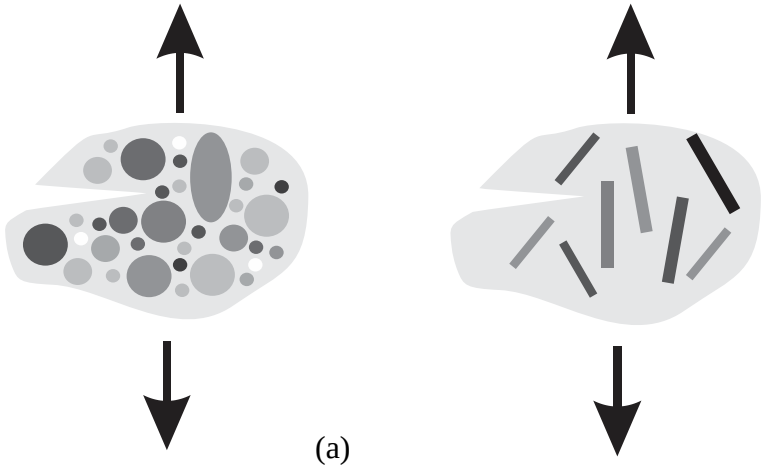

(a) (b)

Figure 4. Potential toughening due to a) particle packing and porosity reduction, and b) fiber toughening [22].

Several complementary techniques such as those based on fracture mechanics, non-linear finite element, and closing pressure formulations have been used to relate the fiber, interface, and matrix properties to the strength, toughness, and fracture response of HPC materials as they affect the toughness. In fiber-reinforced concretes, the critical volume percent of fibers for the transition from strain softening to hardening, or distributed cracking, is available from [3], [7], [23], and [24].

Figure 5(a) and (b) show the contribution of fibers to the resistance to crack propagation. Whether they are continuous fibers or short uniformly-distributed fibers, in unnotched or notched specimens, the results in terms of toughening are similar in nature. As a single crack grows in the concrete, it crosses one, or several fibers which remain intact and result in a bridge across the two crack faces. Additional force applied to the specimen would attempt to open the crack, which is resisted by the bridged fibers, therefore, the fiber may start to debond, while still transferring the load. The fibers, therefore, create the bridging mechanism by forming a closing pressure, that resists cracking opening and increases the material's fracture toughness. Propagation of a matrix

crack, resisted by the debonding of fibers in an unnotched specimen with continuous fibers, is shown in Figure 6 (a). Note that the bridging zone may contain the entire sample width. Propagation of a crack in a notched specimen with short fibers would also result in crack closure due to stress-crack width relationship, however, in this case, the bridging zone is rather limited and dimensionally related to the number of fibers that are able to transfer load. Several studies have shown that if the bridging zone is sufficiently large, it would actually increase the strength of the material significantly. The strengthening of the matrix phase by means of a critical volume percent of fibers was also studied using micromechanics [25], [26]. Another approach includes a model to describe the stages of fiber pullout and crack growth toughening. Using closed-loop pullout experiments, the interfacial region can be characterized as the non-linear response of the ascending part of the pullout curve which affects the stiffness of the pullout force versus slip response. To consider incremental crack growth, an algorithm allowing for gradual fiber debonding is used to allow for the crack opening to take place. To simulate the changes in compliance and of the pullout-slip response, nonlinear fracture models based on R-Curves have recently been used [27], [28].

Figure 6 shows the bridging effect of fibers in the samples with 1% and 3% fiber content. It demonstrates that the crack bridging is due to the presence of fibers.

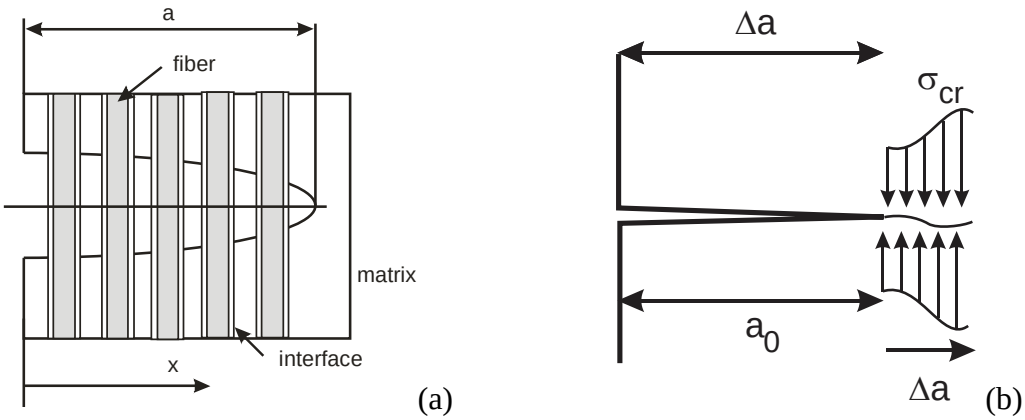

Figure 5. Propagation of a matrix crack, resisted by the debonding of fibers in (a) an unnotched specimen with continuous fibers, and/or b) a notched specimen which results in crack closure due to stress-crack width relationship [22].

(a) (b)

Figure 6. Bridging effect of fibers on samples with: (a) 1% fiber content; (b) 3% fiber content.

1.3 Mechanical Testing and Effect of Fiber Reinforcement In UHPC Beams

Two sets of mixtures are evaluated and selected as ideal candidate samples to be evaluated using flexural tests. These mixtures are the quaternary OPC-fly ash-micro silica-limestone binder mixture ($F_{17.5}M_{7.5}L_5$) designated as FML and the ternary OPC-micro silica-limestone binder mixture ($M_{20}L_{30}$) designated as ML (see Table 1).

Table 1. Mixture proportions of UHPCs, optimized aggregate and paste compositions.

Content of materials (lb/yd3)	$F_{17.5}M_{7.5}L_5$	$M_{20}L_{30}$
OPC	1595	1321
Fly ash (F)	280	0
Micro silica (M)	120	265
Limestone (L)	79	396
Coarse aggregate (#4)	580	555
Coarse aggregate (#8)	145	138
Coarse aggregate (#10)	145	138
Fine aggregate (Coarse or Medium Sand)	290	278
Fine aggregate (Fine Sand)	290	278
Water	280	288
Fiber (1%)	126	126
Superplasticizer (% of solids content by mass of binder)	1.25	1.45

A series of ten sets of concrete beams from different mixture formulations are used in the flexural tests. The variables in these experiments included: two specimen sizes, the effect of notched versus unnotched samples, two different mixing methods, two fiber volume percents, and monotonic and cyclic tests.

Table 2 shows the scope of the flexural tests. The $M_{20}L_{30}$ mixture (referred to as ML mixture) is used only in small beams, 2”x 2.5” x 14” (51 mm x 64 mm x 356 mm), cured for 28 days at 0% and 1% fiber volume. The $F_{17.5}M_{7.5}L_5$ mixture (referred to as FML mixture) is used to evaluate the influence of specimen size, fiber volume percent, and curing age. The FML mixture is selected based on its higher 28-day compressive strength. This mixture also had a more economical set of ingredients based on material costs than the $M_{20}L_{30}$ mixture.

Table 2. Mixtures and test details for the flexural response of UHPC beams.

Set ID	Mix Design	Beam Series	No. of Replicates	Beam Size*	Fiber Content (% by volume)	Curing Period (days)	Testing Method	Mixing Method
1	M20L30 (ML)	ML_S_0_28_4PB_D	3	Small 2"×2.5"×14"	0%	28	4PB	Drill Mixer
2		ML_S_1_28_4PB_D	6		1%	28		
3	F17.5M7.5L5 (FML)	FML_S_0_28_4PB_D	6		0%	28		
4		FML_S_1_28_4PB_D	6		1%	28		
5		FML_S_1_14_4PB_C	3		1%	14		Croker Mixer
6		FML_S_1_28_4PB_C	3		1%	28		
7		FML_L_3_28_4PB_C	3	Large (4"×4"×16")	3%	28		
8		FML_L_1_14_4PB_C	3		1%	14		
9		FML_L_1_28_4PB_C	3		1%	28		
10		FML_L_3_28_3PB_C	3		3%	28	3PB-Fracture (Cyclic)	

*The nominal dimension of the small beams is 2"×2.5"×14" and of the large beams 4"×4"×16".

A servo-hydraulic MTS 810 mechanical testing machine equipped with the flexural fixture, two displacement transducers, and software capable of controlling the test and recording/analyzing the data are used. The test setup is shown in Figure 7. The two-transducer arrangement uses a setup attached to the concrete specimen directly above the support members and at the specimen so the spurious deformations are excluded from the measured response. Four-point bending tests are performed on replicate UHPC beams corresponding to the mixture designs shown in Table 2. A spring-loaded Linear Variable Differential Transformer (LVDT) was mounted at the center of the beam to measure the mid-span deflection with a range of 3.8 mm. Results are used for parameter estimation such as the initial stiffness, post-peak residual strength, and toughness.

A loading rate of 2.2 N/sec was used and the deflection measured. This initial loading range covers about 30% of the initial linear load-deflection response and is

followed by the subsequent steps that are both displacements controlled at rates of 8.5 μm/sec and 1.7 μm/sec, as specified in Table 3.

Table 3. Flexural test procedure used in the MTS station manager to control the test

Phase	Control Mode	Loading Rate	Phase Limit
1	Load	2.2 N/sec	134 N
2	Actuator (Deflection)	8.5 μm/sec	3.8 mm
3	Actuator (Deflection)	1.7 μm/sec	19 mm

The raw experimental data collected from the test is analyzed using a MATLAB code. The code calculates post-cracking parameters that represent the role of the fiber efficiency in carrying the load in the crack propagation phase of testing. Parameters such as load capacity, residual strength, and toughness are computed at two deflection limits of L/600 and L/150, where L is the span of the beam.

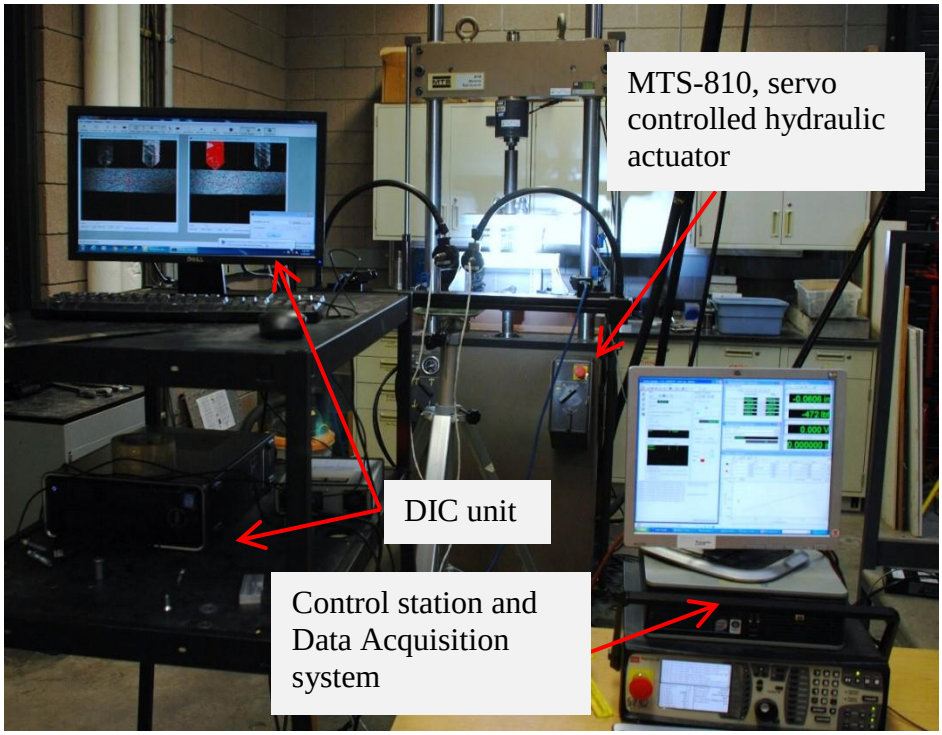

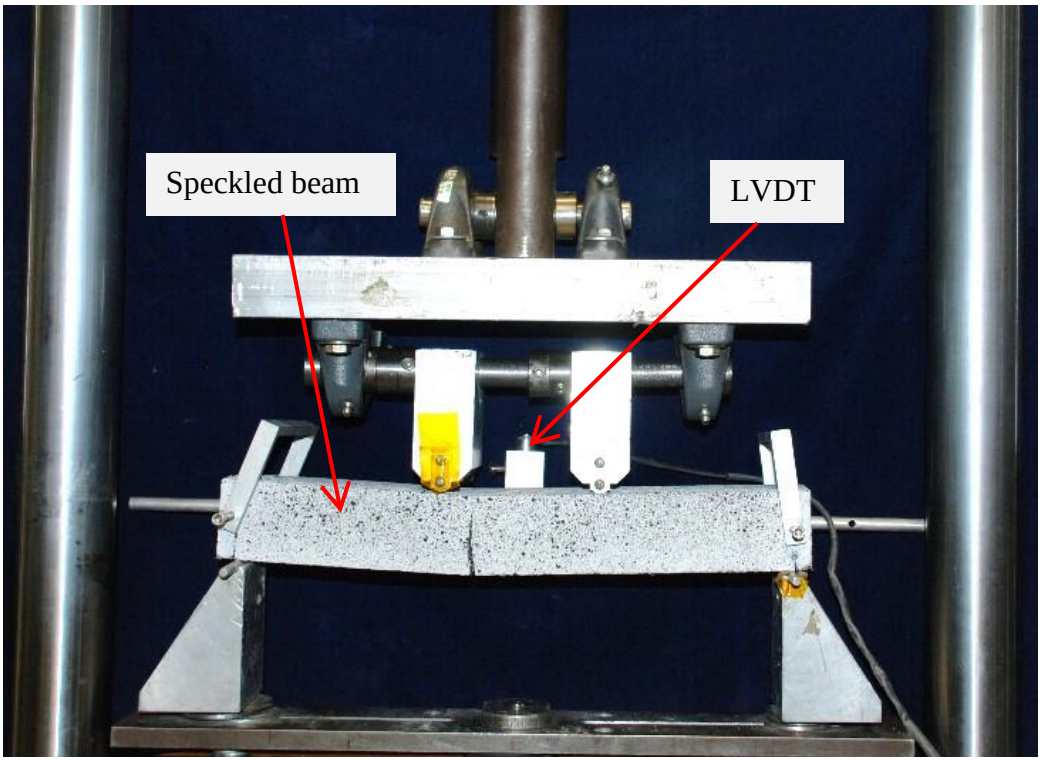

Figure 7. Experimental setup used for standard four-point bending tests on UHPC beams.

1.4 Introduction to Digital Image Correlation (DIC)

Traditional displacement measuring techniques such as Linear Variable Differential Transformer (LVDT) measure the deformation of a single point on the specimen. Digital Image Correlation (DIC) is a more advanced technique that can capture the entire displacement field at every point on the surface of the specimen. As a non-contact optical speckle-tracking measurement method, DIC obtains full-field surface deformations through consecutive post-processing of digital images taken at specific time intervals. This method has been widely applied for composites, fabrics, structural materials, etc. [29]–[31]. The principle and applications of DIC are well documented [29], [32], [33]. This method is superior to alternative strain measurement systems at an isolated spot or within a gage length by conventional devices such as LVDT,

extensometer, clip gage, or strain gages, since the latter result in single values and are insufficient to study the spatial variations or changes due to non-homogeneous deformations.

Application of DIC to specimens that undergo cracking provides a unique opportunity to keep track of the beam's deformations and crack growth during the test by measuring full field deformations and crack opening. In order to perform DIC, a speckle pattern is prepared on the specimen surface using flat paint to create a random texture that is non-periodic and with a clear contrast of gray levels as shown in Figure 8**.** A single camera can be used to obtain two-dimensional deformation pattern in the sample. For three-dimensional displacement measurements, multiple images are needed; hence two cameras from different angles are pointed toward the beam to capture the deformation. Post-processing of the data provides the three-dimensional (u, v, and w) displacements [34], [35].

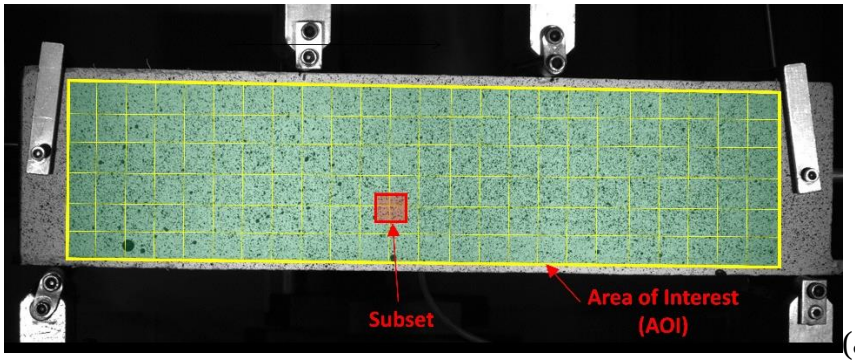

(a)

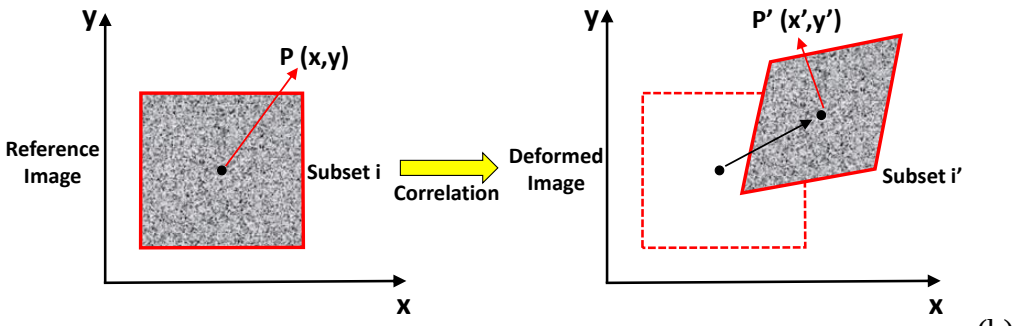

Figure 8. Basic principle for DIC method: (a) Illustration of the area of interest (AOI) and subset, (b) schematic presentation of a reference and deformed subset.

A CCD (Charged-Coupled Device) camera was used to record images every second. A commercial software, Vic-2D 2009, developed by Correlated Solutions Inc., was used to conduct image analysis [36]. As shown in Figure 8, post-processing of the data starts by manually specifying an area of interest (AOI) in the software. This area is divided by the software into an evenly spaced virtual grid. The displacements are computed at each point of the virtual grids $P(x, y)$ by tracking the movement of each point from the reference image (before deformation) to the images in the deformed state of the specimen $P'(x', y')$. The computation is based on the assumption of a certain window of deformation and the maximum likelihood of matching the intensity of the grid between the undeformed and deformed images. The cross-correlation function is a mathematical computation of the likelihood of displacement within the grid and is conducted by pattern matching of the grid speckles.

The red square in Figure 8(a) is defined as a subset (a set of pixels) and its grayscale distribution is used in the identification of a certain subset of deformed images. The tracking of the subset is conducted using selected correlation functions such as cross-correlation (CC) or normalized cross-correlation (NCC). Subsequently, the strain fields

can be derived by smoothing and differentiating the displacement fields. Figure 9 shows the speckled beam after cracking, at different loading stages. Figure 9(a) shows the initial stage of the deformation in the beam.

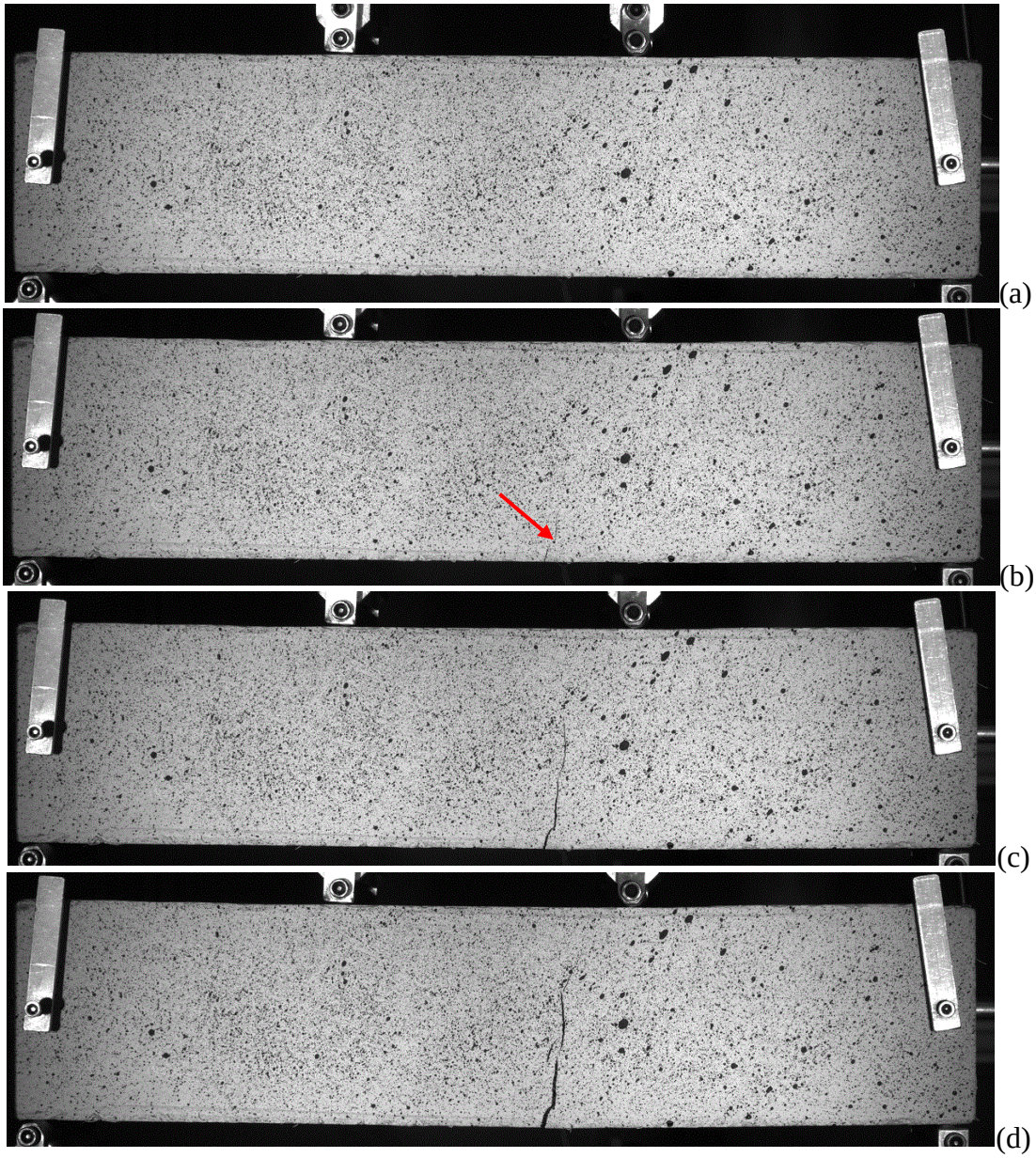

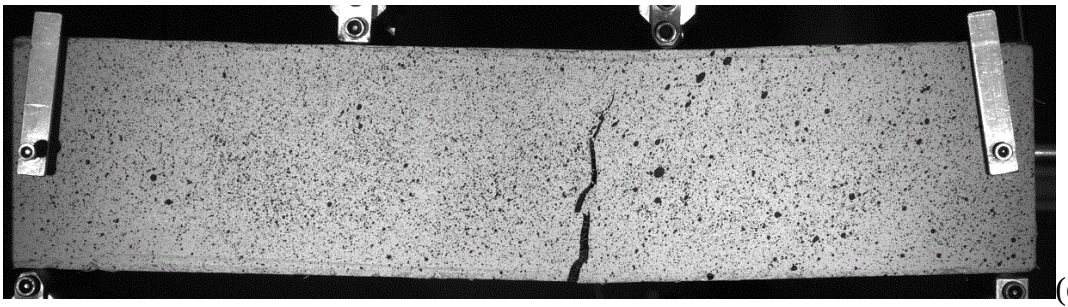 (e)

Figure 9. Speckled beam at different stages of testing.

1.5 Analysis of Plain UHPC and Effect of Fiber Reinforcement on the Flexural Response

Figure 10 compares the flexural response of a UHPC control specimen with a UHPC sample containing 1% steel fibers by volume (Vf = 1%). As shown in the figure, the unreinforced UHPC beam (Vf = 0%) behaves as a brittle material and the load-deflection response increases linearly up to a load of 799 lbs, which is equivalent to a mid-span deflection of 0.004 in. At this point, the failure is imminent as a crack forms in a sample which propagates to the full depth of the specimen. The brittle response is clearly shown in the figure and the entire load-carrying capacity is exhausted as a single crack propagates without any resistance from the matrix. This figure also shows the flexural response of the beam containing 1% fiber volume. Note that significant ductility is obtained with the addition of the fibers. This ductility enhancement can be studied at various stages of load-deformation response as discussed below:

1) The first cracking point in the fiber-reinforced specimen is identified by the initiation of nonlinearity in the ascending response and shown to be at higher loads as compared to the plain unreinforced UHPC. This

nonlinearity is related to the crack initiation and takes place prior to reaching the maximum load, with a distinct separation from the first cracking point. The nonlinear pre-peak zone corresponds to the stable growth of microcracks, which leads to the accumulation of damage at the peak load.

2) The peak load for the fiber-reinforced specimen (with 1% fiber volume) is 22% higher, compared to the unreinforced control specimen.

3) The post-peak response, however, is significantly dominant in the fiber reinforced specimen and the sample is able to carry a significant portion of the maximum load even beyond the peak.

Figure 10 (a) shows that the incorporation of 1% steel fibers has a beneficial effect on the flexural behavior and the post-peak response of the sample. While there is no post-peak response to the unreinforced specimen due to its brittle behavior, the fiber-reinforced specimens demonstrate a considerable non-linear response after the occurrence of the first crack.

The flexure testing was terminated at an ultimate mid-span deflection of 4 mm for the fiber-reinforced specimens. This value is nearly 40 times greater than the mid-span deflection at the first cracking point in the unreinforced UHPC beams. Additionally, the load carrying capacity at this level is as high as 60% of the peak load. This indicates that after reaching the peak load, the sample is capable of maintaining a large percent of load carrying capacity for a significant range of deformation. The peak load sustained by the

UHPC beams containing 1% fiber volume is about 976 pounds, 22% higher than the peak load of 799 pounds in the unreinforced UHPC beams.

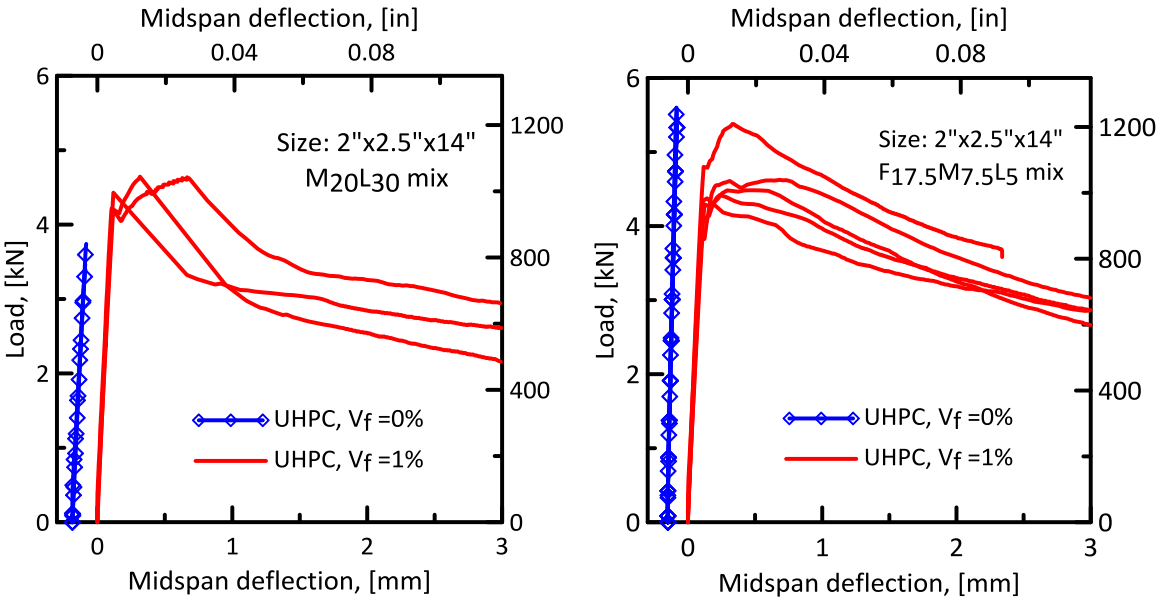

Figure 10. Fiber effect, with and without 1% fiber on: (a) ML; (b) FML samples.

Figure 10 (b) shows similar results for the effect of fibers on the mix FML. Post-cracking results due to the role of fibers are shown for samples with 1% fiber volume of FML samples and compared to the control samples containing no fiber. Similar results are obtained for specimens which show an improvement in a load-carrying capacity beyond the first cracking point as well as a strain softening region beyond the peak load.

1.6 Effect of Fiber Volume Percent on the Flexural Response of the UHPC Beams

The area under the load-deflection curve is used as a measure of energy absorption in terms of flexural toughness or the ductility of the material. The rapid loss of load-bearing capacity beyond the peak load in the unreinforced UHPC mixtures indicates

a brittle failure and minimal flexural toughness. In the case of the fiber-reinforced specimens, the energy absorption is significantly enhanced. The flexural toughness values are calculated in accordance with ASTM C 1609 at the mid-span deflections of L/600 (area under load-deflection curves from 0 to L/600) and L/150 (area under load-deflection curves from 0 to L/150), where L is the nominal span of the beam (in this case, for small beams, L=14 in).

Figure 11 shows the effect of the inclusion of 1% fiber volume on the toughness of the UHPC beams. The absorbed energy in the fiber-reinforced UHPCs is two to three orders of magnitude higher than that obtained for the unreinforced UHPCs at the peak load. Furthermore, there is no significant post-peak response for the unreinforced UHPC samples while the fiber-reinforced specimens show forty times higher toughness values at a mid-span deflection of L/150 than those of samples without fiber, in which the toughness was measured at the deflection corresponding to the cracking.

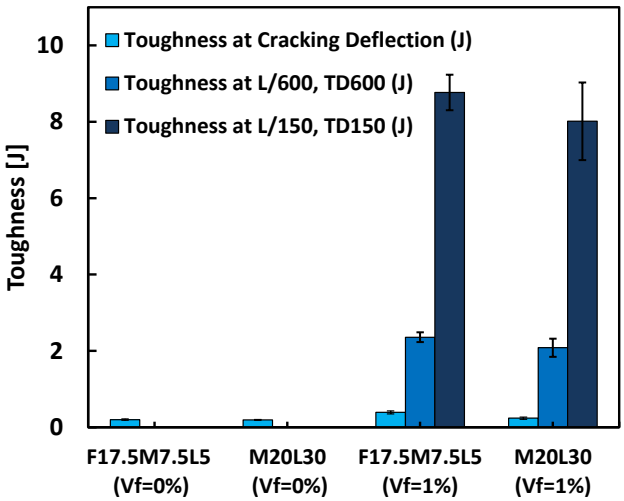

Figure 11. Comparison of toughness between FML and ML mixtures with and without fiber reinforcement (1% fiber volume).

Figure 12 shows the effect of fiber content on the flexural load-deflection response, comparing two samples with fiber volumes of 1% and 3%. The addition of fibers significantly improves the pre-peak response and doubles the flexural load-bearing capacity of the specimen. Post-peak response is also improved significantly by the increase in the volume percent of fibers.

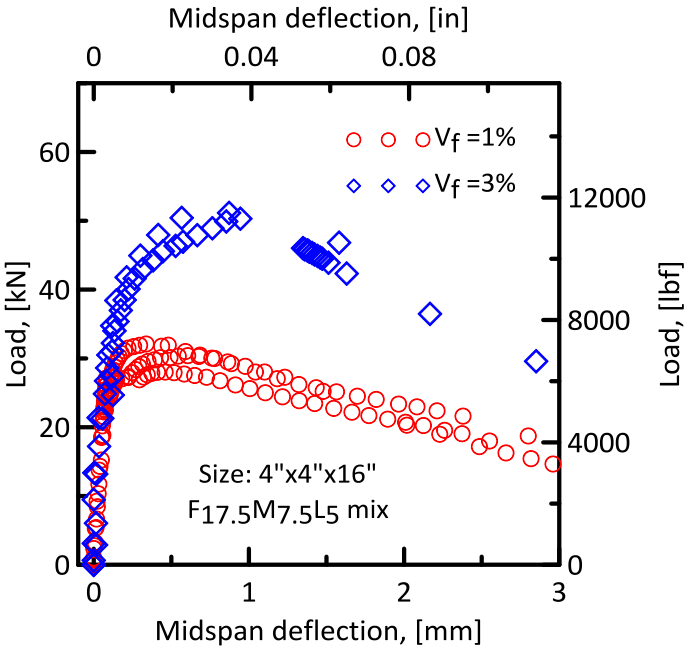

Figure 12. Effect of fiber volume percent on the load-deflection response of large beams after 28 days of curing.

Figure 13 shows the plot of equivalent flexural stress versus midspan deflection for the fiber-reinforced FML specimens. The elastic equivalent flexural stress can be defined as the nominal stress, calculated based on the assumptions of linear elasticity by dividing the load by the section modulus of the uncracked specimen, as shown in Eq (1).

Nominal flexural stresses as high as 3000 psi (20 MPa) are calculated for the specimen with 3% steel fibers.

$$\sigma_n = \frac{PL}{bd^2} \quad (1)$$

Here σ_n is the nominal elastically equivalent flexural stress, P is the load, L is the length of the beam, and b and d are the width and depth of the section.

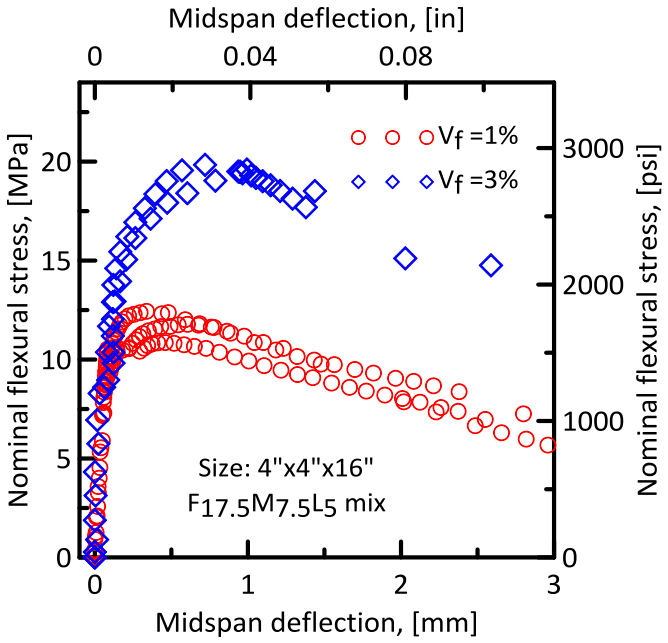

Figure 13. Effect of fiber volume percent on the nominal flexural response of the large beams after 28 days of curing.

Figure 14 compares the flexural strengths of the beams containing 1% and 3% fiber volume. Samples containing 3% fibers show significantly higher flexural strengths as well as higher residual strength in the post-peak region. The post-crack response greatly improves the toughness and is primarily a function of the fiber content in the mixture.

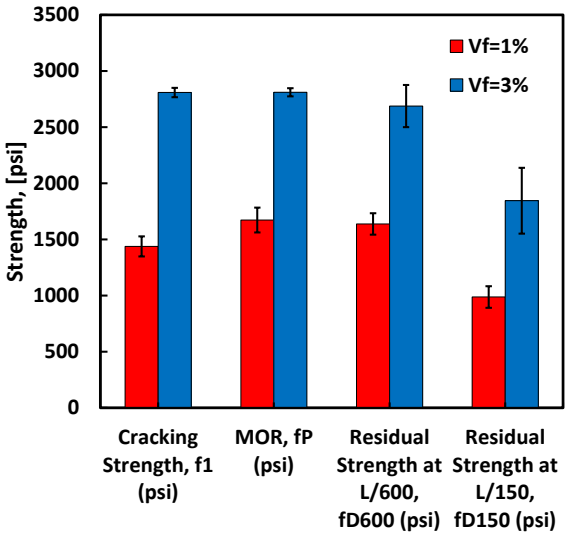

Figure 14. Effect of fiber volume percent on the flexural parameters of large beams, 4" x 4" x 16" (102 mm x 102 mm x 406 mm), after 28 days of moist curing (FML mixture).

1.7 Effect of Binder Composition

The influence of binder composition on the flexural response is shown in Figure 15. This figure shows a comparison of the strength values for the FML and ML mixtures. The FML mixture shows better flexural behavior (Figure 15a) and higher flexural strength (Figure 15b) than the ML mixtures. The post-peak response of this mixture also shows a higher residual strength than the ML mixture. This improvement is attributed to the improved interaction between the matrix and fibers in the FML mixture. Because of this, the FML mixture was chosen for the remaining tests, as shown in Table 7-1. The remaining experiments are conducted using the FML mixture, to address the effect of different sizes and curing periods (14 and 28 days). The following sections present the key conclusions only.

Post-cracking parameters are also calculated. Parameters such as load capacity, residual strength, and toughness are computed at two deflection limits of L/600 and L/150, where L is the span of the beam.

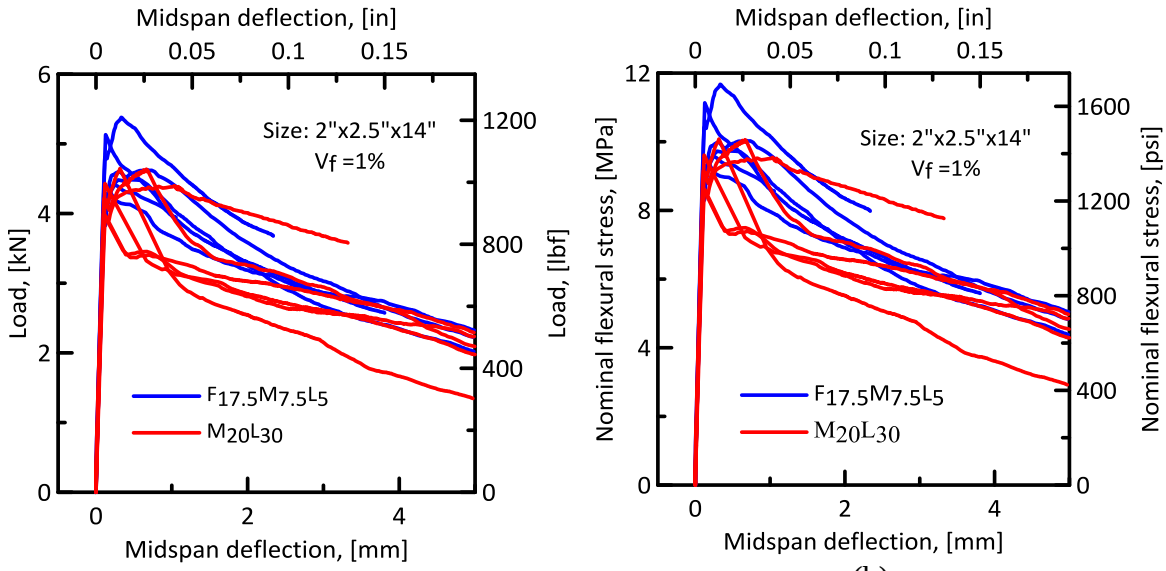

(a) (b)

Figure 15. Effect of mixture design on the flexure response for the small beams (2" x 2.5" x 14") with 1% fiber volume: (a) Load-deflection; (b) Nominal stress-deflection.

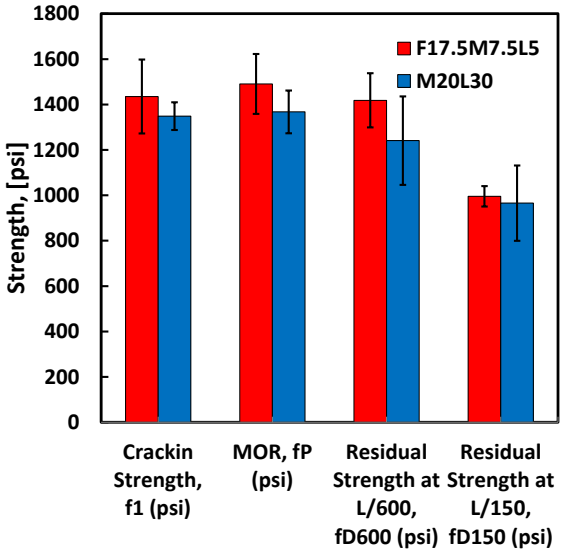

Figure 16. Strength parameters for the tested beams for FML and ML mixtures (the error bars correspond to one standard deviation from the mean, calculated for a total of six replicate samples).

1.8 Effect of Mixing Method

In addition to the hand mixing, the high shear mixer was also used as another method of mixing. Two batches of samples were prepared and mixed with Croker Mixer, which is sown in Figure 17.

Figure 17. Mixing material with Croker Mixer.

Figure 18 shows the effect of mixing method on the flexural response of the FML mixtures incorporating 1% fibers. The two mixing methods are i) a drill mixer, and ii) a high-volume, high-shear Croker mixer. The load-deflection results show that the mixtures cast using the high-volume, high-shear mixer are stronger in flexure and have a higher residual flexural strength than those cast using the hand-drill mixer. This can be attributed to the better mixing, dispersion, and uniform fiber distribution obtained using the high-shear mixer (also see Figure 19).

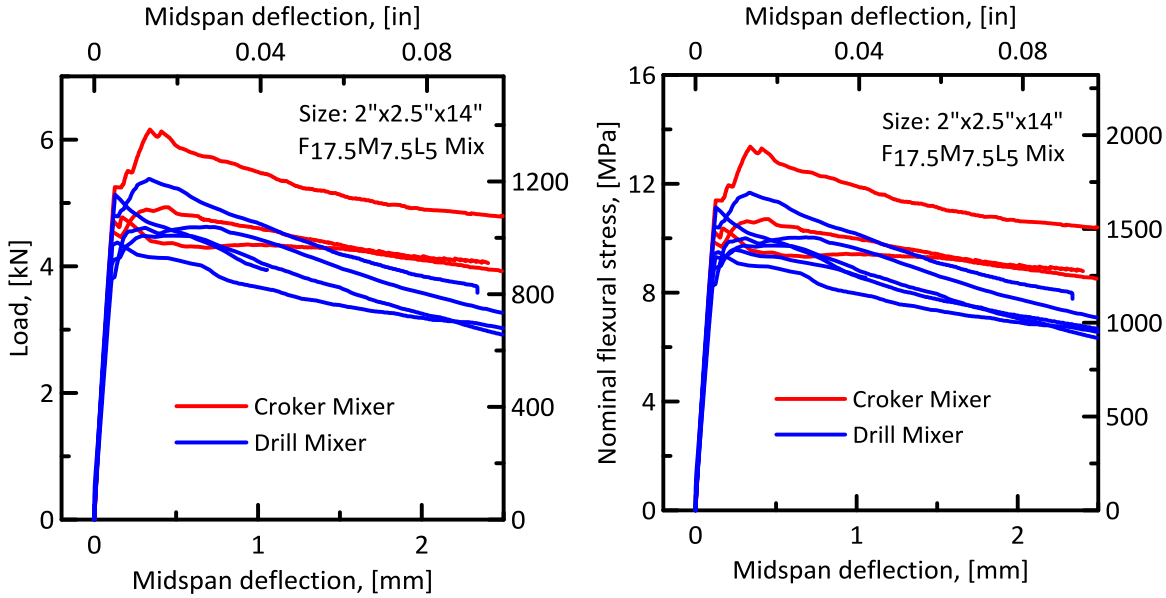

Figure 18. Effect of mixing method.

The comparative analysis of the flexural results for hand-drill and high-shear mixers is shown in Figure 19. Beams made using the high-shear mixer have about 12% higher flexural strength, at different stages of loading, than those made with the hand-

drill mixer. The improved performance using the high-shear mixer is due to the uniform dispersion of powders and fibers in the mixture.

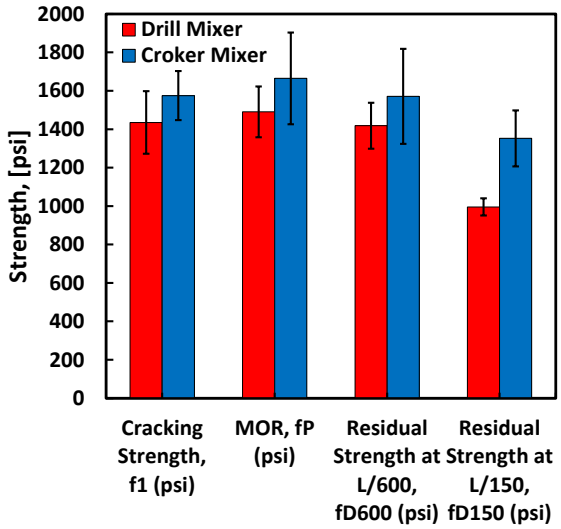

Figure 19. Comparison of flexural strengths obtained via drill mixer and high-shear (Crocker) mixer for small beams with 1% fiber content after 28-day curing period.

1.9 Effect of Specimen Size

Figure 20 compares the effect of specimen size, measured by the load-deflection curves and flexural stress-deflection curves for the small, 2"x 2.5" x 14" and large, 4" x 4" x 16" beams. The figure shows that there is no significant difference in first-cracking stress, maximum stress, and residual strength between small and large specimens. However, the strain is higher for the large beams and shows more smooth post-peak response than for the small beams. This may be due to the greater depth of the large specimens, which promote better crack growth, than of the smaller beams that are only 2" deep. This results in a higher bending and deformation capacity for the larger beams. It is

also observed that the small beams show a higher maximum stress, about 5% than to the large beams.

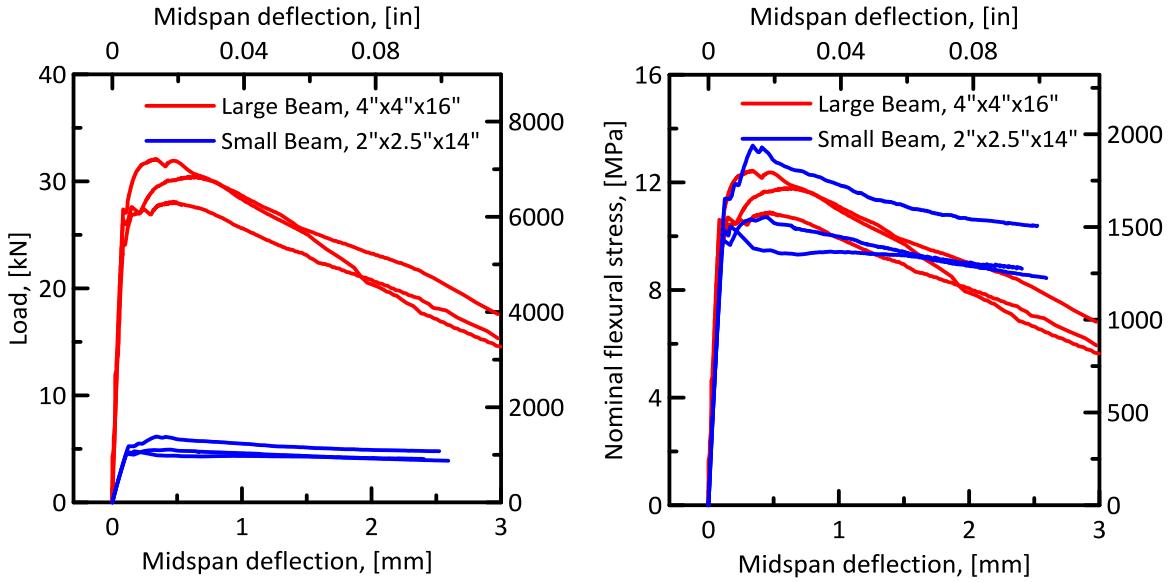

Figure 20. Size effect (2x2.5x14in beams vs. 4x4x16in beams).

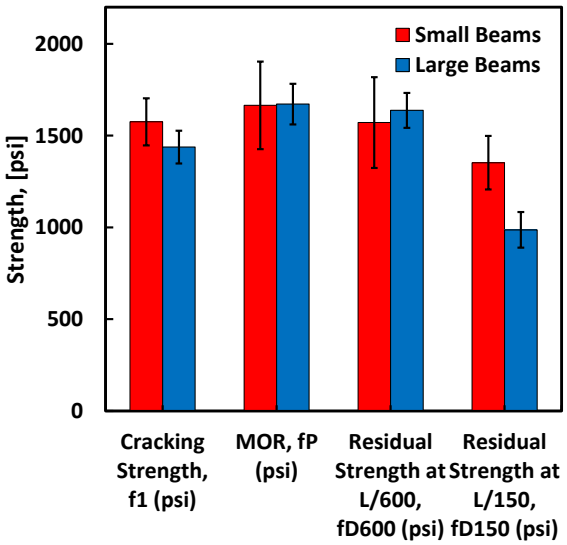

Figure 21. Size effect: (a) small beams, 2”x 2.5” x 14” (51 mm x 64 mm x 356 mm); (b) large beams, 4” x 4” x 16” (152 mm x 152 mm x 406 mm); $F_{17.5}M_{7.5}L_5$ mixes after 28 days.

1.10 Effect of Curing Duration

Figure 22 compares the effect of curing period on the load-deflection response of the small beams after 14 and 28 days of curing. The strength of the small beams was almost 43% higher after 28 days than after 14 days of curing. A similar ratio is maintained for the residual strength of small beams, which is 47% higher after 28 days than after 14 days of curing.

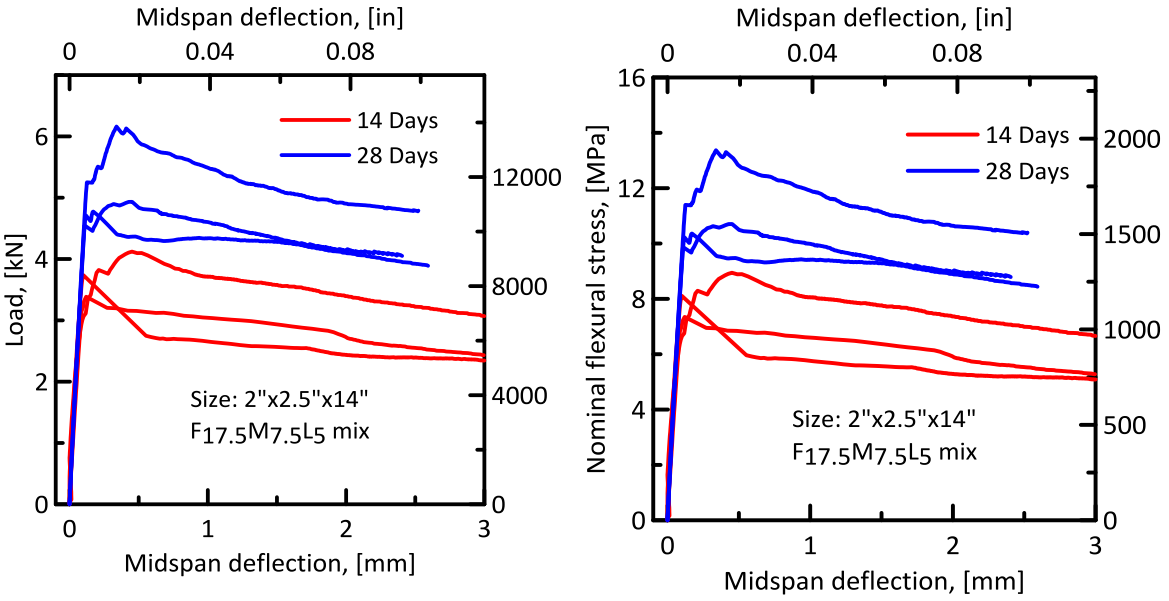

Figure 22. Effect of moist curing on the load-deflection response of the small beams, 2”x 2.5” x 14” (51 mm x 64 mm x 356 mm).

Figure 23 shows the same trend of strength increase due to curing of the large beams. However, the increase in strength is lower than for the small beams.

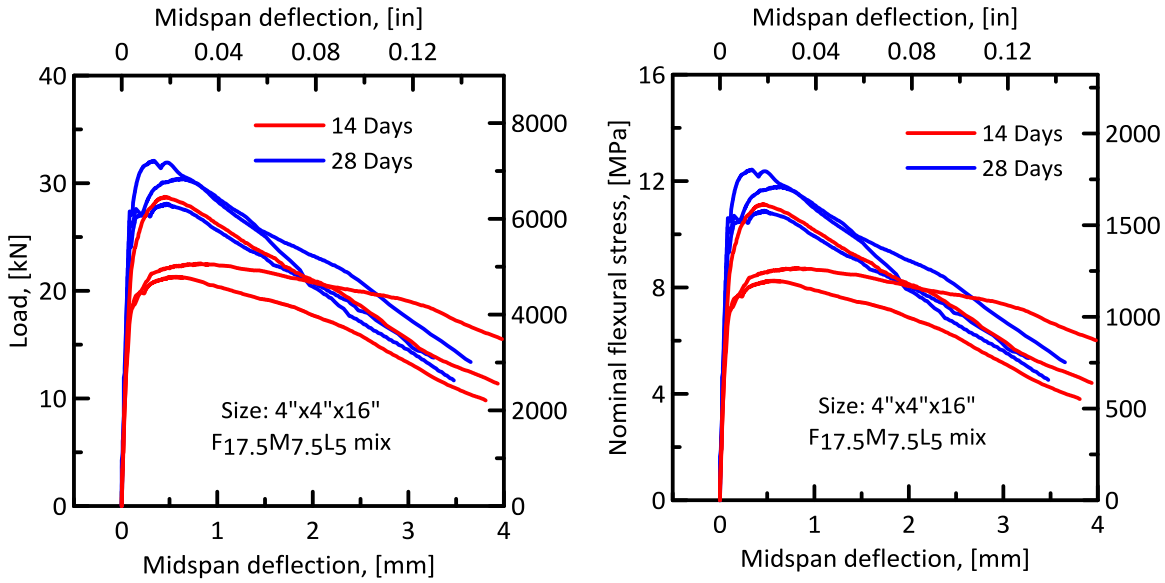

Figure 23. Effect of moist curing on the load-deflection response of the large beams, 4” x 4” x 16” (152 mm x 152 mm x 406 mm).

Figure 24 (a) shows a comparative graph of the effect of the curing duration on the small beams with 1% fibers. Beams cured for 28 days have a 50% higher flexural strength than those cured for only 14 days. This increase is observed at all stages of the loading process. Figure 24 (b) shows a bar chart of the effect of curing duration on the large beams with 1% fiber content. After 28 days of curing, the beams show as much as 30% higher strength than after 14 days.

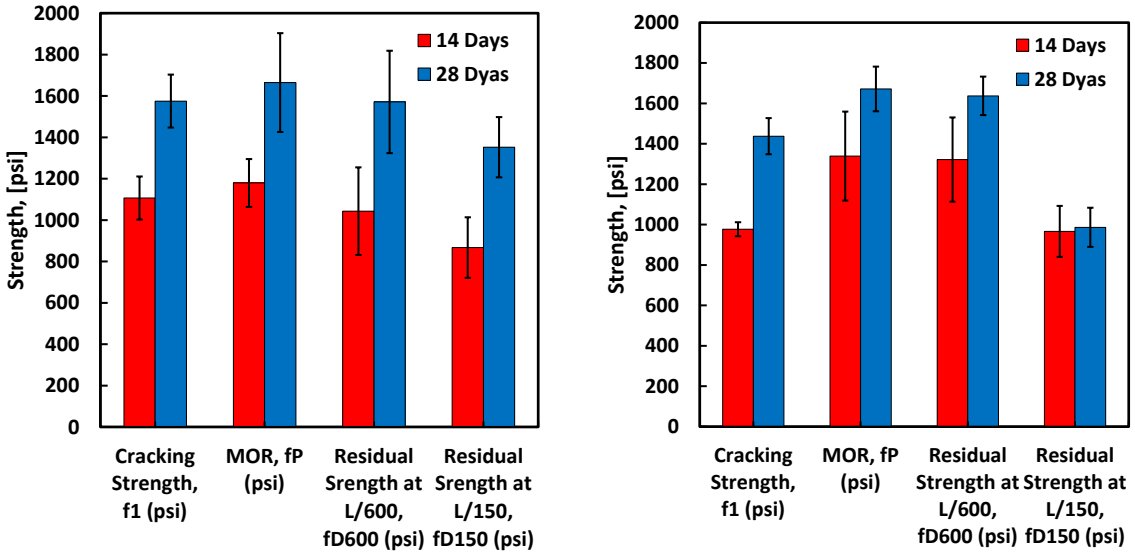

Figure 24. Effect of curing duration on the strength parameters of: (a) small beams, 2"x 2.5" x 14"; (b) large beams, 4" x 4" x 16" (152 mm x 152 mm x 406 mm), with 1% fiber content.

As a summary, a list of average values for each set of experimental tests is presented in Table 4. The last column of Table 7-4 shows that, in almost all of the fiber-reinforced beams, at least 80% of the maximum bending strength is maintained until the equivalent deflection of L/150.

Table 4. Average of experimental parameters for each set of tests according to ASTM C1609.

Test Set	Beam Series	No. of Replicates	First Peak Deflection, δ_1 (in)	First Peak Load, P1 (lb)	First Peak Strength, f1 (psi)	Deflection at Maximum Load, δ_p (in)	Peak Load, Pp (lb)	MOR, fP (psi)	Load at L/600, PD600 (lb)	Residual Strength at L/600, fD600 (psi)	Toughness at L/600, TD600 (in-lb)	Load at L/150, PD150 (lb)	Residual Strength at L/150, fD150 (psi)	Toughness at L/150, TD150 (in-lb)	Equivalent Flexural Strength at L/150, Re_3 (%)
1	ML_S_0_28_4PB_D	3	0.004 (0.0001)	799.7 (39.4)	1163.0 (57.3)	0.004 (0.0001)	799.7 (39.4)	1119.6 (55.2)	0.0	0.0	0.0	0.0	0.0	0.0	0.0
2	ML_S_1_28_4PB_D	6	0.004 (0.0003)	927.6 (41.9)	1349.0 (60.9)	0.015 (0.02)	976.9 (67.3)	1367.7 (94.2)	886.5 (139.2)	1241.2 (194.9)	17.0 (3.9)	689.7 (118.7)	965.5 (166.1)	70.1 (9.9)	75.9 (10.0)
3	FML_S_0_28_4PB_D	6	0.003 (0.0001)	1138.9 (104.6)	1656.2 (152.1)	0.003 (0.0001)	1138.9 (104.6)	1594.5 (146.4)	0.0	0.0	0.0	0.0	0.0	0.0	0.0
4	FML_S_1_28_4PB_D	6	0.005 (0.0001)	986.9 (112.1)	1435.2 (163.0)	0.013 (0.0001)	1064.6 (94.2)	1490.4 (131.9)	1013.2 (85.5)	1418.5 (119.6)	20.9 (1.1)	711.2 (32.2)	995.7 (45.0)	77.6 (4.1)	82.6 (2.4)
5	FML_S_1_14_4PB_C	3	0.004 (0.0001)	761.1 (71.9)	1106.8 (104.5)	0.009 (0.0001)	842.6 (82.7)	1179.6 (115.8)	745.2 (151.3)	1043.2 (211.9)	15.8 (1.7)	619.3 (104.5)	867.0 (146.3)	63.1 (9.6)	80.2 (8.4)
6	FML_S_1_28_4PB_C	3	0.005 (0.0001)	1083.2 (88.1)	1575.1 (128.0)	0.013 (0.006)	1189.1 (170.7)	1664.8 (238.9)	1122.4 (176.6)	1571.4 (247.3)	22.0 (2.4)	966.0 (104.2)	1352.4 (145.8)	94.4 (11.1)	85.3 (2.2)
7	FML_L_3_28_4PB_C	3	0.032 (0.006)	11410.2 (166.9)	2807.6 (41.1)	0.034 (0.003)	11417.2 (145.5)	2809.7 (35.8)	10920.1 (764.1)	2687.4 (188.0)	187.7 (52.8)	7493.3 (1191.3)	1844.1 (293.2)	1032.7 (11.3)	86.1 (1.2)
8	FML_L_1_14_4PB_C	3	0.003 (0.0001)	3971.6 (141.7)	977.3 (34.9)	0.024 (0.007)	5441.1 (894.9)	1339.0 (220.2)	5371.3 (847.9)	1321.8 (208.7)	117.3 (17.2)	3926.6 (511.8)	966.3 (126.0)	492.2 (57.5)	86.6 (4.9)
9	FML_L_1_28_4PB_C	3	0.003 (0.0001)	5842.5 (363.2)	1437.6 (89.4)	0.019 (0.006)	6793.2 (450.1)	1671.8 (110.8)	6653.5 (386.0)	1637.4 (95.0)	149.3 (9.2)	4008.9 (392.9)	986.6 (96.7)	575.1 (28.2)	80.7 (3.9)

* Numbers in the parenthesis refer to the standard deviations (±stdv).

1.11 Characterization of Crack Growth Mechanisms Using Digital Image Correlation (DIC)

The objectives of this section are to address the mechanisms of crack formation and propagation as well as of multiple crack formation and crack opening. Using DIC method the access to a full-field deformation is provided. However, these captured movements inherently, reflect not only the movement of the beam itself but also the movement due to the leaping in the fixtures, supports, testing machine deformations, etc. To eliminate the effect of these type of deformations and calculating the original movement in the beam itself there are some methods which are briefly discussed here.

One of the algorithms which can be used is called rigid body filter. This method calculates the average movement of the total area of interest (AOI) and then subtract the movement at a specific point inside the AOI from the average to achieve the relative movement of that point. The theory behind this approach is the assumption that the average movement of the AOI is an index of rigid body movement due to the support movement, leaping in the fixtures, machine deformations and so forth. Another approach is to consider one point as the reference point and then calculate the deformations at the specific points, by subtracting their movement from the reference point. The weak point of one reference point is that it cannot capture the rotation of the sample. However, it is still possible to increase the number of reference points to have a more accurate rigid body motion including displacements and rotations. Therefore, a full field view from all over the sample during the tests and DIC procedure is highly recommended to have the best options for choosing as the reference points.

In this section, the three-point rigid body is chosen as the rigid-body movement algorithm to eliminate the rigid-body movement of the sample during the DIC procedure. These three points are chosen in a way to be as close as possible to the neutral axis at the supports (see Figure 25). It is suggested that these three points be chosen from both side of the sample (i.e. support locations) to be able to capture the rotation of the sample due to the unequal vertical movement at the supports. By taking this course of action, there will be three points which will move such that they are located on a rigid surface, without any relative movement to each other. However, the movement for other points on the AOI can be captured and subtracted from this rigid body movement to have an accurate deformation for the sample.

It is to mention that the selection of the points completely depends on the sample geometry, supports (boundary conditions) and the parameters which are to be calculated. For example, if the movement along the axis is to be captured, it would be better to choose the reference points from one side of the sample. However, this is only affecting the results of the movements and deformations but not strains. The strain is independent of rigid movement.

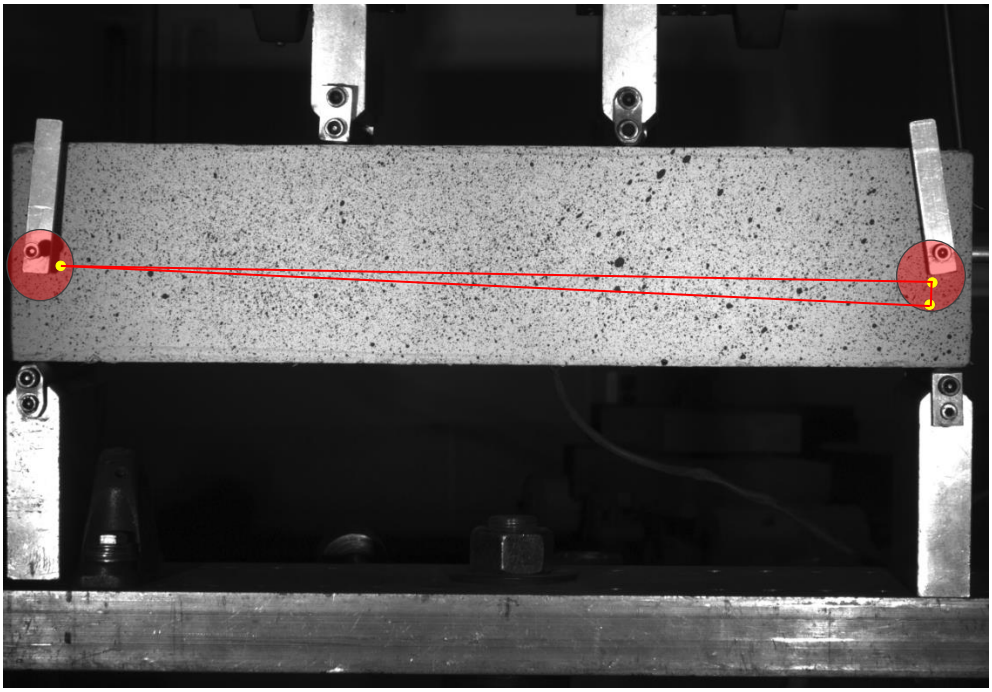

Figure 25. Three-point reference for rigid body movement of the sample.

The objectives of this section are to address the mechanisms of crack formation and propagation as well as of multiple crack formation and crack opening. This section presents experimental results for one small beam with 1% fiber and two large beams with 1% and 3% fiber. All samples are tested after 28 days of curing.

One of the first benchmarks of these experiments was to validate the two measurements of sample deflection at the loading point. By comparing the measurements using DIC and LVDT-based instrumentation, the accuracy of the two methods is checked against one another. In addition, the researchers chose up to four stages of deformation (designated A through D) that correspond to critical stages of loading. Each stage is listed in Table 5.

Table 5. Different stages of data analysis using DIC method.

Stage	Characteristic
A	Initiation of the deformation
B	Initiation of the non-linear response
C	Response to the peak load
D	End of the DIC data analysis (beam failure)

Figure 26 shows that during the loading process stable crack forms and propagates throughout the depth of a small beam with 1 percent fiber content after 28 days of curing period. These results are only possible in the case of fiber reinforced UHPC since it is not possible to control the rate of crack growth in plain UHPC. Addition of fibers stabilizes the crack growth and allows for incremental measurement of crack extension. Stages A and B show a uniform loading in the sample. Cracks are not observable at stages A and B (representing nominal tensile stress level of 290 and 900 psi) when the load reaches stage C (tensile stress of 970 psi) we observe two cracks forming which the crack on the left dominates the response and additional load causes it to grow significantly. At level D only a main crack is operational and a second crack in the process of forming.

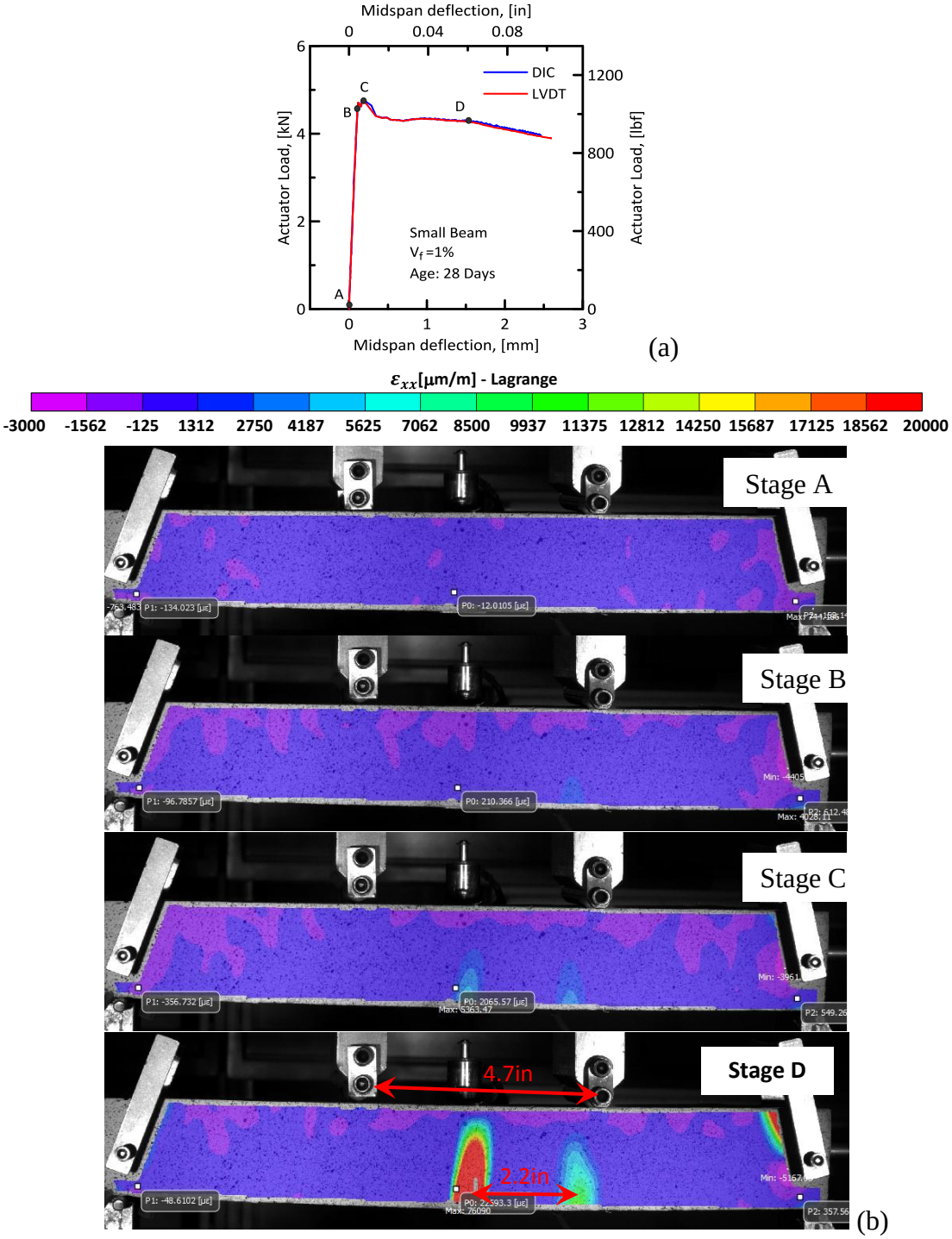

Figure 26. Small beam with 1% fiber, after 28 days of curing: (a) Load-deflection curves, the comparison between DIC results and LVDT results; (b) DIC results at different stages of the test.

For the large and small beams with 1 percent, fiber content at least two cracks occurred in the tension fiber. As the load increases, one of the cracks becomes dominant and the other one will be closed, due to the stress redistribution after crack growth. As the figure demonstrates, the cracking length is about 50 percent of the loading distance. The same trend was observed in the other small beams with 1 percent fiber content. For the large beams, this value is about 70 percent of the loading distance.

Stresses and strains along the section depth for each one of the four stages have been calculated (with the back-calculation process) and are shown in Figure 27. This figure shows that, as the moment increases, the neutral axis moves toward the compressive part of the section. Furthermore, the stress diagram shows that the compressive part remains in the linear response region. This was also observed in other beams and shows that our assumption, in the simplified solution, that the compressive part of the FRC-UHPC section does not fail is acceptable. On the other hand, a stress softening behavior, due to the low (1 percent) fiber content, is detected. At the same time, a comparison with the model shows that the crack has extended as much as 1.7 inches (44 millimeters), or about 84 percent of the beam depth, and the nature of stress distribution over the cracked zone is dominated by the flexural cracking. Comparison of the stresses and the applied moments match, since for the applied bending moment at point D this is equivalent to 2,255 pound-inches, a moment equal to 2,341 pound-inches in accordance with the stress distribution was obtained as well.

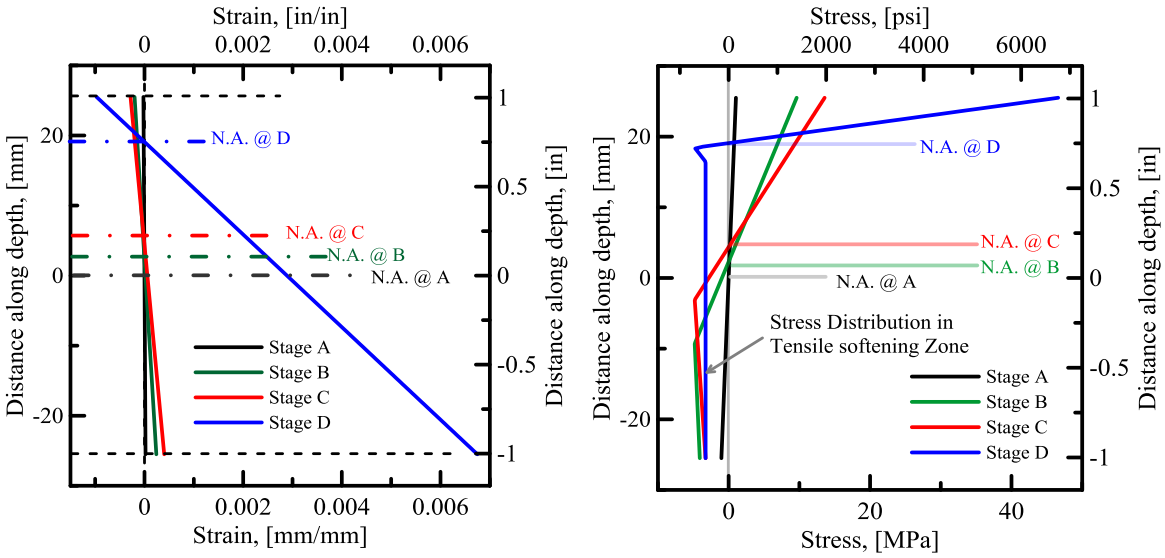

Figure 27. (a) Strain and (b) stress along the section depth, for a small beam with 1% fiber, after 28 days of curing (FML_S_1_28_4PB_C_B3).

A comparison between the results from LVDT and DIC for the large beams with 1 percent fiber (Figure 28) shows good agreement between the results from both methods. As in small beams, two cracks form in the large beams with 1 percent fiber. At stage C, which corresponds to the maximum load, the crack has grown as much as 3.35 inches (85 millimeters), or 84 percent of the height of the beam. While the load increases, one of the cracks becomes dominant and the other will be closed. The cracking length is about 70 percent of the loading distance. At stage D, the main crack is still visible and is opening significantly. There is a significant degree of unloading, as evidenced by the smaller secondary crack.

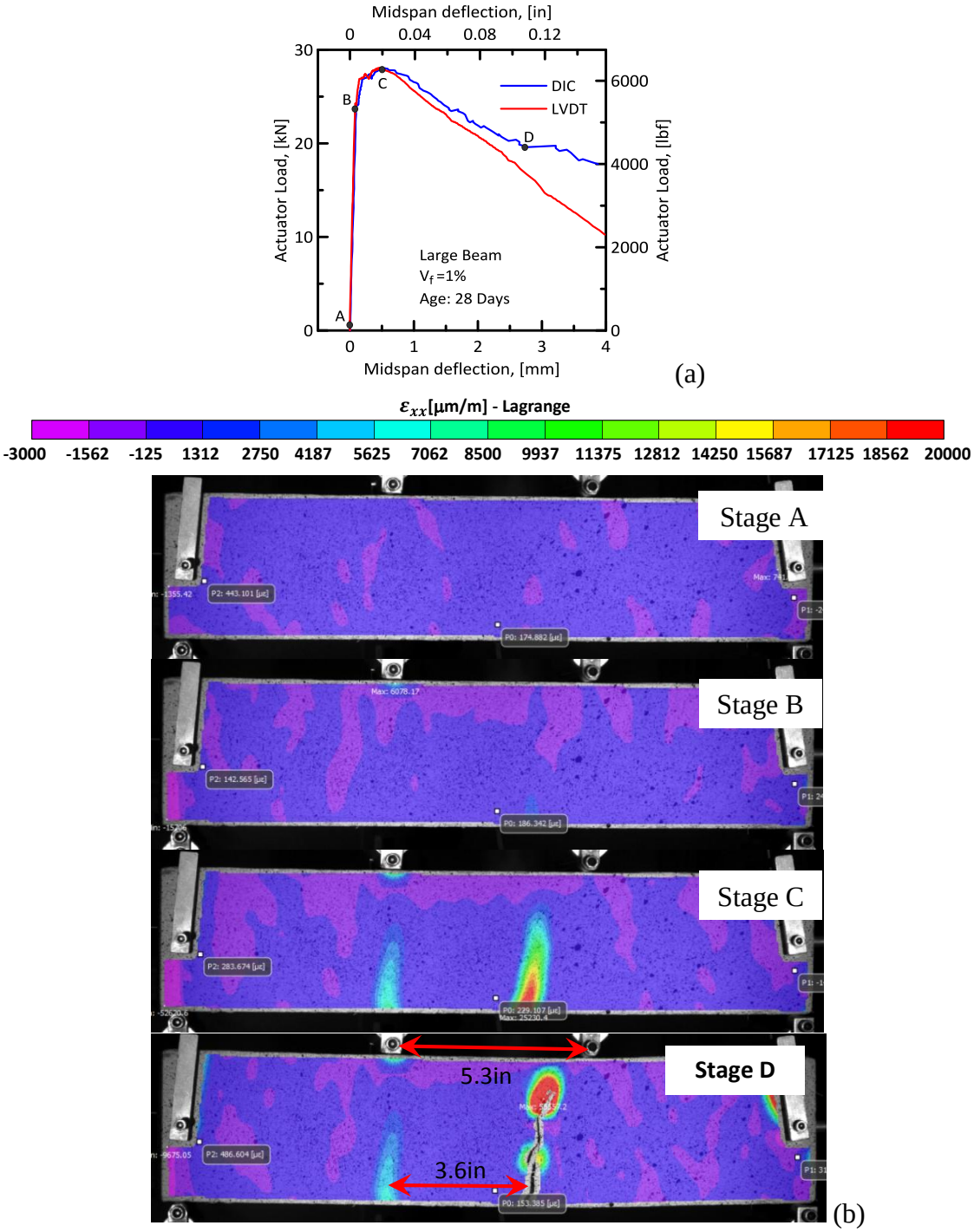

Figure 28. Large beam with 1% fiber, after 28 days of curing: (a) Load-deflection curves, the comparison between DIC results and LVDT results; (b) DIC results at different stages of the test.

Figure 29 shows the stresses and strains along the section depth for each one of the four stages obtained from the back-calculation process. As the moment increases, the neutral axis moves toward the compressive part of the section. At stage D, before failure, only 8 percent of the section is under compression and the rest is under tension. It can be seen from the stress diagram that the compressive part remains in the linear response region. This was also observed in other beams. Due to the low fiber content, a stress softening behavior is detected in the tensile zone. A comparison between Figure 27 and Figure 29 shows that as the beam size increases, the deformation capacity increases considerably. Strain levels for the large beam, at different stages, are much higher than for the small beam.

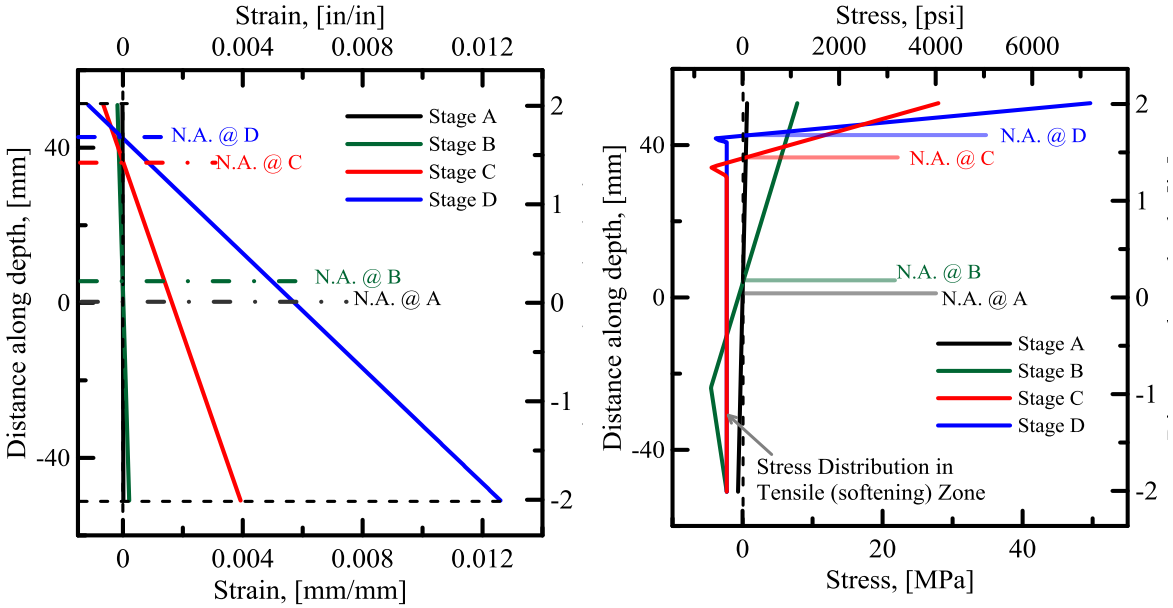

Figure 29. (a) Strain and (b) stress along the section depth, for a large beam with 1% fiber, after 28 days of curing (FML_L_1_28_4PB_C_B2).

The results for one of the large beams with 3 percent fiber content, after 28 days of the curing period, are presented in Figure 30. DIC contours show a distributed cracked rejoin which is about 90 percent of the loading distance. The same cracking trend, a distributed cracked rejoin with at least three major cracks, was monitored for all of the beams with 3 percent fiber content. Like the beams with 1 percent fiber, one of the cracks becomes the major crack and the rest are closed as the load increases. On the other hand, as the fiber content increases, the distance between the major cracks decreases. The major crack's distance in the large beams with 1 percent fiber content is about 4 inches, while this parameter in the beams with 3 percent fiber content is about 2 inches, which represents a 50 percent decrease. This shows that there is a more distributed cracking pattern in the samples with higher fiber content and higher energy dissipation.

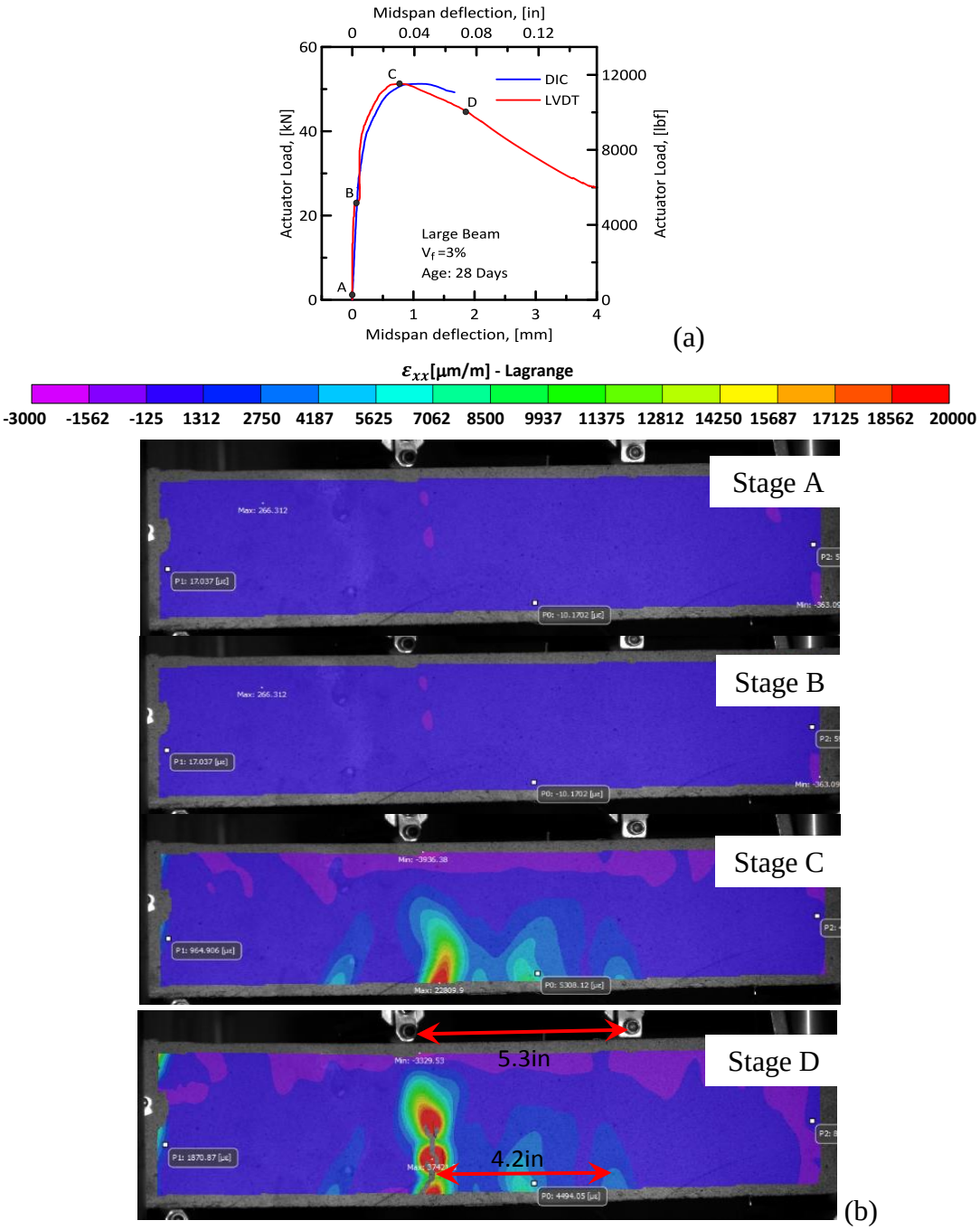

Figure 30. Large beam with 3% fiber, after 28 days of curing: (a) Load-deflection curves, the comparison between DIC results and LVDT results; (b) DIC results at different stages of the test.

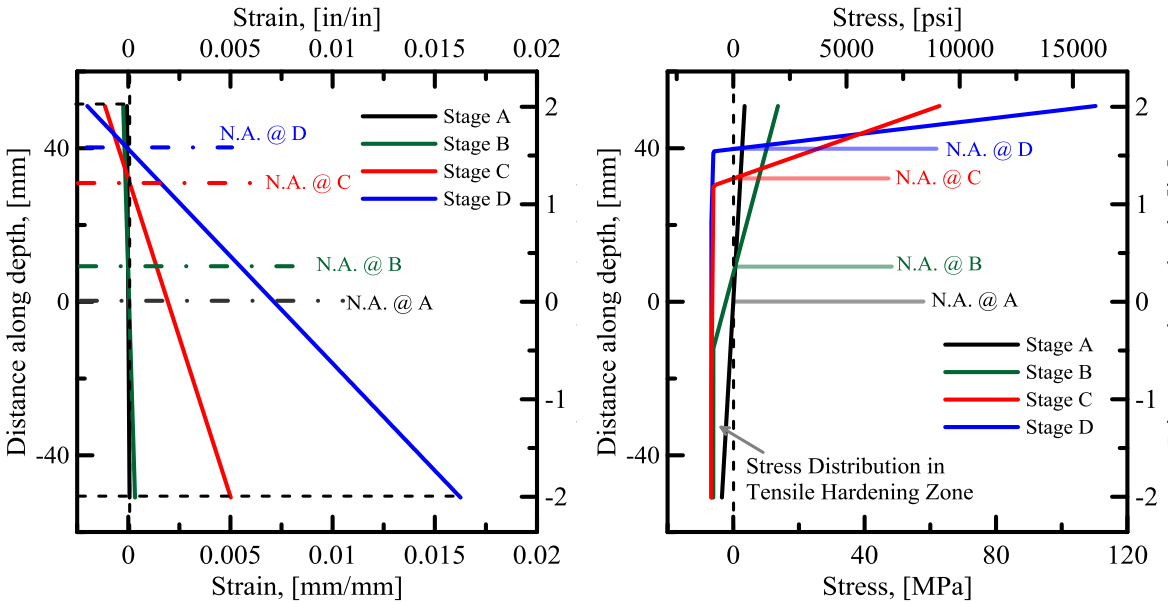

Figure 31. (a) Strain and (b) stress along the section depth, for a large beam with 3% fiber, after 28 days of curing (FML_L_3_28_4PB_C_B2).

Figure 31 shows the stresses and strains along the section depth for each one of the four stages obtained from the back-calculation process for the large beams containing 3 percent fiber content. As the applied moment on the beam increases, the flexural crack extends upwards and neutral axis moves toward the compressive part of the section. The portion of the area carrying compression force is about 14 percent of the gross section area, which is 6 percent greater than that in the same section with lower fiber content. This is because as the fiber volume fraction increases, the crack growth is arrested by the fibers and less of the section enters the tensile phase of the response. In spite of the beam with 1 percent fiber content, for this set of beams, a strain-hardening type of response is observed. For this type of the response, a perfectly plastic stress-strain diagram can be assigned to the material. Compressive failure was observed in none of the beams and the material remained in the linear-elastic region during the loading process.

1.12 Fracture Tests (Cyclic)

One of the areas of improvement in UHPC as compared to plain concrete is its exceptional response to repeated cyclic loading such as earthquake loads as well as fatigue loading. This is especially in the reverse cyclic and tension loading-unloading cycles. A detailed literature search of the fatigue studies conducted on UHPC has been presented by Abbas et al. (Abbas et al., 2016). A fatigue test helps determine a material's ability to withstand cyclic loading conditions. By design, a material is selected to meet or exceed service loads that are anticipated in fatigue testing applications. Cyclic fatigue tests produce repeated loading and unloading in tension, compression, bending, torsion, or combinations of these stresses. Additional papers for discussion in the fatigue test results can be found in the literature [13], [37].

Graybeal and Hartmann [38] conducted flexural fatigue tests on 2-inch (51-mm)-square beams. In one set of tests, uncracked specimens are loaded to produce different stress ranges. Most specimens survived more than 6 million cycles of loading. In the second series of tests, the specimens are pre-cracked and then tested for fatigue with loads cycling from 10 to 60 percent of the cracking load. One specimen failed after 9,950 cycles, while the other failed after 129,700 cycles. In these tests, some of the steel fiber reinforcement was observed to have fractured rather than pulling out of the UHPC matrix.

Behloul et al. (2005) [39] conducted flexural fatigue tests on 4- by 4- by 16-inch (100- by 100- by 400-mm) prisms made of two different UHPC formulations. Prior to fatigue loading, the specimens are loaded to produce a crack opening of 0.012 inches (0.3

mm). The specimens are then cycled at 5 Hz between 10 and 90 percent of the first cracking strength. After 1 million cycles, the specimens are loaded statically, and the results are compared with specimens not subjected to fatigue loading. The fatigue loading appeared to have no effect on the overall mechanical behavior.

Herein the results of the cyclic tests on the large notched beams, 4” x 4” x 16” (152 mm x 152 mm x 406 mm), are presented. Fracture cyclic tests are conducted using a closed loop, servo-hydraulic MTS test frame, and cyclic three-point bending (3PB) procedure. The beams are loaded along the notch to monitor crack growth, as shown in Figure 32. An Instron clip-on gage type extensometer was used to measure the crack mouth opening displacement (CMOD). A Linear Variable Differential Transformer (LVDT) with a range of ±4 mm was used to measure the deflection of the midspan. Initially, the testing procedure was controlled monotonically under load control to apply load on the specimen equivalent to about 10% of the peak load. The feedback control was then switched to CMOD control at a constant rate of 0.004 in/min up to the peak load. The first unloading cycle started at the peak load and the specimen was unloaded to about 1% of the peak load, under load control. Cycles of loading-unloading are then applied under CMOD and load control until 10 such loading-unloading cycles are completed at 1.2 mm of crack opening. A schematic side view of the test setup is presented in Figure 33. Three beams are tested and the results are shown in Figure 34 to Figure 36.

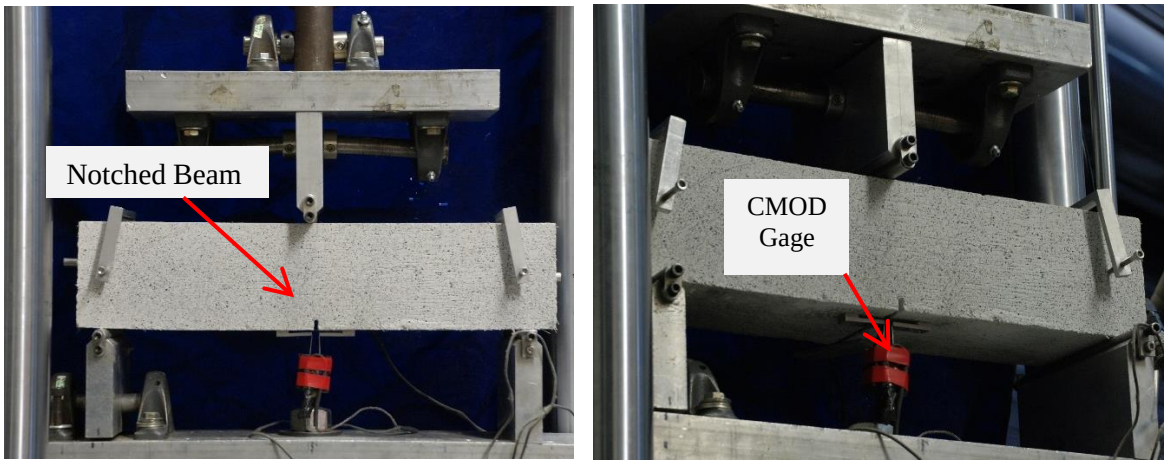

Figure 32. Fracture test setup.

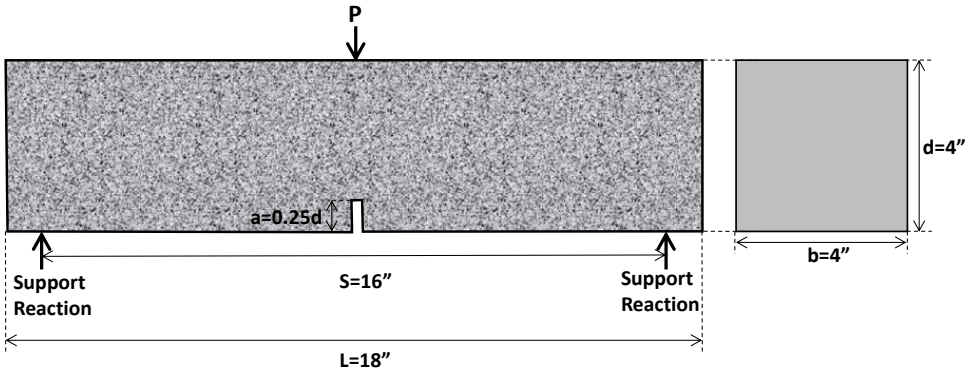

Figure 33. Schematic side view of the 3PB test setup and the beam dimension.

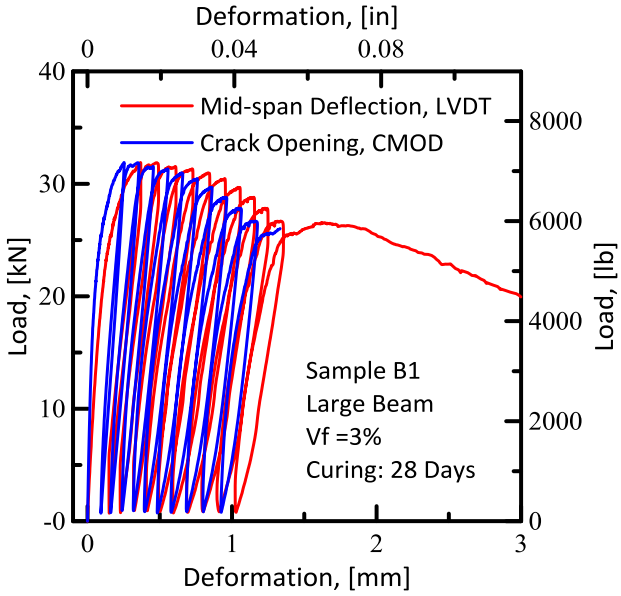

Figure 34. Cyclic test results: (a) Mid-span deflection against load; (b) CMOD against the load, for the large beams with 3% fiber content after 28 days of curing.

Figure 35 represents load against midspan deflection and crack opening. These plots are obtained after ten cycles of loading and unloading of another beam under 3PB-fracture tests.

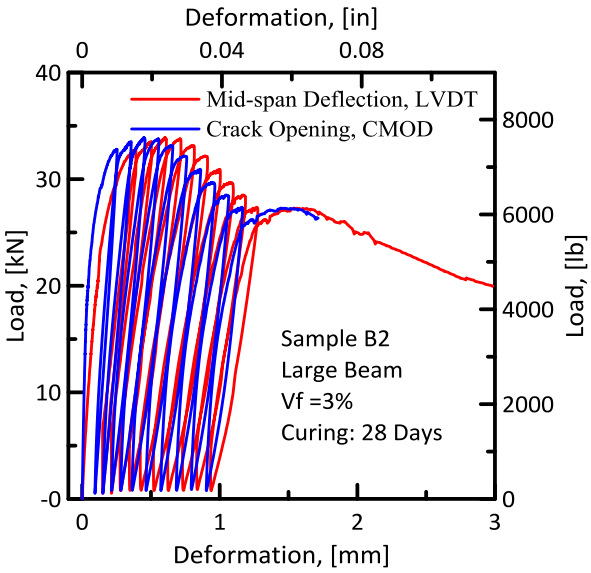

Figure 35. Cyclic test results: Mid-span deflection (LVDT) and Crack Mouth Opening (CMOD) against the load, for the large beams with 3% fiber content after 28 days of curing.

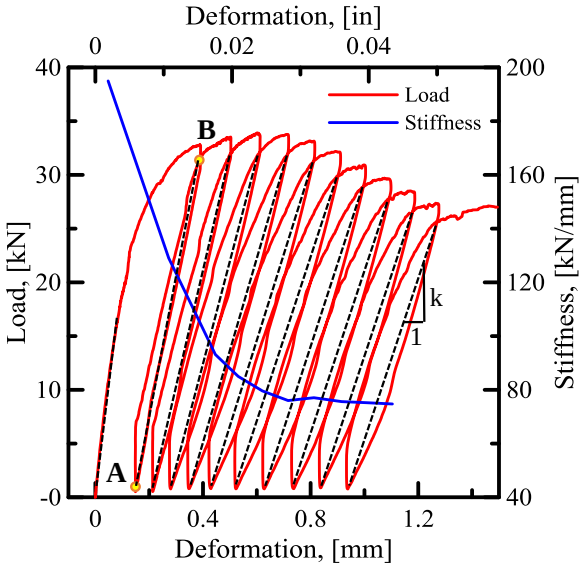

Figure 36. Chosen the part of the cyclic load-deflection response that is used for the stiffness degradation calculation (Sample B2).

Figure 36 shows a part of the load-deflection loops, which are used for the stiffness degradation curves. For doing the calculations, nodes at the minimum point of unloading, points A, and the points located at the joints of loading and unloading curves, points B, are chosen to calculate the stiffness for each loop, black dashed lines in the figure.

$$k = \frac{P_B - P_A}{D_B - D_A} \tag{2}$$

In this equation, P is the loading, D is the displacement and the subscripts represent the equivalent point in which the parameter is extracted.

Displacement at the midpoint of line AB was chosen as the equivalent deflection of each loop to plot the stiffness versus deformation.

As it is shown in the figure, at the start of the cyclic loading there is a sudden drop in the stiffness, but, as the number of cycles increases, it converges to a stable stiffness value, i.e., 78 kN/mm in this specific test. The remaining stiffness of the UHPC section is about 40% of its initial value; i.e., 195 kN/mm. This shows that the section is still able to keep its stiffness after numerous cycles of loading and unloading.

1.13 Tensile Tests and Effect of Strain Rate

Direct tension tests at different strain rates, ranging from 0.04 1/sec to 100 1/sec, were performed on the UHPC samples with 3% fiber content to capture the effect of the strain rate on the mechanical properties of the UHPC. It is noted that the gage length in these set of samples is 2 inches, so the strain rate is half of the stroke speed. The test setup and the tested samples are shown in Figure 37.

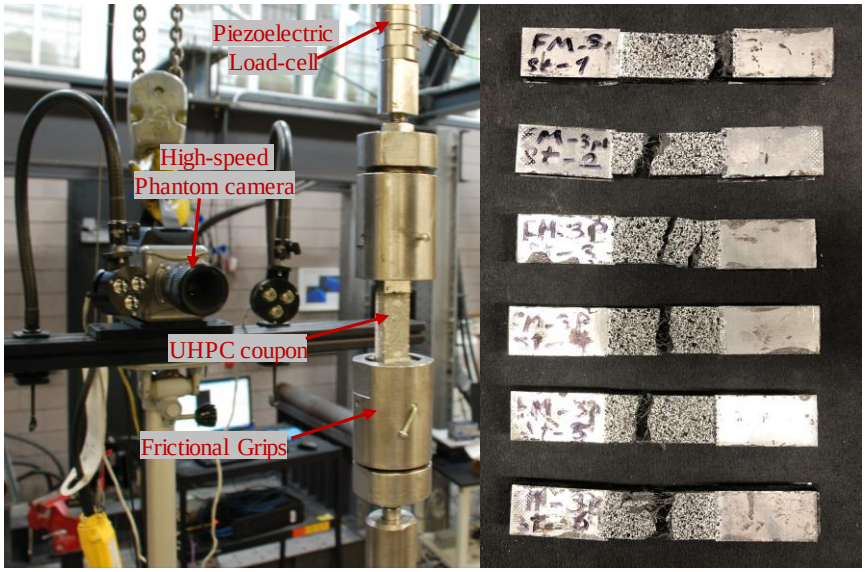

Figure 37. Direct tension tests at different strain rates on UHPC coupons with 3% steel fiber.

The results for different strain rate are shown in Figure 38. This figure shows that as the strain rate increases, the ultimate strengths and the strain that the peak-stress will increase as well. For the quasi-static tests, the average peak stress is around 824 psi (5.7 MPa) and the average strain at peak-stress is about 1.5%. At the strain rate of 25 1/sec, the average peak-stress is around 1334 psi (9 MPa) that is 62% higher than the static strength. The peak strain is about 1.57%, which is it is 0.05% higher compared to the static samples.

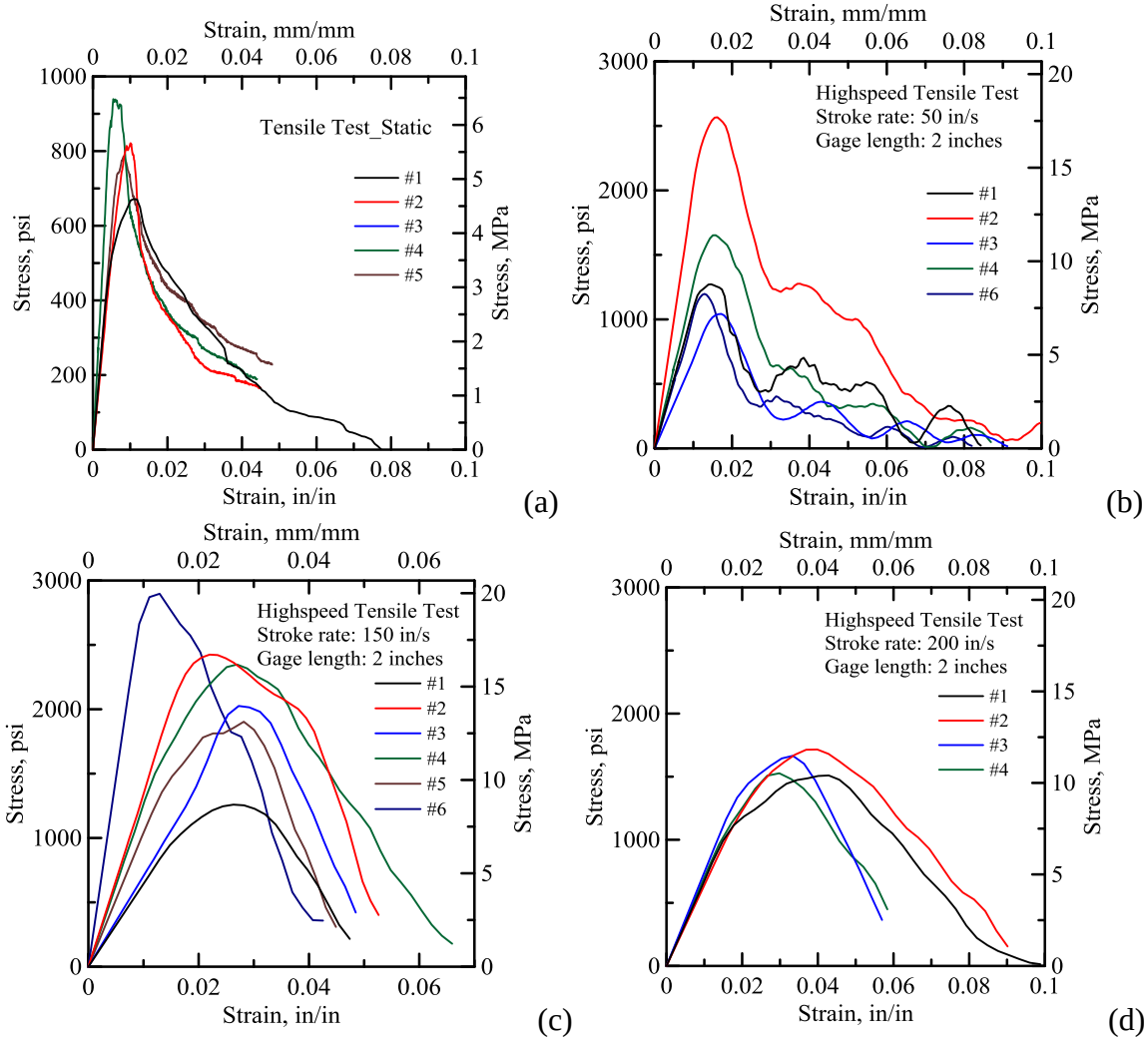

Figure 38. Effect of strain rate on mechanical properties of UHPC.

For the higher strain rate, the same approach is observed. At a nominal strain rate of 75 1/sec, the peak stress is near 1990 psi (14 MPa) that shows a 141% increase compared to the quasi-static tests. The strain is also showing an increasing trend (see Figure 39). At higher strain rate the ultimate strength of the samples showed more uniformity compared to the lower strain rates and the post-peak fluctuations are also fewer than the lower strain rates. Comparative graphs of the effect of strain rate on the peak stress and the peak strain (strain at peak stress) are shown in Figure 39.

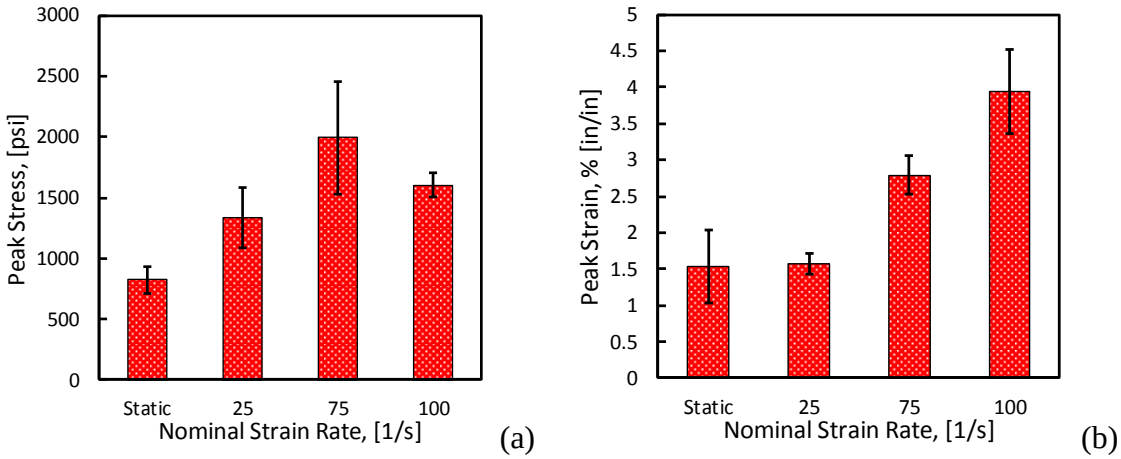

Figure 39. Comparative graphs of the effect of the strain rate on the: (a) peak stress; and (b) peak strain, for UHPC coupons with 3% fiber content.

A summary of the results of the direct tensile tests is presented in Table 6.

Table 6. Summary of direct tensile tests.

Test Set	Nominal Strain Rate (1/sec)	# of Replicates	Actual Strain Rate (1/s)	Peak Stress (psi)	Peak Strain, % (in/in)
FML_3p_st	Quasi-static	6	-	823.77 (±113.35)	1.53 (±0.51)
FML_3p_50	25	6	27.30 (±1.23)	1334.20 (±244.02)	1.57 (±0.14)
FML_3p_150	75	6	69.48 (±2.79)	1991.94 (±463.60)	2.79 (±0.26)
FML_3p_200	100	5	113.03 (±6.90)	1604.48 (±101.69)	3.95 (±0.58)

Another important issue that should be considered in doing the tensile tests on UHPC and, more generally, in FRC composites is the effect of fiber distribution (and orientation) on the tensile response of the small coupons. A bundle of fibers with proper orientation can create outlying results. This issue is shown in Figure 40. These samples are cut from the same original panel with the same fiber content. However, some of the fibers were bundled and created outlying results. This phenomenon is also showing the effect of proper mixing process on the fiber distribution (and orientation) and the strength of FRC as well. In the case of improper mixing, while there are some areas inside the UHPC with high strength, at the bundle locations, there will be also some areas with less amount of fibers and low strength as well.

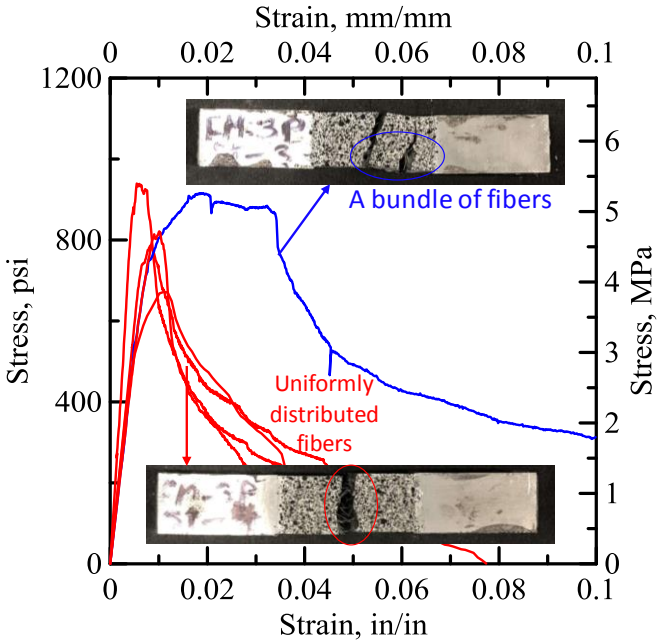

Figure 40. Effect of fiber distribution on the tensile strength of UHPC coupons.

1.14 Summary

- One of the most useful mechanical properties of UHPC is its resistance to cracking and its enhanced tensile strength and ductility. Generally speaking, in all FRC materials, including HPC and UHPC, the resistance to cracking and its propagation in the brittle matrix is significantly increased by steel fibers. This resistance to crack growth is, therefore, more due to the higher percentage of fibers used in UHPC. As the amount of fibers increases, the more ductile behavior is expected and observed.
- Flexure tests are generally used to determine the flexural modulus or flexural strength of a material. Unlike a compression test or tensile test, a flexure test does not measure fundamental material properties. When a specimen is placed under flexural loading, all three fundamental stresses are present: tensile, compressive, and shear. The flexural properties of a specimen are the result of the combined effect of all three stresses as well as − to a lesser extent − the geometry of the specimen and the rate at which the load is applied. Results of the flexural tests can be correlated to the fundamental tension, compression and shear response.
- Steel fibers are added to concrete to improve the structural properties, particularly tensile and flexural strength. The level of improvement in the mechanical properties depends on several factors, such as shape, size, volume, percent, and distribution of fibers.
- The results of the flexural response for the beams are very sensitive to the fiber volume percent. As the micro-cracks develop, the stress in fiber increases gradually with the increase of crack opening.
- Addition of 1% of straight steel fibers to the UHPC mixture affects the post-peak flexural behavior by increasing the toughness values up to 40 times. The absorbed energy (toughness) in the fiber-reinforced beams is two to three times higher than the toughness of the unreinforced beams at peak load.
- Unreinforced beams don’t show a considerable post-peak behavior, while the fiber-reinforced beams show a high level of energy absorption after the post-peak. The total absorbed energy (toughness) at L/150 is 40 times higher than the energy measured at the peak load for unreinforced beams.
- A comparison between two different fiber volume percents, while holding other parameters constant, reveals that the E-modulus of the beams with a 3% fiber volume is 20% higher than this value for a beam with a 1% fiber volume. Furthermore, the ultimate strength of the beams with 3% fiber volume is 70% higher than that in the beams with 1% fiber content.

- $F_{17.5}M_{7.5}L_5$ beams have a superior flexural behavior compared to the $M_{20}L_{30}$ beams. This means that the partial replacement of micro-silica and limestone with fly ash is a good approach to make stronger members and joints. However, the portions and values are very important in the mix design of the UHPC material and a small change in the portions can cause a dramatic change in the results.
- Mixing procedure and methods have a considerable effect on the results. Beams mixed with the high-shear mixer have a residual strength 12% greater than that of beams made using the hand-drill. This can be attributed to a more uniform fiber distribution during the mixing procedure. The more uniform distribution of the admixtures and fibers may be a reason for this better performance.
- Although there is no meaningful difference between the maximum stresses in the beams of different sizes, there is a significant increase in the strain for the large beams. This may be due to the greater depth of the large beams, which can provide more space for crack growth than the small beams.
- As the curing period increases, the strength and post-peak response of the beams increase as well.
- This increase in strength due to an extended curing period is larger in the small beams than in the large beams.
- The loading capacity of small beams after 28 days is almost 43% higher than that of the beams tested after 14 days of curing. The same holds true of the residual strength: the average residual stress for 28-day beams is 47% higher than that of 14-day beams.
- The UHPC section with 3% fiber volume of steel fibers can maintain 40% of its initial stiffness even after numerous cycles of loading and unloading.
- At higher strain rates, the ultimate strength and strain capacity of the UHPC samples may increase by 141% and 158%, respectively.

2 DEVELOPMENT OF STRUCTURAL DESIGN PROCEDURES FOR UHPC BEAMS AND JOINTS

UHPC materials are designed to exhibit noticeable ductility, energy absorption capacity, and post-cracking strength under tension by employing a relatively high dosage of fiber reinforcement [40]. The use of fibers improves the mechanical response behavior by increasing the stiffness and residual strength in the serviceability range of loading which is the dominant mode of loading during the life of a structure. The improvement in mechanical response is accomplished by preventing the cracks from opening and therefore restraining excessive deformations [41]. Unreinforced UHPC materials are extremely strong in compression and brittle in tension and flexure. In order to increase UHPC's ductility even when used with conventional reinforcement, a proportion of reinforcement must be replaced by steel fibers to provide both flexural capacity and ductility. The improvement in the load-bearing capacity and ductility depend on the fiber parameters such as type, shape, aspect ratio, bond strength, and volume fraction [42]. Furthermore, fiber reinforcement improves shear resistance by transferring tensile stresses across flexural cracks and enhances aggregate interlock by reducing the spacing and width of diagonal cracks. The enhanced post-cracking tensile strength and improved crack control due to the distributed fiber reinforcement can improve shear behavior and may potentially substitute or reduce conventional transverse reinforcement [43]. Results have shown that even a limited amount of diffused steel fiber reinforcement increases the post-cracking toughness and ductility of concrete considerably [44]–[47].

Computational models provide opportunities for robust analysis and design with Hybrid UHPC. Various research groups have accomplished extensive work in the

development, design, analysis, and fieldwork with FRC in order to develop design guides [3], [48], [49]. Several procedures for the design of UHPC use formulations based on a strain compatibility analysis, which can be extended to a serviceability-based design by incorporation of full material stress-strain relationship. The material models can be implemented in finite element and elastic-plastic solution methodologies in order to close the gap among properties, analysis, modeling, and design. The tensile characteristics of UHPC can be defined in the context of fiber content and response after the matrix has fully cracked. The general terms of strain softening and/or strain-hardening are defined, and additional sub-classes of deflection-softening and -hardening may be outlined based on the behavior in bending [23].

UHPC mixtures exhibit tensile strain softening or strain-hardening depending on the amount and effectiveness of fiber contribution to the overall composite. The bridging force is expressed in terms of an average smeared tensile residual strength parameter which applies over a large strain range. By representing the bridging force as an average effective tensile stress-crack width relationship (or stress-strain relationship for a specimen of finite width referred to as a localized plastic hinge), one can model the material property as nonlinear spring elements to simulate the residual capacity of a cracked section [23], [50].

Use of UHPC concrete in the structural design of beams, columns, thin sections, link slabs, and panels is an important area of opportunity. With the use of a high-volume fraction of fibers, UHPC design components can be also applied to hybrid flexural and shear reinforcement as well as the connection of precast components in the field. ACI

guidelines have recently been developed for general flexural design, elevated slabs, tunnel lining, etc [ACI-544-8R, ACI-544-7R, ACI 544-6R]. The methodology for analysis and design is based on the minimum and ultimate strength as well as sustainability and serviceability requirements. Serviceability can be designed based on user-defined and specified strain, crack width, deflection, or curvature ductility. Design for serviceability requires a better understanding of the load path and state of nonlinear behavior vis-à-vis cracking. Determination of design parameters such as load capacity at a certain level in the load-deformation history is, therefore, an important aspect of the modeling.

Simplified equations to account for the contribution of fibers to the tensile and shear response, cracking strength, and post-crack softening response are widely used to evaluate the mechanical performance. In many situations, direct interpretation of results primarily based on the strength can be misleading, since the interactions due to variables are not considered. For example, the interaction of factors such as longitudinal reinforcement, compression block, tension residual strength field, and fiber reinforcement make the interpretation of the results quite challenging. Different cracking mechanism often yields to conservative interpretations which underestimate the effect of real parameters [51], [52]. Structural or quasi-full-scale tests, however, represent the concrete volume, modes of failure, and competing mechanisms more realistically and the overall toughness or ductility is a function of such interacting mechanisms. Many of these interacting parameters can be integrated into a representative plastic hinge element and its mechanical properties. Such models integrate cross-sectional dimensions with the tensile

and compressive stress-strain, as well as the reinforcement's contribution. The nonlinear hinge can then be used in a non-linear structural model.

A schematic drawing of the idealized plastic hinge which relates the axial and bending moment with the stress distribution and average curvature across the section is shown in Figure 41. Note that the entire length of the element, L_p is taken as a non-linear hinge which due to cracking exhibits large-scale rotation. This rotation engages the reinforcement and fibers which cross the crack and therefore the stress across the section can be related to the deformation using the moment-curvature (M-ϕ) that is obtained for a single cross-section.

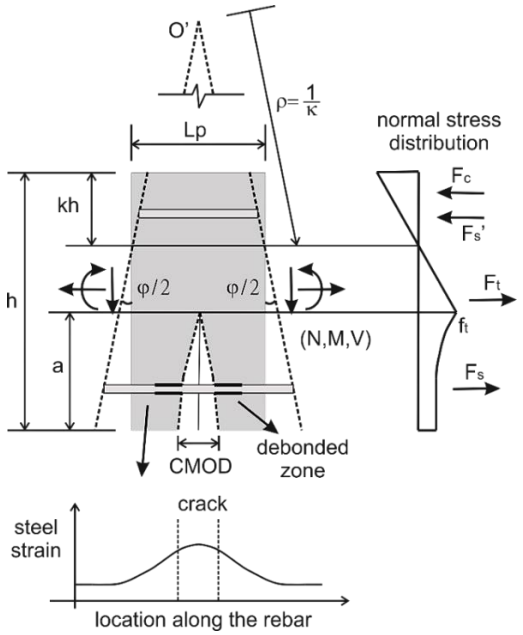

Figure 41. Schematic presentation of the localized zone for a beam section as a non-linear hinge, normal stress distribution and strain distribution in steel rebar [53].

Simplified equations to account for the contribution of fibers to the tensile and shear response, cracking strength, and post-crack softening response, are widely used to evaluate the mechanical performance. In many situations, direct interpretation of a test primarily based on the strength can be misleading since the interactions due to variables

are not considered. For example, the interaction of factors such as longitudinal reinforcement, compression block, tension residual strength field, and fiber reinforcement make the interpretation of the results quite challenging. Different cracking mechanism often yields to conservative interpretations which underestimate the effect of real parameters [51], [52]. Structural or quasi-full scale tests, however, represent the concrete volume, modes of failure, and competing mechanisms more realistically and the overall toughness or ductility is a function of such interacting mechanisms.

2.1 Generalized Yield Hinge Modeling Plan

This section addresses the methods employed in the analysis of flexural UHPC members. Closed form relationships based on the non-linear design of reinforced concrete are used in the calculation of the load-deflection response of UHPC [3], [7], [8]. The procedures are followed from the recent code-based guidelines and are briefly addressed here. Procedures to calibrate the test methods to obtain material properties from experiments are discussed as well. Equations that relate the material properties to the structural design and analysis procedures of UHPC are also discussed. In order to develop serviceability-based design procedures, one has to formulate the problem using a strain compatibility approach that tracks the path of loading. Computations are extended to hybrid reinforcement systems with flexural rebars in conjunction with UHPC in beams and joints.

The developed procedures are used in obtaining material properties from the flexural data using procedures that are based on back-calculation of material properties from the experimental results. Model simulations are compared with other results

available in the literature. Performance of flexural reinforced UHPC concrete beam sections tested under different types of loading is addressed using a combination of fibers and rebars. The objective is to validate the proper design procedures for UHPC flexural members as well as connection elements used with UHPC. The proposed solutions can be used to reduce total reinforcement by means of increasing the ductility of the UHPC mixtures in order to meet the required flexural reinforcement. In addition, the cracking and ductility response can be analyzed as well as the serviceability deflection level estimated from moment-curvature expressions for homogenized UHPC Concrete.

2.2 Simplified Approach for Incorporation of Fibers in Flexural Model

This section presents the classic ACI approach, based on the Whitney rectangle concept, for computing the bending capacity of a plain UHPC beam. This is an ultimate limit state approach based on strength analysis. In ordinary reinforced concrete design the contribution of tensile concrete is ignored due to its low magnitude. The present method employs linear strain distribution, but it ignores the stress-strain constitutive relationship by assuming a constant compressive stress block and a constant residual stress distribution in the tensile region. Due to this simplification, the approach is unable to simulate all stages of the flexural process, although it can be used as a simplified approach for designing the FRC and HRC sections. The basic assumptions of plane sections remaining plane are used. It is assumed that the tensile strength of concrete is $\sigma_{cr} = E\varepsilon_{cr}$ and the residual strength is represented by parameter μ ($0< \mu <1$), representing a fraction of the tensile strength that is transmitted after cracking. This

indicates that the stress crack width relationship is a constant function and equal to $\mu\sigma_{cr}$ in tension.

Figure 42 presents a constitutive model for homogenized strain softening and hardening FRC with two fundamental material parameters: Elastic modulus, E, (equal in tension and compression) and first cracking tensile strain, ε_{cr}. Two non-dimensional parameters: Normalized post-peak tensile strength μ, and compressive to tensile strength ratio, ω, were also defined. The compressive response in Figure 42(a) is represented as an elastic-plastic response with an initial modulus defined as γE up to the compressive strength of $\omega\gamma\sigma_{cr}$, Parameter ω represents the ratio of compressive to tensile strain. In most of the cases, elastic modulus for tension and compression are equal and therefore $\gamma = 1$. Thus, parameter ω can be considered as the ratio of compressive to tensile strength, $\sigma_{cy} = \omega\sigma_{cr}$.

The tension model in Figure 42(b) is described by a trilinear response with an elastic range defined by E, and then post-cracking modulus E_{cr}. By setting E_{cr} to either a negative or a positive value, the same model can be used to simulate strain softening or strain hardening materials. The third region in the tensile response is a constant stress defined with stress σ_{cst} in the post-crack region. The constant stress level μ can be set to any value at the transition strain, resulting in a continuous or discontinuous stress response. Two strain measures are used to define the first cracking and transition strains (ε_{cr} , ε_{trn}). The tensile response terminates at the ultimate tensile strain level of ε_{tu}.

The parameter μ represents the ratio of the post-peak tensile strength to the cracking tensile strength $\mu = \sigma_P / \sigma_{cr}$ and may be a function of the fiber volume fraction, geometry, stiffness, and bond. Figure 42(b) describes the compression model with stress increasing linearly up to the yield strain $\varepsilon_{cy} = \omega\varepsilon_{cr}$, and remaining perfectly plastic until the termination point at the ultimate compressive strain $\varepsilon_{cu} = \lambda_{cu}\varepsilon_{cr}$. The non-dimensional strain measures β_{tu} and λ_{cu} are defined as limits for terminating the algorithm. They also facilitate a simplified parametric model based on serviceability limit state (SLS) and ultimate limit state (ULS) criteria for the design of FRC flexural members [3]. The model can be implemented both for strain softening and strain hardening FRC. As an extension to the model, one can also consider a combination of fibers and plain reinforcement in the context of hybrid reinforced concrete (HRC) which addresses structural members that combine continuous reinforcement with randomly distributed chopped fibers in the matrix. An analytical model for predicting the flexural behavior of HRC, which is applicable to conventional reinforced concrete and FRC, presented by Mobasher et al. (2015) [54], will be discussed in the next section as well.

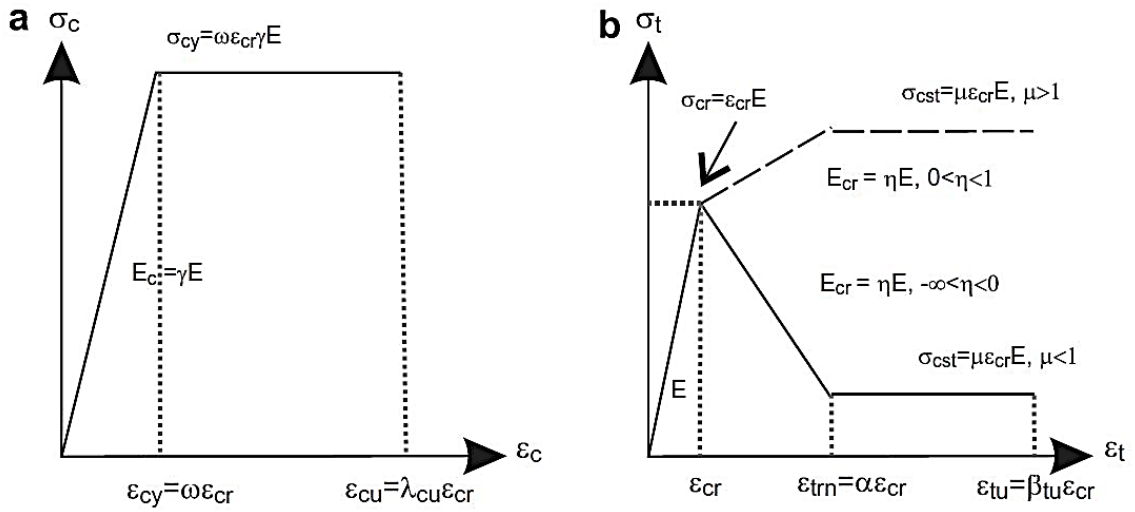

Figure 42. Material models for homogenized fiber reinforced concrete: (a) compression model and (b) tension model [7].

Material parameters required for the simplified models are summarized as follows:

Cracking tensile strain, $\varepsilon_{cr} = \dfrac{\sigma_{cr}}{E}$ (3)

Normalized tensile strain at peak strength, $\alpha = \dfrac{\varepsilon_{peak}}{\varepsilon_{cr}}$ (4)

Normalized post-crack modulus, $\eta = \dfrac{E_{cr}}{E}$ (5)

Normalized yield compressive strain, $\omega = \dfrac{\sigma_{cy}}{E\varepsilon_{cr}} = \dfrac{\sigma_{cy}}{\sigma_{cr}}$ (6)

Normalized tensile strain at bottom fiber, $\beta = \dfrac{\varepsilon_t}{\varepsilon_{cr}}$ (7)

Normalized compressive strain at top fiber, $\lambda = \dfrac{\varepsilon_c}{\varepsilon_{cr}}$ (8)

Designing with UHPC differs from designing with normal concrete, due to differences in stress-strain diagrams. The stress-strain relationship in compression has a similar shape for UHPC and normal concrete but the fibers cause a different stress-strain relation in tension. Normal concrete has a small tensile capacity that will be neglected whenever the concrete has cracked, and the reinforcement is activated. However, the fibers in UHPC provide a tensile capacity that co-operates with reinforcement as well. For design purposes, VSL Australia [55] has developed an idealized stress-strain relationship as shown in Figure 43. In this research, for design purposes, the VSL approach has been chosen. This approach is compared with the typical stress-strain compressive relationship and the method proposed by [56]. The proposed models are shifted to the right for better clarity.

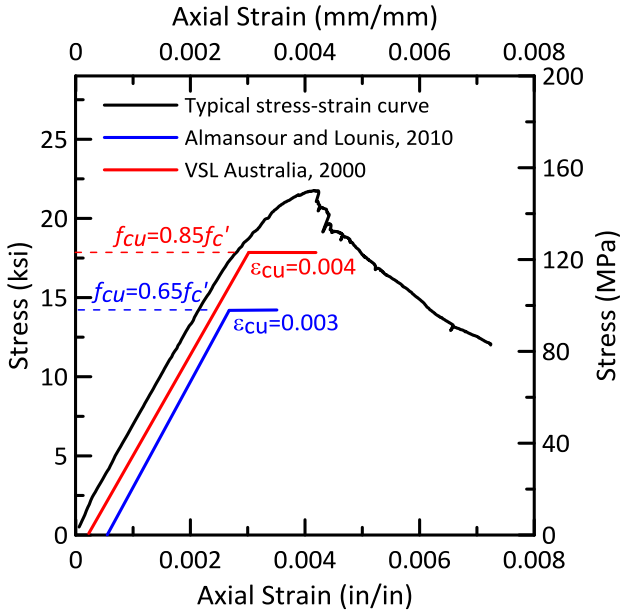

Figure 43. Comparison between design stress-strain relationships in compression.

2.2.1 Design Approach for Fiber Reinforced Concrete (FRC)

Figure 44 shows the stress-strain block diagrams for an FRC section. In this case, due to the low tensile strength, it is very unlikely that we have a compressive failure in the section. Accordingly, a linear elastic response, with a maximum compressive stress value of $\sigma_{cy} = E_c \varepsilon_{cy}$, is chosen. As shown, the tensile response of the section is replaced with a uniform distributed loading equal to $\mu\sigma_{cr}$ representing the tensile post crack capacity.

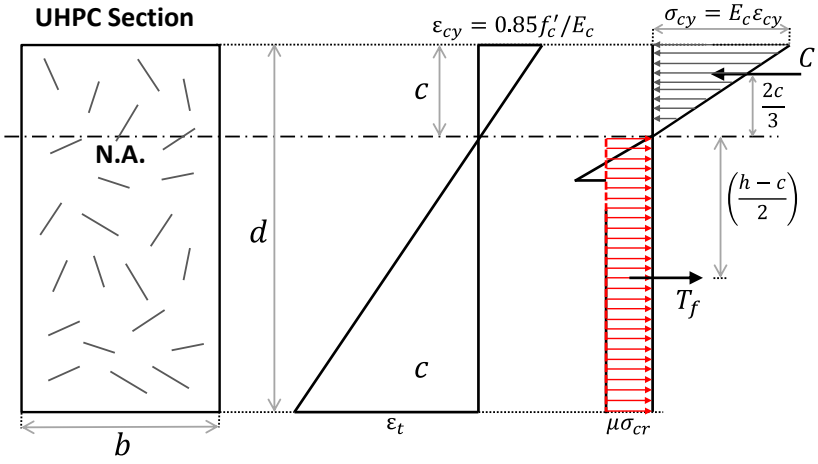

Figure 44. FRC cross-section stress-strain diagrams.

The first step to achieve the moment capacity of the section is to calculate the depth of the neutral axis, c. The section is in a stable status and the tensile and compressive forces are equal to each other. This can be used to calculate c.

$$C = \frac{b}{2} c \times \sigma_{cy} = \frac{bc}{2} \times E_c \varepsilon_{cy} \tag{9}$$

$$T_f = b(h-c) \times \mu\sigma_{cr} = \mu b(h-c) \times E_c \varepsilon_{cr} \tag{10}$$

By requiring $T_f = C$, we have

$$c = \frac{2h\mu\varepsilon_{cr}}{\varepsilon_{cy}+2\mu\varepsilon_{cr}} = \frac{2\mu}{\omega+2\mu}\times h \tag{11}$$

Based on the current research, the range for cracking strain, ε_{cr}, is between 0.00010 to 0.00017, but a more accurate value can be obtained using $\varepsilon_{cr} = E_c / \sigma_{cr}$, tensile tests, back-calculation approach (which will be discussed in the next section), or empirical relationship between tensile and compressive strength, i.e. $\sigma_{cr} = 6.7\sqrt{f_c'}$ in U.S. customary units, psi (and $\sigma_{cr} = 0.56\sqrt{f_c'}$ in SI customary units, MPa), for ordinary concrete; or $\sigma_{cr} = 0.04 f_c'$, for UHPC [57]. A similar approach can be used for E_c with the empirical relationship between elastic modulus and compressive strength, i.e. $E_c = 57000\sqrt{f_c'}$ in U.S. customary units, psi (and $E_c = 4700\sqrt{f_c'}$ in SI customary units, MPa) for ordinary concrete; or $E_c = 49000\sqrt{f_c'}$, for UHPC [57]. Since these equations are empirical relationships based on the tests on FRC beams, for UHPC sections, the more accurate approach is to test the samples, based on the applicable standard, and then conduct a back-calculation procedure in accordance with ACI-544-8R, in order to get the accurate value of residual strength, $\mu\sigma_{cr}$. By using the data reported under flexural tests, from the previous section, one can obtain σ_{cr} values in the range of 700 ($\pm$70) psi and 1050 ($\pm$50) psi for beams with 1% and 3% fiber content, respectively. The μ values laid between 0.55 ($\pm$0.07) and 0.85 ($\pm$0.07) for beams with 1% and 3% fiber content, respectively.

The moment capacity of the section can be calculated as

$$M_n = T_f(\frac{h-c}{2} + \frac{2}{3}\mathrm{c}) \tag{12}$$

By substituting c, from Eq. (11) into (12)

$$M_n = \frac{\omega\mu(3\omega+8\mu)}{(\omega+2\mu)^2} \times M_{cr} \tag{13}$$

Where

$$M_{cr} = \frac{\sigma_{cr} bh^2}{6} \tag{14}$$

Assuming the compressive strength is limited to $0.85 f_c'$ (i.e., $\beta_2 = 0.85$), the normalized compressive strength ω is shown as:

$$\omega = \frac{\varepsilon_{cy}}{\varepsilon_{cr}} \approx \begin{cases} \dfrac{\beta_2 f_c'}{\sigma_{cr}} = \dfrac{0.85 f_c'}{6.7\sqrt{f_c'}} = 0.127\sqrt{f_c'} & (f_c' \text{ in psi}) \\ \dfrac{\beta_2 f_c'}{\sigma_{cr}} = \dfrac{0.85 f_c'}{0.56\sqrt{f_c'}} = 1.518\sqrt{f_c'} & (f_c' \text{ in MPa}) \end{cases} \quad \text{, for FRC} \tag{15}$$

$$\omega = \frac{\varepsilon_{cy}}{\varepsilon_{cr}} \approx \frac{\beta_2 f_c'}{\sigma_{cr}} = \frac{0.85 f_c'}{0.04 f_c'} = 21.25 \quad \text{, for UHPC}$$

Therefore, if one uses a value of to 21 in eq. (13), the nominal moment capacity as a function of the cracking moment can be expressed within 0.5% degree of accuracy as $M_n = 2.85\mu M_{cr}$, based on the suggested values by [57]. Later in this chapter, it is shown that the analytical solution for the ultimate design capacity is $M_n = 3\mu M_{cr}$ which is very much in line with the experimental predictions of $M_n = 2.85\mu M_{cr}$.

2.2.2 Design Approach for Hybrid Reinforced Concrete (HRC)

Hybrid reinforced concrete (HRC) is referred to as a structural member that combines continuous reinforcement with FRC matrix [54]. Combinations of FRC and rebars, or welded wire mesh, may be used to meet the strength criteria [49], [58]–[60]. An approach similar to that for FRC can be implemented to derive the moment capacity for reinforced UHPC sections by taking into account the contribution of steel rebars which is known as hybrid reinforced section (HRC). Figure 46 shows the stress-strain block diagrams for an HRC section. In spite of the FRC section, the plastic compressive failure is likely in this case, therefore, a uniform compressive tension is assumed for the compressive part of the section, $\beta_2 f_c'$. β_2 can be chosen as 0.85 for UHPC. As the figure shows, the tensile response of the section is replaced with a uniform distributed loading over the tensile part of the section.

As Figure 45(a) shows, the tensile response of the section is replaced with a uniform distributed loading over the tensile part of the section. Figure 45(b) shows the stress-strain block diagrams for an HRC section. In spite of the FRC section, the plastic compressive failure is likely in this case, so a uniform compressive tension is assumed for the compressive part of the section, $\beta_2 f_c'$. β_2 can be chosen as 0.85 for UHPC (see Figure 43)(ACI Committee 239).

By mixing the properties of FRCs with those of other type of composites, high strength and an excellent ductility are achievable for a broad range of composites such as textile-reinforced concrete (TRC), high-performance FRC, ultra-high-performance FRC, and ultra-high-performance hybrid reinforced concrete (UHPHRC). This strain-hardening

behavior enhances the durability of concrete structures, because of the ability to (a) arrest the width of cracks and (b) carry tensile stresses (due to the bridging effect of fibers) [22], [62]. The arrangement of the rebars within a cross-section of width *b* and depth *h* (Figure 45d) shows that the depth of the center of gravity of the reinforcement is at a distance $d = \alpha h$.

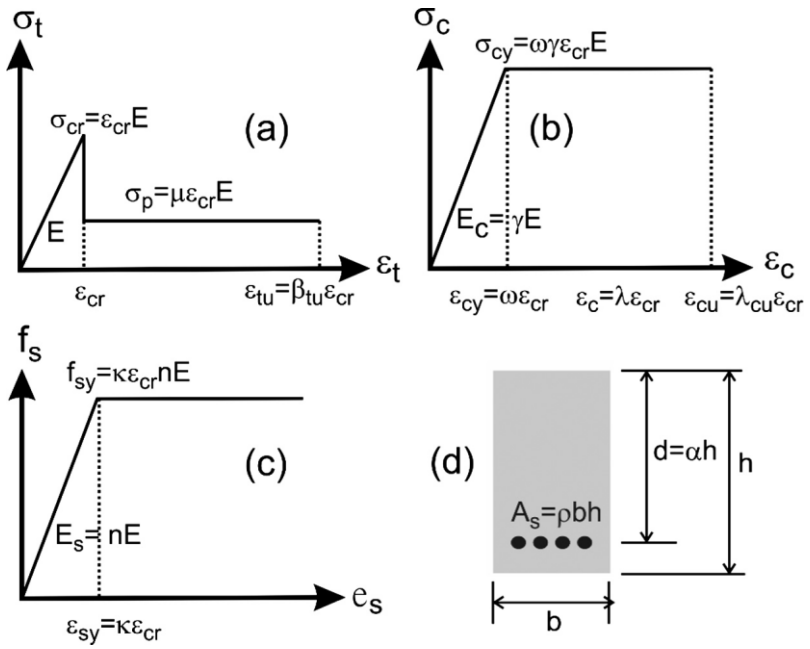

Figure 45. Material model for single reinforced concrete design (a) tension model; (b) compression model; (c) steel model; (d) beam cross-section [54].

In this report, the HRC analytical model presented by Mobasher et al. , [54], is used in a design approach applied to the UHPFRC members. Equations to determine the moment-curvature relationship, ultimate moment capacity, and minimum flexural reinforcement ratio was explicitly derived (Mobasher et al. 2015, [54]). Figure 45 represents all three distinct material models used in the derivation of analytical expressions of moment-curvature and load–deflection of HRC beams which includes the

interaction of compression and tension failure of FRC as well as a failure by tension yielding of steel.

Parameter-based tensile and compressive strain-stress diagrams of composite and steel sections are shown in Figure 45 for a typical hybrid-FRC cross-section. Reinforcement material parameters required for the simplified models are summarized as follows:

Normalized yield strain of steel, $\kappa = \frac{\varepsilon_{sy}}{\varepsilon_{cr}}$ (16)

Normalized elastic modulus of steel, $n = \frac{E_s}{E_c}$ (17)

Reinforcement ratio, $\rho_g = \frac{A_s}{bh}$ (18)

Normalized reinforcement depth, $\alpha = \frac{d}{h}$ (19)

Figure 45a represents the material (a) tensile and (b) compressive constitutive stress-strain responses for FRC. Figure 45c represents the elastic perfectly plastic model for steel reinforcement. The arrangement of the rebars within a cross-section of width *b* and depth *h* is shown in Figure 45d shows that the depth of the center of gravity of the reinforcement is at a distance $d = \alpha h$.

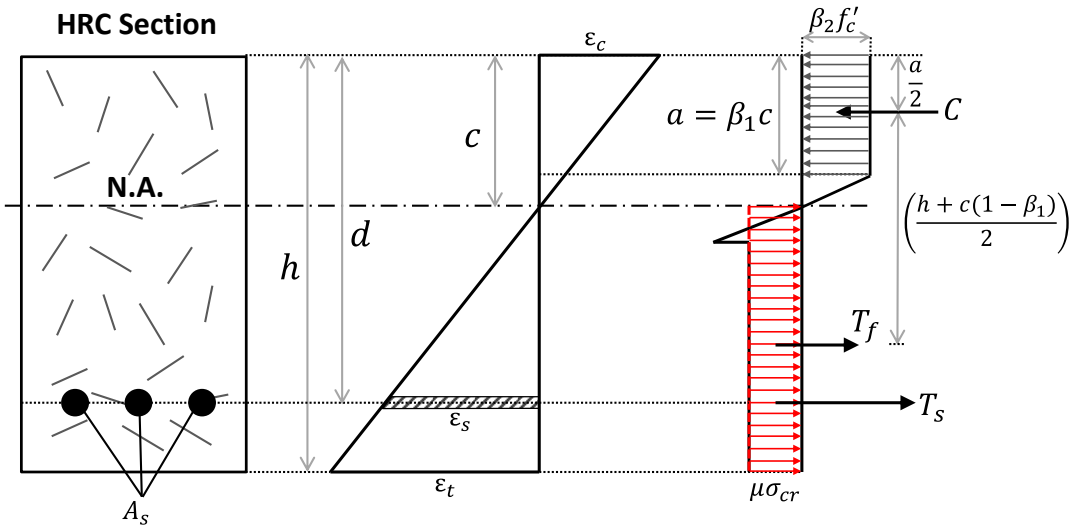

Figure 46. FRC cross-section stress-strain diagrams.

Similar to the process that was used for the FRC section, the first step is to calculate the depth of the neutral axis by putting tensile and compressive forces equal to each other. It is noted that the tensile force due to the cover concrete is ignored.

$$C = ab \times \beta_2 f_c' \tag{20}$$

$$T_f = b(h-c) \times \mu\sigma_{cr} \tag{21}$$

$$T_s = A_s f_y = \rho_g bhf_y \tag{22}$$

Requiring the equilibrium of internal forces, i.e. $C = T_f + T_s$, the depth of the neutral axis can be calculated as

$$c = \frac{hb\mu\sigma_{cr} + A_s f_y}{b(\beta_1\beta_2 f_c' + \mu\sigma_{cr})} = \frac{\mu + \rho\kappa n}{\beta_1\omega + \mu} \times h \tag{23}$$

Where

$$\beta_1 = \begin{cases} 0.85 & \text{for } f_c' \le 4000 \text{ psi} \\ 0.85 - 0.05\left(\dfrac{f_c' - 4000}{1000}\right) & \text{for } 4000 < f_c' \le 8000 \text{ psi} \\ 0.65 & \text{for } f_c' > 8000 \text{ psi} \end{cases} \quad (24)$$

And $\beta_2 = 0.85$ (see Figure 43). The moment capacity of the section can be calculated as

$$M_n = T_f\left(\frac{h + c(1-\beta_1)}{2}\right) + \mathrm{T}_s\left(\alpha h - \frac{\beta_1 c}{2}\right) \quad (25)$$

Substituting Eqs. (21) to (23) into above equation, the capacity of the section can be obtained.

$$M_n = 3\left[\mu(1-A)\left(1 + A(1-\beta_1)\right) + 2\rho\kappa n\left(\alpha - \frac{A\beta_1}{2}\right)\right] \times M_{cr} \quad (26)$$

Where

$$A = \frac{\mu + \rho\kappa n}{\beta_1\omega + \mu} \quad (27)$$

M_{cr} can be obtained using Eq. (14). Balanced reinforcement can be calculated assuming that the steel reinforcement and compressive concrete yield at the same time. Based on this assumption, the depth of the neutral axis, in a section with balanced reinforcement, can be calculated as follows

$$c_b = \frac{\varepsilon_{cy}}{\varepsilon_{sy} + \varepsilon_{cy}} d \quad (28)$$

Using the equilibrium of internal forces, i.e. $C = T_f + T_s$, amount of the balanced reinforcement, ρ_b, can be calculated. Substituting this value into Eq. (20) to Eq. (22), and $C = T_f + T_s$ we have

$$\rho_b = \frac{\beta_1 \beta_2 \varepsilon_{cy} f_c' - \varepsilon_{sy} \mu \sigma_{cr}}{(\varepsilon_{sy} + \varepsilon_{cy}) f_y} = \frac{\beta_1 \omega^2 - \kappa \mu}{(\kappa + \omega) n \kappa} \tag{29}$$

If the reduction factors are assumed equal to 1 (β_1 and $\beta_2 = 1$), then $\omega = 25$ and

$$\rho_b = \frac{625 - \kappa \mu}{(\kappa + 25) n \kappa} \tag{30}$$

To have a ductile failure it is necessary that the reinforcement ratio is less than the balanced ratio, $\rho_g < \rho_b$. A solved example, using this method, is presented in the appendix. For steel rebar Grade 60 and UHPC with $f_c' = 20$ ksi, if $\kappa = 15$ and $n = 5$ then

$$\rho_b = 0.21 - \frac{\mu}{200} \tag{31}$$

Given the fact that μ is usually less than 1, it can be concluded that ρ_b is independent of μ.

2.3 Closed-Form Solutions for Flexural Response of FRC Beams (Model for UHPC)

The simplified approach was based on the ultimate limit state (ULS) design. In this section, another approach, which can be used for the serviceability limit state (SLS) design is presented. The generalized fiber-reinforced concrete model used in this section is based on the idealized model suggested by Lim et al, 1987 [63] and presented in the

form of closed-form solutions by Soranakom and Mobasher, 2007 [7]. The proposed constitutive law for general fiber-reinforced concrete materials consisting of an elastic-perfectly plastic model for compression and an elastic-constant post-peak response for tension.

Figure 47 shows the various interaction of all the parameters of the elastic and inelastic zones of tension and compression response based on a linear strain distribution. The constitutive response relates the strains to stresses, forces, and the bending moment. Note that the interaction of any two zones in the tension and compression behavior results in a specific stress distribution which must be solved in closed form to get the location of neutral axis for that specific sets of values. After solving for the depth of neutral axis, the value of moment and curvature are calculated at each range of applied strain and used to construct the moment-curvature response for that case.

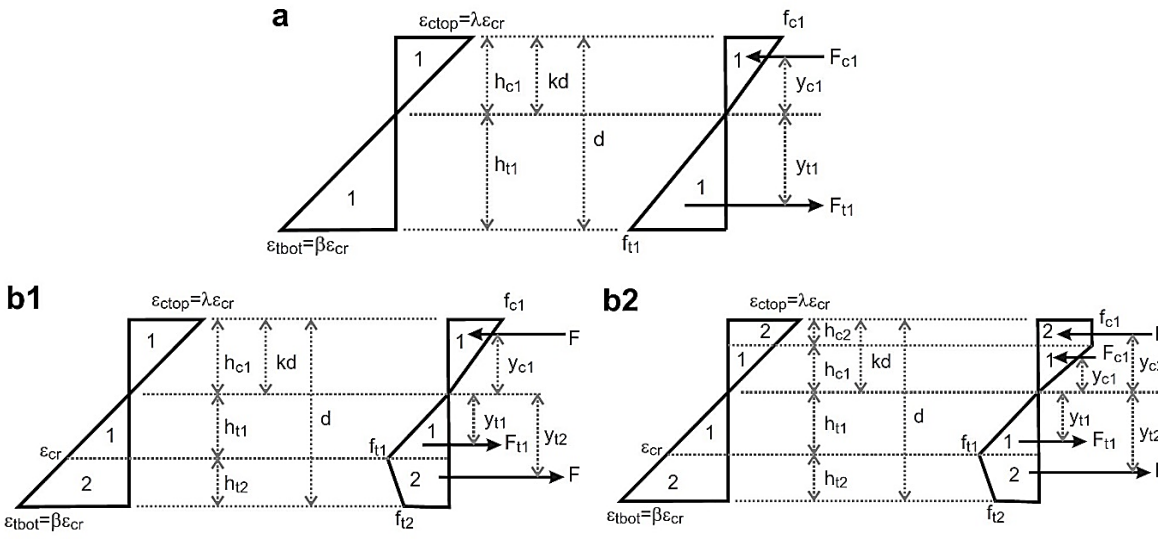

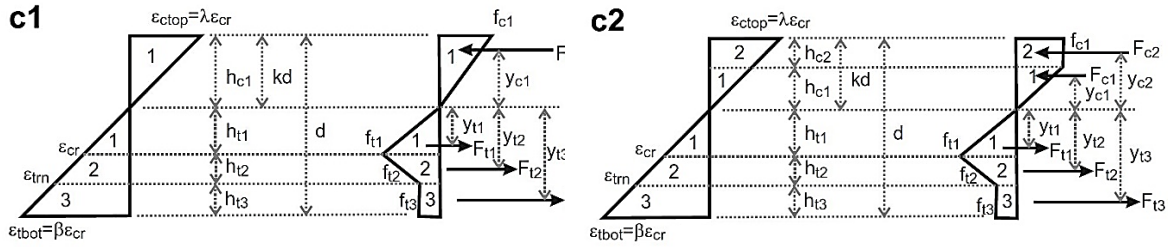

Figure 47. Stress-strain diagram at different stages of normalized tensile strain at the bottom fiber (β): (a) Elastic for compression and tension, $0 \le \beta \le 1$ and $0 < \lambda \le \omega$); (b.1) Elastic for compression but non-linear for tension, $1 < \beta \le \alpha$ and $0 < \lambda \le \omega$), (b.2) Plastic for compression and non-linear for tension, $1 < \beta \le \alpha$ and $\omega < \lambda \le \lambda_{cu}$), (c.1) Elastic for compression but non-linear for tension, $\alpha < \beta \le \beta_{tu}$ and $0 < \lambda \le \omega$, (c.2) Plastic for compression and non-linear for tension, $\alpha < \beta \le \beta_{tu}$ and $\omega < \lambda \le \lambda_{cu}$ [7].

The moment capacity of a beam section according to the imposed tensile strain at the bottom fiber ($\varepsilon_t = \beta\varepsilon_{cr}$) can be derived by the following steps: (1) determine linear strain and stress distributions, (2) force components by integration of stresses, (3) solve for the depth of neutral axis location, *k*, by force equilibrium, and obtain the strain-curvature relationship. The internal moment is obtained from the force and strain distribution. Based on the tensile response of the concrete, three major ranges were defined. In the first range, both compression and tension parts of the section behave in an elastic manner. In the second range, the component of the cross section that is under the tensile stress exceeds the tension cracking stress, therefore the section is in the post-peak transition range. The compressive part may be linear or non-linear. Therefore, this tension cracking criteria introduced two ranges identified as 2.1 or 2.2 depending on the compression zone being linear, or non-linear. In the third range, the segment above the neutral axis that is under compressive stress may follow the linear or non-linear portion of the stress-strain response, while the tensile part of the section has already reached to

the residual tensile response. For this section, only Range 2-1 is described, and the bases for the other ranges will be the same. At this Range, the tensile part of the section is cracked but the compressive part is still in the linear part of its response. Force component and its centroid to the neutral axis in each zone can be expressed as:

$$\frac{F_{c1}}{bh\sigma_{cr}} = \frac{\beta\gamma k^2}{2(1-k)}; \qquad \frac{y_{c1}}{h} = \frac{2}{3}k \tag{32}$$

$$\frac{F_{t1}}{bh\sigma_{cr}} = \frac{(1-k)}{2\beta}; \qquad \frac{y_{t1}}{h} = \frac{2}{3}\frac{(1-k)}{\beta} \tag{33}$$

$$\frac{F_{t2}}{bh\sigma_{cr}} = \frac{(1-k)(\beta-1)(\eta\beta-\eta+2)}{2\beta}; \quad \frac{y_{t2}}{h} = \frac{2\eta\beta^2-\eta\beta-\eta+3\beta+3}{3\beta(\eta\beta-\eta+2)}(1-k) \tag{34}$$

where F and y are the force and its centroid, respectively; subscripts *c1*,*t1*,*t2* designate compression zone 1, tension zone 1 and 2, respectively; b and h are the width and the height of the beam, respectively. The neutral axis parameter k is found by solving the equilibrium of net internal forces equal to zero, $F_{c1} + F_{t1} + F_{t2} = 0$.

$$k = \frac{C_1 - \sqrt{\beta^2 C_1}}{C_1 - \beta^2}; \; C_1 = \eta\left(\beta^2 - 2\beta + 1\right) + 2\beta - 1 \tag{35}$$

The nominal moment capacity M_n is obtained by taking the first moment of force about the neutral axis, $M_n = F_{c1}y_{c1} + F_{t1}y_{t1} + F_{t2}y_{t2}$, and expressed as a product of the normalized nominal moment m_n and the cracking moment M_{cr} as follows:

$$M_n = m_n M_{cr} \tag{36}$$

$$m_n = C_2\frac{k^2-2k+1}{\beta^2} + \frac{2\beta k^3}{1-k}; \text{ where } C_2 = C_1 + 2C_1\beta - \beta^2 \tag{37}$$

Additional discussions of these methodologies and equations have been presented in the original Soranakom and Mobasher publication which has been incorporated in ACI 544-8R, ACI544-6R, and ACI544-7R [64], [65].

Table 7 presents the general derivation of all potential combinations for the interaction of tensile and compressive response. The methodology used in the design of conventional reinforced concrete according to ACI-318 [66] is adopted next. The nominal moment capacity of a flexural member M_n must be decreased by a reduction factor to account for variability in materials and workmanship. The reduced capacity must be greater than the ultimate moment M_u due to factored loading by ACI Sec. 9.2, i.e., $\phi_r M_n \geq M_u$, where ϕ_r is the reduction factor for strain-hardening FRC and taken as 0.65, equal to the reduction factor for compressive failure of plain concrete stipulated by ACI Sec. C.3.5. Despite the post-crack flexural response of HPFRC is ductile such that it can sustain large deflections after cracking, it fails abruptly with little warning after passing the ultimate moment. For this reason, a conservative reduction factor for compressive failure of plain concrete is adopted.

According to bilinear tension and elastic compression models, shown in Figure 45, the maximum moment capacity is obtained when the normalized tensile strain at the bottom fiber ($\beta = \varepsilon_t/\varepsilon_{cr}$) reaches the tensile strain at peak strength ($\alpha = \varepsilon_{peak}/\varepsilon_{cr}$). However, the simplified equations (35)-(37) for moment capacity are applicable to the compressive stress in the elastic region only. The elastic condition must be checked by computing the normalized compressive strain developed at the top fiber λ and compare it to the normalized yield compressive strain ω. The general solutions for all the cases are presented in Table 7. Using the strain diagram in Figure 47, one can obtain the relationship between the top compressive strain and bottom tensile strain as follow:

$$\frac{\varepsilon_c}{kh} = \frac{\varepsilon_t}{(1-k)h} \tag{38}$$

By substituting $\varepsilon_c = \lambda\varepsilon_{cr}$ and $\varepsilon_t = \beta\varepsilon_{cr}$ in Eq.(13), then limit the maximum compressive strain to the yield compressive strain $\varepsilon_{cy} = \omega\varepsilon_{cr}$. Finally, the condition can be expressed in a normalized form as:

Table 7. Neutral axis parameter k, normalized moment m and normalized curvature ϕ for each stage of normalized tensile strain at bottom fiber (β) [54].

Stage	K	$m = M/M_{cr}$	$\phi'_1 = \phi/\phi_{cr}$
1 $0 < \beta \leq 1$	$k_1 = \begin{cases} \frac{1}{2} & \text{for } \gamma=1 \\ \frac{-1+\sqrt{\gamma}}{-1+\gamma} & \text{for } \gamma \neq 1 \end{cases}$	$m_1 = \frac{2\beta\left[(\gamma-1)k_1^3 + 3k_1^2 - 3k_1 + 1\right]}{1-k_1}$	$\phi'_1 = \frac{\beta}{2(1-k_1)}$
2.1 $1 < \beta \leq \alpha$ $0 < \lambda \leq \omega$	$k_{21} = \frac{D_{21} - \sqrt{D_{21}\gamma\beta^2}}{D_{21} - \gamma\beta^2}$ $D_{21} = \eta\left(\beta^2 - 2\beta + 1\right) + 2\beta - 1$	$M'_{21} = \frac{(2\gamma\beta - C_{21})k_{21}^3 + 3C_{21}k_{21}^2 - 3C_{21}k_{21} + C_{21}}{1-k_{21}}$ $C_{21} = \frac{(2\beta^3 - 3\beta^2 + 1)\eta + 3\beta^2 - 1}{\beta^2}$	$\phi'_{21} = \frac{\beta}{2(1-k_{21})}$
2.2 $1 < \beta \leq \alpha$ $\omega < \lambda \leq \lambda_{cu}$	$k_{22} = \frac{D_{22}}{D_{22} + 2\omega\gamma\beta}$ $D_{22} = D_{21} + \gamma\omega^2$	$M'_{22} = (3\gamma\omega + C_{22})k_{22}^2 - 2C_{22}k_{22} + C_{22}$ $C_{22} = C_{21} - \frac{\gamma\omega^3}{\beta^2}$	$\phi'_{22} = \frac{\beta}{2(1-k_{22})}$
3.1 $\alpha < \beta \leq \beta_{tu}$ $0 < \lambda \leq \omega$	$k_{31} = \frac{D_{31} - \sqrt{D_{31}\gamma\beta^2}}{D_{31} - \gamma\beta^2}$ $D_{31} = \eta\left(\alpha^2 - 2\alpha + 1\right)$ $+ 2\mu\left(\beta - \alpha\right) + 2\alpha - 1$	$M'_{31} = \frac{(2\gamma\beta - C_{31})k_{31}^3 + 3C_{31}k_{31}^2 - 3C_{31}k_{31} + C_{31}}{1-k_{31}}$ $C_{31} = \frac{(2\alpha^3 - 3\alpha^2 + 1)\eta - 3\mu\left(\alpha^2 - \beta^2\right) + 3\alpha^2 - 1}{\beta^2}$	$\phi'_{31} = \frac{\beta}{2(1-k_{31})}$
3.2 $\alpha < \beta \leq \beta_{tu}$ $\omega < \lambda \leq \lambda_{cu}$	$k_{32} = \frac{D_{32}}{D_{32} + 2\omega\gamma\beta}$ $D_{32} = D_{31} + \gamma\omega^2$	$M'_{32} = (3\gamma\omega + C_{32})k_{32}^2 - 2C_{32}k_{32} + C_{32}$ $C_{32} = C_{31} - \frac{\gamma\omega^3}{\beta^2}$	$\phi'_{32} = \frac{\beta}{2(1-k_{32})}$

The table shows that the moment and curvature can be obtained as a function of the strain in the tensile fiber of the section, β . Figure 48 represents the typical moment-curvature diagrams with different fiber contents. Fiber-reinforced sections exhibit post-peak residual strength depending on their fiber content. As the amount of the fiber increases, the maximum bending capacity of the section and the residual (post-peak) strength increases as well.

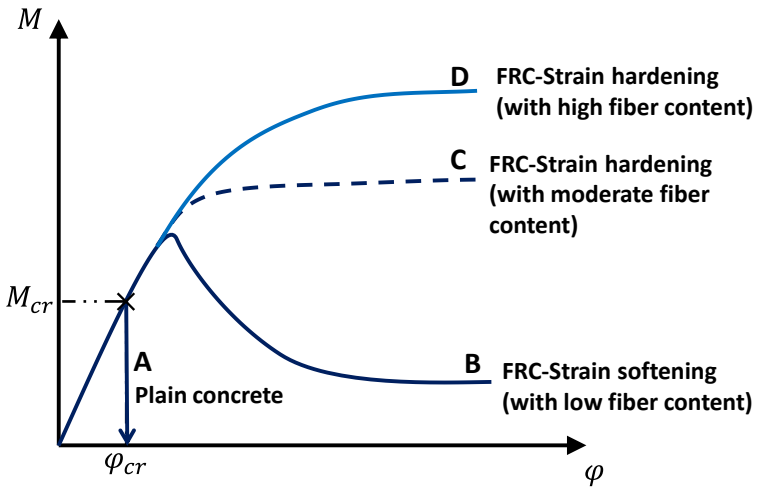

Figure 48. Typical moment-curvature diagrams for FRC sections with various fiber content.

2.4 Design Based on Serviceability Limit State (SLS)

A sustainability-based approach is a powerful method to give us an understanding of what is happening during the flexural procedure and crack growing. Using this approach makes it possible to follow different section deformation stages, in tension and compression layers, and enable us to predict the exact response of the section under given bending moment. Having the moment-curvature diagrams, it is possible to simulate the load-deflection response of a beam, using a moment-area method or any other approaches.

The first step in this approach is to specify the desired deflection (curvature) of the section and then to calculate the equivalent tensile strain at the bottom fiber as a normalized value ($\varepsilon_t = \beta\varepsilon_{cr}$). Then it is possible to calculate the relevant moment capacity for that specific tensile strain by putting the equivalent β value into the equations given in [7], [8], [3], [54].

For the strain-hardening type of behavior, which is observable in UHPC materials, other tensile responses have been presented to describe and simulate the bending behavior of the section, as close as possible to the results from the experiments to provide a better understanding of the nature of the FRC material response based on a sustainability-based approach. A general strain hardening tensile, and an elastic-perfectly plastic compression model as derived by Soranakom and Mobasher [8], [40] is shown in Figure 49. Similarly, the tensile response is defined by tensile stiffness, E, first crack tensile strain ε_{cr}, ultimate tensile capacity, ε_{peak}, and post-crack modulus E_{cr}. In order to simplify material characteristics of strain-hardening FRC, and yet obtain closed-form design equation generation several assumptions are made. Equations can be simplified to idealized bilinear tension and elastic compression models as shown ignoring the post-peak ranges in both tension and compression.

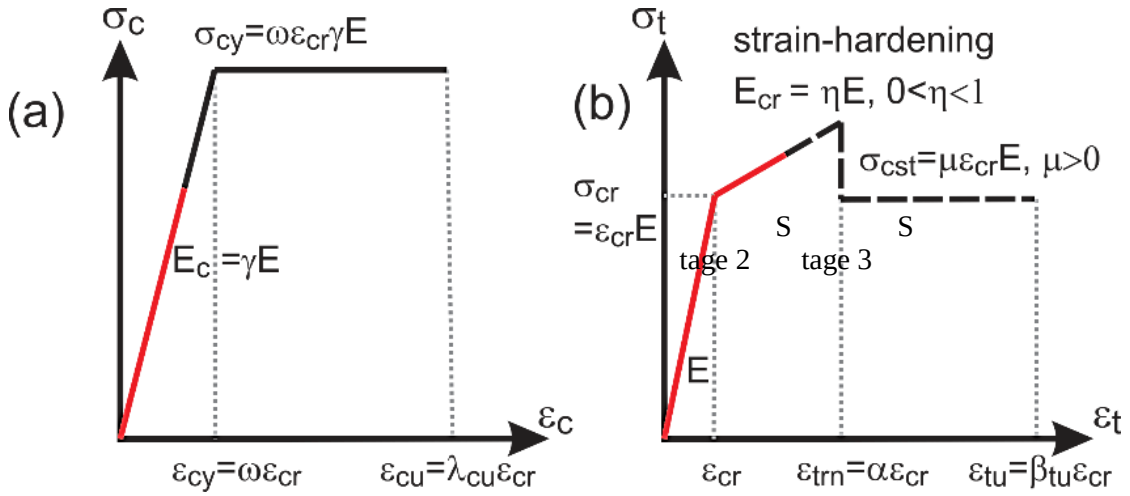

Figure 49. Material models and simplified portions for serviceability limits for strain-hardening FRC: (a) compression model; and (b) tension model.

Moment capacity of a beam section according to the imposed tensile strain at the bottom fiber ($\varepsilon_t = \beta\varepsilon_{cr}$) can be derived based on the assumed linear strain distribution as shown in Figure 47. By using material models in Figure 49, the corresponding stress diagram can be obtained, similar to Figure 47, in which the stress distribution is subdivided into two compression zones 1 and 2, tension zones 1 and 2 [40].

The case represented by case 2.1, where the tensile behavior is in elastic-plastic while the compressive behavior is still elastic is studied in this section. Equations for other cases can also be developed. The general solution presented in Table 7 can be simplified as follows. The location of the neutral axis represented as a function of applied tensile strain β is represented as:

$$k_{21} = \frac{\sqrt{A_{21}}}{\sqrt{A_{21}} + \beta\sqrt{\gamma}} \qquad A_{21} = \eta(\beta^2 + 1 - 2\beta) + 2\beta - 1 \tag{39}$$

This equation can be easily simplified by assuming the tension and compression stiffnesses as the same ($\gamma = 1$). Furthermore, for an elastic perfectly plastic tension material ($\eta = 0$) the equation reduces to:

$$k_{21} = \frac{\sqrt{2\beta - 1}}{\sqrt{2\beta - 1} + \beta} \tag{40}$$

Table 8 presents the case of ($\gamma = 1$), for different values of post-crack stiffness $\eta =$ 0.5, 0.2, 0.1, 0.05, 0.01, and 0.001. Note that the neutral axis is a function β and can be used in the calculation of the moment, or the moment-curvature relationship. This general response is shown in Figure 50 and show that with an increase in applied tensile strain, the neutral axis compression zone decreases, however, this decrease is a function of post-crack tensile stiffness factor. The black line represents the elastic perfectly-plastic response of the section, $\eta = 0.0$. Blue lines belong to the strain-softening response and the red curves stand for the strain-hardening type of the behavior. The moment-curvature relationship in this range is ascending, however, its rate is a function of the post-crack tensile stiffness. The parameter based fit equations in the third and fourth column are obtained by curve fitting the simulated response from the closed form derivations and are applicable within 1% accuracy of the closed form results. Using these equations, one can generate the moment capacity and moment-curvature response for any cross section using basic tensile material parameters in the 2.1 range as defined in Table 8.

Table 8. Location of the neutral axis, moment, and moment-curvature response of a composite material with $\gamma = 1$ and $\eta =$ 0.0001- 0.5.

η	A_{21}, ($k_{21} = \frac{\sqrt{A_{21}}}{\sqrt{A_{21}} + \beta}$)	$M'(k)$	$M'(\varphi)$
0.5	$0.5(\beta^2 + 1 - 2\beta) + 2\beta - 1$	$1.364 + 2.377\times10^{-8}\exp(k^{-3.5})$	$0.503 + 0.686\varphi$
0.2	$0.2(\beta^2 + 1 - 2\beta) + 2\beta - 1$	$1.538 + 0.00115\exp(k^{-2})$	$1.097 + 0.383\varphi$
0.1	$0.1(\beta^2 + 1 - 2\beta) + 2\beta - 1$	$2.124 + 0.00595\exp(k^{-1.5})$	$1.459 + 0.233\varphi$
0.05	$0.05(\beta^2 + 1 - 2\beta) + 2\beta - 1$	$1.001 + 0.06872\exp(k^{-1})$	$1.73 + 0.1376\varphi$
0.01	$0.01(\beta^2 + 1 - 2\beta) + 2\beta - 1$	$0.7293 + 0.2582\exp(k^{-0.5})$	$1.208 + 0.4004\sqrt{\varphi}$
0.0001	$0.0001(\beta^2 + 1 - 2\beta) + 2\beta - 1$	$6.42 - 3.527\exp(k^{1.5})$	$3.014 - 2.028/\sqrt{\varphi}$
-0.001	$-0.001(\beta^2 + 1 - 2\beta) + 2\beta - 1$	$9.669 - 7.043\exp(k^{2.5})$	$2.649 - 2.201/\varphi$

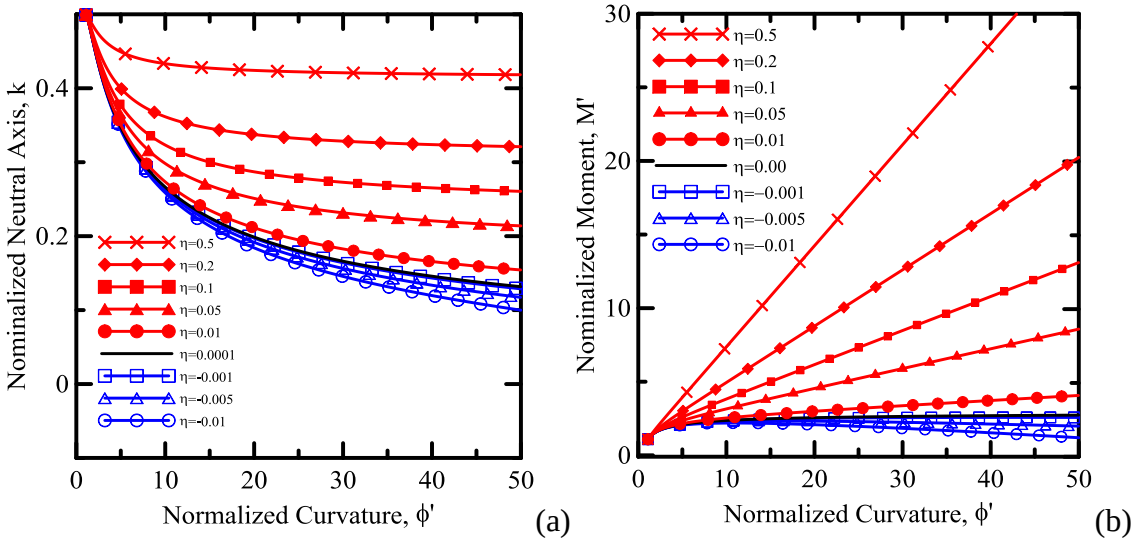

Figure 50. Effect of a) Depth of Neutral axis on the Moment capacity of a section and b) the moment-curvature response in the Range 2.1

The same approach can be used for other stages as well. The results for stage 3.1 of Table 7, linear-elastic compression ($0 < \lambda < \omega$) and non-linear tensile (residual strength) response ($\alpha < \beta \le \beta_{tu}$), are presented here. The general solution presented in

Table 7 can be simplified as follows. The location of the neutral axis represented as a function of applied tensile strain β is represented as:

$$k_{31} = \frac{\sqrt{A_{31}}}{\sqrt{A_{31}} + \beta\sqrt{\gamma}} \qquad A_{31} = \eta(\alpha^2 + 1 - 2\alpha) + 2\mu(\beta - \alpha) + 2\alpha - 1 \tag{41}$$

At stage 3.1, η, α and μ can be related to each other using this equation

$$\eta = \frac{\mu - 1}{\alpha - 1} \tag{42}$$

Therefore, instead of η, it is possible to do the calculation as a function of μ. This equation can be easily simplified by assuming the tension and compression stiffnesses as the same ($\gamma = 1$). Furthermore, for an elastic perfectly plastic tension material ($\eta = 0$ and $\mu = 1$) the equation reduces to:

$$k_{31} = \frac{\sqrt{2\beta - 1}}{\sqrt{2\beta - 1} + \beta} \tag{43}$$

This equation found to be as same as Eq. (40) at stage 2.1, assuming an elastic perfectly plastic tensile response. The values for α can be various, ranging from 17 to 160 for different sets of tests in this research. Table 9 presents the case of ($\gamma = 1$ and $\alpha = 51$, a general value for UHPC material), for different values of post-crack stiffness $\mu =$ 1.00, 0.67, 0.33, and 0.00. β_{tu} is assumed to be equal to 200.

$$A_{31} = 2\mu\beta - 52\mu + 51 \tag{44}$$

Note that the neutral axis is a function β and can be used in the calculation of the moment, or the moment-curvature relationship. This general response is shown in Figure 51 and

shows that with an increase in applied tensile strain, the neutral axis compression zone decreases, however, this decrease is a function of the post-crack tensile stiffness factor. The moment-curvature relationship in this range is descending, however, its rate is a function of the post-crack tensile stiffness. The parameter based fit equations in the third and fourth column are obtained by curve fitting the simulated response from the closed form derivations and are applicable within 1% accuracy of the closed form results. Using these equations, one can generate the moment capacity and moment-curvature response for any cross section using basic tensile material parameters in the range 3.1 as defined in Table 9.

Table 9. Location of the neutral axis, moment, and moment-curvature response of a composite material with $\gamma = 1$, $\alpha = 51$ and $\mu = 0.00$- 1.00.

μ	A_{31}, ($k_{31} = \frac{\sqrt{A_{31}}}{\sqrt{A_{31}} + \beta}$)	$M'(k)$	$M'(\varphi)$
1.00	$2\beta - 1$	$5.041 - 2.038\exp(k)$	$-4.736 + 1.752\exp(\varphi^{-0.5})$
0.67	$1.34\beta + 16.16$	$-2347 + 2349\exp(k^5)$	$-5362 + 5364\exp(\varphi^{-3})$
0.33	$0.66\beta + 33.84$	$-227.9 + 228.9\exp(k^3)$	$-519.7 + 520.7\exp(\varphi^{-2})$
0.00	51	$-65.86 + 65.86\exp(k^2)$	$-844.7 + 844.7\exp(\varphi^{-2})$

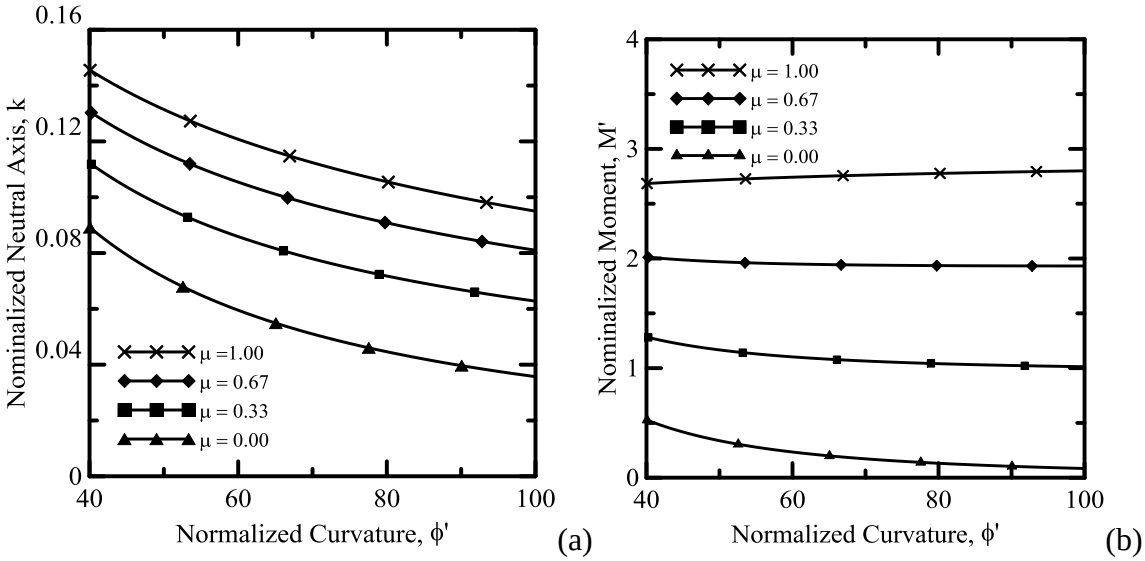

Figure 51. Effect of a) Depth of Neutral axis on the Moment capacity of a section and b) the moment-curvature response in the Range 2.1.

In this range (i.e., 3.1), the normalized moments and curvatures are a function of β, α, and μ. If the value for β being set on a specific value, desirable for design proposes based on the current codes for concrete design, then the moment and curvature values can be obtained for different values of α and μ. Figure 52 demonstrates a 3D plot of moment and curvature diagrams assuming that $\beta = \beta_{tu} = 50$. It can be observed that as the amount of μ and α increases the bending capacity of the section increases as well. Furthermore, there is a singularity in the curvature at $\mu = 0$ and $\alpha = 0$ that is due to the fact that at this point there is not any post-cracking response and therefore the bending capacity of the section at range 3.1 is equal to zero. The same plots can be achieved for other β values.

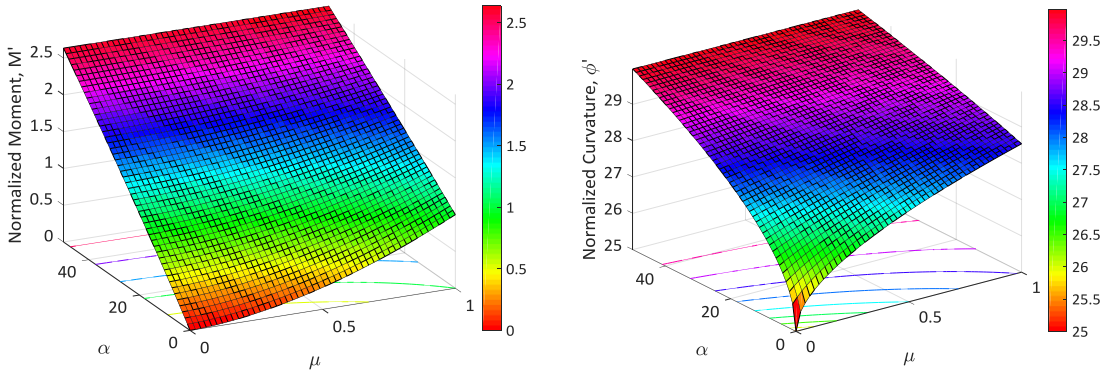

Figure 52. 3D plot of the moment and curvature diagrams ($\lambda = 1, \omega = 30$, and $\beta = \beta_{tu} = 50$).

It is also possible to do the same calculations for stages 2.2 and 3.2, for the plastic compression, but since the design of the sections is based on the assumption that there is no brittle failure there is no need to do this calculation for design proposes. A general derivation of all potential combinations for the interaction of tensile and compressive response is presented in [8]. Figure 53 illustrates the superimposed results from each range (i.e., ranges 1, 2-1, and 3-1) and the final simulated moment-curvature diagram. This figure clearly shows that as the curvature (and therefore the strain in the lower fiber of the section, β) increases, the calculated moment moves from one range to another one. It is to mention that the compressive failure is unlikely in the FRC sections and as a result, the ranges 2-2 and 3-2 are inactive in this case. However, for the HRC sections, the occurrence of the compressive failure is possible. This will be discussed in the section for the HRC section.

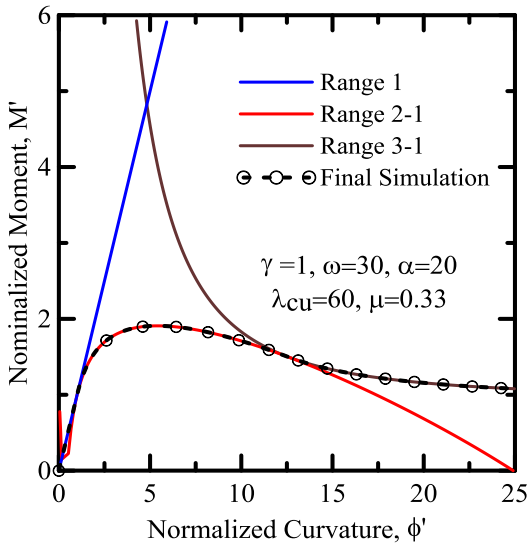

Figure 53. Superimposed responses of each range and the final simulated moment-curvature diagram.

The ultimate bending capacity of the section (i.e., M_{∞} when the section passes the maximum capacity and undergoes high strain levels) is a function of residual strength and can be obtained using Eq. (47) for FRC section (without rebar) or Eq. (54) for HRC section (with rebar), no matter the material has a strain-softening response (such as normal FRC) or a strain-hardening response (such as UHPC). It is noted that by taking this approach, in the strain-hardening type of response, we are ignoring the peak response, after crack and before reaching the residual strength. For strain softening type of response, clearly, there is not such a peak response after crack happening, and the section goes directly to the residual strength stage. This approach is used in the Ultimate Limit approach for the section design, which will be presented in the next section.

Figure 54 illustrates the effect of parameters μ and β on the normalized moment and curvature diagrams. The results of parametric studies of the normalized moment and curvature

diagrams as a function of normalized tensile strain, β, for different levels of post-crack tensile strength (residual strength) parameter, μ. It shows that as the residual tensile strength increases from the brittle response ($\mu = 0.0$) to ductile response ($\mu = 1.0$), the moment and bending capacity of the section increases as well. From these curves, the normalized value for the moment and curvature can be obtained, at a specific tensile strain. Noted that for $\mu = 0.33$, which is extremely closed to the critical residual tensile strength, $\mu_{crit} = 0.34$, the flexural response is virtually perfectly-plastic; and beyond this value, the flexural response shifts from strain-softening to strain hardening response.

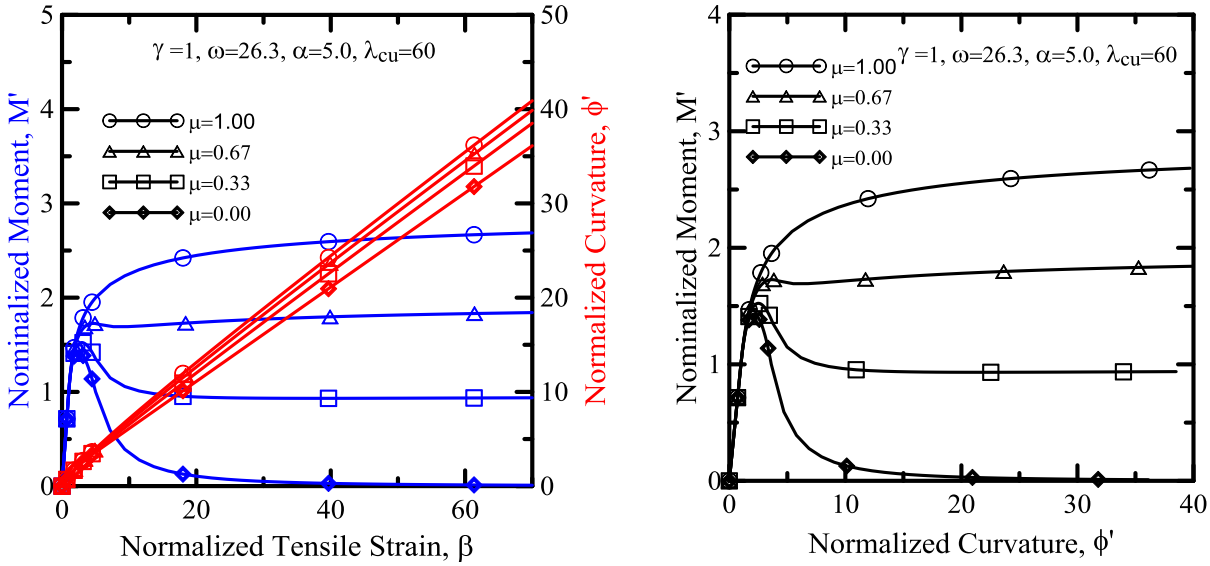

Figure 54. Parametric studies of the normalized moment and curvature diagrams as a function of normalized tensile strain, β, for different levels of post-crack tensile strength (residual strength) parameter, μ.

Figure 55 shows a parametric study on the effect of the parameter α on the moment-curvature response of the section. It is found that as the α parameter increases, the response of the section becomes closer to an elastic perfectly plastic type of the response.

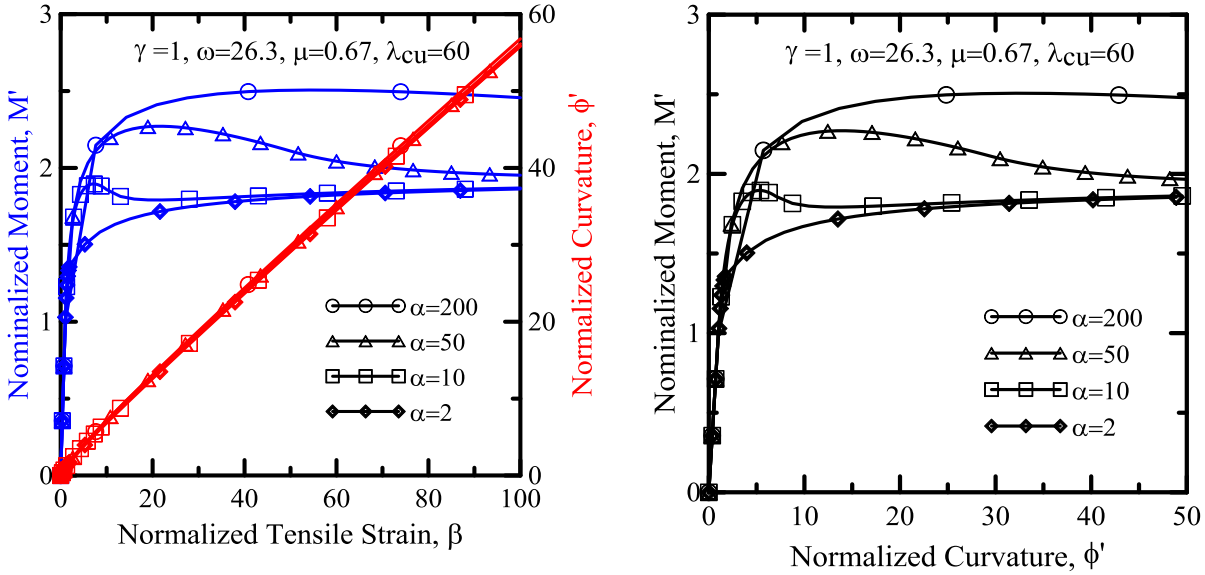

Figure 55. Parametric studies of the normalized moment and curvature diagrams as a function of normalized tensile strain, β, for different levels of α parameter.

2.5 Load Deflection Computation

Moment-curvature diagrams are calculated for the sections depending on the number and interaction of flexural stages (see Figure 56). For any given curvature, the lowest magnitude of the moment from the stages was selected as the governing load, which would allow the transition from one loading stage to the other. The final moment-curvature diagram is a composite of the several interacting flexural stages. To have a load-deflection response for a beam element, it is necessary to have the moment-curvature response for various sections (elements) along the beam

length and then calculate the deflection using moment-area method or direct integration. For a statically determinate simply supported beam, equilibrium is used to obtain support reactions and moment distribution along the length of the beam directly from the applied forces. Using the moment-curvature distribution, this response is converted to the curvature distribution along the length using a look-up table.

The slope and deflection distributions along the length of the beam are obtained by applying the slope-deflection method to the curvature distribution. The strain at the tensile fiber is increased incrementally at a control point such as the midpoint and used to establish the curvature distribution, which is in turn used to calculate both moment distributions used in the deflection computation [7].

Figure 56 and Figure 57 show the typical moment-curvature diagram for the four-point bending test and the moment distribution along the beam length. The three depicted patterns of curvature distribution are needed in the derivations for the mid-span deflection. Figure 57(a) shows the curvature distribution before cracking (Stage A). After cracking (stages B and C), as the post-crack curvature increases, the moment continues to increase as shown by the red line in Figure 57(b). At stage B, after reaching the maximum loading, the moment cannot go higher than the maximum bending capacity; thus it decreases at the levels below the maximum moment. At this point, two type of responses are possible, depend on the location of the section along the axis. If the section is located in the non-localized length, (L_n) crack will be closed during the unloading (Stage C1), but if the section is located on the localized length (L_l) the crack opening will continue (Stage C2). The same approach can be taken for 3PB tests and another type of RC sections as well [7], [67].

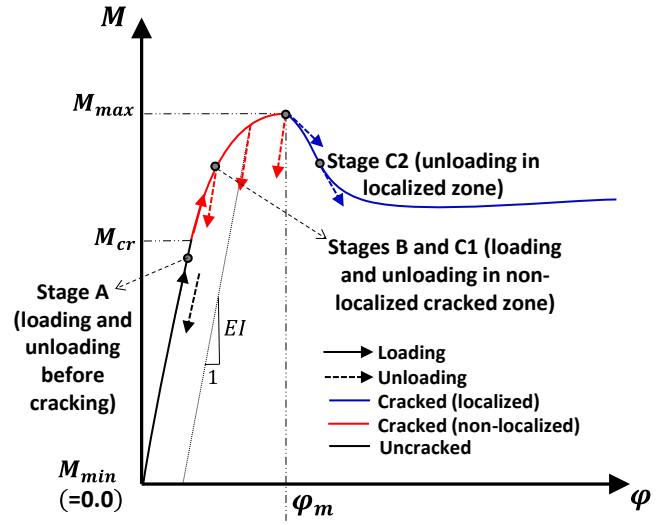

Figure 56. Generalized M-C diagram; during different stages of loading and unloading.

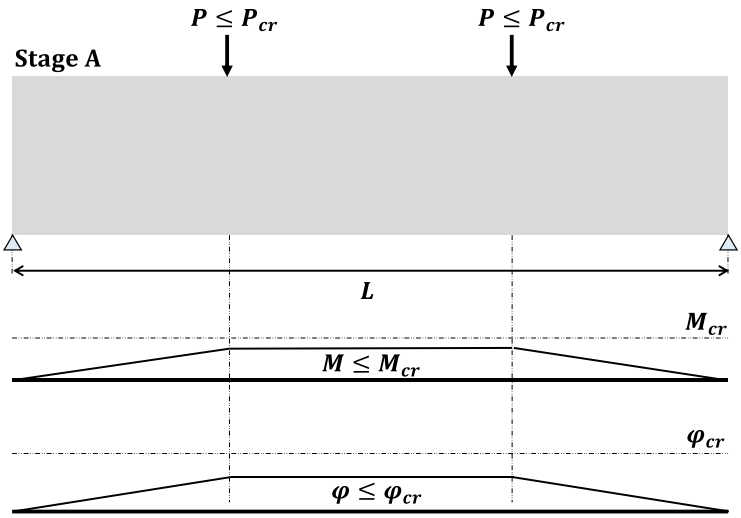

(a)

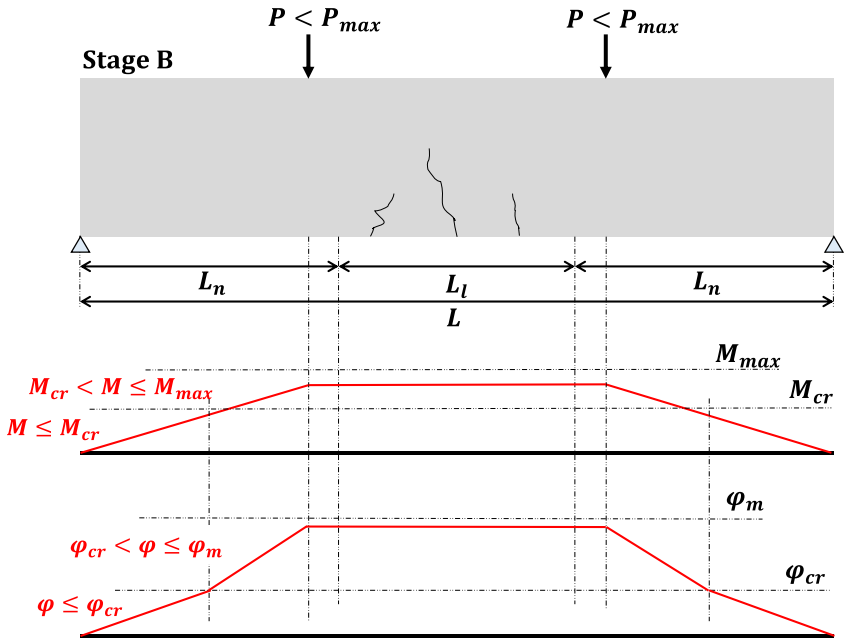

(b)

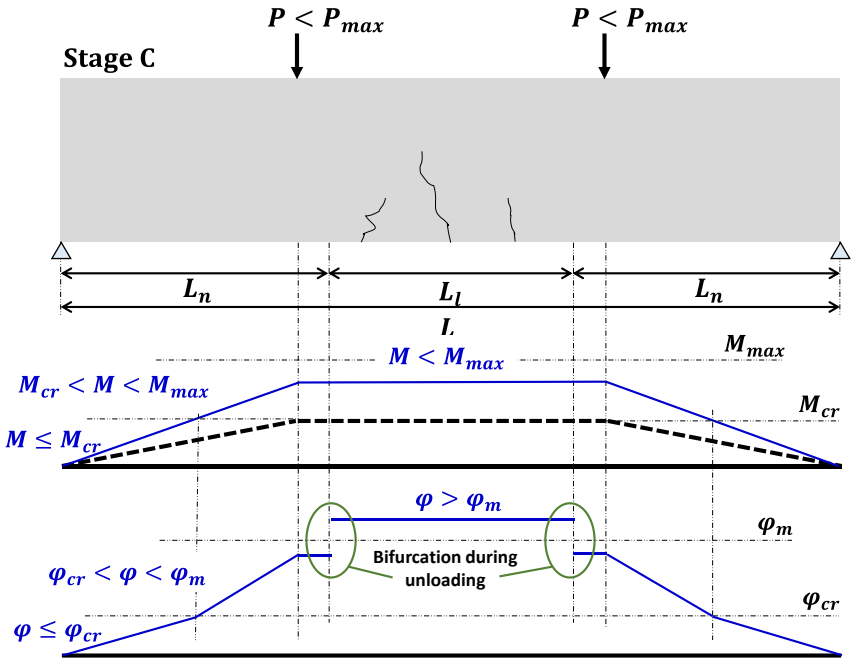

(c)

Figure 57. Moment and curvature distribution in FRC beams at different stages: (a) Stage A: un-cracked section; (b) Stages B: cracked beam, loading at localized and non-localized zones; (c) Stages C: cracked beam, unloading at localized and non-localized zones.

The procedures for the calculation of the load-deflection are described in detail in earlier publications [7], [54], [65].

2.6 Applications of the FRC constitutive model

2.6.1 Computation of Material Tensile Property Using Inverse Analysis

In this section, an inverse analysis procedure is used in order to obtain the basic tensile material properties from the experimental tests. Using this approach, one can obtain design parameters from experiments and simulate the flexural response of any member by starting from a known or back-calculated tensile and compressive constitutive model. This approach enables us to simulate the responses of various specimens in the context of load-deflection. Using the procedures that have been developed in ACI4544-8R [64, p. 544] [65] it is will be possible to obtain a model fit to the experimental data. The output of the model is the material property values. Material properties obtained from this model can be used in finite element analysis (FEA), structural design or any other type of numerical analysis method.

The experimental results of the current research were exhibited in the previous section. In this section, only the comparative simulation results and the back-calculated parameters are given in the following figures. Furthermore, the average of the back-calculated parameters for each set of tests is listed in Table 10.

The first step for the inverse analysis is to import the experimental data as two columns representing the load and deflection experimental results. This is followed by the values for the beam dimensions and the test method (3PB or 4PB). There is also an Excel spreadsheet developed for this purpose which can be found on ACI web site [65].

We start the simulation by fitting the initial linear response with the linear part of the experimental results by only changing Young's modulus parameter to obtain the best fit for Young's modulus of the linear elastic phase. This done by increasing or decreasing the value of the Elastic modulus (Young's modulus) *E*. Normal FRC has a Young's modulus in the range of 3000-5000 ksi (20-35 GPa), however, for UHPC this value can be as high as 9400 ksi (65 GPa).

Next, the value of first crack strain ε_{cr} is chosen to fit the approximate point where the linear elastic behavior ceases and non-linear behavior begins. This parameter depends on the type of FRC being tested, the first crack flexural strength of the sample, the fiber type and fiber dosage all contribute to the point where cracking is observed. In this research, a range between 100 and 170 microstrains was used. The next step is to address the post-peak response of the section. The post cracking slope for strain hardening is represented by E_{cr} which is normalized by the parameter η. This parameter is dependent on the values of α and μ through below equation, after some manipulations on Eqs.(3) to (5) (also see Figure 42).

$$\eta = \frac{E_{cr}}{E} = -\frac{(1-\mu)}{(\alpha-1)} \tag{45}$$

By manipulating α and μ the post-cracking slope can be fitted to the load-deflection curve. The parameter α adjusts the horizontal location of the transition point, while μ adjusts the vertical position of the transition point and the vertical position of the tail of the curve. Increasing μ will raise the post-crack residual portion of the simulated curve. The parameter η is automatically calculated per Eq. (45) and should reflect the post-crack slope, as negative in the softening case and/or positive in the hardening case. Both responses have been observed for UHPC samples with 1 percent (strain-softening) and 3 percent (strain-hardening) fiber content.

The relationship between the parameters α and μ have other effects on the shape of the simulated curve. Changes made in ε_{cr} will also require changes to the parameters α and μ to realign the simulation curve. Parameter β_{tu} depends on the user's preference on the termination point of the simulation curve. In some cases, the entire deflection curve is not necessary, so appropriate adjustments can be made.

Figure 58 represents the effect of fiber content on large UHPC specimens (4" × 4" × 16") tested after 28 days of curing. Note that the capacity of the section increases significantly from 1% to 3% of fibers. The post-peak response also remains at the same elevated level for a large range of displacements. With a residual strength of at around 970 psi after 3 mm of deflection, samples with 3% fibers have as much as twice the residual strength of the 1% fiber samples. The simulated tensile curve for these specimens shows that the strain softening response at the V_f=1% content is now replaced with strain hardening level.

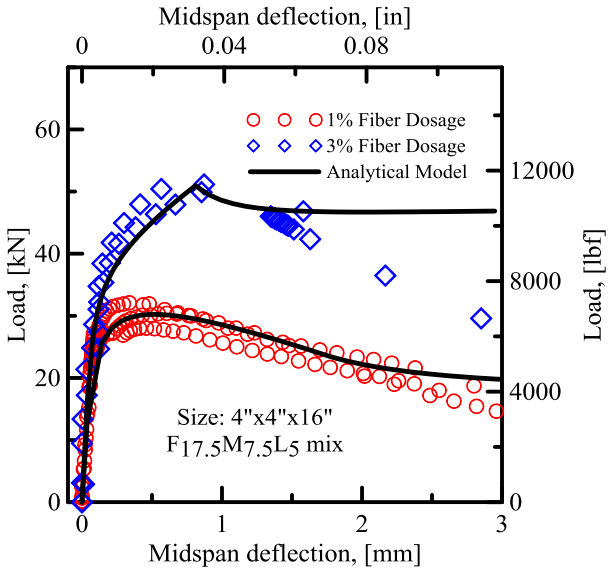

(a)

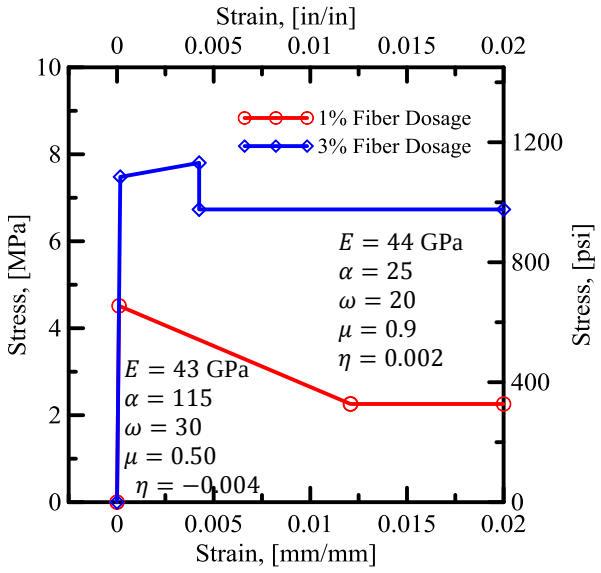

(b)

Figure 58. Effect of fiber volume fraction, large beam after 28 days curing: (a) load-deflection curves; (b) stress-strain diagrams.

The first crack strength of beams with 3% fiber content is about 1100 psi (7.5 MPa) which is significantly higher than the first crack strength of 650 psi (4.5 MPa) for the beams with 1% fiber content. On the other hand, the residual strength of the section, in samples with 3% fiber content is three times higher than that in the samples with 1% fiber content (it shows an increase from 320 to 987 psi). The slope of the post-crack transition zone, after crack and before stable residual strength, is a negative value for strain softening and positive for strain hardening. The back-calculated parameters are also presented in Figure 58. The same approach has been chosen for other sets of data in the experimental program. The average of all back-calculated parameters for each set of analysis is listed in Table 10.

Figure 59 represents the effect of mix design for the two mixtures of ML and FML on large size specimens ($4" \times 4" \times 16"$) tested after 28 days of curing, Note that the flexural capacity of the material FML is higher than the ML mixtures. This is due to the better interaction between the matrix and fibers, however, both these systems are close to one another from a general response point of view. The tension back-calculation responses are similar to a strain softening response simulating both samples. A tensile strength of 625 psi and 790 psi and a nominal residual strength of approximately 400 to 380 psi are obtained for FML and ML mixtures respectively.

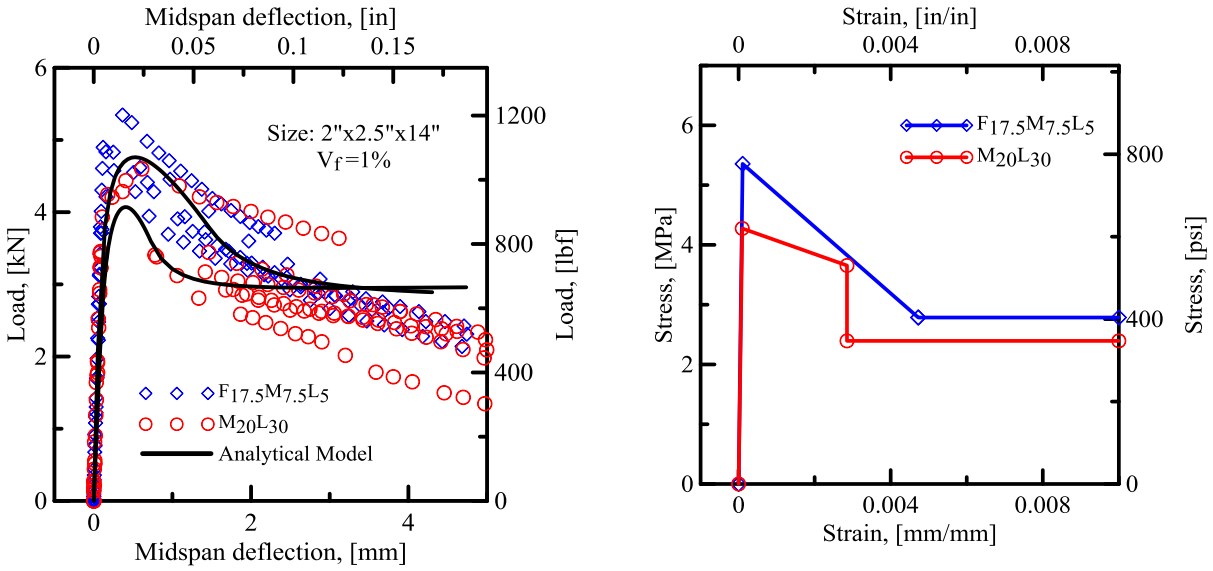

Figure 59. Effect of mix design on the flexure response and tensile stress-strain.

Effect of mixing method is shown in Figure 60, Note that the two samples selected as representatives are quite close to the overall samples. If we choose the two similar samples, it is observed that the tensile responses also fall into a similar category, i.e., strain-softening, with an almost similar tensile response. In practice, one can fit the curves independently and report all of the data, or attempt to fit a representative simulation to the collection of all experimental data.

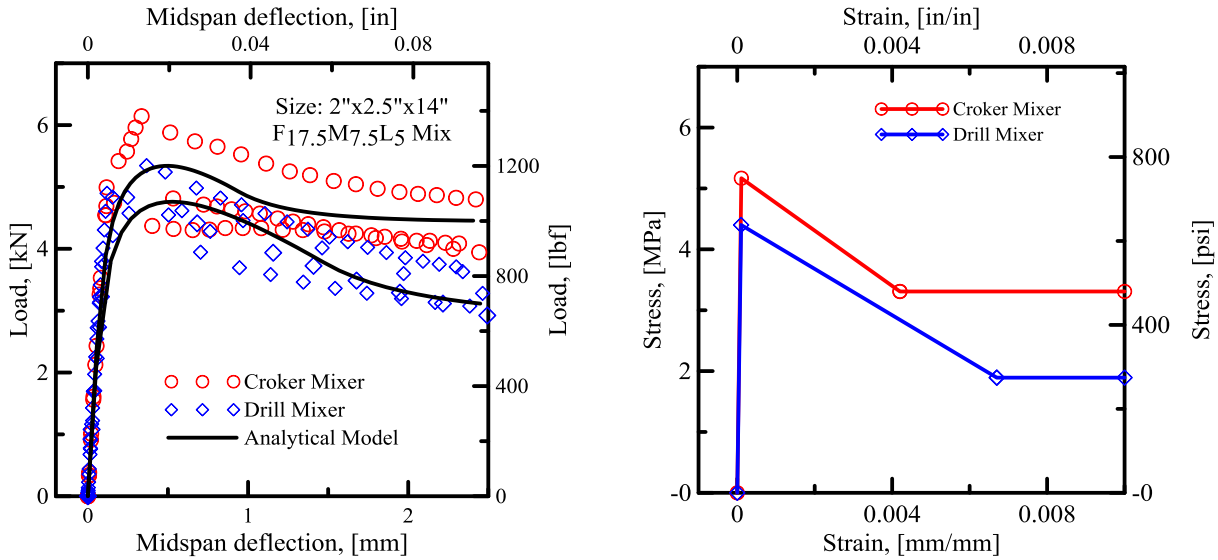

Figure 60. Effect of mixing method.

Effect of specimen size is shown in Figure 61. Note that while the geometry of the two samples is different the proposed procedure uses a rather constant stress-strain response in the post-cracking stage in order to simulate the load deflection results. It is also noted that the post-cracking residual stress for the large beam samples is higher than the smaller beams. This may be attributed to the small size beam not having sufficient depth for the growth of the crack and full activation of all the fibers in the path of the crack before the crack reaches the full depth of the beam. The size effect is therefore shown in this figure as a dominant response and larger specimens, therefore, yield more accurate results.

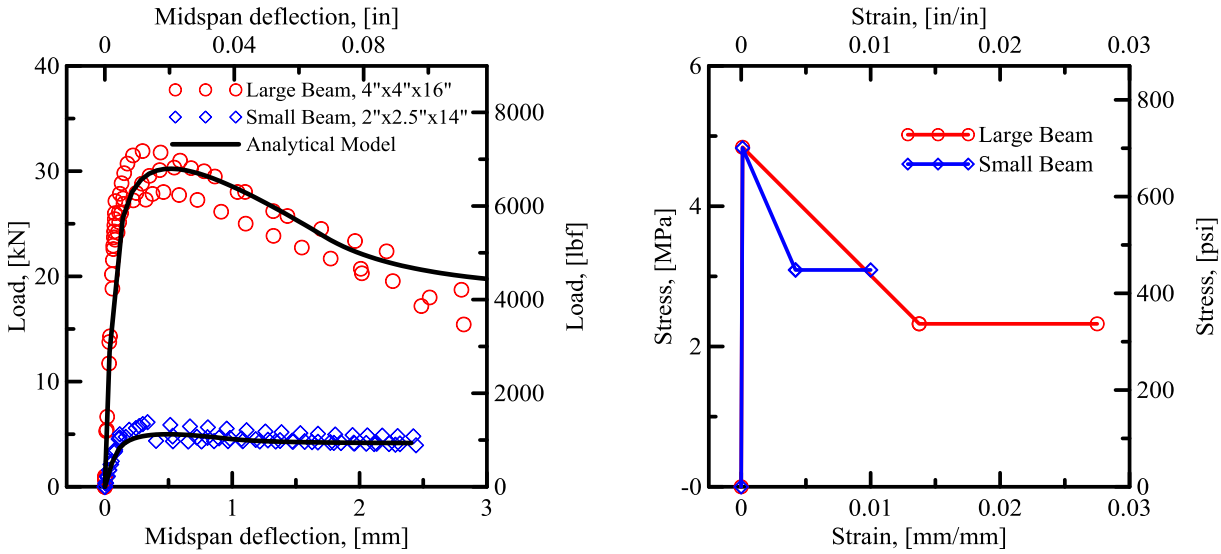

Figure 61. Size effect (2x2.5x14in beams vs. 4x4x16in beams).

Effect of curing on the large and small beams are shown in Figure 62 and Figure 63. Note that in both these cases increasing the curing period increases the strength and ductility significantly. The larger beams show a strength measure that is of the same order to magnitude obtained from the smaller beams. While in the small beams, increasing the curing period increases the tensile strength and residual strength by 60% and 50% respectively, in the large beam this increase is around 10% for both tensile and residual strengths.

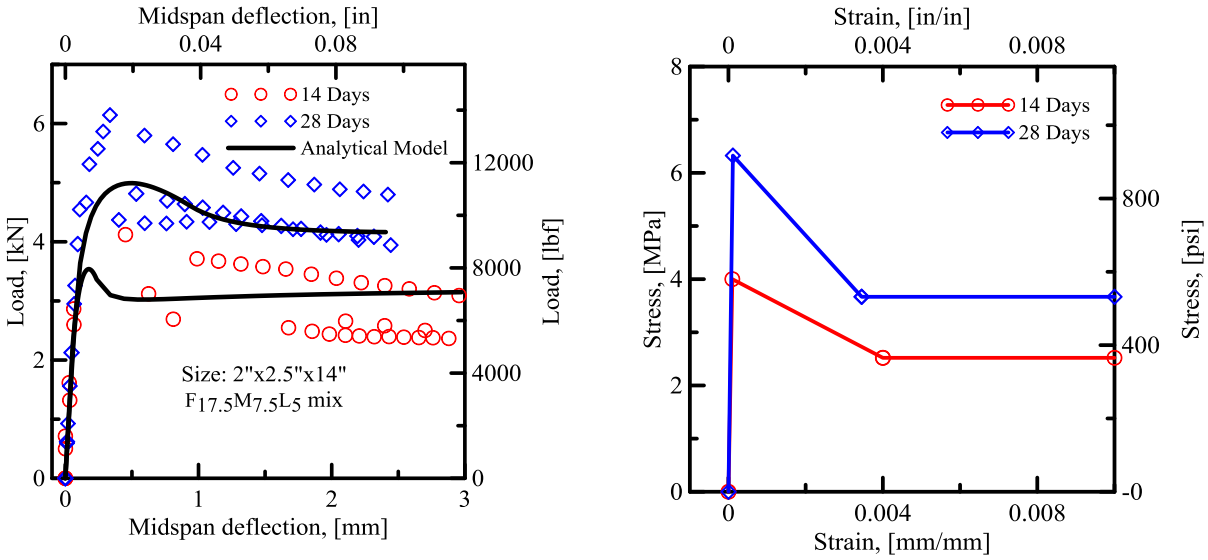

Figure 62. Effect of curing period on small beams (2x2.5x14in).

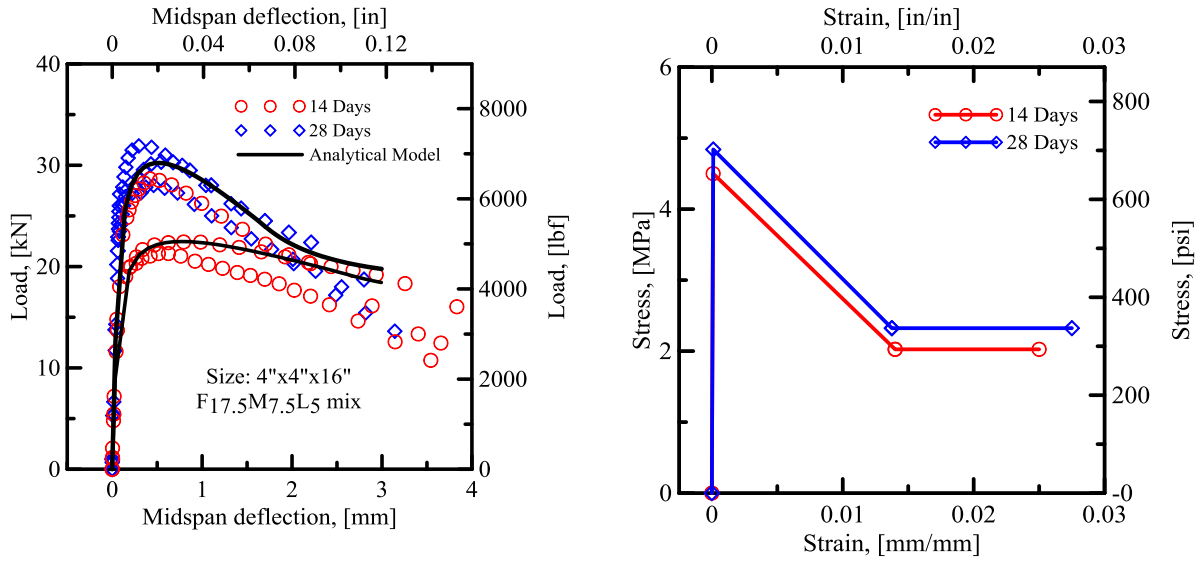

Figure 63. Effect of curing period on large beams (4x4x16in).

A summary of all the back-calculated parameters is presented in Table 10.

Table 10. Average of inverse analysis parameters for each set of tests according to Soranakom and Mobasher, 2008 [1].

Test Set	Beam Series	No. of Replicates	Elastic Modulus, E (ksi)	Cracking Tensile Strain εcr (micro-strain)	Cracking Strength (psi)	α, Transition Strain/ Cracking Strain	γ, Normalized compressive modulus	ω, Normalized Compressive Yield Strain	η, Modulus Ratio	μ, Normalized Residual Tensile Strength	β_{tu}, Normalized Tensile Strain	Compressive Strength (ksi)
1	ML_S_0_28_4PB_D	3	6346.9 (±229.4)	99 (±6.7)	628 (±65)	--	--	--	--	--	--	17.4 (±0.7)
2	ML_S_1_28_4PB_D	6	6599.2 (±177.6)	100 (±8.4)	660 (±68)	17 (±8)	0.98 (±0.04)	30.3 (±1.4)	-0.025 (±0.025)	0.51 (±0.07)	197 (±45)	19.6 (±0.7)
3	FML_S_0_28_4PB_D	6	6425.5 (±391.0)	91 (±3.7)	585 (±61)	--	--	--	--	--	--	20.2 (±0.8)
4	FML_S_1_28_4PB_D	6	6787.8 (±402.5)	98 (±4.4)	665 (±64)	64 (±11)	0.96 (±0.05)	32.6 (±1.1)	-0.009 (±0.0013)	0.46 (±0.04)	218 (±61)	20.8 (±1.0)
5	FML_S_1_14_4PB_C	3	6284.9 (±509.4)	100 (±0.1)	628 (±51)	17 (±11)	1.00 (±0.01)	28.4 (±0.1)	-0.037 (±0.039)	0.53 (±0.12)	163 (±12)	17.6 (±1.4)
6	FML_S_1_28_4PB_C	3	7203.6 (±685.4)	110 (±9.0)	792 (±121)	25 (±18)	1.0 (±0.01)	30.0 (±0.1)	-0.012 (±0.004)	0.63 (±0.05)	127 (±12)	22.0 (±3.6)
7	FML_L_3_28_4PB_C	3	6381.7 (±98.9)	170 (±0.1)	1084 (±11)	33 (±11)	1.0 (±0.01)	20.6 (±0.8)	0.002 (±0.0002)	0.85 (±0.07)	250 (±1)	21.8 (±0.1)
8	FML_L_1_14_4PB_C	3	5463.1 (±921.1)	100 (±0.1)	546 (±92)	160 (±53)	1.0 (±0.01)	29.3 (±1.2)	-0.003 (±0.001)	0.55 (±0.09)	263 (±23)	16.0 (±3.1)
9	FML_L_1_28_4PB_C	3	6526.7 (±383.7)	110 (±0.9)	707 (±55)	110 (±18)	1.0 (±0.01)	30.0 (±0.1)	-0.005 (±0.001)	0.48 (±0.03)	250 (±1)	21.2 (±1.7)

2.7 Comparison with other experimental results

The back-calculation procedure was applied to experimental flexural results of UHPC mixtures conducted by our research colleagues and partners using mixtures developed at Missouri Science and Technology University. Meng et al. [68], tested UHPC beams with a dimension of 400x75x75 mm (16x3x3 inch). These were notched specimens and the test results were in accordance with JCI method [69]. Effect of notch-to-depth ratio was evaluated at a level of N/D= 1/6 corresponding to the notch depth of 12.5 mm (1/2 inch) [70]. Using a constant rate of the mid-span deflection as the control parameter, loading rates ranging from 0.05 mm/min (0.002 inch/min) to 5.00 mm/min (0.2 inch/min) were used in accordance with available test methods [71]. Figure 64 shows the schematics of the testing system. Figure 64 compares the simulated and experimental flexural stress-deflection responses of the UHPC beams with different notch depths and loading rates.

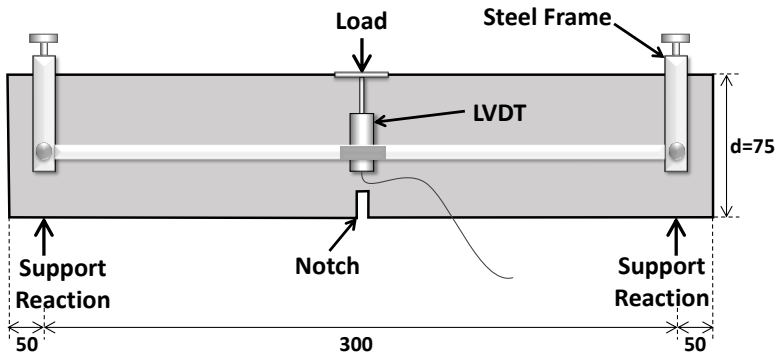

Figure 64. Flexural test setup and notched beam specimen. Unit: mm, [68].

The two tests are different because the stress and strain states in tension and bending are not the same. With a tensile test, the maximum tensile stresses occur throughout the entire volume (and surface area) of the test piece; in bending (where the

sample sees tensile stress above the neutral axis and compressive stresses below), the maximum tensile stresses are conversely concentrated in a small region on the top surface above the neutral axis. Accordingly, for similarly sized test pieces, the tensile sample sees the maximum stresses throughout its entire gauge length, i.e., over a much larger volume than the corresponding bend sample. In brittle materials which are highly sensitive to the defect population, this change in statistical sampling volume means that strength and fracture properties measured in tensile tests are likely to be somewhat lower than the corresponding properties measured in bending because there is a higher statistical probability of finding a larger defect.

The flexural strength would be the same as the tensile strength if the material were homogeneous. In fact, most materials have small or large defects in them which act to concentrate the stresses locally, effectively causing a localized weakness. When a material is bent only the extreme fibers are at the largest stress so, if those fibers are free from defects, the flexural strength will be controlled by the strength of those intact 'fibers'. However, if the same material was subjected to only tensile forces then all the fibers in the material are at the same stress and failure will initiate when the weakest fiber reaches its limiting tensile stress. Therefore, it is common for flexural strengths to be higher than tensile strengths for the same material. Conversely, a homogeneous material with defects only on its surfaces (e.g., due to scratches) might have a higher tensile strength than flexural strength.

2.8 Development of Ultimate Limit State Design Procedures for UHPC

In this section, we use the original closed-form derivations discussed at the beginning of the section, and use them as a basis for the design of the UHPC beam sections.

The ultimate bending capacity of the section can be used in a design approach based on the ultimate limit state ($\beta = \beta_{tu}$). A minimum number of parameters for use in this model are three which include: the ratio of compressive to tensile strength, ω the post-crack tensile residual strength, $\mu\sigma_{cr}$ and the allowable compressive or tensile strain from a serviceability point of view ($\beta_{tu}\varepsilon_{cr}$). The parameters for the constitutive models are obtained from either ASTM C1609/C1609M or BS EN 14651:2005 based on the recommendations of a parametric design method as discussed in (ACI 544.8R-16, 2016).

The solution for the plain fiber reinforced concrete section is presented first for the case in Figure 47 specified by a cracked section under tension and the maximum compressive strain at the elastic-plastic compression zone. For the given applied strain distribution, the location of neutral axis is assumed as *kd* and the using the strain and stress profile across the section, the force equilibrium equation obtained. The neutral axis depth *k* is found by solving the equilibrium of net internal forces, or $F_s + F_{c1} + F_{c2} + F_{t1} + F_{t2} = 0$ representing the forces due to internal stresses. As defined for a specified serviceability limit for maximum allowable compressive strain, compressive strain cannot be more than compression yield strain, $0 < \lambda \le \omega$ and $\beta = \beta_{tu}$, therefore the neutral axis depth is obtained as (stage 3.1):

$$k = \frac{\mu + \beta_{tu}\left(-2\mu + \sqrt{\mu(2\beta_{tu} - 1)}\right)}{\beta_{tu}^{\,2} - 2\mu\beta_{tu} + \mu} \tag{46}$$

Eq. (46) is for the plain FRC section. The full derivation for a hybrid reinforced case is presented by Mobasher et al. (2015). A brief summary of their procedure will be presented in the next section. The magnitude of the moment M_n is obtained by taking the first moment of internal forces about the neutral axis, $M_n = F_{c1}y_{c1} + F_{c2}y_{c2} + F_{t1}y_{t1} + F_{t2}y_{t2}$, calculated as shown in Eqs. (47) and (48) as

$$M_n = \left(\frac{\left(3\mu\beta_{tu}^{\,2} - \mu - 2\beta_{tu}^{\,3}\right)k^3 + \left(3\mu - 9\mu\beta_{tu}^{\,2}\right)k^2 + \left(9\mu\beta_{tu}^{\,2} - 3\mu\right)k - 3\mu\beta_{tu}^{\,2} + \mu}{\left(k-1\right)\beta_{tu}^{\,2}} \right) M_{cr} \tag{47}$$

where

$$M_{cr} = \frac{\sigma_{cr} bh^2}{6} \tag{48}$$

If one conducts an asymptotic analysis to compute the moment capacity in the limit case, a simplified design equation for normalized moment capacity is obtained. This resembles a case when the cracked section in flexure opens significantly to go beyond serviceability limit, however, due to the presence of fibers, the section can still transmit the flexural load applied. The moment capacity, in this case, is defined by the limit case of compressive cracking strain λ_{cu} reaching a relatively large number (Soranakom and Mobasher 2009, [3]). In order to simplify the calculation of several specified moments, one can compute the neutral axis parameter k_∞, by substituting $\lambda_{cu} = \infty$, to obtain the normalized moment at very large strains, m_∞ as shown in Eq.(49). The equation for ultimate moment capacity is derived by substituting m_∞ for m_{cu}. Thus, the design equation for nominal moment capacity M_n is expressed in Eq.(49).

$$k_\infty = \lim_{\lambda \to \infty} k = 0, \qquad m_\infty = 3\mu, \qquad M_n = m_\infty M_{cr} = 3\mu M_{cr} \tag{49}$$

The limit between the strain-hardening and strain-softening response of the section can be achieved by putting m_∞ equal to the normalized cracking moment ($m_\infty = 1$). Rewriting equation (49) will give the critical value for the residual tensile strength, μ_{crit}.

$$\mu_{crit} = \frac{1}{3} \tag{50}$$

The LRFD basis for the ultimate strength design is based on the reduced nominal moment capacity $\phi_p M_n$ exceeding the ultimate demand moment M_u ($\phi_p M_n \geq M_u$) which is determined by linear elastic analysis using factored load coefficients according to ACI318 section 9.2 (ACI 318-14). A reduction factor ϕ_p is used to apply to the post-crack tensile strength, and the value ϕ_p = 0.75-0.9 has been tentatively used based on statistical analysis of limited test data in the earlier work. In order to further simplify Eq.(49), from the previous equations, an empirical relationship between tensile and compressive strength is used, i.e. $\sigma_{cr} = 6.7\sqrt{f_c'}$ in U.S. customary units (and $\sigma_{cr} = 0.56\sqrt{f_c'}$ in SI customary units). However, this relationship can be used only for normal concrete. FHWA [57] has suggested that the tensile strength of the UHPC is equivalent to 4% of its compressive strength, i.e., $\sigma_{cr} = 0.04 f_c'$. For typical fiber based system the residual strength of FRC in flexure is approximately three times its residual strength in tension, (Bakhshi et al. 2014, [72]). Based on the experiments in this research, this value for the UHPC material is 2.42 (see Figure 65).

$$f^{D}_{150} = 2.42\mu\sigma_{cr} \tag{51}$$

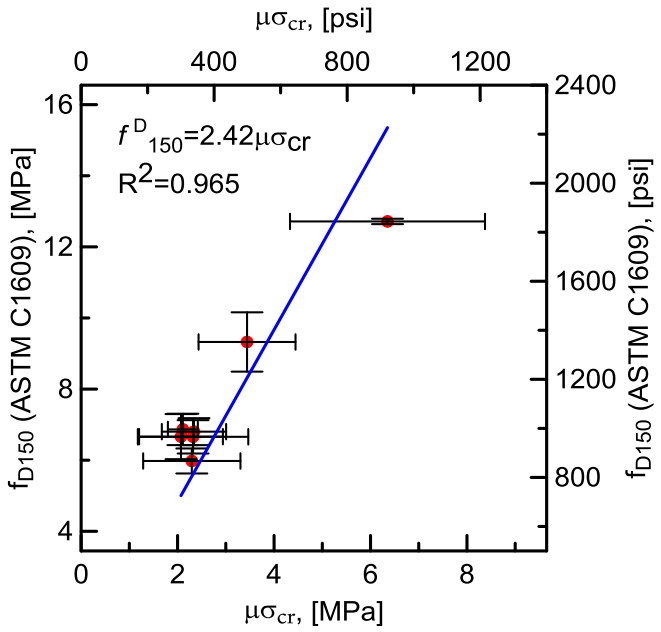

Figure 65. Comparison of residual strength ($\mu\sigma_{cr}$) with ASTM C1609 residual parameter. (f^{D}_{150}).

Substituting Eq.(51) into Eq.(49) , we have

$$M_n = \frac{3f^{D}_{150}}{2.42\sigma_{cr}} M_{cr} = \frac{31f^{D}_{150}}{f_c'} M_{cr} \tag{52}$$

However, these equations are estimations of the relationship between the experimentally obtained standard's parameters, such as $f_{eq,3}$ or f^{D}_{150}, and the normalized residual strength, μ. These equations are empirical relationships, and more accurate approach is to test the samples, based on the relevant standard, and then doing the back-calculations, according to ACI-544-8R, to get the accurate value of residual strength. A detailed approach for the back-calculation can be found in [3], [7], [54]. The same approach was done on the research performed by other groups and other experimental relationships were obtained as it is shown in Figure 66.

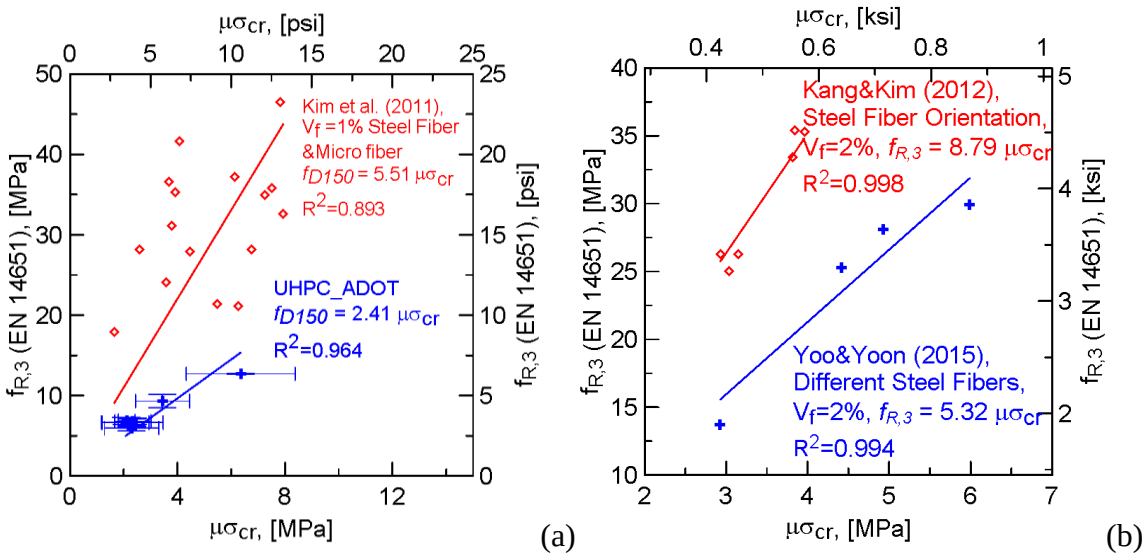

Figure 66. Correlation between residual strength ($\mu\sigma_{cr}$) with: (a) ASTM C1609 residual parameter (f^{D}_{150}); and (b) EN 14651 ($f_{R,3}$).

Using a Load and Resistance Factor Design (LRFD) approach, The nominal moment capacity of a flexural member M_n must be adjusted by a reduction factor to account for variability in materials and workmanship according to ACI-318 Sec. 9.2, [66], where ϕ_r is the reduction factor:

$$\phi_r M_n \geq M_u \tag{53}$$

2.9 Hybrid Reinforced Concrete (HRC) Beams

In a similar manner to the FRC section, closed form solutions are achievable at different stages of loading and deformation. All detailed derivations can be found in [54]. However, as an ultimate limit approach the ultimate moment capacity as a function of residual tensile strength and reinforcement (at $\beta = \beta_{tu}$) can be used as a convenient design tool for combinations of reinforcements, calculated as shown in Eq.(54).

$$M_n \approx m_\infty M_{cr} = \frac{6\rho_g n\kappa(\mu\alpha - \mu + \alpha\omega) + 3\omega\mu - 3(\rho_g n\kappa)^2}{\omega + \mu} M_{cr} \quad (54)$$

Figure 67 shows a design chart for the parametric design model with various grades of steel at the ultimate moment capacity. Flexural design using this chart requires ultimate moment M_u due to factored loads normalized with respect to cross-sectional geometry. The demand ultimate moment capacity M_u' is obtained from this chart used to select any combination of normalized residual tensile strength μ, grade of steel, and reinforcement ratio ρ_g that meets the demand for M_u'. It is shown that the moment capacity is strongly dependent on the amount of the reinforcement ratio. Results are scaled to numerical values using the section cracking moment M_{cr}. An Excel Spreadsheet has been developed as design guides for both the FRC and HRC and is available for use as well. (Mobasher et. al 2015 [54]).

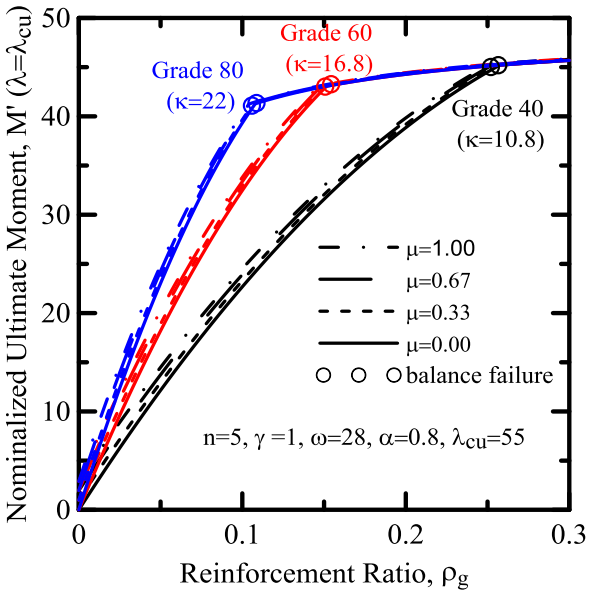

Figure 67. Design chart for normalized ultimate moment capacity (determined at $\lambda = \lambda_{cu}$) for different levels of post crack tensile strength μ and reinforcement ratio ρ_g (1 MPa=145 Psi) .

A parametric study is carried out on the effect of parameters μ and β on the normalized moment and curvature diagrams with two different values of reinforcement ratio, ρ_g . illustrates the results of the first set of simulations. In this set of simulation, it was assumed that the section has a ductile failure ($\rho_g \le \rho_{bal}$). For this purpose, a longitudinal set of steel rebars, Grade 60, with a ratio of 7% was chosen. Other parameters are same as the parameters that were used in Figure 67.

Figure 68 shows both the moment and curvature as a function of the tensile strain in the flexural concrete beam section. This figure demonstrates that residual tensile strength provides extra moment capacity for the section, however, it also increases the stiffness of the section. In fact, the fibers in FRC sections play the same role as the longitudinal reinforcements in ordinary RC sections.

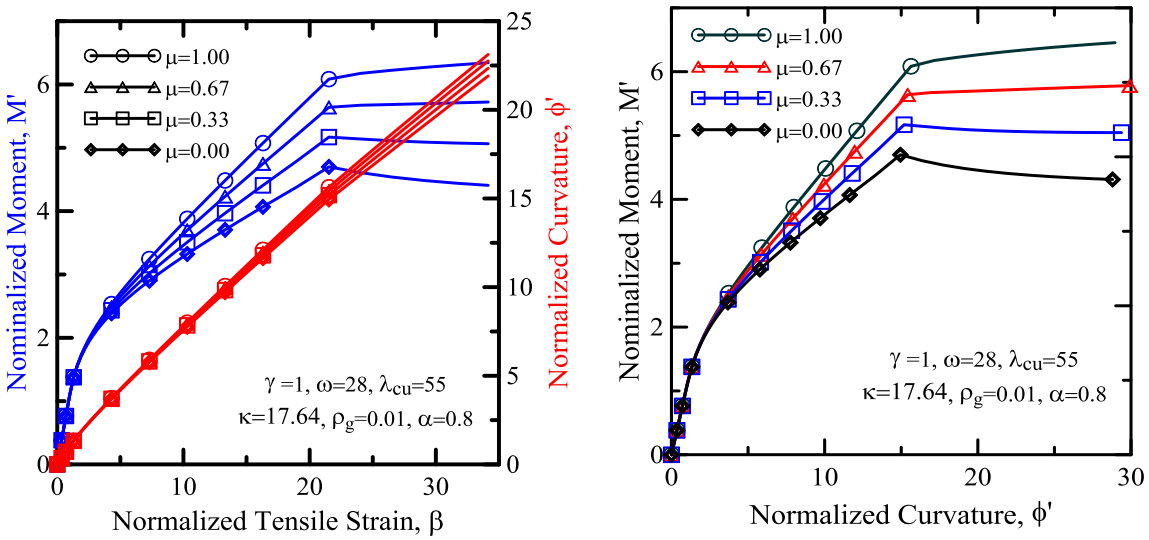

Figure 68. Parametric studies of the normalized moment and curvature diagrams as a function of normalized tensile strain, β , for different levels of post-crack tensile strength (residual strength) parameter, μ (with 1% longitudinal reinforcement, Steel rebar-Grade 60).

Figure 69 shows both the moment and the curvature as a function of the tensile strain in the lower fiber of the concrete section. This figure illustrates that residual tensile strength provides extra moment capacity for the section and increases the stiffness of the section as well. On the other hand, compared to a section with a decreased amount of longitudinal reinforcement (such as 1 percent or less), the effect of fibers in HRC sections with a higher amount of reinforcement is smaller.

Figure 70 shows the results of the other set of simulations. In this set, it was assumed that the section has a brittle failure ($\rho_g > \rho_{bal}$). For this purpose, a longitudinal set of steel rebars, grade 60 with a reinforcement ratio of 16 percent was chosen. Other parameters are the same as those used in Figure 67. A comparison between this figure and Figure 69 shows that, although the moment capacity of the section increases, the ductility decreases considerably, in such a way that the ultimate normalized curvature decreases from 31 to 22 (a 30 percent decrease) and the failure mode changes from ductile to brittle.

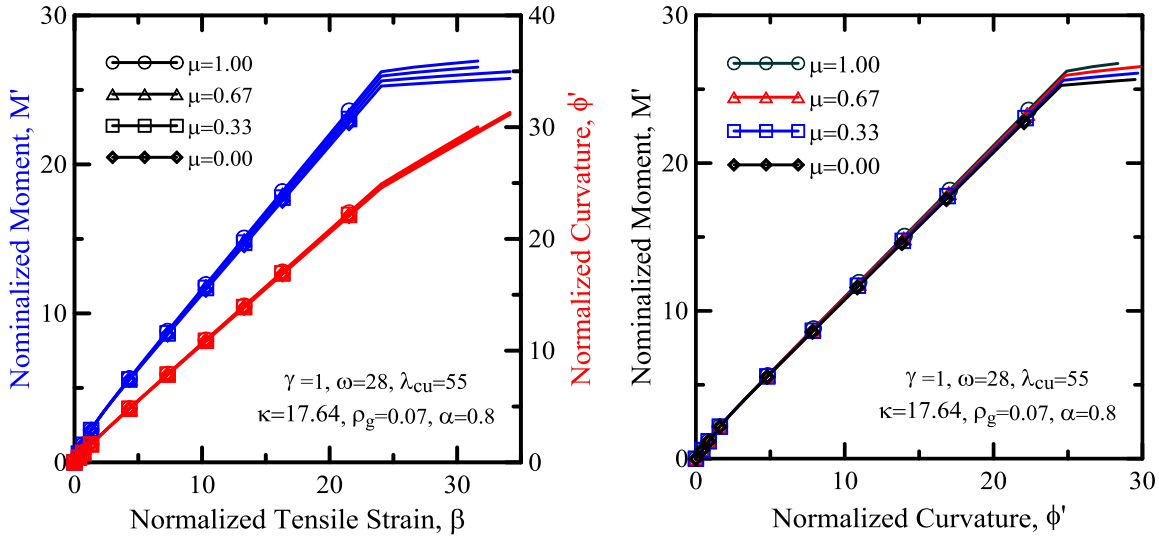

Figure 69. Parametric studies of the normalized moment and curvature diagrams as a function of normalized tensile strain, β, for different levels of post-crack tensile strength (residual strength) parameter, μ (with 7% longitudinal reinforcement, Steel rebar-Grade 60).

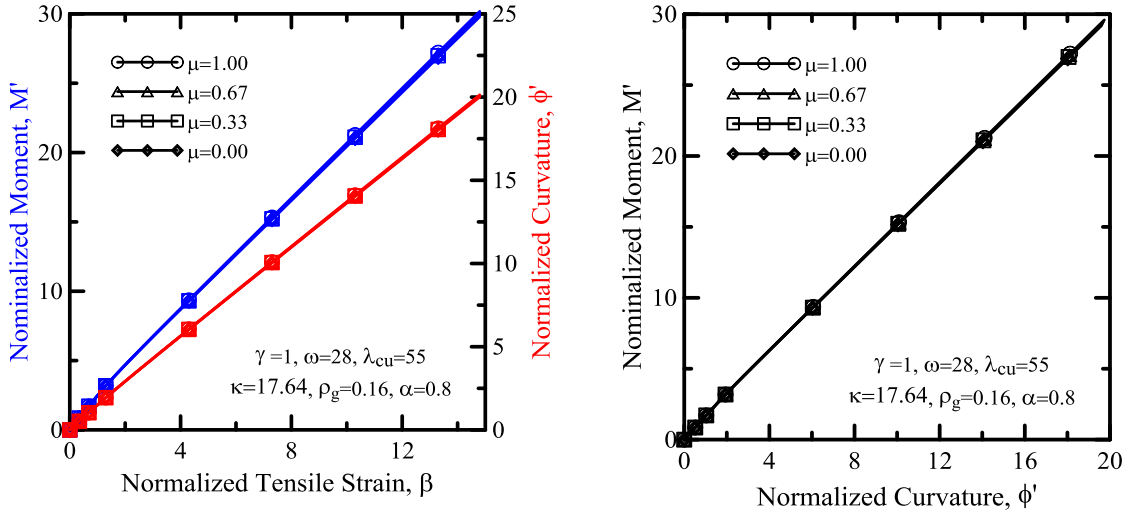

Figure 70. Parametric studies of the normalized moment and curvature diagrams as a function of normalized tensile strain, β, for different levels of post-crack tensile strength (residual strength) parameter, μ (with 16% longitudinal reinforcement, Steel rebar-Grade 60).

Figure 71 illustrates the effect of the reinforcement ratio on the normalized moment and curvature diagrams with no fiber reinforcement, $\mu = 0.0$. Again, as the amount of the reinforcement increases, the ductility of the section decreases, and the failure mode changes from ductile to brittle, so that for 10 percent reinforcement the response of the section is completely brittle, causing a compressive failure. However, for the reinforcements less than 8 percent there is a ductile failure, followed by a compressive failure as deformation continues. Crosses represent the brittle compressive failure before the reinforcement yields.

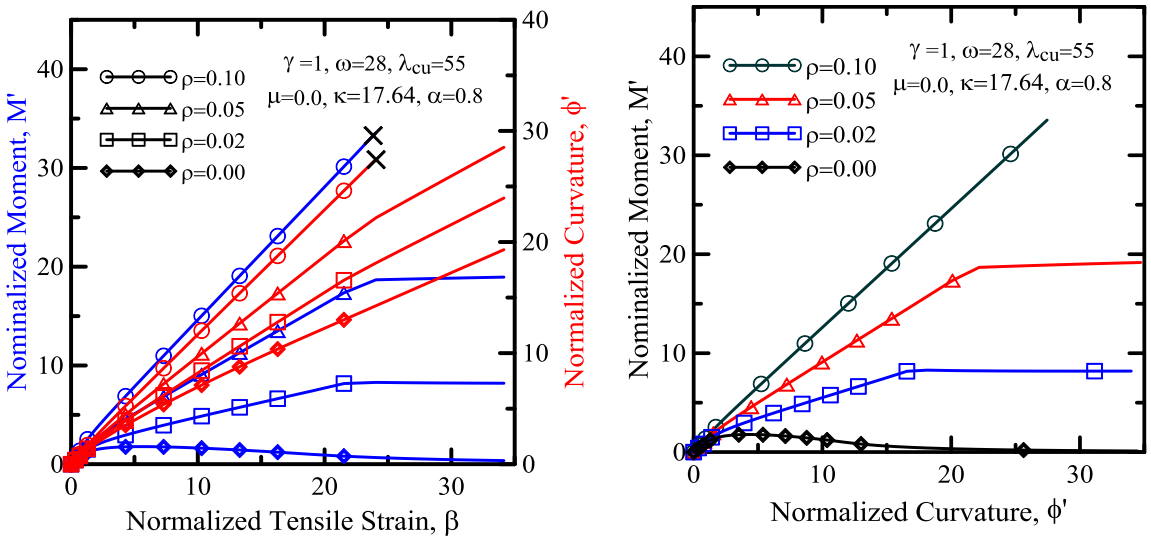

Figure 71. Parametric studies of the normalized moment and curvature diagrams as a function of normalized tensile strain, β, for different levels of longitudinal reinforcement, with no fiber reinforcement (residual tensile strength equal to zero).

Figure 72 illustrates the effect of the reinforcement ratio on the normalized moment and curvature diagrams with the perfectly-plastic tensile response, $\mu = 1.0$. In this case, the section has a good moment capacity and ductility with 5 percent of reinforcement, and as the amount of the reinforcement increases, so does the stiffness of the section and the failure mode changes from ductile to brittle. Using these figures it is possible to evaluate a specific moment and curvature for a specific value of tensile strain in the lower fiber of the beam, by drawing a vertical line from the interested tensile strain value; then the intersection with the curvature (red) curves and the moment (blue) curves will be the equivalent curvature and moment for that tensile strain value. This method can be used in serviceability limit state.

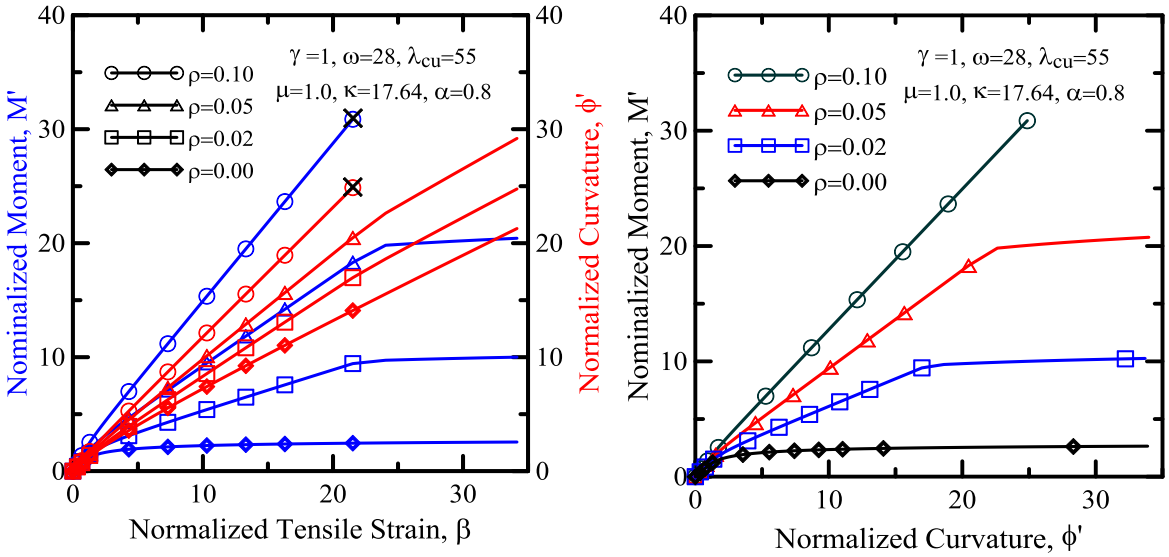

Figure 72. Parametric studies of the normalized moment and curvature diagrams as a function of normalized tensile strain, β, for different levels of longitudinal reinforcement, with perfectly-plastic tensile response ($\mu = 1.0$).

Using these figures it is possible to evaluate a specific moment and curvature for a specific value of tensile strain in the lower fiber of the beam, by drawing a vertical line from the interested tensile strain value and then the intersection with the curvature (red) curves and the moment (blue) curves will be the equivalent moment and curvature for that tensile strain value. This Method can be used in serviceability limit state.

2.9.1 Comparison with other experimental results on HRC

Yang et al. (2010), [33] provided some experimental test results for the flexural behavior of ultra-high performance concrete (UHPC) beams. The experimental parameters comprised the amount of rebar and the placing method for the UHPC. The flexural behavioral features were inspected with respect to test results on UHPC beams with rebar ratios less than 0.02 and steel fibers with a volumetric ratio of 2%. Before

doing the bending tests on the beam samples, they performed some basic compressive tests, on cylindrical specimens with a diameter of 100 mm and a height of 200 mm, to obtain the material properties of the UHPC, such as compressive strength and Young's modulus. For the flexural tests, the experimental program included tests on a total of 14 beam specimens with rectangular cross-sections. The beam specimens included a basic specimen without rebar, which was designated as specimen NR in Table 11. The other specimens had varying rebar ratios that were gained by changing the amount of rebar and the number of layers. For this study, two different set of samples with two sets of rebars (i.e., sections R-13 and R-14) are simulated using HRC-TL model (two samples from R13 and one sample from R14). R13 rebars had a nominal diameter of 13 mm and R14 rebars had a nominal diameter of 14mm.

Table 11. Parameters used in experiments by Yang et al. , [33] (All dimensions in mm)

Specimen	**R13**	**R14**
Cross section	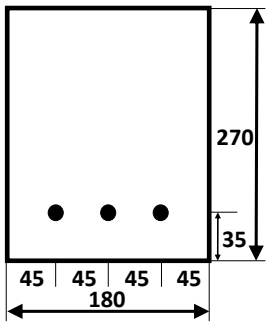	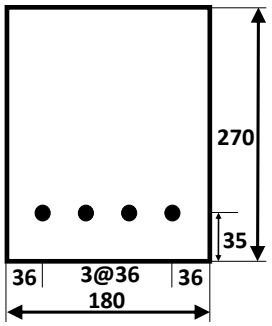
Rebar	3-13mm ϕ, 1 layer	4-13 mm ϕ, 1 layer
Rebar area (mm^2)	380.1	506.8
Rebar ratio	0.009	0.012
Batch number	2	3

The arrangement of the beam and the test setup is shown in Figure 73. Electrical resistance strain gauges were used to measure the strain of the concrete and steel rebar. Five strain gauges were placed on the side surface of the beam at midspan to measure strain at different heights. The loads were applied to the beams at the top face using hydraulic actuator in the form of four-point loading method, as shown in Figure 73. A loading steel frame was installed between the beam and the actuator to transfer the load from actuator to the bean at the specified points.

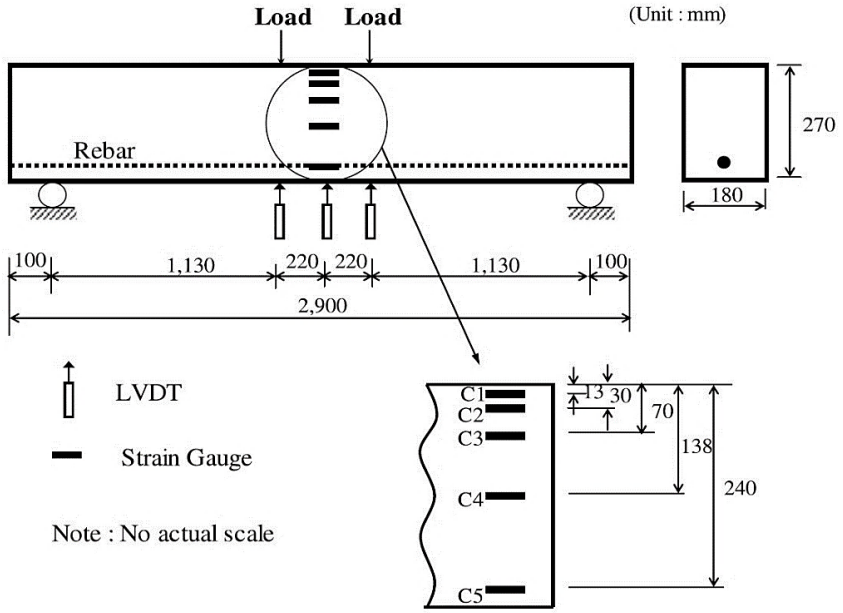

Figure 73. Instrumentation used for the beam flexural test.

For the simulation part, a MATLAB code is used which is developed based on the parameters and stress-strain diagrams which was introduced at the start of this section. More detailed description of the mathematical approach and the closed form solutions can be found in Yao et al., 2017 [40]. The comparison graphs for these sets of simulations are represented here. It was observed that all simulated samples reach to their maximum tensile capacity before a strain of 0.5% and then their tensile capacity decreases to zero in tensile strain of 2%, which is comparable to the ultimate tensile capacity of the steel rebars.

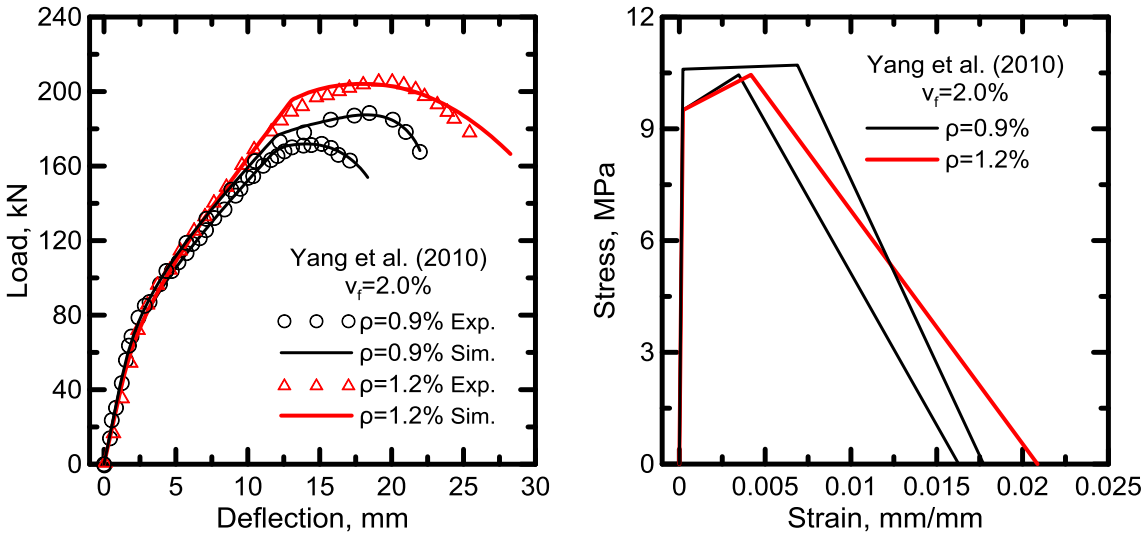

(a) (b)

Figure 74. a) Simulated load-deflection curves; b) Stress-strain graphs for tensile behavior.

Figure 75 demonstrates the comparison between the experimental strain distributions, at different elevations along the beam depth (C1 to C5, also see Figure 73) [25], and the simulated results obtained from the constitutive model. These simulated results are calculated based on the linear strain distribution along the beam section (see Figure 46). The required values (i.e., the depth of the neutral axis, strains at lower and upper fibers of the section) are attained from the back-calculation process and then the strains, at different elevations, can be determined based on the linear strain distribution along the beam depth. This figure shows that there is a very good agreement between the experimental and simulated results, which proves that the assumption of linear strain distribution along the beam depth is an acceptable assumption at both pre-peak and post-peak regions.

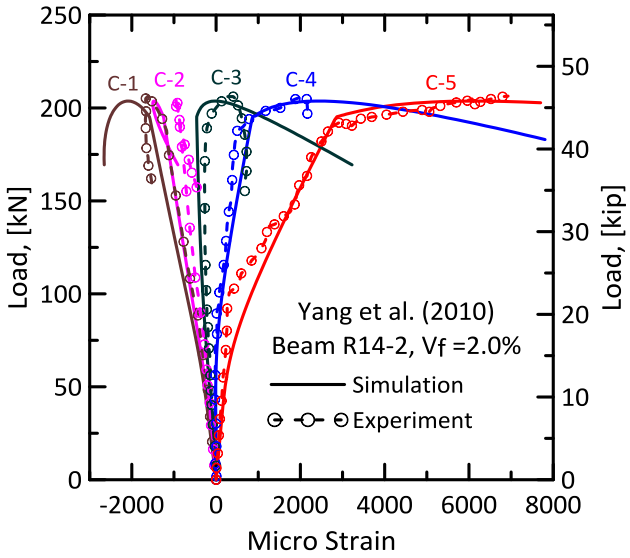

Figure 75. Comparison between simulated and experimental strain distribution along the beam depth, C-1 to C-6 strain gages (Yang et al., 2010) [25].

Another test data set which is used as a basis for simulations is the research done by Kamal et al. , [34]. In their research, they evaluated the behavior of ultra-high strength concrete beams, the effect of adding fibers and explored their effect on the performance and strength of the reinforced concrete beams. A total of twelve simple concrete beams with and without shear reinforcements were tested. The main variables taken into consideration were the type of fibers and the percentage of longitudinal reinforcement as well as the presence or absence of the web reinforcement. Two types of fibers were used including steel and polypropylene fibers. Plain steel fibers with 0.2 mm diameter and 13 mm length with an aspect ratio (L/D) 65 were used. The polypropylene fibers used were produced by SI Concrete systems, USA with 20 mm length and aspect ratio (L/D) 12.5.

The beams were designed to have acceptable resistance against flexure failure. Simply supported beams ($100\times150\times1000\,\text{mm}$) were cast and tested until failure. The beams under investigation were either reinforced with two bottom rebars of 10mm

diameter (reinforcement ratio $\rho = 1.2\%$) or 12mm diameter (reinforcement ratio $\rho = 1.7\%$). The geometrical and reinforcement details of the tested beams are shown in Figure 76.

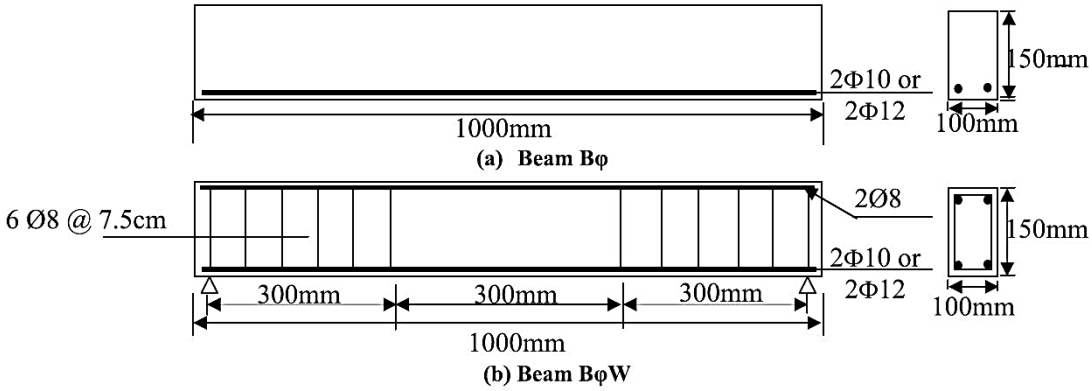

Figure 76. Geometrical and reinforcement details of the tested beams [73].

A test beam was defined by letter B followed by the diameter of the two reinforcing main bars (10 or 12 mm), followed by the letter W in case of beams having web reinforcement and either P or S denoting the beam of polypropylene or steel fibers. In this research B10(S and P) and B12(S and P) are chosen as the reference for analytical simulation using HRC-TL model. The simulated load-deflection curves and stress-strain diagrams for B10 and B12 beams are shown in Figure 77. In these samples, the number after B refers to the rebar number and S and P stand for steel and polymeric fibers, respectively.

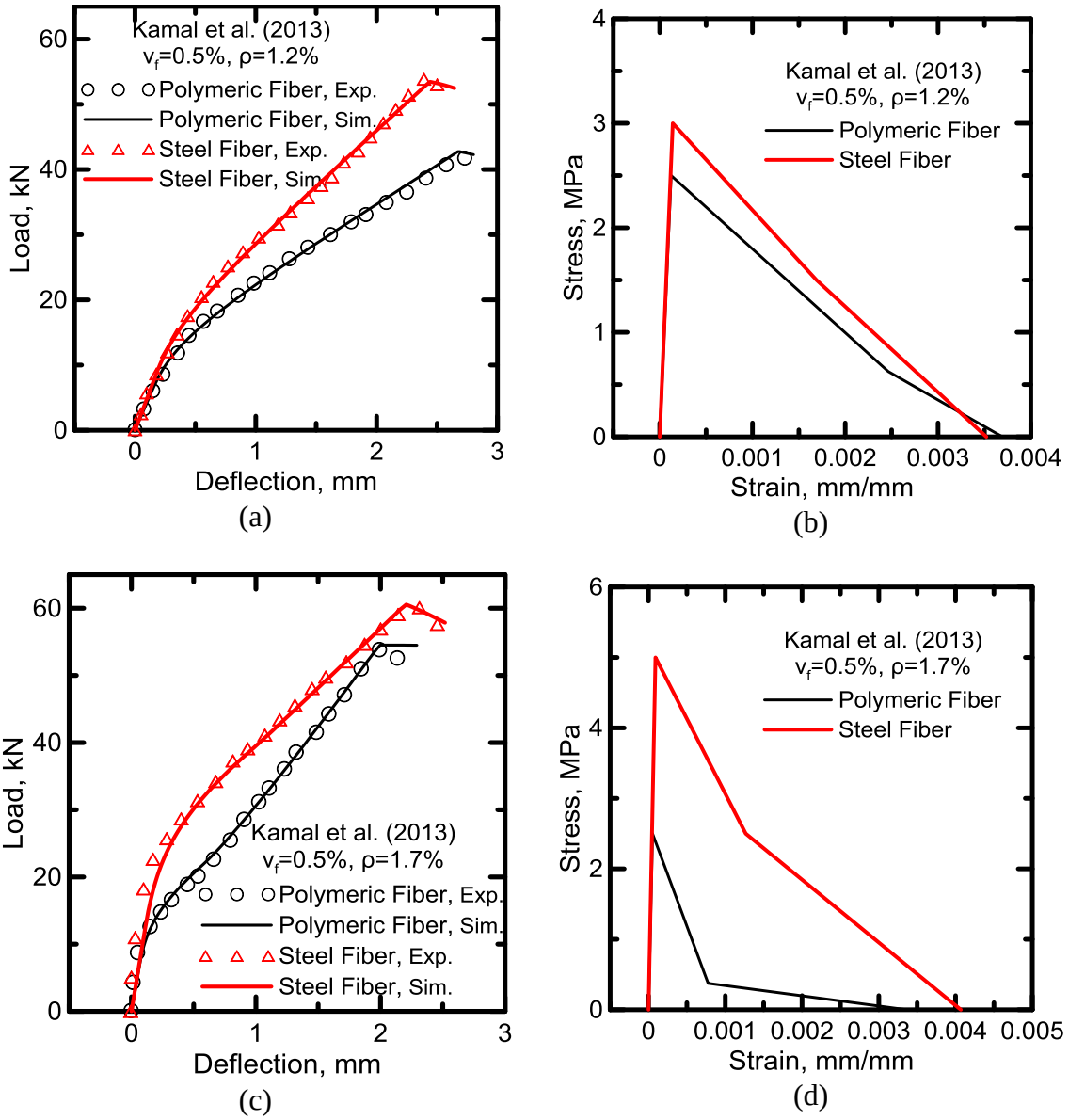

Figure 77. (a) Simulated load-deflection curves, and (b) Stress-strain graphs for tensile behavior for B10 samples; (c) Simulated load-deflection curves, and (d) Stress-strain graphs for tensile behavior for B12 samples.

Kaka and Chao [74] investigated a new concept of replacing prestressed concrete structures with non-prestressed ultra-high-performance fiber-reinforced concrete (UHP-FRC) structural members. This would facilitate accelerated construction of such bridges. Potential application of this proposed concept of replacing prestressed members with

non-prestressed UHP-FRC members offers efficient design and construction practices by eliminating the issues with prestressing. They performed compression and direct tensile tests on UHPC samples. Direct tension test (no reinforcing bar in the specimen) indicated that after a UHP-FRC cracks, it can maintain high tensile strength (about 7 MPa) up to a strain of 0.01. Therefore, adding a large amount of longitudinal reinforcement not only increases the flexural strength of UHP-FRC beams, but it can also enhance the mechanical behavior of UHP-FRC on the tensile side of the beam. Allowing a higher amount of reinforcing bars leads to smaller stress in tensile reinforcement even at higher load [74].

Four simply supported beams, one made of reinforced concrete (RC) and three made of UHP-FRC were monotonically loaded to failure. All beam specimens had a width of 9 in. (229 mm), a height of 16 in. (406 mm), and a span length of 134 in. (3404 mm). A 20-in. (508 mm) constant moment region was at the mid-span of all specimens. For Specimens RC and UHP-FRC #1, the shear span to effective-depth ratio, the a/d ratio, was 4.75; it was 3.93 for Specimens UHP-FRC #2 and UHP-FRC #3. lists the design parameters of beams used in this experimental program. Specimens RC and UHP-FRC #1 used ASTM A615 reinforcing bars, while Specimens UHP-FRC #2 and UHP-FRC #3 used ASTM A1035 high-strength corrosion-resistant low-carbon chromium reinforcing bars to reduce the reinforcement congestion. Shear reinforcement was used in Specimens RC and UHP-FRC #1 to ensure a flexural failure mode, while no shear reinforcement was used in Specimens UHP-FRC #2 and UHP-FRC #3 to investigate the shear capacity of UHP-FRC in flexural members. Figure 2 illustrates the testing setup and details of RC and UHP-FRC #2 beams.

Table 12. Design parameters of RC and UHP-FRC specimens (UT Arlington research) [74].

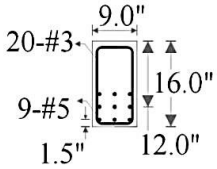

RC #1

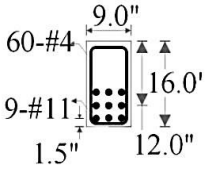

UHP-FRC #1

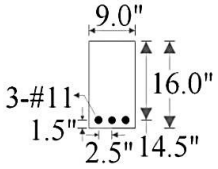

UHP-FRC #2

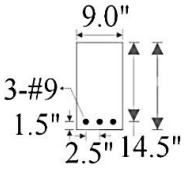

UHP-FRC #3

Specimen	Effective depth (d), in. (mm)	*a/d*	ρ (%)	V_f (%)	Targeted, f'c (ksi) (MPa)	Measured, f'c (ksi) (MPa)
RC1	12.0 (305)	4.75	2.58 (60S)	0	5 (35)	5 (35)
UHP-FRC #1	12.0 (305)	4.75	13.0 (60S)	3.0	22 (152)	21 (145)
UHP-FRC #2	14.5 (368)	3.93	3.59 (100S)	3.0	22 (152)	20.8 (143)
UHP-FRC #3	14.5 (368)	3.93	2.30 (100S)	3.0	22 (152)	20.8 (143)

Reinforcement ratio for Specimen UHP-FRC #1 with Gr. 60 reinforcing bars was five times that of the RC beam which resulted in a ratio of ρ = 13%, corresponding to nine No. 11 reinforcing bars (Figure 2b and Table 12). The reinforcement areas were considerably reduced in Specimens UHP-FRC #2 and UHP-FRC #3 with Grade 100 reinforcing bars.

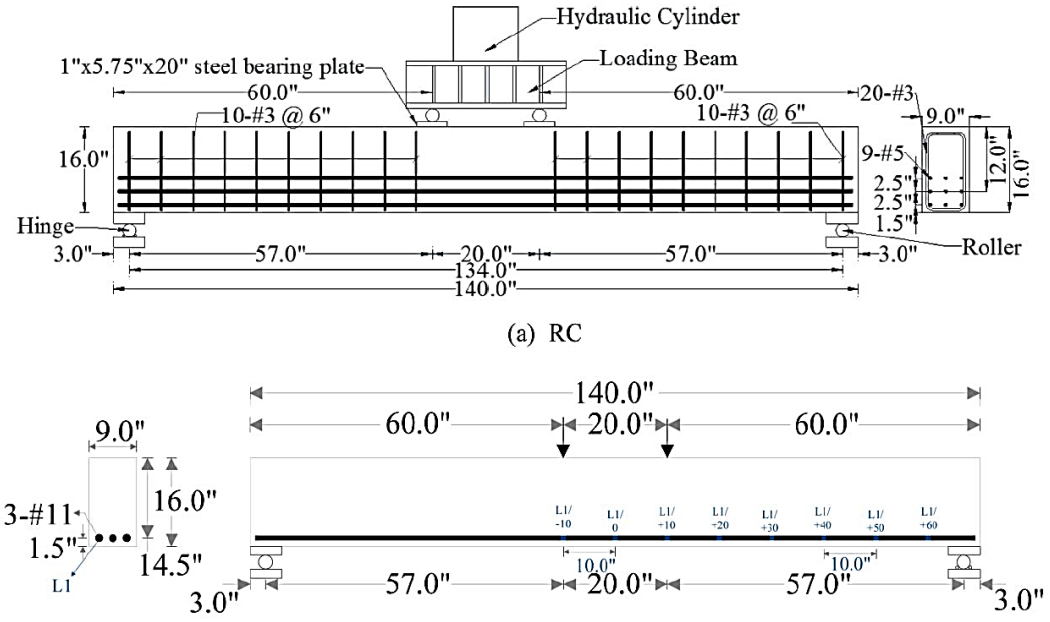

Figure 78. Testing setup and details of RC and UHP-FRC #2 beams; Unit: inch (1 in. = 25.4 mm) (UT Arlington research) [74].

The comparison graphs between the experimental results and the simulated results, using the constitutive analytical model are presented in below figures.

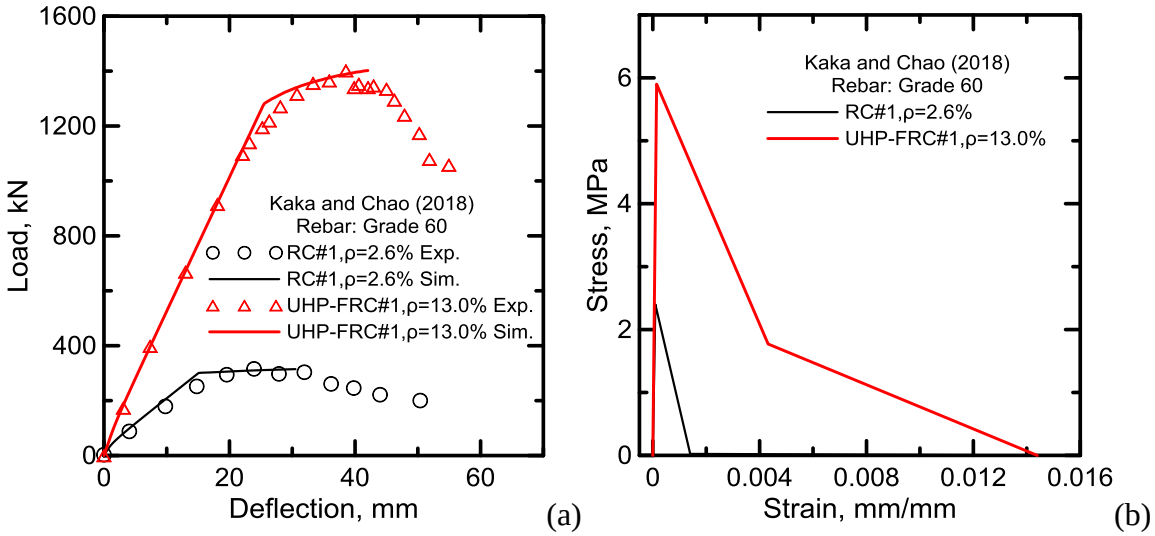

Figure 79. a) Simulated load-deflection curves; b) Stress-strain graphs for tensile behavior.

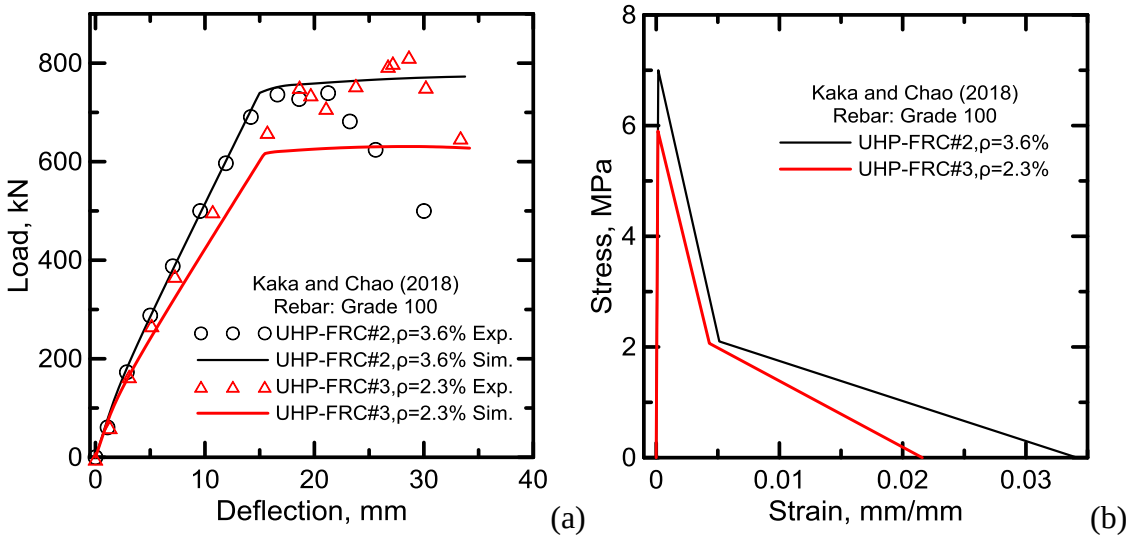

Figure 80. a) Simulated load-deflection curves; b) Stress-strain graphs for tensile behavior.

Qi et al. [75] presented the results of experimental and theoretical studies undertaken to assess the flexural performance of high-strength steel-ultra-high-performance fiber reinforced concrete (HSS-UHPFRC) beams. A total of nine HSS-UHPFRC beams were tested, and the influence of fiber volume fraction, fiber type, longitudinal reinforcement ratio, and concrete strength on the flexural response was evaluated. The results indicated that sufficient longitudinal reinforcement should be provided in a UHPFRC beam to avoid abrupt failure and possible catastrophic collapse.

Nine beams with dimensions and reinforcement details shown in Figure 81and Table 13 were prepared and tested in bending to investigate the effect of fiber volume fraction, fiber type, longitudinal reinforcement ratio, and concrete strength on the flexural behavior of HSS-UHPFRC beams.

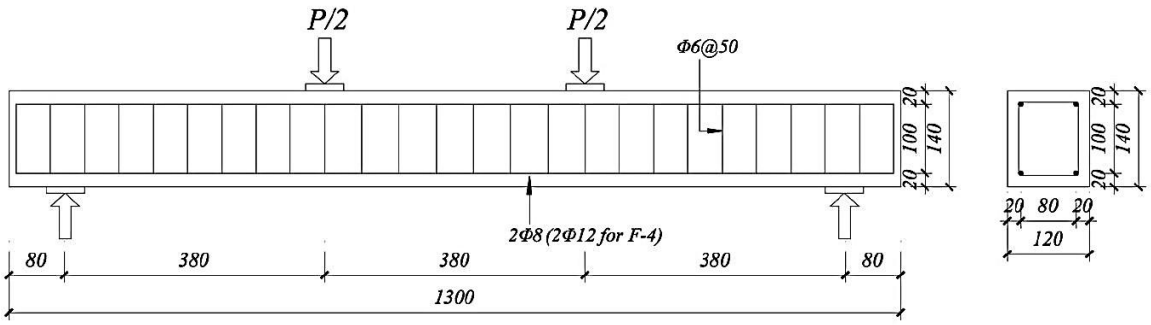

Figure 81. Dimensions and cross section of specimens [75].

The fiber volume fraction of 2% was adopted for the majority of the beams in this study. The fibers are cylindrical, straight high-tensile-strength steel fibers, and are coated with a thin layer of copper to provide lubrication during the drawing process and to prevent them from corrosion. For the rebars, the yield strengths are 760.9 MPa and 889.7 MPa for Φ12 and Φ8 longitudinal reinforcement, respectively, while the yield strength is 417.2 MPa for Φ6 transversal reinforcement.

Table 13. Beam properties and test parameters [75].

Beam	Ultra-high-performance concrete mix	b (mm)	d (mm)	ρ_f (%)	ρ_s (%)	ρ_v (%)	Test parameter
F-1	A	120	120	2	0.7	0.94	Benchmark beam
F-2	D	120	120	0.5	0.7	0.94	ρ_f
F-3	E	120	120	1	0.7	0.94	ρ_f
F-4	A	120	120	2	1.57	0.94	ρ_s
F-5	A	120	120	2	/	/	ρ_s
F-6	F	120	120	2	0.7	0.94	Fiber type
F-7	G	120	120	2	0.7	0.94	Fiber type
F-8	B	120	120	2	0.7	0.94	f_{cu}
F-9	C	120	120	2	0.7	0.94	f_{cu}

Note: b = width of the web; d = effective depth; ρ_f = fiber fraction volume; ρ_s = longitudinal reinforcement ratio; ρ_v = transverse reinforcement ratio.

Beam F-1 is the benchmark beam. Beams F-2 and F-3 contain less fiber compared to Beam F-1. Beam F-4 was similar to F-1 with the exception that the longitudinal reinforcement ratio was higher. Beam F-5 was designed as a pure UHPFRC beam without additional reinforcement with the purpose of verifying whether longitudinal

reinforcement could be removed. Beams F-6 and F-7 were designed with different steel fiber types, while Beams F-8 and F-9 were designed with varying concrete strengths.

All beams had the same geometric dimensions with a rectangular cross section. The length of the beam is 1,300 mm and the effective span is 1,140 mm. The height and width of the beams are 140 and 120 mm, respectively. Stirrups were provided in all beams, except for Beam F-5. The rebar spacing was 50 mm, resulting in a stirrup ratio of 0.94%, to ensure flexural failure mode. Considering steel fibers as a part of longitudinal reinforcement, all beams were designed to have longitudinal reinforcement ratio below 2%. Thus, two deformed steel bars with the diameter of 8 mm (12 mm for Beam F-4) were embedded at the tension side of the beams as passive reinforcement. The longitudinal reinforcement ratio was 1.57% for Beam F-4 and 0.7% for other beams. Mixtures proportions and the material properties can be found in the original paper [75].

The comparisons between the experimental results and the simulated results, using the constitutive analytical model are presented in below figures.

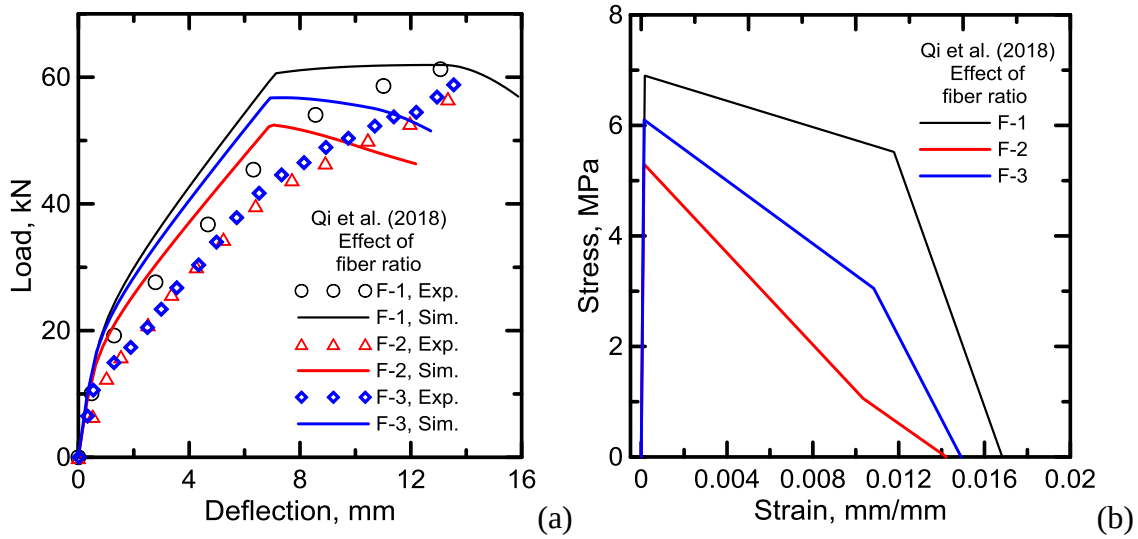

Figure 82. a) Simulated load-deflection curves; b) Stress-strain graphs for tensile behavior.

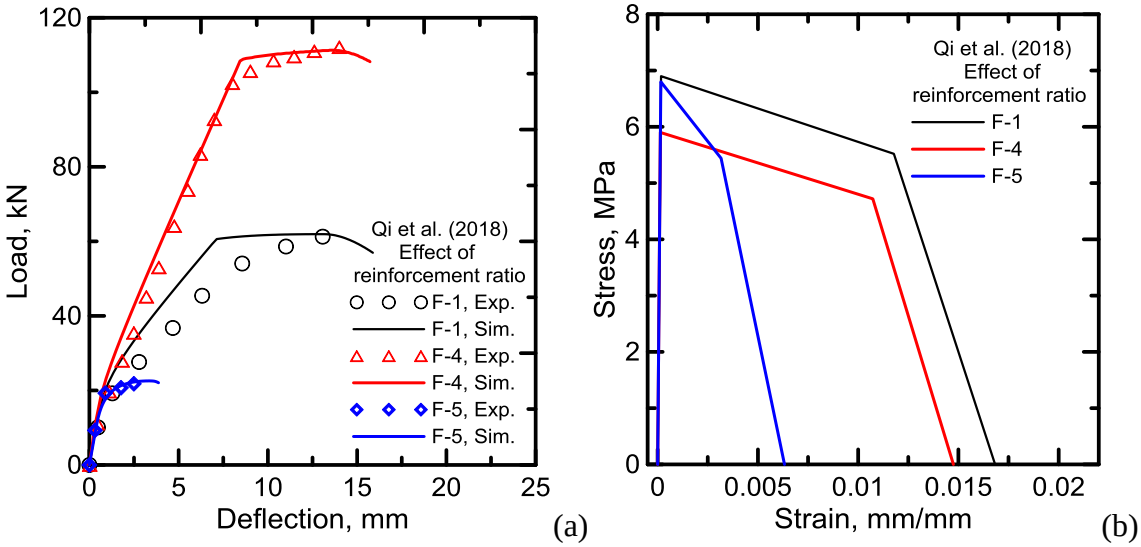

Figure 83. a) Simulated load-deflection curves; b) Stress-strain graphs for tensile behavior.

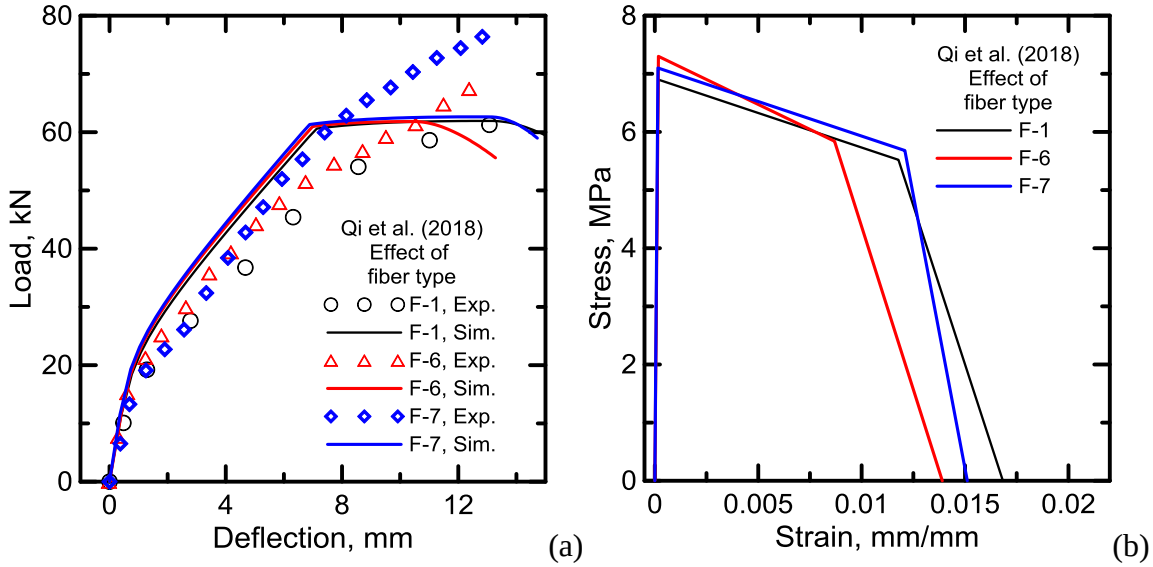

Figure 84. a) Simulated load-deflection curves; b) Stress-strain graphs for tensile behavior.

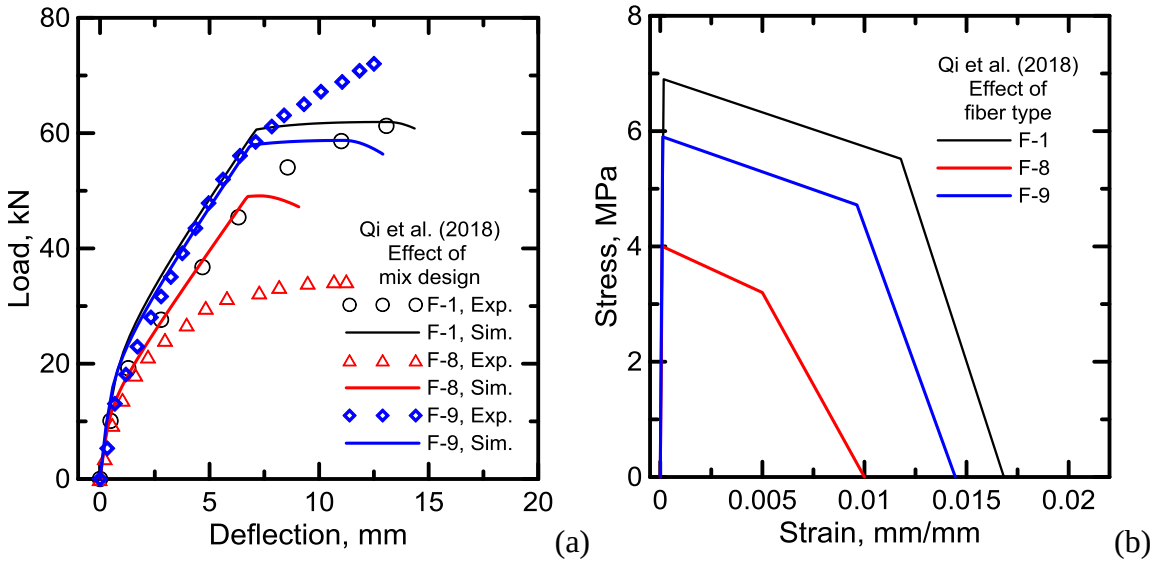

Figure 85. a) Simulated load-deflection curves; b) Stress-strain graphs for tensile behavior.

All back-calculated parameters are listed in Table 14.

Table 14. Summary of the back-calculated parameters using constitutive analytical model for HRC sections.

Experimental Research	Sample ID	Reinforcement ratio, r (%)	Elastic Modulus, E (ksi)	Compressive Strength (ksi)	Cracking Tensile Strain $\mu\varepsilon_{cr}$	Cracking Strength (ksi)	Υ, Normalized compressive modulus	ω, Normalized Compressive Yield Strain	μ, Normalized Residual Tensile Strength	β_{tu}, Normalized Tensile Strain
Yang et al. (2010)	R13-1	0.8	7208	25.9	190	1.37	0.9	21.0	1.05	85
	R13-2	0.8	7368	26.5	210	1.55	0.9	19.0	1.01	85
	R14-1	1.2	6382	26.5	210	1.34	0.9	22.0	0.95	110
Kamal et al. (2013)	B10	0.7	870	17.7	47	0.41	0.9	48.0	0.00	8
	B10-P	0.6	2944	13.6	120	0.35	0.8	48.0	0.25	30
	B10-S	0.8	3089	17.1	140	0.43	0.9	44.0	0.50	25
	B12	0.8	3379	16.1	110	0.37	0.9	48.0	0.00	30
	B12-P	1.0	7005	19.0	60	0.42	0.9	50.3	0.16	65
	B12-S	0.8	8021	15.6	90	0.72	0.8	27.0	0.50	45
Kaka & Chao (2018)	RC-1_60S	2.5	3626	3.8	100	0.36	0.7	15.0	0.01	155
	UHPC-1_60S	12.7	5947	14.0	140	0.83	0.7	24.0	0.30	100
	UHPC-2_100S	3.6	5947	14.0	140	0.83	0.7	24.0	0.35	80
	UHPC-3_100S	2.5	5947	14.0	140	0.83	0.7	24.0	0.35	150
Qi et al. (2018)	F-1	0.7	5947	15.5	170	1.01	0.9	17.0	0.80	100
	F-2	0.7	5947	12.9	130	0.77	0.9	18.5	0.20	110
	F-3	0.7	6527	12.3	140	0.91	0.9	15.0	0.50	110
	F-4	1.6	6382	11.9	130	0.83	0.9	16.0	0.80	110
	F-5	0.0	6237	15.3	160	1.00	0.9	17.0	0.80	60
	F-6	0.7	6092	15.8	170	1.04	0.9	17.0	0.80	80
	F-7	0.7	6817	15.6	150	1.02	0.9	17.0	0.80	100
	F-8	0.7	5802	14.1	100	0.58	0.9	27.0	0.80	100
	F-9	0.7	7107	17.7	120	0.85	0.9	23.0	0.80	120

Back-calculated stress-strain graphs show that the steel fibers have better performance compared to the polymeric fibers with the same fiber content. On the other hand, a comparison between the results of this research with the previous one (Yang et al., 2010) demonstrates that the fiber content has a considerable effect on the tensile response of the FRC section. While in the later research (with 0.5% fiber content) the

ultimate tensile strain of the section is about 0.4%, in the previous research (with 2% fiber content) this parameter was about 2%, which is five times higher. The same is true about the tensile strength. While the tensile strength in the samples with 2% fiber content is around 10 MPa, this value for the samples with 0.5% fiber content is about 3 MPa, on average.

Another important issue is that in most of the experimental research performed so far, a reinforcement ratio of less than 2 percent was chosen. However, as the parametric studies demonstrated, due to the high compressive strength of UHPC it is possible to employ more reinforcement (up to 15 percent for UHPC section with a compressive strength more than 20 ksi and grade 60 rebars). This enables proper exploitation of the advantages of UHPC's high compressive strength.

2.10 Design and Analysis of UHPC Joints Based on Constitutive Analytical Approach

One of the largest and specific challenges facing bridge authorities is the long-term durability of bridge decks which receive continuous impact loading from trucks and changing environmental conditions. The years of continuous flexural and thermal stresses and exposure to corrosive elements create long-term deterioration and maintenance issues for bridge decks. While Cast-In-Place (CIP) concrete decks with High-Performance Concrete (HPC) and corrosion resistant reinforcement can significantly extend the deck life, it creates high user inconvenience and is problematic for bridge deck replacement in high traffic areas. The use of HPC precast deck panels is a

common method to speed construction and reduce the user inconvenience; however, the joining of the precast system is a source of potential maintenance or even failure [76].

Joints are considered as the vulnerable link in a structure and usually, deterioration of the structure originates from the joints. Joints convey the stresses from super-structure to sub-structure and during the process are subjected to large stresses. However, the introduction of new methodologies and innovative material technologies facilitates the implementation of new solutions. One of the solutions to this problem is the composite UHPC material which offers superior technical characteristics including ductility, strength, and durability while providing highly moldable products, with a high-quality surface aspect and a short bond development length [77], [78]. Ultra-high performance concrete (UHPC), when used as a jointing material in conjunction with reinforced high-performance concrete (HPC) panels, provides a synergistic, new approach for reconstruction of bridge superstructures.

Opportunities to modify and improve upon prefabricated element connection details exist by taking advantage of the material and durability properties that UHPC has to offer. In addition to the high compressive and post-cracking tensile strengths, the dense, discontinuous pore structure and steel fiber reinforcement of UHPC provide further material property benefits. Improvements include better internal distribution of stresses, better confinement of embedded rebar, and reduced rebar development and splice lengths. Currently, the most popular application of UHPC in U.S. bridge construction is for connections between prefabricated bridge deck elements [79]. UHPC was successfully used by New York State (see Figure 86) and Iowa State Department of

Transportations (DoT) in many bridges as various components, and proved to help with Accelerated Bridge Construction (ABC) which makes its use economical and time-saving [80]. The performance of prefabricated bridge systems is highly contingent on the design of connections and joints.

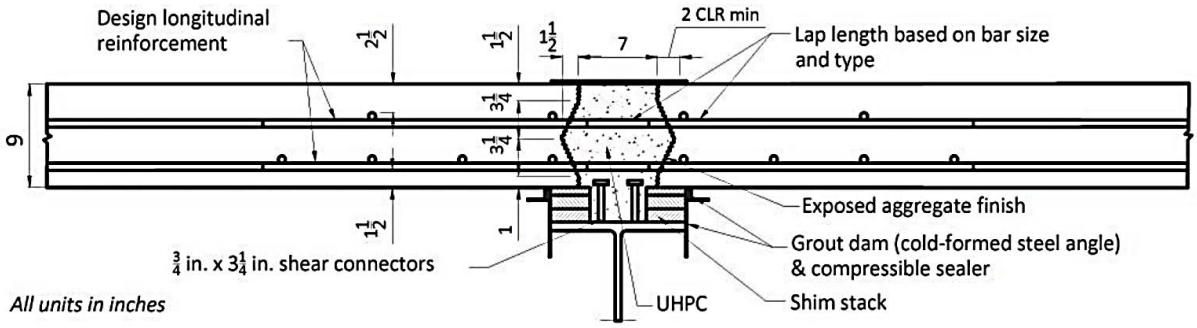

Figure 86. Combined UHPC deck-level and composite connections as deployed by NYSDOT on I-81 near Syracuse, NY [57].

Figure 87. Filling the transverse (LLC) joints with UHPC [76].

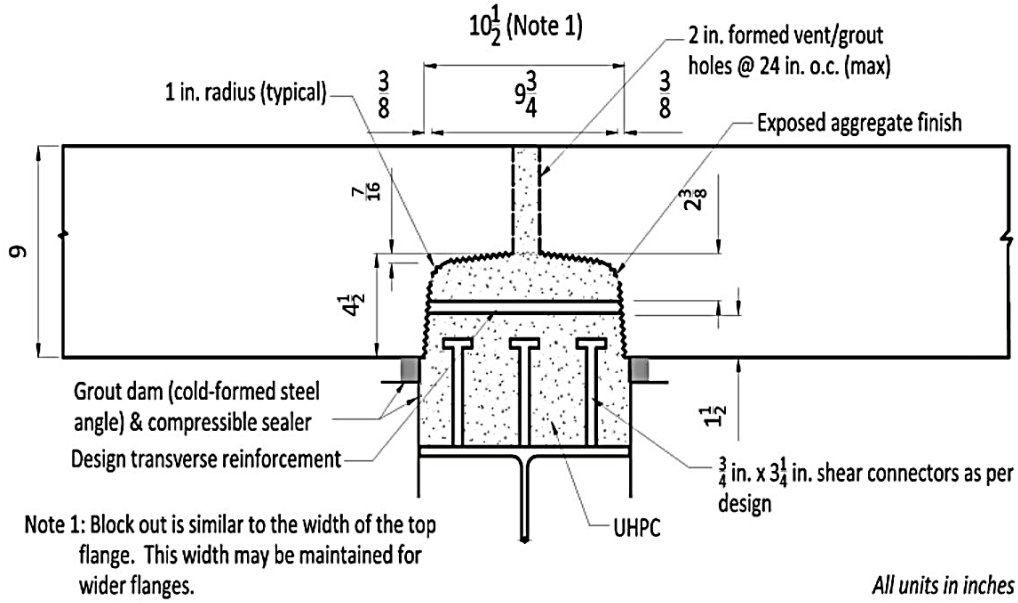

Figure 88. UHPC composite connection between deck panel and steel girder [57].

Figure 89. Longitudinal connection detail above first interior girder line with shear studs stopping below the bottom mat of rebar [57].

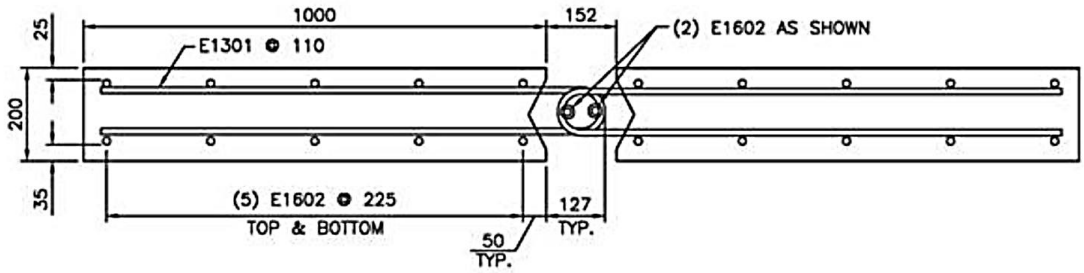

Figure 90. Prototype panel (pairs) for testing joint fill performance [76].

The advanced properties of UHPC allow for simple reinforcement details inside the connection region while using conventional non-shrink grouts, the flexural reinforcement in the connection region requires hooked or U-shaped bars to meet the length requirements [81]. Besides, additional bars are usually required to withstand secondary loads such as temperature and shrinkage. Using UHPC, there is no need for

hooked flexural reinforcement or lacer bars, thus greatly simplifying the detailing and increasing the constructability [79].

To design the UHPC joint, the similar approach for FRC and HRC sections can be used. First, it is necessary to have the moment-curvature response to the section and then use that response to simulate the load-deflection response of the element, similar to what we had for FRC and HRC sections. For this purpose, we need to consider the most general case which covers all of the possible situations with a different type of materials (i.e., curve C in Figure 48). It is possible to simplify the model as a beam with two different sections. Section 1 for the beam body parts and Section 2 for the joint. This is depicted in Figure 91.

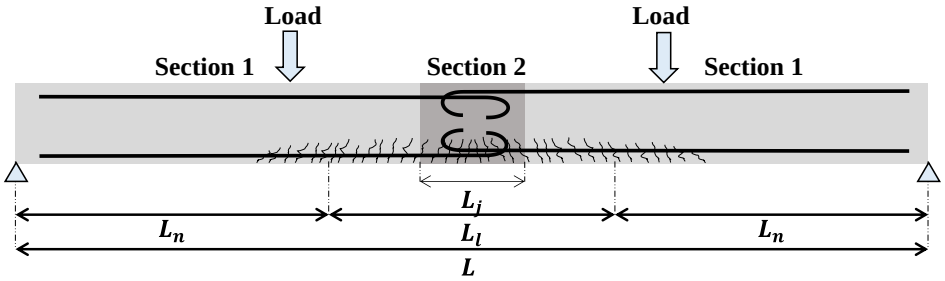

Figure 91. Typical RC beam with a joint at the middle part under four-point loading.

In this figure, L_j represents the joint length and L_n and L_l represent non-localized and localized zones, respectively. As shown, the joint (Section 2) is totally located in the localized zone. Furthermore, a part of Section 1 is also located in the localized zone. It is noted that in the localized zone, it is assumed that the cracks continue to growth even after unloading, but the cracks, located in the non-localized zone, will be closed after

unloading. This kind of response in different segments of the beam affects the load-deflection response of the beam as well. The material in the joint is made

Clearly, each section has its own M-C diagram. Each section is divided into several subsection, or element, along with the beam axis. The moment due to the external loading will be calculated for each element and the corresponding curvature is extracted from the related M-C diagram. The mid-span deflection can be calculated using the moment-area method and direct integration of the element curvatures along the beam axis [82]. This process is performed using a MATLAB code for a generalized beam with two different sections and two type of external loading, i.e., four-point and three-point bending tests, see Figure 92.

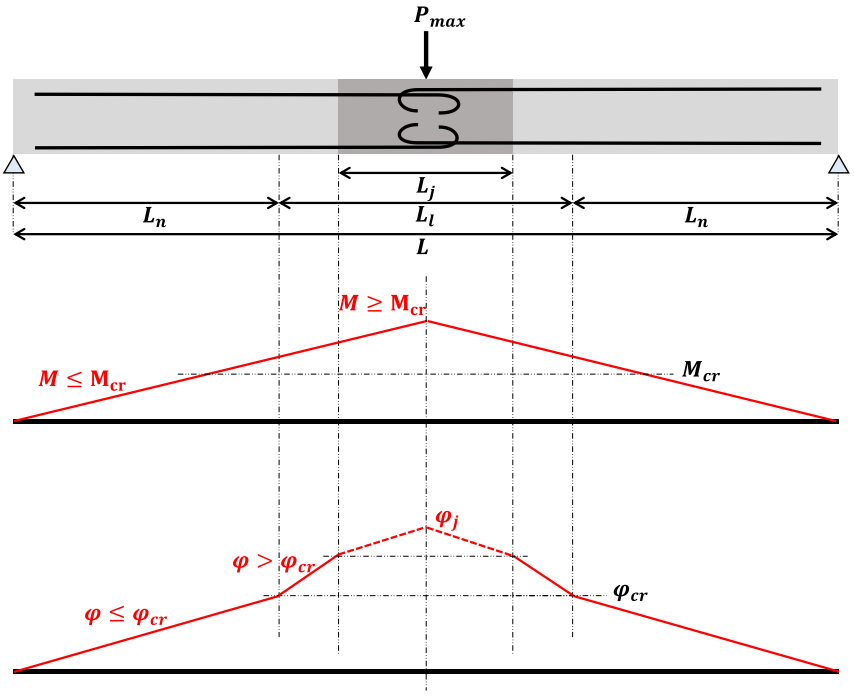

(a)

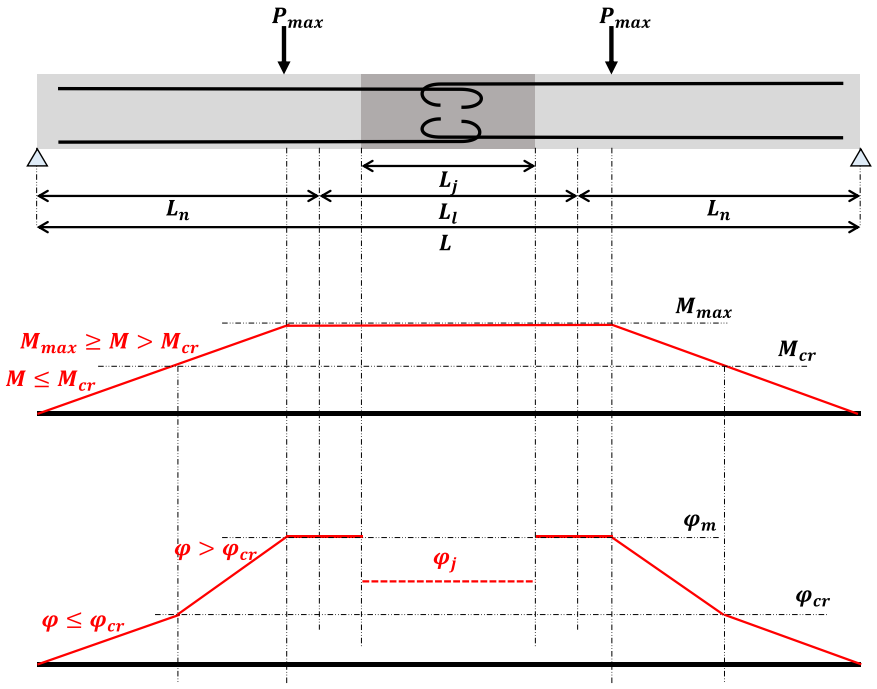

(b)

Figure 92. Schematic drawing of moment and curvature distributions: (a) 3PB; (b) 4PB.

In these diagrams, it is assumed that the stiffness of the joint (section 2) is higher than the stiffness of the element (section 1). These figures demonstrate the schematic views of the moment and curvature diagrams at the maximum loading and bending moment. As it was mentioned before, each section has its own M-C diagram and this relationship is only linear for the initial part of the response. To generalize the solution, as much as possible, it is trying to consider a generalized form of M-C diagram which is applicable for the different type of the RC, FRC, HRC and UHPC sections. Amongst all types of M-C diagrams in Figure 48, curve C has the most comprehensiveness. It has an increasing part at the first segment, then a decreasing segment and finally another increasing segment. This behavior can be used to define other types of M-C diagrams, as well.

The same approach, similar to section 8.4, is applicable for a beam with a UHPC joint at the middle. The difference is that in this case there are two different sections along the beam axis. The moment-curvature (M-C) diagrams for HRC sections, single or double reinforced, can be obtained using the models that were presented in the previous section. To obtain a general solution to calculate the load-deflection response of a beam with a joint at the middle, a general form of the moment-curvature diagrams should be utilized for each section. Deferent forms of a typical M-C diagram for FRC sections were shown in Figure 48.

The main purpose of this study is to provide an analytical solution for the joints in the bridges with a concrete deck. It is clear that in this case there are two different type of concrete. A normal concrete with reinforcement and an HRC section which can be a fiber reinforced concrete (FRC) or an ultra-high performance concrete (UHPC) with rebar (usually double reinforced).

2.10.1 Parametric Study and Comparison with Experimental Data

An experimental study on six commercially-available UHPC materials was conducted by FHWA (Haber et al. , [79], [83]). The objective of the study was to obtain a comprehensive set of mechanical and physical properties for the field-cast UHPC materials that are used in the closure pours. The objective of the closure pours is to connect adjacent prefabricated bridge elements; these are employed in many ABC projects in North America. The mix designs for components for each of the UHPC types are listed in Table 15. The UHPC-class materials were assessed using 14 different

ASTM, AASHTO, or FHWA-TFHRC-developed test methods. Their 4PB test setup is shown in Figure 93.

Table 15. Components of each type of proprietary UHPC material [83].

ID		U-A	U-B	U-C	U-D	U-E	U-F
Mix Design		lb/yd^3	lb/yd^3	lb/yd^3	lb/yd^3	lb/yd^3	lb/yd^3
Pre-blended dry powders		3503	3516	3600	3700	3236	3725
Water		278	354	268	219	379	241
Chem admix	Liquid	23	48	na	89	73	65.7
	Solid	na	na	Pre-blended	na	na	1.5
Steel fiber content (2%) Short / Long Fibers		277	88/ 179	272	263	263	284
Tensile strength, ksi		160	≥305	348	399	399	399
Length, in		1.18	0.5 / 0.79	0.5	0.5	0.5	0.5
Diameter, in		0.022	0.012	0.012	0.008	0.008	0.008
E_c, ksi		7500	6300	6300	7200	5300	--
f_c', ksi		21	22	19	18	17	--
σ_{cr}, ksi		1.06	1.10	0.76	1.23	1.01	--

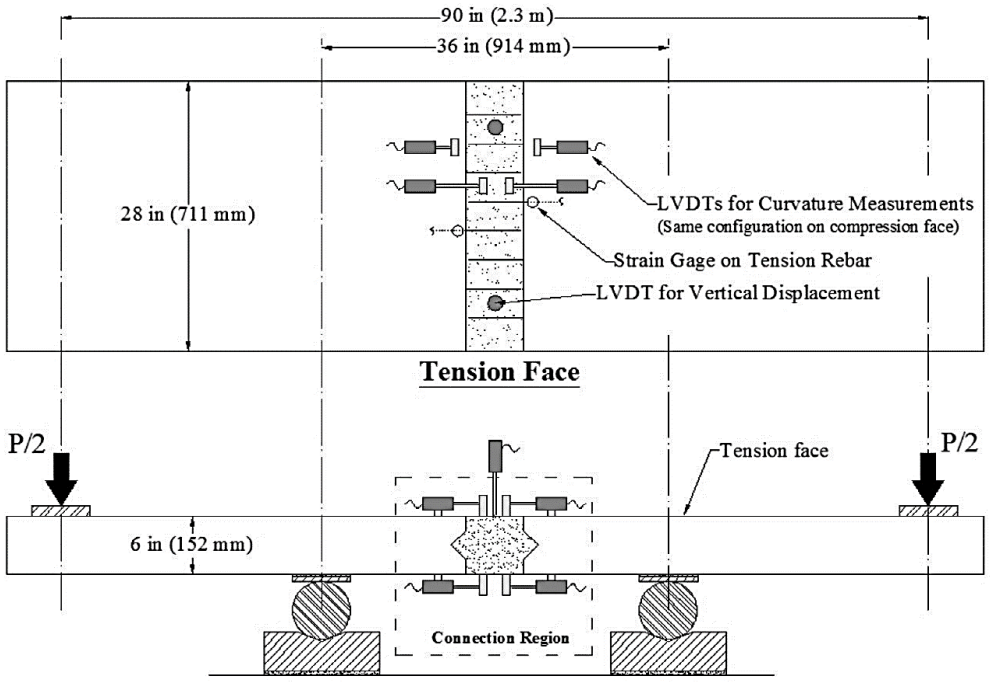

(a)

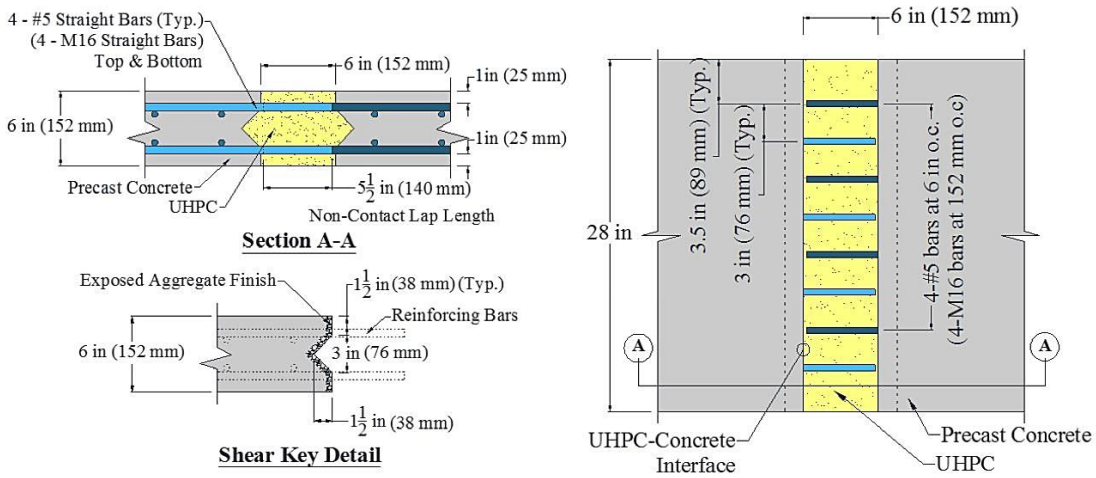

(b)

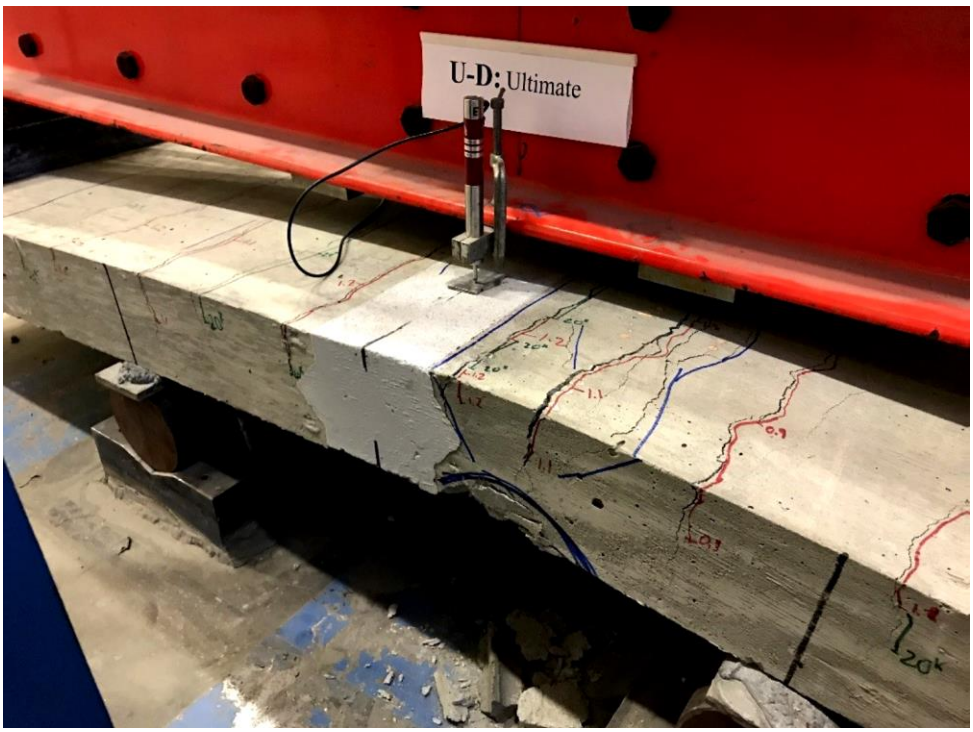

(c)

Figure 93. Instrumentation and loading configuration of 4PB test setup [79].

The Haber team performed 4PB tests on five sets of beams, each made of a different commercially available UHPC material. Four sets of tests were used in the back-

calculations and load-deflection simulations. The details of each mix design and the comprehensive tests (including compression, tension, and bending) can be found in the original research [79].

The objective of the current study is to simulate the full-scale tests conducted using these materials in order to develop a design guideline and procedure.

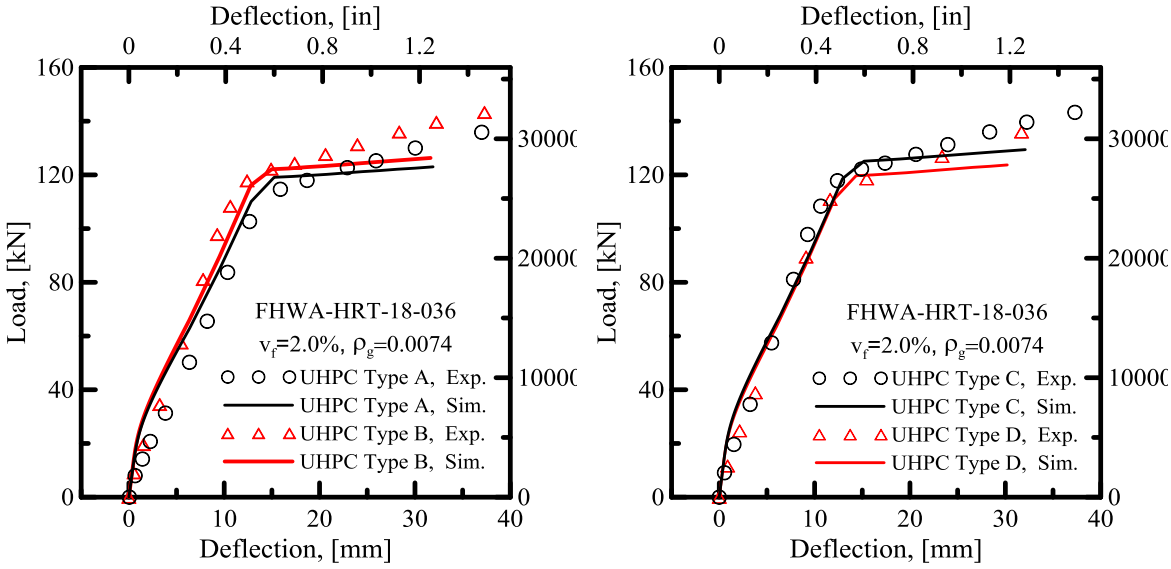

Figure 94. Results from inverse analysis and comparison with the experimental data.

Haber employed 0.74 percent reinforcement, which is acceptable for normal RC members with UHPC joints. For members fully made of UHPC, however, it is possible to use up to 15 percent reinforcement, grade 60). A parametric study on this beam-joint system is presented next. The dimensions and material properties are as follows (Figure 93):

Table 16. Material properties of the joint and the slab concrete.

Properties	RC	UHPC joint
L	90 inches	
L_j (joint length)	--	0.5, 1.0, and 1.5 ft
b (section width in inches)	28	28
d (section depth in inches)	6	6
E (ksi)	4600	6700
$f_{c1}^{'}$ (ksi)	4.3	19
σ_{cr} (psi)	500	1200
ω	9	17
γ	1	1
μ	0	1
E_s (ksi)	29000	29000
$\rho_s (= \rho_s')$	0.0074	0.0074
f_{sy} *(ksi)*	61	61

Figure 95 shows the moment-curvature responses for both sections, i.e., RC used as the standard section and the UHPC joint. The moment capacity of the section is dominated by the capacity of the weaker section (RC section); therefore the moment capacity cannot exceed this value (42 kN-m) and, although the UHPC is cracked, it does not reach its maximum moment capacity and never enters its localized region (after maximum moment). However, these curves show that making stronger joints will not help to improve the capacity of the member and that the member itself, not the joint, dominates the capacity of the entire structural configuration.

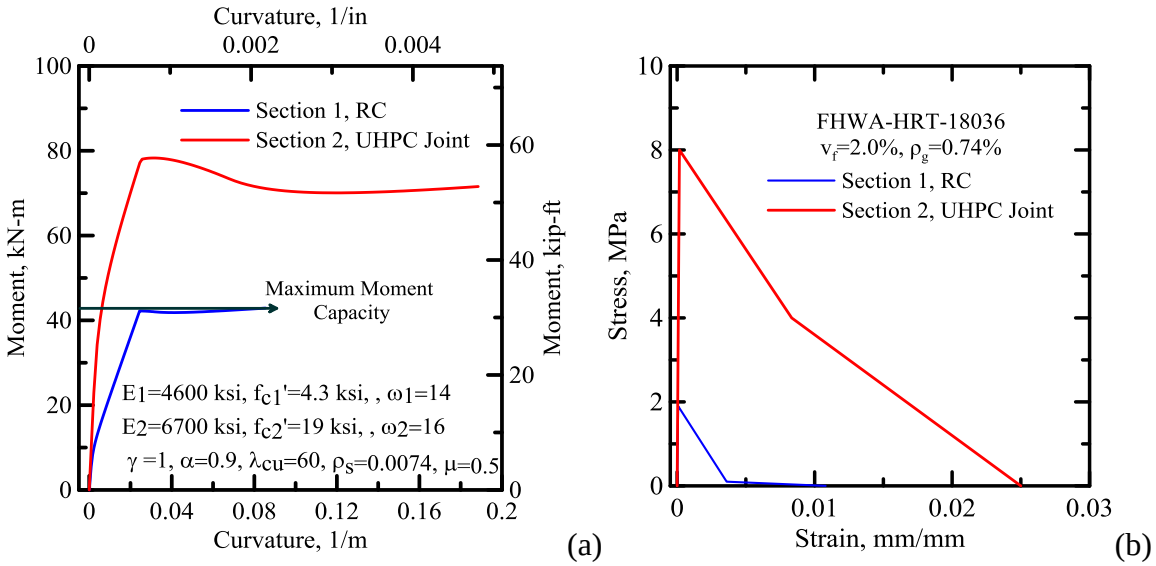

Figure 95. Moment-curvature response for two different sections (RC and UHPC joint).

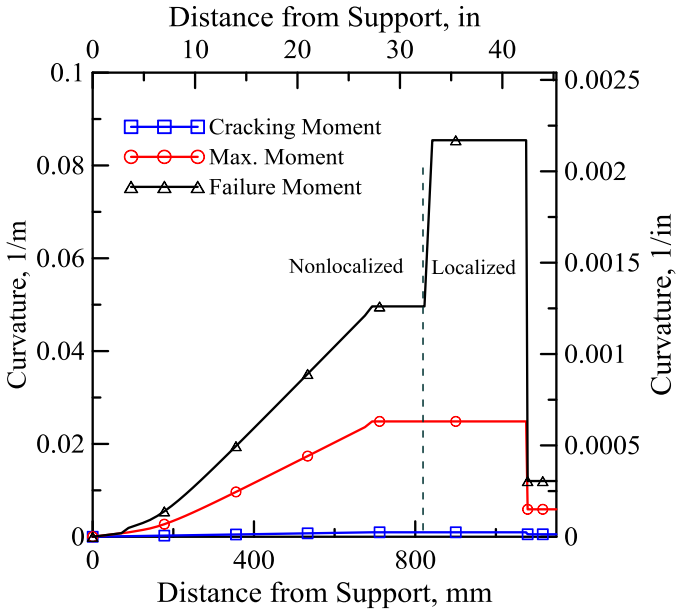

Figure 96. Curvature distribution along the beam axis (for half of the simulated beam).

Figure 96 demonstrates the curvature distribution along the beam axis obtained from the MATLAB simulation. Before reaching the maximum moment (the red curve in the figure), there is no difference between the curvature in the localized and non-localized zones. During the unloading, however, there is a significant difference between the

curvature in the two due to the localization. The curvature in the joint never reaches its maximum capacity and the localization never happens at this part. As the joint length increases, the stiffness of the member is expected to increase as well. Figure 97 shows the effect of the joint length on the load-deflection response of the beam-joint element under 4PB simulation.

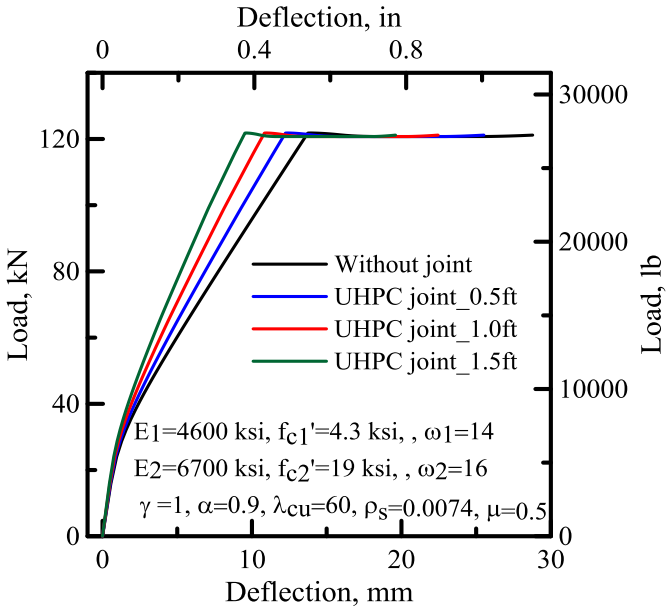

Figure 97. The effect of the joint length on the load-deflection response of the example beam-joint element.

In this simulation, it is assumed that the joint is made of UHPC and the beam element of normal concrete. As the length of the UHPC joint increases, the stiffness of the system increases so the mid-span deflection decreases. On the other hand, it was shown that the extra strength in the UHPC joint cannot be used as long as the RC section itself is not able to carry that extra strength, therefore, a UHPC joint which is about 20% stronger than the RC section can be a rational design.

2.10.2 Solved Example Problems for – Parametric Based Design for UHPC

The sample problem can be constructed in three different cases:

Case A - The sizes of the beam and the residual strength of the material are known; the maximum allowable load is required for a given geometry.

Case B - Size of the beam and the loading condition (moment demand) are known; the level of residual strength is required.

Case C - The residual strength of the material and the loading condition (moment demand) are known; the size of the section is required.

- Case A- Calculation of the moment capacity of a given section

The aim of this section is to use the simplified ultimate strength approach and compare the parametric design of FRC with the solutions obtained from ACI 544.8R-16, in order to illustrate the process of obtaining moment capacity for a section and compute the allowable service load.

- Problem Statement- Compute the maximum allowable load on a simply supported beam with a span of $L = 10$ ft (3.04 m) and a rectangular section 6 in × 12 in (152 mm × 305 mm). UHPC concrete has a compressive strength, $f_c^{'}$, of 22 ksi (151.6 MPa) . Design for a material with $f^{D}_{150} = 580$ psi (4 MPa) . Assume a concrete density as $\rho_c = 150$ lb/ft^3 (2402.7 kg/m^3) and compute

unfactored moment by assuming $\phi = 1$ (ϕ is strength reduction factor, which is less than one in accordance with ACI 318-14 Section 10.5.1[66].

For an illustration of the calculation and comparison, Case A is addressed in this example. Figure 98 shows a schematic side view of the simply supported beam under a center loading.

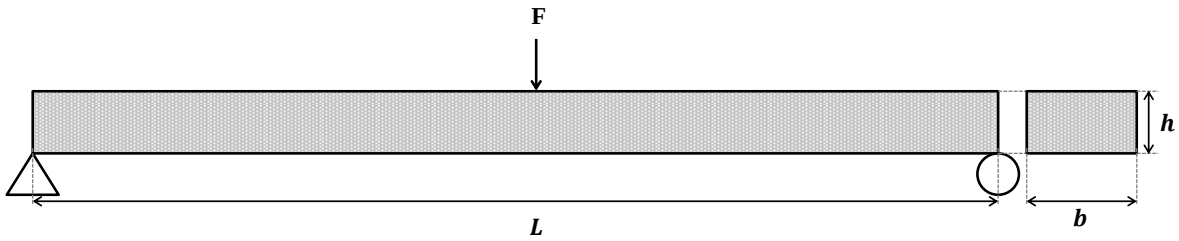

Figure 98. Sample problem, simply supported beam with center point loading.

- Step 1: Define geometric and material parameters

$L = 10$ ft (3.3 m), $b = 12$" (0.3 m), $h = 6$" (0.15 m), $\phi = 1$, $f_c' = 22$ ksi (151.6 MPa)

Assume $\gamma = 1$, thus: $E_c = E$; also $\sigma_{cr} = 0.04 f_c'$

$$E = 49000\sqrt{f_c'} = 7.27 \times 10^6 \text{ psi } (50 \text{ GPa})$$

$$\sigma_{cr} = 0.04 f'_c = 0.04 \times 22000 = 880 \text{ psi } (6.07 \text{ MPa})$$

$$\varepsilon_{cr} = \frac{\sigma_{cr}}{E} = \frac{880 \text{ psi}}{7270000 \text{ psi}} = 1.21 \times 10^{-4}$$

$$\varepsilon_{cy} = \beta_2 \times \frac{f_c'}{E} = 0.85 \times \frac{22000 \text{ psi}}{7270000 \text{ psi}} = 0.85 \times 0.003 = 2.57 \times 10^{-3}$$

β_{tu} is the normalized ultimate tensile strain in the section, since it is assumed that the section will maintain its residual tensile strength. This value is expected to be imposed as a large number. In this example, it is considered to be equal to 50, i.e., $\beta_{tu} = \varepsilon_{tu} / \varepsilon_{cr} = 50$. Therefore, the maximum tensile strain allowed is $\varepsilon_{tu} = 0.0055$ or 0.55%.

- Step 2: Calculate demand moment

$$M_u = M_{DL} + M_F$$

Where M_{DL} is moment due to dead weight and M_F is the moment due to point load.

$$\text{w} = \frac{72 \text{ in}^2}{144} \times 150 \text{ lb/ft}^3 = 75 \text{ lb/ft} = 6.25 \text{ lb/in} \left(1.09 \text{ kN/m}\right)$$

$$M_{DL} = \frac{wL^2}{8} = \frac{75 \text{ lb/ft} \times 10^2 \text{ ft}^2}{8} = 937.5 \text{ lb-ft} = 11250 \text{ lb-in} \left(1.27 \text{ kN-m}\right)$$

For a simply supported beam the maximum moment is at the center of the beam:

$$\phi \text{M}_\text{n} = M_u = 937.5 + \frac{F \times 10}{4} \text{ lb-ft} = 11250 + 30F \text{ lb-in}$$

- Step 3: Calculate the cracking moment

The cracking moment is given by:

$$M_{cr} = \frac{1}{6} \sigma_{cr} b h^2 = \frac{1}{6} (880 \text{ psi}) \times 12'' \times (6'')^2 = 63360 \text{ lb-in} = 5.28 \text{ kips-ft } (7.16 \text{ kN-m})$$

- Step 4: Determine post-crack tensile strength (ACI 544.8R-16)

Use the formula for plain FRC (according to Eq.(52))

$$M_n = \frac{31 f^{D}_{150}}{f_c'} M_{cr}$$

$$= \left[\frac{31 \times 580}{22000} \right] \times 5.28 = 4314 \text{ lb-ft } (5.84 \text{ kN-m})$$

$$\phi M_u = M_n \Rightarrow \left(937.5 + \frac{F \times 10}{4} \right) = 4314 \text{ lb-ft}$$

$$F = 1350.6 \text{ lb } (6.0 \text{ kN})$$

- Simplified Approach:

Here the results of the previous method are compared with the results from the simplified approach. From Eq.(13) we have

$$M_n = \frac{\omega\mu(3\omega + 8\mu)}{(\omega + 2\mu)^2} \times M_{cr}$$

Where

$$\omega = \frac{\varepsilon_{cr}}{\varepsilon_{cr}} = \frac{2.57 \times 10^{-3}}{1.21 \times 10^{-4}} = 21.25 \text{ and } \mu = \frac{f^{D}_{150}}{2.42\sigma_{cr}} = \frac{580}{2.42 \times 880} = 0.27$$

Thus

$$M_n = 50895 \text{ lb-in} = 4241 \text{ lb-ft } (5.75 \text{ kN-m})$$

Moment capacity obtained from the simplified method is 11 percent higher than the value obtained from the ULS method. The simulated moment-curvature diagram for this example is shown in Figure 99. Both ULS and the simplified approach give an

acceptable result. However, before reaching the ultimate state, the section is able to carry higher bending moments than the ultimate moment capacity.

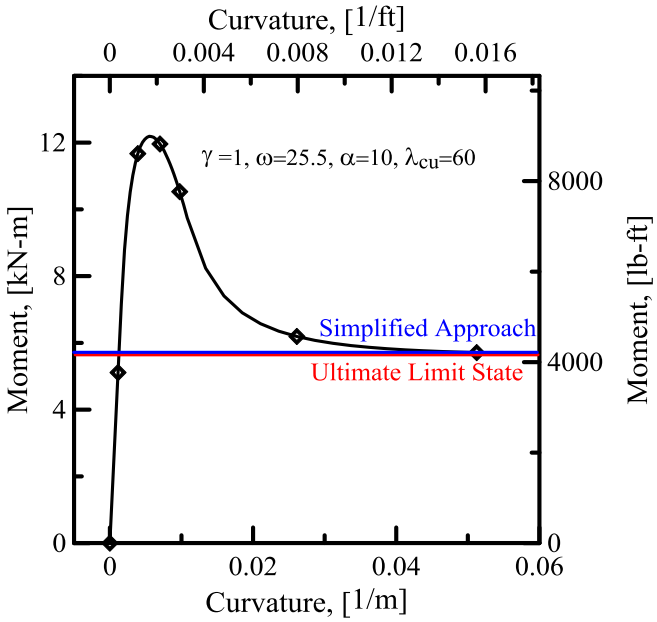

Figure 99. Comparison between different analytical models.

- Case A- Calculation of the moment capacity of a given reinforced joint

This part presents a design example for the reinforced section with a joint at the middle section of the beam. The design procedure will be calculated using the solutions obtained from ACI 544.8R-16, to illustrate the process of obtaining moment capacity for a UHPC joint under specific loading conditions and compute the allowable service load. All of the dimensions are similar to the previous example; only the parameters for the reinforcement and the UHPC joint are extra parameters in this example.

- Problem Statement- Compute the maximum bending capacity of the UHPC joint as a function of allowable load, F, on a simply supported single reinforced beam

with a span of $L = 10\text{ ft}\ (3.04\text{ m})$ and a rectangular section 6in × 12in (152 × 305 millimeters). The reinforcement consisted of 3 Grade 60 #4 rebars, $E_s = 30\times10^6$ psi (210 GPa) (see Figure A.1.b), with a yield strength σ_{sy} (or f_y) of 74 ksi (510 MPa), yield strain ε_{sy} of 0.24 percent, and the reinforcement depth is $d = 5\text{in}$. Two loads with a loading gage of L/3 are applied on top of the beam and the joint length, $L_j = 6\text{in}$ (152 mm).

Normal concrete has $f_{c1}^{'} = 6$ ksi (41.4 MPa) and $\sigma_{cr1} = 0.3$ ksi (2 MPa); UHPC concrete has $f_{c2}^{'} = 22$ ksi (151.6 MPa) and $\sigma_{cr2} = 1.2$ ksi (8.27 MPa). Design for a UHPC material with $f^{D}_{150} = 580$ psi (4 MPa). Assume a concrete density as $\rho_c = 150\text{ lb/ft}^3$ (2402.7 kg/m^3) for both normal concrete and UHPC.

To illustrate the calculation, Figure 100 shows a schematic side view of the simply supported beam under two equal loadings.

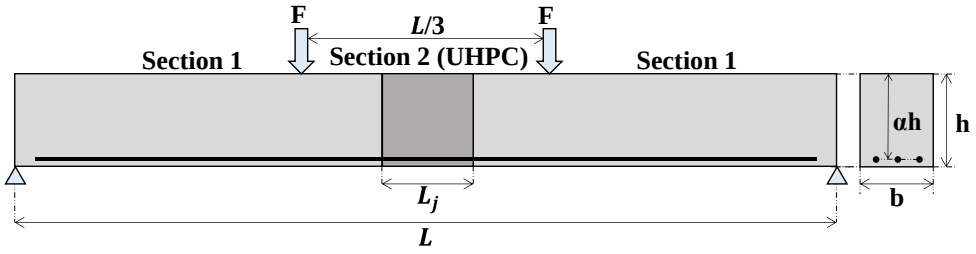

Figure 100. Sample problem, simply supported beam with center point loading.

- Step 1: Define geometric and material parameters

  $L = 10$ ft (3.3 m), $b = 12$" (0.305 m), $h = 6$" (0.152 m), $\phi = 1$

Also,, $\sigma_{cr2} = 0.04 f_{c2}'$ and $E_{c2} = 49000\sqrt{f_{c2}'}$, thus:

$$E_{c1} = 57000\sqrt{f_{c1}'} = 4.4\times10^{6} \text{ psi } (30 \text{ GPa})$$

$$\sigma_{cr1} = 6.7\sqrt{f_{c1}'} = 519 \text{ psi (3.6 MPa)}$$

$$E_{c2} = 49000\sqrt{f_{c2}'} = 7.27\times10^{6} \text{ psi (50 GPa)}$$

$$\sigma_{cr2} = 0.04 f'_{c} = 0.04\times 22000 = 880 \text{ psi } (6.07 \text{ MPa})$$

$$\varepsilon_{cr1} = \frac{\sigma_{cr1}}{E_{c1}} = \frac{519 \text{ psi}}{4400000 \text{ psi}} = 1.18\times10^{-4}$$

$$\varepsilon_{cr2} = \frac{\sigma_{cr2}}{E_{c2}} = \frac{880 \text{ psi}}{7270000 \text{ psi}} = 1.21\times10^{-4}$$

β_{tu} is the normalized ultimate tensile strain in the section. Since it is assumed that the section will maintain its residual tensile strength, this value is expected to be imposed as a large number. In this example, it is considered to be equal to 50, i.e. $\beta_{tu} = \varepsilon_{tu} / \varepsilon_{cr} = 50$. Therefore, the maximum tensile strain allowed is $\varepsilon_{tu} = 0.0055$ or 0.55%.

ω is the ratio of compressive strength to tensile strength and obtained as

$$\omega = \beta_2 \times \frac{f_c^{'}}{\sigma_{cr}} = 0.85 \times \frac{22000 \text{ psi}}{880 \text{ psi}} = 21.25$$

- Step 2: Calculate the demand moment

$$M_u = M_{DL} + M_F$$

Where, M_{DL} is the moment due to dead weight and M_F is the moment due to point load.

$$\mathrm{w} = \frac{72\ \mathrm{in}^2}{144} \times 150\ \mathrm{lb/ft}^3 = 75\ \mathrm{lb/ft} = 6.25\ \mathrm{lb/in}\left(1.09\ \mathrm{kN/m}\right)$$

$$M_{DL} = \frac{wL^2}{8} = \frac{75\ \mathrm{lb/ft} \times 10^2\ \mathrm{ft}^2}{8} = 937.5\ \mathrm{lb\text{-}ft} = 11250\ \mathrm{lb\text{-}in}\left(1.27\ \mathrm{kN\text{-}m}\right)$$

For a simply supported beam the maximum moment is at the center of the beam:

$$\phi \mathrm{M_n} = M_u = 937.5\ \mathrm{ft} + \frac{F \times 10}{3}\ \mathrm{lb\text{-}ft}$$

- Step 3: Calculate the cracking moment

Is this problem there are two different sections. The RC section is likely to fail before UHPC joint failure, so the design should be based on the properties of the beam section (section 1). However, the purpose of this example is to introduce the design process of the UHPC joint section and its bending capacity. Therefore, the calculations for the RC section are not represented here and only the comparative results are demonstrated in Figure 101.

Cracking moment of the joint is given by:

$$M_{cr} = \frac{1}{6}\sigma_{cr} b h^2 = \frac{1}{6}(880\ \mathrm{psi}) \times 12'' \times (6'')^2 = 63360\ \mathrm{lb\text{-}in} = 5.28\ \mathrm{kips\text{-}ft}\ (7.16\ \mathrm{kN\text{-}m})$$

- Step 4: Minimum and balanced reinforcement

Minimum reinforcement is given by (ACI Committee 318, 2014)

$$\rho_{\min} = \text{Max}[\frac{200}{f_y}, \frac{3\sqrt{f_c'}}{f_y}] = \text{Max}[\frac{200}{74000}, \frac{3\sqrt{22000}}{74000}] = \text{Max}[0.0027, 0.006] = 0.006$$

For this example we have

$$\rho_g = \frac{3 \times 0.2 \text{ in}^2}{12 \times 5 \text{ in}^2} = 0.01 \geq \rho_{\min}, \text{ Passed}$$

To calculate the balanced reinforcement ρ_{bal} from Eq.(29) we have

$$\rho_b = \frac{\beta_1 \omega^2 - \kappa\mu}{(\kappa + \omega) n \kappa}$$

From Eqs.(16) to (19) and Eq. (51)

$$\kappa = \frac{\varepsilon_{sy}}{\varepsilon_{cr}} = \frac{2.4 \times 10^{-3}}{1.21 \times 10^{-4}} = 20$$

$$n = \frac{E_s}{E_c} = \frac{30 \times 10^6 \text{ psi}}{7.27 \times 10^6 \text{ psi}} = 4.1$$

$$\mu = \frac{f^D_{150}}{2.42\sigma_{cr}} = \frac{580 \text{ psi}}{2.42 \times 880 \text{ psi}} = 0.27$$

Thus

$$\rho_b = \frac{0.65 \times 0.85 \times 21.25^2 - 0.27 \times 20}{(20 + 0.27) \times 4.1 \times 20} = 0.082 >> \rho_g, \text{ Passed}$$

The current reinforcement is much lower than the balanced reinforcement (i.e., $\rho_g << \rho_b = 8\%$).

- Step 5: Determine post-crack tensile strength (ACI 544.8R-16)

Use the formula for the single reinforced section, according to Eq. (54)

$$M_n \approx m_\infty M_{cr} = \frac{6\rho_g n\kappa\left(\mu\alpha - \mu + \alpha\omega\right) + 3\omega\mu - 3\left(\rho_g n\kappa\right)^2}{\omega + \mu} M_{cr}$$

Where

$$\alpha = \frac{d}{h} = \frac{5 \text{ in}}{6 \text{ in}} = 0.83$$

Thus

$$M_n = 4.74 \times M_{cr} = 4.87 \times 63360 = 307 \text{ kip-in} = 25600 \text{ lb-ft (34.7 kN-m)}$$

$$\phi M_u = M_n \Rightarrow \left(937.5 + \frac{F \times 10}{3}\right) = 25600 \text{ lb-ft}$$

$$F = 7.4 \text{ kip } (32.9 \text{ kN})$$

- Simplified approach:

Here the results of the ULS method is compared with the results from the simplified approach. From Eq.(26) we have

$$M_n = 3\left[\mu(1-A)\left(1 + A(1-\beta_1)\right) + 2\rho\kappa n\left(\alpha - \frac{A\beta_1}{2}\right)\right] \times M_{cr}$$

Where

$$A = \frac{\mu + \rho\kappa n}{\beta_1\omega + \mu}$$

Thus

$M_n = 307.2$ kip-in $= 25.6$ kip-ft (34.71 kN-m)

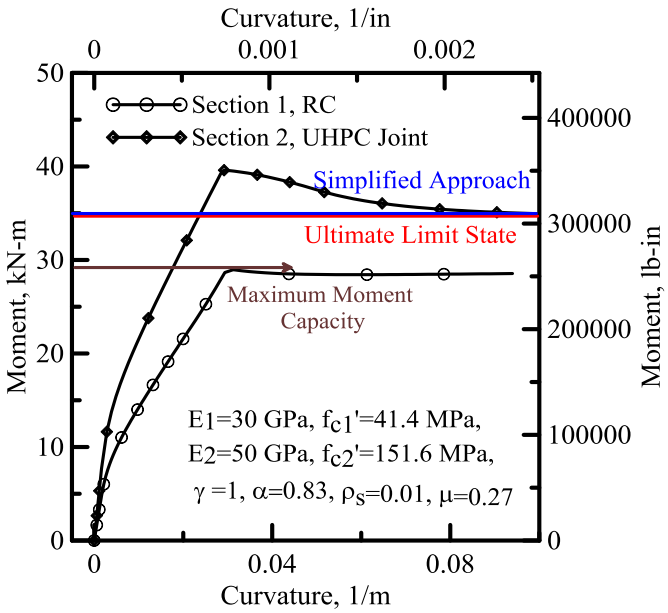

Figure 101. Comparative results for different design approaches (1 MPa = 145 psi).

This figure shows a comparison between different design methods for the UHPC joint (section 2). As can be observed from the figure, there is a very good agreement between different approaches at ULS. However, the RC section (section 1) has a lower bending strength (about 20 percent) and will dominate the failure of the element, regardless of the UHPC joint's strength. Therefore, the proper design approach is to first design the RC beam and then control the joint.

2.11 Summary

Several analytical approaches were presented to evaluate the flexural capacity of the FRC, HRC and UHPC sections. The presented approaches can be used in ultimate limit state and serviceability limit sate designs. Their accuracy was also investigated

through comparison with the experimental results from the current research on UHPC samples and several experiments by other groups as well. The simulation results show a good agreement between the experimental and simulated results, around 8% difference in the non-linear part of the load-deflection curves.

A model was also developed for the cast in place UHPC joints in the precast bridge segments. The simulation results showed that the proposed analytical approach is able to accurately predict the load-deflection curves for the precast bridge decks with the cast in place UHPC joints. The effect of the joint length and the material properties of the joint were studied in several parametric studies and comparative graphs. Two solved examples were also presented to show the application of the given analytical approaches for design purposes.

3 FRC SECTIONS REINFORCED WITH FIBER REINFORCED POLYMER (FRP) AND TEXTILE REINFORCED CONCRETE (TRC)

The issue of upgrading the existing civil engineering infrastructure has been one of great importance for over a decade. Deterioration of bridge decks, beams, girders and columns, buildings, parking structures, and others may be attributed to aging, environmentally induced degradation, poor initial design and/or construction, lack of maintenance, and to accidental events such as earthquakes. The infrastructure's increasing decay is frequently combined with the need for upgrading so that structures can meet more stringent design requirements (e.g. increased traffic volumes in bridges exceeding the initial design loads), and hence the aspect of civil engineering infrastructure renewal has received considerable attention over the past few years throughout the world. At the same time, seismic retrofit has become at least equally important, especially in areas of high seismic risk.

Recent developments related to materials, methods, and techniques for structural strengthening have been enormous. One of today's state-of-the-art techniques is the use of fiber reinforced polymer (FRP) composites, which are currently viewed by structural engineers as "new" and highly promising materials in the construction industry [84]–[86].

The reasons why composites are increasingly used as strengthening materials of reinforced concrete elements may be summarized as follows: immunity to corrosion; low weight (about ¼ of steel), resulting in easier application in confined space, elimination of the need for scaffolding and reduction in labor costs; very high tensile strength (both static and long-term, for certain types of FRP materials); stiffness which may be tailored to the design requirements; large deformation capacity; and practically unlimited

availability in FRP sizes and FRP geometry and dimensions. Composites suffer from certain disadvantages too, which are not to be neglected by engineers: contrary to steel, which behaves in an elastoplastic manner, composites, in general, are linear elastic to failure (although the latter occurs at large strains) without any significant yielding or plastic deformation, leading to reduced ductility. Additionally, the cost of materials on a weight basis is several times higher than that for steel (but when cost comparisons are made on a strength basis, they become less unfavorable). Moreover, some FRP materials, e.g. carbon and aramid, have incompatible thermal expansion coefficients with concrete. Finally, their exposure to high temperatures (e.g. in case of fire) may cause premature degradation and collapse (some epoxy resins start softening at about 45- 70 o C). Hence FRP materials should not be thought of as a blind replacement of steel (or other materials) in structural intervention applications. Instead, the advantages offered by them should be evaluated against potential drawbacks, and final decisions regarding their use should be based on consideration of several factors, including not only mechanical performance aspects, but also constructability and long-term durability [87].

Other types of the material that are being used for strengthening and reinforcement proposes are the textile reinforced concrete (TRC) materials. TRC is a composite material that combines the advantages of fiber-reinforced concrete and ordinary RC [88]. Due to the superior corrosion resistance of fiber materials [e.g., alkali-resistant (AR-glass), carbon, aramid, and basalt], the concrete cover is no longer needed as special chemical protection [88]. The thickness of TRC members depends primarily on the necessary value to ensure a proper anchorage of the reinforcement and to avoid splitting failure [89].

The application of TRC to strengthen different types of existing structure members, including plates or beams [90], [91], columns [92], beam-column joints [93], masonry [94], shells [95], and other structural members have been investigated [96]. The results show that using TRC as the reinforcement material is an effective way to strengthen the structure. TRC not only improves the load-bearing and seismic resistance capacity of the structure and restricts the extension of cracks in the structures, but it also overcomes a series of drawbacks of fiber-reinforced polymers [97]. The replacement of the organic binders with inorganic ones—for example, cement-based mortars—allows the reduction or elimination of some disadvantages related to the use of polymeric resins, such as the toxicity, loss of resistance to high temperatures, and less compatibility with the substrate [94], [97]. Other reinforced systems based on the use of cementitious mortars, such as CFCM, TRM, BRM, and FRCM, all prove the effectiveness of cement-based composites for strengthening RC structures[96], [98].

Based on the existing application of TRC and FRP reinforced RC members, and in view of the structural design, this study attempts to propose some analytical solutions based on the constitutive model, which was discussed in the previous sections. Using this concept, the mechanical characteristics of the RC structures and design approaches may be improved significantly. The TRC (or FRP) layer allows for the uniform distribution of cracks throughout the tensile zone of the component. Thus, the main crack's propagation is delayed and the role of the tensile steel bar is utilized better, leading to better performance of the RC structures in the service stage. Therefore, future maintenance costs can be reduced. Furthermore, if the tensile force of the textile is considered, the steel reinforcement replaced with the textile may be subtracted. Due to the corrosion

resistance of fiber materials and the excellent crack pattern (smaller crack width and spacing) of this component, the concrete cover on the steel bar may be reduced, which leads to decreasing the dead weight of the structures.

In this project, the same constitutive approach is chosen to predict the behavior of an HRC beam section reinforced with TRC (FRP) plates. The related formulations are derived, and the results will be compared with the experimental results and also with the results from the literature.

Figure 102 presents three distinct material models used in the derivation of the parametric response of FRP-HRC beams. Material parameters are described as two intrinsic parameters: tensile modulus E and the first cracking tensile strain ε_{cr} while other variables are normalized with respect to these intrinsic parameters. Figure 102a shows an idealized tension model with an elastic range of stress increases linearly with E up to the first cracking tensile strength coordinates (ε_{cr}, σ_{cr}). In the post-crack region, the stress is constant at $\sigma_P = \mu\sigma_{cr} = \mu\varepsilon_{cr}E$ and terminates at the ultimate tensile strain $\varepsilon_{tu} = \beta_{tu}\varepsilon_{cr}$.

Figure 102b shows the elastic-perfectly plastic compression response with a modulus $E_c = \gamma E$. The plastic range initiates at strain $\varepsilon_{cy} = \omega\varepsilon_{cr}$ corresponding to yield stress $\sigma_{cy} = \omega\gamma\varepsilon_{cr}E$ and terminated at $\varepsilon_{cu} = \lambda_{cu}\varepsilon_{cr}$. Figure 102c is the elastic-perfectly plastic steel model using yield strain and stress of $\varepsilon_{sy} = \kappa\varepsilon_{cr}$ and $f_{sy} = \kappa n\varepsilon_{cr}E$ as defined by normalized parameters: κ and n. No termination level is specified for steel strain. Geometrical parameters are also normalized with the beam dimensions of width b and full depth h, as shown in Figure 102d with steel parameters defined as area $A_s = \rho_g bh = \rho_g bd/\alpha$ at the reinforced depth $d = \alpha h$. The reinforcemethe nt ratio ρ_g is

defined per gross sectional area bh, and differs slightly from the conventional definition based on term bd used in reinforced concrete nomenclature.

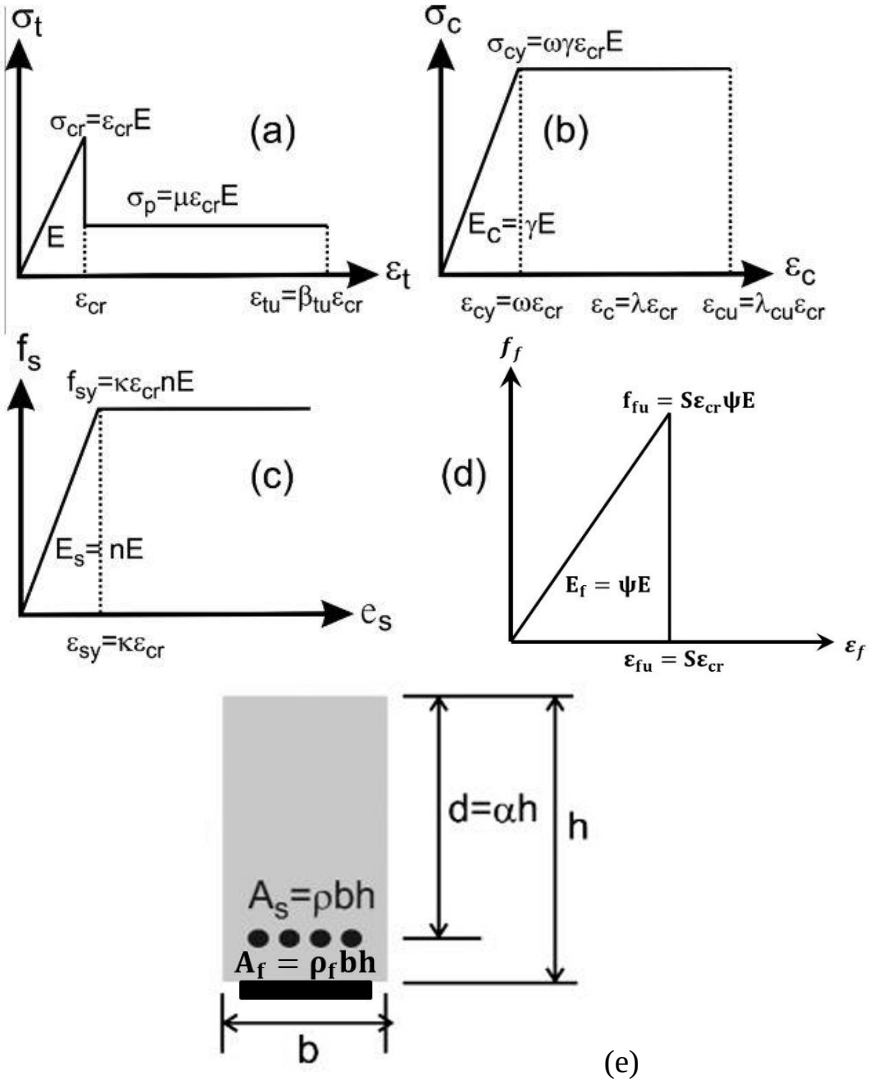

Figure 102. Material model for single reinforced concrete design (a) tension model; (b) compression model; (c) steel model; (d) FRP model; (e) Beam cross section.

The material models for tension and compression of FRC and the model for steel rebar are presented as:

$$\sigma_t(\varepsilon_t)=\begin{cases}E\varepsilon_t & 0\le\varepsilon_t\le\varepsilon_{cr}\\ \mu E\varepsilon_{cr} & \varepsilon_{cr}<\varepsilon_t\le\varepsilon_{tu}\\ 0 & \varepsilon_t\le\varepsilon_{tu}\end{cases};\quad \frac{\sigma_t(\beta)}{E\varepsilon_{cr}}=\begin{cases}\beta & 0\le\beta\le 1\\ \mu & 1<\beta\le\beta_{tu}\\ 0 & \beta>\beta_{tu}\end{cases} \tag{55}$$

$$\sigma_c(\varepsilon_c)=\begin{cases}E_c\varepsilon_c & 0\le\varepsilon_c\le\varepsilon_{cy}\\ E_c\varepsilon_{cy} & \varepsilon_{cy}<\varepsilon_c\le\varepsilon_{cu}\\ 0 & \varepsilon_c\le\varepsilon_{cu}\end{cases};\quad \frac{\sigma_c(\lambda)}{E\varepsilon_{cr}}=\begin{cases}\gamma\lambda & 0\le\lambda\le\omega\\ \gamma\omega & \omega<\lambda\le\lambda_{cu}\\ 0 & \lambda>\lambda_{cu}\end{cases} \tag{56}$$

$$f_s(\varepsilon_c)=\begin{cases}E_s\varepsilon_s & 0\le\varepsilon_s\le\varepsilon_{sy}\\ E_s\varepsilon_{sy} & \varepsilon_s>\varepsilon_{sy}\end{cases};\quad \frac{f_s(\chi)}{E\varepsilon_{cr}}=\begin{cases}n\chi & 0\le\chi\le\kappa\\ n\kappa & \chi>\kappa\end{cases} \tag{57}$$

$$f_f(\varepsilon_f)=\begin{cases}E_f\varepsilon_f & 0\le\varepsilon_f\le\varepsilon_{fu}\\ 0 & \varepsilon_f>\varepsilon_{fu}\end{cases} \tag{58}$$

FRP behavior is considered linear before failure; and after failure, the tensile strength falls down to zero.

3.1.1 Stage 1

This is a pre-crack stage. Concrete is not cracked, and all materials are in the elastic region. In this case, schematic section strains and stresses can be shown as follows:

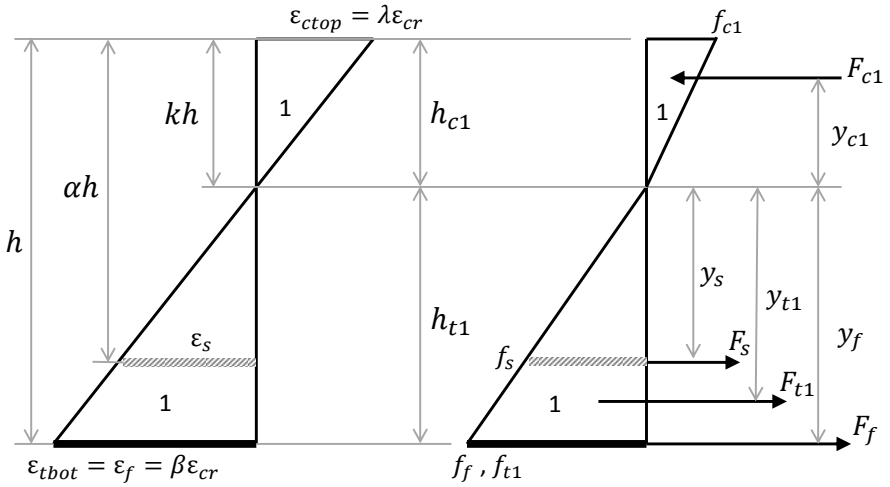

Figure 103. Strain and stress diagram at stage 1($0<\beta\le 1$) and ($0<\lambda\le\omega$), elastic compression–elastic tension.

3.1.2 Stage 2

This is a post-crack stage. In his stage, the compressive concrete is in the elastic range and has a linear behavior while the tensile concrete has cracked. In this case, there are two sub-scenarios. In the first one, the steel has not yielded and the FRP plate has not failed. In the second scenario, the steel has yielded but there are two possible sub-scenarios for FRP plate. The FRP plate may remain in the elastic region or fail, due to debonding or rupture. It is not probable that FRP fails before steel rebar yielding. These steps can be summarized as follows:

Table 17. Post crack sub-stages while the compressive concrete is still linear (stage 2)

Substage	Compressive Concrete	Tensile Concrete	Steel	FRP
2.1	Linear Elastic	Cracked	Un-yielded	Linear
2.2.1	Linear Elastic	Cracked	Yielded	Linear
2.2.2	Linear Elastic	Cracked	Yielded	Failed

In this case, schematic section strains and stresses can be shown as follows:

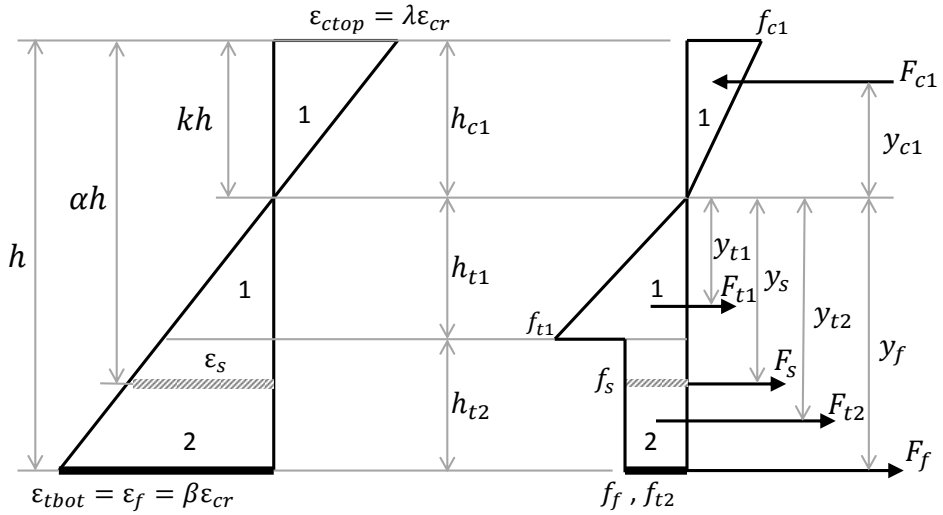

Figure 104. Strain and stress diagram at stage 2 ($1 \leq \beta \leq \beta_{tu}$) and ($0 < \lambda \leq \omega$), elastic compression – post crack tension.

3.1.3 Stage 3

In his stage, the compression concrete is in the plastic region and has a non-linear behavior and the tensile concrete is cracked. In this case, there are two sub-scenarios. In the first one, the steel has not yielded and the FRP plate has not failed. In the second scenario, the steel has yielded but there are two possible sub-scenarios for FRP plate. The FRP plate may remain in the elastic region or fail, due to debonding or rupture. Again, it is not probable that FRP fails before steel rebar yielding (see Figure 106). These steps can be summarized as follows:

Table 18. Post crack sub-stages while the compressive concrete is non-linear (stage 3)

Substage	Compressive Concrete	Tensile Concrete	Steel	FRP
3.1	Non-linear Plastic	Cracked	Un-yielded	Linear
3.2.1	Non-linear Plastic	Cracked	Yielded	Linear
3.2.2	Non-linear Plastic	Cracked	Yielded	Failed

In this case, schematic section strains and stresses can be shown as follows:

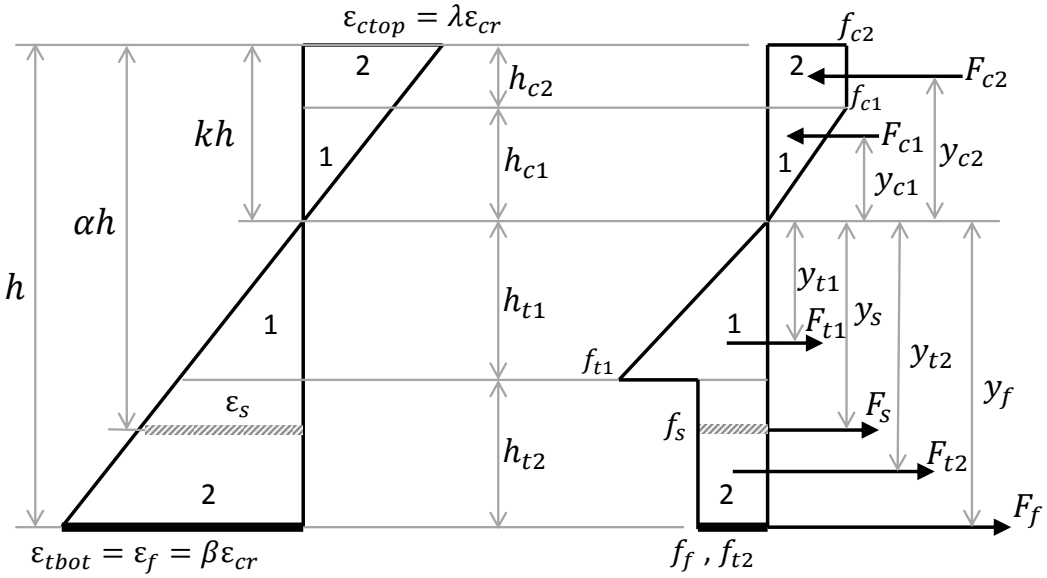

Figure 105. Strain and stress diagram at stage 3 ($1 \leq \beta \leq \beta_{tu}$) and ($\omega \leq \lambda \leq \lambda_{cu}$), plastic compression – post crack tension.

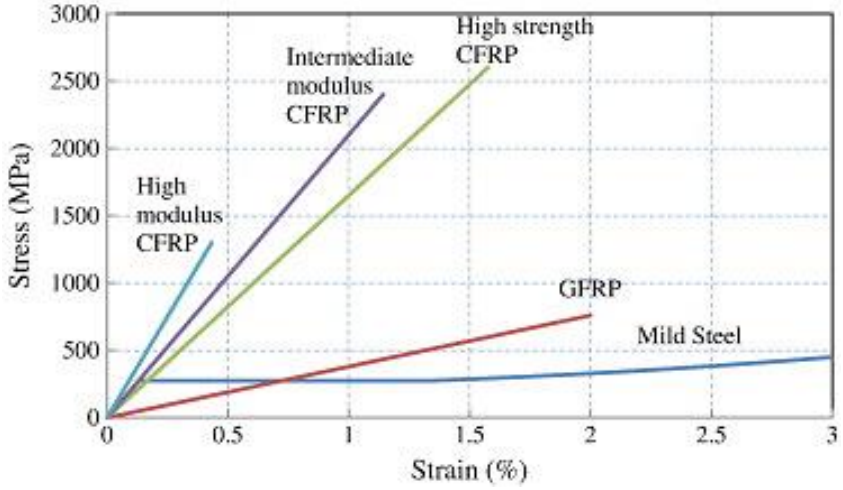

Figure 106. Comparison between stress-strain curves for steel and different types of FRP [14].

As it is shown in Figure 106, the assumption that the CFRP fails after steel yielding is a realistic assumption. This assumption required us to use values for S according to the below equation:

$$S \geq \frac{\kappa}{2(\alpha - 0.5)} \tag{59}$$

In this project, the calculations for each stage and sub-stage will be done and the results from the simulation will be compared to the experimental results.

3.2 Calculations

3.2.1 Stage 1, ($\mathbf{0 < \beta \leq 1}$) and ($\mathbf{0 < \lambda \leq \omega}$):

During Stage 1 the tensile and compressive zones are both elastic. This derivation is shown to familiarize the average person based on elastic mechanics of materials approach. Note that due to differences in the elastic modulus the neutral axis may not be at the center of the rectangular section, i.e. k=0.5 only in the case where γ=1. So the

general case of $\gamma > 1$ is presented here. According to Figure 105, the depth of Neutral axis is defined as:

$$h_{c1} = kh\,, \quad h_{t1} = (1-k)h \tag{60}$$

The stresses are obtained based on the stress at the tension fiber or $\beta\varepsilon_{cr} \leq \varepsilon_{cr}$

$$f_{c1} = \frac{\gamma\beta k}{1-k} E\varepsilon_{cr}\,, \qquad f_{t1} = E\varepsilon_{cr}\beta \tag{61}$$

$$f_s = \frac{(\alpha-k)}{1-k} nE\beta\varepsilon_{cr}\,, \quad f_f = \psi E\ \beta\varepsilon_{cr} \tag{62}$$

Tensile and compressive forces and their line of action are obtained by integration of the stresses across the depth:

$$F_{c1} = \int_{z=0}^{h_{c1}} \sigma(z) b\ dz = \int_{z=0}^{h_{c1}} \frac{\gamma\beta k}{1-k} E\varepsilon_{cr} b\ dz = \frac{\beta\gamma k^2}{2(1-k)} bhE\varepsilon_{cr} \tag{63}$$

$$F_{t1} = \int_{z=0}^{h_{t1}} \sigma(z) b\ dz = \int_{z=0}^{h_{t1}} E\varepsilon_{cr}\beta b\ dz = \frac{\beta}{2}(1-k) bhE\varepsilon_{cr} \tag{64}$$

$$F_s = A_s f_s = \frac{n\rho_g(\alpha-k)}{1-k} \beta bhE\varepsilon_{cr} \tag{65}$$

$$F_f = A_f f_f = \psi\beta\rho_f bhE\varepsilon_{cr} \tag{66}$$

Moment arms for each part of the section are as follows

$$y_{c1} = \frac{2}{3}kh \tag{67}$$

$$y_{t1} = \frac{2}{3}(1-k)h \tag{68}$$

$$y_s = (\alpha-k)h \tag{69}$$

$$y_f = (1-k)h \tag{70}$$

The Force and moment equilibrium require that:

$$\sum F = 0 \rightarrow F_{c1} - F_{t1} - F_s - F_f = 0 \tag{71}$$

Solution to this equation in terms of the value of neutral axis k is defined as k_1 obtained as:

$$k_1 = \begin{cases} \dfrac{B_3}{2B_2} & \gamma = 1 \\ -\left(\dfrac{B_2 - \sqrt{B_2^2 + B_1 B_3}}{B_1}\right) & \gamma \neq 1 \end{cases} \tag{72}$$

Where

$$B_1 = \gamma - 1 \tag{73}$$

$$B_2 = \rho_f \psi + \rho_g n + 1 \tag{74}$$

$$B_3 = 1 + 2\rho_g n\alpha + 2\rho_f \psi \tag{75}$$

For the moment in the section, we have

$$\sum M = F_{c1} y_{c1} + F_{t1} y_{t1} + F_s y_s + F_f y_f \tag{76}$$

The normalized values for the section moment, curvature and stiffness can be obtained using the cracking values M_{cr}, ϕ_{cr} and K_{cr}

$$M_i = M_i' M_{cr}; \quad M_{cr} = \frac{1}{6} b h^2 E \varepsilon_{cr} \tag{77}$$

$$\phi_i = \phi_i' \phi_{cr}; \quad \phi_{cr} = \frac{2\varepsilon_{cr}}{h} \tag{78}$$

$$K_i = K_i' K_{cr}; \quad K_{cr} = \frac{1}{12} b h^3 \tag{79}$$

Accordingly, the magnitude of the normalized internal moment can be obtained by substituting k_1 into equation (72).

$$M_1' = \frac{2\beta(B_1 k_1^3 + 3B_2 k_1^2 - 3B_3 k_1 + B_4)}{1 - k_1} \tag{80}$$

Based on the geometry of the section, the curvature is obtained as a function of depth of the neutral axis:

$$\phi_1' = \frac{1}{2}\left(\frac{\beta}{1-k_1}\right) \tag{81}$$

And

$$K_1' = \frac{M_1'}{\phi_1'} = 4B_1k_1^3 + 12B_2k_1^2 - 12B_3k_1 + 4B_4 \tag{82}$$

Where

$$B_4 = 3\rho_f\psi + 3\rho_g n\alpha^2 + 1 \tag{83}$$

The same approach can be chosen for the other stages. The results are summarized in several tables as follows:

Table 19. Normalized height of compression and tension zones for each stage of normalized tensile strain at bottom fiber (β).

Zone	Normalized height	Stage 1 ($\mathbf{0 < \beta \leq 1}$), ($\mathbf{0 < \lambda \leq \omega}$)	Stage 2 ($\mathbf{0 < \beta \leq 1}$), ($\mathbf{0 < \lambda \leq \omega}$)			Stage 3 ($1< \mathbf{\beta \leq \beta_{tu}}$), ($\mathbf{\lambda > \omega}$)		
			2.1	2.2 ($\varepsilon_s > \varepsilon_{sy}$)		3.1	3.2 ($\varepsilon_s > \varepsilon_{sy}$)	
				2.2.1	2.2.2 ($\varepsilon_f > \varepsilon_{fu}$)		3.2.1	3.2.2 ($\varepsilon_f > \varepsilon_{fu}$)
Compression	$\frac{h_{c2}}{h}$	--	--			$\left(1+\frac{\omega}{\beta}\right)k - \frac{\omega}{\beta}$		
	$\frac{h_{c1}}{h}$	k	k			$\frac{\omega(1-k)}{\beta}$		
Tension	$\frac{h_{t1}}{h}$	$1-k$	$\frac{1-k}{\beta}$			$\frac{1-k}{\beta}$		
	$\frac{h_{t2}}{h}$	--	$\frac{(1-k)(\beta-1)}{\beta}$			$\frac{(1-k)(\beta-1)}{\beta}$		

Table 20. Normalized stress at vertices in the stress diagram for each stage of normalized tensile strain at bottom fiber (β).

Zone	Normalized stress	Stage 1 ($\mathbf{0 < \beta \leq 1}$), ($\mathbf{0 < \lambda \leq \omega}$)	Stage 2 ($\mathbf{0 < \beta \leq 1}$), ($\mathbf{0 < \lambda \leq \omega}$)			Stage 3 ($1< \mathbf{\beta \leq \beta_{tu}}$), ($\mathbf{\lambda > \omega}$)		
			2.1	2.2 ($\varepsilon_s > \varepsilon_{sy}$)		3.1	3.2 ($\varepsilon_s > \varepsilon_{sy}$)	
				2.2.1	2.2.2 ($\varepsilon_f > \varepsilon_{fu}$)		3.2.1	3.2.2 ($\varepsilon_f > \varepsilon_{fu}$)
Compression	$\frac{f_{c2}}{E\varepsilon_{cr}}$	--	--			$\gamma\omega$		
	$\frac{f_{c1}}{E\varepsilon_{cr}}$	$\frac{\gamma\beta k}{1-k}$	$\frac{\gamma\beta k}{1-k}$			$\gamma\omega$		
Tension	$\frac{f_{t1}}{E\varepsilon_{cr}}$	$1-k$	1			1		
	$\frac{f_{t2}}{E\varepsilon_{cr}}$	--	μ			μ		
	$\frac{f_s}{E\varepsilon_{cr}}$	$\frac{(\alpha-k)}{1-k}n\beta$	$\frac{(\alpha-k)}{1-k}n\beta$	$n\kappa$		$\frac{(\alpha-k)}{1-k}n\beta$	$n\kappa$	
	$\frac{f_f}{E\varepsilon_{cr}}$	$\psi\,\beta$	$\psi\,\beta$		0	$\psi\beta$		0

Table 21. Normalized force component for each stage of normalized tensile strain at bottom fiber (β).

Zone	Normalized stress	Stage 1 ($\mathbf{0 < \beta \leq 1}$), ($\mathbf{0 < \lambda \leq \omega}$)	Stage 2 ($\mathbf{0 < \beta \leq 1}$), ($\mathbf{0 < \lambda \leq \omega}$)			Stage 3 ($1< \mathbf{\beta \leq \beta_{tu}}$), ($\boldsymbol{\lambda > \omega}$)		
			2.1	2.2 ($\varepsilon_s > \varepsilon_{sy}$)		3.1	3.2 ($\varepsilon_s > \varepsilon_{sy}$)	
				2.2.1	2.2.2 ($\varepsilon_f > \varepsilon_{fu}$)		3.2.1	3.2.2 ($\varepsilon_f > \varepsilon_{fu}$)
Compression	$\frac{F_{c2}}{bhE\varepsilon_{cr}}$	--	--			$\gamma\omega\left(k-\frac{\omega(1-k)}{\beta}\right)$		
	$\frac{F_{c1}}{bhE\varepsilon_{cr}}$	$\frac{\beta\gamma k^2}{2(1-k)}$	$\frac{\beta\gamma k^2}{2(1-k)}$			$\frac{\gamma\omega^2(1-k)}{2\beta}$		
Tension	$\frac{F_{t1}}{bhE\varepsilon_{cr}}$	$\frac{\beta}{2}(1-k)$	$\frac{(1-k)}{2\beta}$			$\frac{(1-k)}{2\beta}$		
	$\frac{F_{t2}}{bhE\varepsilon_{cr}}$	--	$\frac{\mu(1-k)(\beta-1)}{\beta}$			$\frac{\mu(1-k)(\beta-1)}{\beta}$		
	$\frac{F_s}{bhE\varepsilon_{cr}}$	$\frac{n\rho_g(\alpha-k)}{1-k}$	$\frac{n\rho_g(\alpha-k)}{1-k}\beta$	$n\kappa\rho_g$		$\frac{n\rho_g(\alpha-k)}{1-k}\beta$	$n\kappa\rho_g$	
	$\frac{F_f}{bhE\varepsilon_{cr}}$	$\psi\beta\rho_f$	$\psi\beta\rho_f$		0	$\psi\beta\rho_f$		0

Table 22. Normalized moment arm of force component for each stage of normalized tensile strain at bottom fiber (β).

Zone	Normalized stress	Stage 1 ($\mathbf{0 < \beta \leq 1}$), ($\mathbf{0 < \lambda \leq \omega}$)	Stage 2 ($\mathbf{0 < \beta \leq 1}$), ($\mathbf{0 < \lambda \leq \omega}$)		Stage 3 ($1< \mathbf{\beta \leq \beta_{tu}}$), ($\boldsymbol{\lambda > \omega}$)		
			2.1	2.2 ($\varepsilon_s > \varepsilon_{sy}$)	3.1	3.2 ($\varepsilon_s > \varepsilon_{sy}$)	
				2.2.1	2.2.2 ($\varepsilon_f > \varepsilon_{fu}$)	3.2.1	3.2.2 ($\varepsilon_f > \varepsilon_{fu}$)
Compression	$\frac{y_{c2}}{h}$	--	--		$\frac{1}{2}\left(\frac{\omega(1-k)}{\beta}+k\right)$		
	$\frac{y_{c1}}{h}$	$\frac{2}{3}k$	$\frac{2}{3}k$		$\frac{2}{3}\frac{\omega(1-k)}{\beta}$		
Tension	$\frac{y_{t1}}{h}$	$\frac{2}{3}(1-k)$	$\frac{2(1-k)}{3\beta}$		$\frac{2(1-k)}{3\beta}$		
	$\frac{y_{t2}}{h}$	--	$\frac{1}{2}\left(\frac{(1-k)(1+\beta)}{\beta}\right)$		$\frac{1}{2}\left(\frac{(1-k)(1+\beta)}{\beta}\right)$		
	$\frac{y_s}{h}$	$(\alpha-k)$	$(\alpha-k)$	$(\alpha-k)$	$(\alpha-k)$	$(\alpha-k)$	
	$\frac{y_f}{h}$	$(1-k)$	$(1-k)$	$(1-k)$	$(1-k)$		$(1-k)$

Table 23. Normalized neutral axis, moment, curvature and stiffness for each stage of normalized tensile strain at bottom fiber (β).

Stage	$\boldsymbol{k}$	$\boldsymbol{M'}$	$\boldsymbol{\phi'}$	$\boldsymbol{K'}$
1	$k_1 = \begin{cases} \frac{B_3}{2B_2} & \gamma = 1 \\ -\left(\frac{B_2-\sqrt{B_2^2+B_1B_3}}{B_1}\right) & \gamma \neq 1 \end{cases}$	$M_1' = \frac{2\beta(B_1k_1^3+3B_2k_1^2-3B_3k_1+B_4)}{1-k_1}$	$\phi_1' = \frac{1}{2}(\frac{\beta}{1-k_1})$	$K_1' = \frac{M_1'}{\phi_1'}$
2.1	$k_{21} = -\frac{C_2-\sqrt{C_2^2-C_1C_3}}{C_1}$	$M_{21}' = \frac{C_4k_{21}^3+3C_5k_{21}^2+3C_6k_{21}+C_7}{(1-k_{21})\beta^2}$	$\phi_{21}' = \frac{1}{2}(\frac{\beta}{1-k_{21}})$	$K_{21}' = \frac{M_{21}'}{\phi_{21}'}$
2.2.1	$k_{221} = -\frac{C_8-\sqrt{C_8^2-C_1C_9}}{C_1}$	$M_{221}' = \frac{C_4k_{221}^3+3C_{10}k_{221}^2+3C_{11}k_{221}+C_{12}}{(1-k_{221})\beta^2}$	$\phi_{221}' = \frac{1}{2}(\frac{\beta}{1-k_{221}})$	$K_{221}' = \frac{M_{221}'}{\phi_{221}'}$

2.2.2	$k_{222} = -\frac{C_{13} - \sqrt{C_{13}^2 - C_1 C_{14}}}{C_1}$	$M'_{222} = \frac{C_4 k_{222}^3 + 3C_{15} k_{222}^2 + 3C_{16} k_{222} + C_{17}}{(1 - k_{222})\beta^2}$	$\phi'_{222} = \frac{1}{2}(\frac{\beta}{1 - k_{222}})$	$K'_{222} = \frac{M'_{222}}{\phi'_{222}}$
3.1	$k_{31} = -\frac{D_2 + \sqrt{D_2^2 - D_1 D_3}}{D_1}$	$M'_{31} = \frac{D_4 k_{31}^3 + 3D_5 k_{31}^2 + 3D_6 k_{31} + D_7}{(1 - k_{31})\beta^2}$	$\phi'_{31} = \frac{1}{2}(\frac{\beta}{1 - k_{31}})$	$K'_{31} = \frac{M'_{31}}{\phi'_{31}}$
3.2.1	$k_{321} = \frac{D_8}{D_1}$	$M'_{321} = \frac{-D_4 k_{321}^2 + 2D_9 k_{321} + D_{10}}{\beta^2}$	$\phi'_{221} = \frac{1}{2}(\frac{\beta}{1 - k_{321}})$	$K'_{321} = \frac{M'_{321}}{\phi'_{321}}$
3.2.2	$k_{322} = \frac{D_{11}}{D_1}$	$M'_{322} = \frac{-D_4 k_{322}^2 + 2D_{12} k_{322} + D_{13}}{\beta^2}$	$\phi'_{322} = \frac{1}{2}(\frac{\beta}{1 - k_{322}})$	$K'_{322} = \frac{M'_{322}}{\phi'_{322}}$

The coefficients used in the tables are as follows:

$$B_1 = \gamma - 1 \tag{84}$$
$$B_2 = \rho_f \psi + \rho_g n + 1 \tag{85}$$
$$B_3 = 1 + 2\rho_g n\alpha + 2\rho_f \psi \tag{86}$$
$$B_4 = 3\rho_f \psi + 3\rho_g n\alpha^2 + 1 \tag{87}$$

$$C_1 = 2\mu - 2\mu\beta + \gamma\beta^2 - 1 \tag{88}$$
$$C_2 = 2\mu\beta + \rho_g n\beta^2 + \rho_f \psi\beta^2 - 2\mu + 1 \tag{89}$$
$$C_3 = -2\mu\beta - 2\rho_g n\beta^2\alpha - 2\rho_f \psi\beta^2 + 2\mu - 1 \tag{90}$$
$$C_4 = -3\beta^2\mu + 2\gamma\beta^3 + 3\mu - 2 \tag{91}$$
$$C_5 = 3\beta^2\mu + 2 - 3\mu + 2\rho_g n\beta^3 + 2\rho_f \psi\beta^3 \tag{92}$$
$$C_6 = -2 - 4\rho_f \psi\beta^3 - 3\beta^2\mu + 3\mu - 4\rho_g n\beta^3\alpha \tag{93}$$
$$C_7 = 6\rho_g n\beta^3\alpha^2 + 2 + 6\rho_f \psi\beta^3 + 3\beta^2\mu - 3\mu \tag{94}$$

$$C_8 = 2\mu\beta + \rho_g n\kappa\beta + \rho_f \psi\beta^2 - 2\mu + 1 \tag{95}$$
$$C_9 = -2\mu\beta - 2\rho_g n\kappa\beta - 2\rho_f \psi\beta^2 + 2\mu - 1 \tag{96}$$
$$C_{10} = 3\beta^2\mu + 2 - 3\mu + 2\rho_g n\kappa\beta^2 + 2\rho_f \psi\beta^3 \tag{97}$$
$$C_{11} = -2 - 4\rho_f \psi\beta^3 - 3\beta^2\mu + 3\mu - 2\rho_g n\kappa\beta^2 - 2\rho_g n\kappa\beta^2\alpha \tag{98}$$
$$C_{12} = 6\rho_g n\kappa\beta^2\alpha + 2 + 6\rho_f \psi\beta^3 + 3\beta^2\mu - 3\mu \tag{99}$$

$$C_{13} = 2\mu\beta + \rho_g n\kappa\beta - 2\mu + 1 \quad (100)$$

$$C_{14} = -2\mu\beta - 2\rho_g n\kappa\beta + 2\mu - 1 \quad (101)$$

$$C_{15} = 3\beta^2\mu + 2 - 3\mu + 2\rho_g n\kappa\beta^2 \quad (102)$$

$$C_{16} = -2 - 3\beta^2\mu + 3\mu - 2\rho_g n\kappa\beta^2 - 2\rho_g n\kappa\beta^2\alpha \quad (103)$$

$$C_{17} = 6\rho_g n\kappa\beta^2\alpha + 2 + 3\beta^2\mu - 3\mu \quad (104)$$

$$D_1 = 1 - 2\mu + 2\mu\beta + \gamma\omega^2 + 2\gamma\omega\beta \quad (105)$$

$$D_2 = -\rho_g n\beta^2 - \rho_f\psi\beta^2 - 2\mu\beta + 2\mu - 1 - \gamma\omega^2 - \gamma\omega\beta \quad (106)$$

$$D_3 = \gamma\omega^2 + 2\rho_g n\beta^2\alpha + 2\rho_f\psi\beta^2 + 2\mu\beta + 1 - 2\mu \quad (107)$$

$$D_4 = \gamma\omega^3 - 3\gamma\omega\beta^2 - 2 + 3\mu - 3\mu\beta^2 \quad (108)$$

$$D_5 = 3\beta^2\mu + 2 - 3\mu + 2\rho_g n\beta^3 + 2\rho_f\psi\beta^3 + \gamma\omega\beta^2 - \gamma\omega^3 \quad (109)$$

$$D_6 = -2 - 4\rho_f\psi\beta^3 - 3\beta^2\mu + 3\mu - 4\rho_g n\beta^3\alpha + \gamma\omega^3 \quad (110)$$

$$D_7 = 6\rho_g n\beta^3\alpha^2 + 2 + 6\rho_f\psi\beta^3 + 3\beta^2\mu - 3\mu - \gamma\omega^3 \quad (111)$$

$$D_8 = \gamma\omega^2 + 2\rho_g n\kappa\beta + 2\rho_f\psi\beta^2 + 2\mu\beta + 1 - 2\mu \quad (112)$$

$$D_9 = \gamma\omega^3 - 3\rho_f\psi\beta^3 - 3\mu\beta^2 - 2 - 3\rho_g n\kappa\beta^2 + 3\mu \quad (113)$$

$$D_{10} = -\gamma\omega^3 + 6\rho_g n\kappa\beta^2\alpha + 6\rho_f\psi\beta^3 + 3\beta^2\mu - 3\mu + 2 \quad (114)$$

$$D_{11} = \gamma\omega^2 + 2\rho_g n\kappa\beta + 2\mu\beta + 1 - 2\mu \quad (115)$$

$$D_{12} = \gamma\omega^3 - 3\mu\beta^2 - 2 - 3\rho_g n\kappa\beta^2 + 3\mu \quad (116)$$

$$D_{13} = -\gamma\omega^3 + 6\rho_g n\kappa\beta^2\alpha + 3\beta^2\mu - 3\mu + 2 \quad (117)$$

3.2.2 Superimposed Results

It is clear that all these modes are not happening at the same time. The occurrence of each mode depends on the material properties and the dimensions. If the section is over reinforced it is very probable that a failure happens in stage 3 and its substages.

However, if the section is well designed, first the steel reinforcements yield and then the FRP plates fail, while the compressive part of the section is still linear. A plot of all possible curve for a specific section ($\rho_g = 0.005$ and $\rho_f = 0.005$) are shown in Figure 107.

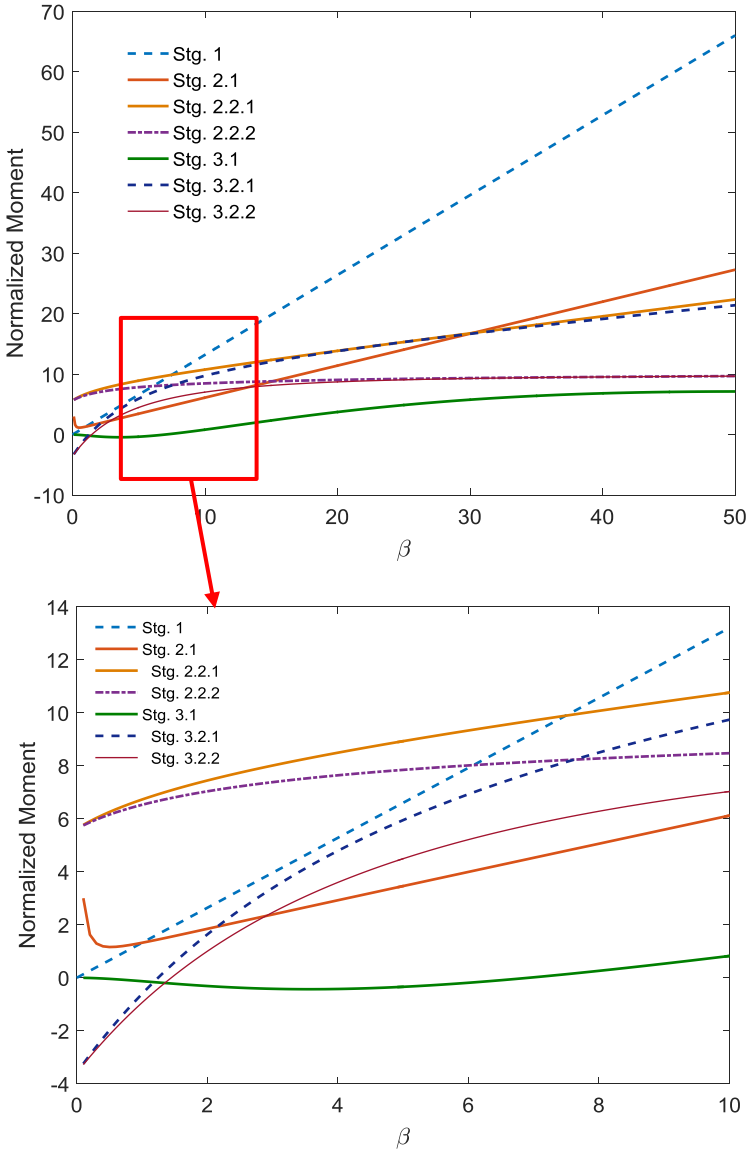

Figure 107. Superimposed curves for different stages.

A closer look at the curves shows that for specific values of beta the normalized moments are negative meaning that these modes are impossible to happen in that range. However, for most of the cases, it is not as easy as this. We need to consider the limit for beta and gamma values and see if they are in what acceptable range for which mode. If there is a well-designed section, compressive failure is not possible and the stage 3 and its substages will be eliminated, one of the possible scenarios for this limited selection of modes is represented in Figure 108.

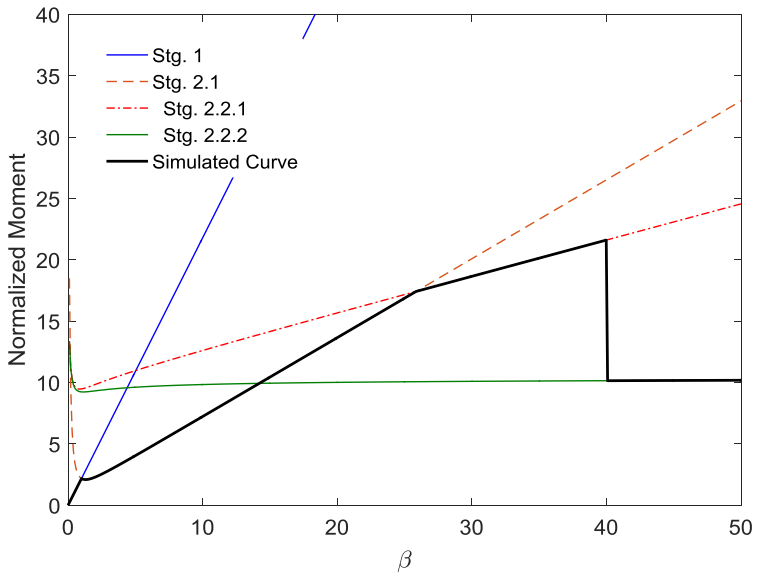

Figure 108. One possible case among numerous possible scenarios during beam deflection.

In this scenario, the beam has linear behavior at the first stage, then it will go through a cracking zone for the tensile part (stage 2.1). Since it is assumed that steel will yield before FRP failure, it will go to the higher mode of stage 2.2.1, in which only steel is yielded but not the FRP. Finally, FRP fails and the normalized moment falls down to

the stage 2.2.2. In this stage, only the residual stresses, due to the steel rebars and fibers, are acting.

3.3 Verification with Experimental Data

In this section, the analytical data will be compared to the experimental data in the literature [99].

3.3.1 Segment's Properties and Test Setup:

Li et al. [99] performed a set of tests on the performances of two different types of fiber reinforced concrete (FRC) beams, which were strengthened with three different types of fiber reinforced polymer (FRP) sheets. Three types of concrete beams were tested, including plain concrete beams for reference, polypropylene fiber (PF) reinforced concrete beams, and polypropylene fiber (PF) together with steel fiber (SF) hybrid reinforced concrete beams. Three strengthening schemes also were used, which were mono-layered carbon fiber reinforced plastic (CFRP) sheet strengthening, mono-layered glass fiber reinforced plastic (GFRP) sheet strengthening and CFRP mixed GFRP bi-layer sheets strengthening.

When monolayer FRP sheets were used to strengthen, the failure pattern was a central rupture in the FRP sheets, because of the proper anchor at ends. The fiber then debonds at the vicinity of FRP rupture. When bi-layer mixed FRP sheets were used, debonding failures occurs. Since the proposed analytical model is not able to consider the debonding failure, only mono-layered samples are chosen for the simulations.

For the FRC samples, a larger steel fiber (SF) content and a smaller polymeric fiber (PF) one were used in the test. All the fiber contents were in the low range (i.e., SF volume content up to 0.9% and PF volume content up to 0.1%). Three types of concrete beams were tested, which were plain concrete beams for reference, PF reinforced concrete beams and PF along with SF hybrid reinforced concrete beams. The physical properties of SFs and PFs used to reinforce test concrete members in this article are shown in Table 24.

Table 24. The physical property of steel and polypropylene fibers.

Fiber Type	Ultimate tension strength (MPa)	Density ρ (kg/m3)	Diameter d (mm)	Elastic Modulus (GPa)	Volume Rate v_f (%)	Fiber Length s (mm)
PF	276	0.91	0.048	3.8	0.1	1.9
SF	410	7.8	0.25	210	0.9	3.4

Four-point bending tests were carried out for rectangular section beams with dimensions of b x h = 120 mm x200 mm, span = 2000 mm, the net span = 1800 mm (see Figure 109). The steel reinforcement ratio of test concrete beam is $\rho = 0.48\%$, the stirrup steel reinforcement ratio is 0.475%, and the shear-span ratio is 4.

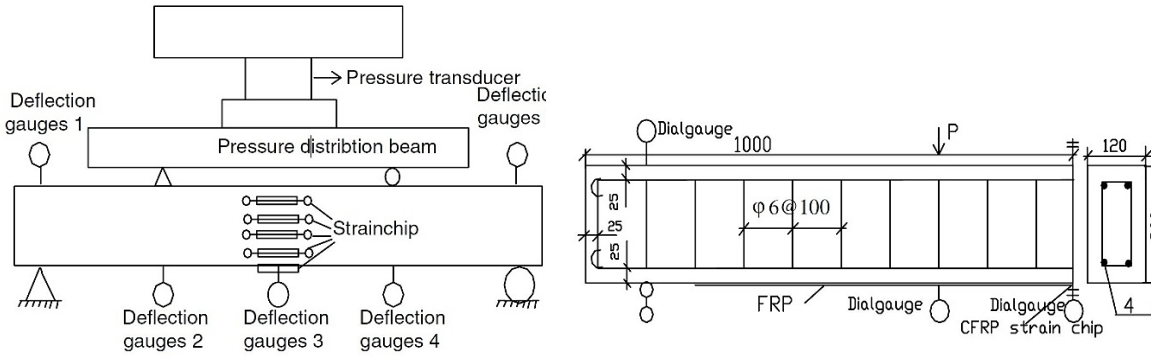

(a) (b)

Figure 109. Test scheme of FRC beams: (a) measure scheme of the test; (b) configuration of FRC beams (measured in mm).

Table 25 is the serial number of test beams strengthened with different FRP sheets. There are 12 beams for test and are divided into three groups, which include plain concrete beams without fiber reinforcement i.e. B00, B01, B02 and B03, 0.1% content PF reinforced concrete beams i.e. B10, B11, B112 and B13, and 0.1% content PFs together with 0.9% content SFs hybrid reinforced concrete beams i.e. B20, B21, B22, and B23, respectively.

Table 25. Concrete beams (sample labels) strengthened with FRP sheets.

Concrete types	Reference beams	Mono-layer GFRP sheet strengthened beams	Mono-layer CFRP sheet strengthened beams	CFRP/GFRP sheets mixed bi-layer strengthened beams
Without fiber reinforcement	B00	B01	B02	B03
PF reinforced concrete beams	B10	B11	B12	B13
SF and PF hybrid reinforced concrete beams	B20	B21	B22	B23

3.4 Simulation Results for Using HRC+FRP Model

In this section, the simulation results based on Li et al. research are presented.

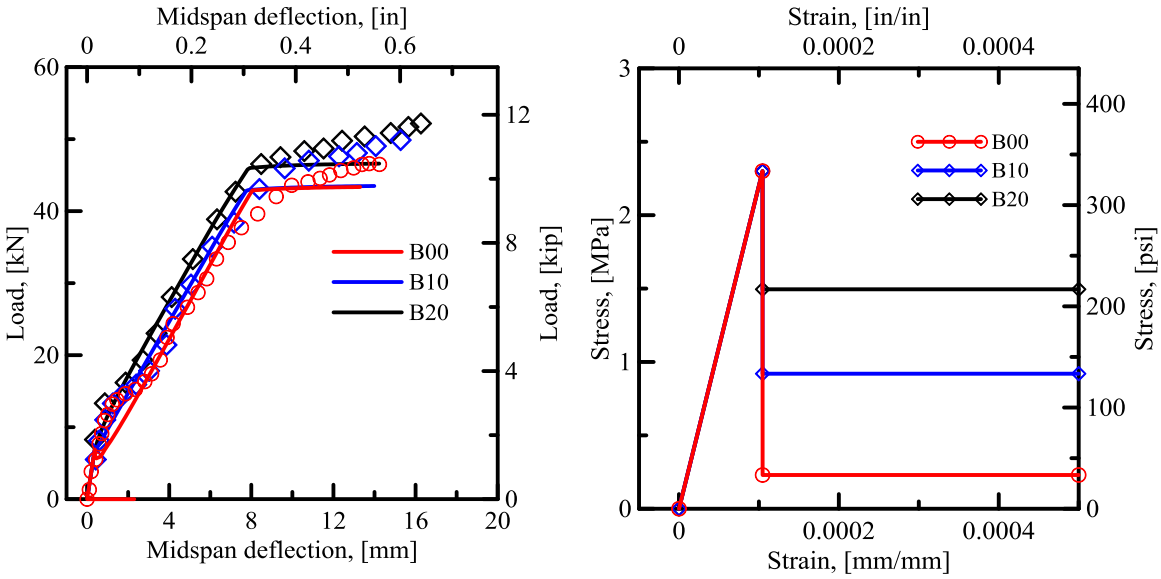

Figure 110. Simulation results for the samples without fiber reinforcement.

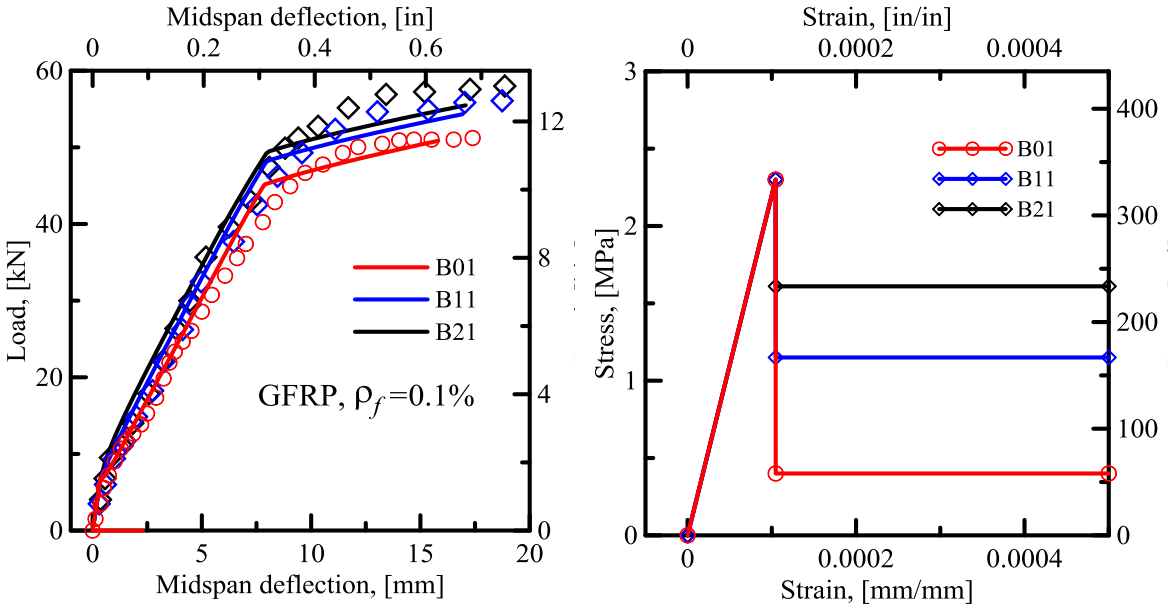

Figure 111. Simulation results for the samples with polymeric fiber reinforcement.

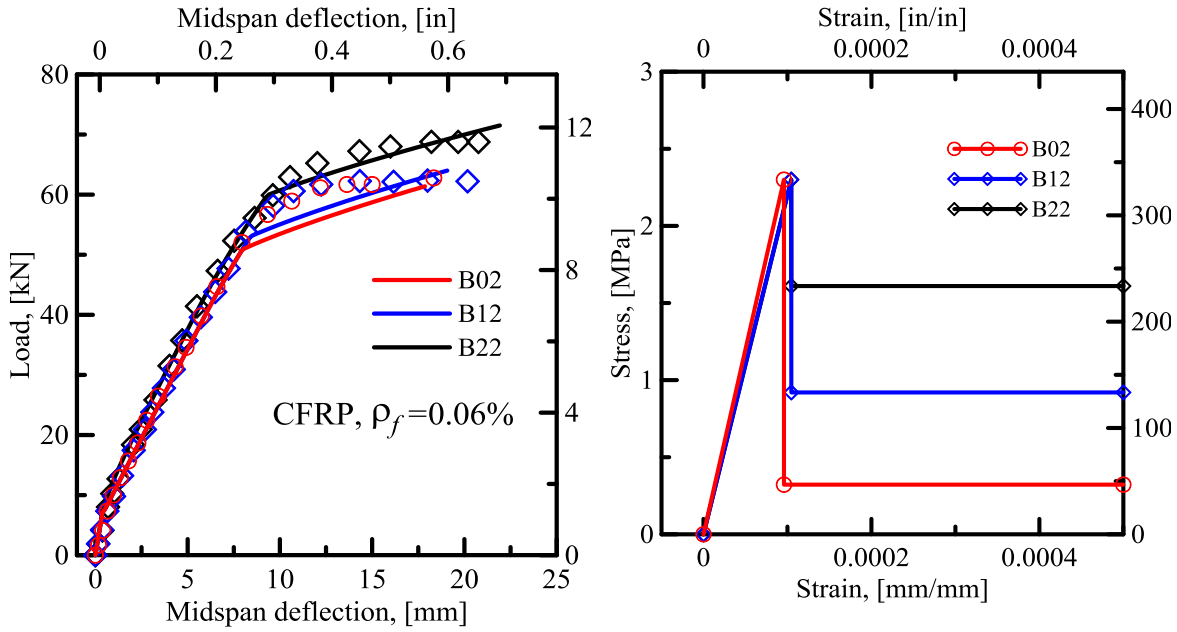

Figure 112. Simulation results for the samples with polymeric and steel fiber reinforcement.

3.5 Parametric Study

In this section, some parametric studies are performed to compare the results due to changing different values such as ρ_g, ρ_f, μ and so forth.

3.5.1 Effect of residual stress due to the fiber content (μ)

The effect of normalized residual strength, μ on the normalized moment M_0 for a typical HRC section with 0.1% rebar reinforcement and 0.1% FRP reinforcement is shown in Figure 113.

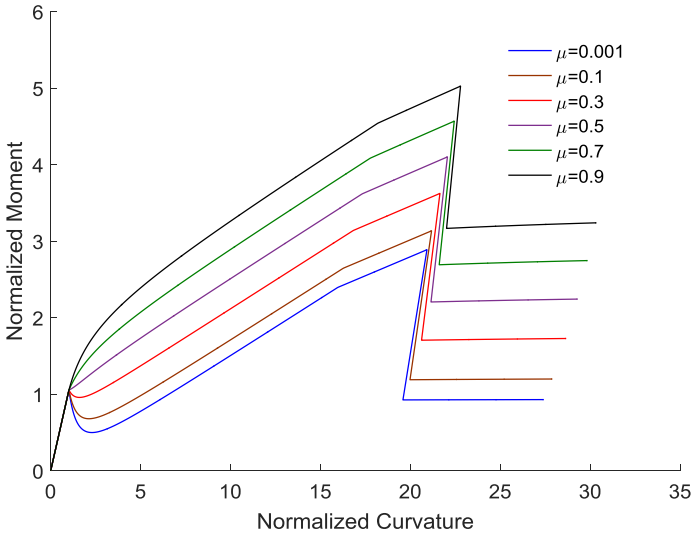

Figure 113. The effect of residual strength, μ on the normalized moment of a typical section.

The strain softening and strain hardening can be observed in the curves, for different values of residual strength, μ. It is observed that, at $\mu = 0.3$ there is a phase change from strain softening type of response to strain hardening type of response.

3.5.2 Reinforcement ratio effect

The effect of the reinforcement on HRC sections reinforced with 0.1% FRP reinforcement and $\mu = 0.1$ was investigated and the results are presented in Figure 114.

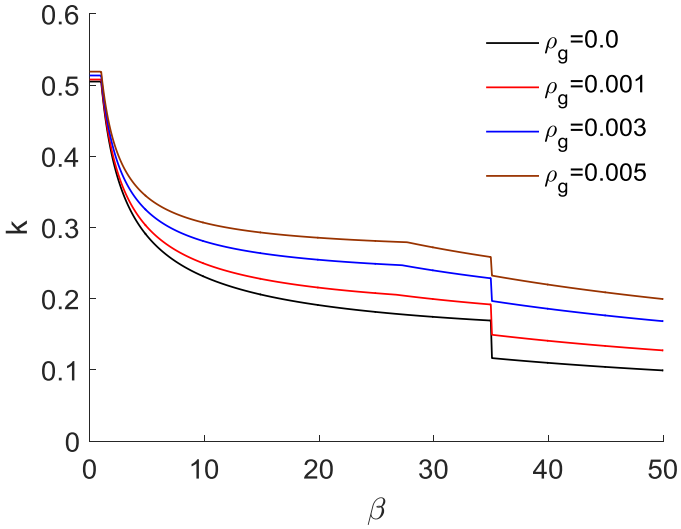
k
β
ρg=0.0
ρg=0.001
ρg=0.003
ρg=0.005

(a)

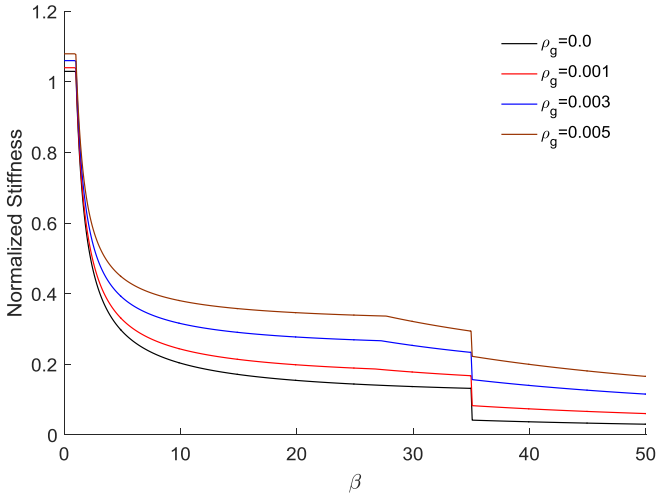
Normalized Stiffness
β
ρg=0.0
ρg=0.001
ρg=0.003
ρg=0.005

(b)

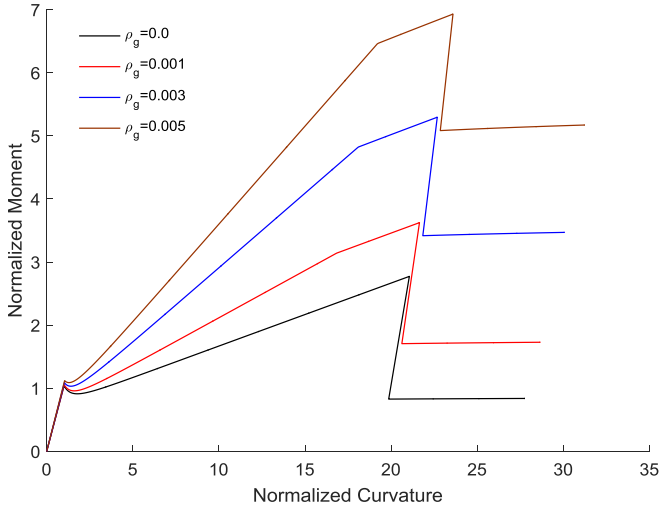
Normalized Moment
Normalized Curvature
ρg=0.0
ρg=0.001
ρg=0.003
ρg=0.005

(c)

Figure 114. Reinforcement effect on: (a) The depth of the neutral axis; (b) Normalized stiffness; and (c) Normalized moment.

As expected, as the amount of reinforcement increases, the ultimate strength of the section increases as well.

3.5.3 Effect of FRP ratio

The effect of the FRP reinforcement on HRC sections reinforced with 0.1% longitudinal reinforcement and $\mu = 0.1$ was investigated and the results are presented in Figure 115.

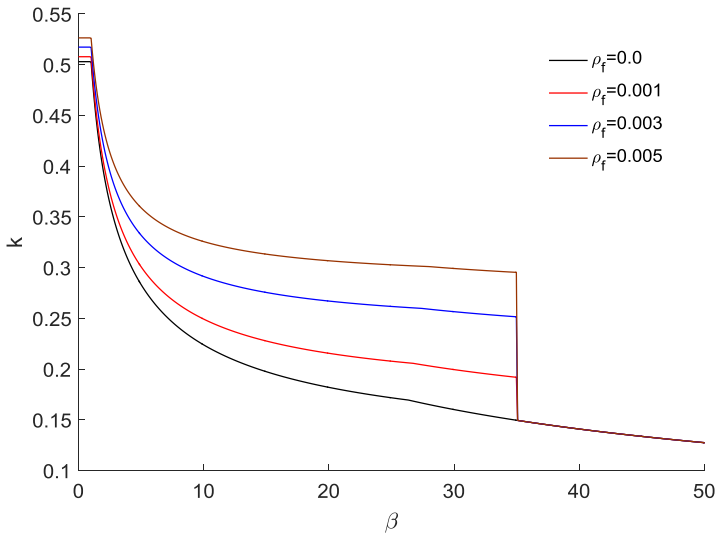

(a)

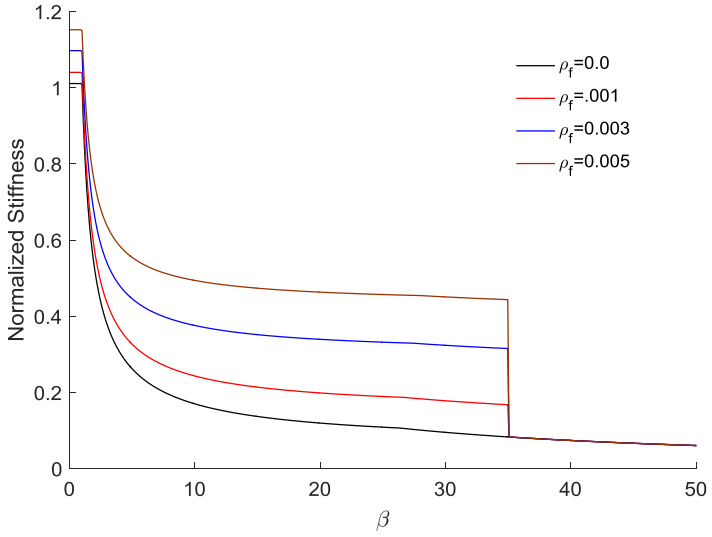

(b)

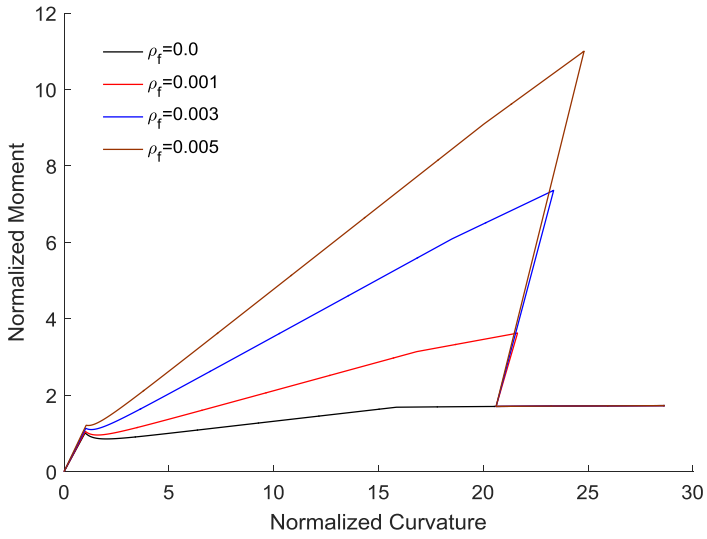

(c)

Figure 115. FRP reinforcement effect on: (a) The depth of the neutral axis; (b) Normalized stiffness; and (c) Normalized moment.

As expected, as the amount of FRP reinforcement increases, the ultimate strength of the section increases as well, but after FRP failure, only the residual strength due to the plastic steel rebars and fibers remains in the section. It is noted that in this set of

parametric studies, only normalized values were calculated, and the actual dimensions of the sections were not of interest.

3.6 Summary

In this section, an analytical solution was presented to simulate the flexural response of the HRC sections strengthened by FRP plates. The simulated results were compared to the experimental results and the comparison plots showed a good agreement between simulated and experimental results. This analytical simulation can be used as a strong tool to initial evaluation of the effect of the FRP plates, with different material properties, Elastic Modulus, and cross-sectional areas, on the load-deflection response of the RC, FRC and HRC sections. This can also be used for the current beams and slabs that need strengthening and rehabilitation as well. Several parametric studies were performed to investigate the effect of reinforcement ratio, FRP plates, and residual strength due to the fiber content.

4 APPLICATION OF ANALYTICAL SOLUTIONS IN TUNNELING SEGMENTS

An important component of tunnel infrastructure is the tunnel lining systems. The functionality of tunnels significantly depends on the structural and durability performance of its lining system. Tunnel linings act as protective barriers against large overburden loads and complex geotechnical surrounding exposure conditions. The use of precast concrete tunnel lining (PCTL) systems in tunneling projects has been increasing as a result of its efficient and economical application in comparison with the conventional in-situ lining technique [100]. PCTL segments are suitable for both soft and hard ground and can serve both as preliminary and final support against large overburden loads [101] (Hung *et al*., 2009).

Tunnel linings are normally constructed in a circular shape using tunnel boring machines (TBMs). During the last years, the evolution of the TBMs and the construction techniques associated with these drilling devices gave the opportunity to plan and construct tunnels under increasingly difficult scenarios. Nowadays, it is possible to construct tunnels under severe conditions and at any range of overburdens, with the possibility of achieving unsuspected drilling rates under high ground and water pressures. These unfavorable conditions imply higher structural requirements in order to resist the increments of ground pressures and the forces imposed by the advances of the TBM, conferring to the segmental tunnel lining a decisive role in the tunnel construction[102].

A number of precast segments are installed at the end of the TBM and assembled in such a way it completes the circle of the tunnel lining [103]. The number of segments required to complete a circle of the tunnel depends on many parameters including the

aspect ratio of the segment, the diameter of the tunnel and the contractor's choice. Typical thickness of segments varies from 200 to 300 mm (8 to 12 in) along with 1000 to 1500 mm (40 to 60 in) width [101]. PCTL allows speedy construction along with superior quality due to enhanced control during precast segment fabrication in precast plants. Moreover, the fabrication of PCTL includes repetitive steps of batching and casting of concrete, which ultimately results in wastage reduction compared to traditional in-situ concrete lining [104].

Multi-disciplinary skills are required for the designing of PCTL segments in order to meet their structural and durability performance. Thus, a detailed life-cycle analysis is required in order to calculate the total fabrication and installation cost of PCTL systems that satisfy specific design performance criteria [101]. Generally, the required service life of tunnel linings is considerably higher than that of other structures (e.g. bridges and buildings)[101]; therefore, special considerations should be given in selecting the PCTL materials to satisfy the structural needs and result in a long-lasting life with minimum maintenance requirements.

Normally, PCTL segments are designed for 100 years of service life with conventional steel rebar reinforced concrete (RC)[101]. However, cases such as the Koblenz Railway Tunnel, Switzerland; the London Underground Railway Tunnel, UK; and the Michigan Northeast Raw Water Tunnel, the USA all suffered premature deterioration before achieving their respective service life. This was mainly attributed to reinforcement corrosion induced by chloride ions penetration [105]. Chloride ions from the underground water can attack the extrados faces of PCTL, while de-icing salts carried

by vehicular tires can attack the intrados faces. Once these chloride ions reach the embedded reinforcing rebar, it disrupts the passive layer around the rebar and corrosion starts. The formation of corrosion products can induce internal pressures in the concrete surrounding the corroded rebar, thus leading to concrete cracking and spalling of the concrete cover [106]. Moreover, as the effective cross-section of the rebar decreases, the load carrying capacity of PCTL segments will decrease, which can jeopardize its structural integrity [107].

From a structural point of view, crack developments in RC PCTL segments during their fabrication, delivery to the job site and installation process using TBM (due for instance to accidental thrust and impact loads) will disturb its normal functioning. In addition, such cracks will facilitate the intrusion of aggressive species, consequently accelerating the corrosion process and leading to decreased structural strength. It was found that the chloride ion diffusion into concrete was directly proportional to the developed crack width [108], [109]. Therefore, an alternative higher strength material may be required for more crack resistant and more durable PCTL segments.

It is well known that steel fiber-reinforced concrete (SFRC) can better resist crack formation through the crack bridging action of steel fibers. Steel fibers can partially or completely replace traditional reinforcing steel cages in several applications [110]. It is believed that steel fibers do not allow the onset and propagation of corrosion current due to their discontinuous and dispersed nature. The use of steel fibers in segmental tunnel linings has considerably increased during the last years [102]. Their main contribution is traditionally related to the avoidance of concrete spalling. Spalling is used to occur in

segment joints due to deficient segment allocation, inadequate segment construction tolerances or joints geometries when the TBM jack forces are applied. Steel fibers act as small links between the detached concrete and the segment avoiding the reparation of the superficial damage. However, steel fibers are not only present at the edges or corners of the segments. Their presence inside the whole element may contribute to the structural resistance of the lining.

SFRC segmental linings have already been successfully utilized in various tunneling projects around the world, such as the Line 9 Subway Barcelona, the Madrid Subway, Spain; the Bright Water Sewer System Seattle, USA; the Channel Tunnel Rail Link, UK and the Second Heine Noord Tunnel, the Netherlands [111]–[113].

However, the complete replacement of conventional rebar cages with steel fiber reinforcement is not always a feasible option due to higher structural strength requirements. Therefore, an alternative high strength and the ultra-durable material are required in order to completely substitute for the conventional steel rebar in PCTL segments without affecting its structural and durability performances. Ultra-high performance fiber-reinforced concrete (UHPFRC or UHPC) is an emerging cement-based composite with compressive strength typically higher than 150 MPa (22 ksi) and almost negligible porosity [114]. Therefore, UHPC can prove to be a more durable and sustainable material for PCTL fabrication.

In addition to improving structural and durability properties, complete substitution of conventional steel rebar reinforcement with UHPC in tunnel linings can eliminate the laborious and costly manufacturing of curved shape reinforcing rebar cages, which

require complicated welding and detailing. Furthermore, the cross-sectional dimensions of the UHPC lining segments can be reduced owing to its high strength properties, leading to more economical construction.

4.1 Initial Estimates Using Analytical Models

In this section, some of the simulations are performed based on the experimental results from other research groups. According to the results from simulations, it was observed that, although in some cases, such as fiber reinforced sections without rebars, the estimations are close to the experimental data, but in some other samples there is a difference between analysis and experimental result, and therefore more accurate numerical/analytical solutions are required.

4.1.1 Simulation results (using FRC model):

Figure 42 presents a constitutive model for homogenized strain softening and hardening of FRC with two fundamental material parameters: Elastic modulus, E, (equal in tension and compression) and first cracking tensile strain, ε_{cr}. Two non-dimensional parameters, normalized post-peak tensile strength μ and compressive to tensile strength ratio ω, were also defined. The compressive response in Figure 42(a) is represented as an elastic-plastic response with an initial modulus defined as γE up to the compressive strength of $\omega\gamma\sigma_{cr}$. Parameter ω represents the ratio of compressive to tensile strain. In most of the cases, elthe astic modulus for tension and compression are equal and therefore $\gamma = 1$. Thus, parameter ω can be considered as the ratio of compressive to tensile strength, $\sigma_{cy} = \omega\sigma_{cr}$.

The tension model in Figure 42(b) is described by a trilinear response with an elastic range defined by E, and then the post-cracking modulus E_{cr}. By setting E_{cr} to either a negative or a positive value, the same model can be used to simulate strain-softening or strain-hardening materials. The third region in the tensile response is a constant stress defined with stress σ_{cst} in the post-crack region. The constant stress level μ can be set to any value at the transition strain, resulting in a continuous or discontinuous stress response. Two strain measures are used to define the first cracking and transition strains (ε_{cr}, ε_{trn}). The tensile response terminates at the ultimate tensile strain level of ε_{tu}.

The parameter μ represents the ratio of the post-peak tensile strength to the cracking tensile strength $\mu = \sigma_P / \sigma_{cr}$ and may be a function of the fiber volume fraction, geometry, stiffness, and bond. Figure 42(b) describes the compression model with stress increasing linearly up to the yield strain $\varepsilon_{cy} = \omega\varepsilon_{cr}$, and remaining perfectly plastic until the termination point at the ultimate compressive strain $\varepsilon_{cu} = \lambda_{cu}\varepsilon_{cr}$. The non-dimensional strain measures β_{tu} and λ_{cu} are defined as limits for terminating the algorithm. They also facilitate a simplified parametric model based on serviceability limit state (SLS) and ultimate limit state (ULS) criteria for the design of FRC flexural members [3]. The model can be implemented both for strain-softening and strain-hardening FRC. As an extension to the model, one can also consider a combination of fibers and plain reinforcement in the context of HRC, which addresses structural members that combine continuous reinforcement with randomly distributed chopped fibers in the matrix. An analytical

model for predicting the flexural behavior of HRC, which is applicable to conventional reinforced concrete and FRC, presented by Mobasher et al. (2015) [54], will be discussed in the next section as well.

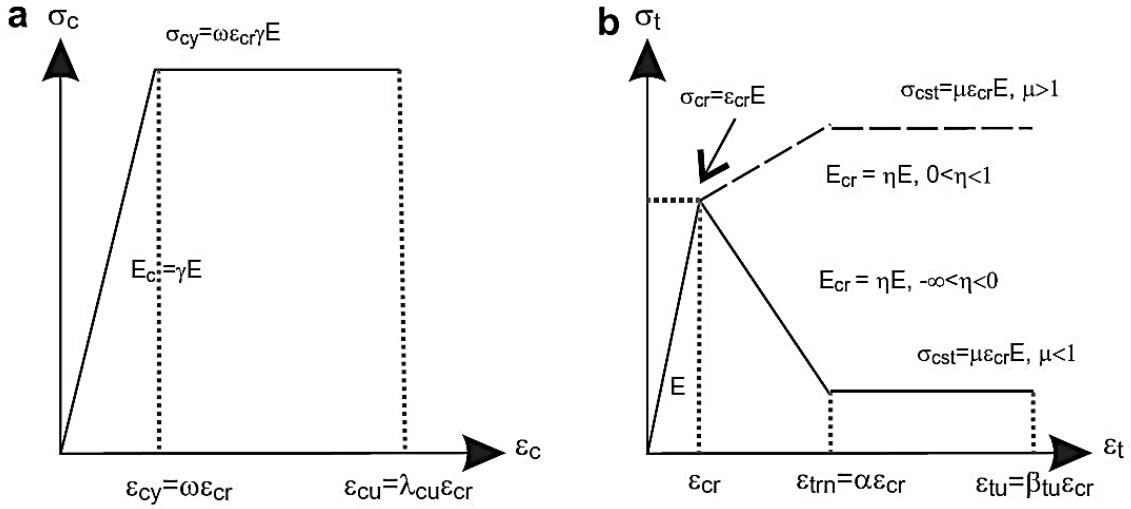

Figure 116. Material models for homogenized fiber reinforced concrete: (a) compression model and (b) tension model [7].

Material parameters required for the simplified models are summarized as follows:

Cracking tensile strain, $\varepsilon_{cr} = \frac{\sigma_{cr}}{E}$ (118)

Normalized tensile strain at peak strength, $\alpha = \frac{\varepsilon_{peak}}{\varepsilon_{cr}}$ (119)

Normalized post-crack modulus, $\eta = \frac{E_{cr}}{E}$ (120)

Normalized yield compressive strain, $\omega = \frac{\sigma_{cy}}{E\varepsilon_{cr}} = \frac{\sigma_{cy}}{\sigma_{cr}}$ (121)

Normalized tensile strain at bottom fiber, $\beta = \frac{\varepsilon_t}{\varepsilon_{cr}}$ (122)

Normalized compressive strain at top fiber, $\lambda = \dfrac{\varepsilon_c}{\varepsilon_{cr}}$ (123)

Figure 47 shows the interactions of the parameters of elastic and inelastic zones of tension and compression response based on a linear strain distribution. The constitutive response relates the strains to stresses, forces, and the bending moment. Note that the interaction of any two zones in the tension and compression behavior results in a specific stress distribution which must be solved in closed form to get the location of neutral axis for that specific set of values. After solving for the depth of neutral axis, the value of moment and curvature are calculated at each range of applied strain and used to construct the moment-curvature response for that case.

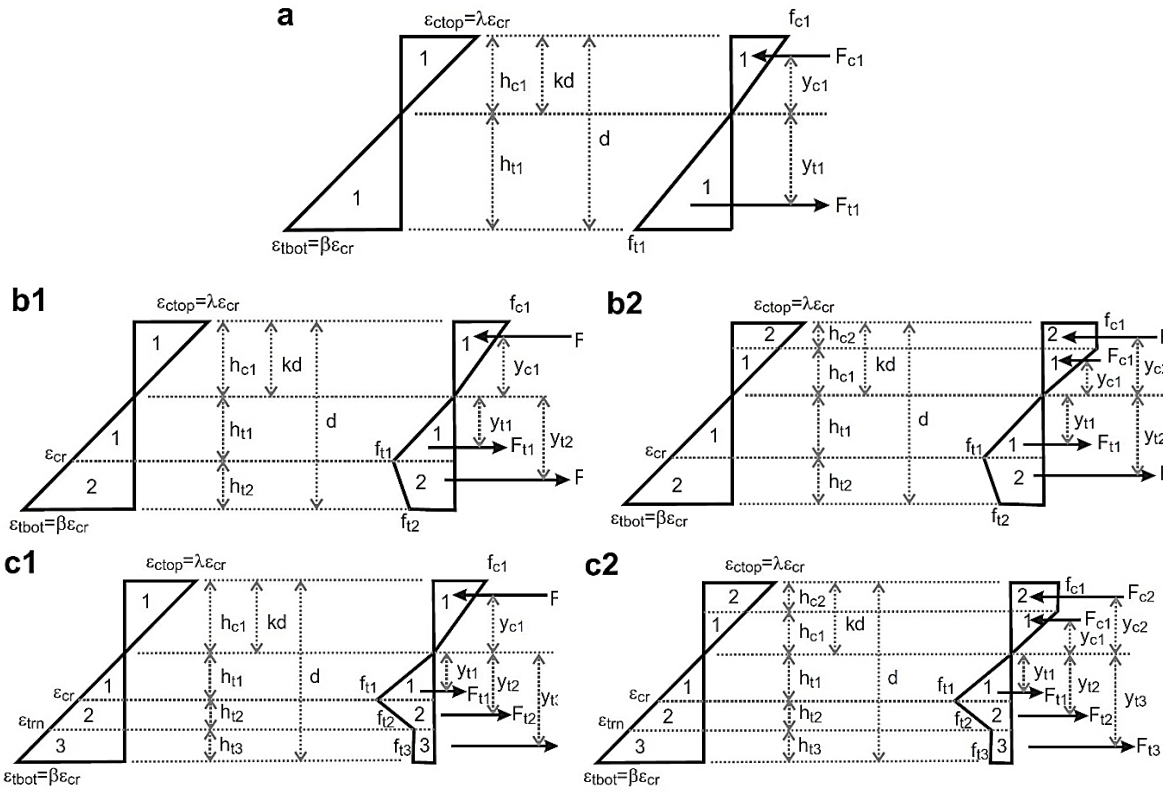

Figure 117. Stress-strain diagram at different stages of normalized tensile strain at the bottom fiber (β): (a) Elastic for compression and tension, $0 \le \beta \le 1$ and $0 < \lambda \le \omega$); (b.1) Elastic for compression but non-linear for tension, $1 < \beta \le \alpha$ and $0 < \lambda \le \omega$); (b.2) Plastic for compression and non-linear for tension, $1 < \beta \le \alpha$ and $\omega < \lambda \le \lambda_{cu}$); (c.1) Elastic for compression but non-linear for tension, $\alpha < \beta \le \beta_{tu}$ and $0 < \lambda \le \omega$; (c.2) Plastic for compression and non-linear for tension, $\alpha < \beta \le \beta_{tu}$ and $\omega < \lambda \le \lambda_{cu}$ [7].

The moment capacity of a beam section according to the imposed tensile strain at the bottom fiber ($\varepsilon_t = \beta\varepsilon_{cr}$) can be derived by the following steps: (1) determine linear strain and stress distributions, (2) force components by integration of stresses, (3) solve for the depth of neutral axis location, *k*, by force equilibrium, and obtain the strain-curvature relationship. The internal moment is obtained from the force and strain distribution. Based on the tensile response of the concrete, three major ranges were defined. In the first range, both compression and tension parts of the section behave in an elastic manner. In the second range, the component of the cross section that is under the tensile stress exceeds the tension cracking stress, therefore the section is in the post-peak transition range. The compressive part may be linear or non-linear. Therefore this tension cracking criteria introduced two ranges identified as 2-1 or 2.2 depending on the compression zone being linear, or non-linear. In the third range, the segment above the neutral axis that is under compressive stress may follow the linear or non-linear portion of the stress-strain response, while the tensile part of the section has already reached to the residual tensile response. For this section, only Range 2-1 is described, and the bases for the other ranges will be the same. At this range, the tensile part of the section is cracked but the compressive part is still in the linear part of its response. Force component and its centroid to the neutral axis in each zone can be expressed as:

$$\frac{F_{c1}}{bh\sigma_{cr}} = \frac{\beta\gamma k^2}{2(1-k)}; \qquad \frac{y_{c1}}{h} = \frac{2}{3}k \tag{124}$$

$$\frac{F_{t1}}{bh\sigma_{cr}} = \frac{(1-k)}{2\beta}; \qquad \frac{y_{t1}}{h} = \frac{2}{3}\frac{(1-k)}{\beta} \tag{125}$$

$$\frac{F_{t2}}{bh\sigma_{cr}} = \frac{(1-k)(\beta-1)(\eta\beta-\eta+2)}{2\beta}; \quad \frac{y_{t2}}{h} = \frac{2\eta\beta^2-\eta\beta-\eta+3\beta+3}{3\beta(\eta\beta-\eta+2)}(1-k) \tag{126}$$

where F and y are the force and its centroid, respectively; subscripts *c1,t1,t2* designate compression zone 1 and tension zones 1 and 2; b and h are the width and the height of the beam. The neutral axis parameter k is found by solving the equilibrium of net internal forces equal to zero, $F_{c1} + F_{t1} + F_{t2} = 0$.

$$k = \frac{C_1 - \sqrt{\beta^2 C_1}}{C_1 - \beta^2} \text{ ; where } C_1 = \eta(\beta^2 - 2\beta + 1) + 2\beta - 1 \tag{127}$$

The nominal moment capacity M_n is obtained by taking the first moment of force about the neutral axis, $M_n = F_{c1}y_{c1} + F_{t1}y_{t1} + F_{t2}y_{t2}$, and expressed as a product of the normalized nominal moment m_n and the cracking moment M_{cr} as follows:

$$M_n = m_n M_{cr} \tag{128}$$

$$m_n = C_2\frac{k^2-2k+1}{\beta^2} + \frac{2\beta k^3}{1-k} \text{ ; where } C_2 = C_1 + 2C_1\beta - \beta^2 \tag{129}$$

Additional discussions of these methodologies and equations are presented in the original Soranakom and Mobasher publication which has been incorporated in ACI 544-8R, ACI544-6R, and ACI544-7R [64], [65].

4.2 Load Deflection Computation

Moment-curvature diagrams are calculated for the sections depending on the number and interaction of flexural stages (see Figure 118). For any given curvature, the lowest magnitude of the moment from the stages was selected as the governing load, which would allow the transition from one loading stage to the other. The final moment-curvature diagram is a composite of the several interacting flexural stages. To have a load-deflection response for a beam element, it is necessary to have the moment-curvature response for various sections (elements) along the beam length and then calculate the deflection using a moment-area method or direct integration. For a statically determinate simply supported beam, equilibrium is used to obtain support reactions and moment distribution along the length of the beam directly from the applied forces. Using the moment-curvature distribution, this response is converted to the curvature distribution along the length using a look-up table.

The slope and deflection distributions along the length of the beam are obtained by applying the slope-deflection method to the curvature distribution. The strain at the tensile fiber is increased incrementally at a control point such as the midpoint and used to establish the curvature distribution, which is in turn used to calculate both moment distributions used in the deflection computation [7].

Figure 56 and Figure 57 show the typical moment-curvature diagram for the four-point bending test and the moment distribution along the beam length. The three depicted patterns of curvature distribution are needed in the derivations for the mid-span deflection. Figure 57(a) shows the curvature distribution before cracking (Stage A). After

cracking (stages B and C), as the post-crack curvature increases, the moment continues to increase as shown by the red line in Figure 57(b). At stage B, after reaching the maximum loading, the moment cannot go higher than the maximum bending capacity; thus it decreases at the levels below the maximum moment. At this point, two type of responses are possible, depend on the location of the section along the axis. If the section is located in the non-localized length, (L_n) crack will be closed during the unloading (Stage C1), but if the section is located on the localized length (L_l) the crack opening will continue (Stage C2). The same approach can be taken for 3PB tests and another type of RC sections as well [7], [67].

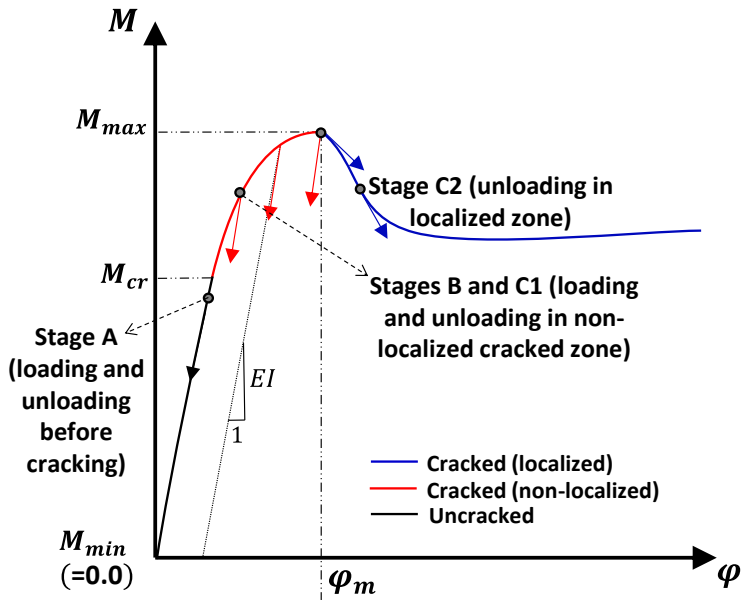

Figure 118. Generalized M-C diagram; during different stages of loading and unloading.

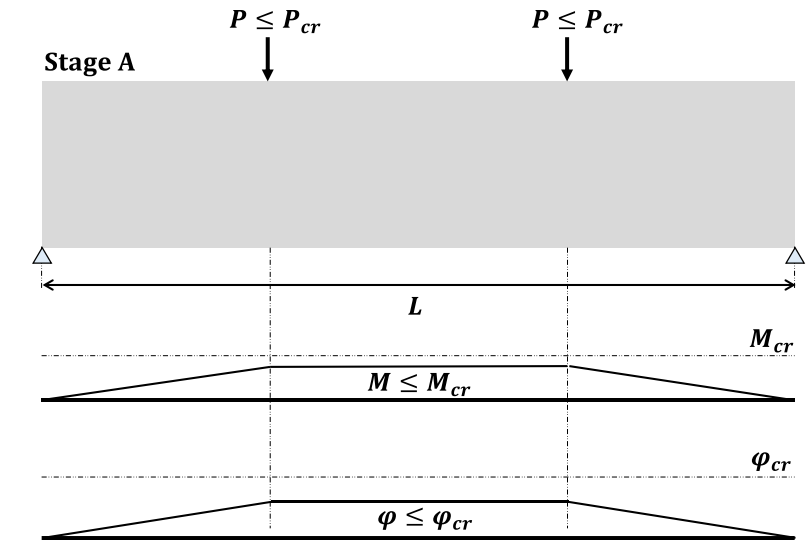
$P \leq P_{cr}$
$P \leq P_{cr}$
Stage A
L
M_{cr}
$M \leq M_{cr}$
φ_{cr}
$\varphi \leq \varphi_{cr}$

(a)

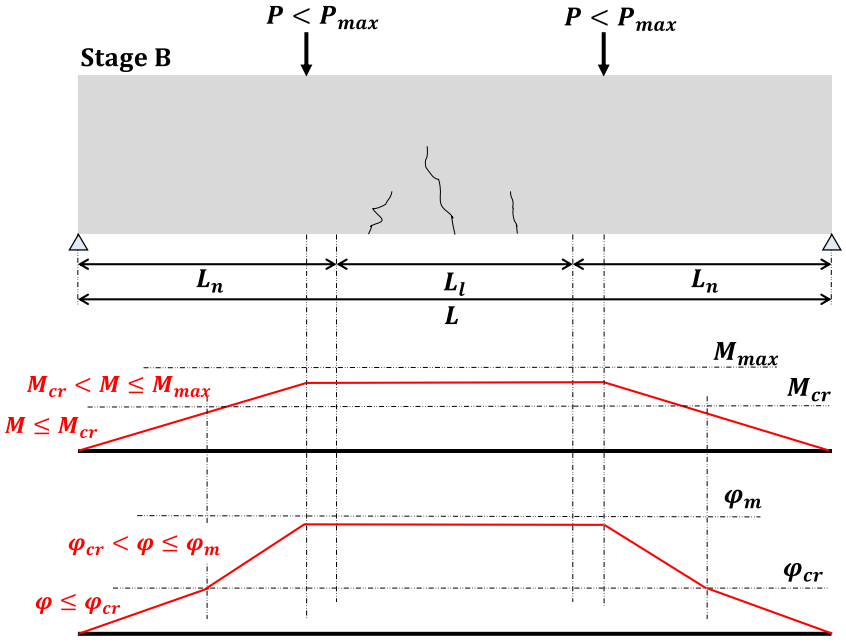
$P < P_{max}$
$P < P_{max}$
Stage B
L_n
L_l
L_n
L
M_{max}
$M_{cr} < M \leq M_{max}$
M_{cr}
$M \leq M_{cr}$
φ_m
$\varphi_{cr} < \varphi \leq \varphi_m$
φ_{cr}
$\varphi \leq \varphi_{cr}$

(b)

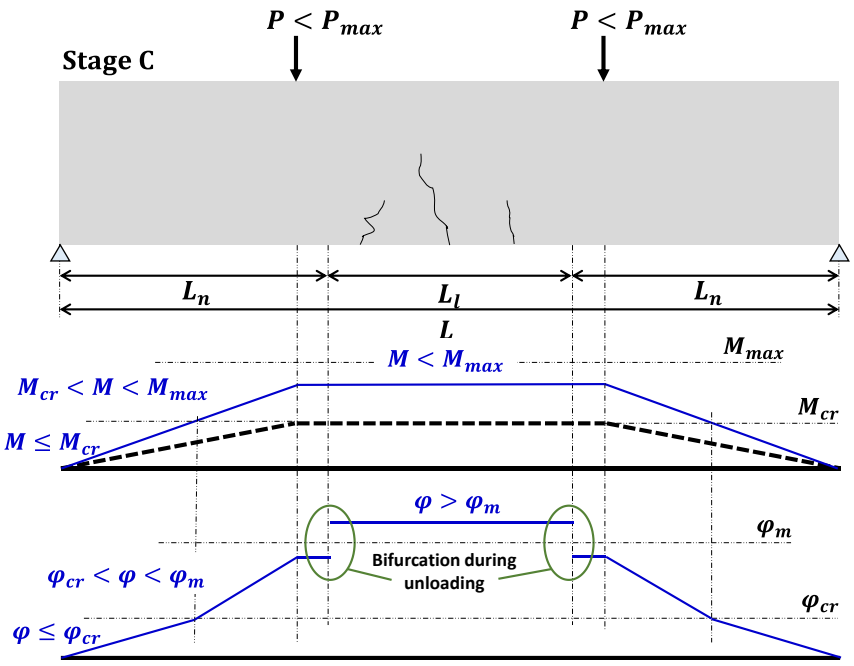

(c)

Figure 119. Moment and curvature distribution in FRC beam at different stages: (a) Stage A: un-cracked section; (b) Stage B: cracked beam, loading at localized and non-localized zones; (c) Stage C: cracked beam, unloading at localized and non-localized zones.

The procedures for the calculation of the load-deflection are described in detail in earlier publications [7], [54], [65].

4.2.1 Hybrid Reinforced Concrete (HRC)

HRC is referred to as a structural member that combines continuous reinforcement with FRC matrix [54]. Combinations of FRC and rebars, or welded wire mesh, may be used to meet the strength criteria [49], [58]–[60]. An approach similar to that for FRC can be implemented to derive the moment capacity for reinforced UHPC sections by taking into account the contribution of steel rebars.

Figure 45 shows the material behavior Mobasher et al. , [54], used to derive an analytical model for predicting the flexural behavior of HRC which is applicable to

conventional and fiber-reinforced concrete (FRC). Figure 45a represents the material (a) tensile and (b) compressive, constitutive stress-strain responses for FRC. Figure 45c represents the elastic, perfectly plastic model for steel reinforcement.

As Figure 45(a) shows, the tensile response of the section is replaced with a uniform distributed loading over the tensile part of the section. Figure 45(b) shows the stress-strain block diagrams for an HRC section. In spite of the FRC section, the plastic compressive failure is likely in this case, so a uniform compressive tension is assumed for the compressive part of the section, $\beta_2 f_c'$.

By mixing the properties of FRCs with those of another type of composites, high strength and an excellent ductility are achievable for a broad range of composites such as textile-reinforced concrete (TRC), high-performance FRC, ultra-high-performance FRC, and ultra-high-performance hybrid reinforced concrete (UHPHRC). This strain-hardening behavior enhances the durability of concrete structures, because of the ability to (a) arrest the width of cracks and (b) carry tensile stresses (due to the bridging effect of fibers) [22], [62]. The arrangement of the rebars within a cross-section of width *b* and depth *h* (Figure 45d) shows that the depth of the center of gravity of the reinforcement is at a distance $d = \alpha h$.

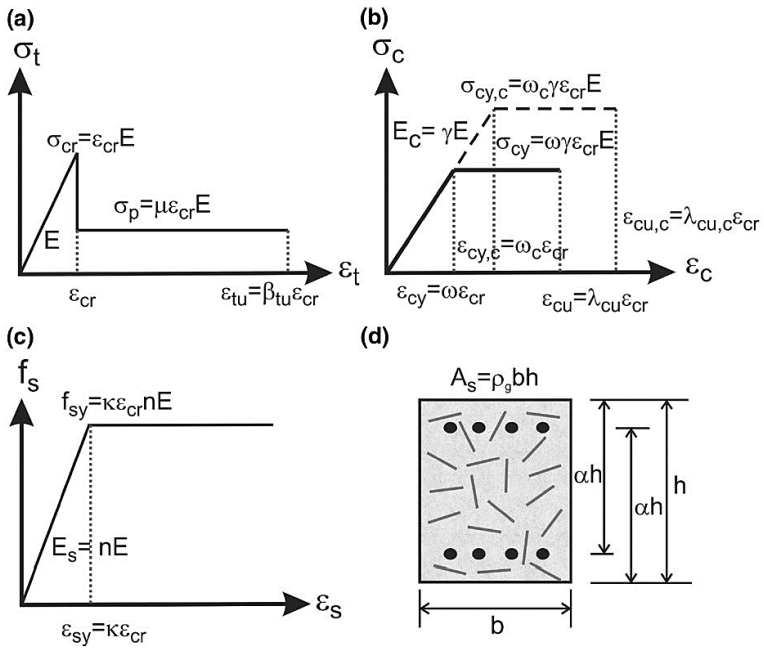

Figure 120. Material model for double reinforced concrete design (a) tension model; (b) compression model; (c) steel model; (d) beam cross section.

In this report, the HRC analytical model presented by Mobasher et al. , [54], is used in a design approach applied to the UHPFRC members. Equations to determine the moment-curvature relationship, ultimate moment capacity, and minimum flexural reinforcement ratio was explicitly derived (Mobasher et al. 2015, [54]). Figure 45 (a) and (b) represent all the combined tensile and compressive response of steel and FRC models used in the analytical expressions of moment-curvature and load–deflection of HRC beams. The derivation includes the interaction of compression and tension failure of FRC, as well as a failure by tension yielding of steel.

Parameter-based tensile and compressive strain-stress diagrams of composite and steel sections are shown in Figure 45(c) for a typical hybrid-FRC cross-section.

Reinforcement material parameters required for the simplified models are shown in Figure 120 and summarized as follows (see Figure 45):

Normalized yield strain of steel, $$\kappa = \frac{\varepsilon_{sy}}{\varepsilon_{cr}} \quad (130)$$

Normalized elastic modulus of steel, $$n = \frac{E_s}{E_c} \quad (131)$$

Reinforcement ratio, $$\rho_g = \frac{A_s}{bh} \quad (132)$$

Normalized reinforcement depth, $$\alpha = \frac{d}{h} \quad (133)$$

A list of the material properties obtained from the experiment and the properties that are used for the analytical simulations is presented in. The simulated curves and the tensile response of the section are presented in Figure 130.

4.2.2 Case Study 1- Analytical Simulations Based on Rinaldi and Meda's Experiments [115]

The loading tests, object of the present report, were carried out on precast tunnel segments in fiber reinforced concrete produced in the Laboratory of Materials and Structures of the Civil Engineering Department of the Rome University. The segments were cast by using segment molds typically used in hydraulic tunnels. Two different kinds of tests were performed, as described in the following: a test simulating the point loads effects on the segments, produced by the TBM machine during the digging phase and a flexural test simulating the behavior of the segments when loaded under bending. In total, 2 segments have been tested.

The tests were performed on elements made in concrete without traditional reinforcement, with a fiber content equal to 40 kg/m3. The adopted fiber was Dramix® 4D 80/60BG with a length of 60 mm. This mix design is typical in precast segment production in terms of cost and performance.

The tests have been carried out on precast segments characterized by a thickness of 250 mm, a length of about 1670 mm and a width of about 1200 mm (Figure 121). The concrete was prepared in a truck mixer. The adopted molds have electrical vibrators in order to compact the concrete. Both the segments were made from the same batch, as well as beams and cubes for the material characterization. The mix design of the concrete adopted for the segment preparation is shown in Table 26. Steel fibers Bekaert Dramix® 4D 80/60BGwere added with a content of 40 Kg/m.

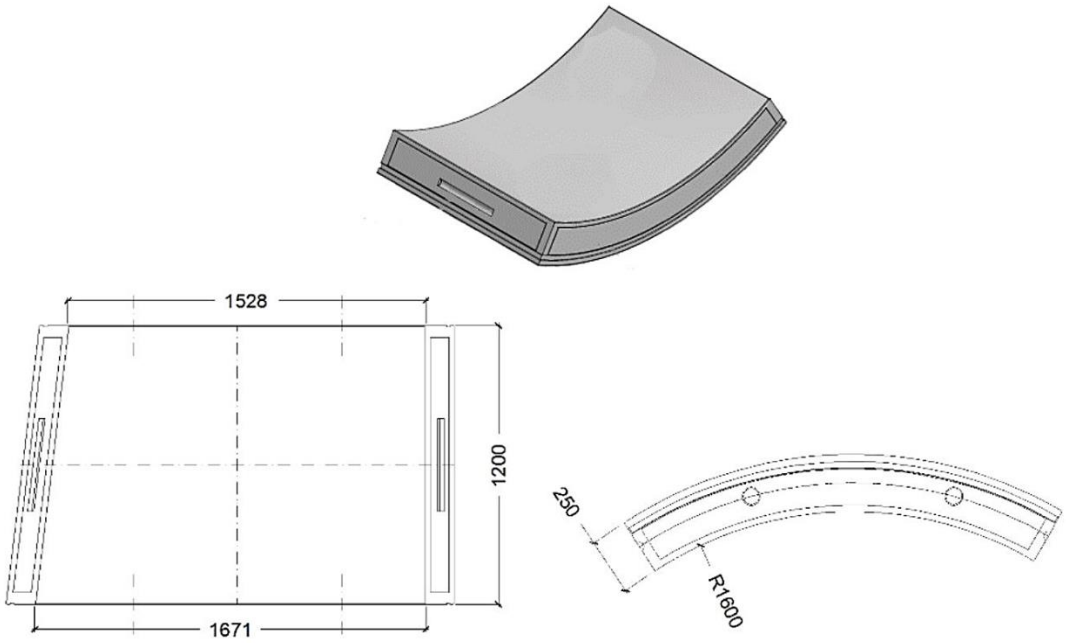

Figure 121. Segment geometry [116].

Table 26. Concrete mix design.

Component	kg/m3
Cement 42.5 R	480
Natural sand (0-4 mm)	422
Crushed sand (0-4 mm)	423
Crushed aggregate (4-16 mm)	519
Crushed aggregate (16-25 mm)	350
Plasticizer	4.8
Water	170
Steel fiber (Dramix® 4D 80/60BG, 60mm)	40 (0.54% volume fraction)

The average compressive strength of the fiber reinforced material, measured on 8 cubes having 150 mm side, was equal to 61.20 MPa. The tensile behavior was characterized through bending tests on nine 150x150x600 mm notched specimens according to the EN 14651. The diagrams of the nominal stress versus the crack mouth opening displacements (CMOD) are plotted in Figure 122. Furthermore, in Table 27 are summarized the values of the stress related to the proportionality limit (fL) and the residual nominal strengths related to four different crack openings - CMOD (0.5, 1.5, 2.5 and 3.5 mm), named fR1, fR2, fR3, fR4.

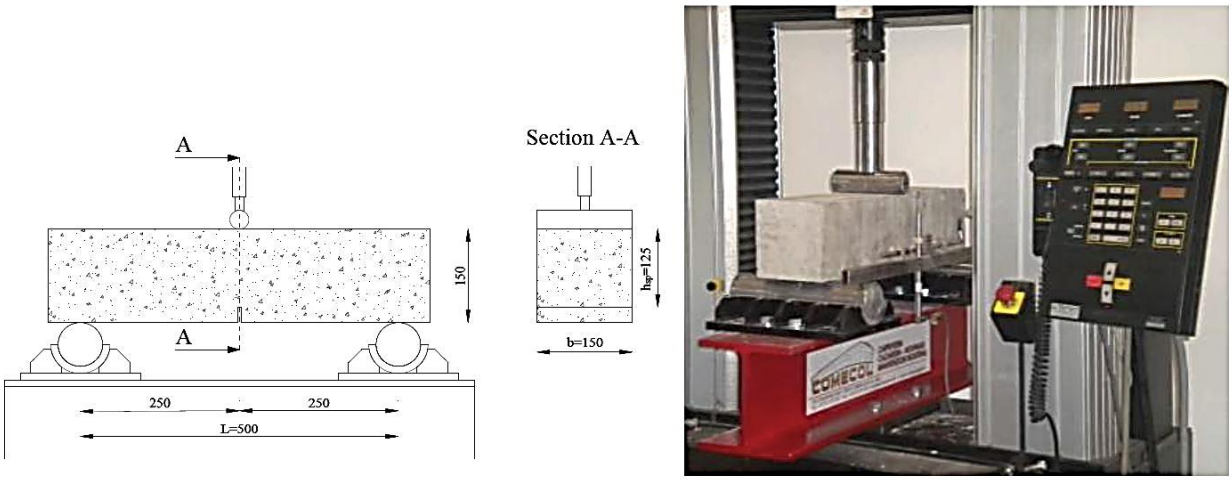

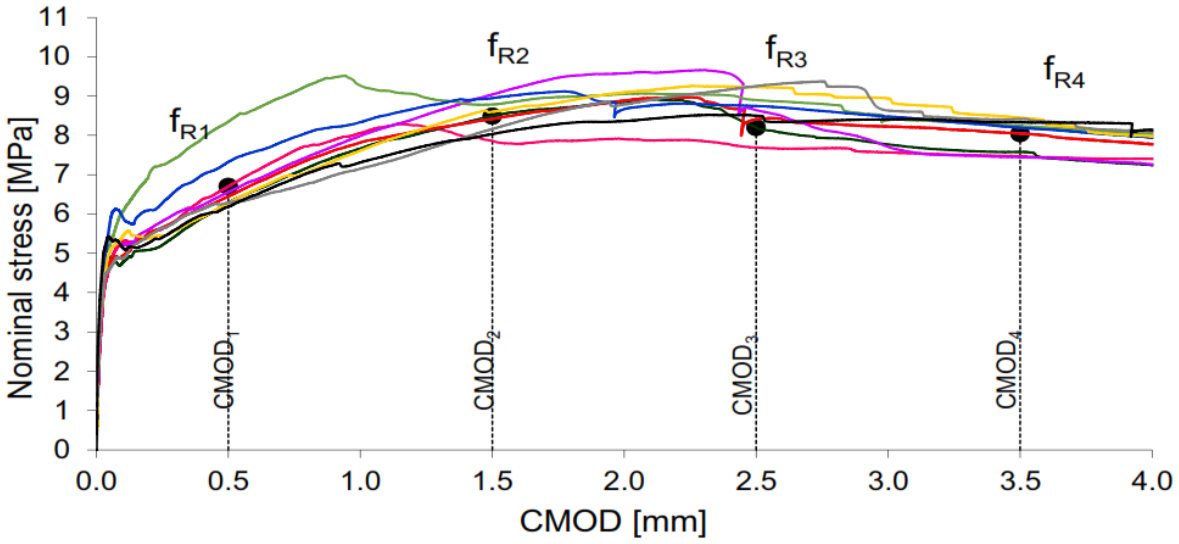

Figure 122. Results of the beam bending tests [116].

Table 27. Results of the beam bending tests [116].

	f_L [Mpa]	f_{R1} [MPa]	f_{R2} [MPa]	f_{R3} [MPa]	f_{R4} [MPa]
Beam_01	4.68	6.70	7.86	7.69	7.47
Beam_02	4.90	6.28	8.49	8.20	7.58
Beam_03	4.78	6.45	8.41	8.42	8.04
Beam_04	5.15	6.56	9.04	8.64	7.44
Beam_05	5.72	7.33	8.95	8.75	8.19
Beam_06	5.03	6.27	8.60	9.23	8.45
Beam_07	5.63	7.75	10.2	8.99	8.54
Beam_08	4.60	6.28	8.16	9.25	8.40
Beam_09	5.43	6.18	8.03	8.50	8.33
Average	5.10	6.64	8.64	8.63	8.05
Characteristic	4.30	5.58	7.26	7.65	7.19

A series of back-calculations were performed to obtain the material properties. These properties will be used in the simulation of the large segments. The back-calculated results and the summary table are shown below.

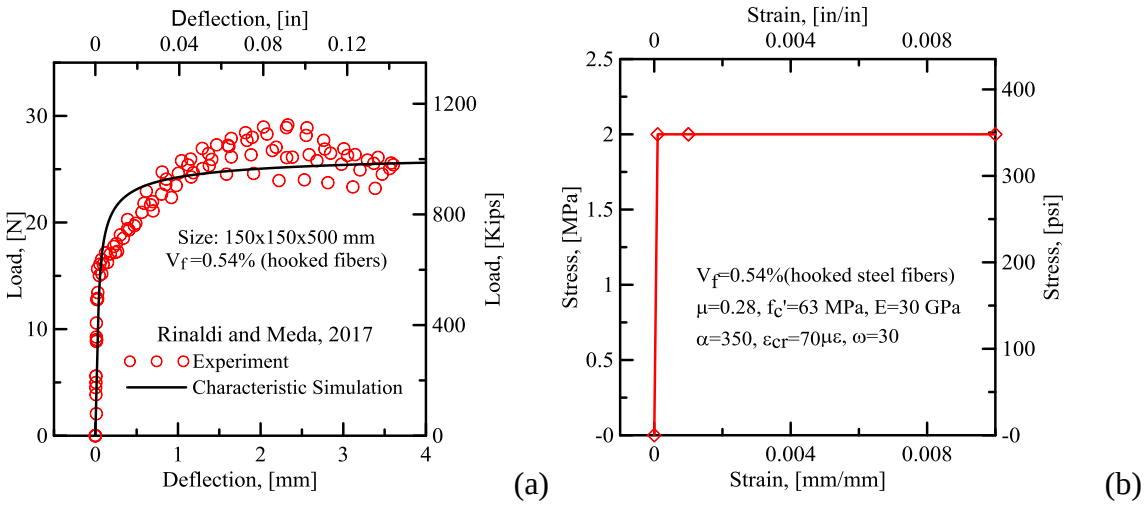

Figure 123. Simulated results and the back-calculated parameters based on 3PB tests.

Table 28. Summary of back-calculated results for the 3PB tests.

Sample ID	Elastic Modulus, E (MPa)	Cracking Tensile Strain ε_{cr}	Cracking Strength (MPa)	α, Transition Strain/ Cracking Strain	ϒ, Normalized compressive modulus	ω, Normalized Compressive Yield Strain	μ, Normalized Residual Tensile Strength	Compressive Strength (MPa)
3PB_Sample 1	20000	0.0001	2	10	0.9	27	1	48.6
3PB_Sample 2	20000	0.0001	2	10	0.9	27	1	48.6
3PB_Sample 3	20000	0.0001	2	10	0.9	27	1	48.6
3PB_Sample 4	21000	0.0001	2.1	10	0.9	27	1	51.03
3PB_Sample 5	19000	0.0001	1.9	10	0.9	27	1	46.17
Average	20000	0.0001	2	10	0.9	27	1	48.6
Std. Dev.	816.4966	0	0.08165	0	0	0	0	2
Coef. of Var.	4.08%	0.00%	4.08%	0.00%	0.00%	0.00%	0.00%	4.08%

The test on the large segments was performed with the loading set-up illustrated in Figure 124, in displacement control, by adopting a 1000kN electromechanical jacket, with a PID control and by imposing a stroke speed of 10 μm/sec.

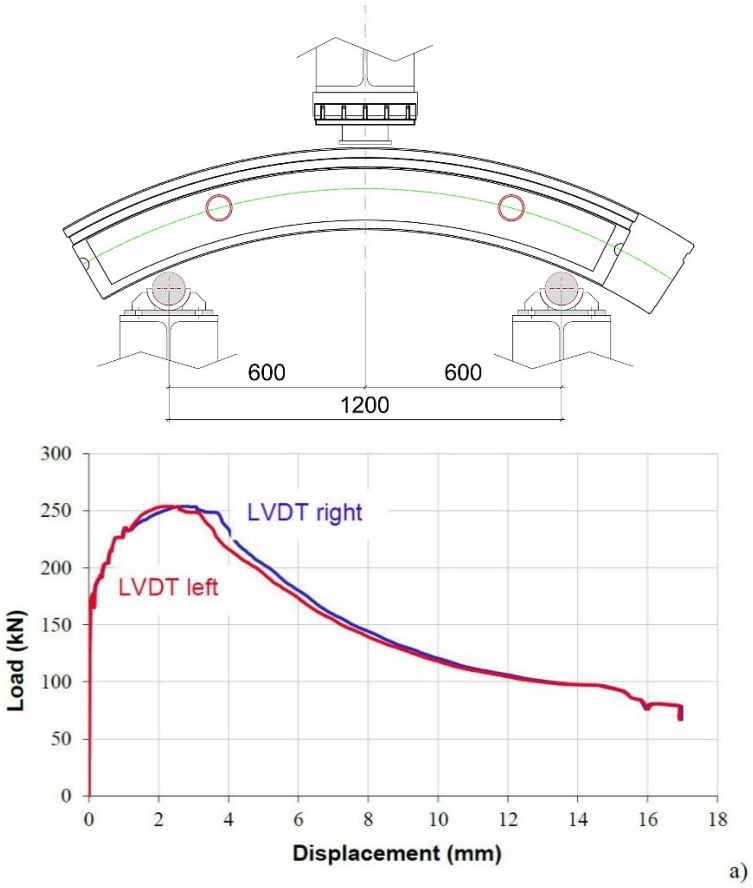

Figure 124. Test setup and Experimental results reported by Meda et al [116].

According to ACI 318:

$$\sigma_{cr} = 0.56\sqrt{f_c'} = 4.4 \text{ MPa}$$

$$E = 4700\sqrt{f_c'} = 36.8 \text{ GPa}$$

$$\varepsilon_{cr} = \frac{\sigma_{cr}}{E} = \frac{4.4}{36800} = 1.19\times10^{-4}$$

ω is the ratio of compressive strength to tensile strength and obtained as

$$\omega = \frac{f_c'}{\sigma_{cr}} = \frac{61.2}{4.4} = 14$$

These values are used as an initial estimation for the simulations. A list of the material properties obtained from the experiment and the properties that are used for the analytical simulations is presented in Table 29. The simulated curves and the tensile response of the section are presented in Figure 126.

Table 29. Experimental properties against simulation properties, Rinaldi and Meda, 2017.

Sample	Property	Experiment	Simulation
Fiber reinforced tunnel segment (FRC), with hooked steel fibers	Fiber content, V_f (%)	0.54	--
	Reinforcement ratio, ρ	0.00	--
	Concrete elastic modulus, E (GPa)	36.8	30
	Compressive strength, f_c' (MPa)	61.2	66
	Cracking tensile strength, σ_{cr} (MPa)	5.1	2.7
	Average residual tensile strength, f_R (MPa)	6.9	--
	Normalized residual strength, μ	--	0.28
	Normalized compressive strength, ω	--	20

Figure 125 shows the moment and curvature distribution along the sample length.

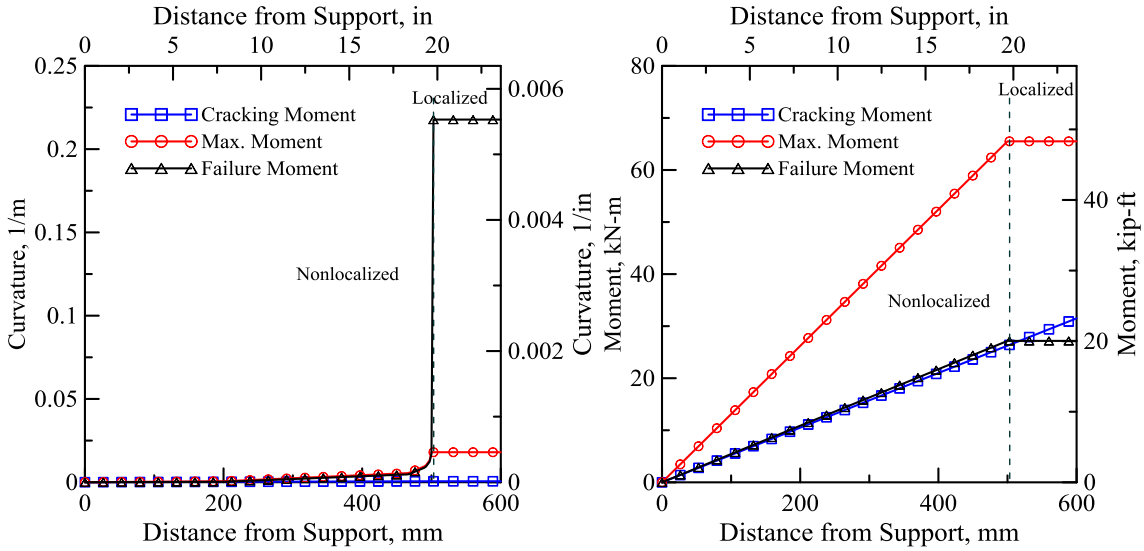

Figure 125. Moment and curvature distribution along the section.

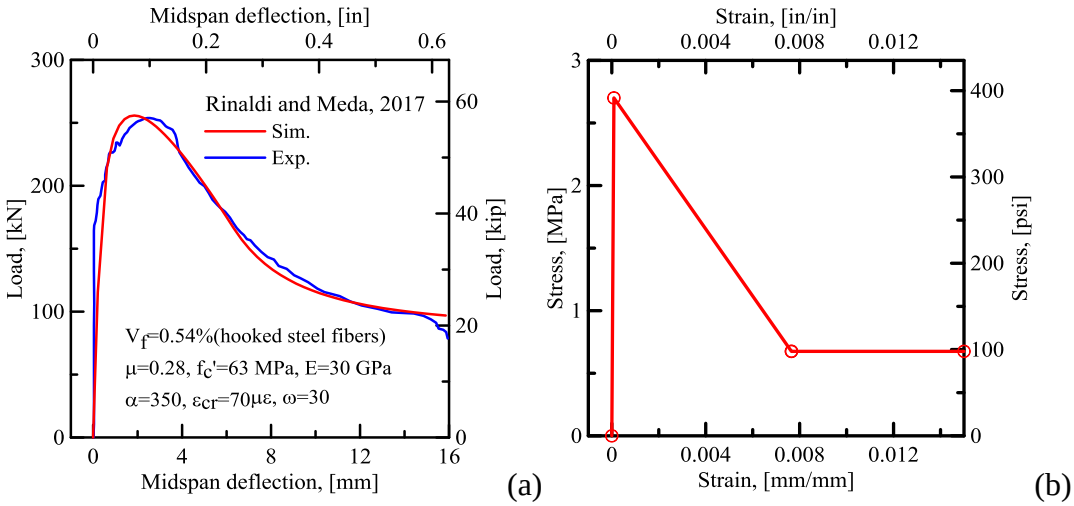

Figure 126. Comparison between analytical simulations and experiments on FRC tunnel segments.

4.2.3 Case Study 2- Analytical Simulations Based on Abbas et al. Experiments [13]

Segment's properties and test setup from the experiments by Abbas et al. [13] are presented here. The length and width of RC and SFRC segments are 3180 mm (125.20 in.) and 1500 mm (59.05 in.), respectively, while the thickness is 235 mm (9.25 in.). Segments are skewed at their ends rather than straight edges. Figure 127 shows the geometrical and reinforcement details of the RC segments.

The concrete mixture compositions and fresh properties for RC and SFRC PCTL segments are **similar**. Cold-drawn hooked-end steel fibers (60 mm [2.36 in.] long and 0.75 mm [0.030 in.] in diameter) having an ultimate tensile strength greater than **1050 MPa** (152.30 ksi) were added at a rate of **1.5% volume fraction**. The target compressive strength for both concretes was **60 MPa** (8700 psi).

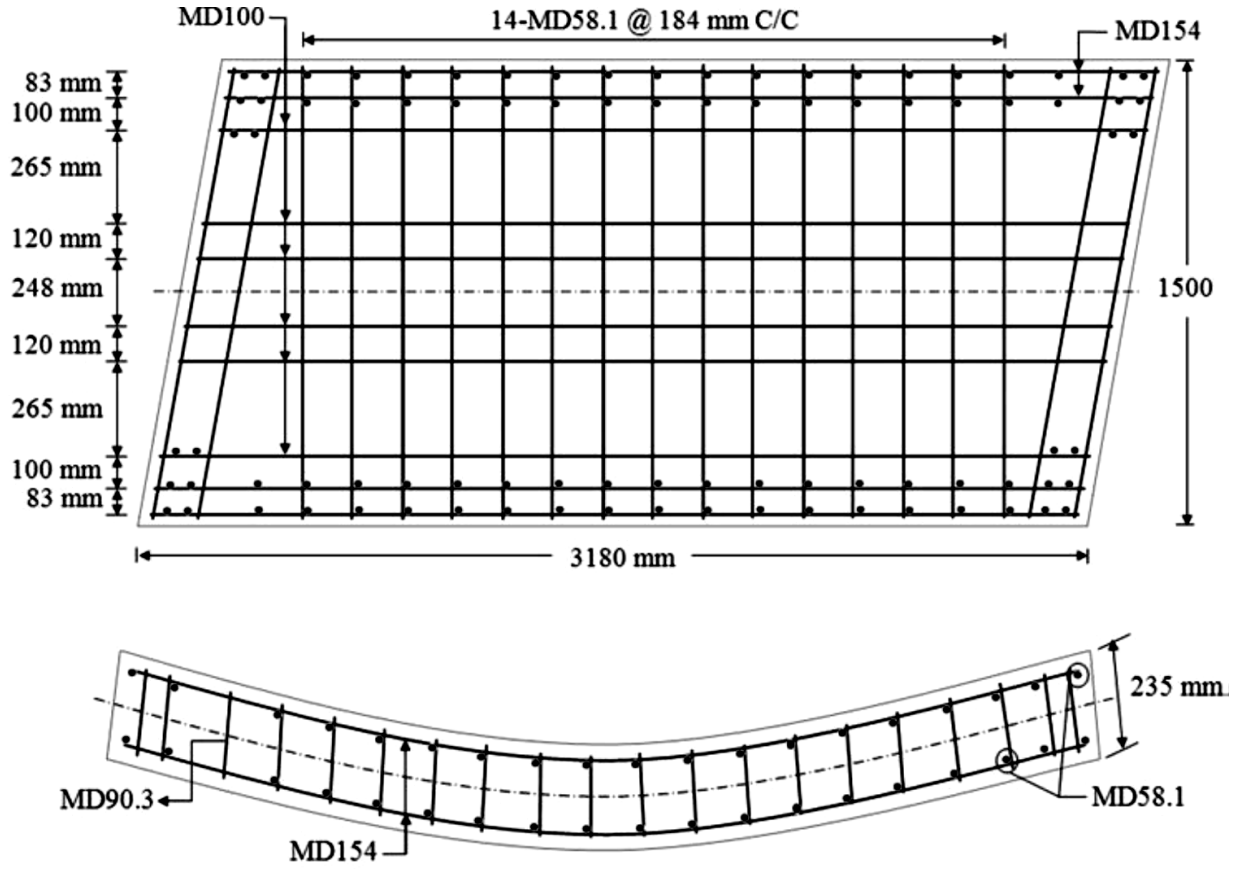

MD90.3 = metric deformed (MD) rebar having cross-section area of 90.3 mm^2 (0.14 in.^{2})

Figure 127. RC segment dimensions and detailing (MD: metric deformed; the number after MD is the cross-section area in mm) Abbas et. al [13].

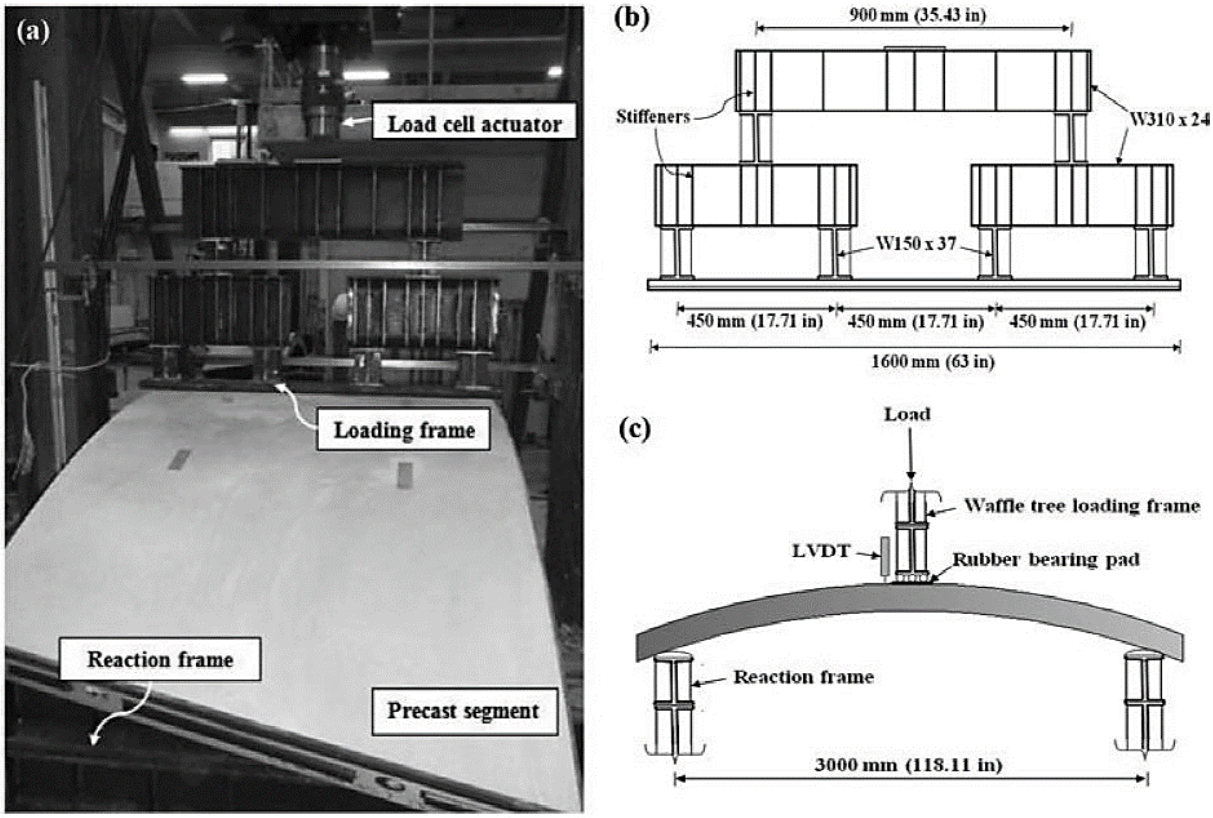

Figure 128. Flexural testing of PCTL segments: (a) instrumentation test setup; (b) waffle tree loading frame; and (c) schematic of flexural test Abbas et.al [13].

For the RC sections, a model developed for HRC sections has been used. Although this model is provided for HRC sections, assuming the residual strength for the tensile response of concrete is equal to zero (μ=0) the effect of fibers will be neglected and the RC section can be simulated as well. Four 150 x 150 x 500 mm (5.90 x 5.90 x 19.70 in.) beams were tested to determine the flexural performance of SFRC using ASTM C1609/C1609M.19 The average beam bending test results of SFRC are shown in Table 30.

To assess the quality of the cast concrete (compressive and tensile strengths), cylindrical cores were taken from both the RC and SFRC PCTL segments. The coring process was conducted at site per ACI 214.4R.20. The average core compressive

strengths for concrete mixtures of RC and SFRC PCTL segments were **60.0 MPa** (8700 psi) and **61.4 MPa** (8900 psi), respectively. The addition of steel fibers did not cause a significant effect on compressive strength, in agreement with previous research.26 The initial splitting tensile strength for RC and SFRC was **7.5 MPa** (1008 psi) and **9.0 MPa** (1030 psi), respectively. This indicates that the addition of 1.5% steel fibers improved the splitting tensile strength by 20% with respect to that of the concrete without steel fibers. This can be attributed due to the crack bridging and arresting property of steel fibers.

According to ACI 318:

$$\sigma_{cr} = 6.7\sqrt{f_c'} = 6.7\sqrt{8700} = 625\,psi\,(4.3\,MPa)$$

$$E = 57000\sqrt{f_c'} = 5300 \text{ ksi } \left(36.5 \text{ GPa}\right)$$

$$\varepsilon_{cr} = \frac{\sigma_{cr}}{E} = \frac{561}{4.8\times10^{6}} = 1.18\times10^{-4}$$

ω is the ratio of compressive strength to tensile strength and obtained as

$$\omega = \frac{f_c'}{\sigma_{cr}} = \frac{8700}{625} = 14$$

Table 30. Bending properties of SFRC. Abbas et.al [13].

δ1, mm	**δp, mm**	***f*1, MPa**	**fp, MPa**	***f*600, MPa**	***f*300, MPa**	***f*150, MPa**	***T*150, MPa**	***R*150, %**
0.067	0.343	7.6	8.1	5.7	3.8	2.7	93.8	52.4

*Notes: δ_1 is net deflection at first peak load; δ_p is net deflection at peak load; f_1 is first peak strength; f_p is peak strength; f_{600}, f_{300}, and f_{150} are residual strength at net deflection of L/600, L/300, and L/150, respectively; T_{150} is area under load-net deflection curve 0 to L/150; and R_{150} is equivalent flexural strength ratio; 1 mm = 0.0.39 in.; 1 MPa = 0.145 ksi.

Table 31. Experimental properties against simulation properties, Rinaldi and Meda, 2017.

Sample	Property	Experiment	Simulation
Ordinary reinforced tunnel segment (RC)	Fiber content, V_f (%)	0.0	--
	Reinforcement ratio, ρ (%)	0.4	--
	Concrete elastic modulus, E (GPa)	36.5	25.0
	Compressive strength, f_c' (MPa)	61.4	38.5
	Cracking tensile strength, σ_{cr} (MPa)	7.6	2.8
	Average residual tensile strength, f_R (MPa)	0.0	--
	Normalized residual strength, μ	--	0.0
	Normalized compressive strength, ω	--	14
Fiber reinforced tunnel segment (SFRC), with steel fibers	Fiber content, V_f (%)	1.5	--
	Reinforcement ratio, ρ (%)	0.0	--
	Concrete elastic modulus, E (GPa)	36.5	25.0
	Compressive strength, f_c' (MPa)	60.0	38.5
	Cracking tensile strength, σ_{cr} (MPa)	7.6	2.8
	Average residual tensile strength, f_R (MPa)	2.7	--
	Normalized residual strength, μ	--	0.1
	Normalized compressive strength, ω	--	14

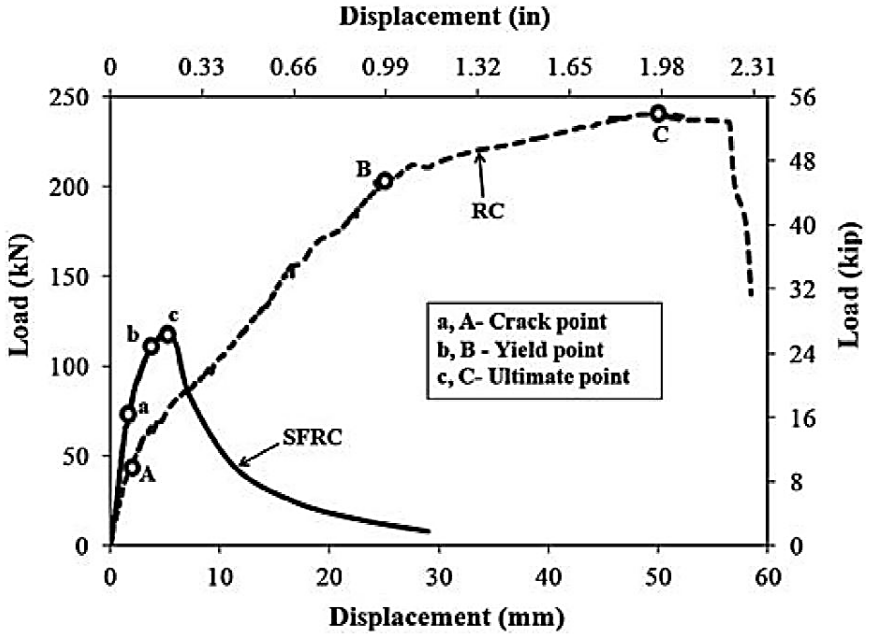

Figure 129. Experimental Data reported by Abbas et al.[13].

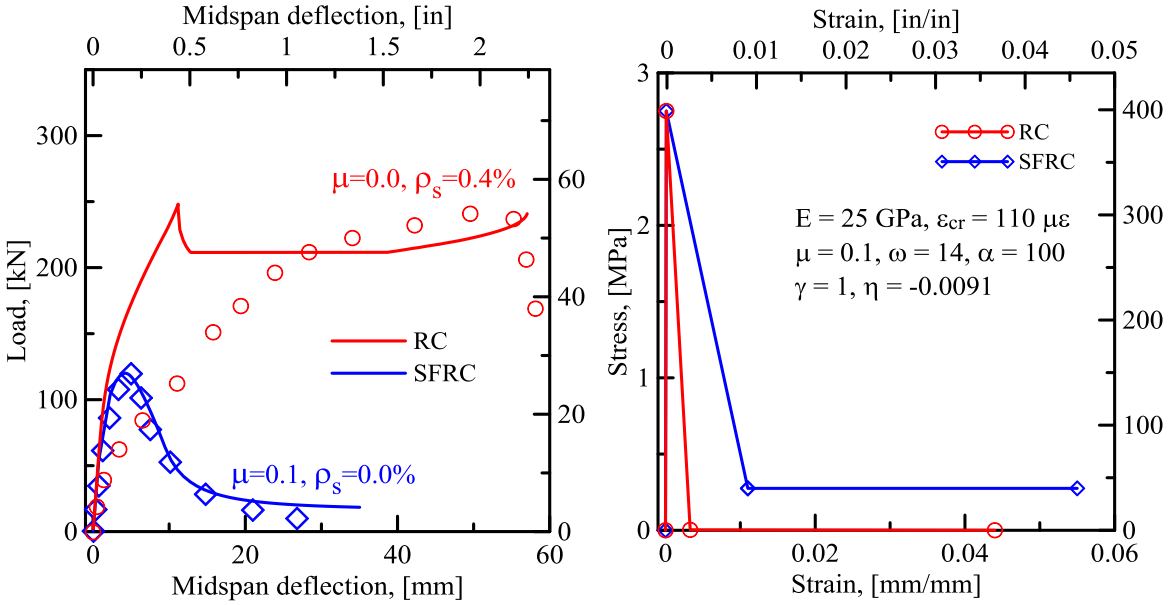

Figure 130. Comparison between analytical simulations and experiments on RC and SFRC tunnel segments.

This figure shows that, although the analytical results are comparable to the experimental results, for the SFRC segments, the simulation results for the RC segments are not very accurate. However, the predicted ultimate strength is close to the experimental results in both cases. In addition, this figure shows that the fiber content provides more loading capacity for the section but this increase is not continuous and as the deflection increases the effect of fibers decreases until it reaches zero.

4.2.4 Case Study 3- Analytical Simulations Based on Plizzari et al. Experiments [116]

Segment's properties and test setup from the experiments by Plizzari et al. [116] are presented here. The segments are parts of a lining ring each made by seven different tunnel segments. The internal diameter is **5.80 m** and the thickness is **0.30 m**, as shown in Figure 127. Concrete mixture C 40/50 was used for all of the segments. The corresponding characteristic values for the concrete mixture are $\boldsymbol{E_c}$**=36.6 GPa,** $\boldsymbol{\sigma_{cr}}$**=2.49 MPa, and** $\boldsymbol{f_c'}$**=41.3 MPa**.

$$\omega = \frac{f_c^{'}}{\sigma_{cr}} = \frac{41.3}{2.49} = 16.6$$

They have also performed some 3PB tests based on EN14651 on the notched samples. Their results, which is shown in Figure 131.

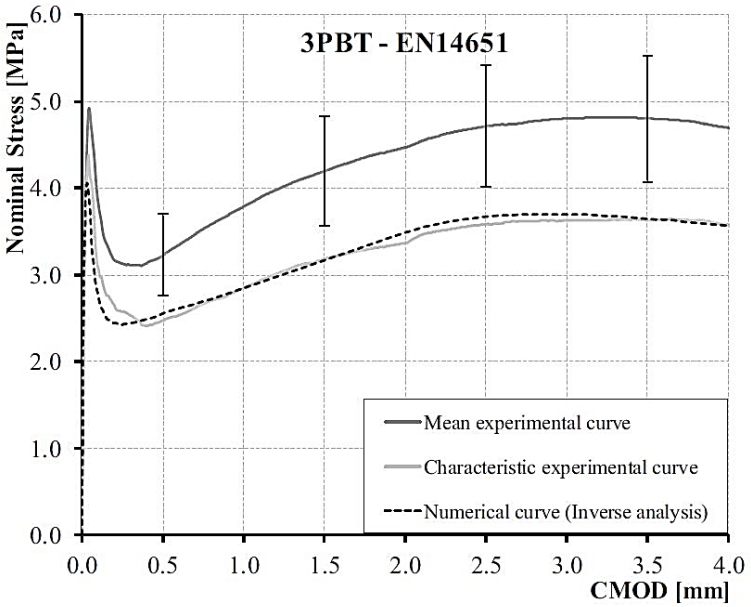

Figure 131. Flexural, 3PB, tests on FRC samples based on EN14651 [116].

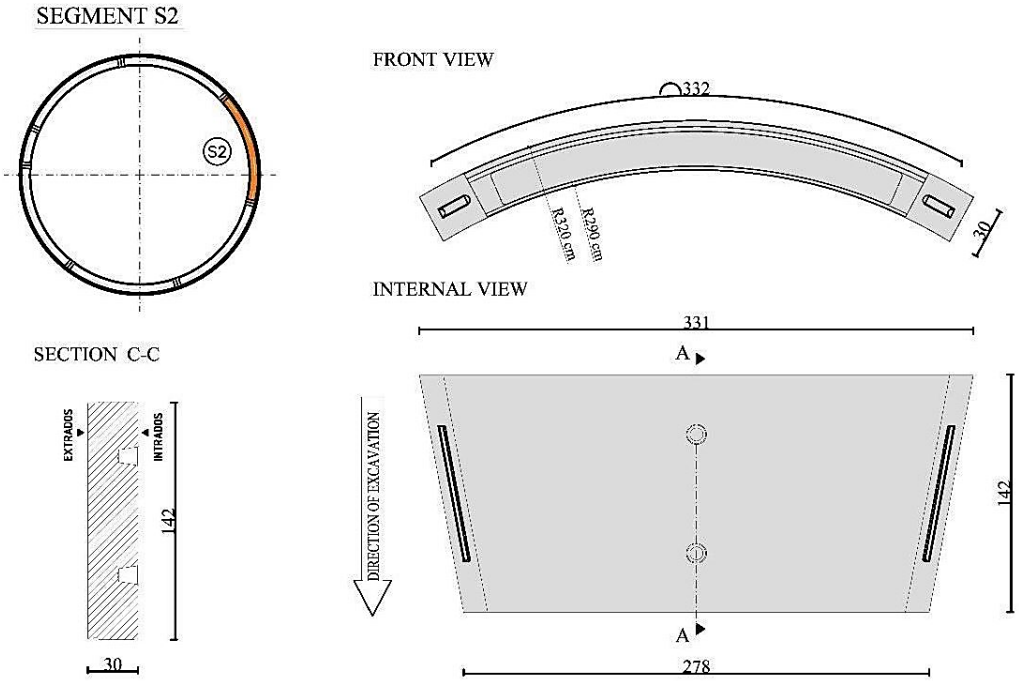

Figure 132. Metro tunnel: segment ring details and adopted precast segment (measured in cm) [116].

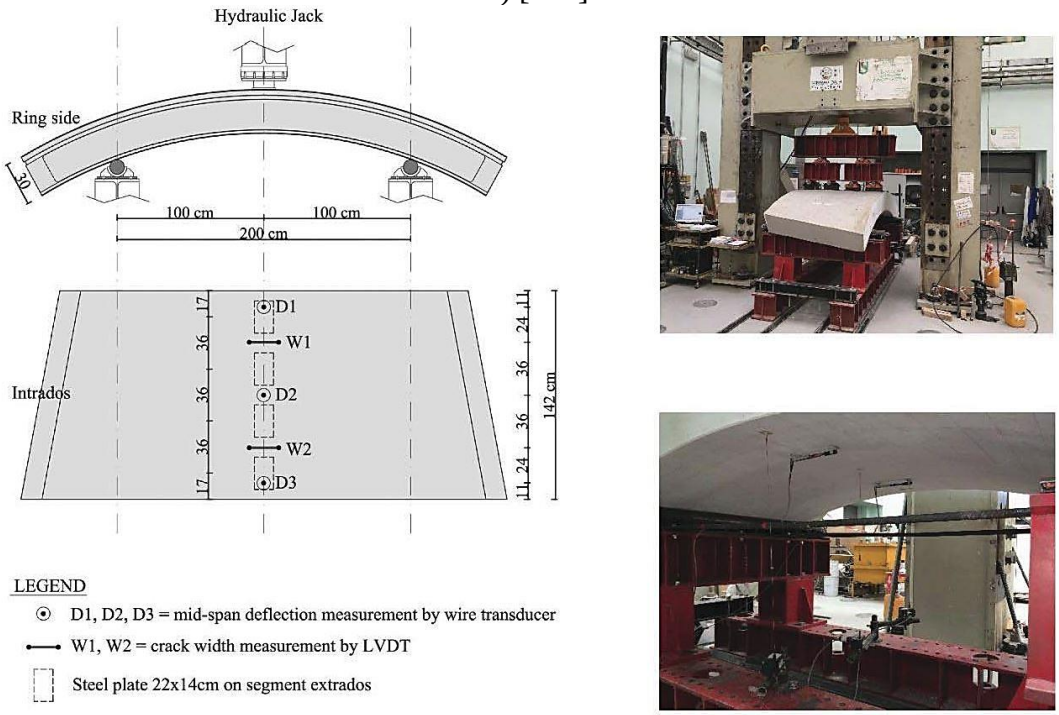

Figure 133. Flexural test setup and instrumentation details [116].

RC segments are reinforced only by conventional reinforcement. The yielding and tensile strengths were **545 MPa** and **634 MPa** for Φ10 bars (imperial bar size). Curved rebars were implemented at a reinforcement ratio of 0.22%. (see Figure 134).

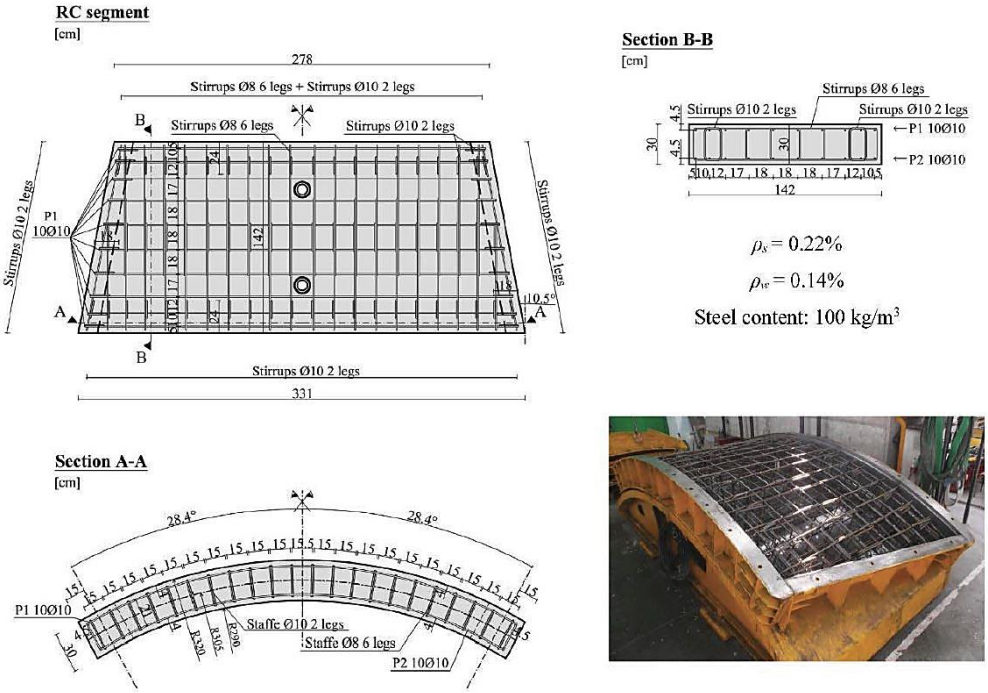

Figure 134. Reinforcement details of RC segments [116].

All concrete parameters for HRC segments are similar to RC sections. The only difference is the added polymeric fibers to the mixture (10 kg/m3 equivalent to 1.1% fiber volume fraction). The properties and the picture of the applied fibers are shown in Figure 135.

Type	Polypropylene
Shape	Embossed
Length l [mm]	54
Diameter Ø [mm]	0.81
Aspect ratio l/Ø	67
Tensile strength [MPa]	552
Elastic modulus [MPa]	6000
Density [kg/m^3]	910

(a)

(b)

Figure 135. Characteristics of the adopted macro-synthetic fiber MasterFiber MAC 2200CB.

Other difference in these segments is the reinforcement ratio and the adopted pattern. A minimum amount of curved rebars concentrated in two chords were applied to provide a longitudinal reinforcement ratio of 0.13%. The same HRC model that was used in the previous section is used here. In a similar approach, assuming the residual strength for the tensile response of concrete equal to zero (μ=0), the effect of fibers will be neglected, and the RC section can be simulated as well.

A list of the material properties obtained from the experiment and the properties that are used for the analytical simulations is presented in Table 32. The simulated curves and the tensile response of the section are presented in Figure 136.

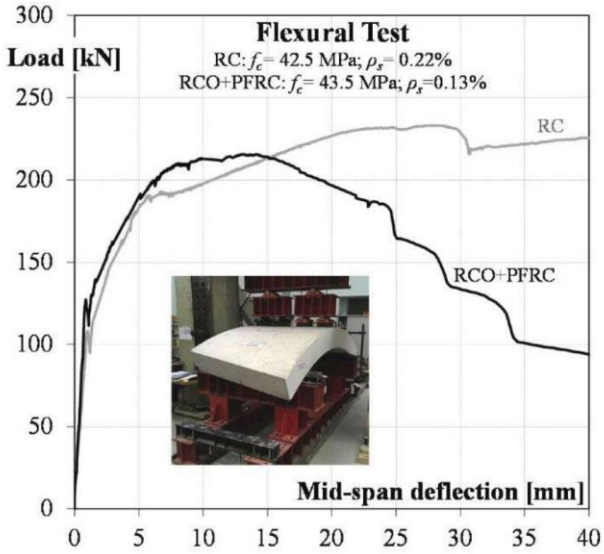

Table 32. Experimental properties against simulation properties, Rinaldi and Meda, 2017.

Sample	Property	Experiment	Simulation
Ordinary reinforced tunnel segment (RC)	Fiber content, V_f (%)	0.0	--
	Reinforcement ratio, ρ (%)	0.2	--
	Concrete elastic modulus, E (GPa)	36.6	20.0
	Compressive strength, f_c' (MPa)	41.2	23.8
	Cracking tensile strength, σ_{cr} (MPa)	2.49	1.4
	Average residual tensile strength, f_R (MPa)	0.0	--
	Normalized residual strength, μ	--	0.0
	Normalized compressive strength, ω	--	16.6
Hybrid reinforced tunnel segment (HRC), reinforcement & polymeric fibers	Fiber content, V_f (%)	1.1	--
	Reinforcement ratio, ρ (%)	0.13	--
	Concrete elastic modulus, E (GPa)	36.6	20.0
	Compressive strength, f_c' (MPa)	41.2	23.8
	Cracking tensile strength, σ_{cr} (MPa)	2.49	1.4
	Average residual tensile strength, f_R (MPa)	1.1	--
	Normalized residual strength, μ	--	0.15
	Normalized compressive strength, ω	--	16.6

The results are shown below. Similar to the simulation results of the experiments by Abbas et al.[13], as the amount of fiber content decreases (and therefore the amount of the reinforcement increases) the accuracy of the model decreases as well.

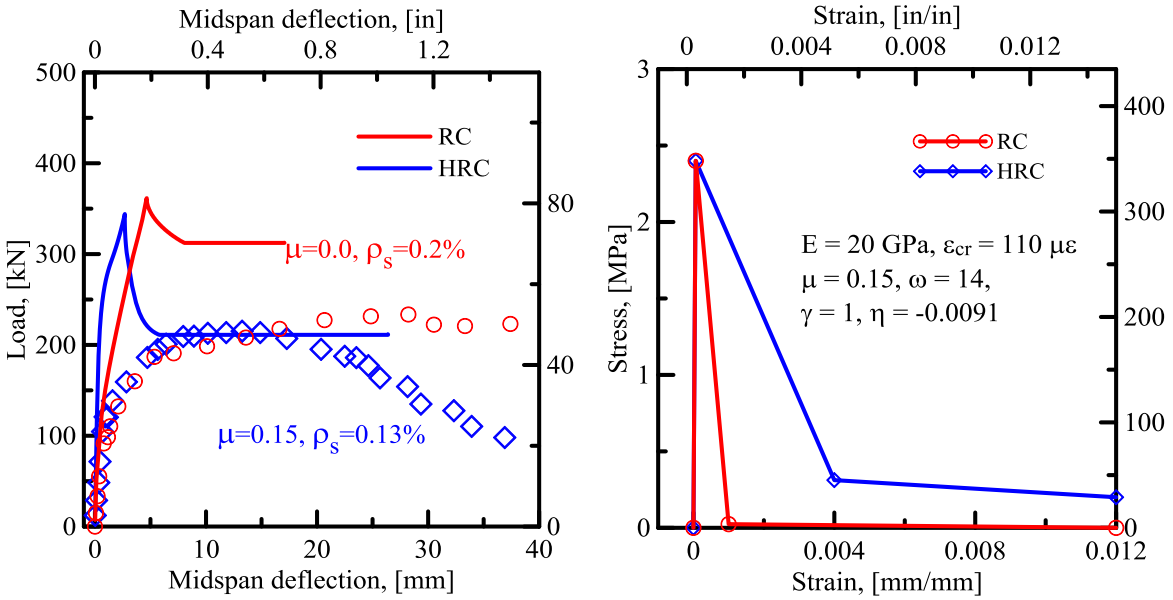

Figure 136. Comparison between analytical simulations and experiments on RC and HRC tunnel segments.

4.3 Simulation of the Tunnel Lining under the Current Test Program

A study was conducted to evaluate the performance of MasterFiber MAC 2200 CB used in proposed tunnel limning for the project. The selected mix design was previously approved for both the Regional Connector and Westside Subway PCTLs (LA County, Westside Subway Extension Project). No charges are being made to the previously used mix design, as the materials have not changed, and the break history has demonstrated compliance with the stated specifications and requirements. Testing was performed in accordance with ASTM C1609-12 “Standard Test Method for Flexural Performance of Fiber Reinforced Concrete (Using Beam with Third-Point Loading)” at an age of 5.5 hours in an oven. The mix design and the test results were obtained from BASF report on FRC Precast Tunnel Segments, Prequalification Testing in September

2018, the information provided on Precast Concrete Tunnel Liners (PCTL). The study was conducted to evaluate the performance of MasterFiber MAC 2200 CB.

4.3.1 Test Program

The following data are obtained from the test results conducted by in-house BASF trials for the tunnel segments.

Table 33. Concrete Mixture.

Mix 1		V_f = 1 %
Cement I/II	lb/yd^3	748
Class F Fly Ash	lb/yd^3	131
Silica Fume	lb/yd^3	45
Coarse Aggregate (#4)	lb/yd^3	340
Coarse Aggregate (#3)	lb/yd^3	1017
Washed Concrete Sand	lb/yd^3	1400
Water	lb/yd^3	283
w/cm	(-)	0.3
MasterFiber MAC 2200 CB	lb/yd^3	15

4.3.2 Test Results from Previous and current BASF studies

Application of the back-calculation approach to the ASTM C1609 was conducted on two sets of data, previous studies conducted in 2014 and 2015. (Reports submitted earlier in 2014 and 2015) as well as data supplied by BASF on Thursday the 6th of September 2018. The following two sets of simulations of 5 and 7.5 lbs/cubic yard mixtures were obtained from BASF studies conducted during 2014 and 2015.

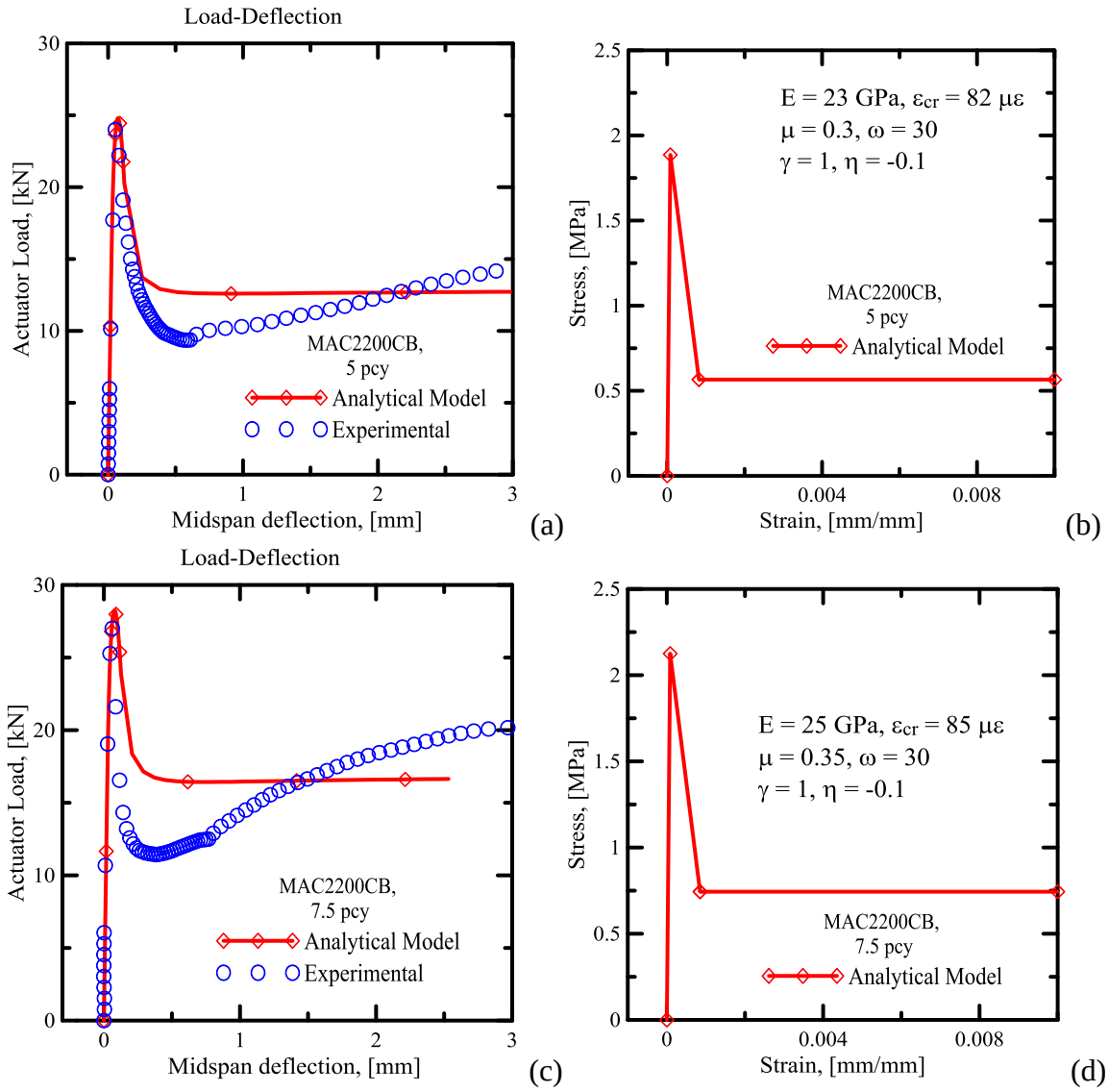

Figure 137. Test data from 2014 and 2015 studies of MAC2200 fibers by ASU. With 5 (top) and 7.5 pcy (bottom) of MAC 2200CB fibers.

Another study was conducted to evaluate the performance of MasterFiber MAC 2200 CB. Testing was performed in accordance with ASTM C1609-12 "Standard Test Method for Flexural Performance of Fiber Reinforced Concrete (Using Beam with Third-Point Loading)" at an age of 5.5 hours in an oven. A summary of data supplied by BASF on Thursday the 6th of September, 2018 is as follows:

Table 34. Plastic Properties and Compressive Strength.

		Mix 1 Vf = 1 %
Slump (ASTM C143-12)	inches	1
Plastic Air (ASTM C231-14)	(%)	2.3
Compressive Strength @ 5.5 hrs Oven Cured (ASTM C39-15)	psi	2910
Compressive Strength @ 5.5 hrs Sure Cure (ASTM C39-15)	psi	3960

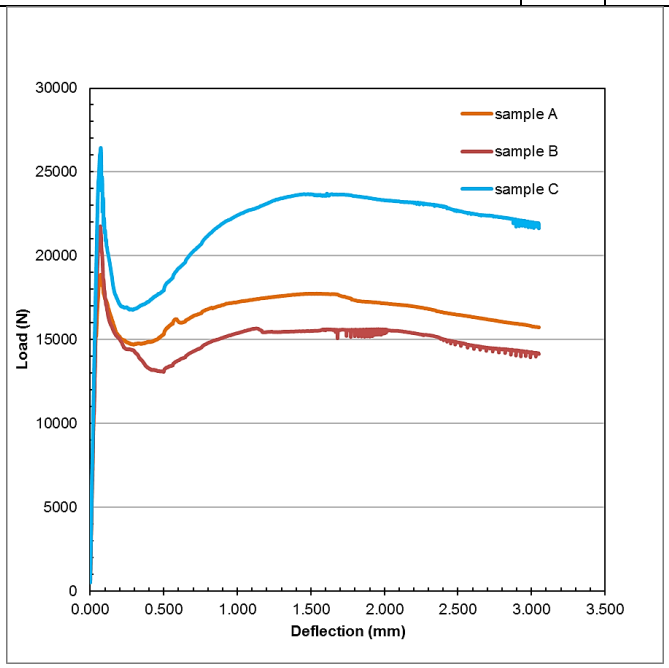

Figure 138. ASTM C1609-12 Test Results @ 5.5 hrs (MasterFiber MAC 2200 CB – 15 lb/yd3).

Back-calculation results of the ASTM C1609 results of four-point bending tests conducted for fiber evaluation is shown in

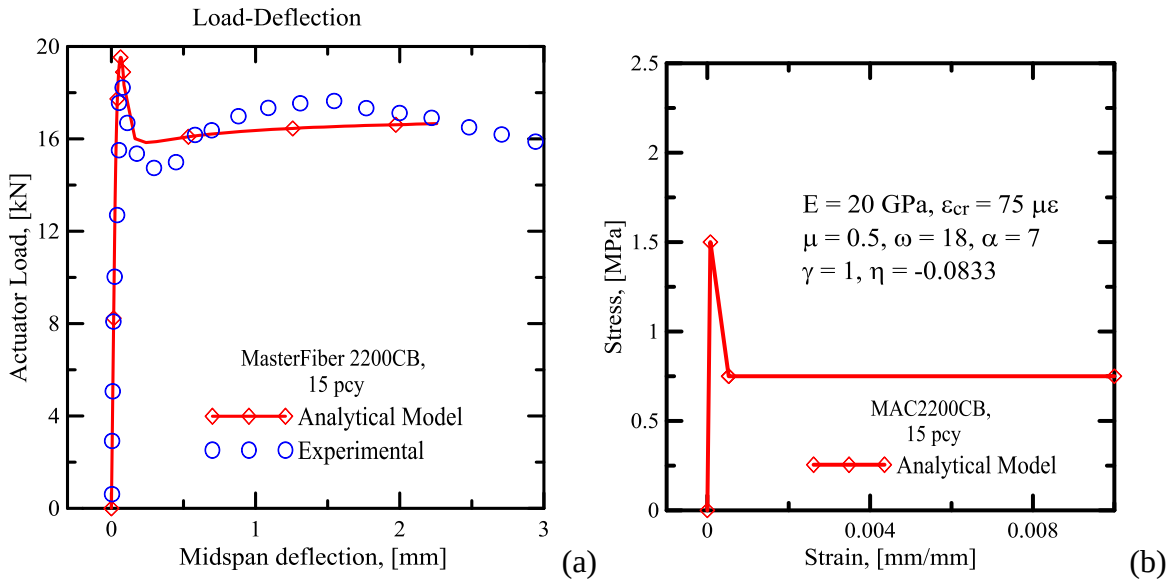

Figure 139. Test data from 2018 studies of MAC2200 fibers by BAST. With 15 pcy of MAC 2200CB fibers.

Table 35. Summary of ASTM C1609-12 Test Results (MasterFiber MAC 2200 CB – 15 lb/yd3).

Sample ID	Width	Depth	δ_1	P_1	P_{600}^{150}	P_{150}^{150}	f_1	f_{600}^{150}	f_{150}^{150}	T_{150}^{150}	$R_{T,150}^{150}$
	(mm)	(mm)	(mm)	(N)	(N)	(N)	(MPa)	(MPa)	(MPa)	(J)	(%)
A	150	150	0.069	18874	16578	15808	2.5	2.2	2.1	49.8	88.0
B	150	150	0.069	21770	14509	14262	2.9	1.9	1.9	44.9	68.8
C	150	150	0.071	26439	20667	21966	3.5	2.8	2.9	65.2	82.3
Average	150	150	0.070	22361	17251	17345	3.0	2.3	2.3	53.3	79.7

4.3.3 Dimensions and Material Properties

Maximum applied a load by the actuator on the beam with a span of $L = 96\text{ in } (2.4\text{ m})$ and a rectangular Section 60in × 12in (1520mm × 305mm) is used. UHPC concrete has $f_c^{'} = 3900$ psi (27 MPa). The longitudinal deformed wire, D20, with an area of 0.2 in^2 (129 mm^2) for each wire has been used for each panel (see Figure 140). The normalized residual strength is obtained from the back-calculations on the small beams, testing based on ASTM C1609. From the previous section, a rage between $\mu =$

0.45 to $\mu = 0.55$ can be assigned to the FRC material. Other parameters are also similar to the previous section. For the steel wires it ,is a ssumed that $f_y = 7500\ psi\ (515\ MPa) and\ 30 \times 10^6\ psi\ (210\ GPa)$. The total weigh of each panel is $W = 9192$ lb (4169 kg).

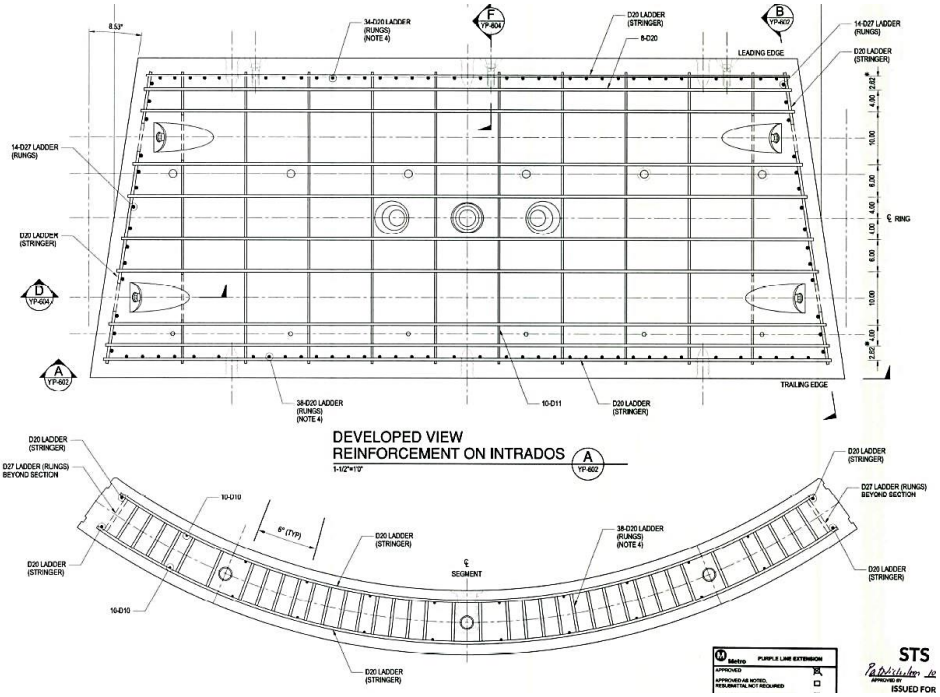

Figure 140. Segment dimensions and reinforcement plan.

4.4 A parametric study based on the results obtained from experimental tests (ASTM C1609)

In this section, a series of simulations on the full-scale samples is performed based on the results obtained from ASTM tests on small beams, which was presented in the previous section. A schematic view of the simulated sample and its dimensions are shown below.

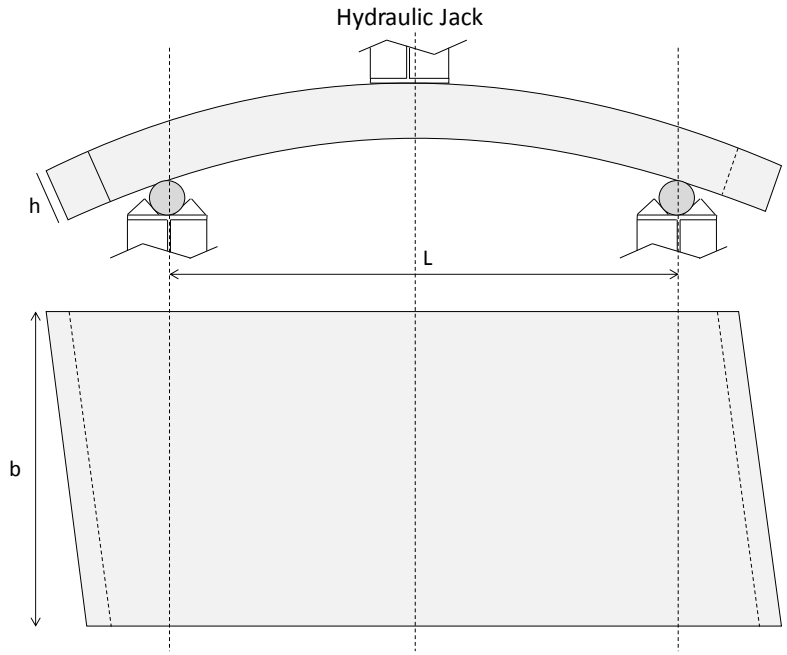

Figure 141. Schematic view of the large tunnel segments used in the analytical simulations.

According to the information given in the previous section and the dimensions shown in the figure, the segment's dimension and the material properties are as follows:

$L = 96$ in (2.4 m), $b = 60"$ (1.52 m), $h = 12"$ (0.305 m), ϕ(safety factor) $= 1$,
$f_c' = 3900$ psi (27 MPa)

Area of one wire: 0.2 in^2 (129 mm^2)

$A_s = 10 \times 0.2 = 2\ in^2$

$A'_s = 10 \times 0.2 = 2\ in^2$

$f_y = 7500\ psi\ (515\ MPa)$

$E_s = 30 \times 10^6\ psi\ (210\ GPa)$

Assume $\gamma = 1$, thus: $E_c = E$; also $\sigma_{cr} = 6.7\sqrt{f_c'} = 6.7\sqrt{3900} = 420\,psi\,(2.9\,MPa)$

$E = 57000\sqrt{f_c'} = 4800 \text{ ksi } (33 \text{ GPa})$

$$\varepsilon_{cr} = \frac{\sigma_{cr}}{E} = \frac{561}{4.8\times10^6} = 1.17\times10^{-4}$$

However, the values obtained from the back-calculation are different from the values obtained from the ACI formulations:

$\varepsilon_{cr} = 8.0\times10^{-5}$

$\sigma_{cr} = 290\,psi\,(2.0\,MPa)$

$E = 3600 \text{ ksi } (25 \text{ GPa})$

This can be due to the fact that the ACI recommendations are based on the 28 days samples not for the oven cured samples. Here the later values are used for the simulation.

β_{tu} is the normalized ultimate tensile strain in the section and since it is assumed that the section will maintain its residual tensile strength. This value is expected to be imposed as a large number. In this example, it is considered to be equal to 50, i.e.

$\beta_{tu} = \varepsilon_{tu} / \varepsilon_{cr} = 50$. Therefore, maximum the tensile strain allowed is ε_{tu} = 0.0055 or 0.55%.

ω is the ratio of compressive strength to tensile strength and obtained as

$$\omega = \frac{f_c^{'}}{\sigma_{cr}} = \frac{3900}{217} = 18$$

Based on these values, the load-deflection diagrams for 3PB tests, at different reinforcement ratios (ρ=0.0%, 0.2%, 0.4%, and 0.6%), and for different residual strengths (μ =0.0%, 20%, 40%, and 60%), can be obtained as follows, using the approach in ACI-544-R8 and the corresponding MATLAB code for the hybrid model. Alist of applied material properties is given in Table 36.

Table 36. Parameters used in the parametric studies.

Sample	Property	Simulation
Ordinary reinforced tunnel segment (RC)	Fiber content, V_f (%)	0.0
	Reinforcement ratio, ρ (%)	0.0, 0.2, 0.4, 0.6
	Concrete elastic modulus, E (GPa)	25.0
	Compressive strength, f_c' (MPa)	27.0
	Cracking tensile strength, σ_{cr} (MPa)	2.0
	Average residual tensile strength, f_R (MPa)	0.0
	Normalized residual strength, μ	0.0
	Normalized compressive strength, ω	14.0
Hybrid reinforced tunnel segment (HRC), reinforcement & polymeric fibers	Fiber content, V_f (%)	--
	Reinforcement ratio, ρ (%)	0.0, 0.2, 0.4, 0.6
	Concrete elastic modulus, E (GPa)	25.0
	Compressive strength, f_c' (MPa)	27.0
	Cracking tensile strength, σ_{cr} (MPa)	2.0
	Average residual tensile strength, f_R (MPa)	0.0, 0.4, 0.8, 1.2
	Normalized residual strength, μ	0.0, 0.2, 0.4, 0.6
	Normalized compressive strength, ω	14.0

The results of the parametric studies are shown in Figure 142.

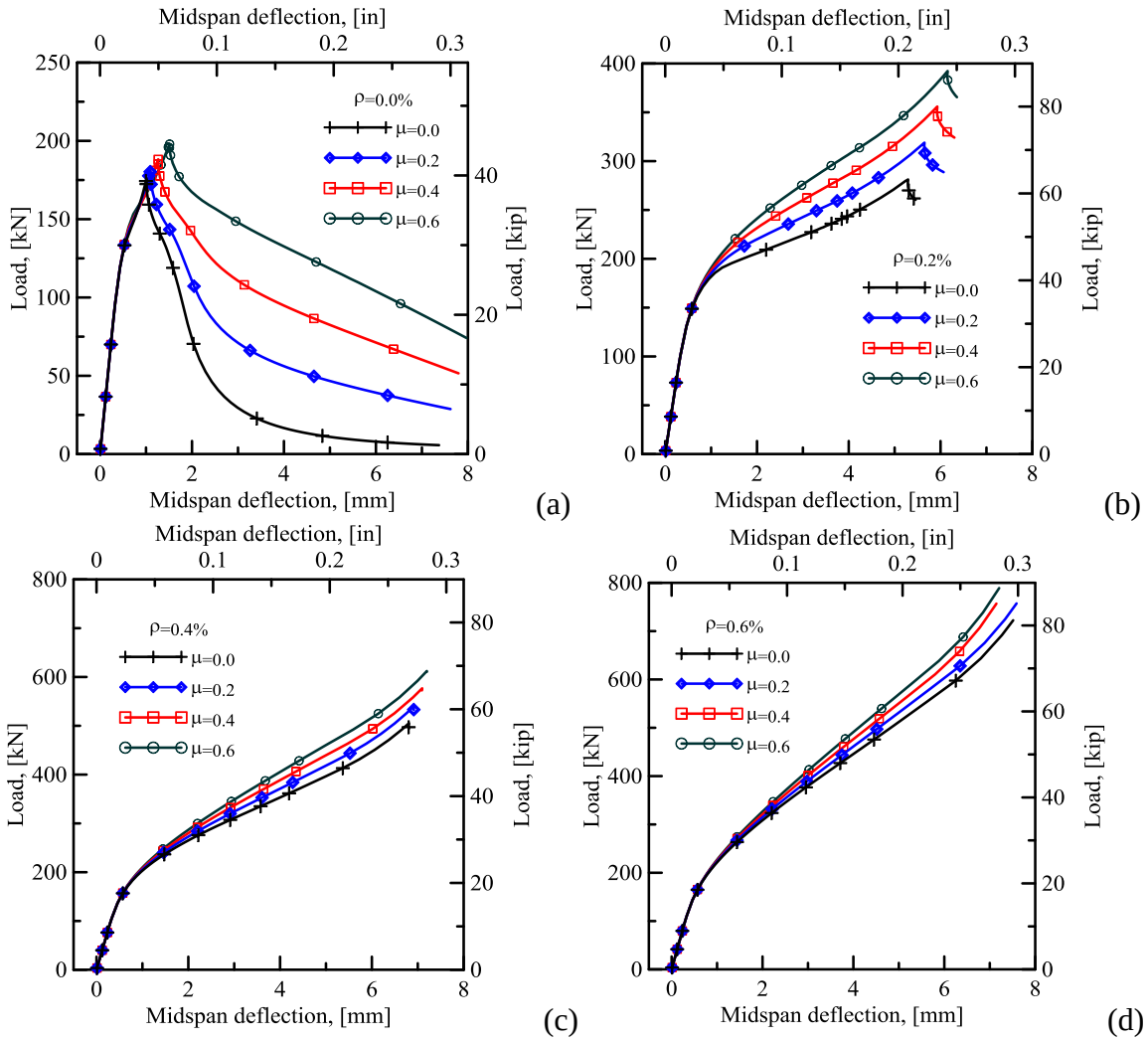

Figure 142. Parametric study on the effect of fiber content and reinforcement ratio.

4.4.1 Effect of fiber content

At this set of experiments, three different fiber contents were utilized (5, 7.5, and 15 pcy). Based on the back-calculated parameters, three different values for normalized residual strength were obtained for each fiber content. In this section, these values will be compared with an ordinary RC section with 0.3% reinforcement and without any fiber

reinforcement, as the control sample. The reinforcement ratio was chosen based on the original plans given by the BASF.

Table 37. Parameters used in the parametric study based on the original tunnel segments.

Sample	Property	Simulation
Ordinary reinforced tunnel segment (RC)	Fiber content, V_f (%)	0.0
	Reinforcement ratio, ρ (%)	0.3
	Concrete elastic modulus, E (GPa)	25.0
	Compressive strength, f_c' (MPa)	27.0
	Cracking tensile strength, σ_{cr} (MPa)	2.0
	Average residual tensile strength, f_R (MPa)	0.0
	Normalized residual strength, μ	0.0
	Normalized compressive strength, ω	14.0
Hybrid reinforced tunnel segment (HRC), reinforcement & polymeric fibers	Fiber content, V_f (%)	--
	Reinforcement ratio, ρ (%)	0.3
	Concrete elastic modulus, E (GPa)	25.0
	Compressive strength, f_c' (MPa)	27.0
	Cracking tensile strength, σ_{cr} (MPa)	2.0
	Average residual tensile strength, f_R (MPa)	0.0, 0.6, 0.7, 1.0
	Normalized residual strength, μ	0.0, 0.3, 0.35, 0.5
	Normalized compressive strength, ω	14.0

The results of the simulations are shown in Figure 143. It shows that the strength of the FRC segments is almost half of the FRC sections.

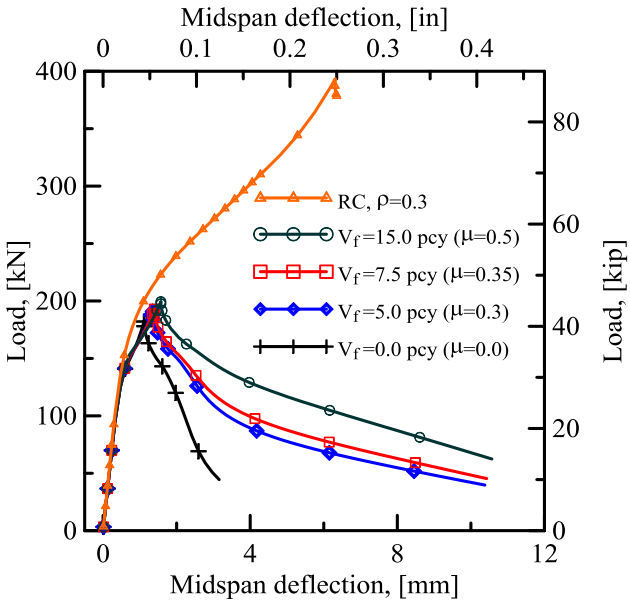

Figure 143. Parametric study on the effect of fiber content for the MAC2200CB type of fibers without any rebar and comparison with ordinary RC section.

4.4.2 Effect of segment length

The effect of the segment length is shown in Figure 144. As it is expected, as the length of the segment decreases, the loading capacity increases as well. Other parameters are the same as those in Table 36.

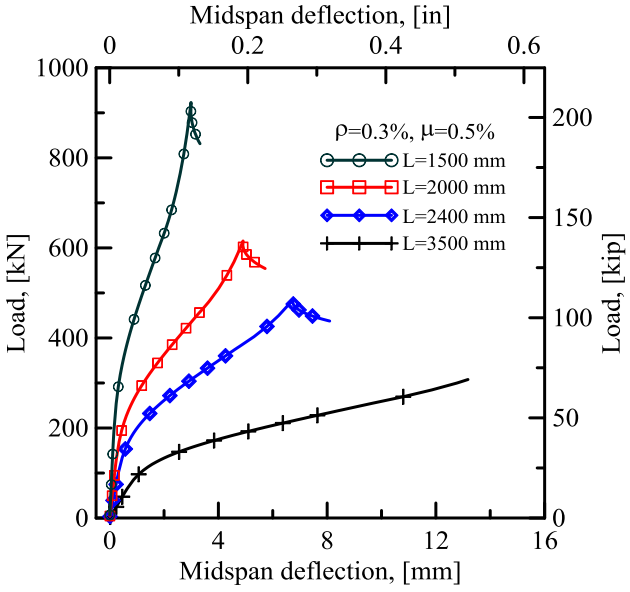

Figure 144. Length effect.

4.5 Parametric study

4.5.1 Effect of fiber and reinforcement ratio on narrow samples (W=1200 mm)

Long Samples (L=2500 mm):

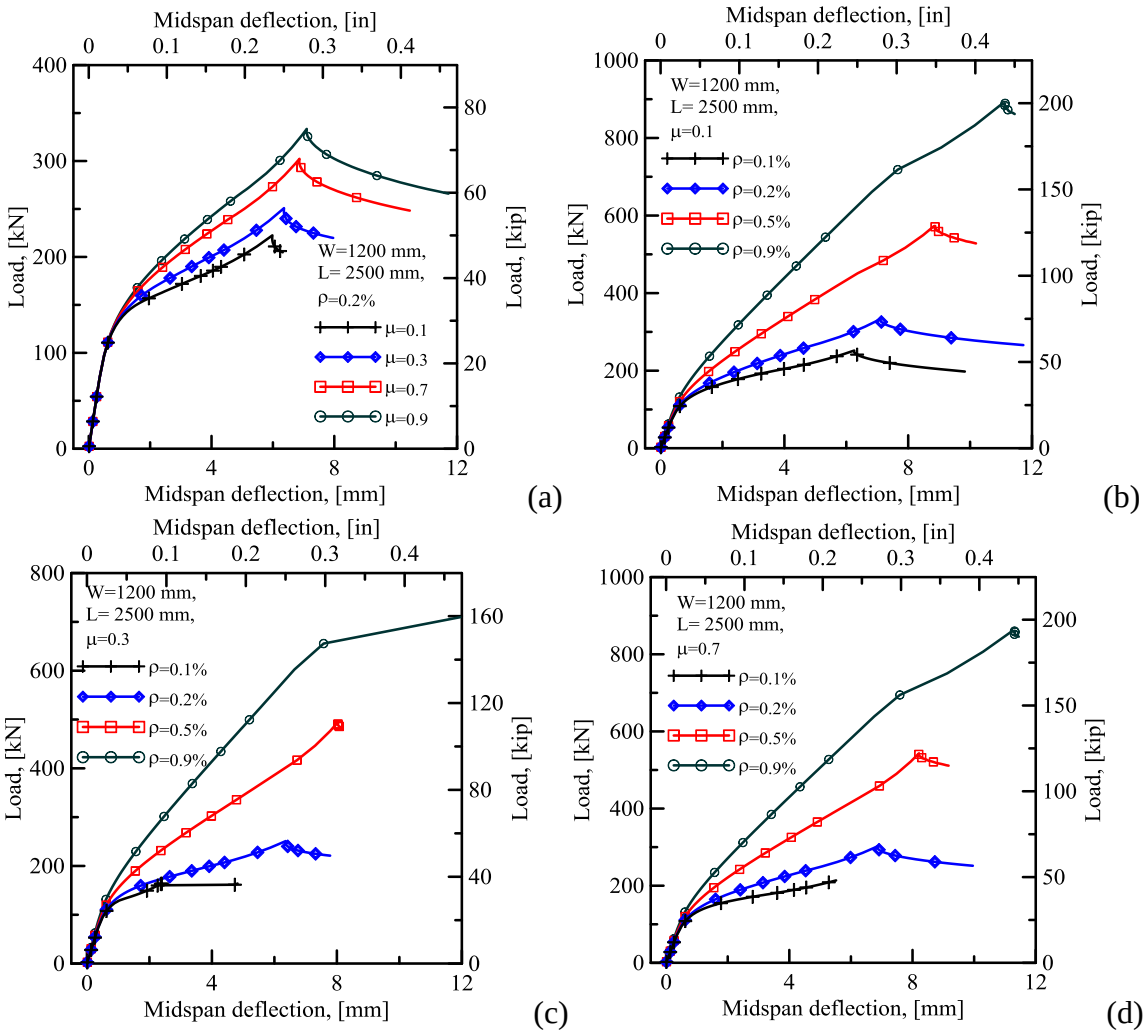

Figure 145. Effect of fiber and reinforcement ratio on narrow-long samples.

Short Samples (L=1500):

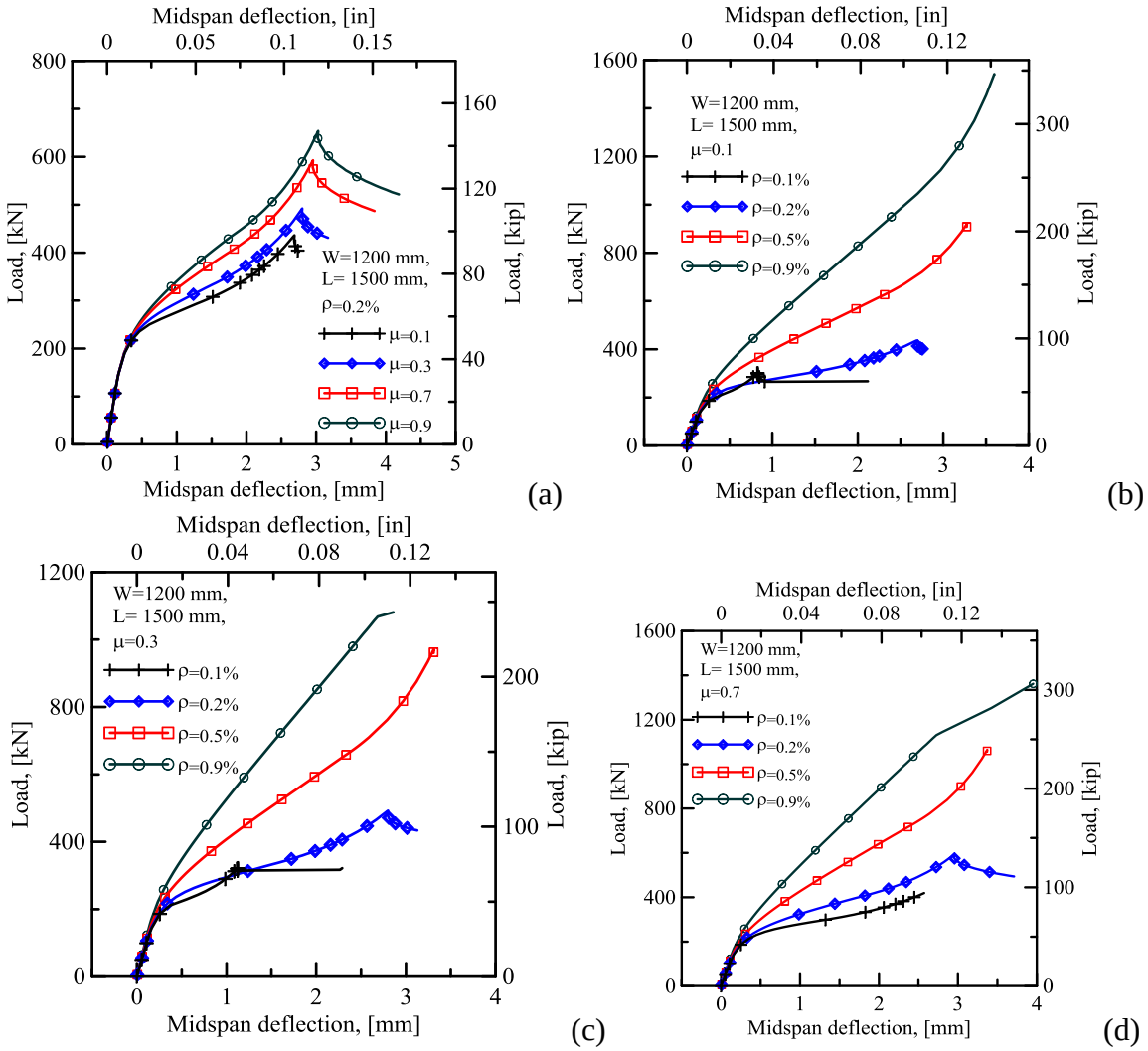

Figure 146. Effect of fiber and reinforcement ratio on narrow-short samples.

4.5.2 Effect of Fiber Content and Reinforcement on the Wide Samples (W=1500 mm)

Long samples (L=2500 mm):

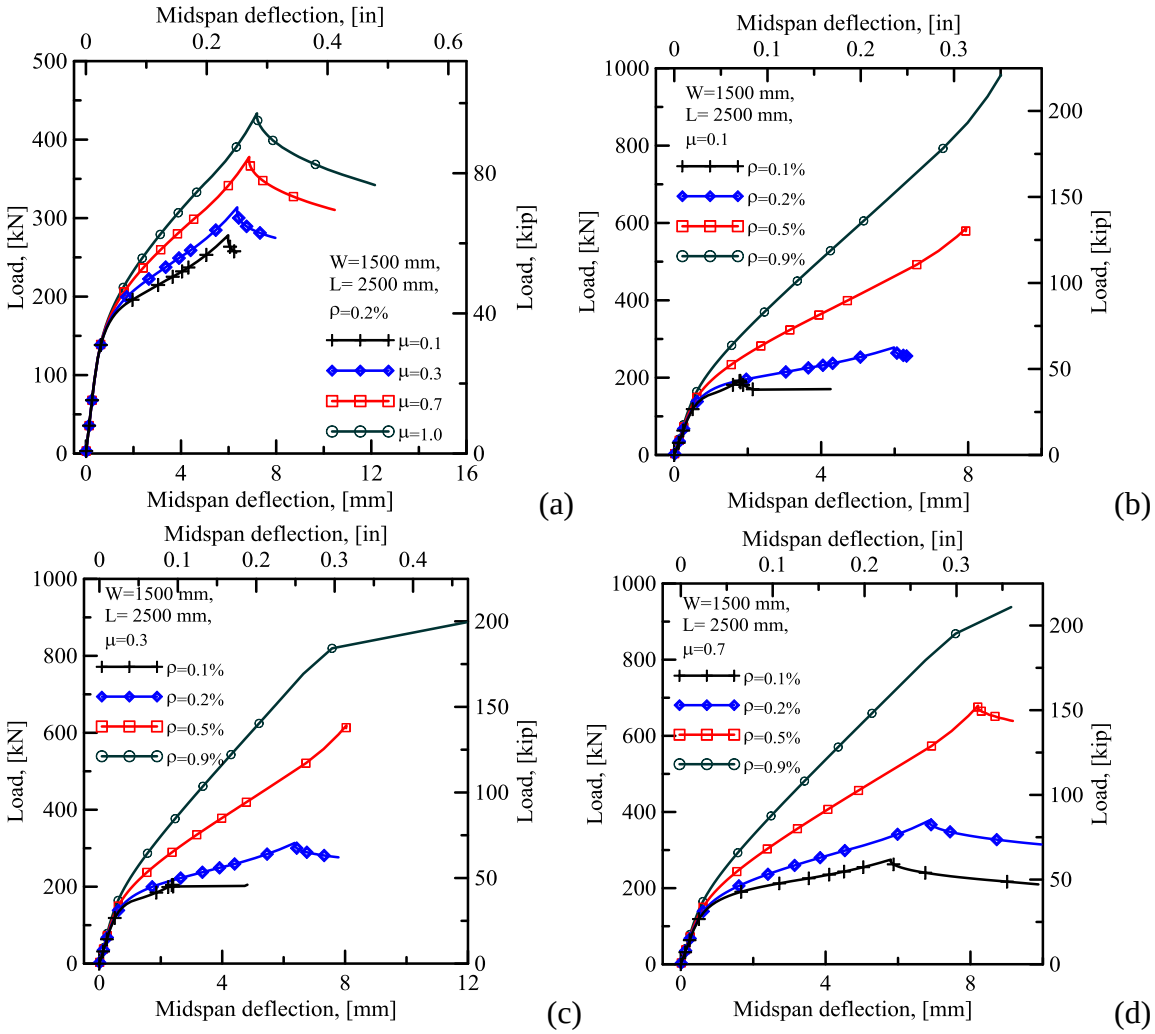

Figure 147. Effect of fiber and reinforcement ratio on wide-long samples.

Short samples (L=1500 mm):

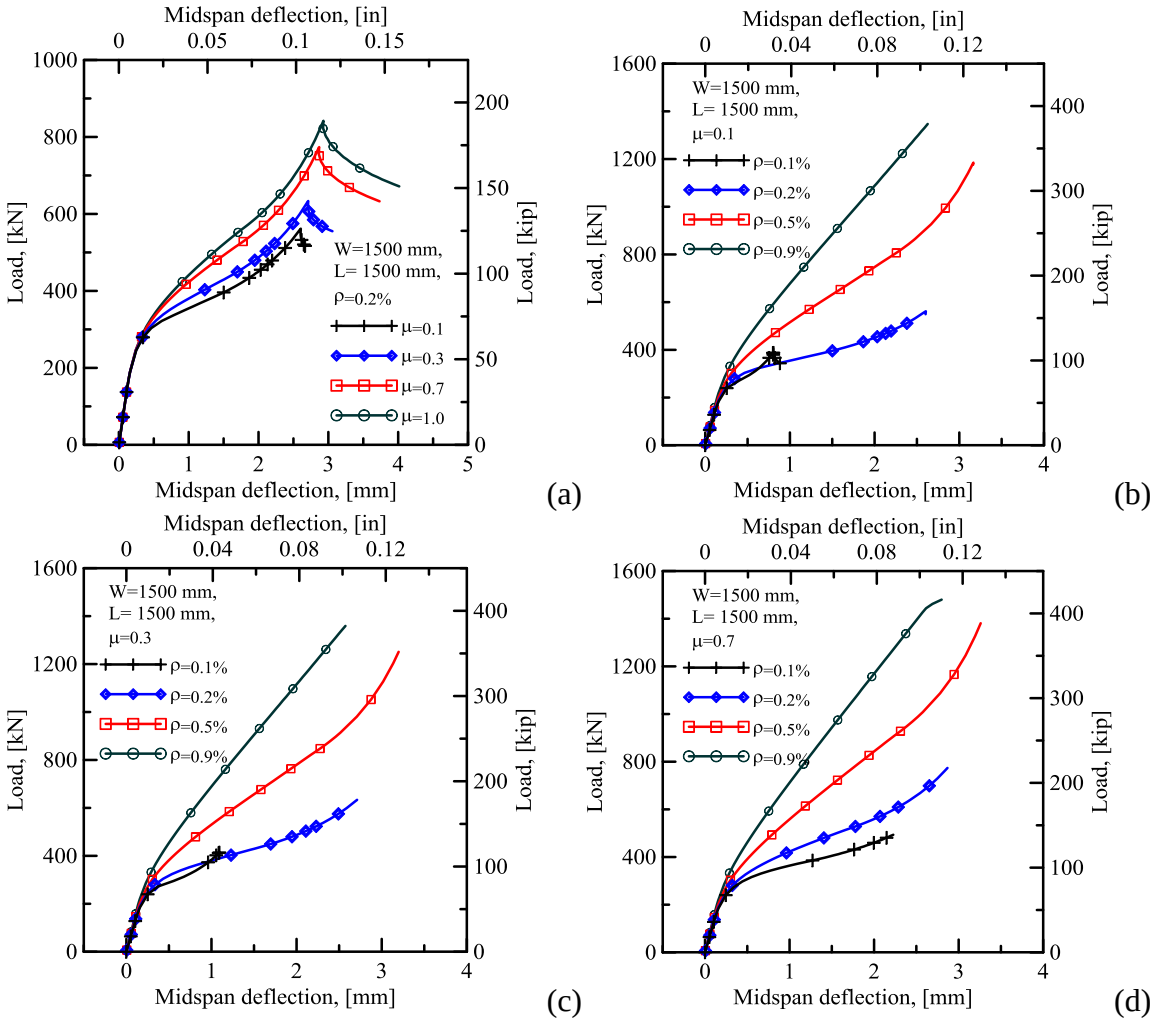

Figure 148. Effect of fiber and reinforcement ratio on wide-long samples.

REFERENCES

[1] K. Sobolev and S. P. Shah, *Nanotechnology in Construction: Proceedings of NICOM5*. Springer, 2015.

[2] F. F. Wafa, "Properties & applications of fiber reinforced concrete," *Eng. Sci.*, vol. 2, no. 1, 1990.

[3] C. Soranakom and B. Mobasher, "Flexural Design of Fiber-Reinforced Concrete," *Mater. J.*, vol. 106, no. 5, pp. 461–469, Sep. 2009.

[4] M. Code, "Fib model code for concrete structures 2010," *Doc. Competence Cent. Siegmar Kästl EK Ger.*, 2010.

[5] M. di Prisco, P. Martinelli, and B. Parmentier, "On the reliability of the design approach for FRC structures according to fib Model Code 2010: the case of elevated slabs," *Struct. Concr.*, vol. 17, no. 4, pp. 588–602, Dec. 2016.

[6] A. C. ACI 544.4R-18, "Guide to Design with Fiber-Reinforced Concrete: reported by ACI Committee 544. ACI 544.4 R-18," 2018.

[7] C. Soranakom and B. Mobasher, "Closed-form solutions for flexural response of fiber-reinforced concrete beams," *J. Eng. Mech.*, vol. 133, pp. 933–941, 2007.

[8] C. Soranakom and B. Mobasher, "Correlation of tensile and flexural responses of strain softening and strain hardening cement composites," *Cem. Concr. Compos.*, vol. 30, pp. 465–477, 2008.

[9] S. Aaleti and S. Sritharan, "Design of Ultrahigh-Performance Concrete Waffle Deck for Accelerated Bridge Construction," *Transp. Res. Rec. J. Transp. Res. Board*, vol. 2406, pp. 12–22, Jul. 2014.

[10] FHWA, "ABC - Accelerated - Technologies and Innovations - Construction - Federal Highway Administration," 2016. [Online]. Available: https://www.fhwa.dot.gov/bridge/abc/. [Accessed: 01-Nov-2016].

[11] "Publication FHWA-HRT-18-036 HRDI-40/3-18(WEB)EHIF - Google Search." [Online]. Available: https://www.google.com/search?q=Publication+FHWA-HRT-18-036+HRDI-40%2F3-18(WEB)EHIF&oq=Publication+FHWA-HRT-18-036+HRDI-40%2F3-18(WEB)EHIF&aqs=chrome..69i57.559j0j8&sourceid=chrome&ie=UTF-8. [Accessed: 25-Apr-2018].

[12] A. Meda, G. A. Plizzari, and P. Riva, "Fracture behavior of SFRC slabs on grade," *Mater. Struct.*, vol. 37, no. 6, pp. 405–411, Jul. 2004.

[13] S. Abbas, M. L. Nehdi, and M. A. Saleem, "Ultra-high performance concrete: Mechanical performance, durability, sustainability and implementation challenges," *Int. J. Concr. Struct. Mater.*, vol. 10, no. 3, pp. 271–295, 2016.

[14] K. Wille, A. E. Naaman, and S. El-Tawil, "Optimizing ultra-high performance fiber-reinforced concrete," *Concr. Int.*, vol. 33, no. 9, pp. 35–41, 2011.

[15] Y. Yao, M. Barzin, S. Rajan, N. Neithalath, and Arizona State University, "Application of 2-D Digital Image Correlation (DIC) method to Damage Characterization of Cementitious Composites under Dynamic Tensile Loads," in *ASU Electronic Theses and Dissertations*, Arizona State University, 2013.

[16] D. R. Sahoo and A. Sharma, "Effect of steel fiber content on behavior of concrete beams with and without stirrups," *ACI Struct. J.*, vol. 111, p. 1157, 2014.

[17] A. E. Naaman, "Setting the Stage, Toward Performance Based Classification of FRC Composites," in *High Performance Fiber Reinforced Cement Composites (HPFRCC 4), Proc. of the 4th Int. RILEM Workshop, 2003*, 2003.

[18] J. G. Van Mier, *Fracture processes of concrete*. CRC press, 2017.

[19] M. Bakhshi, B. Laungrungrong, A. Bonakdar, and B. Mobasher, "Economical Concrete Mix Design Utilizing Blended Cements, Performance-Based Specifications, and Pay Factors," Arizona Department of Transportation, ADOT AZ633, 2013.

[20] A. Bentur and S. Mindess, *Fiber Reinforced Cementitious Composites, London and New York*. Elsevier Applied Science, 1990.

[21] B. Mobasher and C. Y. Li, "Mechanical properties of hybrid cement-based composites," *ACI Mater. J.*, vol. 93, pp. 284–292, 1996.

[22] B. Mobasher, *Mechanics of fiber and textile reinforced cement composites*. CRC press, 2011.

[23] A. E. Naaman and H. W. Reinhardt, "Proposed classification of HPFRC composites based on their tensile response," *Mater. Struct.*, vol. 39, no. 5, pp. 547–555, Jun. 2006.

[24] P. Tjiptobroto and W. Hansen, "Tensile strain hardening and multiple cracking in high-performance cement-based composites containing discontinuous fibers," *Mater. J.*, vol. 90, no. 1, pp. 16–25, 1993.

[25] I. H. Yang, C. Joh, and B.-S. Kim, "Structural behavior of ultra high performance concrete beams subjected to bending," *Eng. Struct.*, vol. 32, no. 11, pp. 3478–3487, Nov. 2010.

[26] J. Yang and J. Ye, “Interfacial stresses in plated beams with cracks,” *Compos. Struct.*, vol. 57, pp. 125–134, 2002.

[27] B. Mobasher and C. Y. Li, “Modeling of stiffness degradation of the interfacial zone during fiber debonding,” *Compos. Eng.*, vol. 5, no. 10–11, pp. 1349–1365, 1995.

[28] C. Ouyang, A. Pacios, and S. P. Shah, “Pullout of inclined fibers from cementitious matrix,” *J. Eng. Mech.*, vol. 120, no. 12, pp. 2641–2659, 1994.

[29] G. Gao, S. Huang, K. Xia, and Z. Li, “Application of Digital Image Correlation (DIC) in Dynamic Notched Semi-Circular Bend (NSCB) Tests,” *Exp. Mech.*, vol. 55, no. 1, pp. 95–104, Jan. 2015.

[30] S. D. Rajan, B. Mobasher, S. Sankaran, D. Naik, and Z. Stahlecker, “Explicit finite element modeling of multilayer composite fabric for gas turbine engine containment systems, Phase III, Part 1: Arizona State University material model and numerical simulations,” *FAA Rep DOTFAAAR-1024 Fed. Aviat. Adm. FAA Wash. DC*, 2010.

[31] D. Zhu, B. Mobasher, and S. D. Rajan, “Dynamic tensile testing of Kevlar 49 fabrics,” *J. Mater. Civ. Eng.*, vol. 23, no. 3, pp. 230–239, 2010.

[32] X. Wang, X. Liu, H. Zhu, and S. Ma, “Spatial-temporal subset based digital image correlation considering the temporal continuity of deformation,” *Opt. Lasers Eng.*, vol. 90, pp. 247–253, Mar. 2017.

[33] H. Z. Xing, Q. B. Zhang, C. H. Braithwaite, B. Pan, and J. Zhao, “High-Speed Photography and Digital Optical Measurement Techniques for Geomaterials: Fundamentals and Applications,” *Rock Mech. Rock Eng.*, vol. 50, no. 6, pp. 1611–1659, Jun. 2017.

[34] S. Das, M. Aguayo, G. Sant, B. Mobasher, and N. Neithalath, “Fracture process zone and tensile behavior of blended binders containing limestone powder,” *Cem. Concr. Res.*, vol. 73, pp. 51–62, 2015.

[35] S. Das *et al.*, “The fracture response of blended formulations containing limestone powder: evaluations using two-parameter fracture model and digital image correlation,” *Cem. Concr. Compos.*, vol. 53, pp. 316–326, 2014.

[36] “Correlated Solutions – VIC-2D™.”.

[37] J. D. Ríos, H. Cifuentes, R. C. Yu, and G. Ruiz, “Probabilistic Flexural Fatigue in Plain and Fiber-Reinforced Concrete,” *Materials*, vol. 10, no. 7, p. 767, 2017.

[38] B. A. Graybeal and J. L. Hartmann, “Strength and durability of ultra-high performance concrete,” in *Concrete Bridge Conference, Portland Cement Association*, 2003.

[39] M. Behloul, G. Chanvillard, P. Pimienta, A. Pineaud, and P. Rivillon, “Fatigue flexural behavior of pre-cracked specimens of special UHPFRC,” *Spec. Publ.*, vol. 228, pp. 1253–1268, 2005.

[40] Y. Yao, X. Wang, K. Aswani, and B. Mobasher, “Analytical procedures for design of strain softening and hardening cement composites,” *Int. J. Adv. Eng. Sci. Appl. Math.*, vol. 9, no. 3, pp. 181–194, 2017.

[41] A. Meda, F. Minelli, and G. A. Plizzari, “Flexural behaviour of RC beams in fibre reinforced concrete,” *Compos. Part B Eng.*, vol. 43, no. 8, pp. 2930–2937, 2012.

[42] B. Singh and K. Jain, “Appraisal of steel fibers as minimum shear reinforcement in concrete beams,” *ACI Struct. J.*, vol. 111, no. 5, p. 1191, 2014.

[43] H. H. Dinh, G. J. Parra-Montesinos, and J. K. Wight, “Shear strength model for steel fiber reinforced concrete beams without stirrup reinforcement,” *J. Struct. Eng.*, vol. 137, no. 10, pp. 1039–1051, 2010.

[44] G. Batson, “Steel fiber reinforced concrete,” *Mater. Sci. Eng.*, vol. 25, pp. 53–58, 1976.

[45] L. Vandewalle, “Influence of Tensile Strength of Steel Fibre on the Toughness of High Strength Concrete,” in *Third International Workshop" High Performance Fiber Reinforced Cement Composites"*, 1999, pp. 331–340.

[46] P. Balaguru, R. Narahari, and M. Patel, “Flexural toughness of steel fiber reinforced concrete,” *Mater. J.*, vol. 89, no. 6, pp. 541–546, 1992.

[47] S.-C. Lee, J.-Y. Cho, and F. J. Vecchio, “Diverse embedment model for steel fiber-reinforced concrete in tension: model development,” *Mater. J.*, vol. 108, no. 5, pp. 516–525, 2011.

[48] M. di Prisco, G. Plizzari, and L. Vandewalle, “Fibre reinforced concrete: new design perspectives,” *Mater. Struct.*, vol. 42, no. 9, pp. 1261–1281, Sep. 2009.

[49] L. Vandewalle, “RILEM TC162-TDF : Test and Design methods for Steel Fibre Reinforced Concrete : Bending test (final recommendation),” *Mater. Struct.*, vol. 35, pp. 579–582, Nov. 2002.

[50] J. A. O. Barros, V. M. C. F. Cunha, A. F. Ribeiro, and J. a. B. Antunes, “Post-cracking behaviour of steel fibre reinforced concrete,” *Mater. Struct.*, vol. 38, no. 1, pp. 47–56, Jan. 2005.

[51] F. Minelli, G. A. Plizzari, and F. J. Vecchio, “Influence of steel fibers on full-scale RC beams under shear loading,” in *High performance concrete, brick-masonry and environmental aspects. Sixth international conference of fracture mechanics of*

concrete and concrete structures FRAMCOS6. Taylor & Francis Group (UK), London/Catania, 2007, vol. 3, pp. 1523–1531.

[52] E. S. Bernard, "Durability of cracked fibre reinforced shotcrete," *Shotcrete More Eng. Dev. Taylor Francis Lond. ES Bernard Ed*, pp. 59–66, 2004.

[53] Y. Yao, M. Bakhshi, V. Nasri, and B. Mobasher, "Interaction diagrams for design of hybrid fiber-reinforced tunnel segments," *Mater. Struct.*, vol. 51, no. 1, p. 35, 2018.

[54] B. Mobasher, Y. Yao, and C. Soranakom, "Analytical solutions for flexural design of hybrid steel fiber reinforced concrete beams," *Eng. Struct.*, vol. 100, pp. 164–177, 2015.

[55] N. Gowripalan and R. I. Gilbert, "Design guidelines for RPC prestressed concrete beams," *Syd. Aust. Sch. Civ. Environ. Eng. Univ. New South Wales*, 2000.

[56] H. Almansour and Z. Lounis, "Innovative design approach of precast–prestressed girder bridges using ultra high performance concrete," *Can. J. Civ. Eng.*, vol. 37, no. 4, pp. 511–521, 2010.

[57] B. Graybeal, "Design and construction of field-cast UHPC connections," 2014.

[58] M. Taheri, J. A. O. Barros, and H. Salehian, "A design model for strain-softening and strain-hardening fiber reinforced elements reinforced longitudinally with steel and FRP bars," *Compos. Part B Eng.*, vol. 42, no. 6, pp. 1630–1640, Sep. 2011.

[59] T. Y. Lim, P. Paramisivam, and S. L. Lee, "Bending behavior of steel-fiber concrete beams," *Struct. J.*, vol. 84, no. 6, pp. 524–536, 1987.

[60] T.-S. Lok and J.-S. Pei, "Flexural behavior of steel fiber reinforced concrete," *J. Mater. Civ. Eng.*, vol. 10, no. 2, pp. 86–97, 1998.

[61] ACI Committee 239, "ACI Committee 239, 'Committee in Ultra-High Performance Concrete,.'"

[62] X. Destrée, Y. Yao, and B. Mobasher, "Sequential Cracking and Their Openings in Steel-Fiber-Reinforced Joint-Free Concrete Slabs," *J. Mater. Civ. Eng.*, vol. 28, no. 4, 2015.

[63] T.-Y. Lim, P. Paramasivam, and S.-L. Lee, "Behavior of reinforced steel-fiber-concrete beams in flexure," *J. Struct. Eng.*, vol. 113, no. 12, pp. 2439–2458, 1987.

[64] ACI 544, "544.7R-16 Report on Design and Construction of Fiber-Reinforced Precast Concrete Tunnel Segments," ACI Committee 544, 2016.

[65] A. C. I. Committee 544, *ACI 544. 8R-16 Report on Indirect Method to Obtain Stress-Strain Response of Fiber-Reinforced Concrete (FRC)*. American Concrete Institute, 2016.

[66] ACI Committee 318 and American Concrete Institute, *Building code requirements for structural concrete (ACI 318-14): an ACI standard : commentary on building code requirements for structural concrete (ACI 318R-14), an ACI report*. 2014.

[67] K. S. R. Iyengar, S. Raviraj, and T. N. Jayaram, "Analysis of crack propagation in strain-softening beams," *Eng. Fract. Mech.*, vol. 69, no. 6, pp. 761–778, 2002.

[68] W. Meng, Y. Yao, B. Mobasher, and H. K. Khayat, "Effects of Loading Rate and Notch-to-Depth Ratio of Notched Beams on Flexural Performance of Ultra-High-Performance Concrete (Under review)," *Cem. Concr. Compos.*, 2017.

[69] J. C. I. Standard, "Method of test for fracture energy of concrete by use of notched beam," JCI-S-001-2003. Japan Concrete Institute (JCI), 2003.

[70] X. X. Zhang, A. M. Abd Elazim, G. Ruiz, and R. C. Yu, "Fracture behaviour of steel fibre-reinforced concrete at a wide range of loading rates," *Int. J. Impact Eng.*, vol. 71, pp. 89–96, Sep. 2014.

[71] S. Pyo, K. Wille, S. El-Tawil, and A. E. Naaman, "Strain rate dependent properties of ultra high performance fiber reinforced concrete (UHP-FRC) under tension," *Cem. Concr. Compos.*, vol. 56, pp. 15–24, Feb. 2015.

[72] M. Bakhshi, C. Barsby, and B. Mobasher, "Comparative evaluation of early age toughness parameters in fiber reinforced concrete," *Mater. Struct.*, vol. 47, no. 5, pp. 853–872, May 2014.

[73] M. M. Kamal, M. A. Safan, Z. A. Etman, and R. A. Salama, "Behavior and strength of beams cast with ultra high strength concrete containing different types of fibers," *HBRC J.*, vol. 10, no. 1, pp. 55–63, 2014.

[74] Kaka Venkatesh Babu and Chao Shih-Ho, "Investigation of Eliminating Prestress in Bridge Girders with the Use of Non-Prestressed Ultra-High-Performance Fiber-Reinforced Concrete Girders," *Struct. Congr. 2018*.

[75] J. Qi, J. Wang, and Z. J. Ma, "Flexural response of high-strength steel-ultra-high-performance fiber reinforced concrete beams based on a mesoscale constitutive model: Experiment and theory," *Struct. Concr.*, vol. 19, no. 3, pp. 719–734, 2018.

[76] F. Vic Perry *et al.*, "Innovative Field Cast UHPC Joints for Precast Bridge Systems–3-span Live Load Continuous," 2010.

[77] B. A. Graybeal, "Fabrication of an optimized UHPC bridge," in *PCI National Bridge Conference, Atlanta, GA, USA*, 2004.

[78] D. Bierwagen, B. Moore, and V. Perry, “Revolutionary Concrete Solutions,” *Constr. Specif.*, 2006.

[79] Zachary B. Haber, Igor De la Varga, B. A. Graybeal, B. Nakashoji, and R. El-Helou, “Properties and Behavior of UHPC-Class Materials.” Mar-2018.

[80] S. Rallabhandhi, *Evaluation of ultra high performance concrete in joints of bridge girders*. Missouri University of Science and Technology, 2016.

[81] L. Li, Z. Ma, M. E. Griffey, and R. G. Oesterle, “Improved longitudinal joint details in decked bulb tees for accelerated bridge construction: Concept development,” *J. Bridge Eng.*, vol. 15, no. 3, pp. 327–336, 2009.

[82] C. Soranakom and B. Mobasher, “Closed-Form Solutions for Flexural Response of Fiber-Reinforced Concrete Beams,” *J. Eng. Mech.*, vol. 133, no. 8, pp. 933–941, 2007.

[83] Z. Haber and B. A. Graybeal, “Performance of Multiple UHPC-Class Materials in Prefabricated Bridge Deck Connections.”

[84] M. Arduini and A. Nanni, “Behavior of precracked RC beams strengthened with carbon FRP sheets,” *J. Compos. Constr.*, vol. 1, pp. 63–70, 1997.

[85] F. Kianmofrad, E. Ghafoori, M. M. Elyasi, M. Motavalli, and M. Rahimian, “Strengthening of metallic beams with different types of pre-stressed un-bonded retrofit systems,” *Compos. Struct.*, vol. 159, pp. 81–95, 2017.

[86] A. F. Ashour, S. A. El-Refaie, and S. W. Garrity, “Flexural strengthening of RC continuous beams using CFRP laminates,” *Cem. Concr. Compos.*, vol. 26, pp. 765–775, 2004.

[87] F. I. Du Béton, “Externally bonded FRP reinforcement for RC structures,” *Bulletin*, vol. 14, p. 138, 2001.

[88] F. Jesse, N. Will, M. Curbach, and J. Hegger, “Load-bearing behavior of textile-reinforced concrete,” *Spec. Publ.*, vol. 250, pp. 59–68, 2008.

[89] J. Hegger, N. Will, O. Bruckermann, and S. Voss, “Load–bearing behaviour and simulation of textile reinforced concrete,” *Mater. Struct.*, vol. 39, no. 8, pp. 765–776, 2006.

[90] A. Brückner, R. Ortlepp, and M. Curbach, “Textile reinforced concrete for strengthening in bending and shear,” *Mater. Struct.*, vol. 39, no. 8, pp. 741–748, 2006.

[91] A. D’Ambrisi and F. Focacci, “Flexural strengthening of RC beams with cement-based composites,” *J. Compos. Constr.*, vol. 15, no. 5, pp. 707–720, 2011.

[92] T. C. Triantafillou, C. G. Papanicolaou, P. Zissimopoulos, and T. Laourdekis, "Concrete confinement with textile-reinforced mortar jackets," *ACI Mater. J.*, vol. 103, no. 1, p. 28, 2006.

[93] Y. A. Al-Salloum, N. A. Siddiqui, H. M. Elsanadedy, A. A. Abadel, and M. A. Aqel, "Textile-reinforced mortar versus FRP as strengthening material for seismically deficient RC beam-column joints," *J. Compos. Constr.*, vol. 15, no. 6, pp. 920–933, 2011.

[94] C. G. Papanicolaou, T. C. Triantafillou, K. Karlos, and M. Papathanasiou, "Textile-reinforced mortar (TRM) versus FRP as strengthening material of URM walls: in-plane cyclic loading," *Mater. Struct.*, vol. 40, no. 10, pp. 1081–1097, 2007.

[95] S. Weiland, R. Ortlepp, B. Hauptenbuchner, and M. Curbach, "Textile Reinforced Concrete for Flexural Strengthening of RC-Structures-Part 2: Application on a Concrete Shell," *Spec. Publ.*, vol. 251, pp. 41–58, 2008.

[96] S. Yin, S. Xu, and H. Lv, "Flexural behavior of reinforced concrete beams with TRC tension zone cover," *J. Mater. Civ. Eng.*, vol. 26, no. 2, pp. 320–330, 2013.

[97] A. Peled, "Confinement of damaged and nondamaged structural concrete with FRP and TRC sleeves," *J. Compos. Constr.*, vol. 11, no. 5, pp. 514–522, 2007.

[98] M. Di Ludovico, A. Prota, and G. Manfredi, "Structural upgrade using basalt fibers for concrete confinement," *J. Compos. Constr.*, vol. 14, no. 5, pp. 541–552, 2010.

[99] L. Li, Y. Guo, and F. Liu, "Test analysis for FRC beams strengthened with externally bonded FRP sheets," *Constr. Build. Mater.*, vol. 22, no. 3, pp. 315–323, 2008.

[100] K. S. Elliott, *Precast concrete structures*. Crc Press, 2016.

[101] C. J. Hung, J. Monsees, N. Munfah, and J. Wisniewski, "Technical manual for design and construction of road tunnels–civil elements," *US Dep. Transp. Fed. Highw. Adm. Natl. Highw. Inst. N. Y.*, 2009.

[102] O. Arnau and C. Molins, "Experimental and analytical study of the structural response of segmental tunnel linings based on an in situ loading test. Part 2: Numerical simulation," *Tunn. Undergr. Space Technol.*, vol. 26, no. 6, pp. 778–788, 2011.

[103] R. G. A. de Waal, "Steel fibre reinforced tunnel segments-for the application in shield driven tunnel linings," PhD Thesis, TU Delft, Delft University of Technology, 2000.

[104] Y. W. Cheong, H. P. Kwan, and A. D. Hariyanto, “QUALITY CONTROL IN PRECAST PRODUCTION A case study on Tunnel Segment Manufacture,” *DIMENSI J. Archit. Built Environ.*, vol. 33, no. 2, 2005.

[105] A. J. Howard, “REPORT ON THE DAMAGING EFFECTS OF WATER ON TUNNELS DURNG THEIR WORKING LIFE,” *Tunn. Undergr. Space Technol.*, vol. 6, no. 1, pp. 11–76, 1991.

[106] K. Uji, Y. Matsuoka, and T. Maruya, “Formulation of an equation for surface chloride content of concrete due to permeation of chloride,” *Elsevier Appl. Sci.*, pp. 258–267, 1990.

[107] J. P. Broomfield, *Steel corrosion in concrete—Understanding, investigation and repair*. Taylor & Francis: London, UK, 2007.

[108] P. S. Mangat and K. Gurusamy, “Long-term properties of steel fibre reinforced marine concrete,” *Mater. Struct.*, vol. 20, no. 4, p. 273, 1987.

[109] C. Tognazzi, J. P. Ollivier, M. Carcasses, and J. M. Torrenti, “Couplage fissuration-dégradation chimique des matériaux cimentaires: premiers résultats sur les propriétés de transfert,” *Ouvrage Géomatériaux Interact.-Modélisations Multi-Echelles Hermes Fr.*, pp. 69–84, 1998.

[110] G. A. Plizzari and G. Tiberti, “Steel fibers as reinforcement for precast tunnel segments,” *Tunn. Undergr. Space Technol.*, vol. 21, no. 3, pp. 438–439, 2006.

[111] A. Kooiman, C. Van der Veen, and M. Djorai, “Steel fibre reinforced concrete (SFRC) tunnel segments suitable for application in the Second Heinenoord Tunnel,” in *Proceedings of the 8th Congress on Challenges for Concrete in the Next Millennium*, 1998, pp. 719–722.

[112] M. R. King and A. J. Alder, “The practical specification of steel fibre reinforced concrete (SFRC) for tunnel linings,” in *Proceedings of Underground Construction 2001 Conference*, 2001.

[113] E. Woods, R. May, J. Hurt, and P. Watson, “Design of bored tunnels on Channel Tunnel rail link, UK,” in *Rapid excavation and tunneling conference proceedings*, 2003, pp. 230–244.

[114] B. A. Graybeal, “Material property characterization of ultra-high performance concrete,” 2006.

[115] “Meda and Rinaldi (AECOM) TESTS ON PRECAST TUNNEL SEGMENT - Google Search.” [Online]. Available: https://www.google.com/search?q=Meda+and+Rinaldi+(AECOM)+TESTS+ON+PRECAST+TUNNEL+SEGMENT&source=lnms&sa=X&ved=0ahUKEwjejsacq

KzdAhUKslQKHU9DCqoQ_AUICSgA&biw=1366&bih=631&dpr=1. [Accessed: 08-Sep-2018].

[116] A. Conforti, G. Tiberti, G. A. Plizzari, A. Caratelli, and A. Meda, “Precast tunnel segments reinforced by macro-synthetic fibers,” *Tunn. Undergr. Space Technol.*, vol. 63, pp. 1–11, 2017.

APPENDIX I

OPTICAL MICROGRAPHS OF CRACK PATTERNS IN FAILED SAMPLES

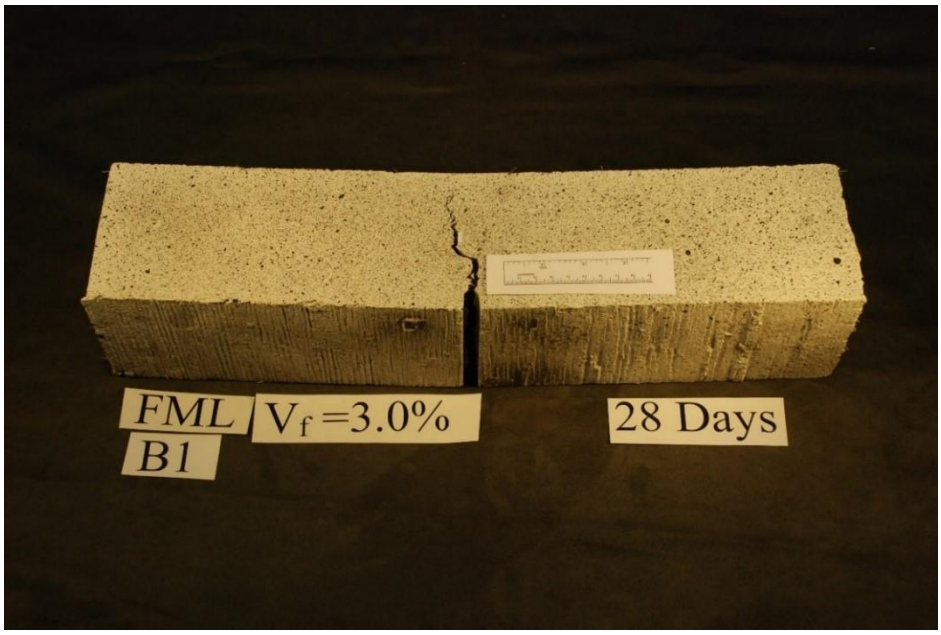

(a)

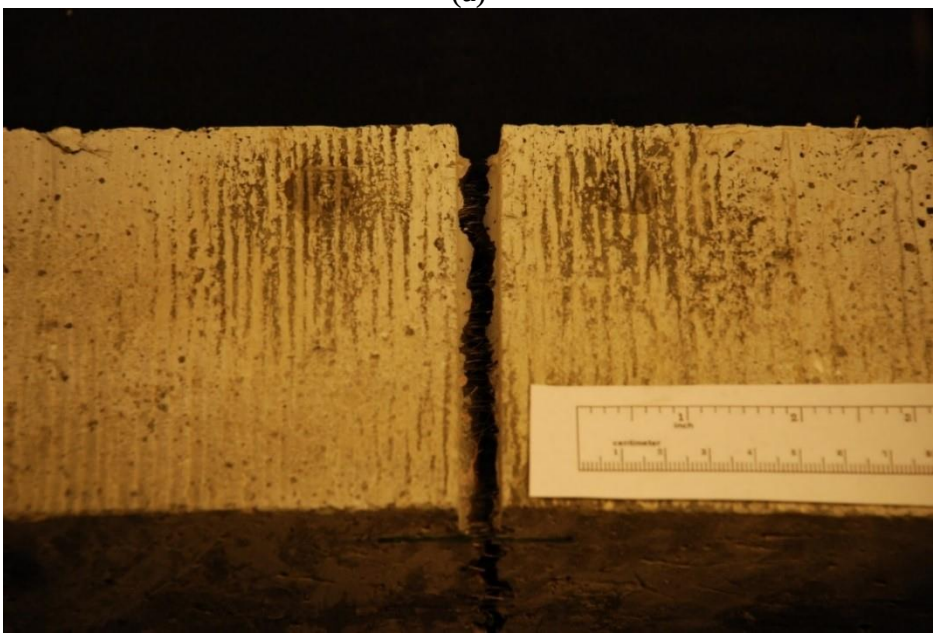

(b)

Figure A. 1. Large beams, 4” x 4” x 16” (102 mm x 102 mm x 406 mm), with 3% fiber content, after 28 days (FML_L_3_28_3PB_C_B1).

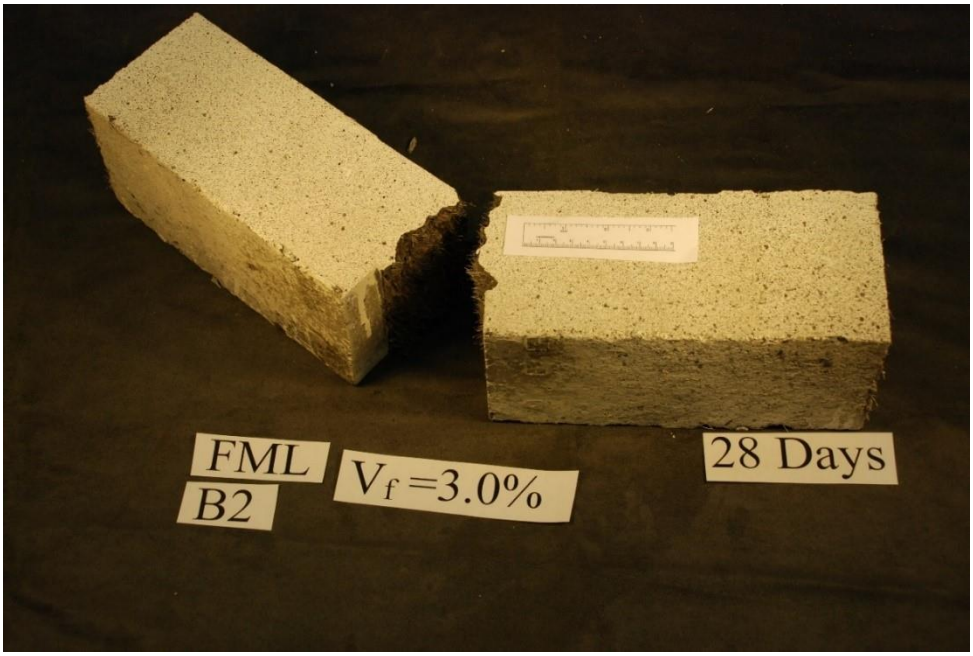

(a)

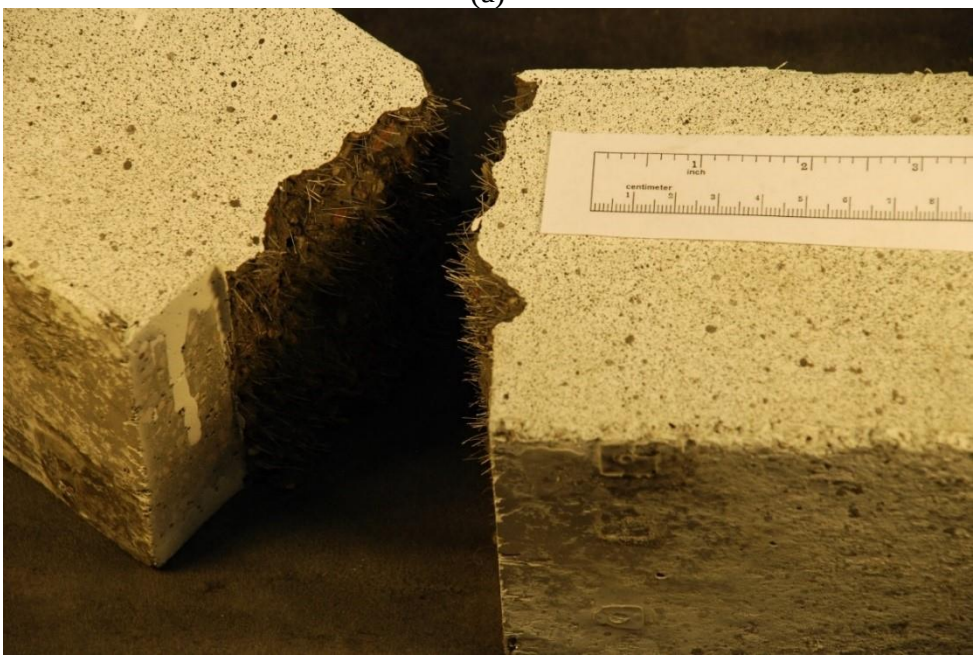

(b)

Figure A. 2. Large beams, 4” x 4” x 16” (102 mm x 102 mm x 406 mm), with 3% fiber content, after 28 days (FML_L_3_28_3PB_C_B2).

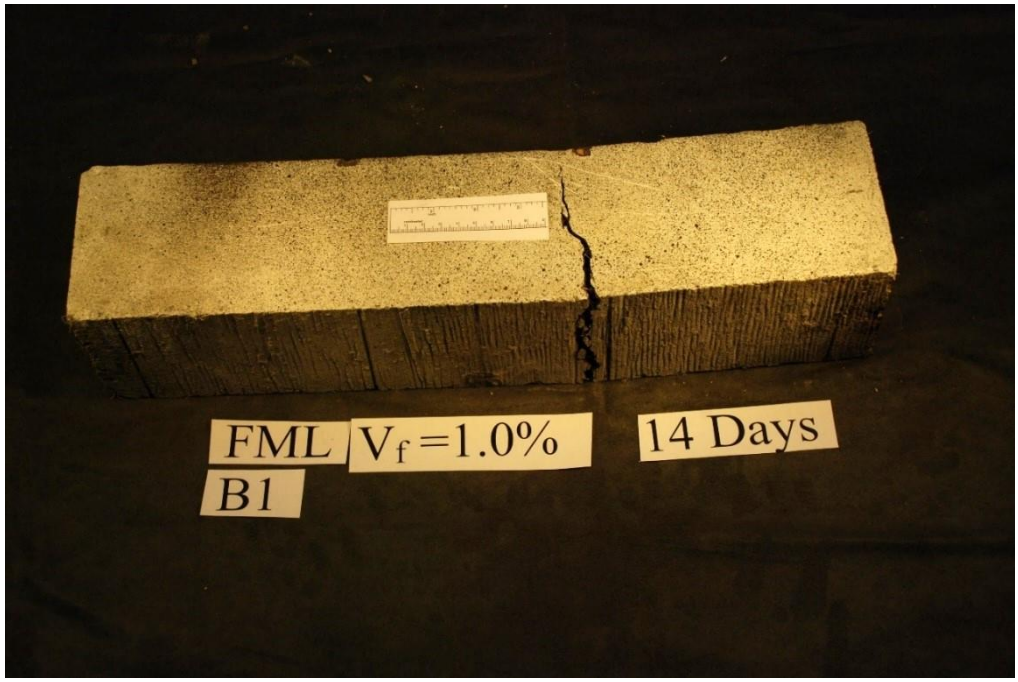

(a)

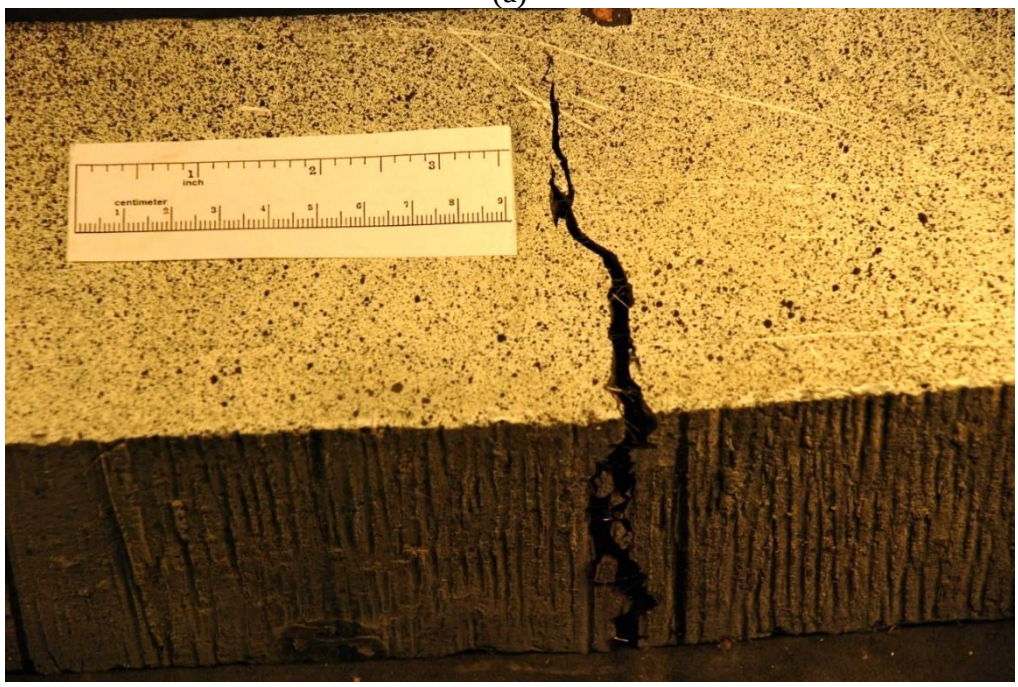

(b)

Figure A. 3. Large beams, 4” x 4” x 16” (102 mm x 102 mm x 406 mm), with 1% fiber content, after 14 days (FML_L_1_14_4PB_C_B1).

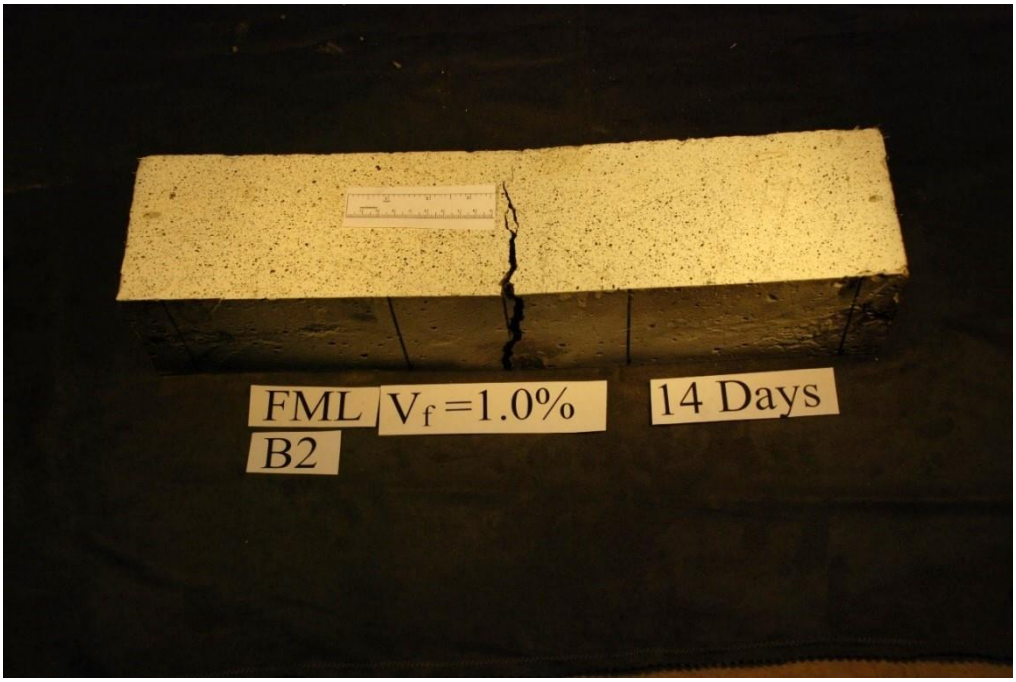

(a)

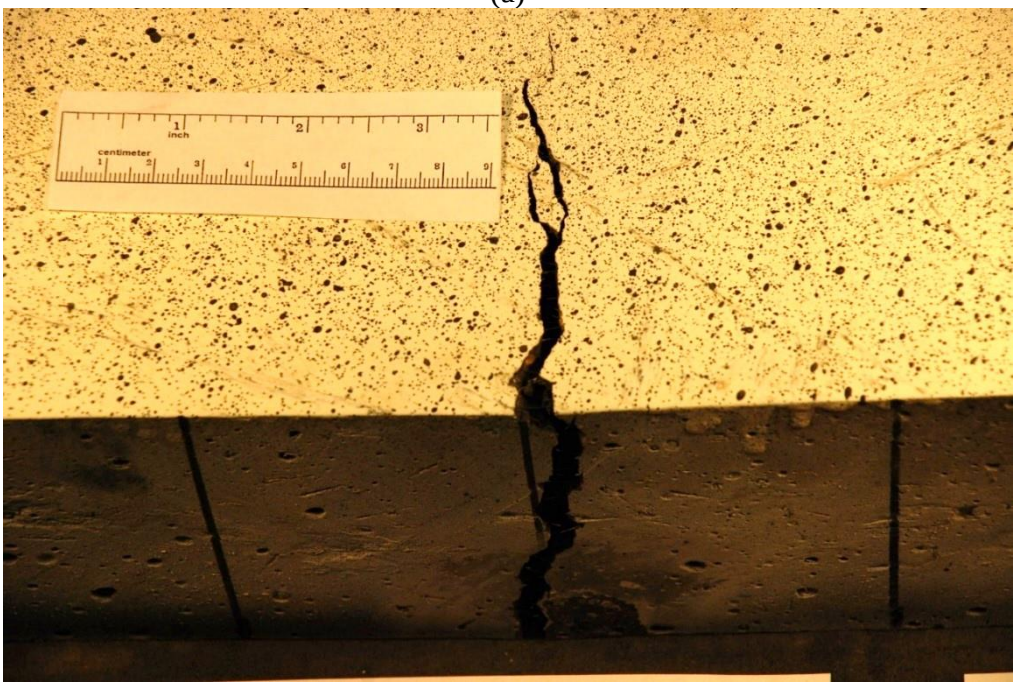

(b)

Figure A. 4. Large beams, 4” x 4” x 16” (102 mm x 102 mm x 406 mm), with 1% fiber content, after 14 days (FML_L_1_14_4PB_C_B2).

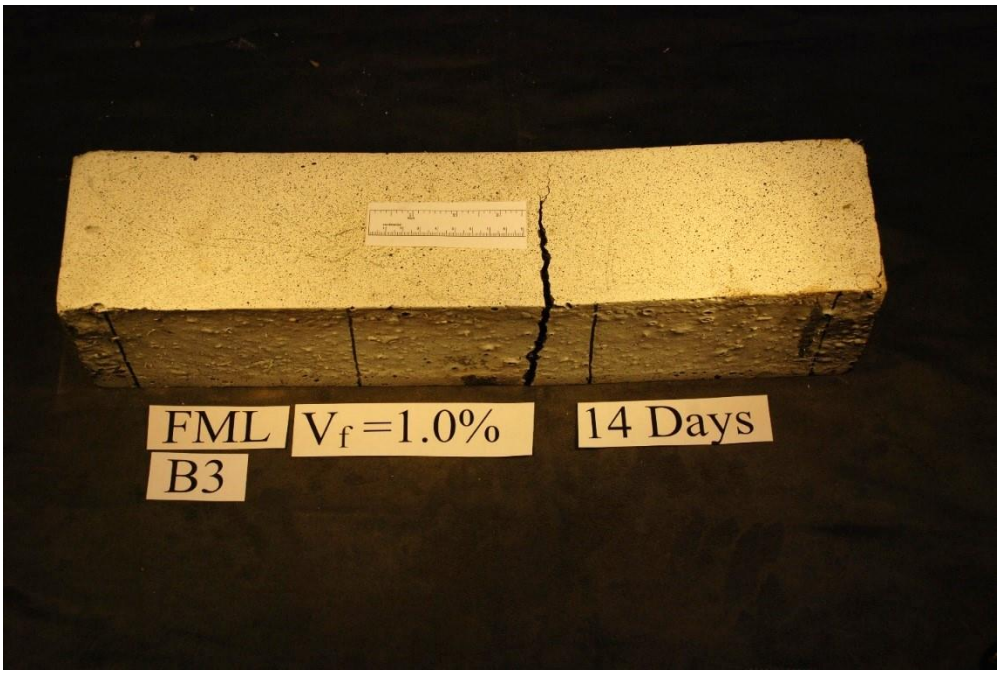

(a)

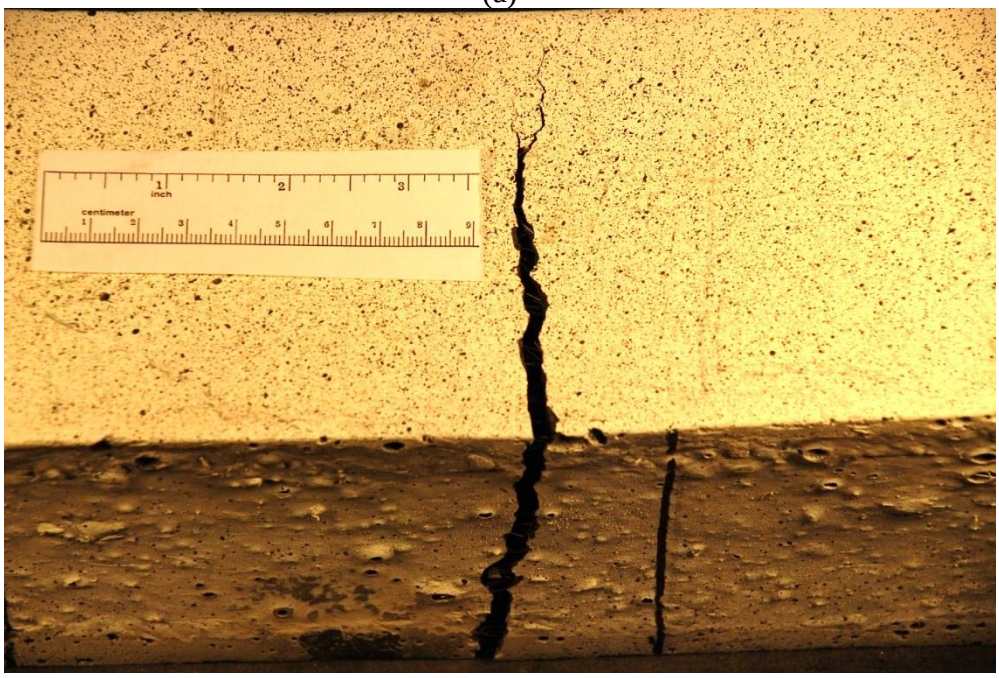

(b)

Figure A. 5. Large beams, 4” x 4” x 16” (102 mm x 102 mm x 406 mm), with 1% fiber content, after 14 days (FML_L_1_14_4PB_C_B3).

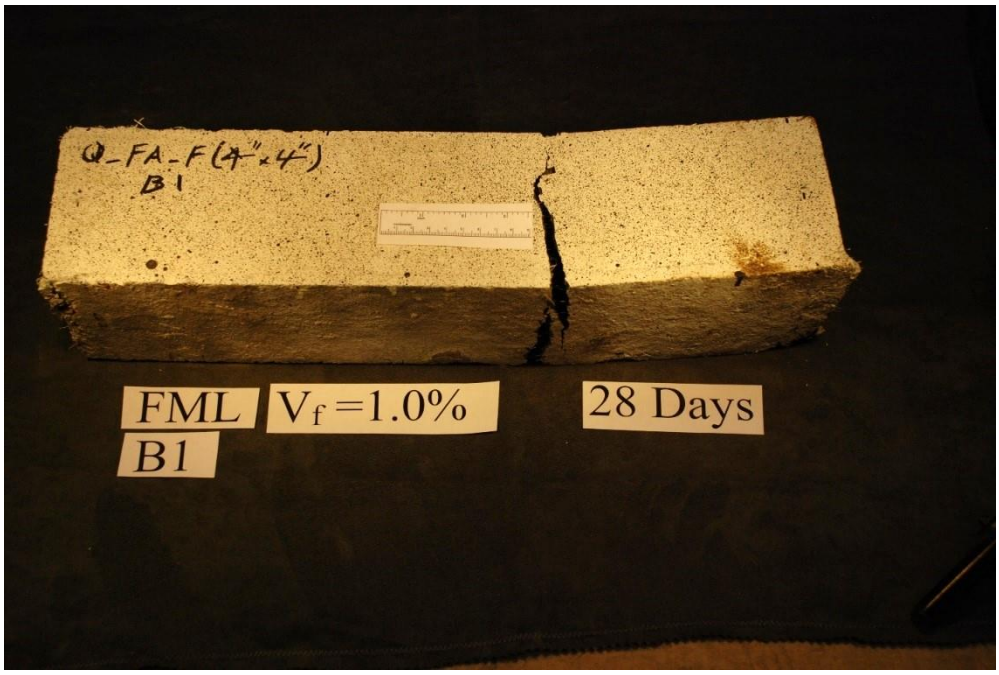

(a)

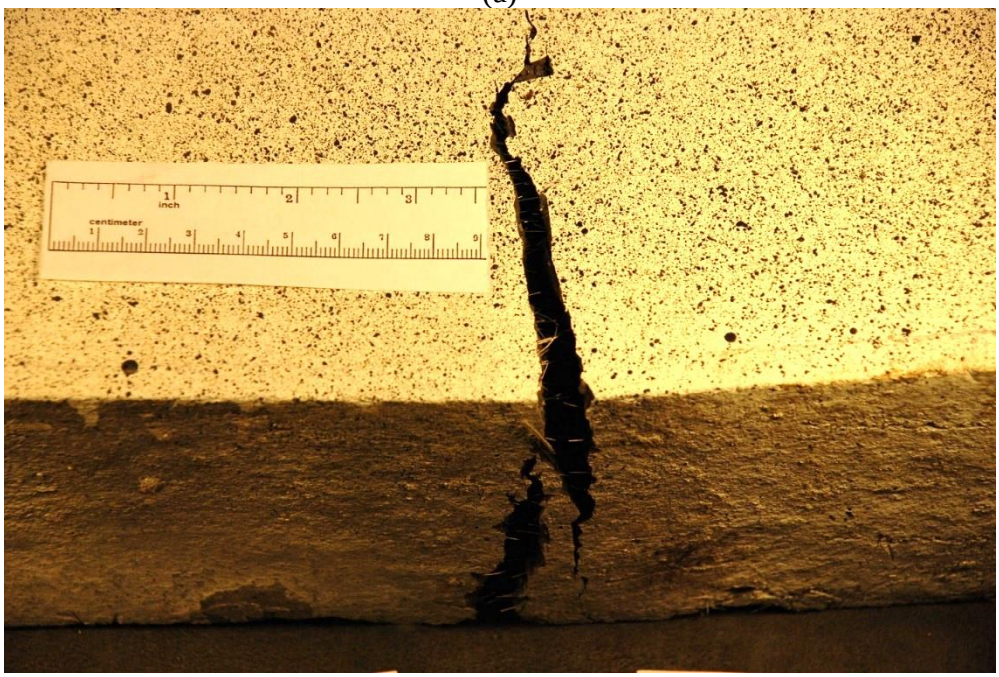

(b)

Figure A. 6. Large beams, 4” x 4” x 16” (102 mm x 102 mm x 406 mm), with 1% fiber content, after 28 days (FML_L_1_28_4PB_C_B1).

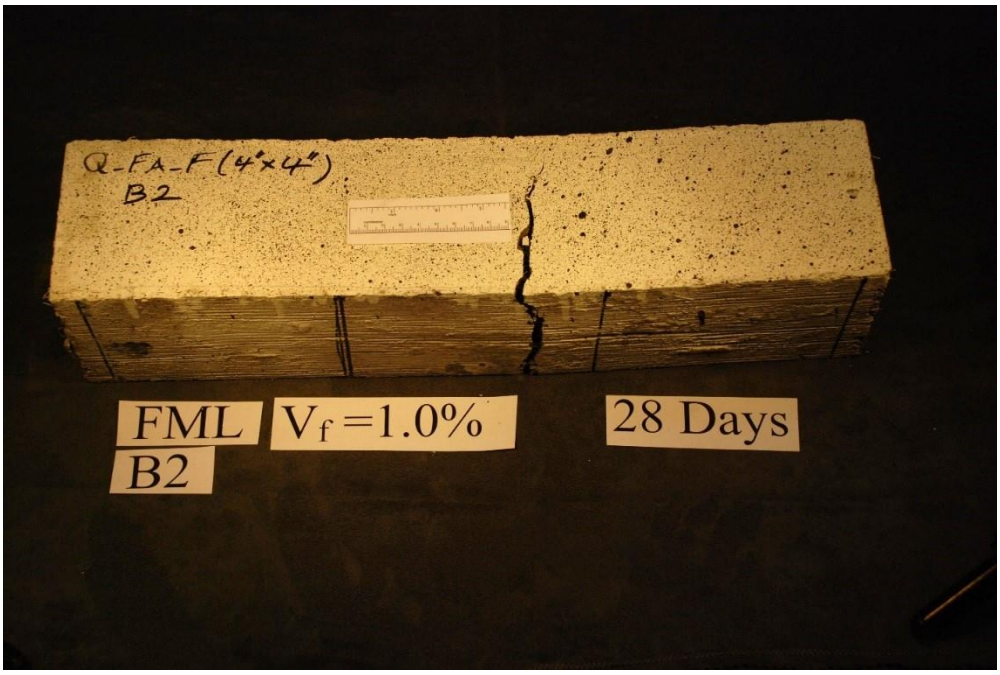

(a)

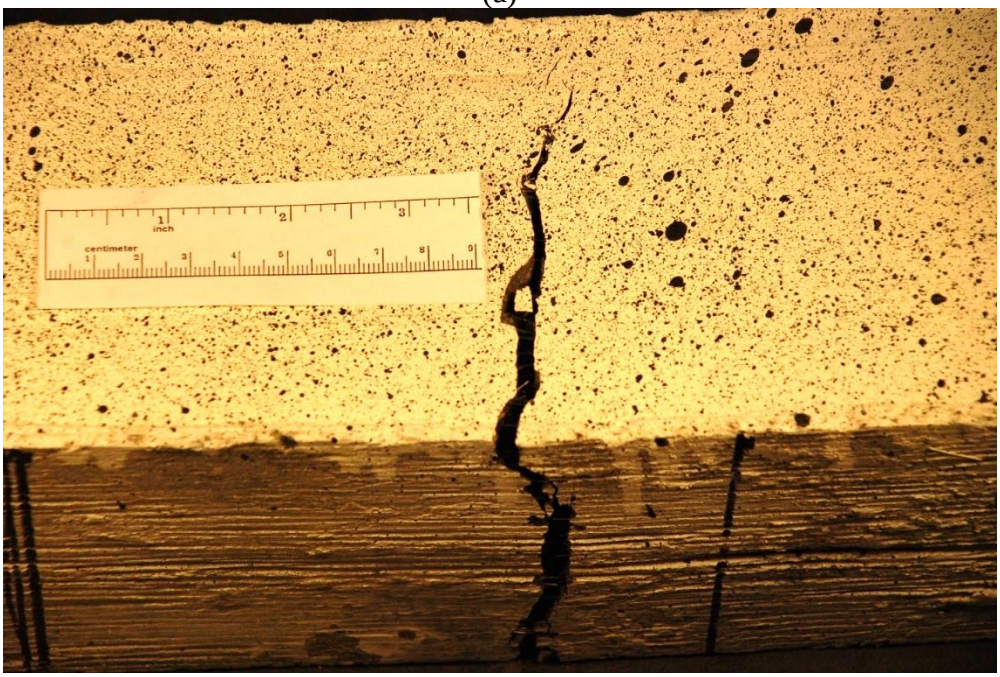

(b)

Figure A. 7. Large beams, 4” x 4” x 16” (102 mm x 102 mm x 406 mm), with 1% fiber content, after 28 days (FML_L_1_28_4PB_C_B2).


Q_FA_F(4"x4")
B3
FML
V_f =1.0%
28 Days
B3

(a)

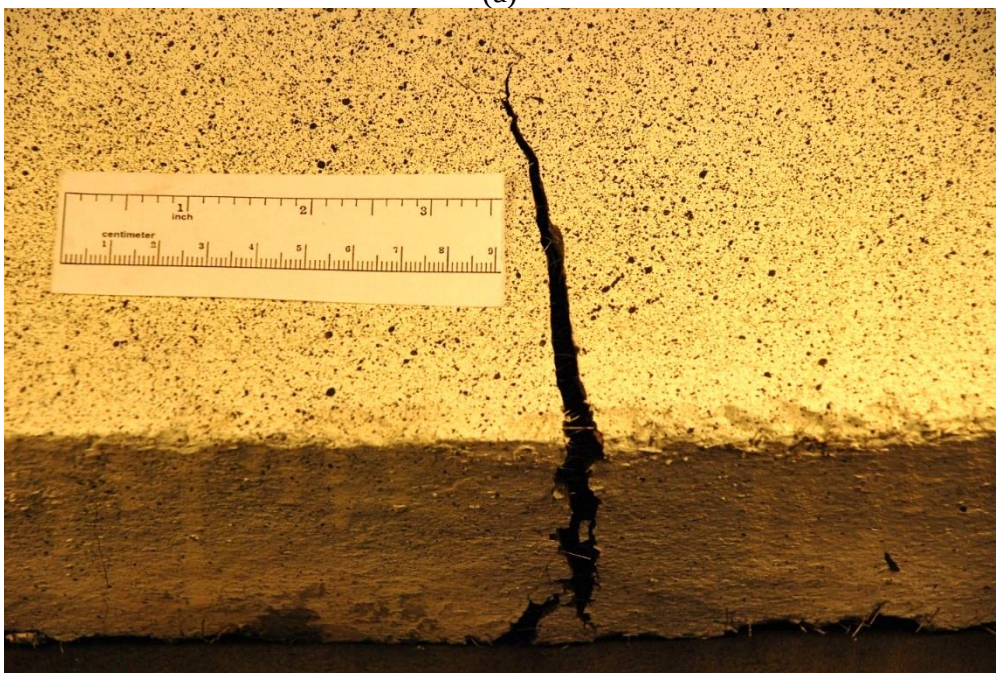
1
inch
2
3
centimeter
1
2
3
4
5
6
7
8
9

(b)

(c)

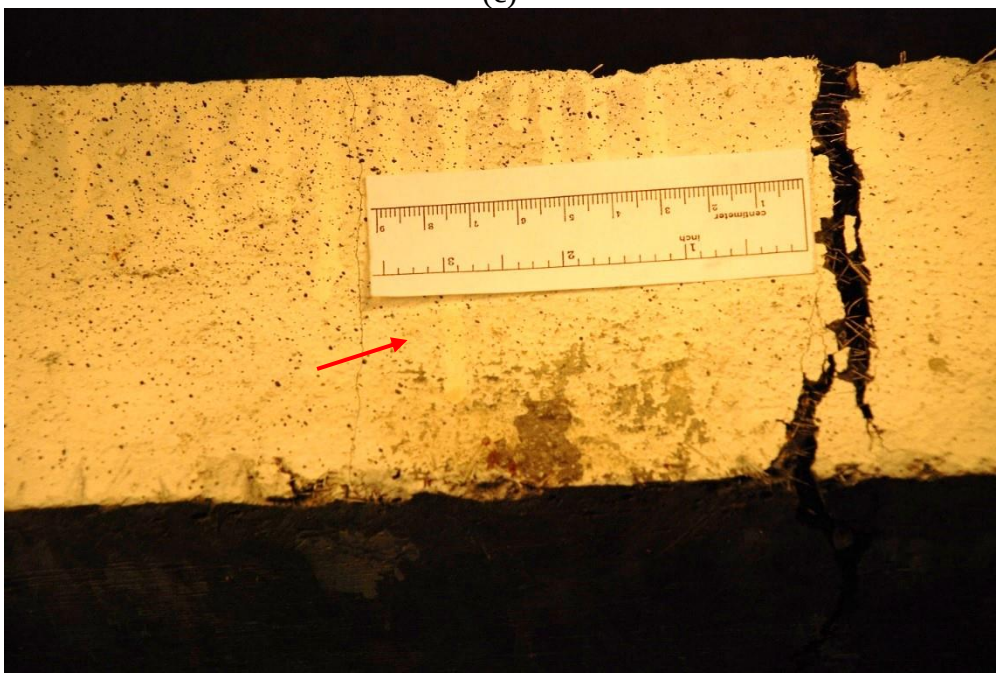

(d)

Figure A. 8. Large beams, 4” x 4” x 16” (102 mm x 102 mm x 406 mm), with 1% fiber content, after 28 days (FML_L_1_28_4PB_C_B3).

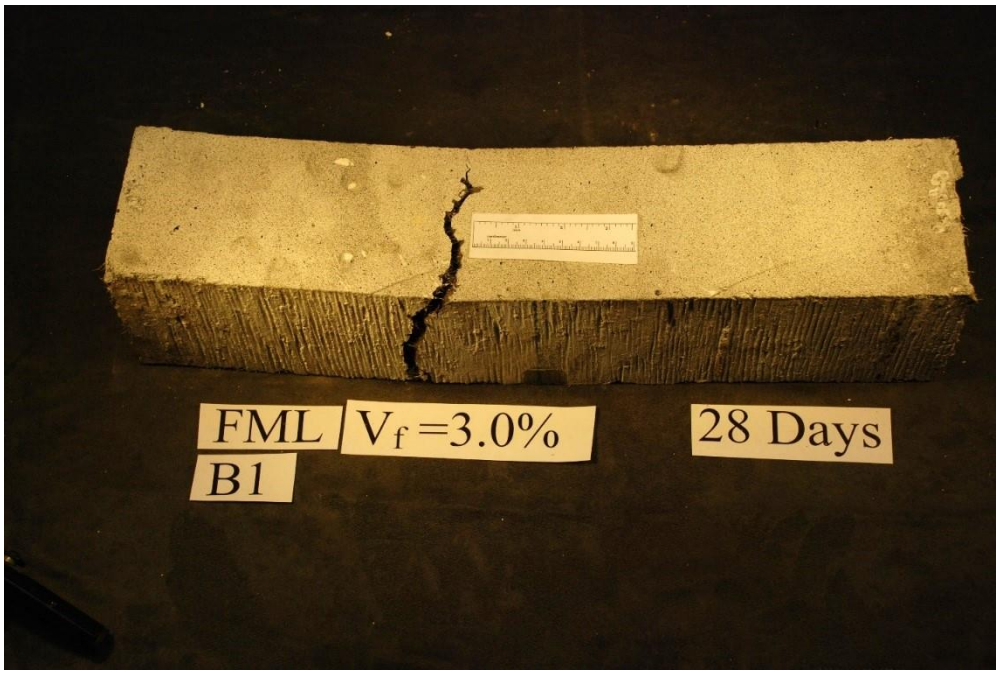

(a)

(b)

Figure A. 9. Large beams, 4” x 4” x 16” (102 mm x 102 mm x 406 mm), with 3% fiber content, after 28 days (FML_L_3_28_4PB_C_B1).

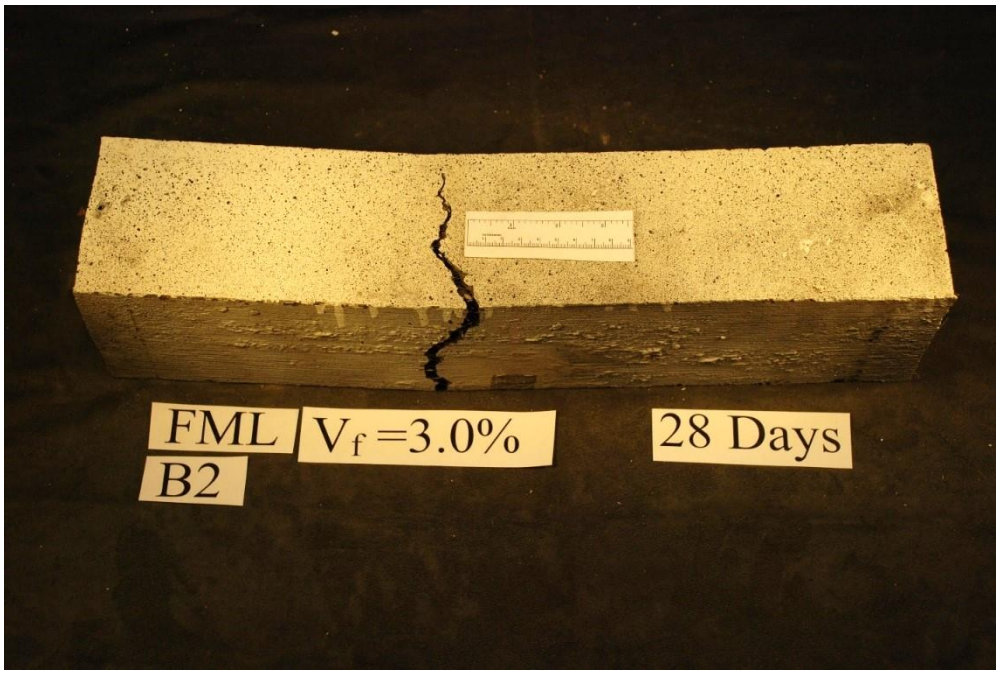

(a)

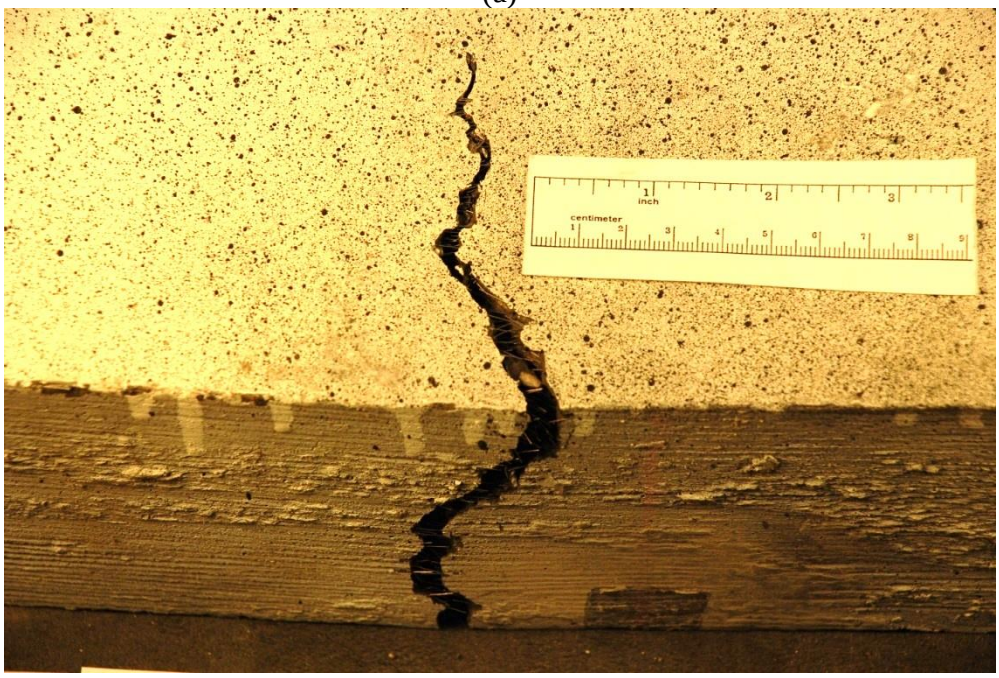

(b)

Figure A. 10. Large beams, 4” x 4” x 16” (102 mm x 102 mm x 406 mm), with 3% fiber content, after 28 days (FML_L_3_28_4PB_C_B2).

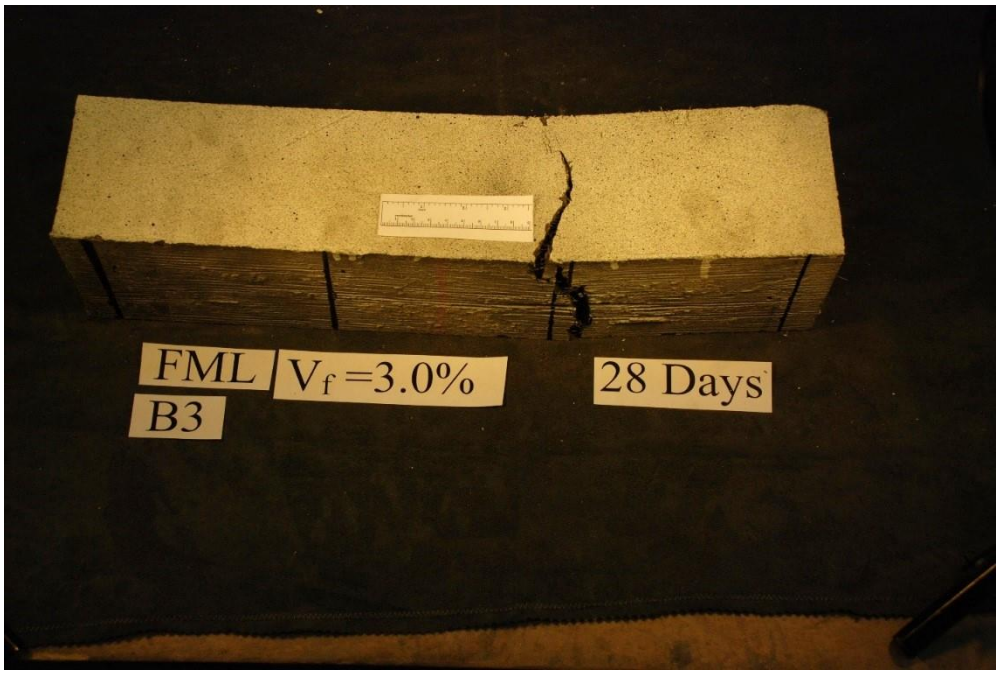

(a)

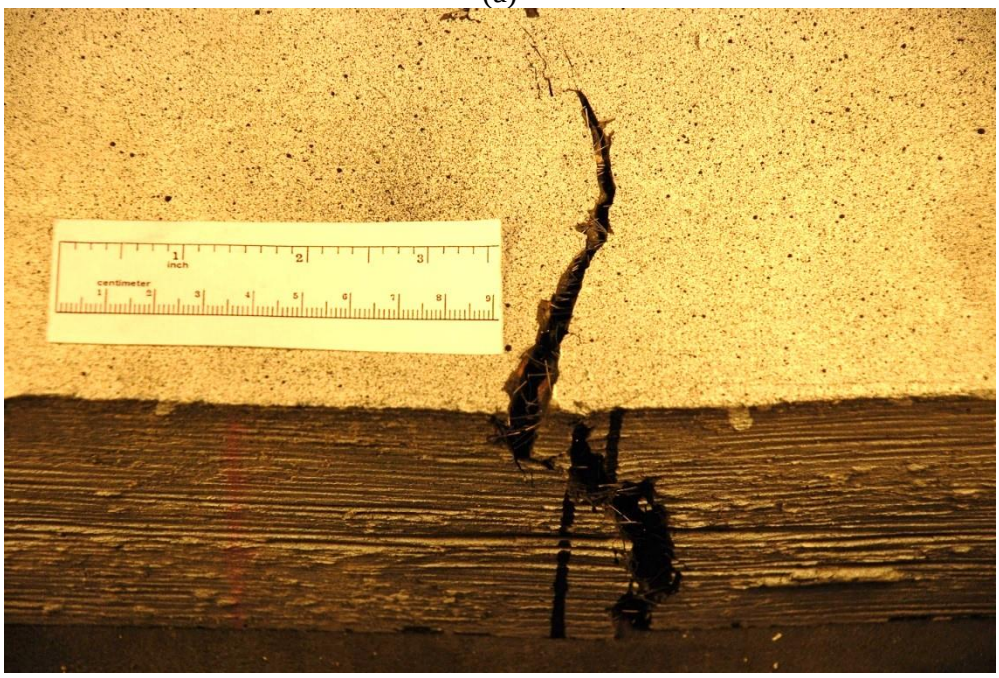

(b)

Figure A. 11. Large beams, 4” x 4” x 16” (102 mm x 102 mm x 406 mm), with 3% fiber content, after 28 days (FML_L_3_28_4PB_C_B3).

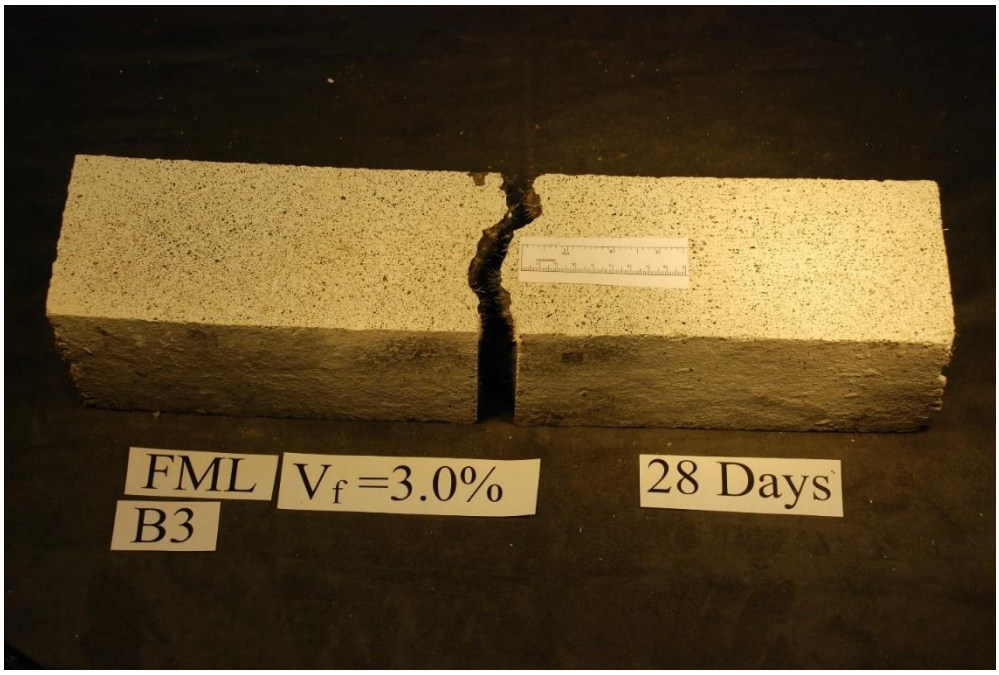

(a)

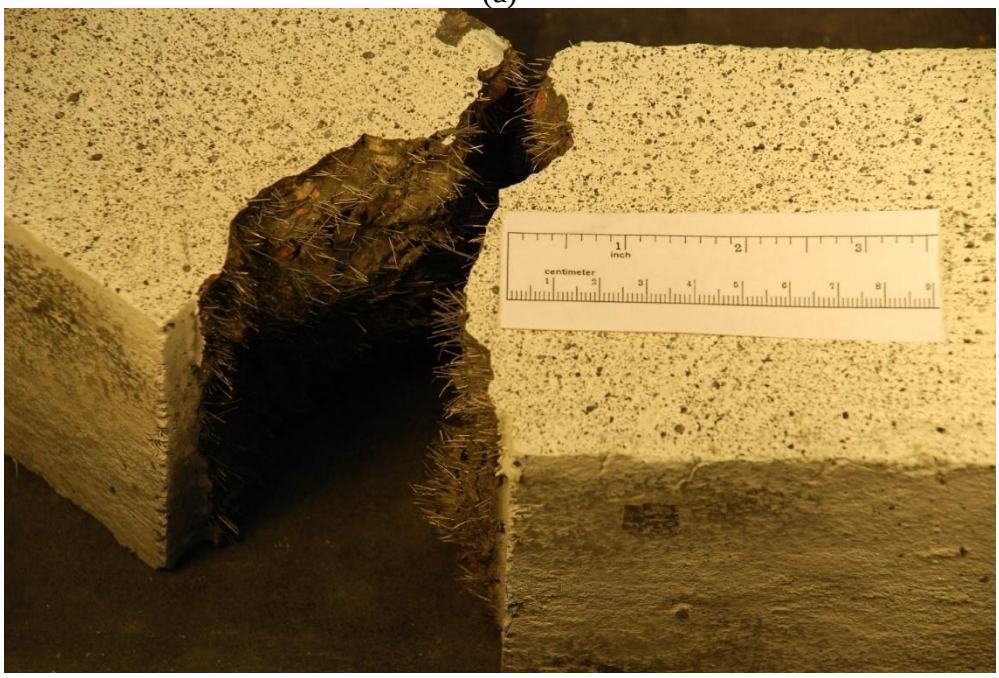

(b)

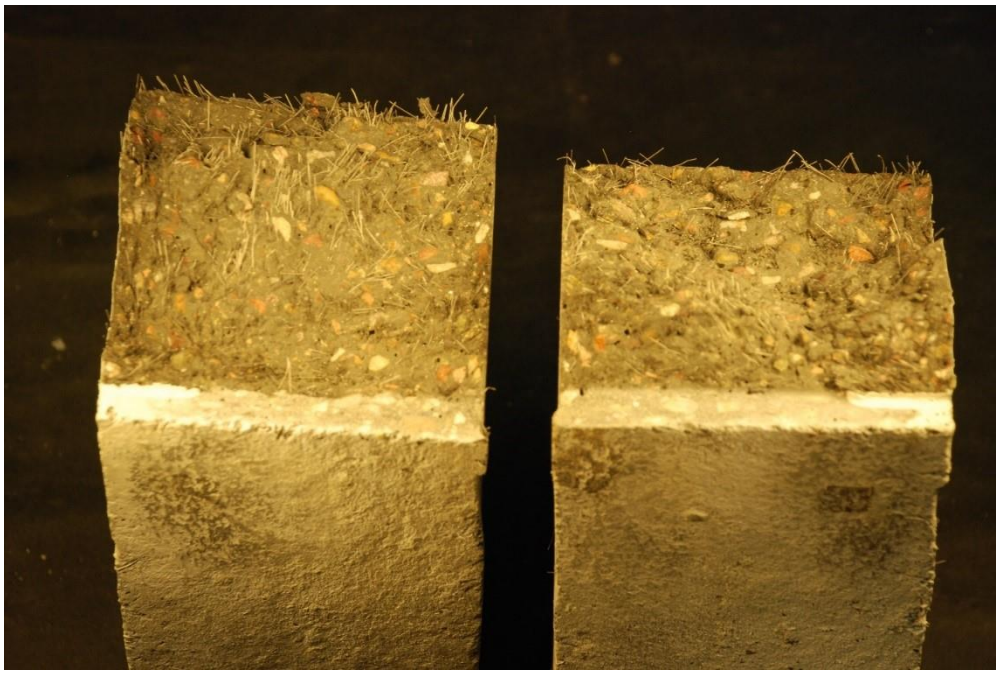

(c)

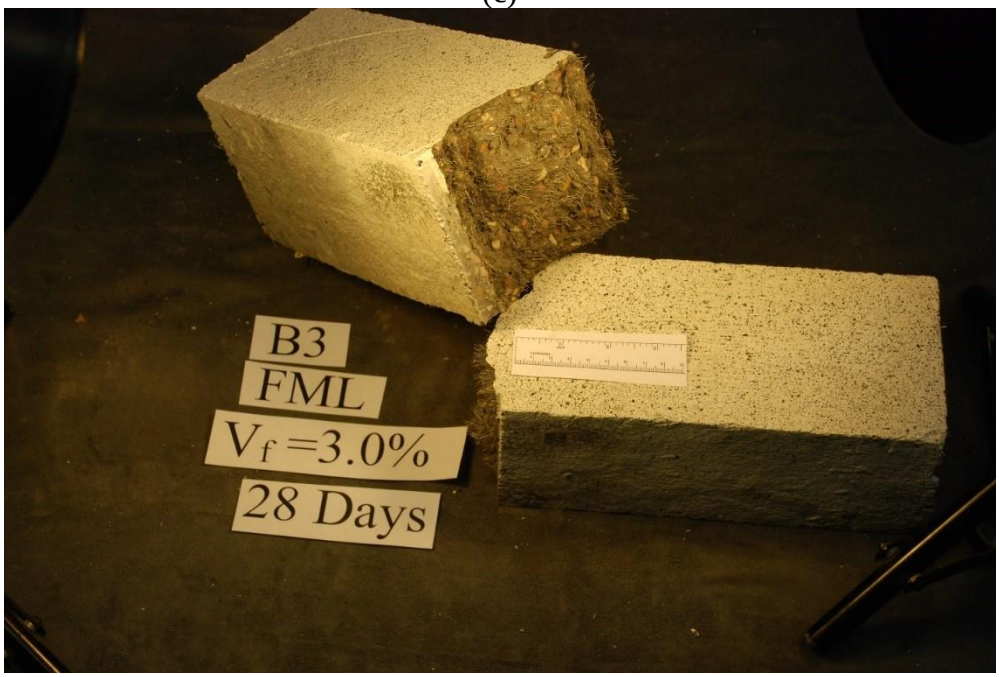

(d)

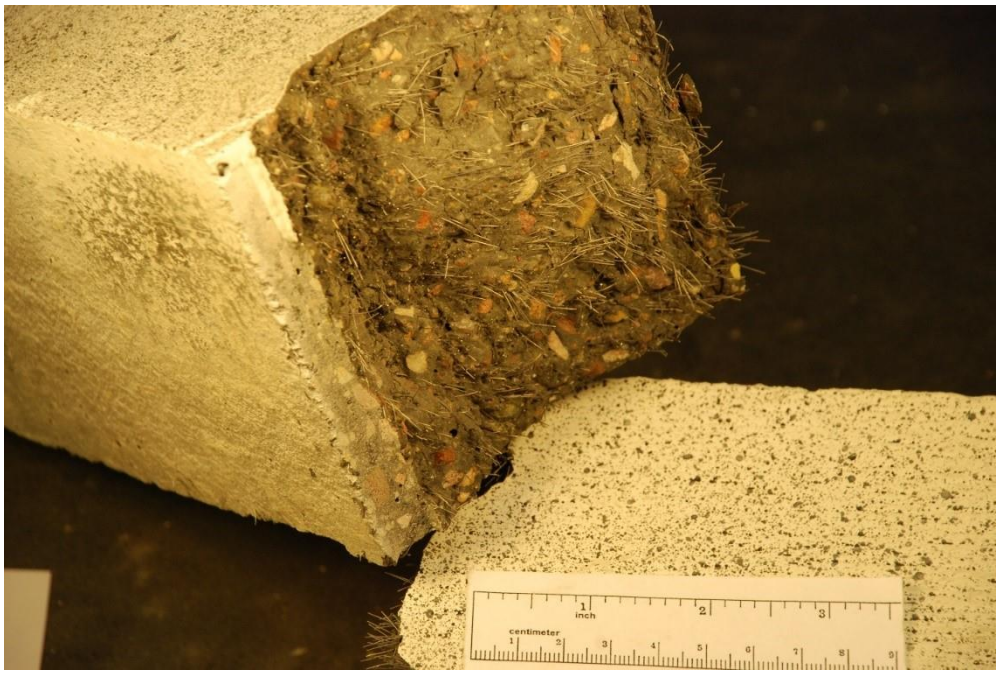

(e)

Figure A. 12. Large beams, 4” x 4” x 16” (102 mm x 102 mm x 406 mm), with 3% fiber content, after 28 days (FML_L_3_28_3PB_C_B3).

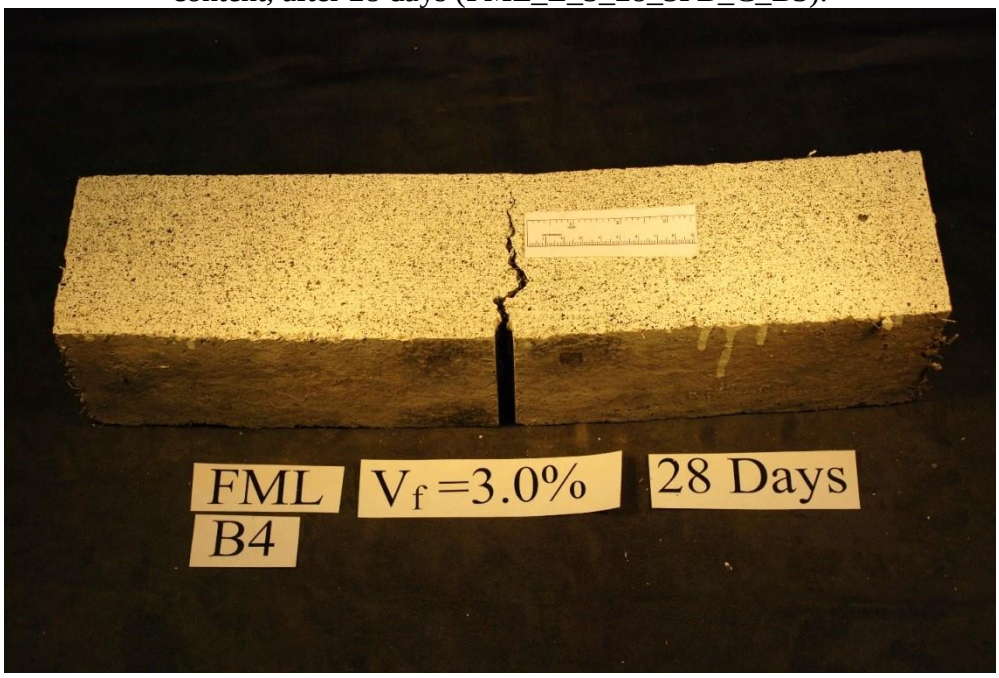

(a)

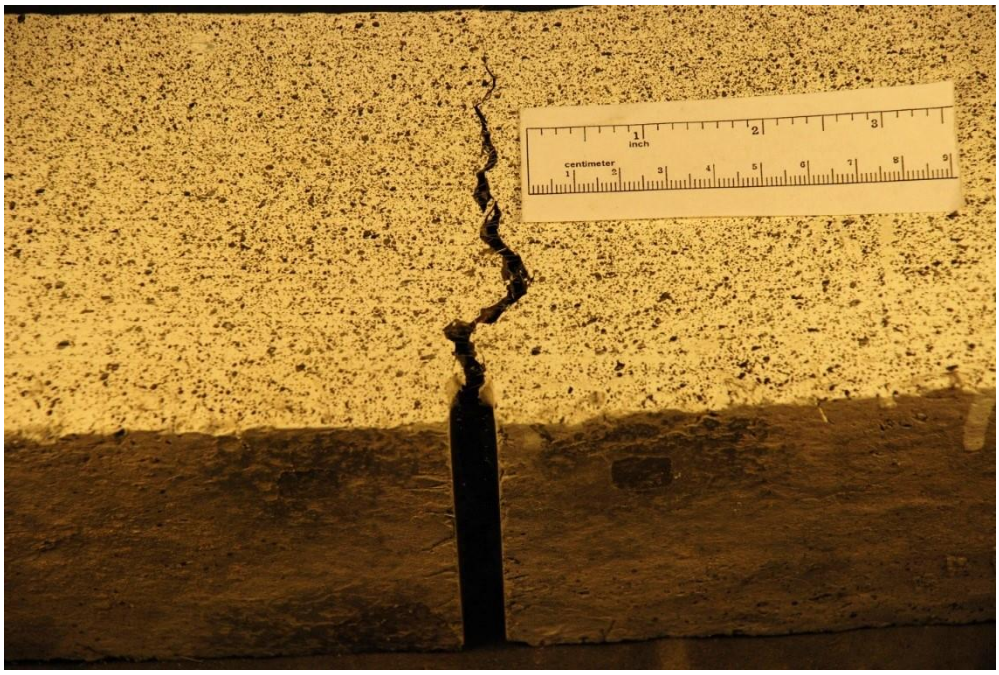

(b)

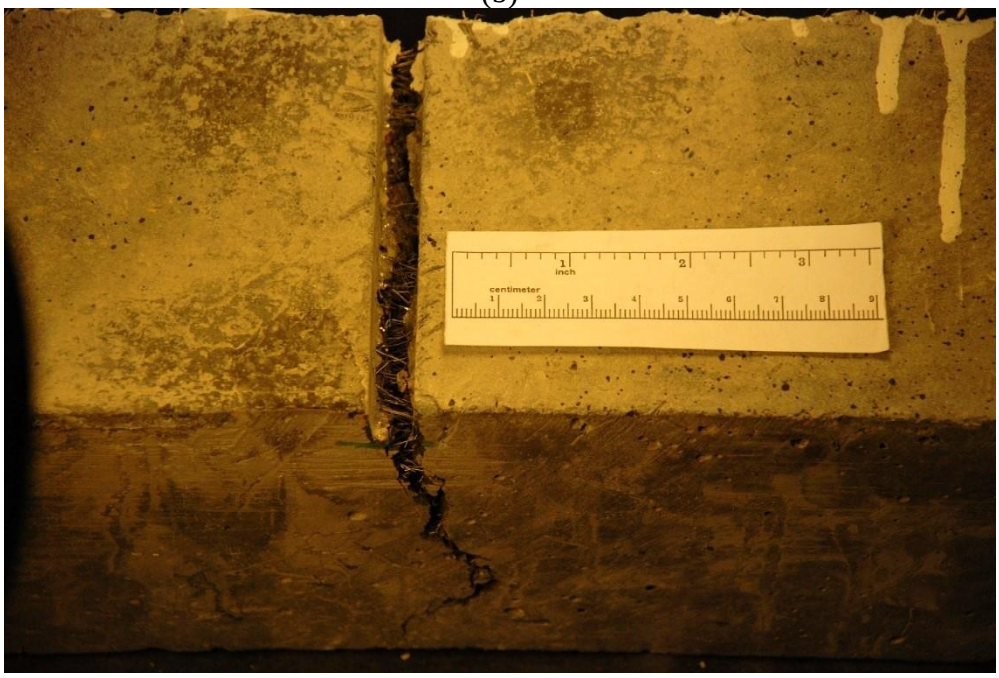

(c)

Figure A. 13. Large beams, 4” x 4” x 16” (102 mm x 102 mm x 406 mm), with 3% fiber content, after 28 days (FML_L_3_28_3PB_C_B4).

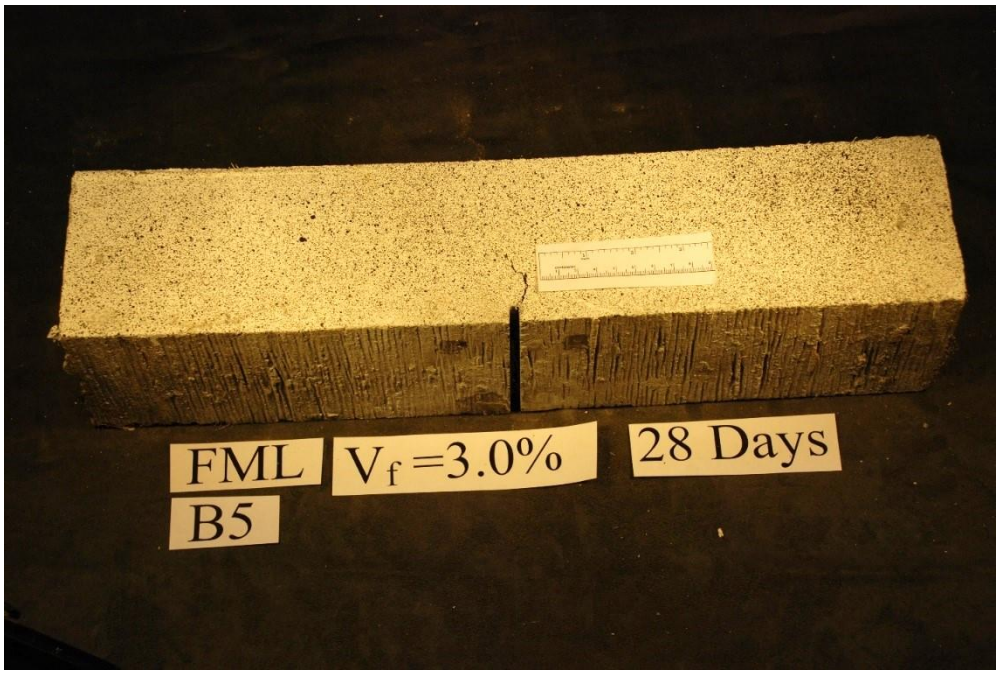

(a)

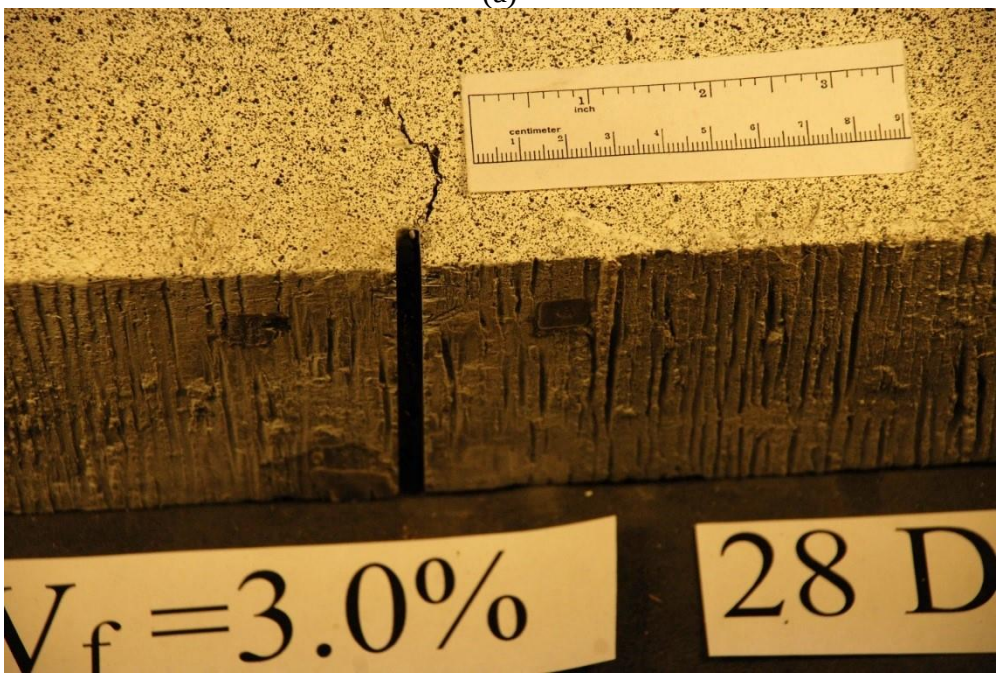

(b)

Figure A. 14. Large beams, 4” x 4” x 16” (102 mm x 102 mm x 406 mm), with 3% fiber content, after 28 days (FML_L_3_28_3PB_C_B5).

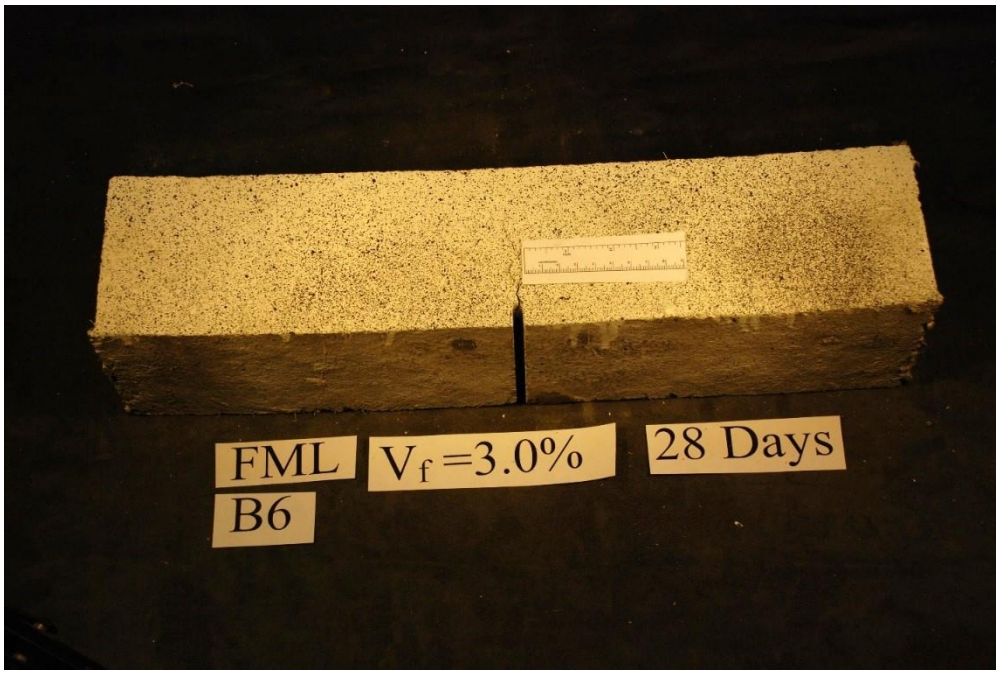

(a)

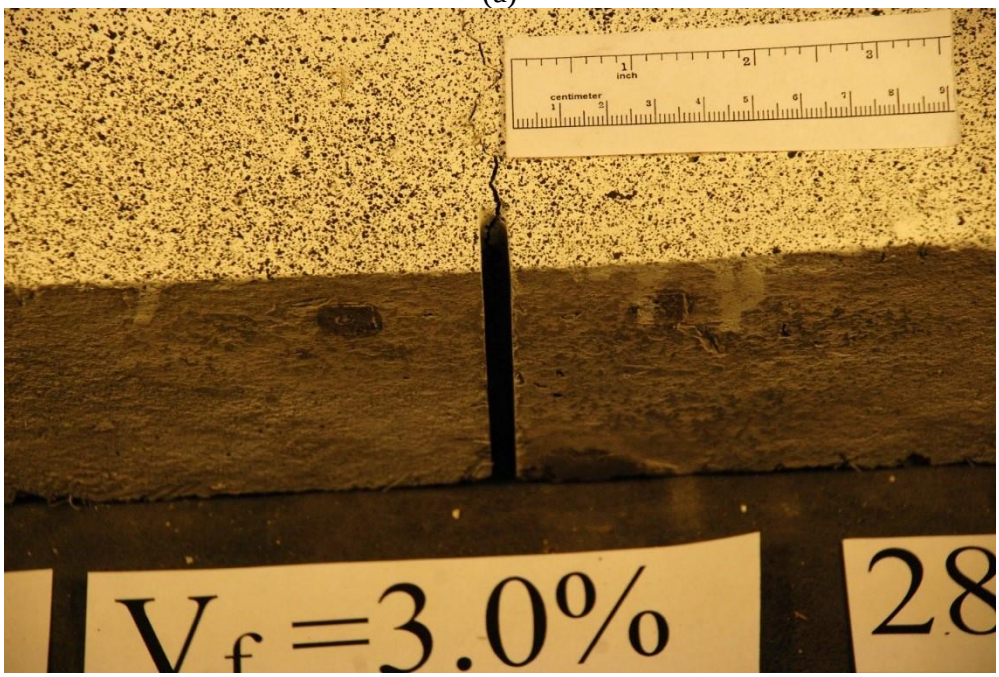

(b)

Figure A. 15. Large beams, 4” x 4” x 16” (102 mm x 102 mm x 406 mm), with 3% fiber content, after 28 days (FML_L_3_28_3PB_C_B6).

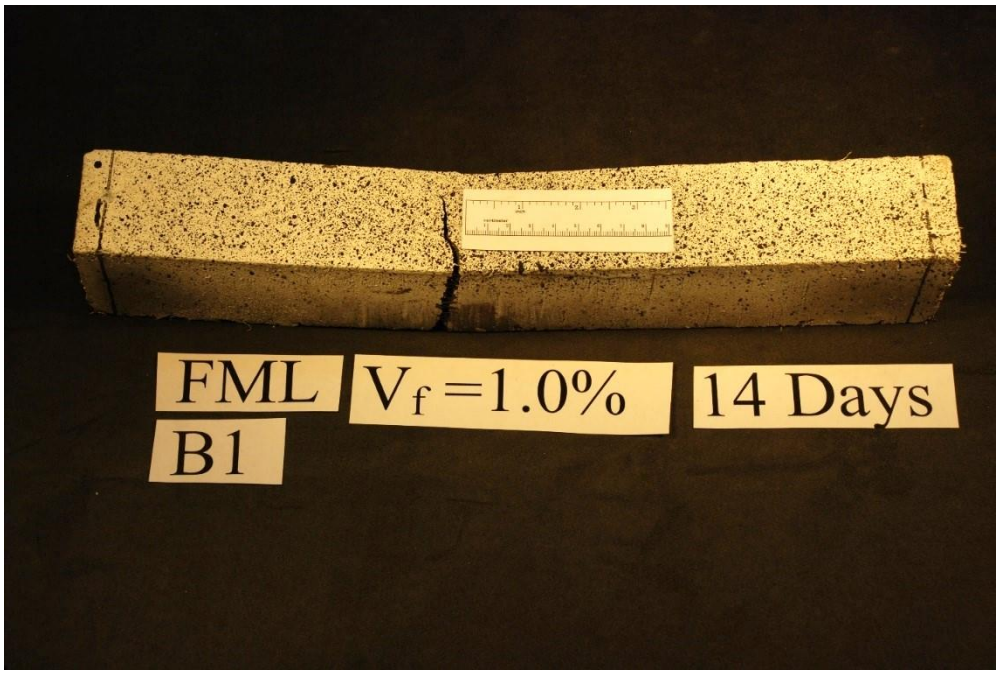

(a)

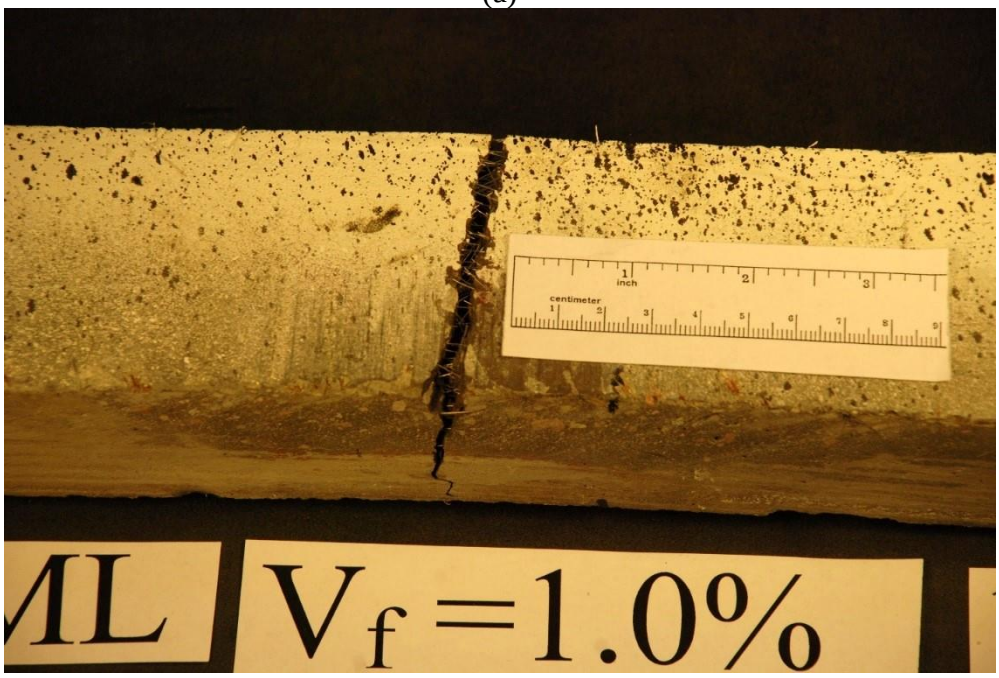

(b)

Figure A. 16. Small beams 2” x 2.5” x 14”, with 1% fiber content, after 14 days (FML_S_1_14_4PB_C_B1).

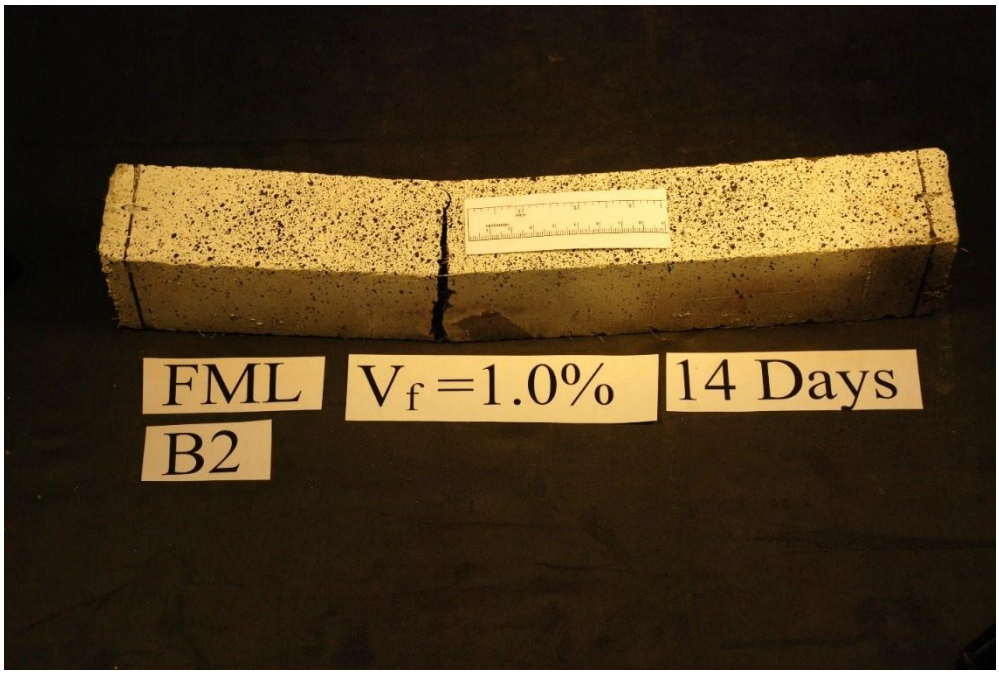

(a)

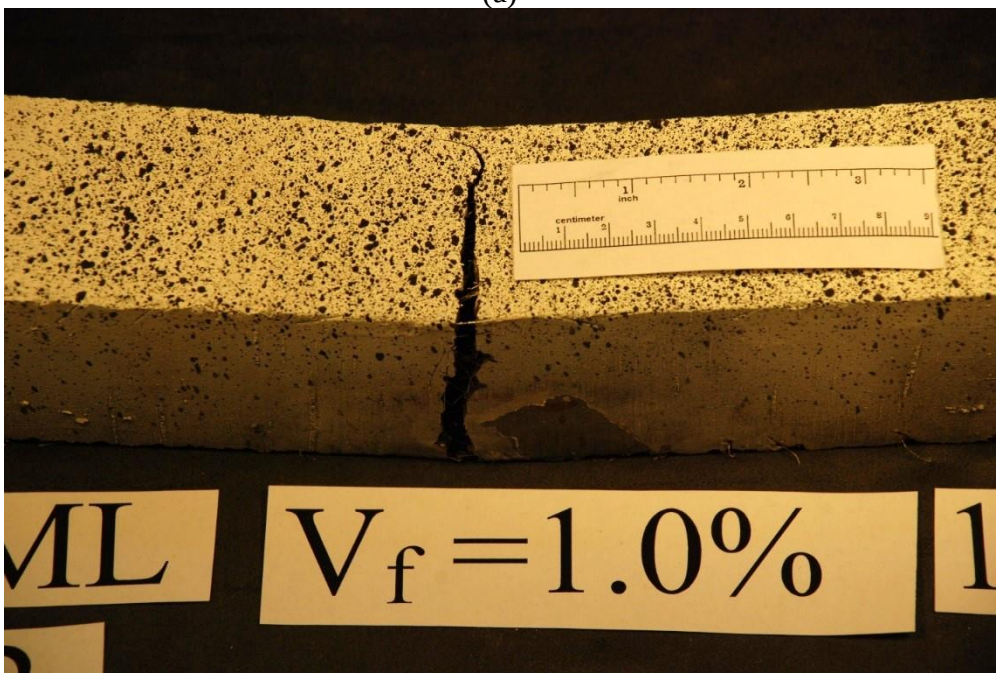

(b)

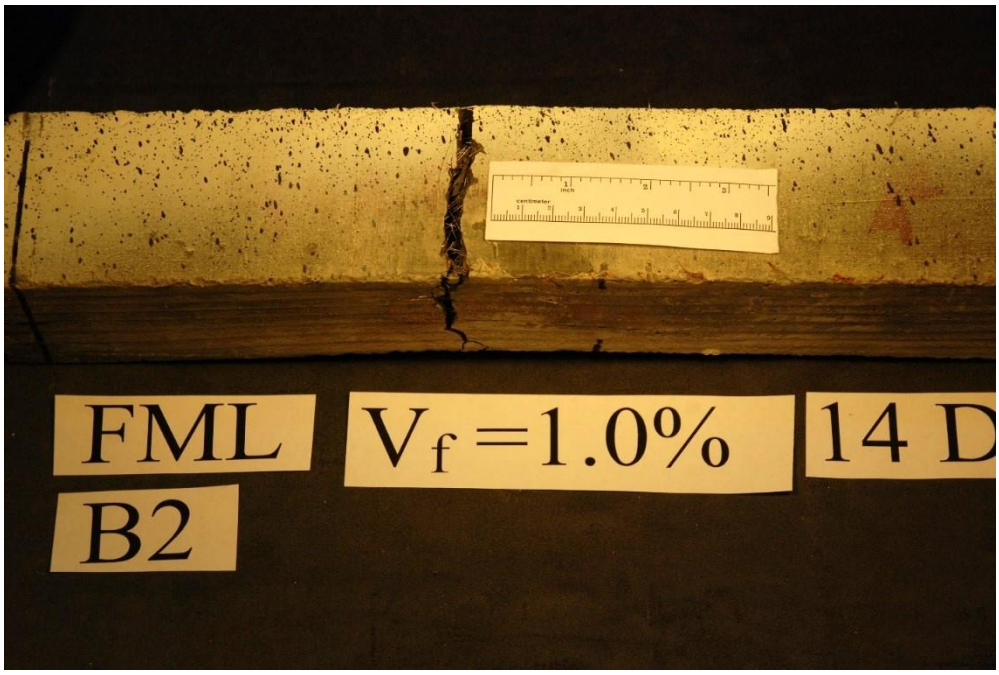

(c)

Figure A. 17. Small beams 2” x 2.5” x 14”, with 1% fiber content, after 14 days (FML_S_1_14_4PB_C_B2).

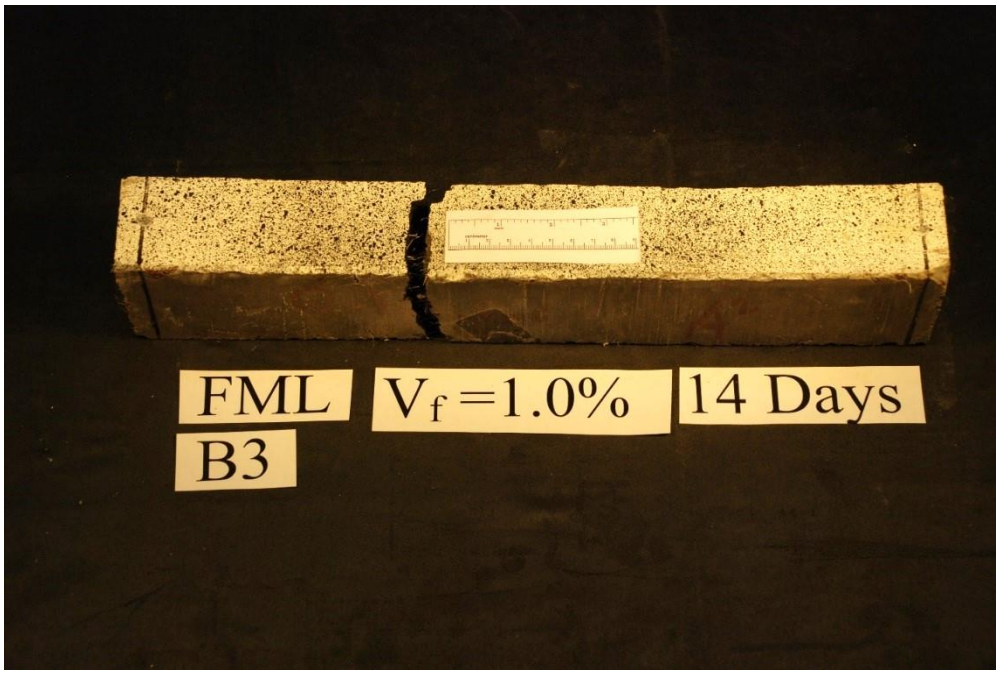

Figure A. 18. Small beams 2” x 2.5” x 14”, with 1% fiber content, after 14 days (FML_S_1_14_4PB_C_B3).

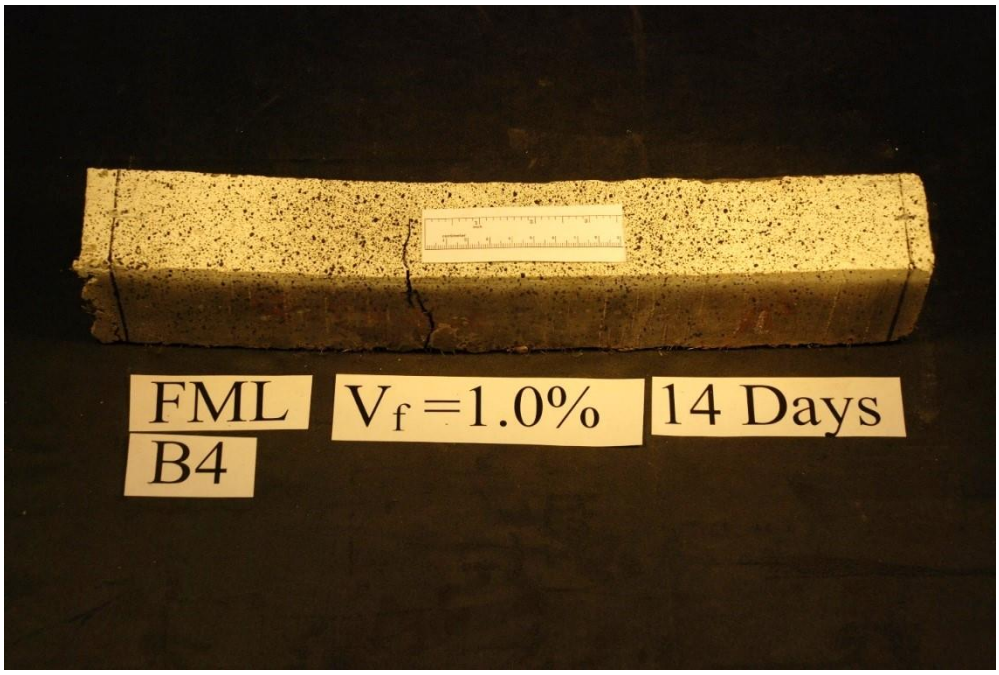

Figure A. 19. Small beams 2” x 2.5” x 14”, with 1% fiber content, after 14 days (FML_S_1_14_4PB_C_B4).

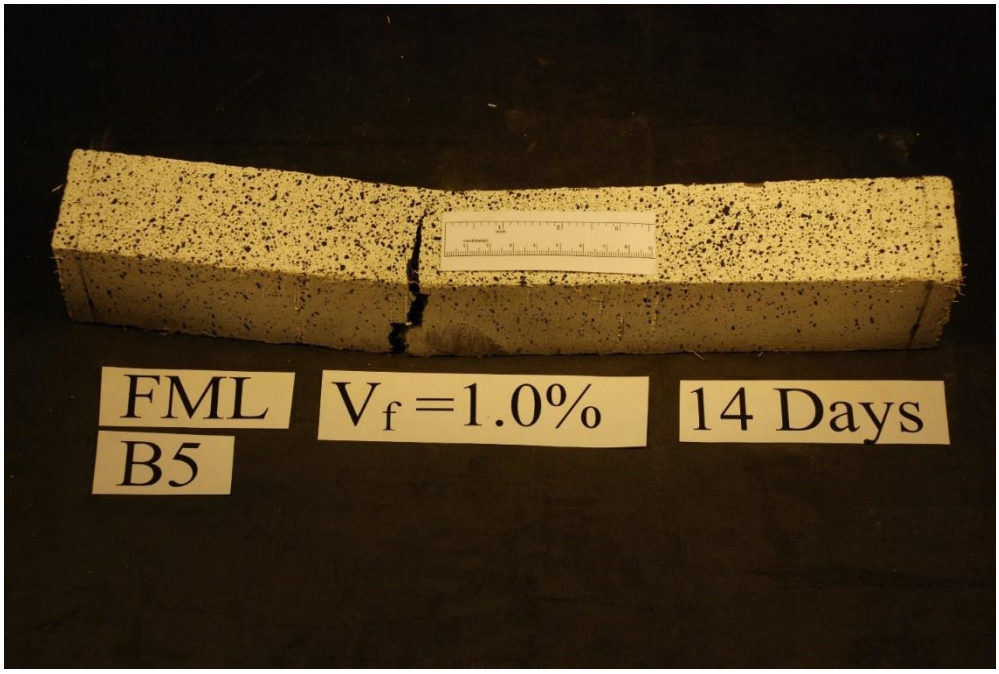

(a)

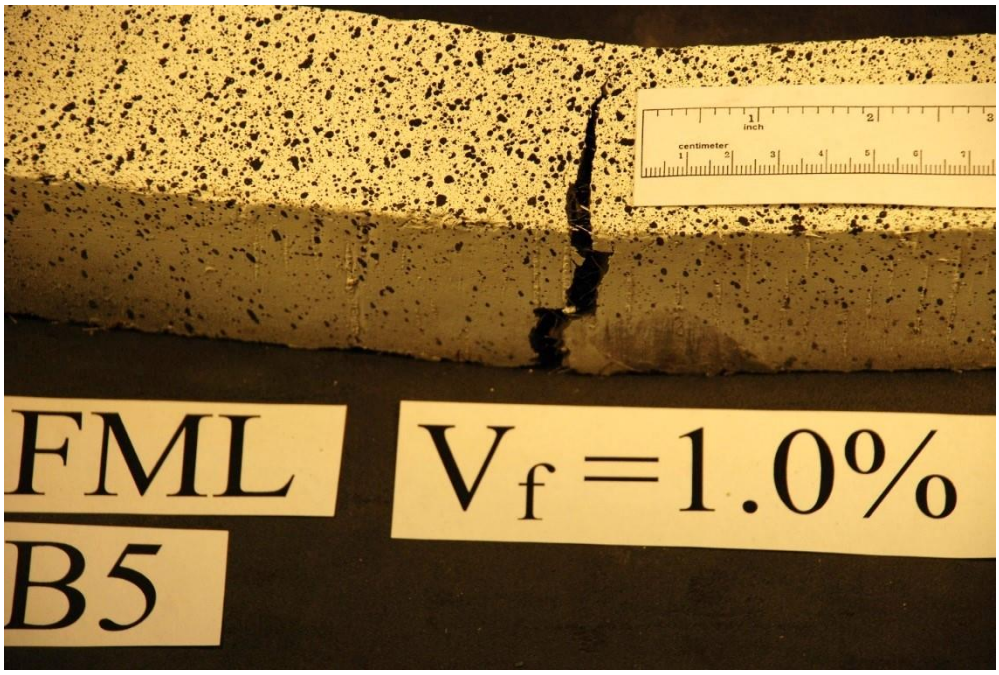

(b)

Figure A. 20. Small beams 2” x 2.5” x 14”, with 1% fiber content, after 14 days (FML_S_1_14_4PB_C_B5).

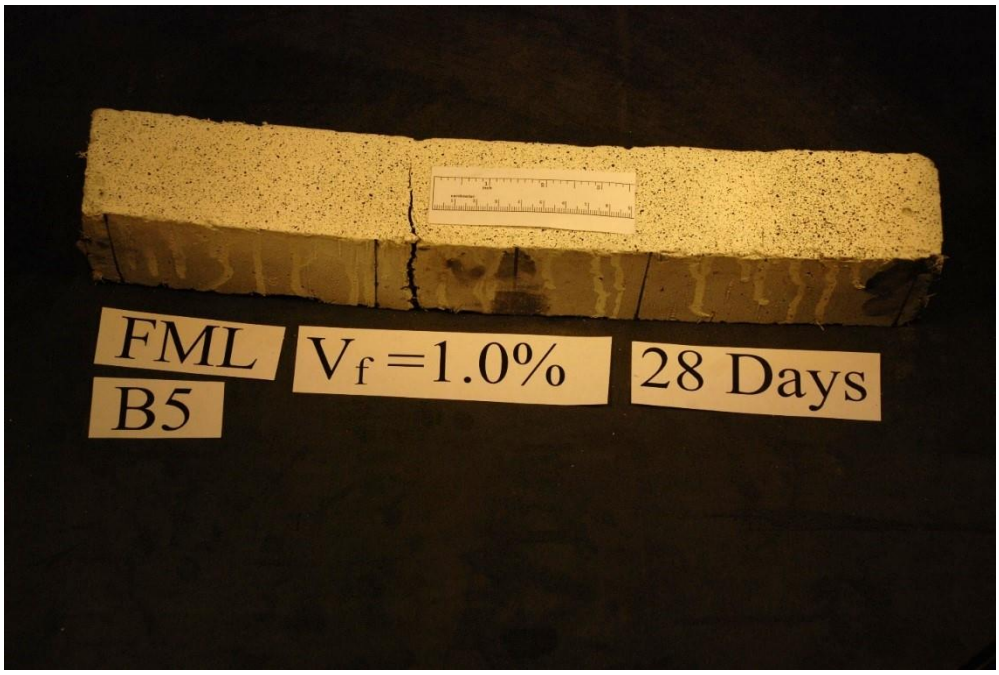

Figure A. 21. Small beams 2” x 2.5” x 14”, with 1% fiber content, after 28 days (FML_S_1_28_4PB_C_B5).

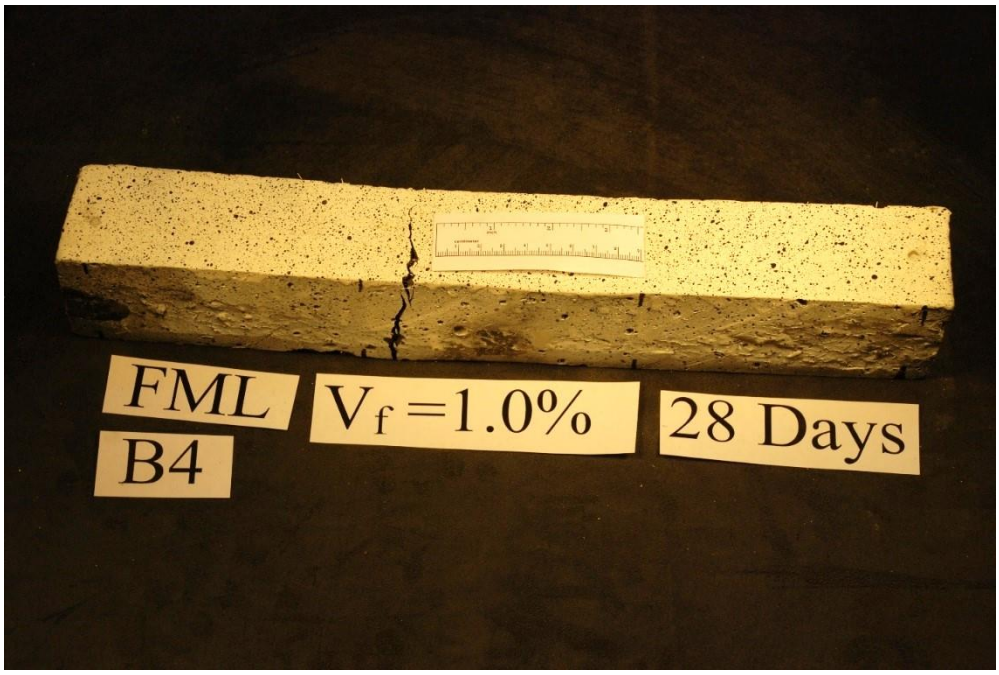

(a)

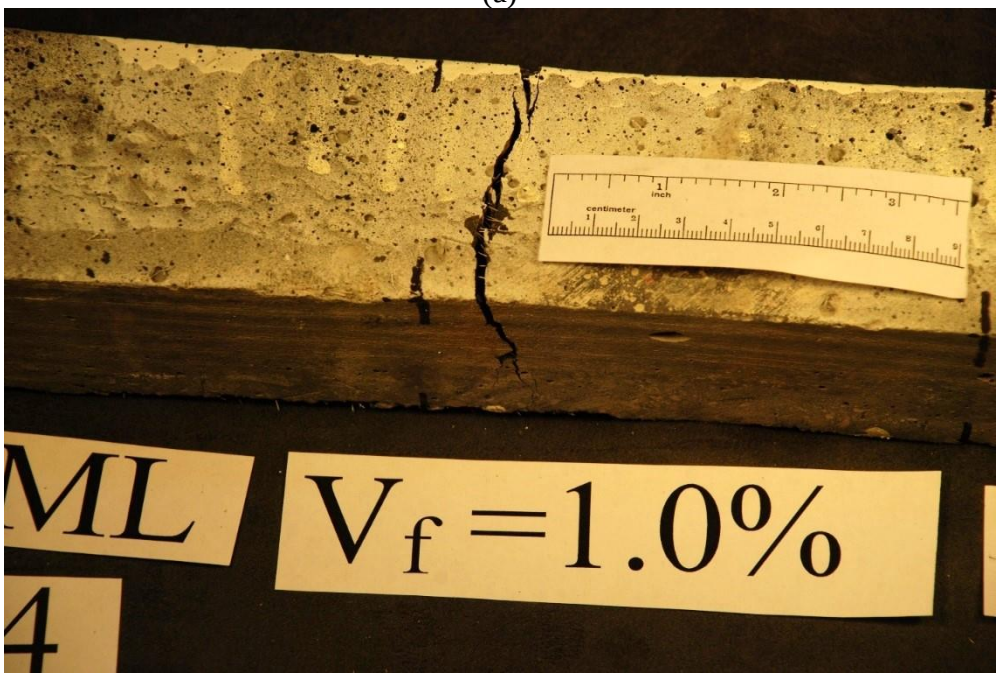

(b)

Figure A. 22. Small beams 2” x 2.5” x 14”, with 1% fiber content, after 28 days (FML_S_1_28_4PB_C_B4).

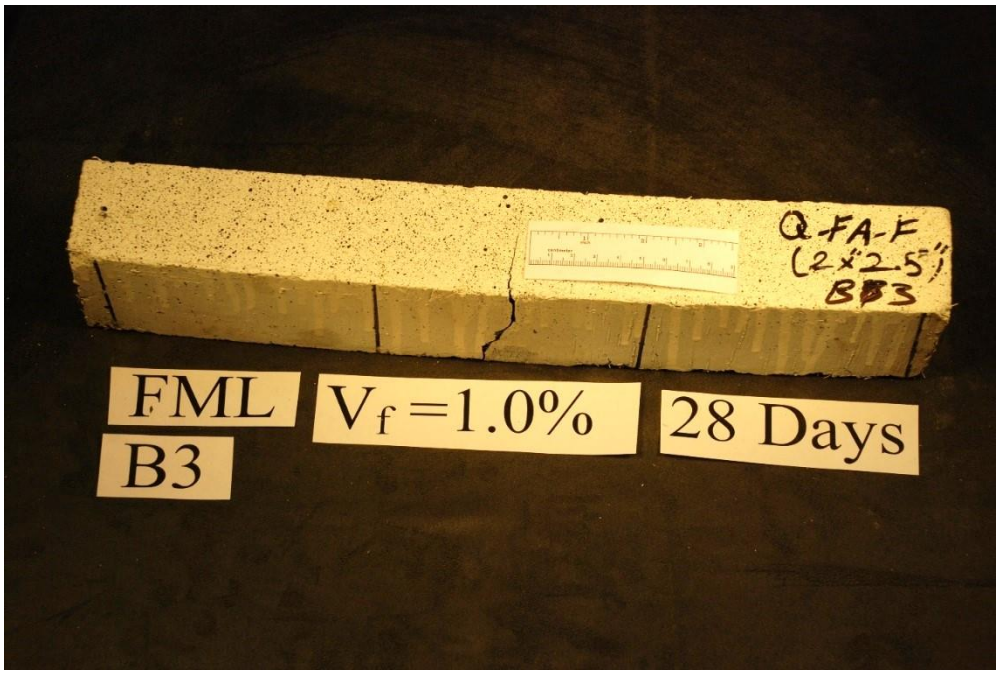

Figure A. 23. Small beams 2” x 2.5” x 14”, with 1% fiber content, after 28 days (FML_S_1_28_4PB_C_B3).

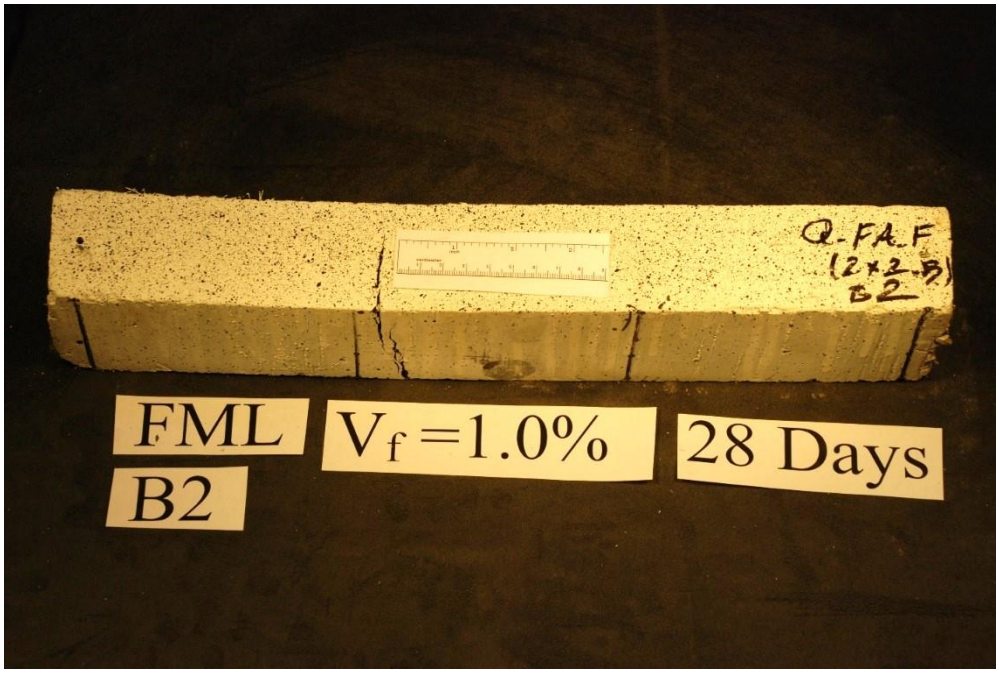

(a)

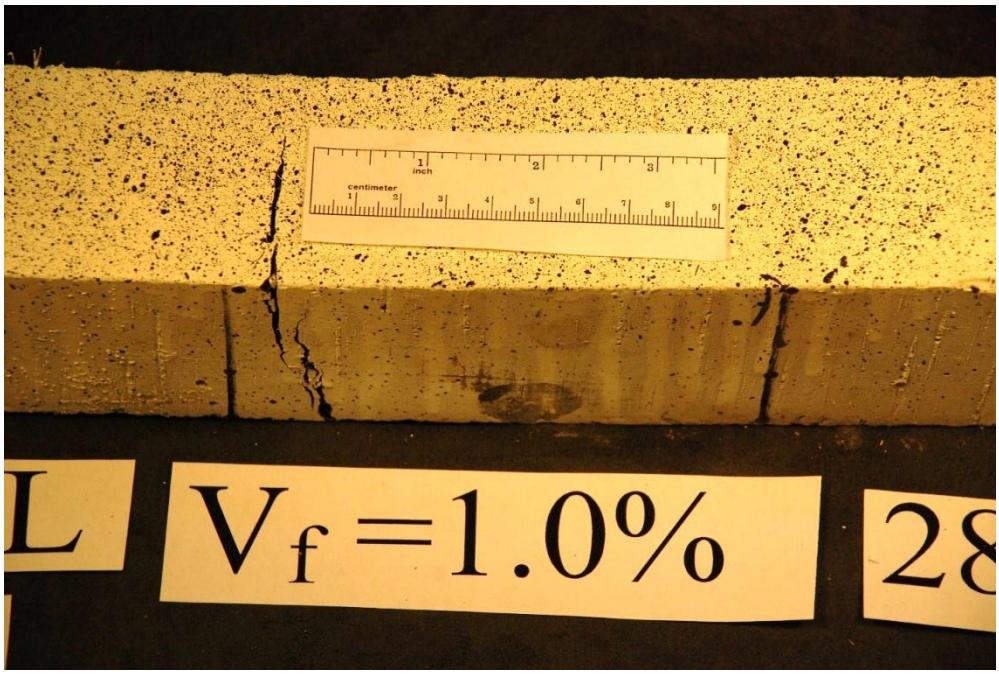

(b)

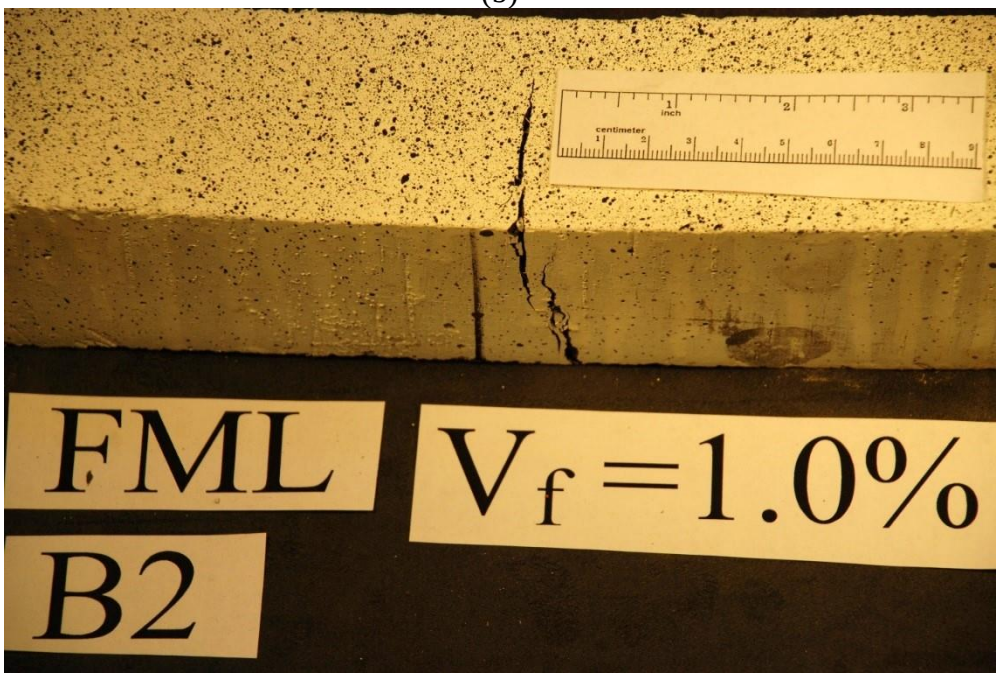

(c)

Figure A. 24. Small beams 2” x 2.5” x 14”, with 1% fiber content, after 28 days (FML_S_1_28_4PB_C_B2).

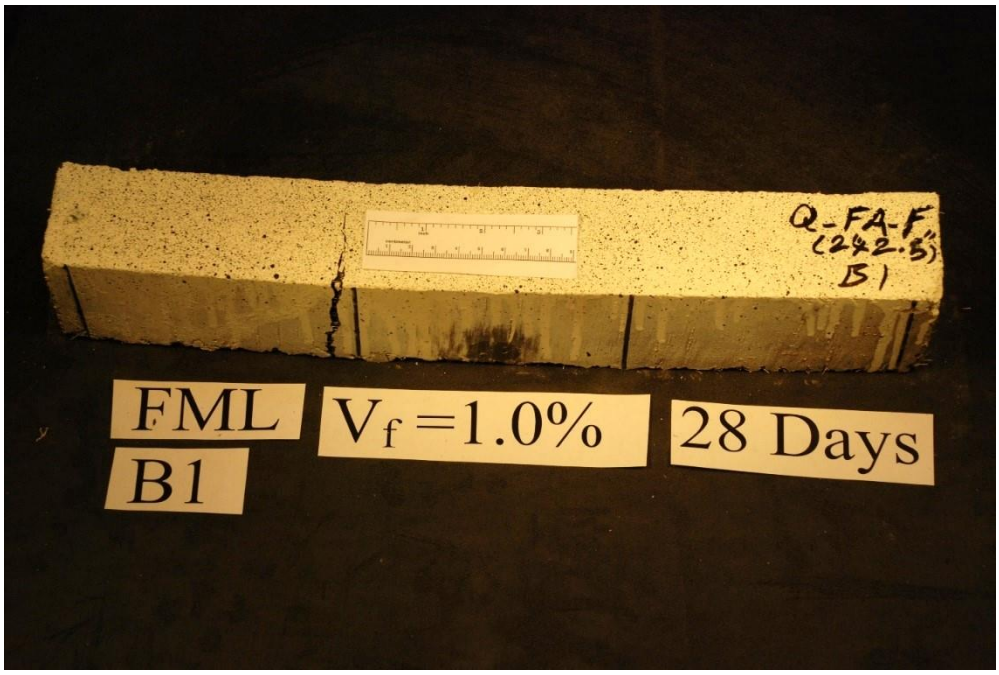

(a)

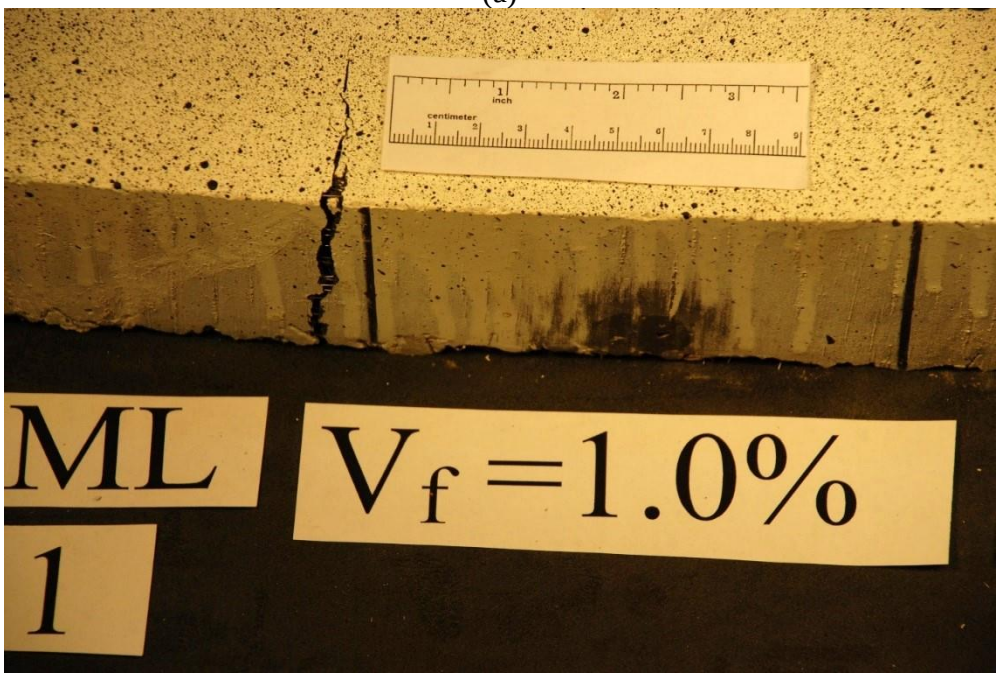

(b)

Figure A. 25. Small beams 2” x 2.5” x 14”, with 1% fiber content, after 28 days (FML_S_1_28_4PB_C_B1).

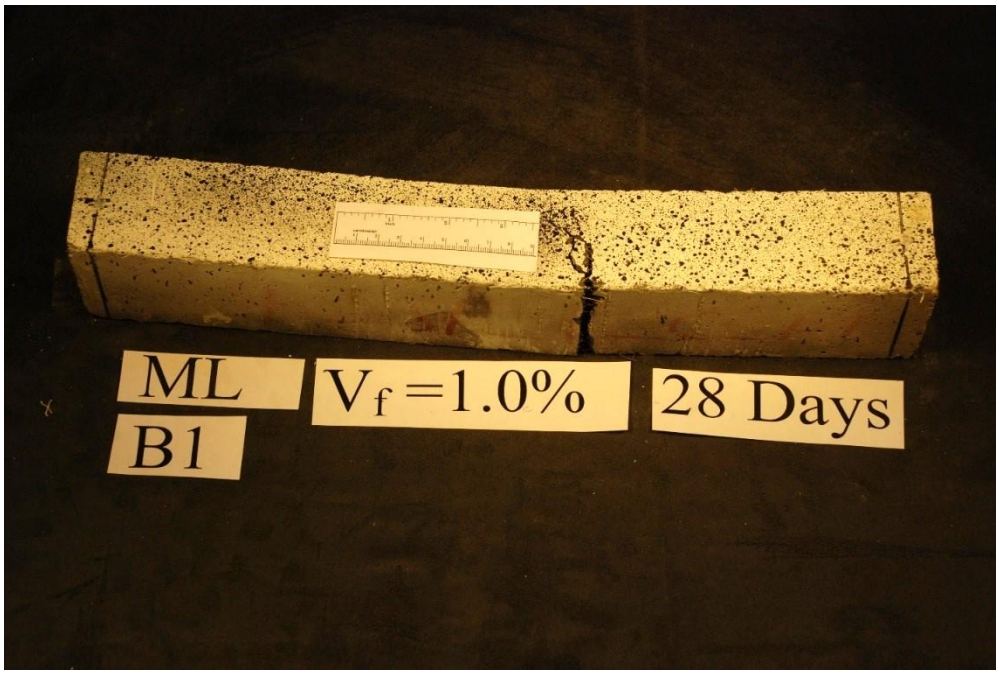

(a)

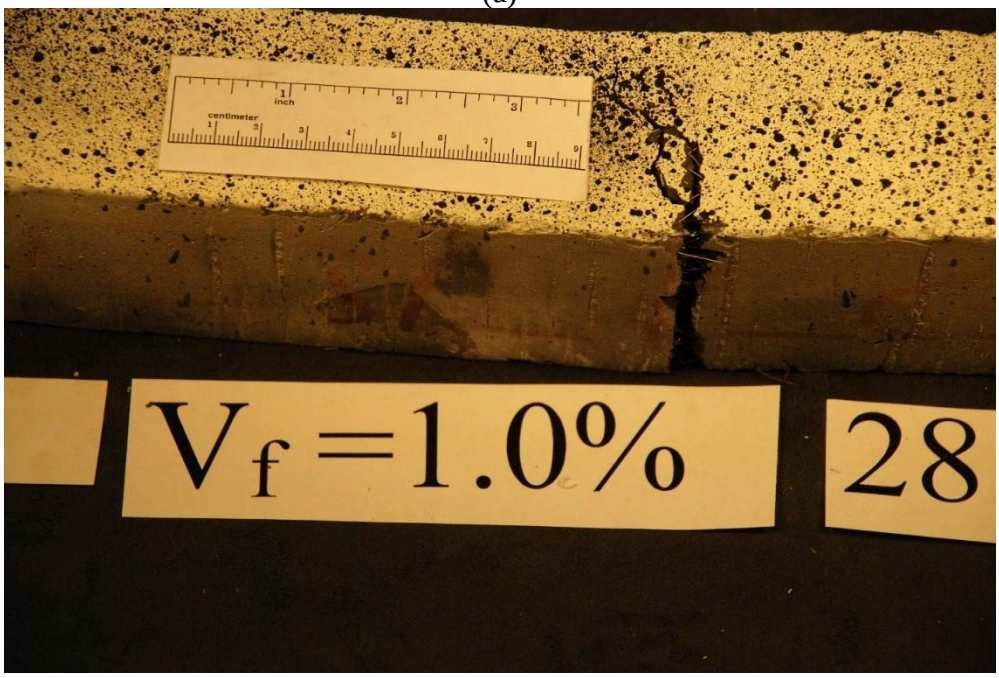

(b)

Figure A. 26. Small beams 2” x 2.5” x 14”, with 1% fiber content, after 28 days (ML_S_1_28_4PB_C_B1).

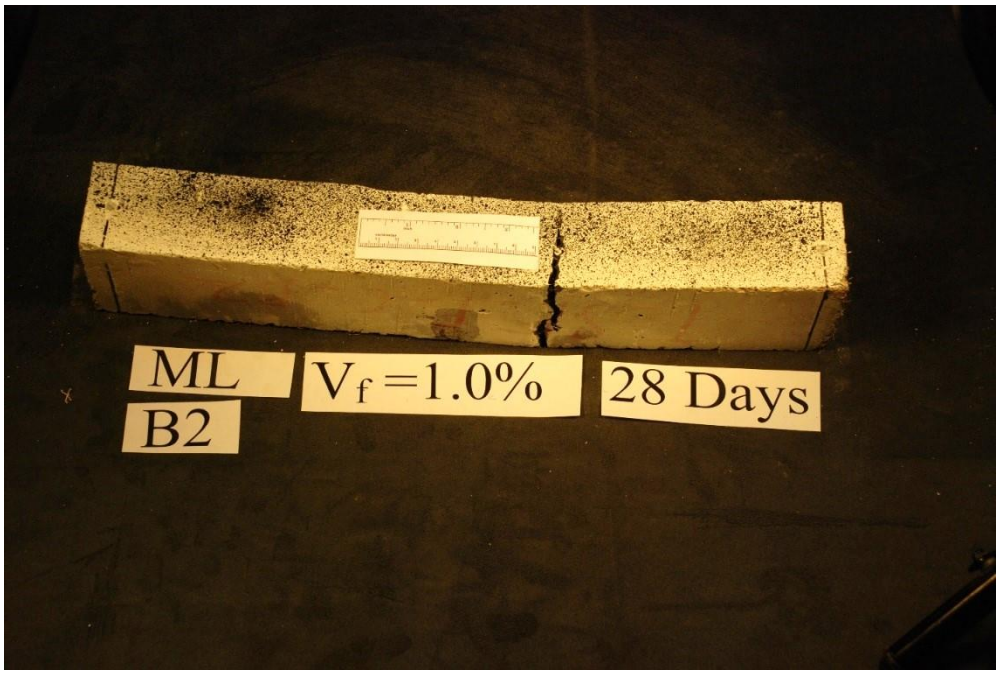

Figure A. 27. Small beams 2” x 2.5” x 14”, with 1% fiber content, after 28 days (ML_S_1_28_4PB_C_B2).

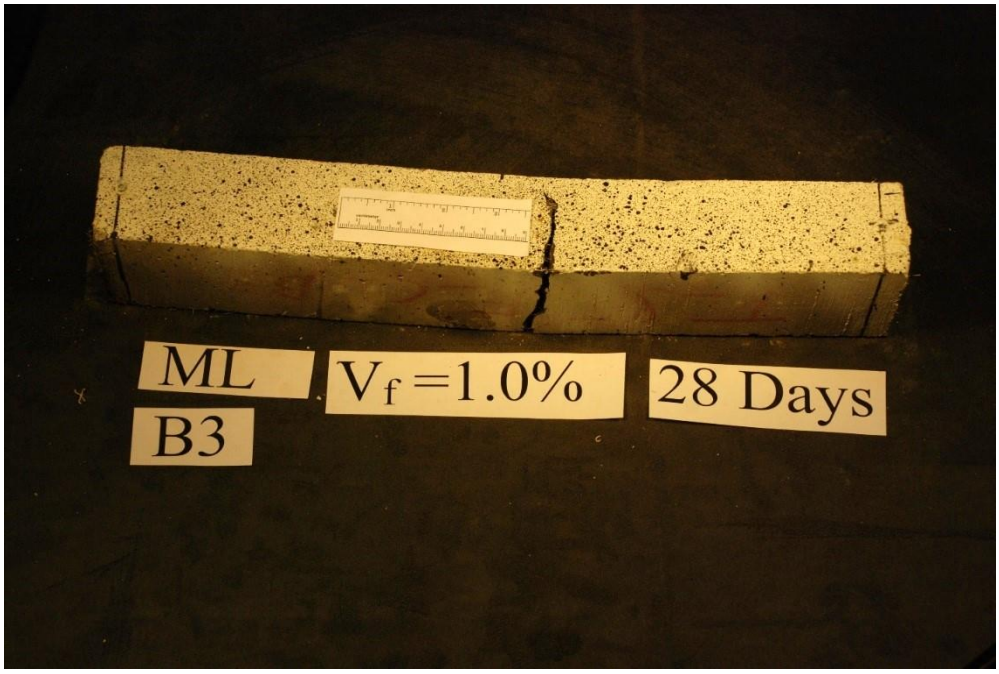

Figure A. 28. Small beams 2” x 2.5” x 14”, with 1% fiber content, after 28 days (ML_S_1_28_4PB_C_B3).

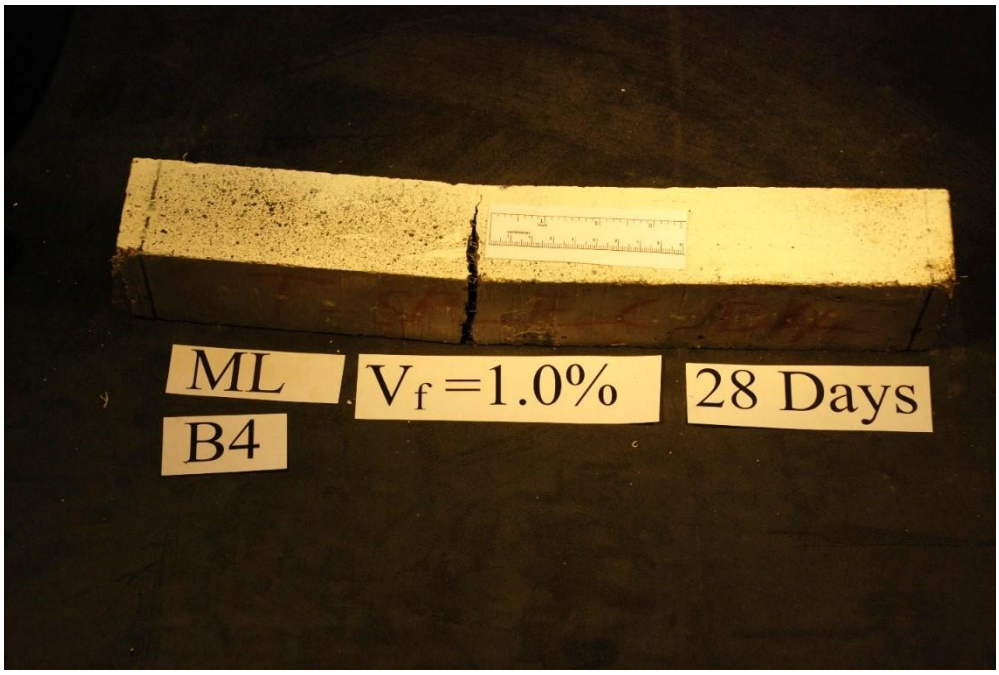

Figure A. 29. Small beams 2” x 2.5” x 14”, with 1% fiber content, after 28 days (ML_S_1_28_4PB_C_B4).

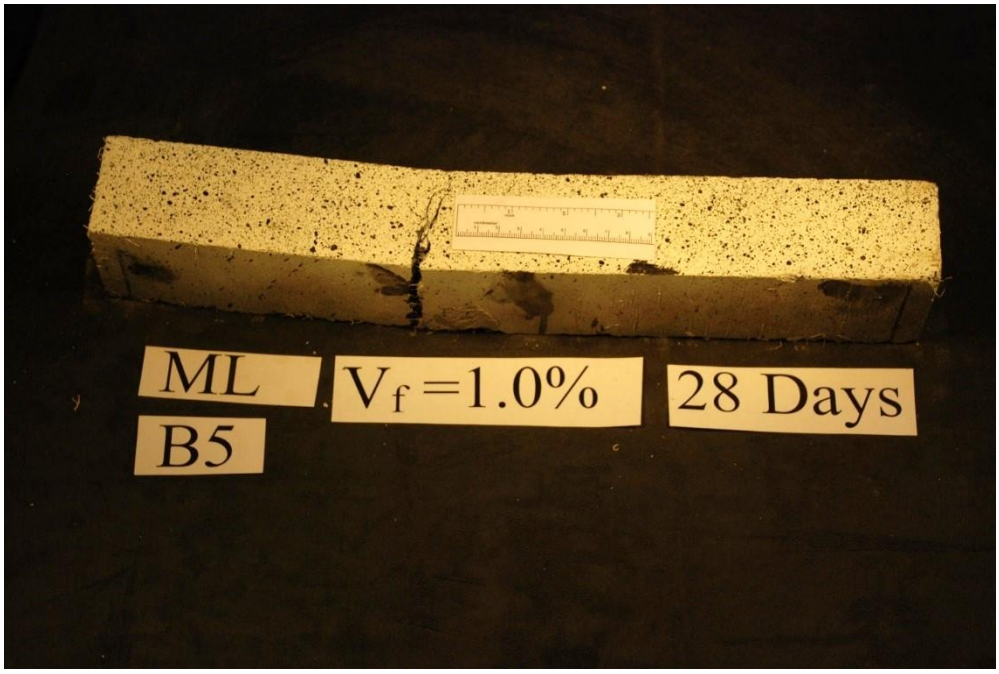

Figure A. 30. Small beams 2” x 2.5” x 14”, with 1% fiber content, after 28 days (ML_S_1_28_4PB_C_B5).

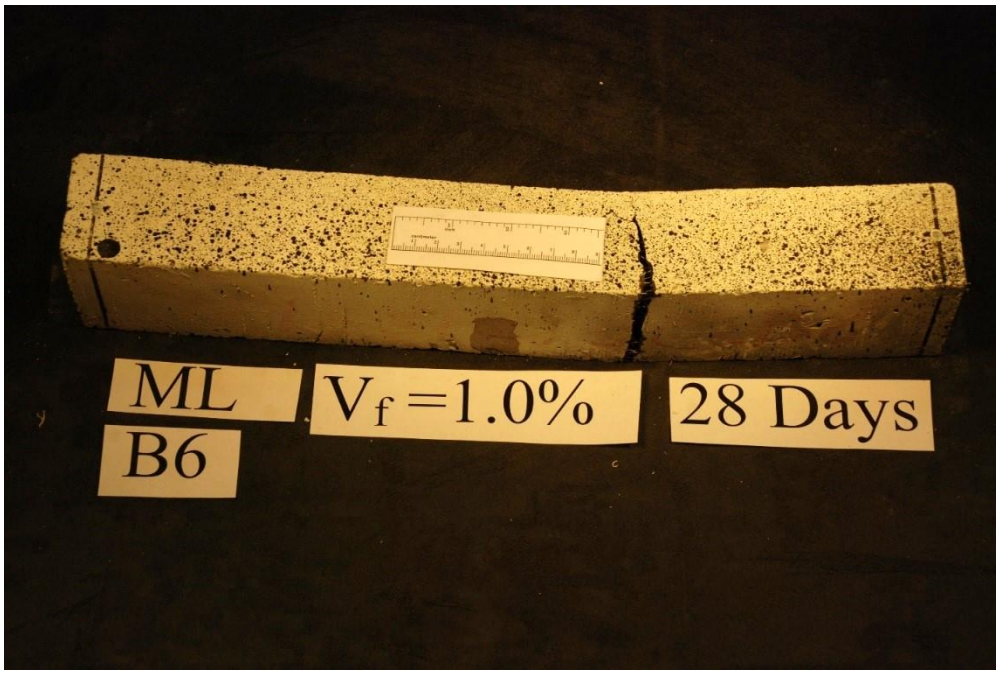

Figure A. 31. Small beams 2” x 2.5” x 14”, with 1% fiber content, after 28 days (ML_S_1_28_4PB_C_B6).

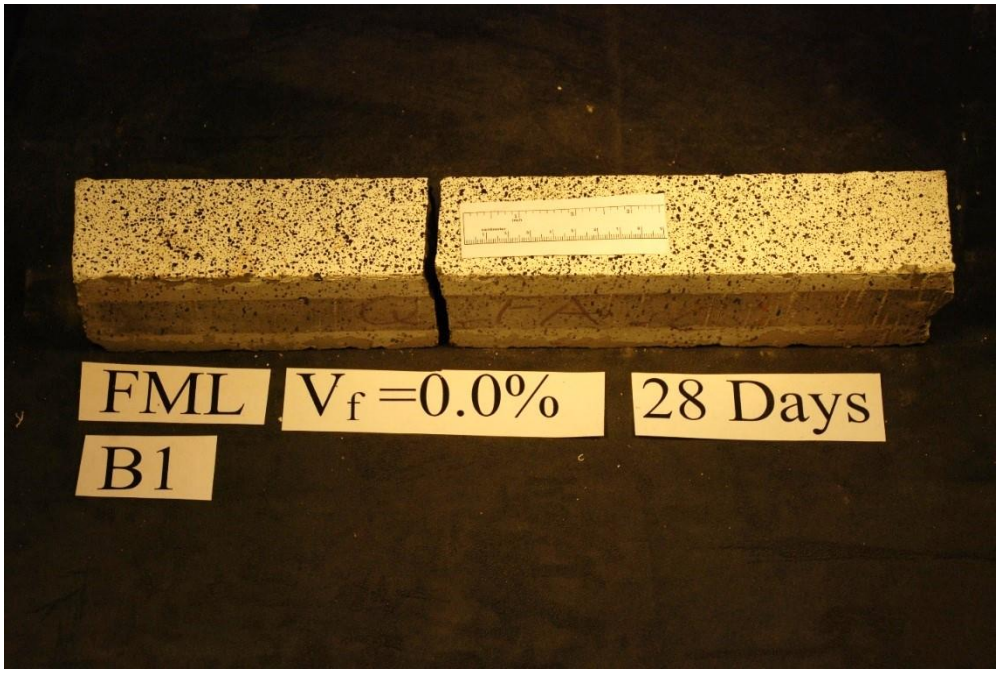

(a)

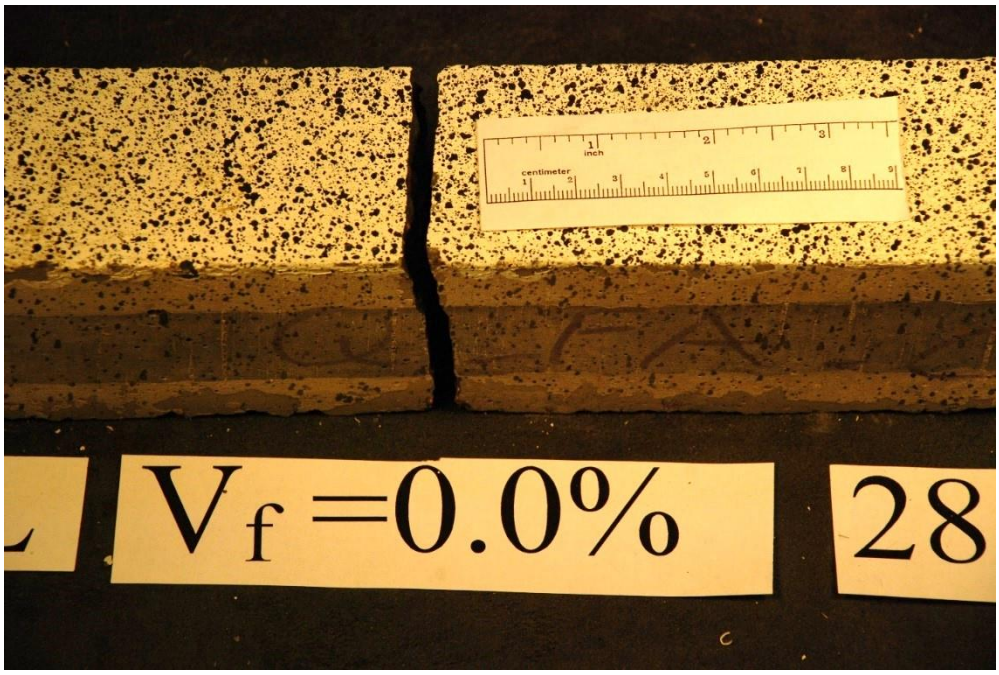

(b)

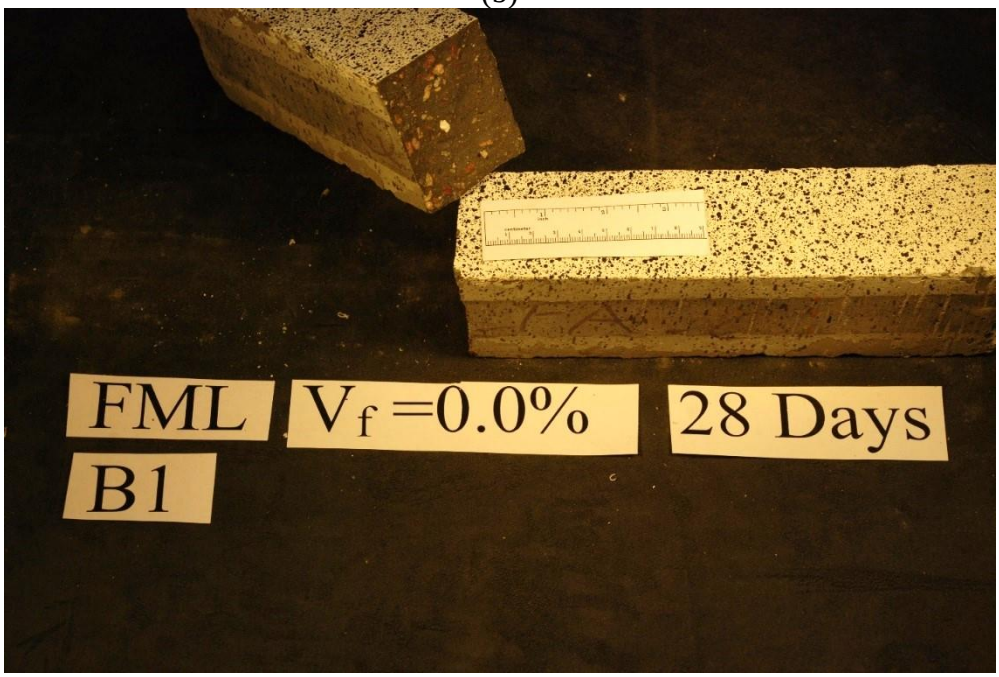

(c)

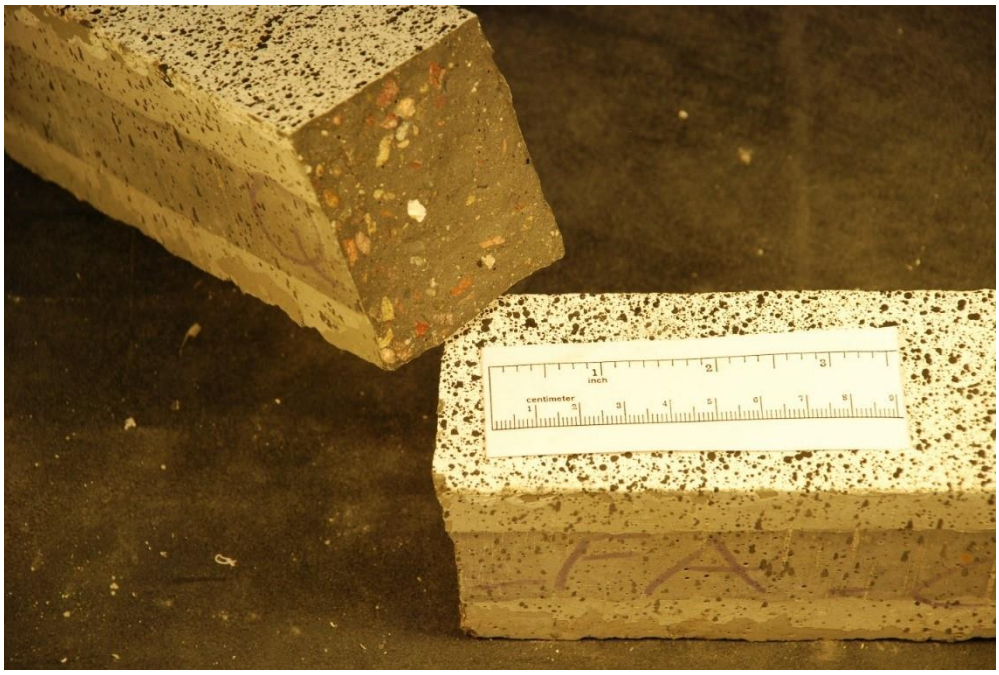

(d)

(e)

Figure A. 32. Small beams 2” x 2.5” x 14”, with 1% fiber content, after 28 days (FML_S_0_28_4PB_C_B1).

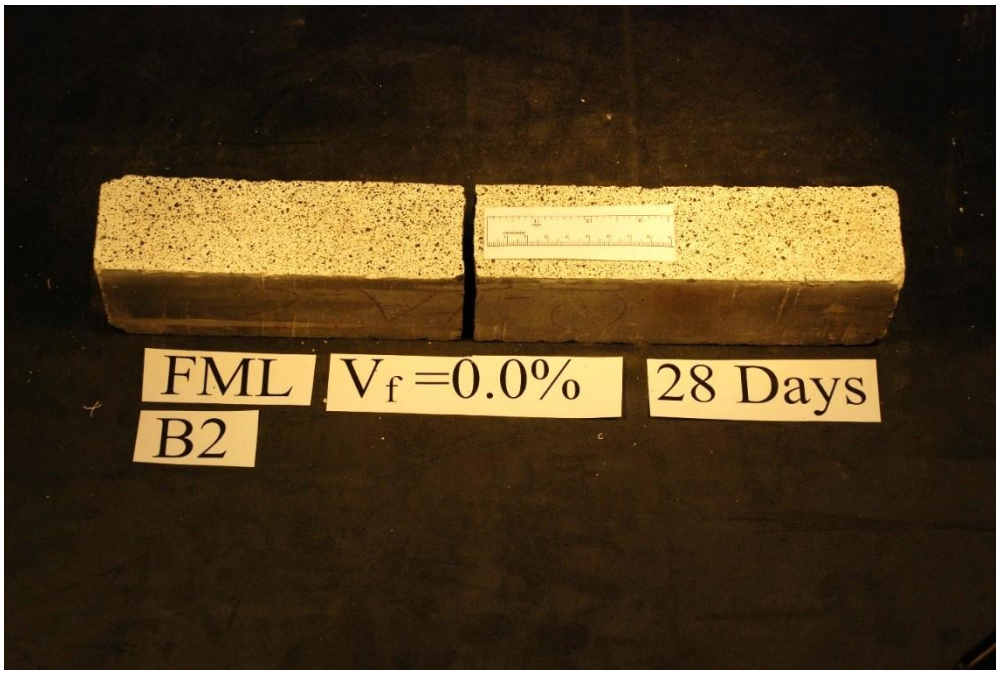

(a)

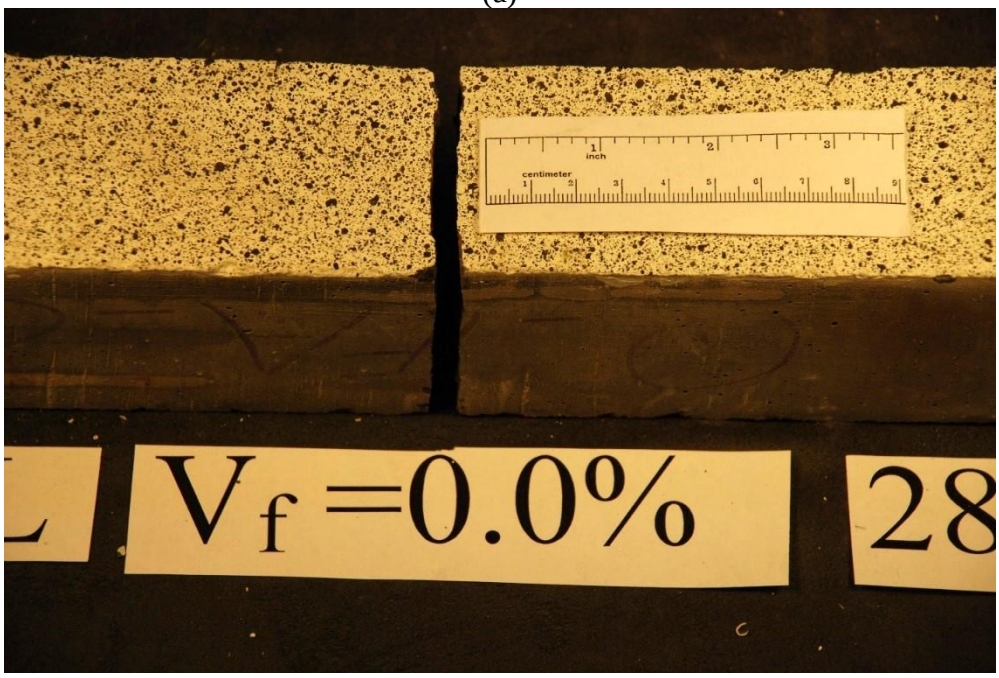

(b)

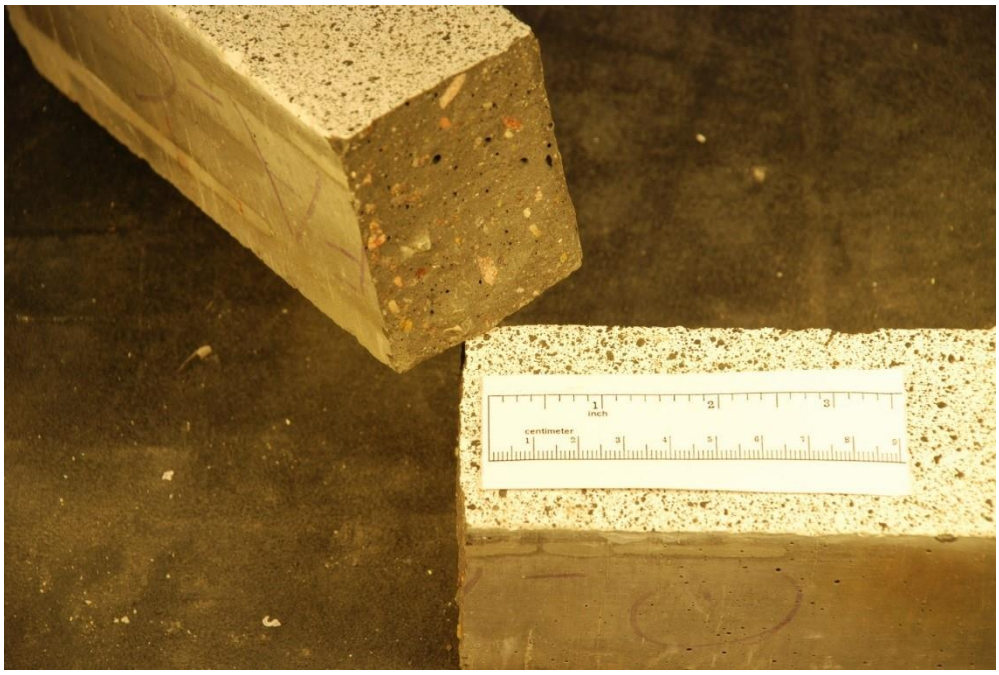

(c)

Figure A. 33. Small beams 2” x 2.5” x 14”, with 1% fiber content, after 28 days (FML_S_0_28_4PB_C_B2).

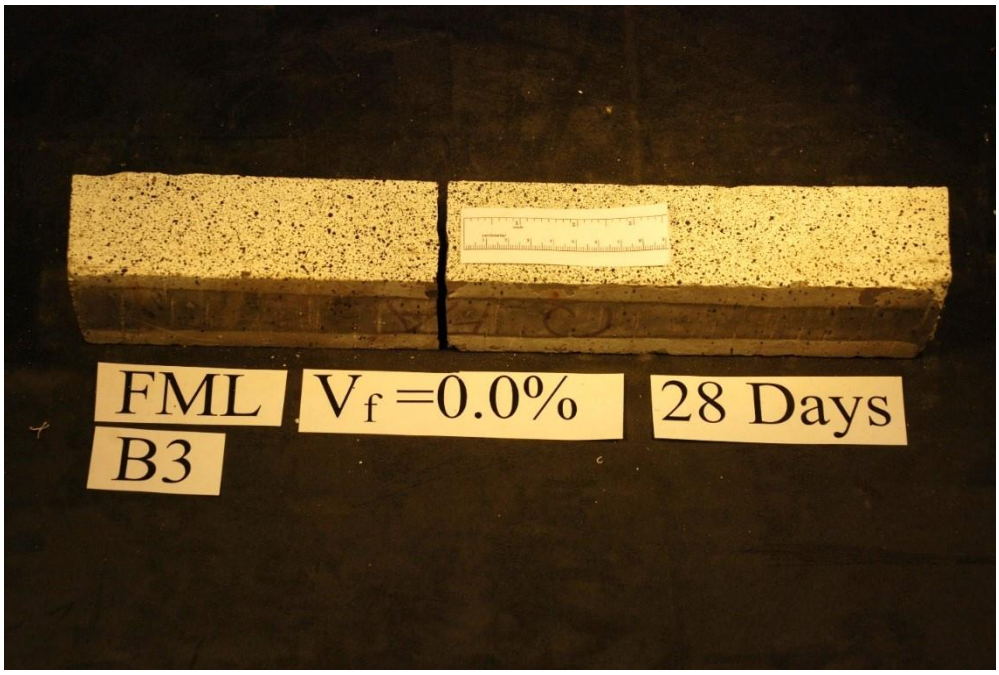

(a)

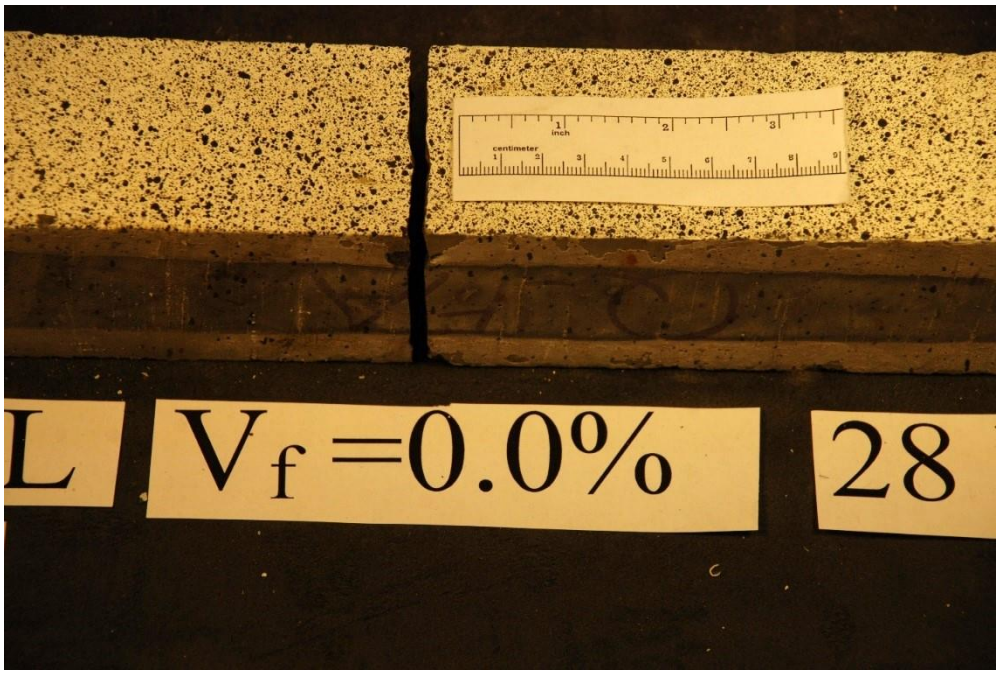

(b)

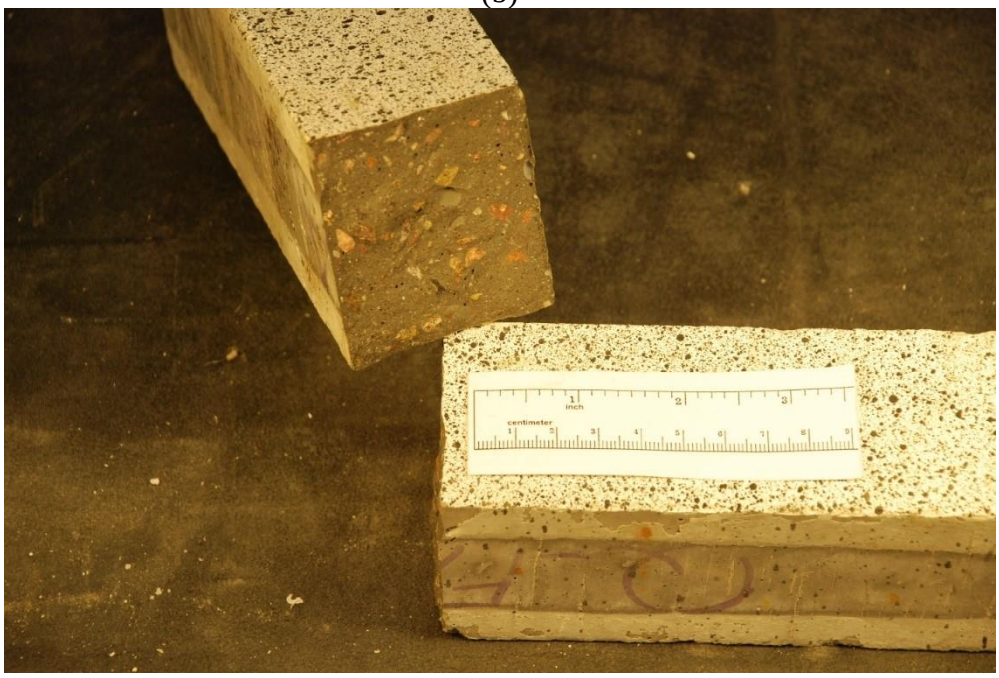

(c)

Figure A. 34. Small beams 2” x 2.5” x 14”, with 1% fiber content, after 28 days (FML_S_0_28_4PB_C_B3).

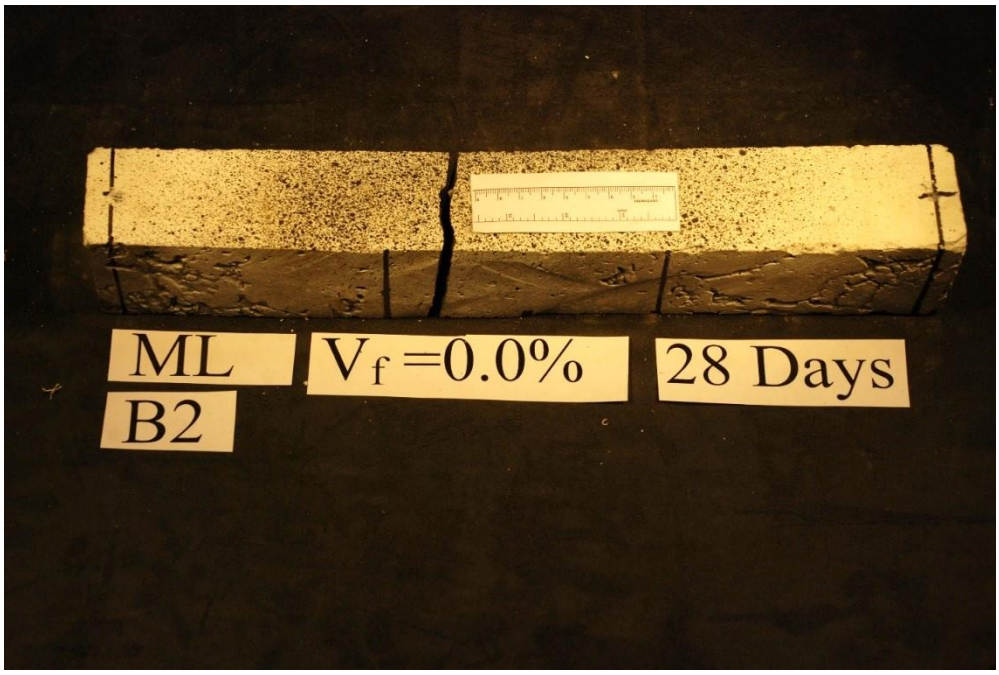

Figure A. 35. Small beams 2” x 2.5” x 14”, with 1% fiber content, after 28 days (ML_S_0_28_4PB_C_B2).

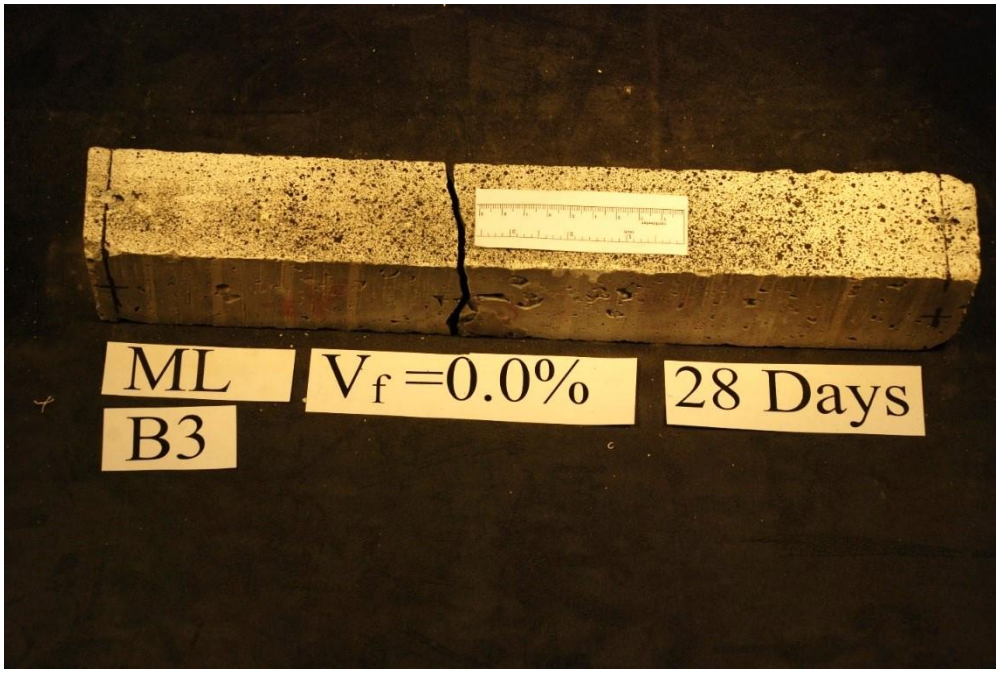

Figure A. 36. Small beams 2” x 2.5” x 14”, with 1% fiber content, after 28 days (ML_S_0_28_4PB_C_B3).

APPENDIX II

BACK-CALCULATIONS

In the following curves (Figure A. 37), the results obtained from the back-calculation process are represented. In this procedure, the material properties of the UHPC are extracted from the 4P-bending test results. Having these parameters enables us to predict the stress-strain diagram for the FRC materials with different properties and use these properties in the future designs using design softwares just by introducing the stress-strain properties to the software, needless to do the experimental tests.

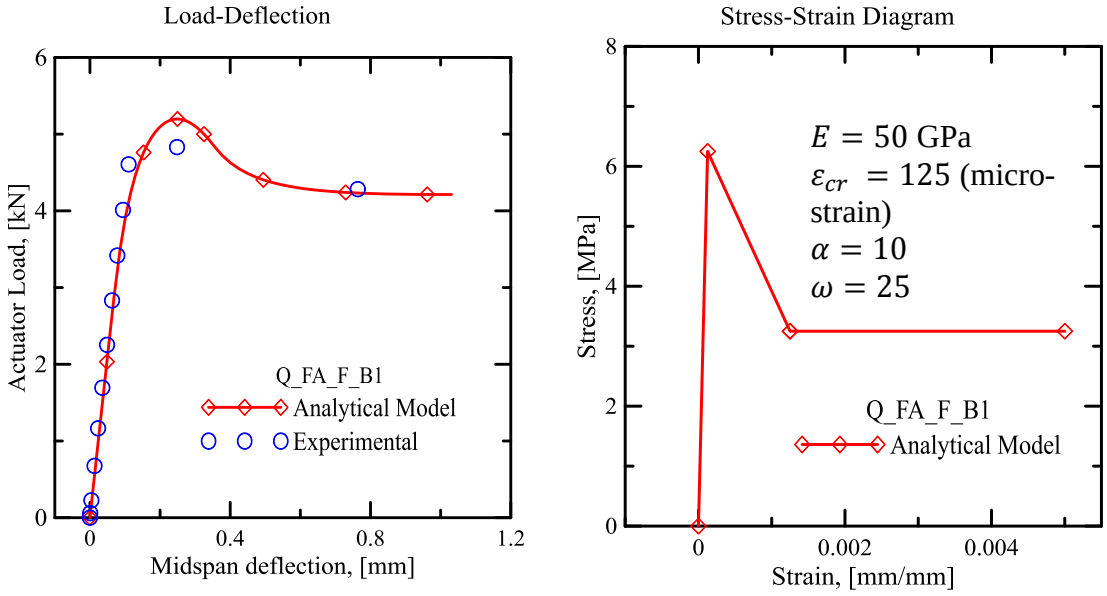

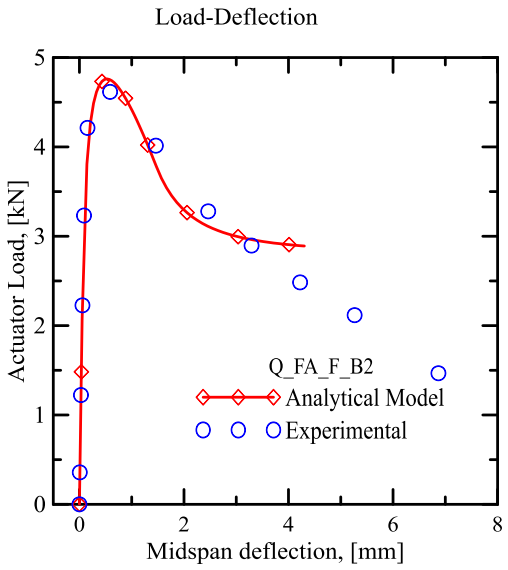
Load-Deflection
Actuator Load, [kN]
Midspan deflection, [mm]
Q_FA_F_B2
Analytical Model
Experimental

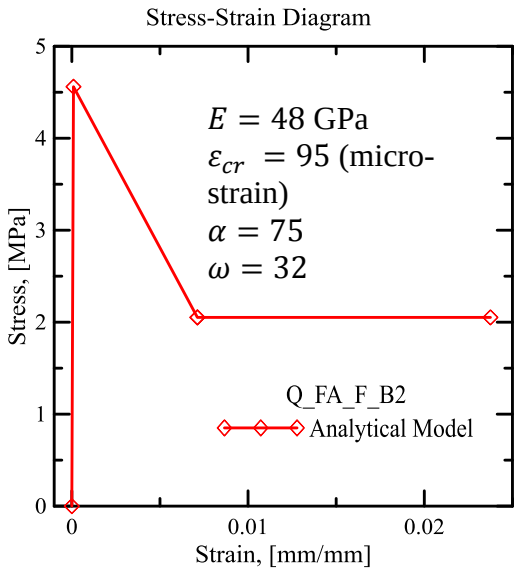
Stress-Strain Diagram
$E = 48$ GPa
$\varepsilon_{cr} = 95$ (micro-strain)
$\alpha = 75$
$\omega = 32$
Stress, [MPa]
Strain, [mm/mm]
Q_FA_F_B2
Analytical Model

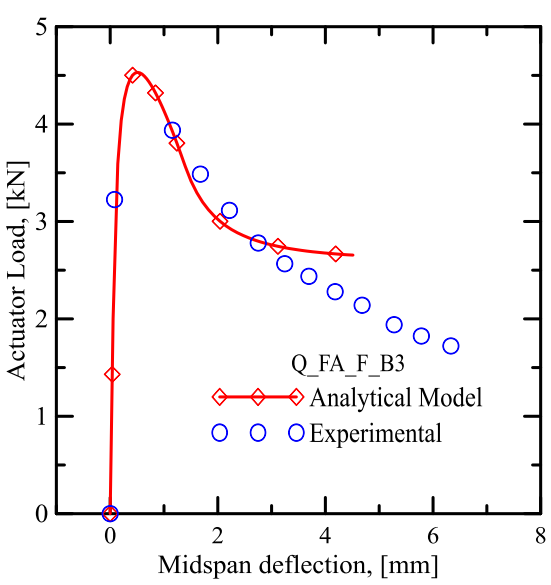
Actuator Load, [kN]
Midspan deflection, [mm]
Q_FA_F_B3
Analytical Model
Experimental

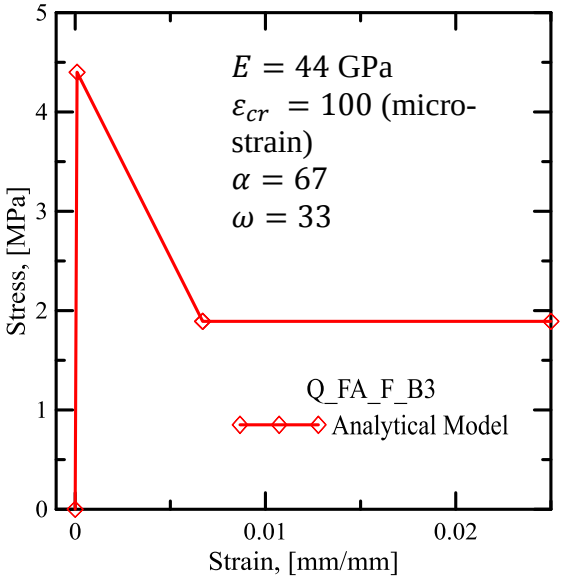
$E = 44$ GPa
$\varepsilon_{cr} = 100$ (micro-strain)
$\alpha = 67$
$\omega = 33$
Stress, [MPa]
Strain, [mm/mm]
Q_FA_F_B3
Analytical Model

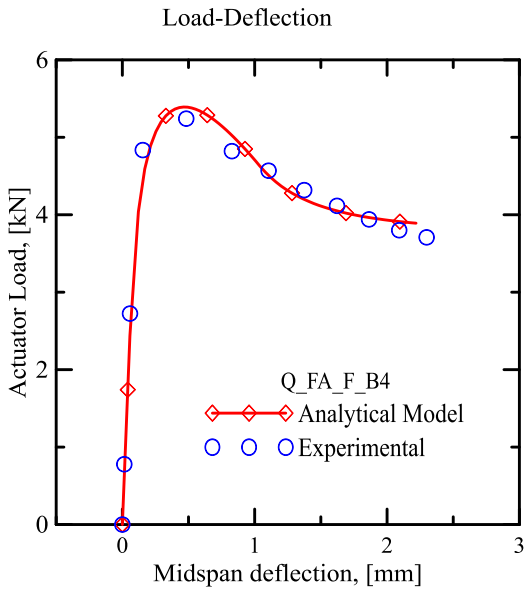
Load-Deflection
Actuator Load, [kN]
Midspan deflection, [mm]
Q_FA_F_B4
Analytical Model
Experimental

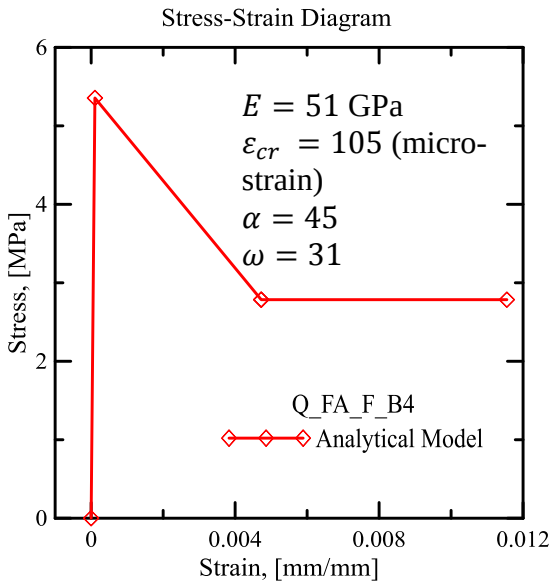
Stress-Strain Diagram
E = 51 GPa
ε_{cr} = 105 (micro-strain)
α = 45
ω = 31
Stress, [MPa]
Strain, [mm/mm]
Q_FA_F_B4
Analytical Model

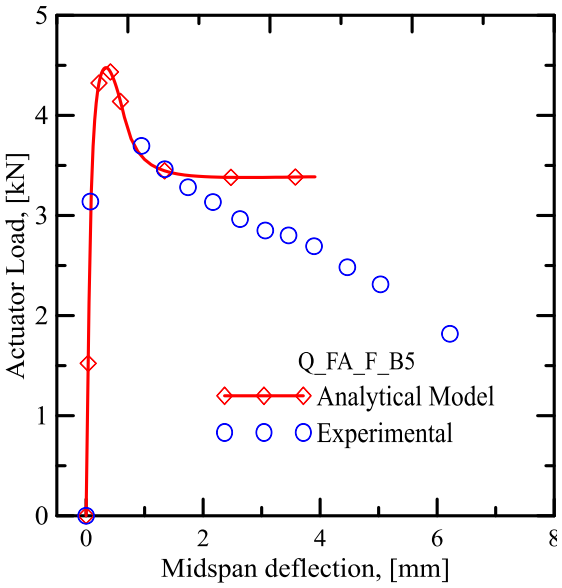
Actuator Load, [kN]
Midspan deflection, [mm]
Q_FA_F_B5
Analytical Model
Experimental

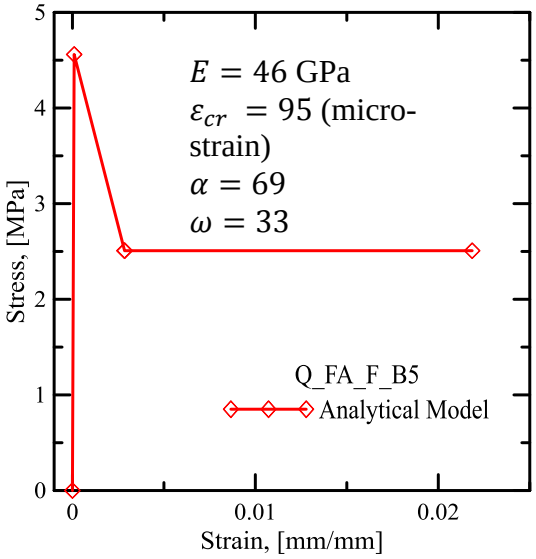
E = 46 GPa
ε_{cr} = 95 (micro-strain)
α = 69
ω = 33
Stress, [MPa]
Strain, [mm/mm]
Q_FA_F_B5
Analytical Model

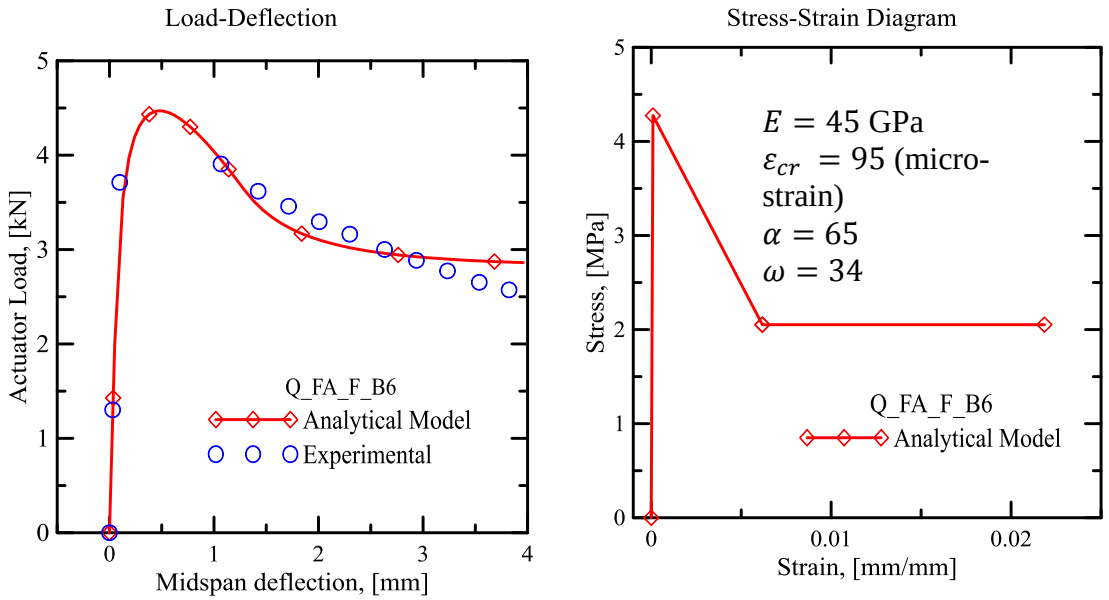

Figure A. 37. Experimental against simulated results for 4P-bendin test (left side) and tensile model (right side) for the UHPC material (Q_FA_F) obtained from test samples 1 to 6, respectively from the top.

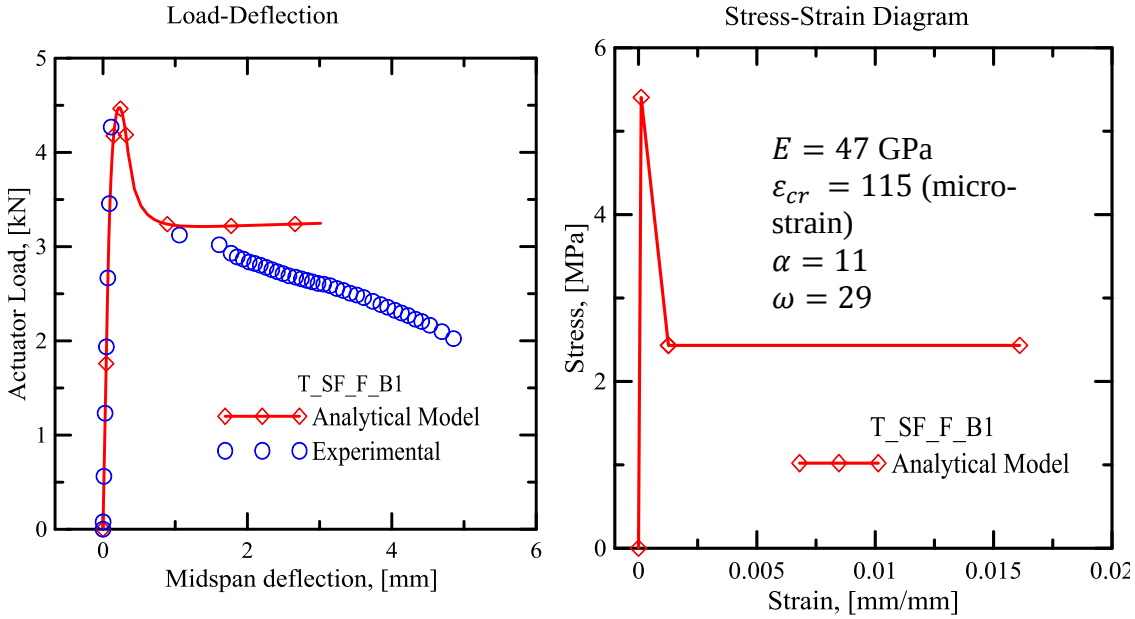

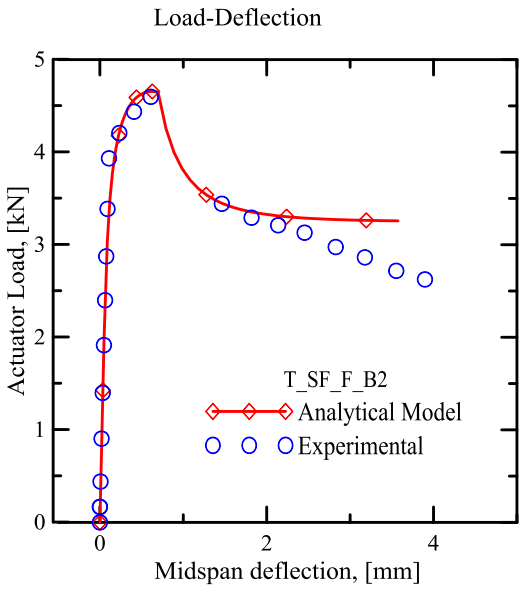
Load-Deflection
Actuator Load, [kN]
Midspan deflection, [mm]
T_SF_F_B2
Analytical Model
Experimental

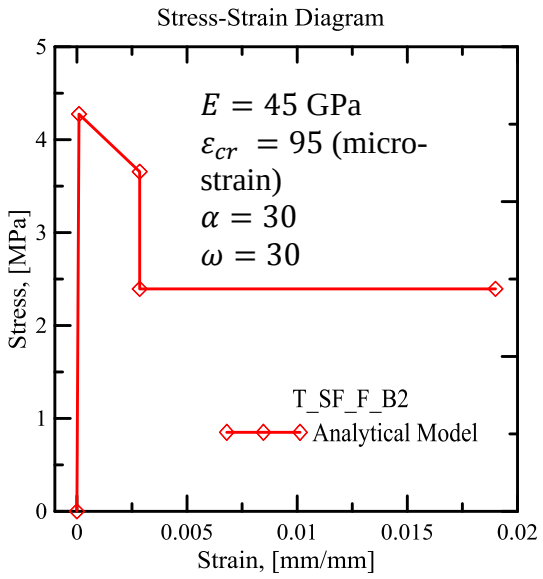
Stress-Strain Diagram
$E = 45$ GPa
$\varepsilon_{cr} = 95$ (micro-strain)
$\alpha = 30$
$\omega = 30$
Stress, [MPa]
Strain, [mm/mm]
T_SF_F_B2
Analytical Model

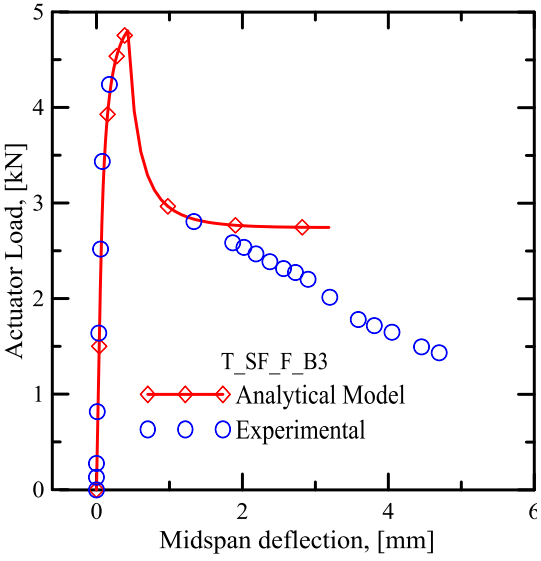
Actuator Load, [kN]
Midspan deflection, [mm]
T_SF_F_B3
Analytical Model
Experimental

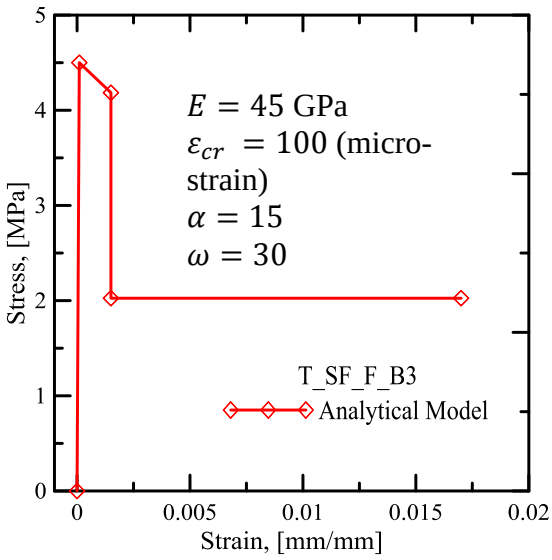
$E = 45$ GPa
$\varepsilon_{cr} = 100$ (micro-strain)
$\alpha = 15$
$\omega = 30$
Stress, [MPa]
Strain, [mm/mm]
T_SF_F_B3
Analytical Model

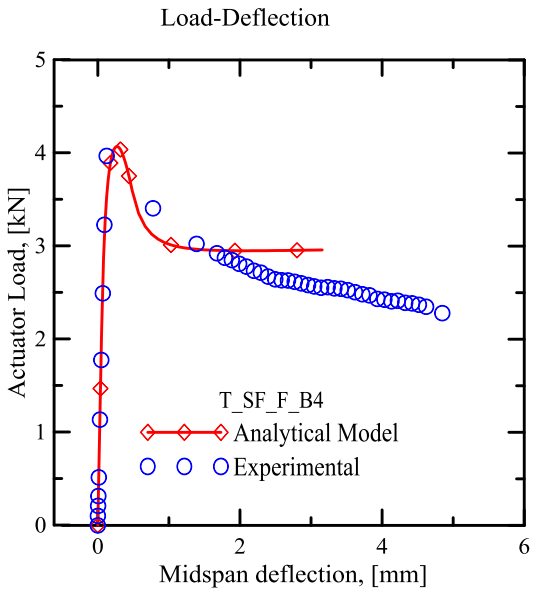
Load-Deflection
Actuator Load, [kN]
Midspan deflection, [mm]
T_SF_F_B4
Analytical Model
Experimental

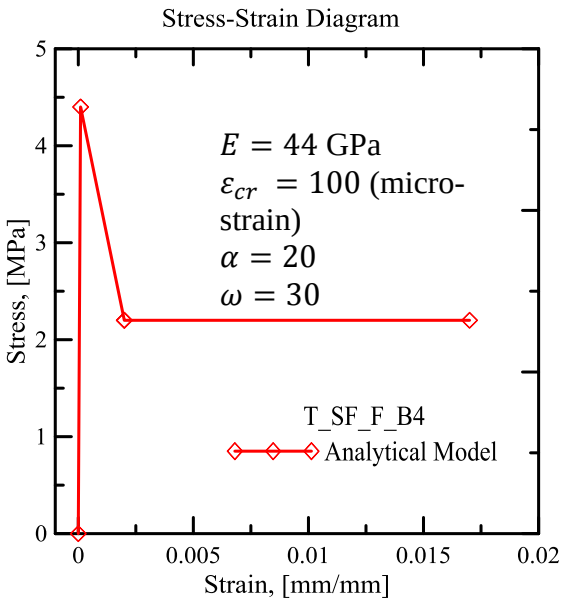
Stress-Strain Diagram
Stress, [MPa]
Strain, [mm/mm]
$E = 44$ GPa
$\varepsilon_{cr} = 100$ (micro-strain)
$\alpha = 20$
$\omega = 30$
T_SF_F_B4
Analytical Model

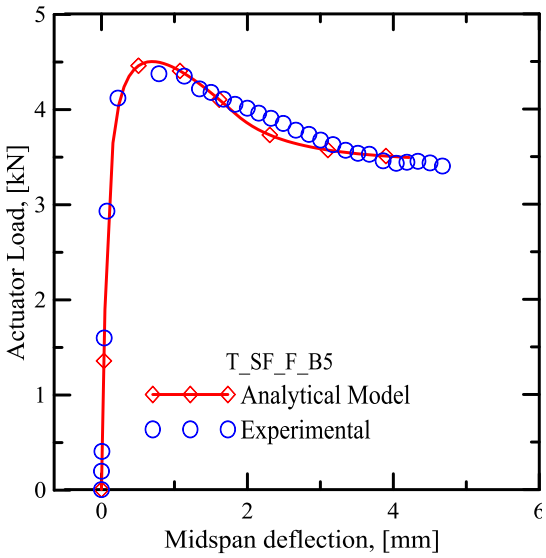
Actuator Load, [kN]
Midspan deflection, [mm]
T_SF_F_B5
Analytical Model
Experimental

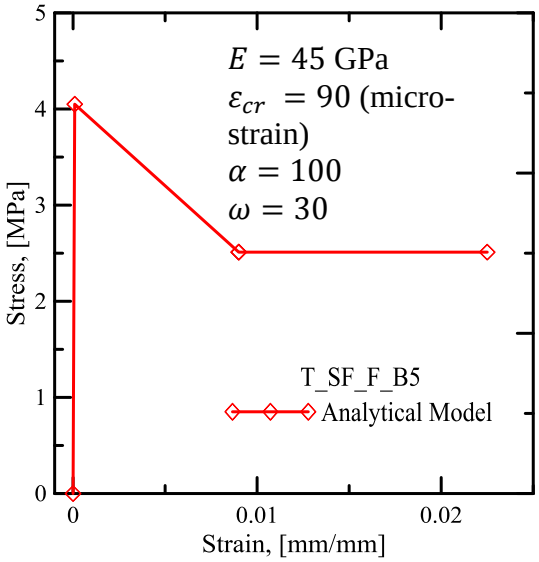
Stress, [MPa]
Strain, [mm/mm]
$E = 45$ GPa
$\varepsilon_{cr} = 90$ (micro-strain)
$\alpha = 100$
$\omega = 30$
T_SF_F_B5
Analytical Model

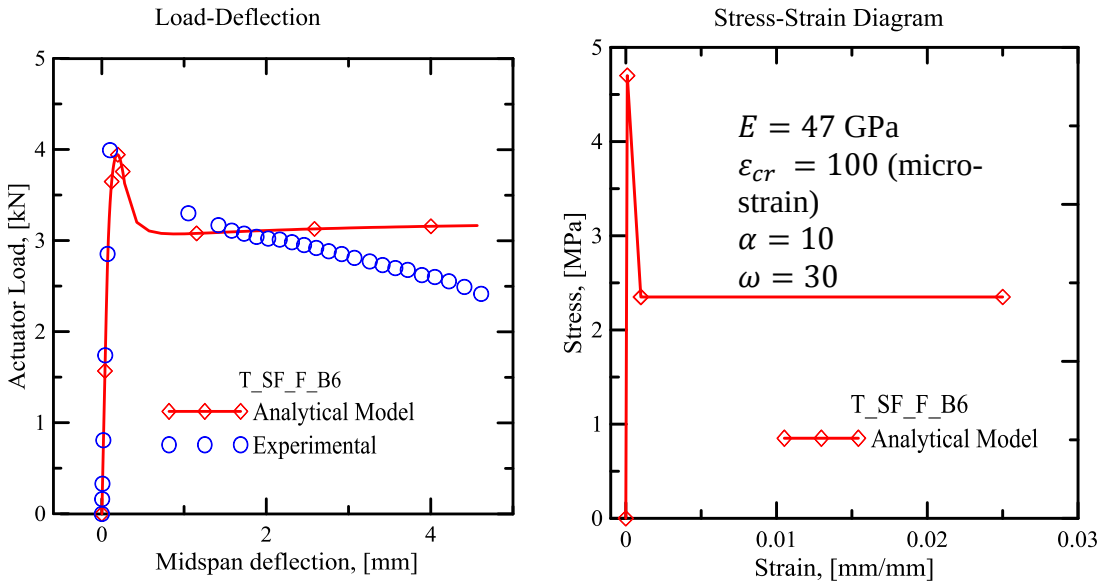

Figure A. 38. Experimental against simulated results for 4P-bendin test (left side) and tensile model (right side) for the UHPC material (T_SF_F) obtained from test samples 1 to 6, respectively from the top.

Summary of back-calculations on hand-mixed samples:

In this section a summary result for all of the six samples is represented.

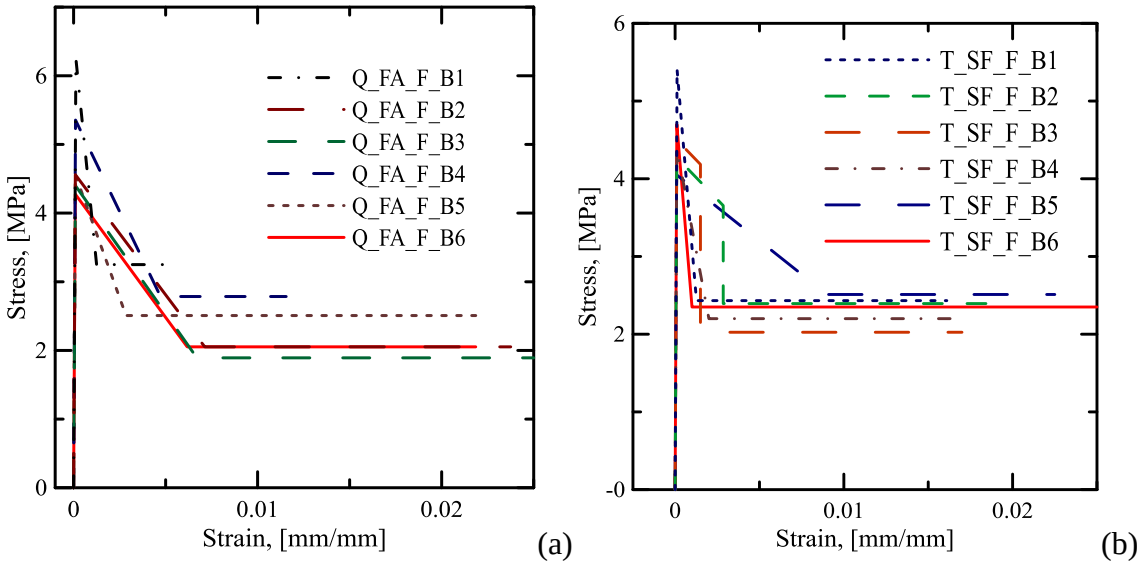

Figure A. 39. Stress-strain diagrams for: (a) Q_FA_F samples; (b) T_SF_F samples.

In this section the results of the back-calculations are represented.

Q_FA_F_C (small beams @ 14 Days):

In the following curves the results obtained from the back-calculation process are represented. In this procedure, the material properties of the UHPC are extracted from the 4P-bending test results. Having these parameters enables us to predict the stress-strain diagram for the FRC materials with different properties and use these properties in the future designs using design softwares just by introducing the stress-strain properties to the software, needless to do the experimental tests.

Figure A. 40 shows the load-deflection curves for the experimental results against analytical simulations (left column) and back-calculated tensile behavior for the FRC material (right column). As is shown, there is a very good agreement between simulated and experimental results. However, the alpha parameter is very sensitive to the post-crack behavior of the sample and is changing greatly as the post-crack response changes. Other parameters show a limited range of variation.

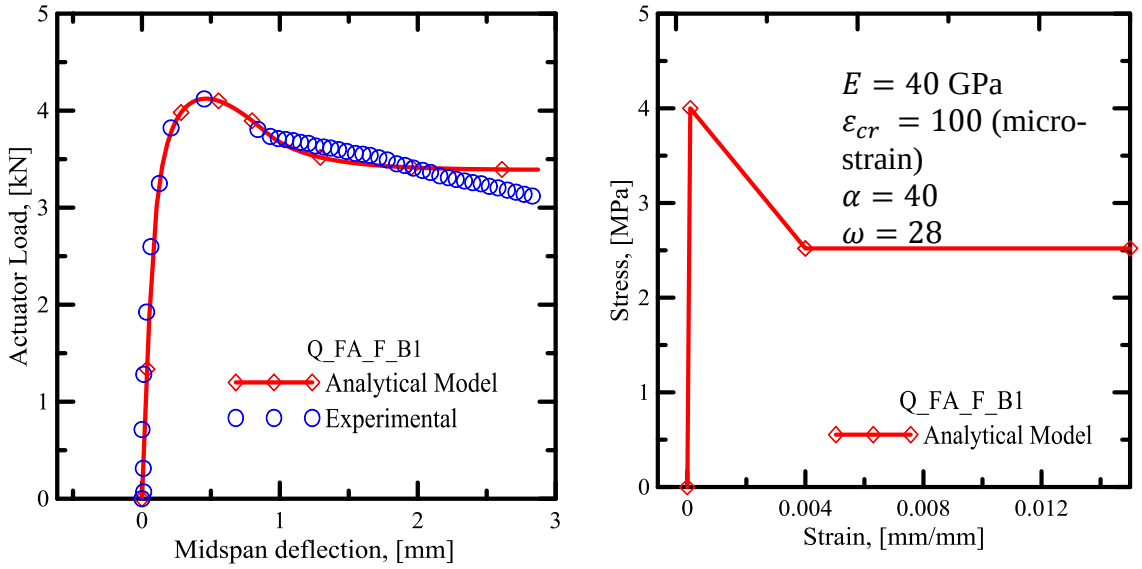

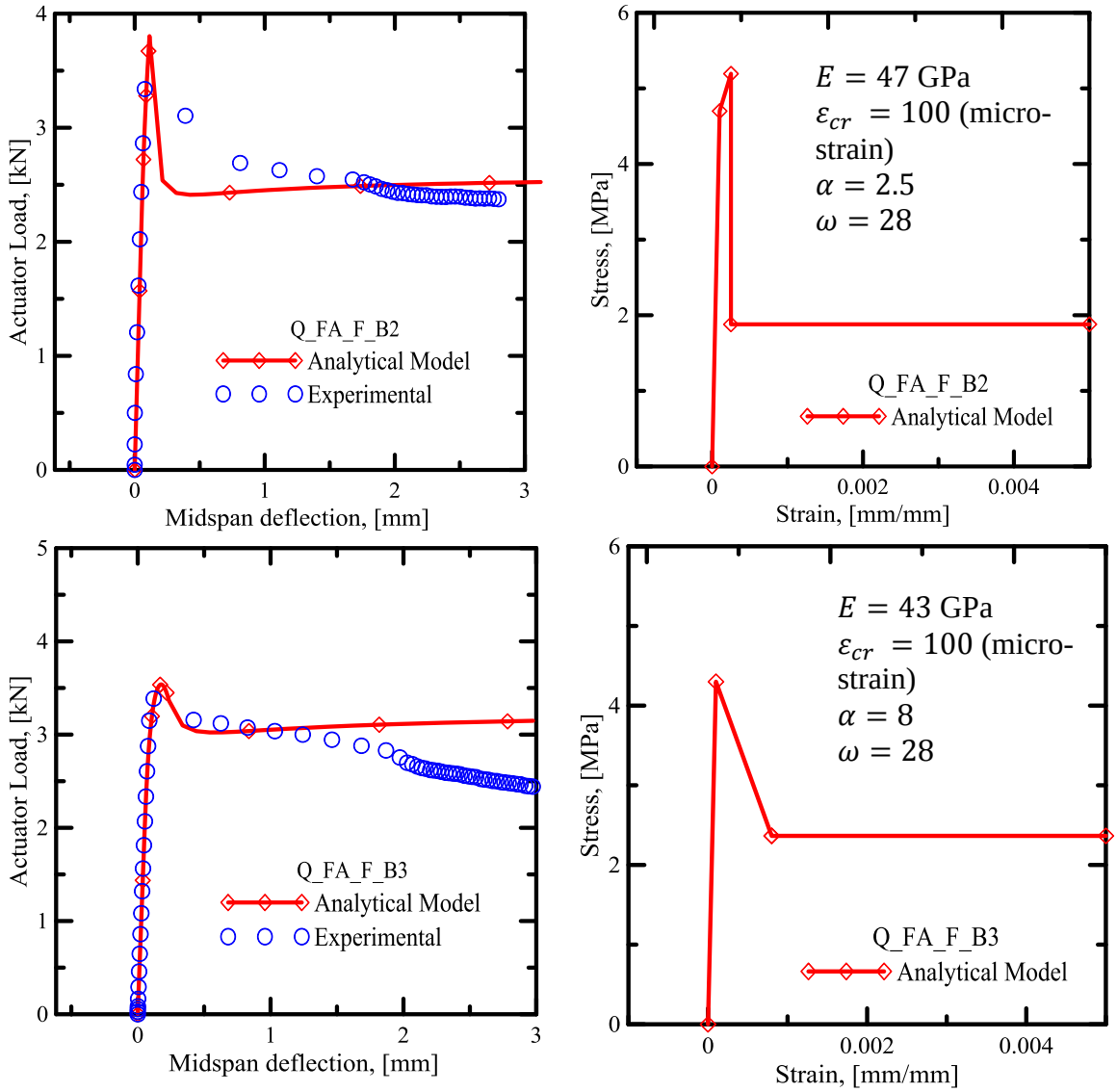

Figure A. 40. Experimental against simulated results for 4P-bendin test (left side) and tensile model (right side) for the UHPC material (Q_FA_F) obtained from the small samples 1 to 3, with 1% of fiber volume fraction at their 14th days, respectively from the top.

Q_FA_F_C (large beams @ 14 Days):

Figure A. 41 shows the load-deflection curves for the experimental results against analytical simulations (left column) and back-calculated tensile behavior for the FRC

material (right column) for the large beam samples tested at their 14th days. As is shown, there is a very good agreement between simulated and experimental results.

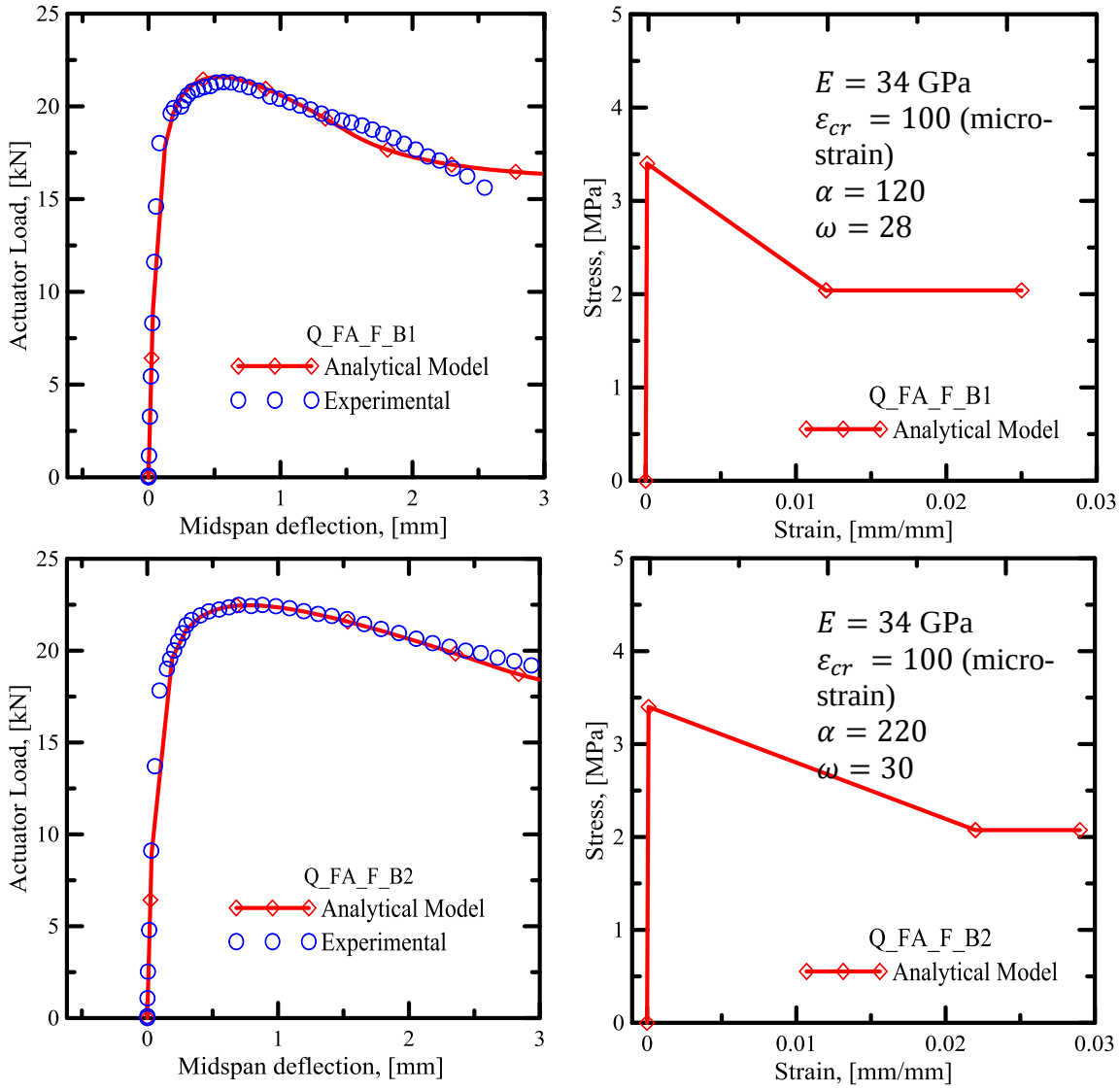

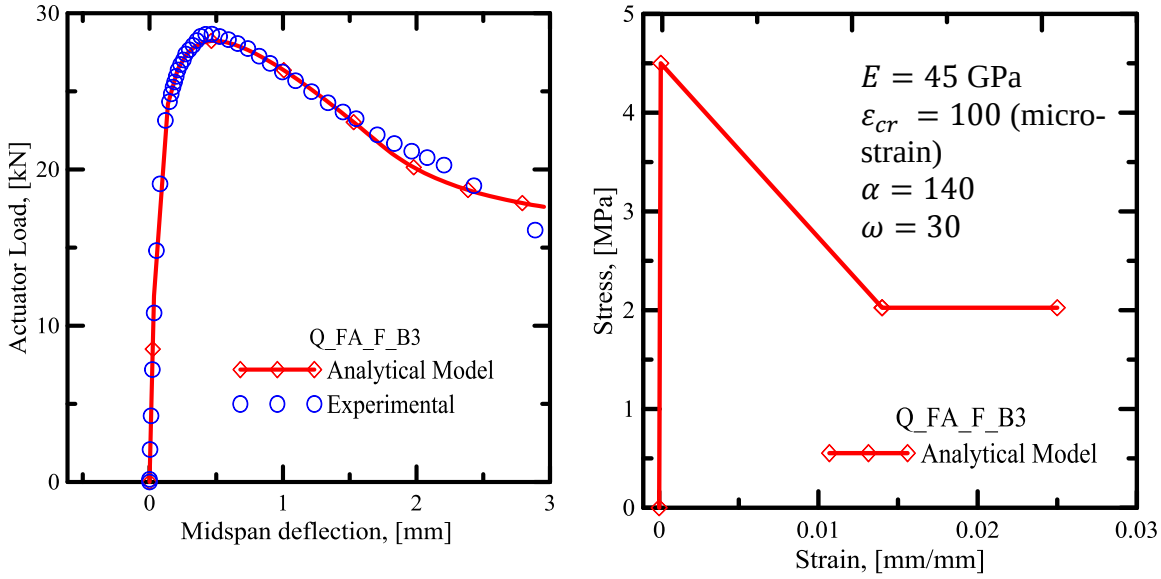

Figure A. 41. Experimental against simulated results for 4P-bendin test (left side) and tensile model (right side) for the UHPC material (Q_FA_F) obtained from the large samples 1 to 3, with 1% of fiber volume fraction at their 14th days, respectively from the top.

Q_FA_F_C (small beams @ 28 Days):

Figure A. 42 shows the load-deflection curves for the experimental results against analytical simulations (left column) and back-calculated tensile behavior for the FRC material (right column) for the small beam samples tested at their 28th days. As is shown, there is a very good agreement between simulated and experimental results.

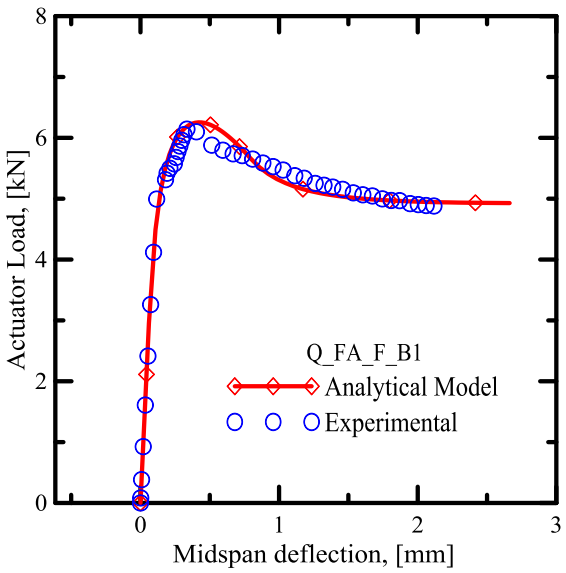
Actuator Load, [kN]
Midspan deflection, [mm]
Q_FA_F_B1
Analytical Model
Experimental

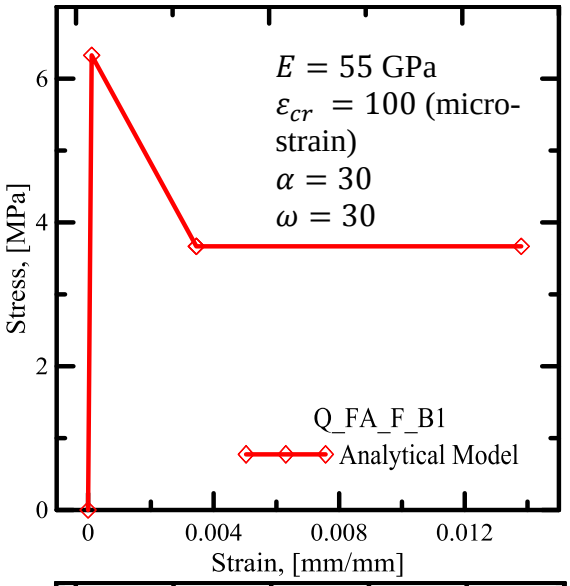
$E = 55$ GPa
$\varepsilon_{cr} = 100$ (micro-strain)
$\alpha = 30$
$\omega = 30$
Stress, [MPa]
Strain, [mm/mm]
Q_FA_F_B1
Analytical Model

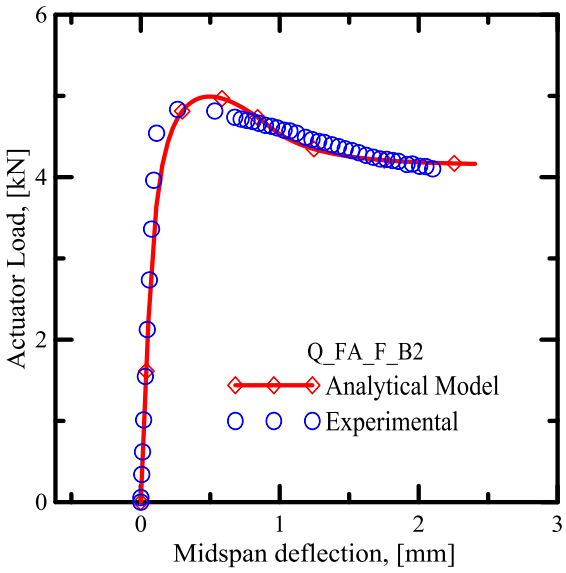
Actuator Load, [kN]
Midspan deflection, [mm]
Q_FA_F_B2
Analytical Model
Experimental

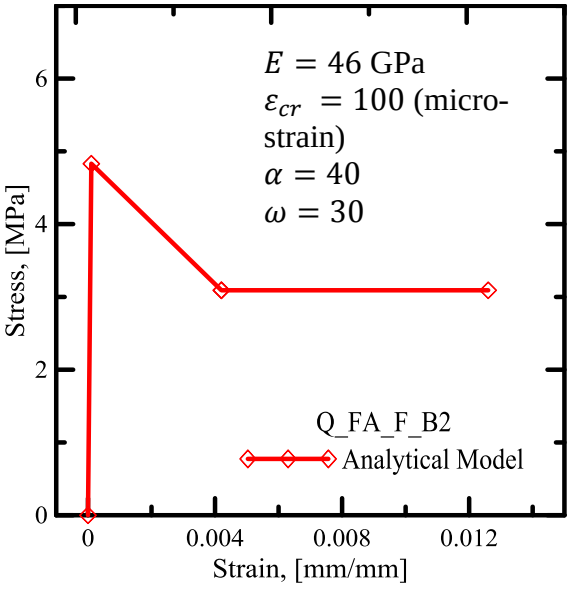
$E = 46$ GPa
$\varepsilon_{cr} = 100$ (micro-strain)
$\alpha = 40$
$\omega = 30$
Stress, [MPa]
Strain, [mm/mm]
Q_FA_F_B2
Analytical Model

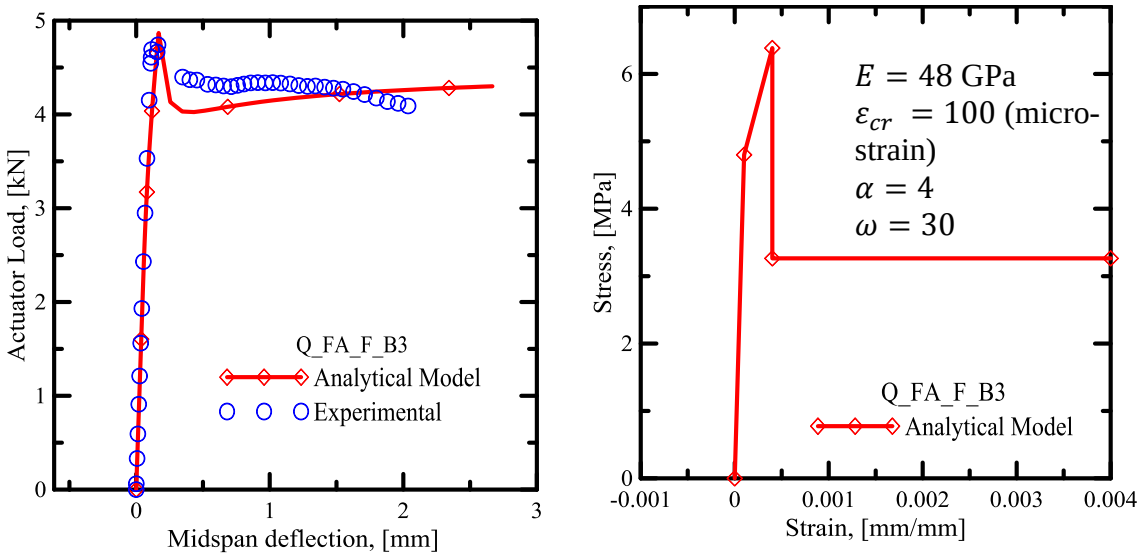

Figure A. 42. Experimental against simulated results for 4P-bendin test (left side) and tensile model (right side) for the UHPC material (Q_FA_F) obtained from the small samples 1 to 3, with 1% of fiber volume fraction at their 28th days, respectively from the top.

Q_FA_F_C (large beams @ 28 Days):

Figure A. 43 shows the load-deflection curves for the experimental results against analytical simulations (left column) and back-calculated tensile behavior for the FRC material (right column) for the large beam samples tested at their 28th days. As is shown, there is a very good agreement between simulated and experimental results.

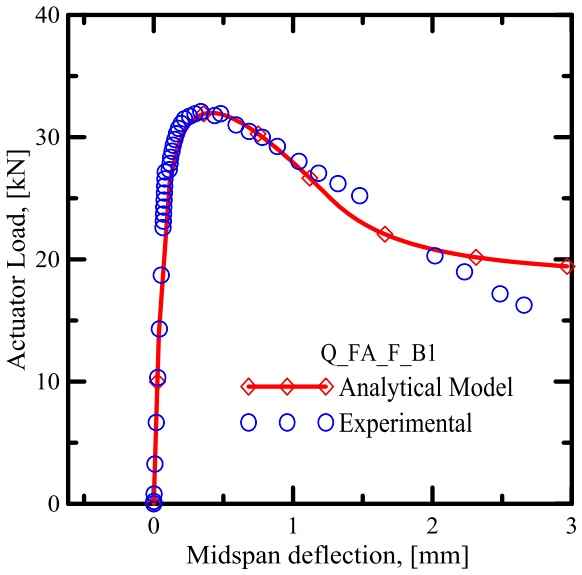
Actuator Load, [kN]
Midspan deflection, [mm]
Q_FA_F_B1
Analytical Model
Experimental

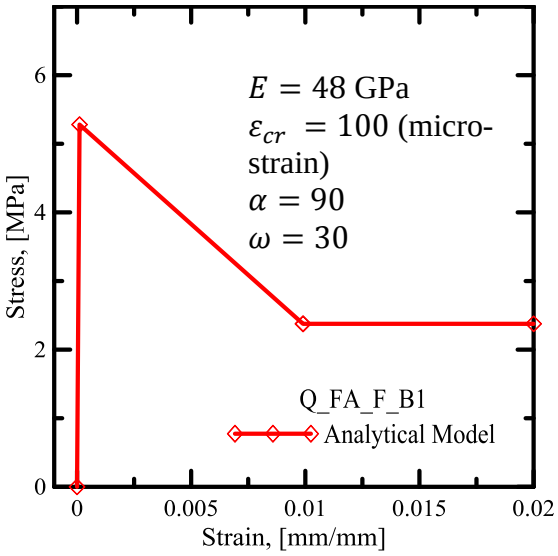
E = 48 GPa
ε_{cr} = 100 (micro-strain)
α = 90
ω = 30
Stress, [MPa]
Strain, [mm/mm]
Q_FA_F_B1
Analytical Model

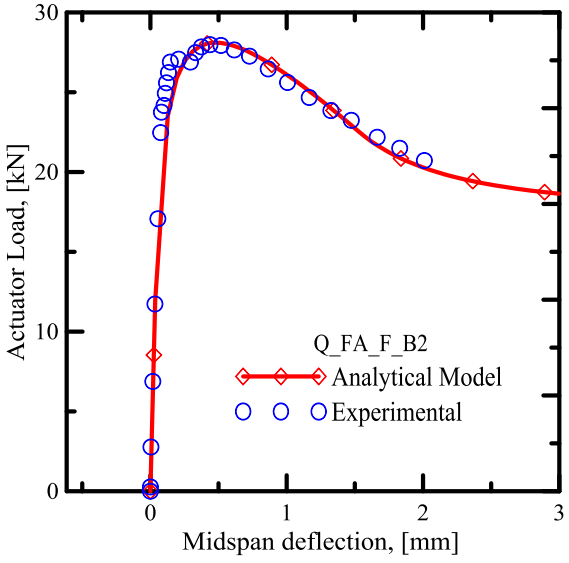
Actuator Load, [kN]
Midspan deflection, [mm]
Q_FA_F_B2
Analytical Model
Experimental

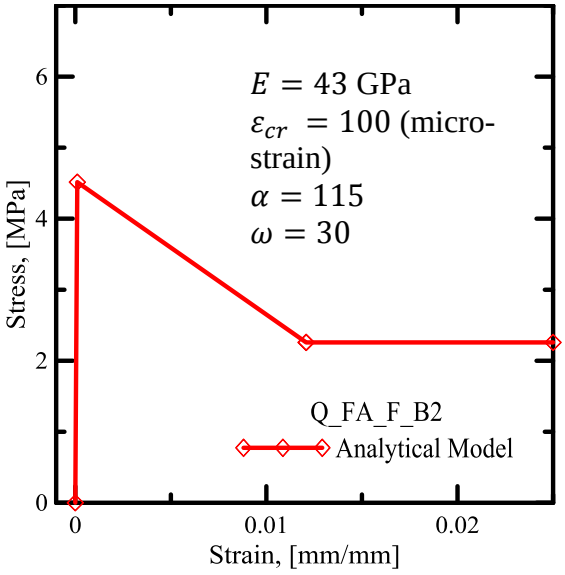
E = 43 GPa
ε_{cr} = 100 (micro-strain)
α = 115
ω = 30
Stress, [MPa]
Strain, [mm/mm]
Q_FA_F_B2
Analytical Model

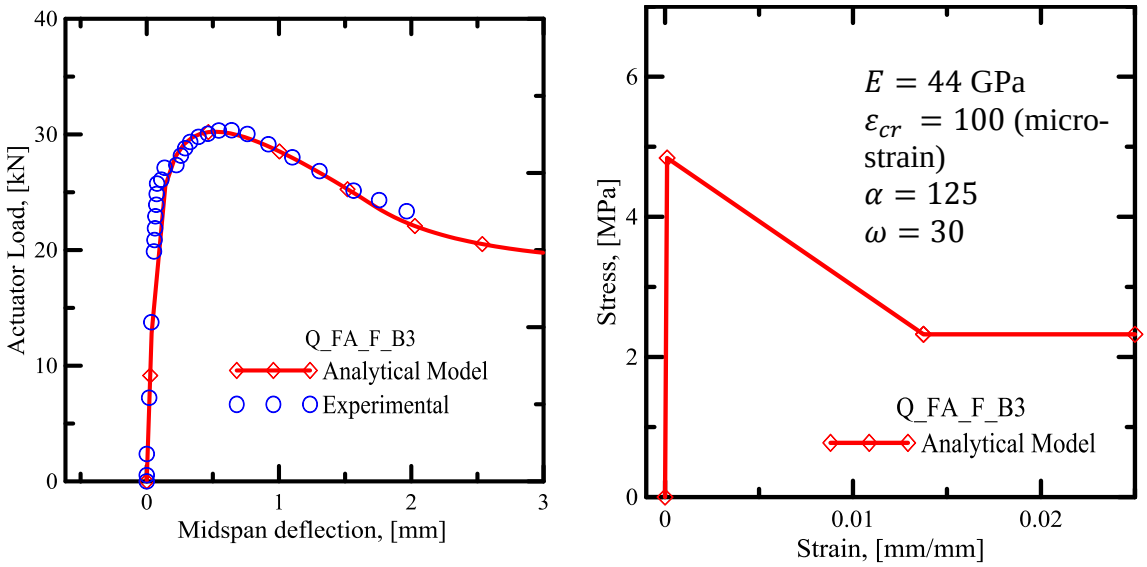

Figure A. 43. Experimental against simulated results for 4P-bendin test (left side) and tensile model (right side) for the UHPC material (Q_FA_F) obtained from the large samples 1 to 3, with 1% of fiber volume fraction at their 28th days, respectively from the top.

Summary of back-calculations on high-shear-mixed samples:

In this section a summary result for all of the six samples is represented.

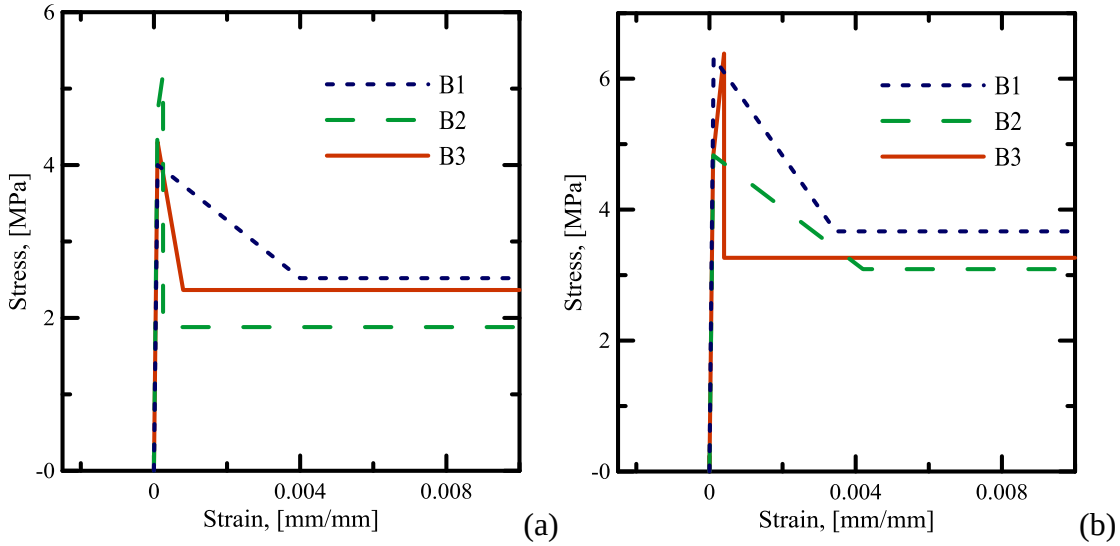

Figure A. 44. Stress-strain diagrams for small beams: (a) 14 days; (b) 28 days.

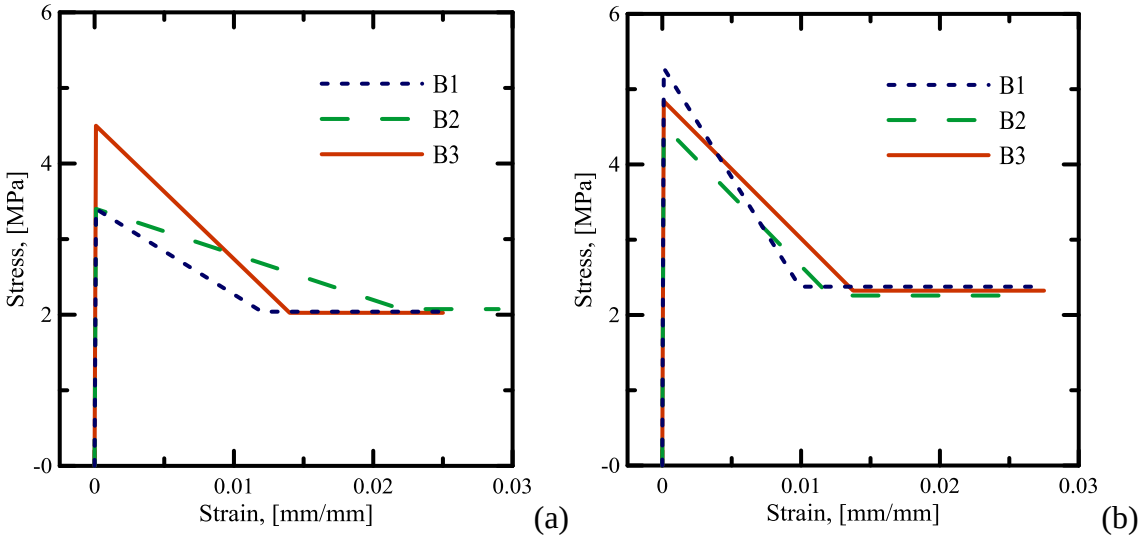

Figure A. 45. Stress-strain diagrams for large beams: (a) 14 days; (b) 28 days.

Back Calculation parameters:

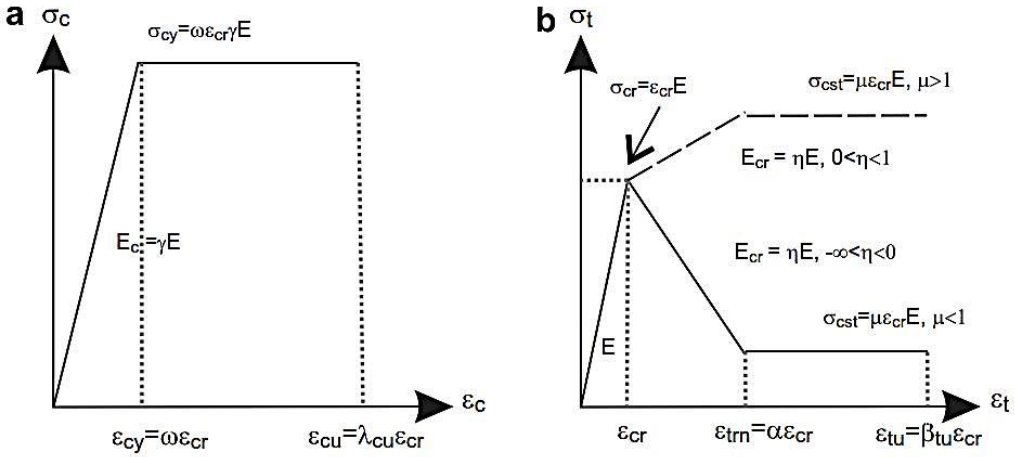

Figure A. 46. Back-calculation parameters: (a) Compressive, (b) Tensile

Table A. 1. Back Calculation parameters for Q_FA_F small samples: (a) 14 days; (b) 28 days.

Sample ID	Elastic Modulus, E (MPa)	Cracking Tensile Strain ε_{cr}	α, Transition Strain/ Cracking Strain	ϒ, Normalized compressive modulus	ω, Normalized Compressive Yield Strain	η, Modulus Ratio	μ, Normalized Residual Tensile Strength	β_{tu}, Normalized Tensile Strain
B1	40000	0.0001	40	1	28	-0.00949	0.63	150
B2	47000	0.0001	2.5	1	28	0.07*	0.4	170
B3	43000	0.0001	8	1	28	-0.06429	0.55	170
Average	43333.33	0.0001	16.83	1.00	28.00	0.00	0.53	163.33
Std. Dev.	3511.88	0	20.25	0.00	0.00	0.07	0.12	11.55
Coef. of Var.	8.10%	0.00%	120.30%	0.00%	0.00%	105.15%	22.17%	7.07%

Sample ID	Elastic Modulus, E (MPa)	Cracking Tensile Strain ε_{cr}	α, Transition Strain/ Cracking Strain	ϒ, Normalized compressive modulus	ω, Normalized Compressive Yield Strain	η, Modulus Ratio	μ, Normalized Residual Tensile Strength	β_{tu}, Normalized Tensile Strain
B1	55000	0.00012	30.0	1.0	30.0	-0.014	0.58	120
B2	46000	0.00011	40.0	1.0	30.0	-0.009	0.64	120
B3	48000	0.00010	4.0	1.0	30.0	0.110*	0.68	140
Average	49667	0.00011	24.7	1.0	30.0	-0.012	0.63	127
Std. Dev.	4726	0.00001	18.6	0.0	0.0	0.004	0.05	12
Coef. of Var.	9.52%	7.16%	75.34%	0.00%	0.00%	31.31%	7.95%	9.12%

*The parameter values for Q_FA_F_B1 sample caused an unacceptable increase in standard deviation, therefore these values are not considered for the statistical calculations.

Table A. 2. Back Calculation parameters for Q_FA_F large samples: (a) 14 days; (b) 28 days.

Sample ID	Elastic Modulus, E (MPa)	Cracking Tensile Strain ε_{cr}	α, Transition Strain/ Cracking Strain	ϒ, Normalized compressive modulus	ω, Normalized Compressive Yield Strain	η, Modulus Ratio	μ, Normalized Residual Tensile Strength	β_{tu}, Normalized Tensile Strain
B1	34000	0.00010	120.0	1.0	28.0	-0.003	0.60	250
B2	34000	0.00010	220.0	1.0	30.0	-0.002	0.61	290
B3	45000	0.00010	140.0	1.0	30.0	-0.004	0.45	250
Average	37667	0.00010	160.0	1.0	29.3	-0.003	0.55	263
Std. Dev.	6351	0.00000	52.9	0.0	1.2	0.001	0.09	23
Coef. of Var.	16.86%	0.00%	33.07%	0.00%	3.94%	37.07%	16.20%	8.77%

Sample ID	Elastic Modulus, E (MPa)	Cracking Tensile Strain ε_{cr}	α, Transition Strain/ Cracking Strain	ϒ, Normalized compressive modulus	ω, Normalized Compressive Yield Strain	η, Modulus Ratio	μ, Normalized Residual Tensile Strength	β_{tu}, Normalized Tensile Strain
B1	48000	0.00011	90.0	1.0	30.0	-0.006	0.45	250
B2	43000	0.00011	115.0	1.0	30.0	-0.004	0.50	250
B3	44000	0.00011	125.0	1.0	30.0	-0.004	0.48	250
Average	45000	0.00011	110.0	1.0	30.0	-0.005	0.48	250
Std. Dev.	2646	0.00000	18.0	0.0	0.0	0.001	0.03	0
Coef. of Var.	5.88%	2.66%	16.39%	0.00%	0.00%	22.26%	5.28%	0.00%

APPENDIX III

DIC ANALYSIS

The results for the DIC are presented here. As it was mentioned in section 4, using DIC method the access to a full-field deformation is provided. However, these captured movements inherently, reflect not only the movement of the beam itself, but also the movement due to the leaping in the fixtures, supports, testing machine deformations, etc. To eliminate the effect of these type of deformations and calculating the original movement in the beam itself there are some methods which are briefly discussed here.

One of the algorithms which can be used, is called rigid body filter. This method calculates the average movement of the total area of interest (AOI) and then subtract the movement at a specific point inside the AOI from the average to achieve the relative movement of that point. The theory behind this approach is the assumption that the average movement of the AOI is an index of rigid body movement due to the support movement, leaping in the fixtures, machine deformations and so forth. This method was used in section 4 to calculate the mid-span deflection.

Another approach, is to consider one point as the reference point and then calculate the deformations at the specific points, by subtracting their movement from the reference point. The weak-point of one reference point is that it cannot capture the rotation of the sample. However, it is still possible to increase the number of reference points to have a more accurate rigid body motion including displacements and rotations. Therefore, a full field view from all over the sample during the tests and DIC procedure is highly recommended to have the best options for choosing as the reference points.

In this section, three-point rigid body is chosen as the rigid-body movement algorithm to eliminate the rigid-body movement of the sample during the DIC procedure. These three points are chosen in a way to be as close as possible to the neutral axis at the supports (see Figure 25). It is suggested that these three points be chosen from both side of the sample (i.e. support locations) to be able to capture the rotation of the sample due to the unequal vertical movement at the supports. By taking this course of action, there will be three points which will move such that they are located on a rigid surface, without any relative movement to each other. However, the movement for other points on the AOI can be captured and subtracted from this rigid body movement to have an accurate deformation for the sample.

It is to mention that the selection of the points is completely depend on the sample geometry, supports (boundary conditions) and the parameters which are to be calculated. For example if the movement along the axis is to be captured, it would be better to choose the reference points from one side of the sample. However, this is only affecting the results of the movements and deformations but not strains. Strain is independent from rigid movement.

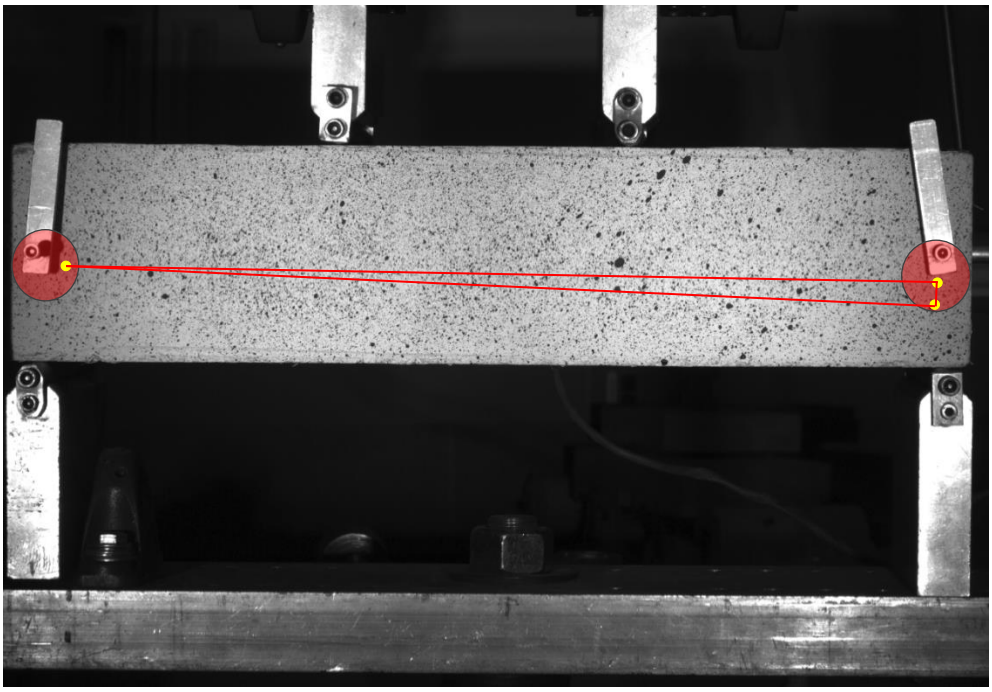

Figure A. 47. Three-point reference for rigid body movement of the sample.

Q_FA_F_C (small beams @ 14 Days):

The first sample (QSB1-1):

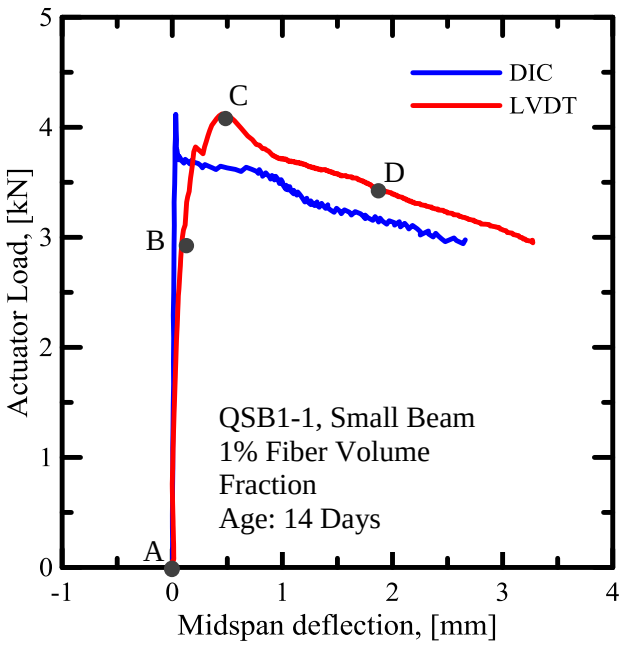

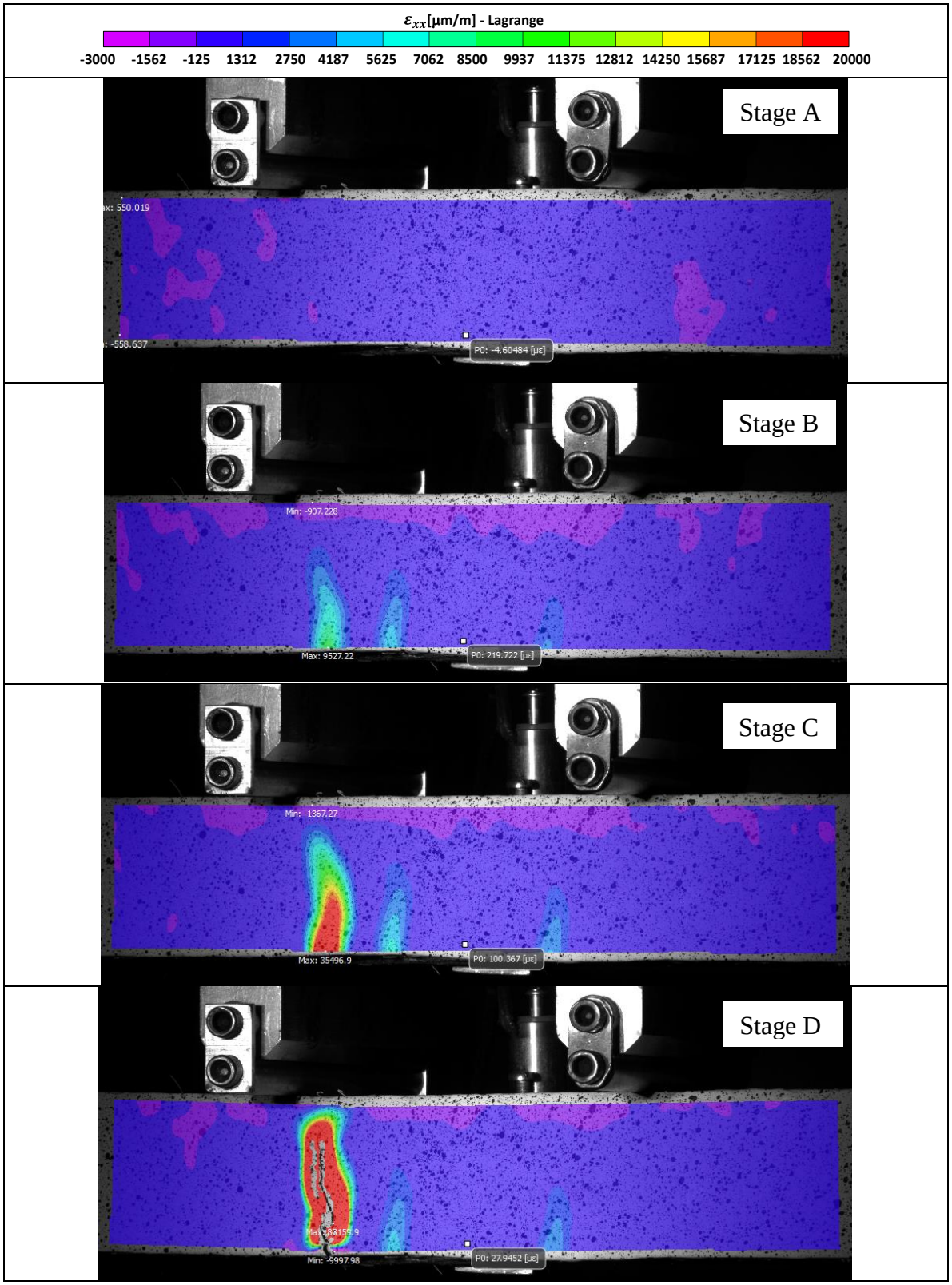
ε_{xx}[μm/m] - Lagrange
-3000 -1562 -125 1312 2750 4187 5625 7062 8500 9937 11375 12812 14250 15687 17125 18562 20000
Stage A
Stage B
Stage C
Stage D

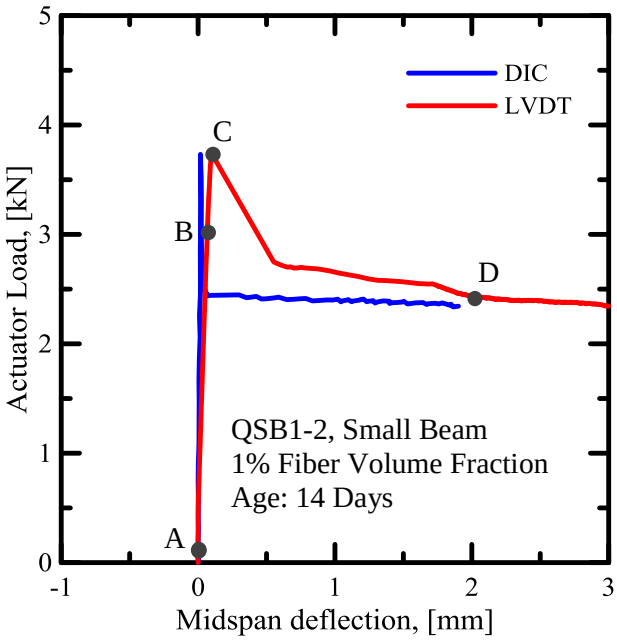
DIC
LVDT
C
B
D
A
QSB1-2, Small Beam
1% Fiber Volume Fraction
Age: 14 Days
Actuator Load, [kN]
Midspan deflection, [mm]
0
1
2
3
4
5
-1
0
1
2
3

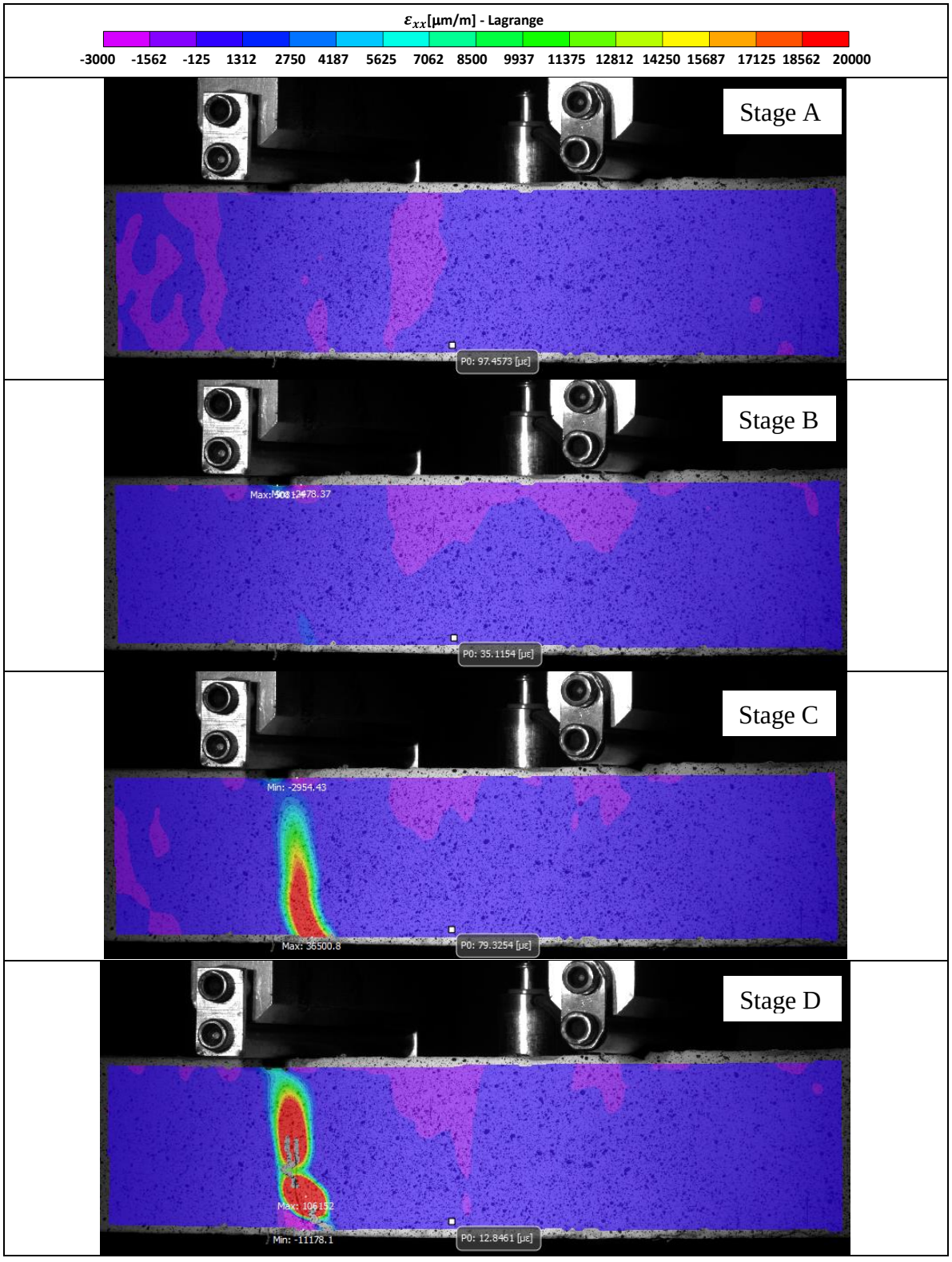
ε_{xx}[µm/m] - Lagrange
-3000 -1562 -125 1312 2750 4187 5625 7062 8500 9937 11375 12812 14250 15687 17125 18562 20000
Stage A
P0: 97.4573 [με]
Stage B
Max: 12478.37
P0: 35.1154 [με]
Stage C
Min: -2954.43
Max: 38500.8
P0: 79.3254 [με]
Stage D
Max: 106152
Min: -11178.1
P0: 12.8461 [με]

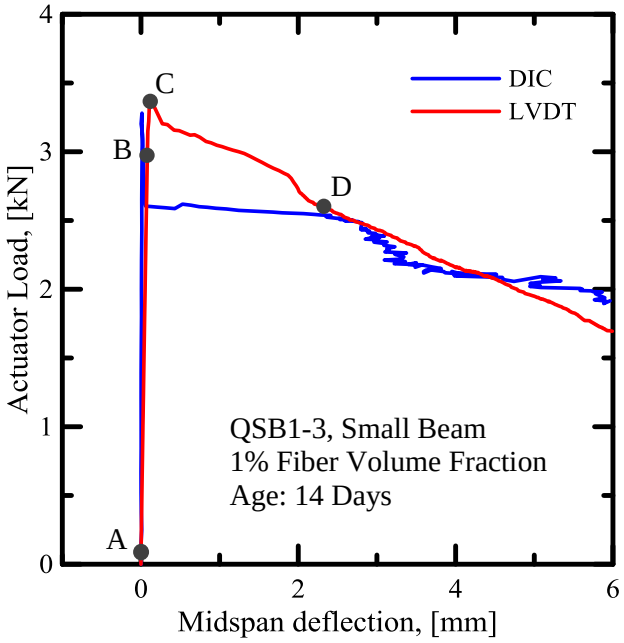
DIC
LVDT
A
B
C
D
QSB1-3, Small Beam
1% Fiber Volume Fraction
Age: 14 Days
Actuator Load, [kN]
Midspan deflection, [mm]
0
1
2
3
4
0
2
4
6

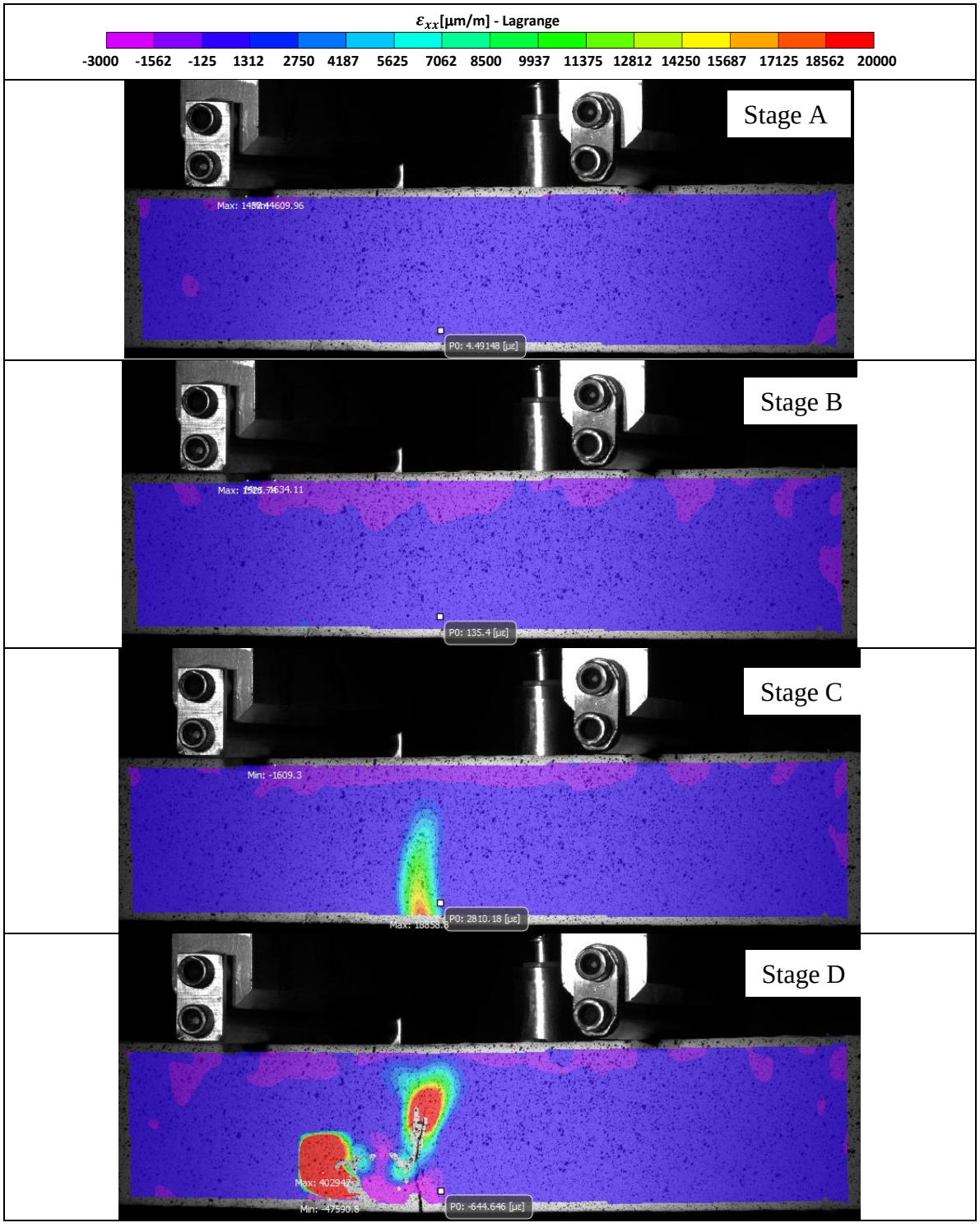
ε_{xx}[µm/m] - Lagrange
-3000 -1562 -125 1312 2750 4187 5625 7062 8500 9937 11375 12812 14250 15687 17125 18562 20000
Stage A
Max: 14609.96
P0: 4.49148 [µε]
Stage B
Max: 1634.11
P0: 135.4 [µε]
Stage C
Min: -1609.3
Max: 18858.6
P0: 2810.18 [µε]
Stage D
Max: 402942
Min: -47590.8
P0: -644.646 [µε]

Q_FA_F_C (large beams @ 14 Days):

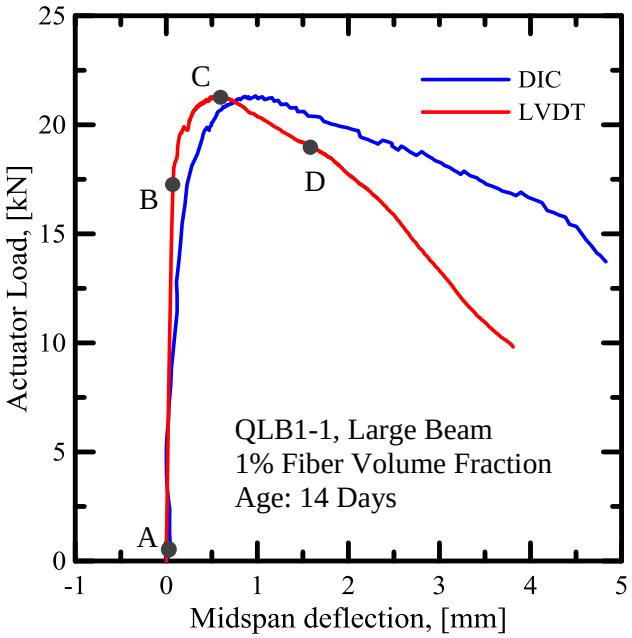

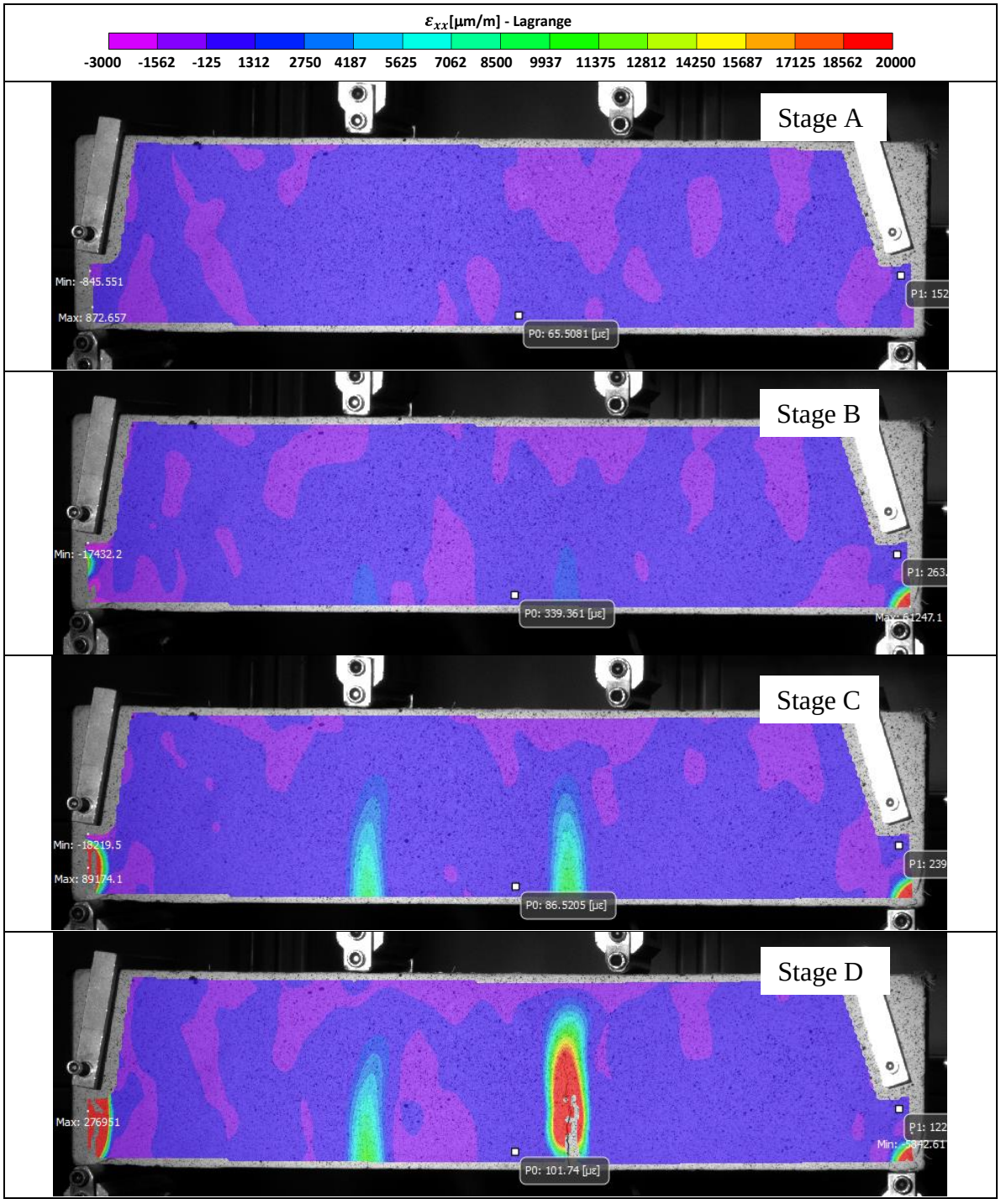
ε_{xx}[µm/m] - Lagrange
-3000 -1562 -125 1312 2750 4187 5625 7062 8500 9937 11375 12812 14250 15687 17125 18562 20000
Stage A
Min: -845.551
Max: 872.657
P0: 65.5081 [µε]
Stage B
Min: -17432.2
P0: 339.361 [µε]
Stage C
Min: -18219.5
Max: 89174.1
P0: 86.5205 [µε]
Stage D
Max: 276951
P0: 101.74 [µε]

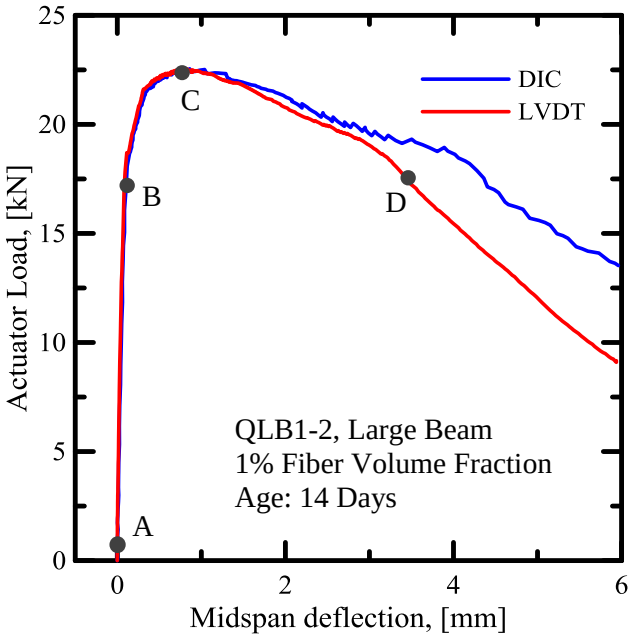
25
20
15
10
5
0
0
2
4
6
Actuator Load, [kN]
Midspan deflection, [mm]
DIC
LVDT
A
B
C
D
QLB1-2, Large Beam
1% Fiber Volume Fraction
Age: 14 Days

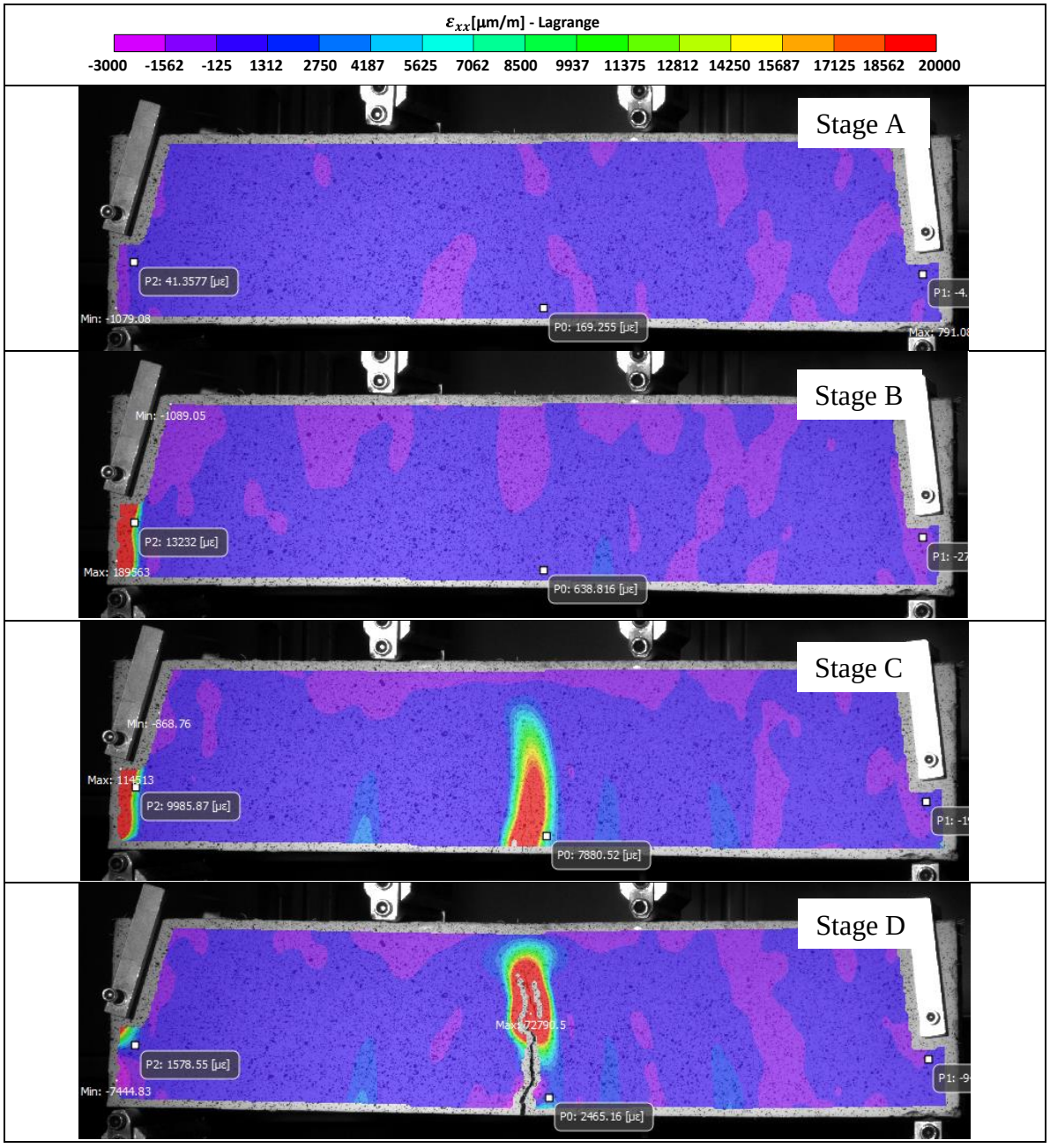
ε_{xx}[µm/m] - Lagrange
-3000 -1562 -125 1312 2750 4187 5625 7062 8500 9937 11375 12812 14250 15687 17125 18562 20000
Stage A
P2: 41.3577 [µε]
Min: -1079.08
P0: 169.255 [µε]
Stage B
Min: -1089.05
P2: 13232 [µε]
Max: 189563
P0: 638.816 [µε]
Stage C
Min: -868.76
Max: 114513
P2: 9985.87 [µε]
P0: 7880.52 [µε]
Stage D
P2: 1578.55 [µε]
Min: -7444.83
P0: 2465.16 [µε]

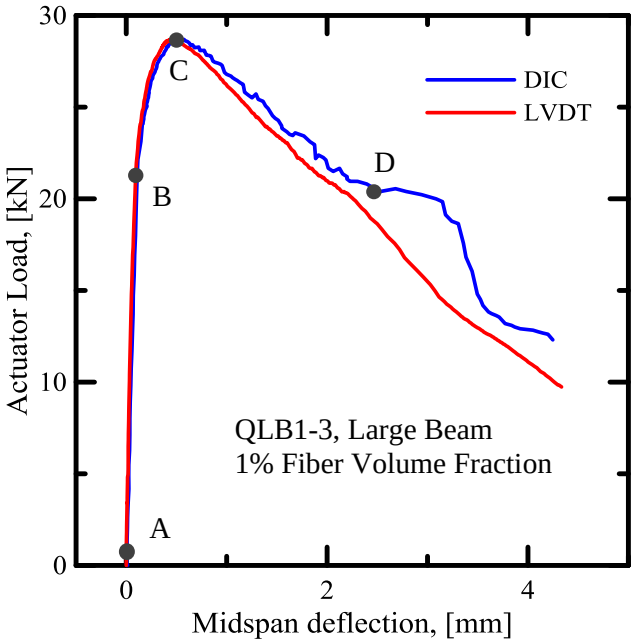
30
20
10
0
0
2
4
Actuator Load, [kN]
Midspan deflection, [mm]
DIC
LVDT
A
B
C
D
QLB1-3, Large Beam
1% Fiber Volume Fraction

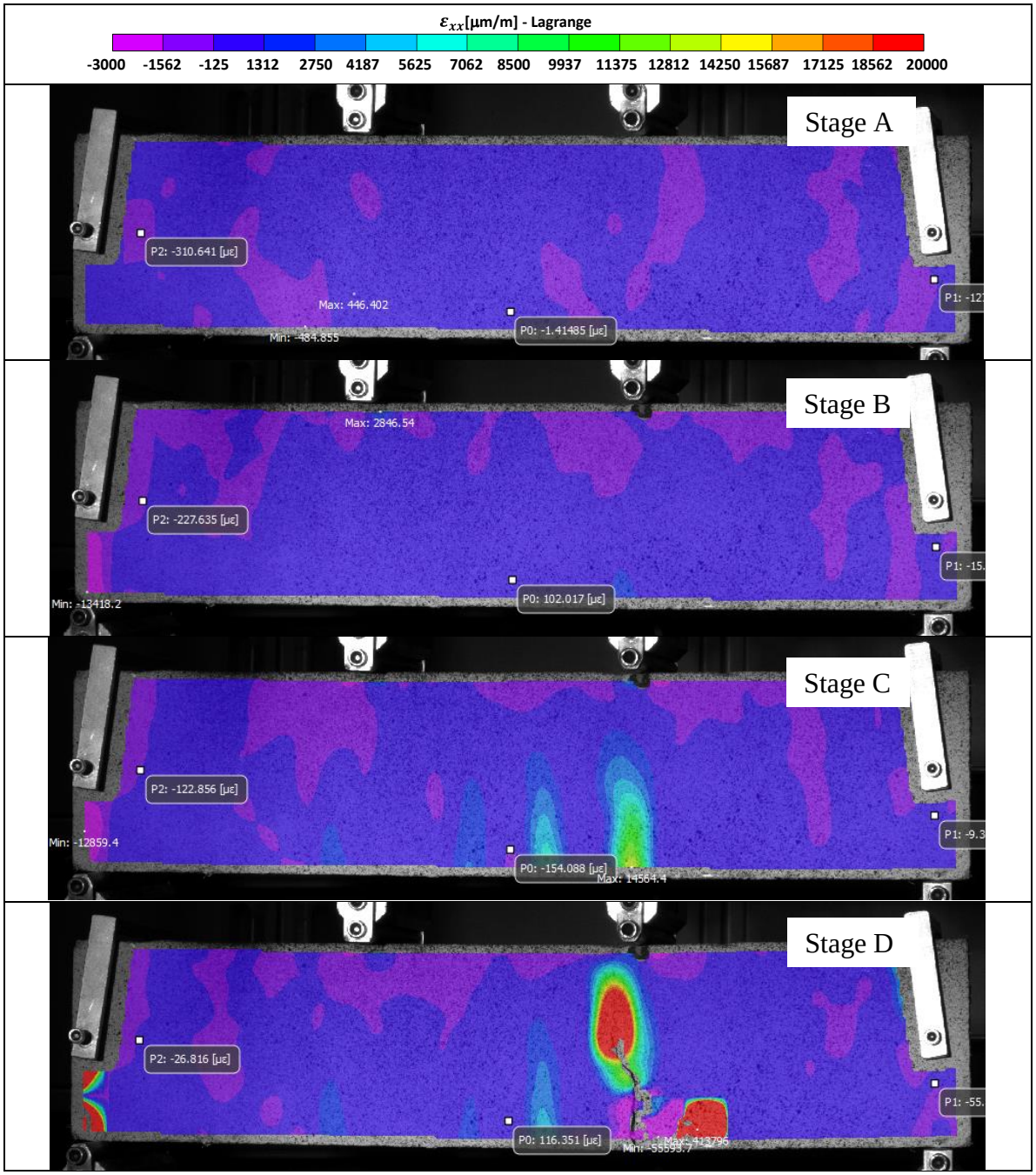
ε_{xx}[µm/m] - Lagrange
-3000 -1562 -125 1312 2750 4187 5625 7062 8500 9937 11375 12812 14250 15687 17125 18562 20000
Stage A
P2: -310.641 [µε]
Max: 446.402
Min: -484.855
P0: -1.41485 [µε]
Stage B
Max: 2846.54
P2: -227.635 [µε]
Min: -13418.2
P0: 102.017 [µε]
Stage C
P2: -122.856 [µε]
Min: -12859.4
P0: -154.088 [µε]
Max: 14564.4
Stage D
P2: -26.816 [µε]
P0: 116.351 [µε]

Q_FA_F_C (small beams @ 28 Days):

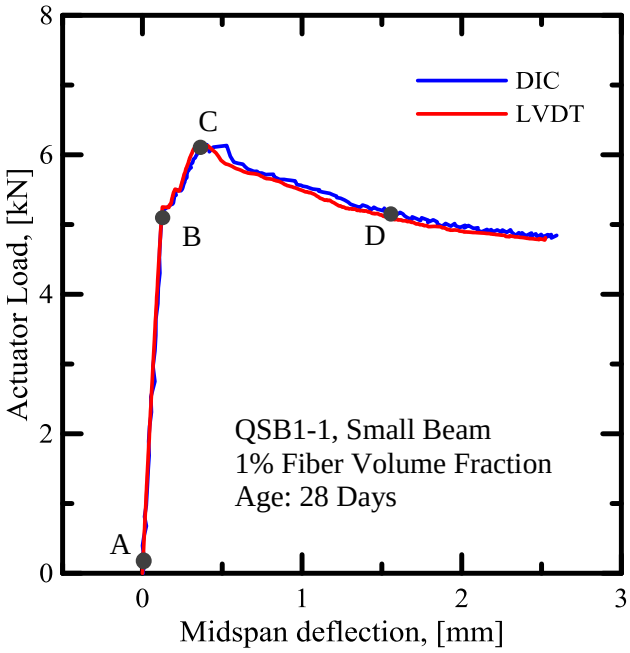

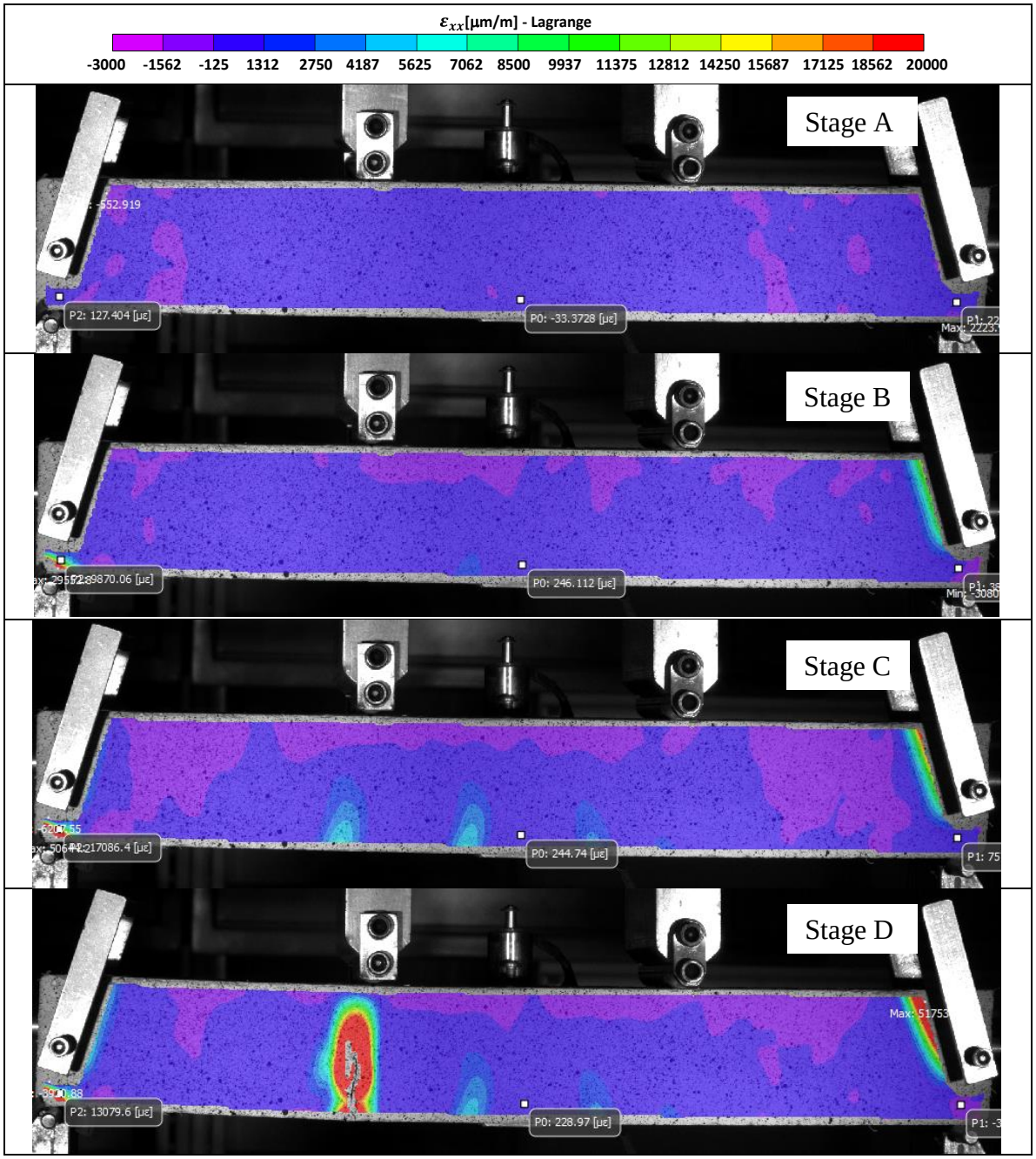
ε_{xx}[µm/m] - Lagrange
-3000 -1562 -125 1312 2750 4187 5625 7062 8500 9937 11375 12812 14250 15687 17125 18562 20000
Stage A
P2: 127.404 [µε]
P0: -33.3728 [µε]
Stage B
P0: 246.112 [µε]
Stage C
P0: 244.74 [µε]
Stage D
P2: 13079.6 [µε]
P0: 228.97 [µε]

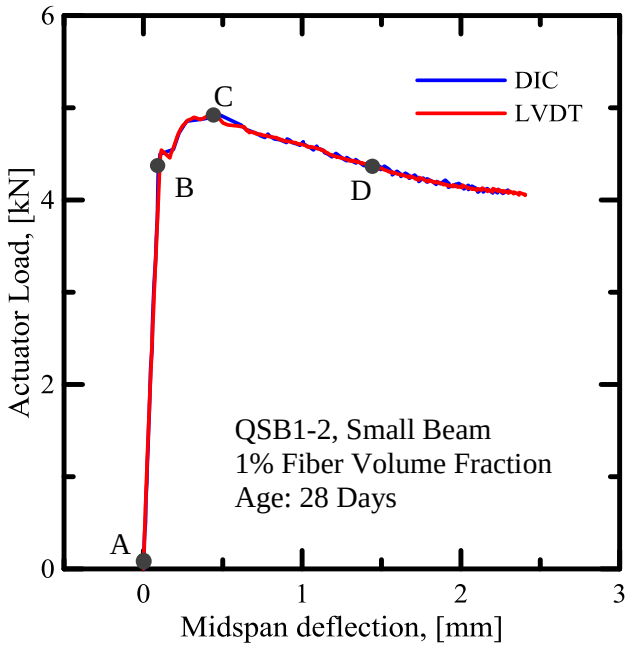
DIC
LVDT
C
B
D
A
QSB1-2, Small Beam
1% Fiber Volume Fraction
Age: 28 Days
Actuator Load, [kN]
Midspan deflection, [mm]
0
2
4
6
0
1
2
3

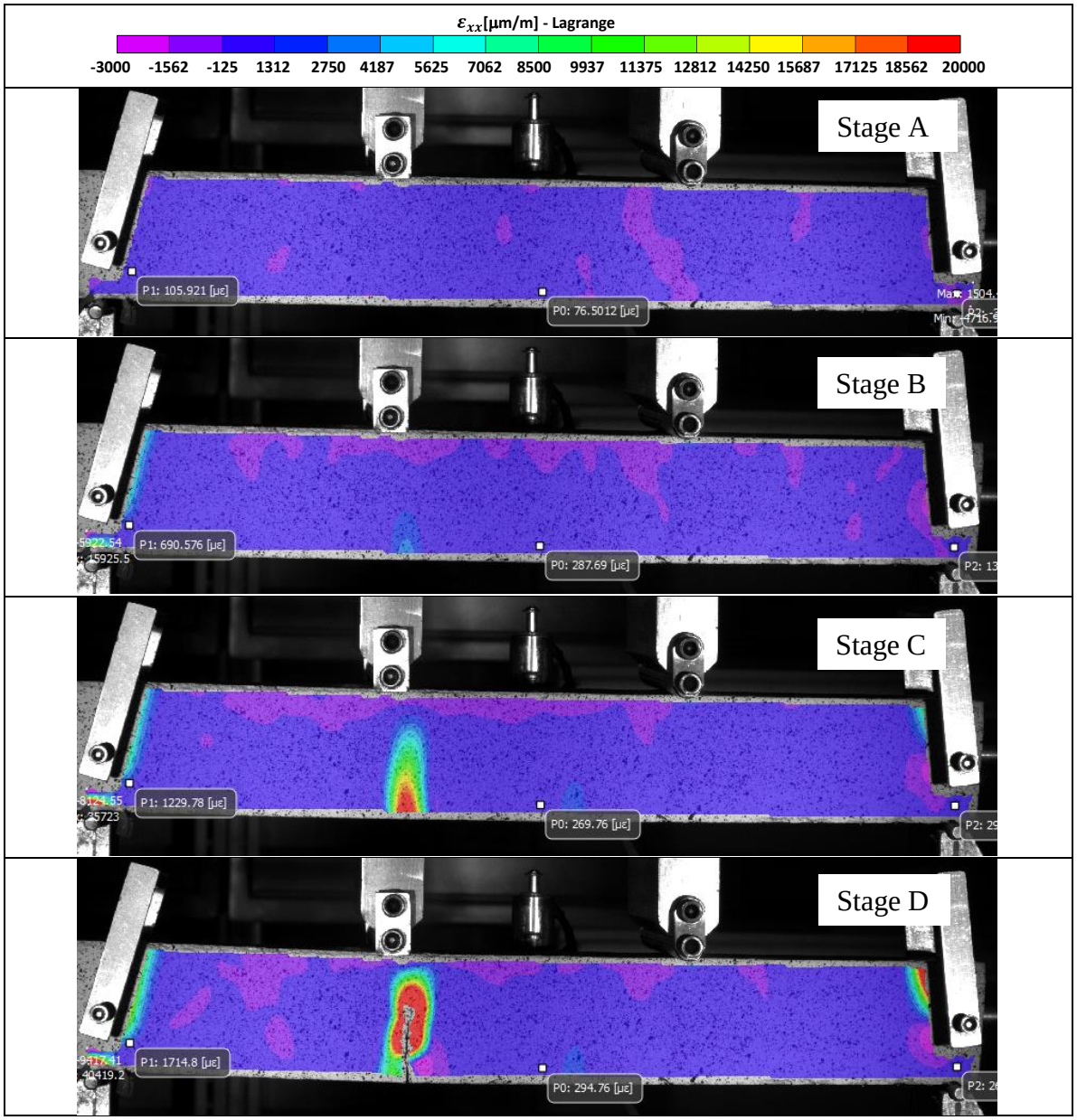
ε_{xx}[µm/m] - Lagrange
-3000 -1562 -125 1312 2750 4187 5625 7062 8500 9937 11375 12812 14250 15687 17125 18562 20000
Stage A
P1: 105.921 [µε]
P0: 76.5012 [µε]
Stage B
P1: 690.576 [µε]
P0: 287.69 [µε]
Stage C
P1: 1229.78 [µε]
P0: 269.76 [µε]
Stage D
P1: 1714.8 [µε]
P0: 294.76 [µε]

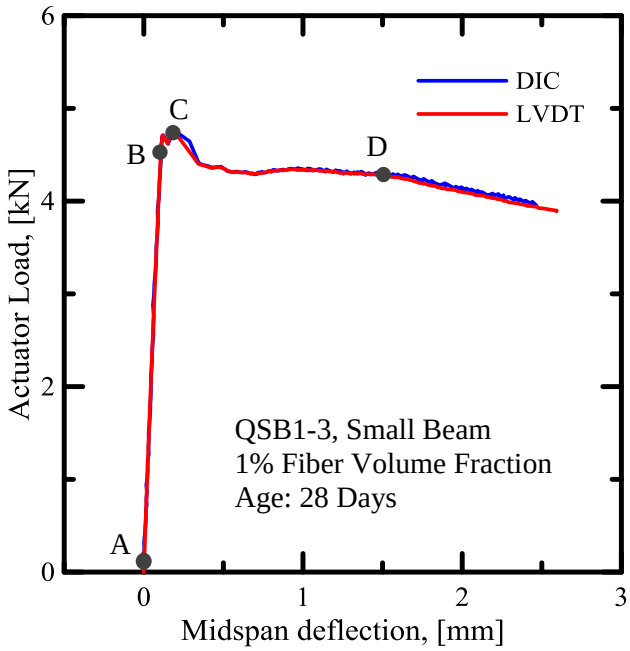
DIC
LVDT
A
B
C
D
QSB1-3, Small Beam
1% Fiber Volume Fraction
Age: 28 Days
Actuator Load, [kN]
Midspan deflection, [mm]
0
2
4
6
0
1
2
3

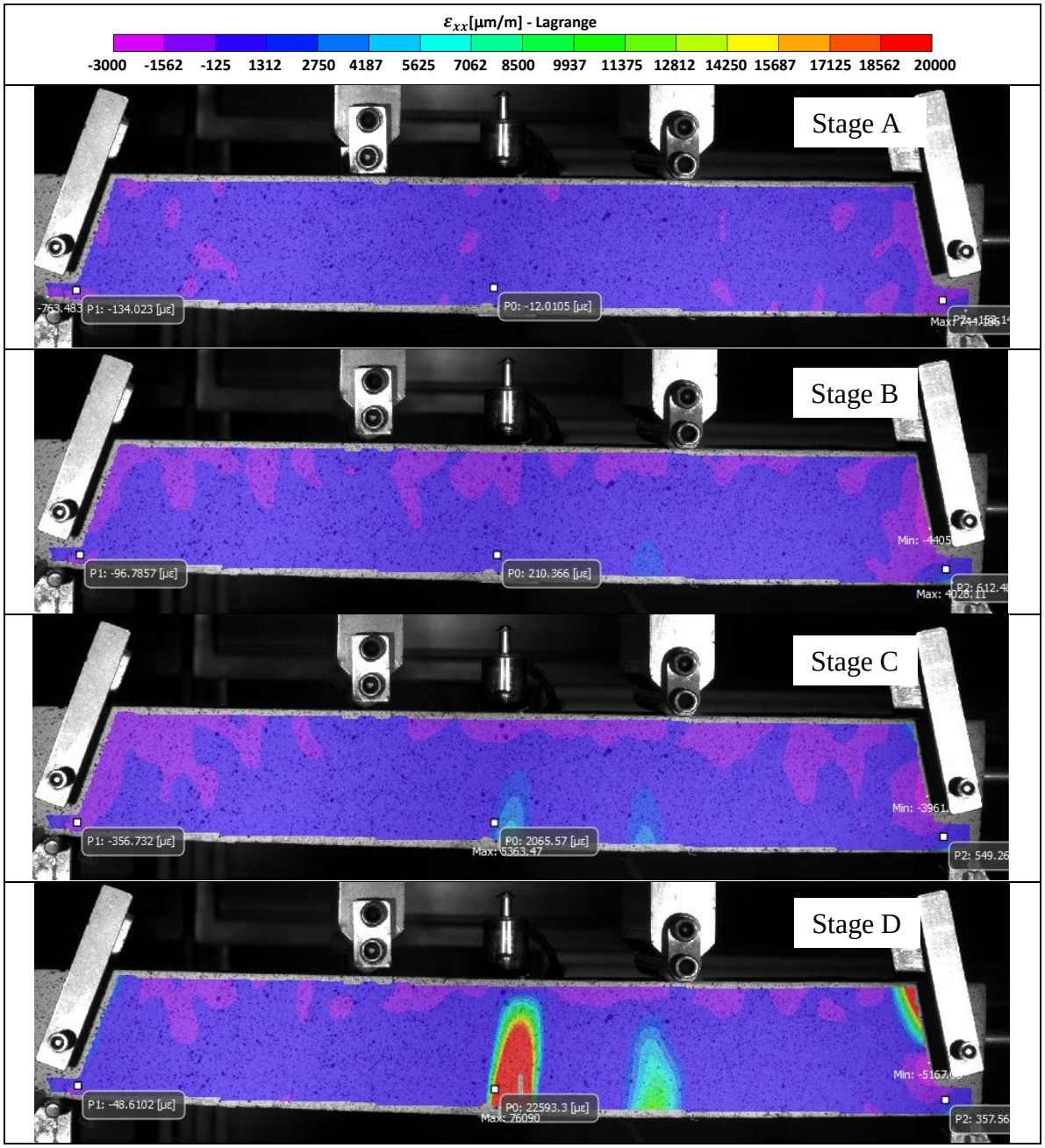
ε_{xx}[µm/m] - Lagrange
-3000 -1562 -125 1312 2750 4187 5625 7062 8500 9937 11375 12812 14250 15687 17125 18562 20000
Stage A
P1: -134.023 [µε]
P0: -12.0105 [µε]
Stage B
P1: -96.7857 [µε]
P0: 210.366 [µε]
Stage C
P1: -356.732 [µε]
P0: 2065.57 [µε]
Max: 6363.47
Stage D
P1: -48.6102 [µε]
P0: 22593.3 [µε]
Max: 76090

Q_FA_F_C (large beams @ 28 Days):

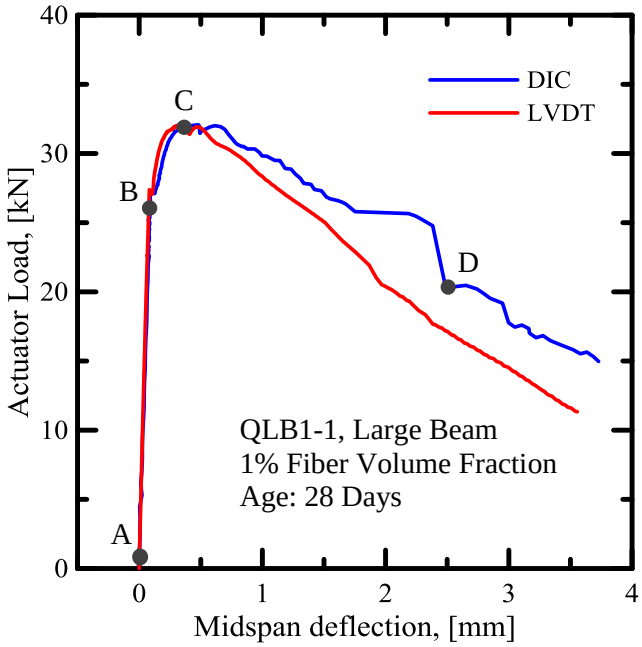

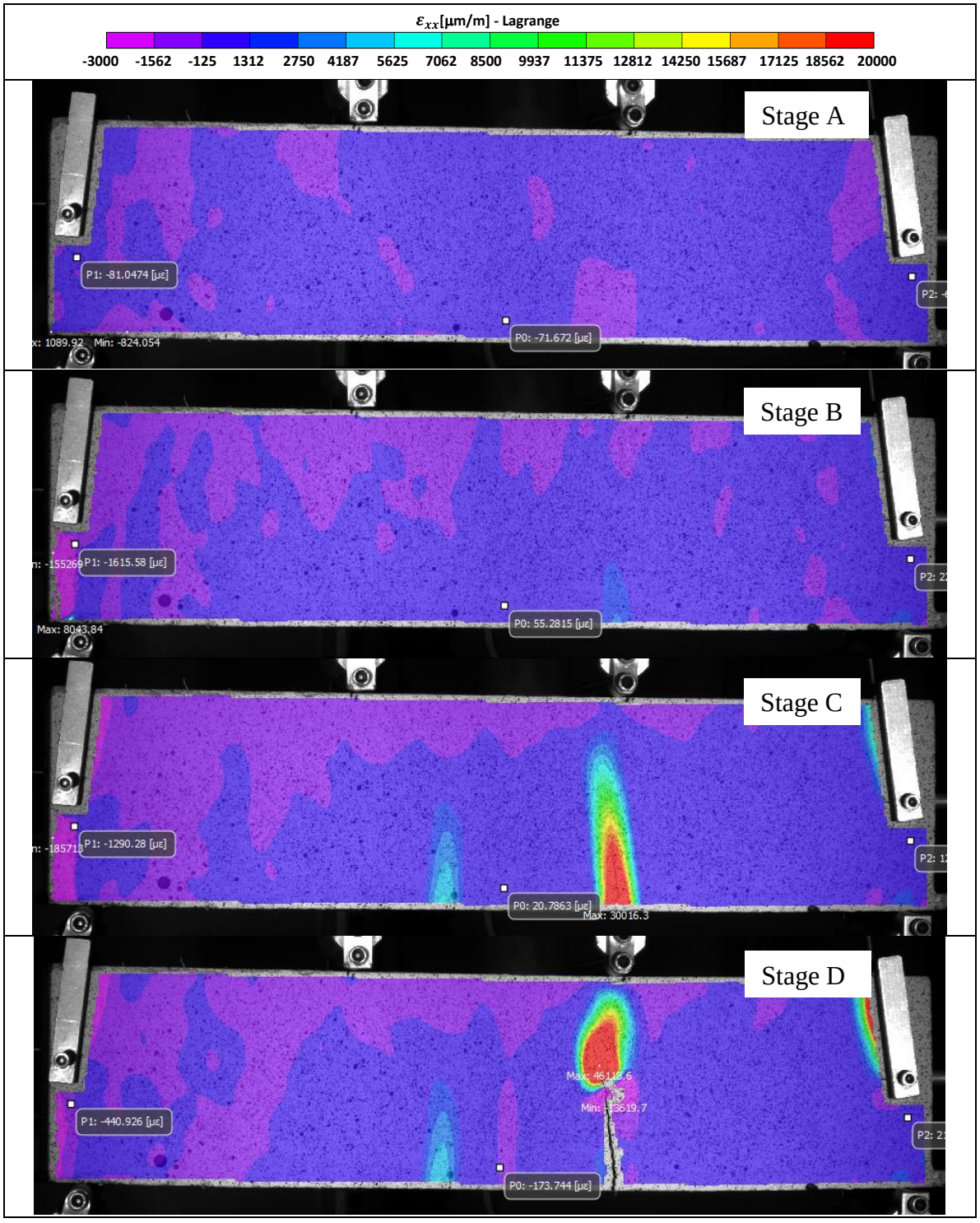
ε_{xx}[µm/m] - Lagrange
-3000 -1562 -125 1312 2750 4187 5625 7062 8500 9937 11375 12812 14250 15687 17125 18562 20000
Stage A
P1: -81.0474 [µε]
P0: -71.672 [µε]
Stage B
P1: -1615.58 [µε]
P0: 55.2815 [µε]
Max: 8043.84
Stage C
P1: -1290.28 [µε]
P0: 20.7863 [µε]
Max: 30016.3
Stage D
P1: -440.926 [µε]
P0: -173.744 [µε]

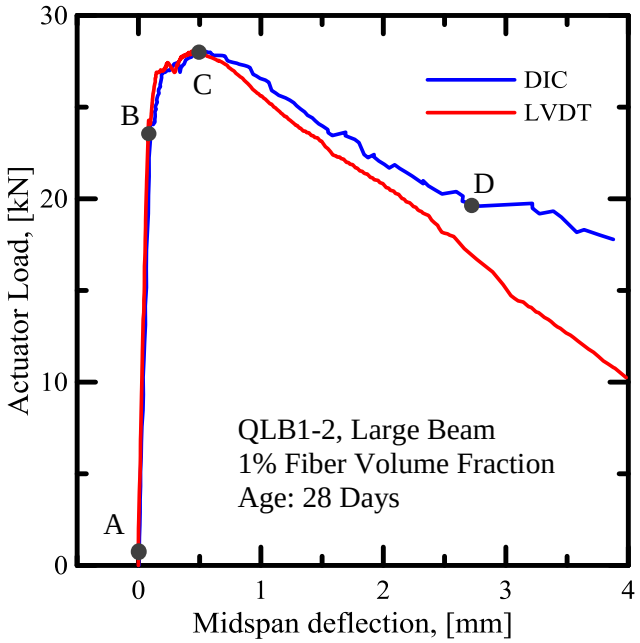
30
20
10
0
Actuator Load, [kN]
0
1
2
3
4
Midspan deflection, [mm]
DIC
LVDT
A
B
C
D
QLB1-2, Large Beam
1% Fiber Volume Fraction
Age: 28 Days

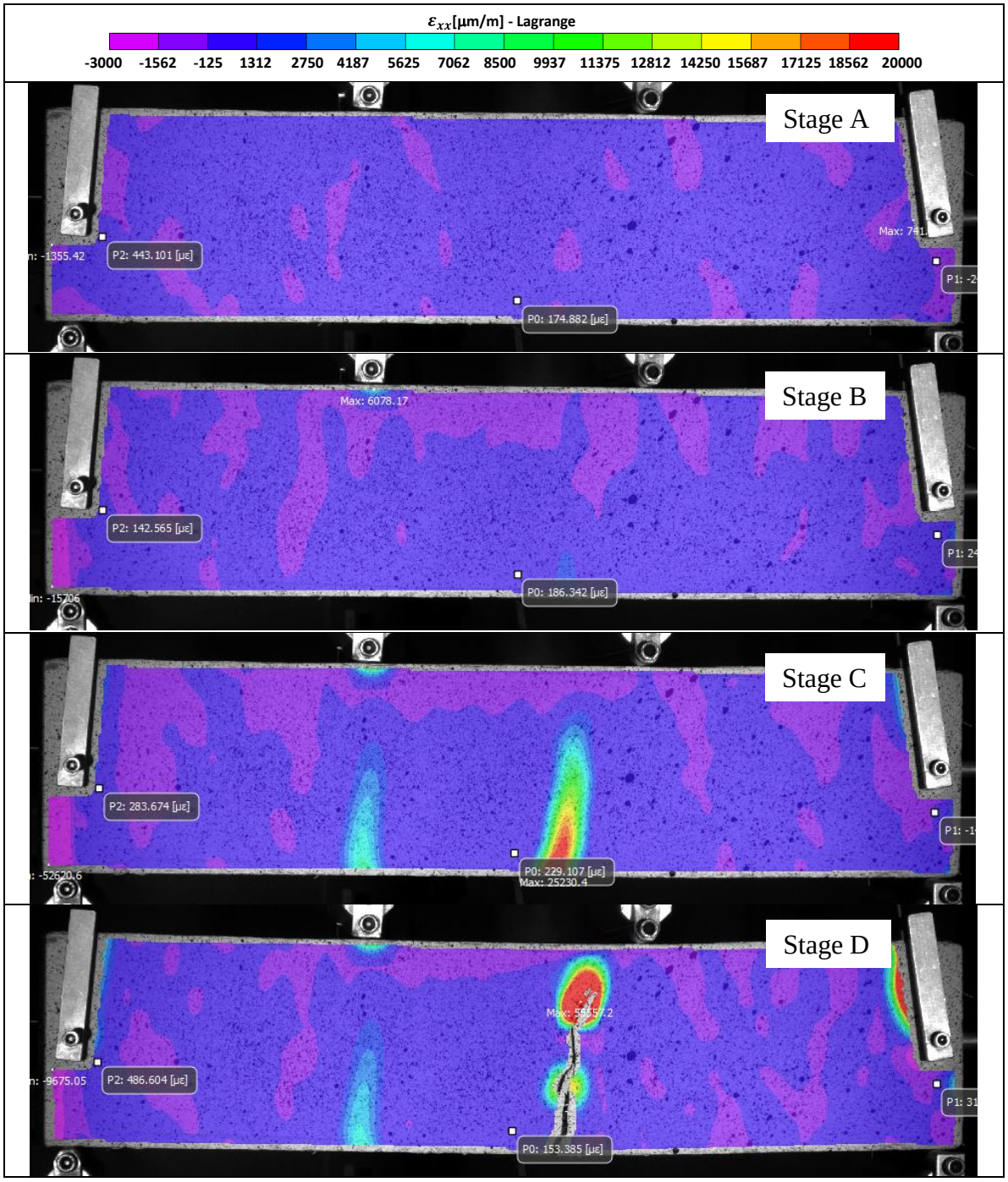
ε_{xx}[µm/m] - Lagrange
-3000 -1562 -125 1312 2750 4187 5625 7062 8500 9937 11375 12812 14250 15687 17125 18562 20000
Stage A
P2: 443.101 [µε]
P0: 174.882 [µε]
Stage B
Max: 6078.17
P2: 142.565 [µε]
P0: 186.342 [µε]
Stage C
P2: 283.674 [µε]
P0: 229.107 [µε]
Max: 25230.4
Stage D
P2: 486.604 [µε]
P0: 153.385 [µε]

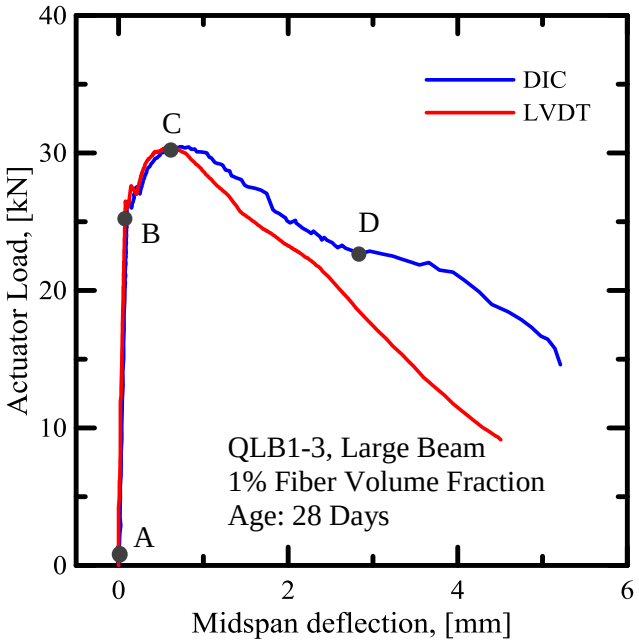
40
30
20
10
0
0
2
4
6
Actuator Load, [kN]
Midspan deflection, [mm]
DIC
LVDT
A
B
C
D
QLB1-3, Large Beam
1% Fiber Volume Fraction
Age: 28 Days

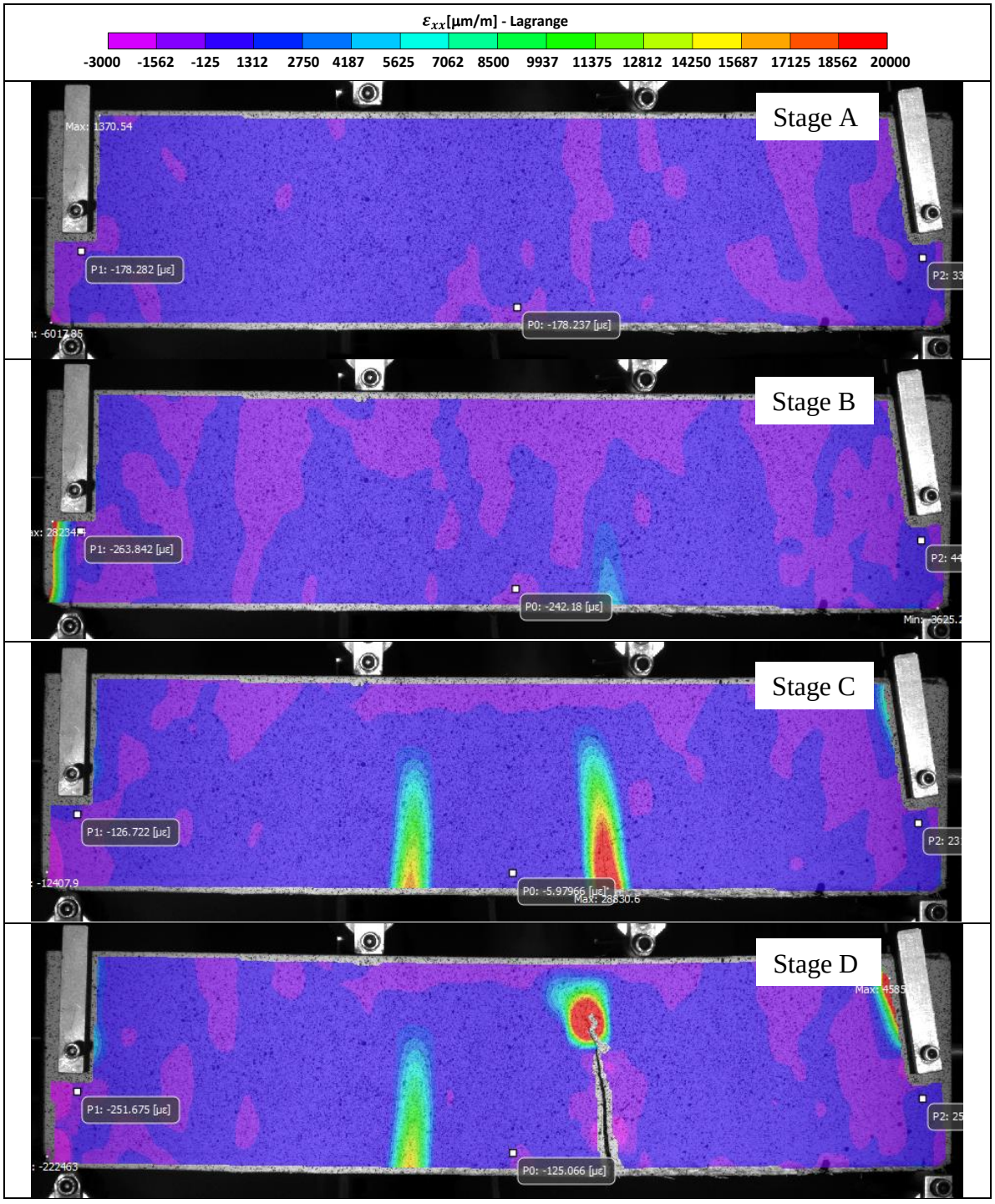
ε_{xx}[µm/m] - Lagrange
-3000 -1562 -125 1312 2750 4187 5625 7062 8500 9937 11375 12812 14250 15687 17125 18562 20000
Stage A
Max: 1370.54
P1: -178.282 [µε]
P0: -178.237 [µε]
Stage B
P1: -263.842 [µε]
P0: -242.18 [µε]
Stage C
P1: -126.722 [µε]
P0: -5.97966 [µε]
Max: 28830.6
Stage D
P1: -251.675 [µε]
P0: -125.066 [µε]

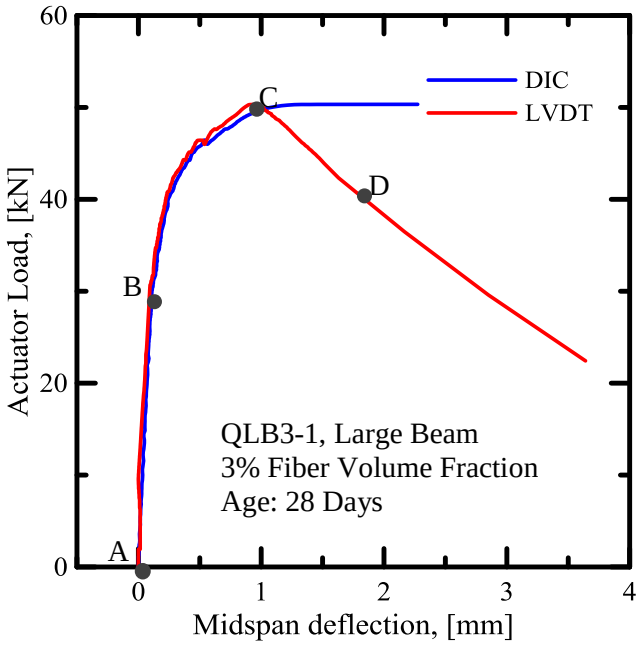
60
40
20
0
Actuator Load, [kN]
0
1
2
3
4
Midspan deflection, [mm]
DIC
LVDT
A
B
C
D
QLB3-1, Large Beam
3% Fiber Volume Fraction
Age: 28 Days

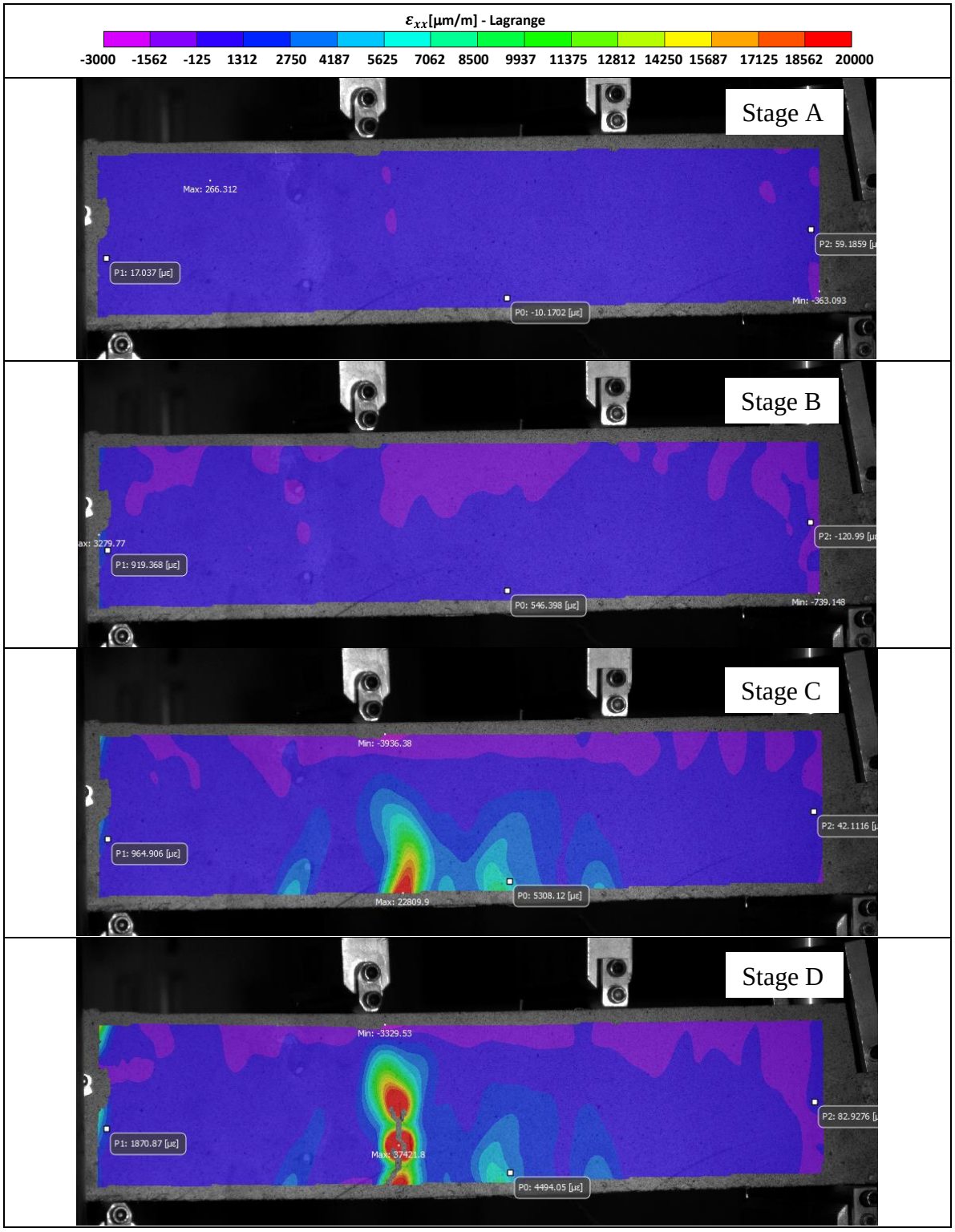
ε_{xx}[µm/m] - Lagrange
-3000 -1562 -125 1312 2750 4187 5625 7062 8500 9937 11375 12812 14250 15687 17125 18562 20000
Stage A
Max: 266.312
P1: 17.037 [µε]
P0: -10.1702 [µε]
Min: -363.093
Stage B
P1: 919.368 [µε]
P0: 546.398 [µε]
Min: -739.148
Stage C
Min: -3936.38
P1: 964.906 [µε]
Max: 22809.9
P0: 5308.12 [µε]
Stage D
Min: -3329.53
P1: 1870.87 [µε]
P0: 4494.05 [µε]

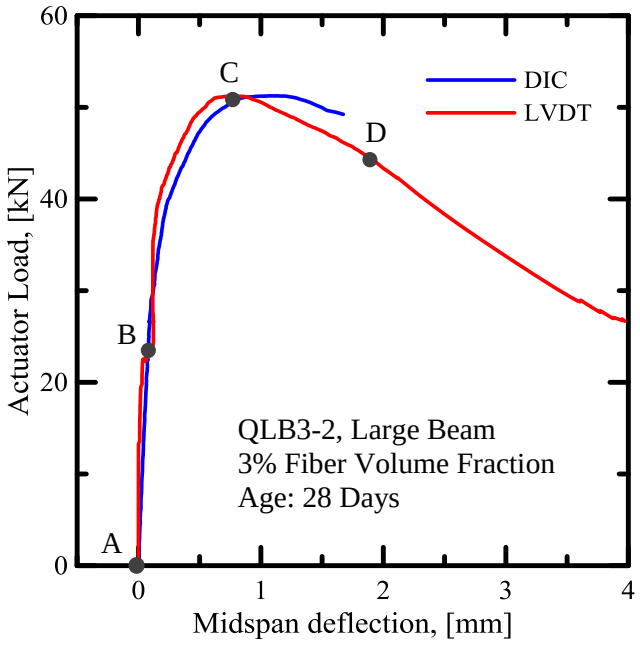
60
40
20
0
Actuator Load, [kN]
0
1
2
3
4
Midspan deflection, [mm]
A
B
C
D
DIC
LVDT
QLB3-2, Large Beam
3% Fiber Volume Fraction
Age: 28 Days

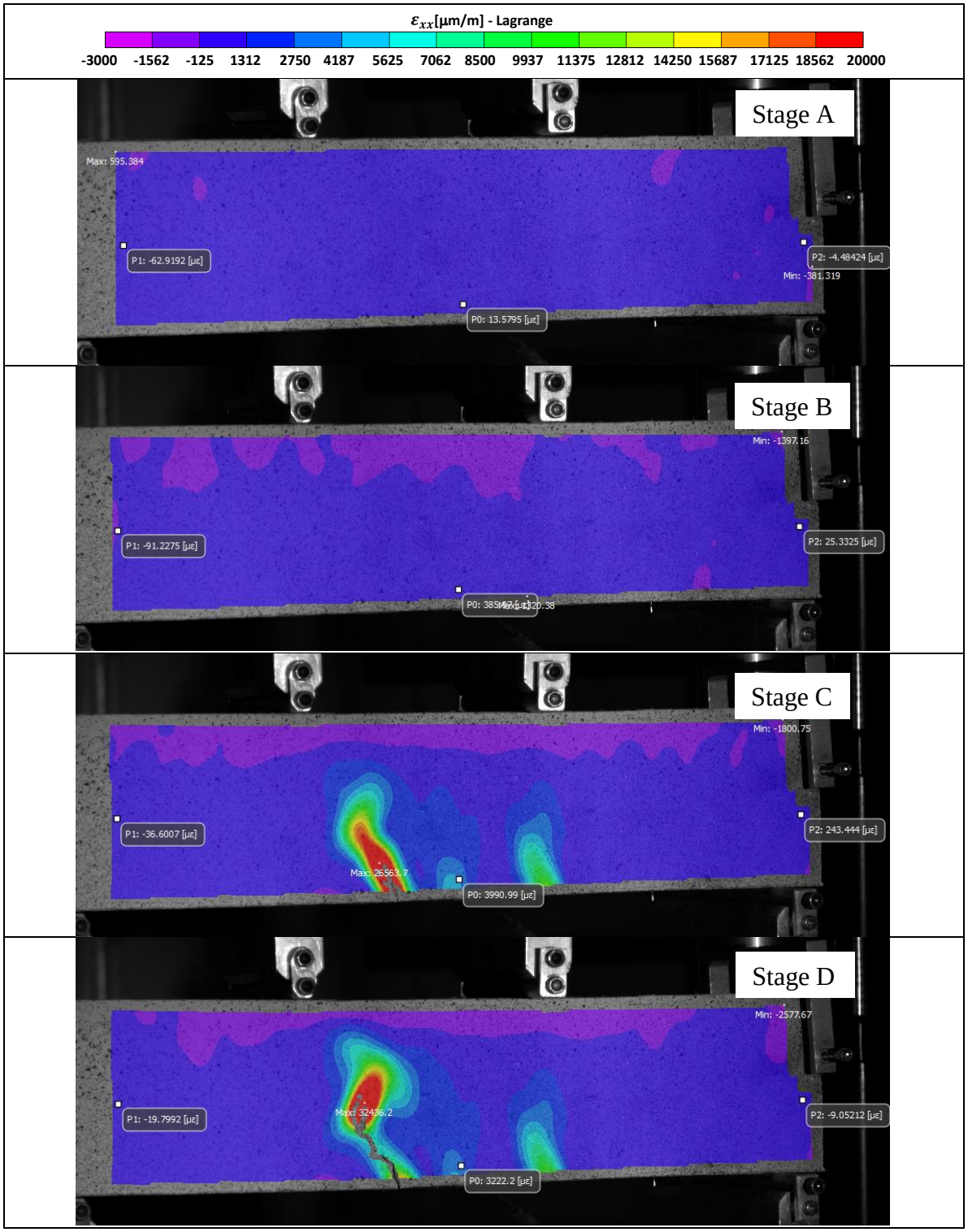
ε_{xx}[µm/m] - Lagrange
-3000 -1562 -125 1312 2750 4187 5625 7062 8500 9937 11375 12812 14250 15687 17125 18562 20000
Stage A
Max: 595.384
P1: -62.9192 [µε]
P2: -4.48424 [µε]
Min: -381.319
P0: 13.5795 [µε]
Stage B
Min: -1397.16
P1: -91.2275 [µε]
P2: 25.3325 [µε]
Stage C
Min: -1800.75
P1: -36.6007 [µε]
P2: 243.444 [µε]
Max: 26563.7
P0: 3990.99 [µε]
Stage D
Min: -2577.67
P1: -19.7992 [µε]
Max: 32436.2
P2: -9.05212 [µε]
P0: 3222.2 [µε]

APPENDIX IV

HIGH-CAPACITY FLEXURAL STEEL FRAME

In other to do the flexural tests on the full scale tunnel segments, a special steel frame was designed and developed. The details of the frame development are presented in this section. The frame is designed to apply bending moment, using one or two actuators at the middle top of the frame, to the large-scale samples, such as beams and full-scale tunnel segments, up to a span of 135 inches (3.4 m). Originally, this frame was designed to impose a load of 50 kips (220 kN). Then after, it was decided to upgrade the frame to enhance its capacity from 50 kips to 200 kips (890 kN).

Several types of analysis were performed, before and after improvement, to make sure that the frame is able to tolerate this amount of loading. The full structural analysis was performed using ETABS 2015. Besides, local FE analysis, using ABAQUS software, was implemented for different parts (such as bolts and plates), members, and joints. Based on the results some improvements were suggested.

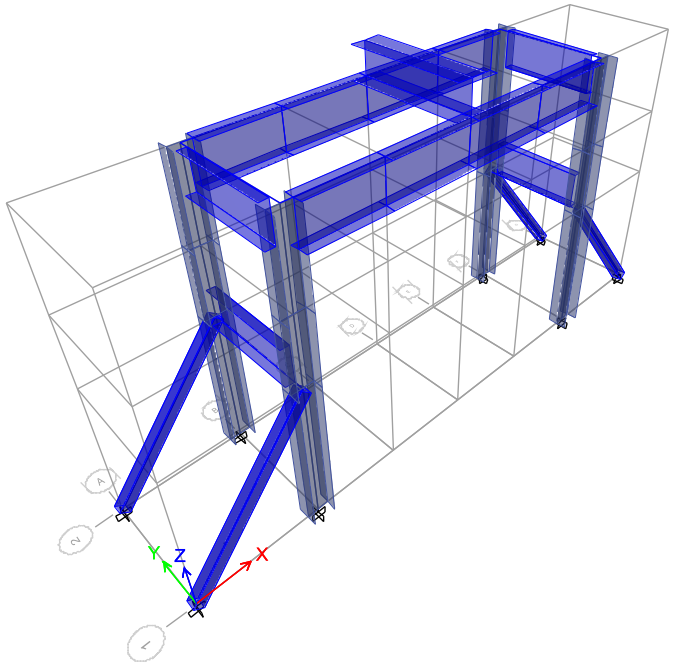

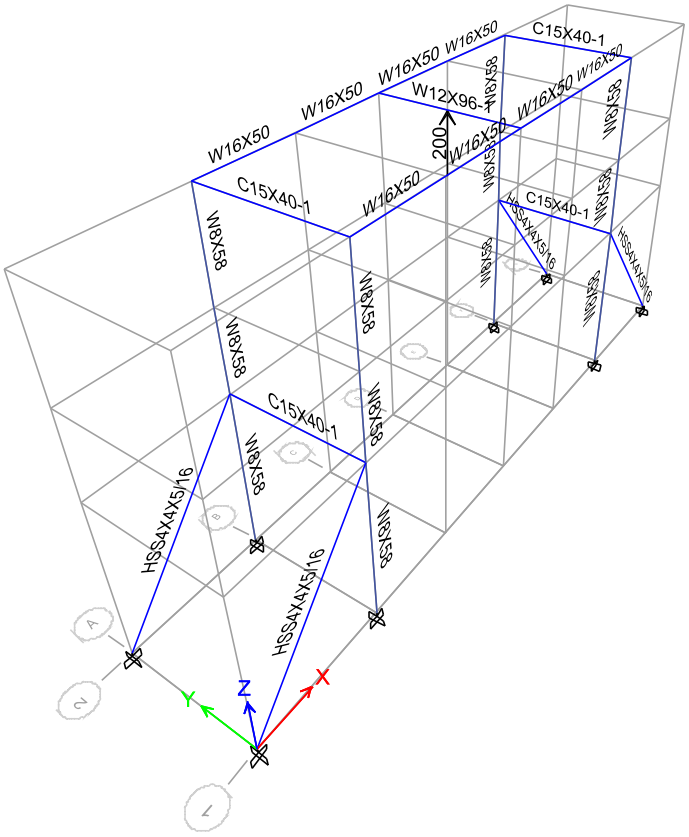

Figure A. 48. Steel frame (before improvement).

This report is divided into two major sections. In the first section, the current frame was analyzed and the results were scrutinized closely. In the second section, some improvements were suggested and the frame was analyzed to make sure that the suggested upgrades satisfy the requirements.

Original Steel Frame:

This frame and the applied loading is shown below. The frame is fixed to the ground. All joints are assumed to be fixed, except the braces that are considered as truss members. A point loading of 200 kips is applied at the center of the top (loading) beam.

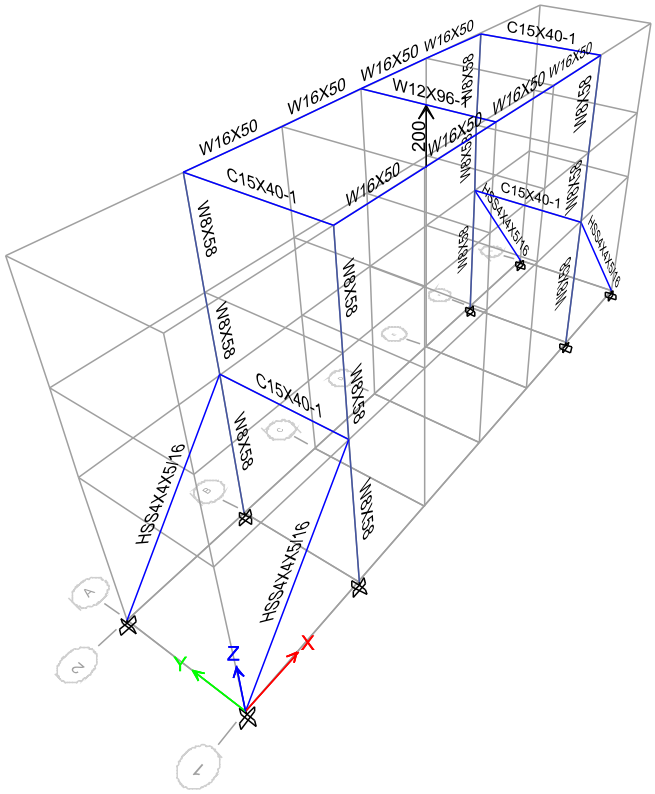

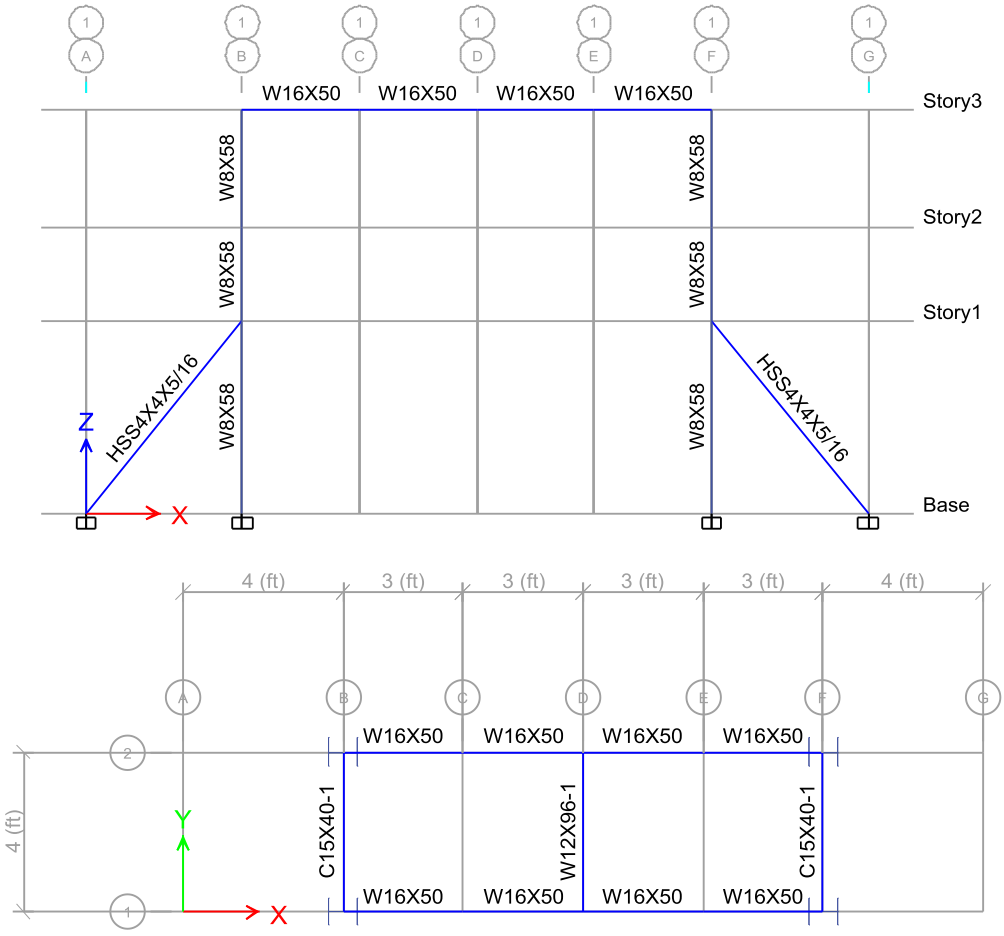

Figure A. 49. Original steel frame and the applied loads.

Flexural Design:

The bending diagrams are shown below. Two major bending moments are happening in the loading beam, BI (W 12X96) and the top beams, BII (W 16X50). The maximum bending moment in the loading beam, BI, is about 200 kip-ft and the factored capacity of the beam is 550 kip-ft.

$$\phi M_n \simeq 550\,\text{kip-ft} > M_u \qquad O.K$$

The other members are the top beams, BII, with maximum bending moments of 210 kip-ft and the flexural capacity of 320 kip-ft.

$$\phi M_n \simeq 320\,\text{kip-ft} > M_u \qquad O.K$$

The bending moment in the other members is not considerable.

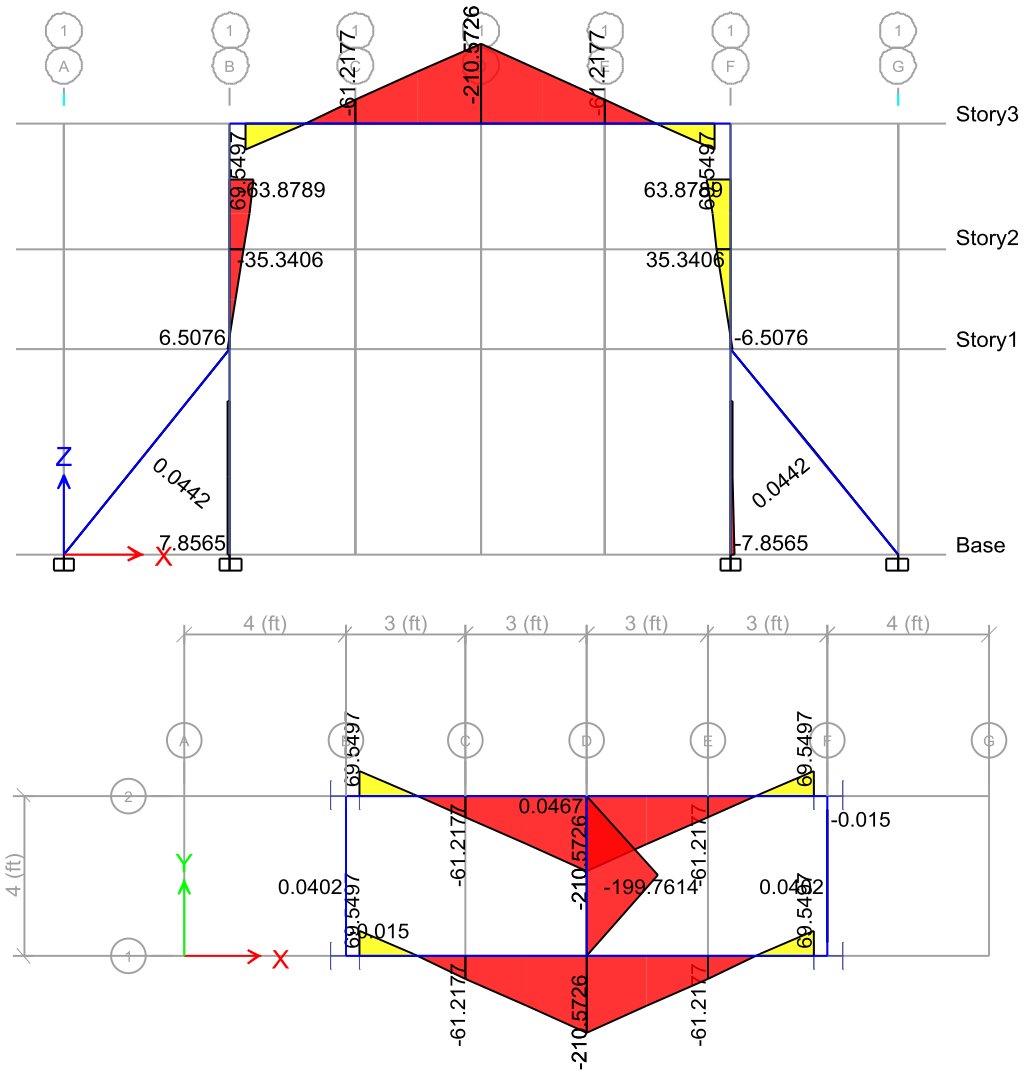

Figure A. 50. Bending moment diagrams, M33_Diagrams (kip-ft).

Shear Design:

Similar to the bending moment, the critical shear forces are occurring in the loading and top beams. The loading beam is under 100 kips shear which its shear capacity (with an SF of 2.5) is

$$F_v = 0.4F_yA_w = 0.4\times 50\times 7.4 \simeq 150\text{kip} > F_u \qquad O.K$$

This provides enough shear capacity for the loading beam. The maximum shear in the top beams is 50 kip and their shear capacity is 122 kip, which provides enough shear capacity for the top beams as well.

$$F_v = 0.4F_yA_w = 0.4\times 50\times 6.1 \simeq 122\text{kip} > F_u \qquad O.K$$

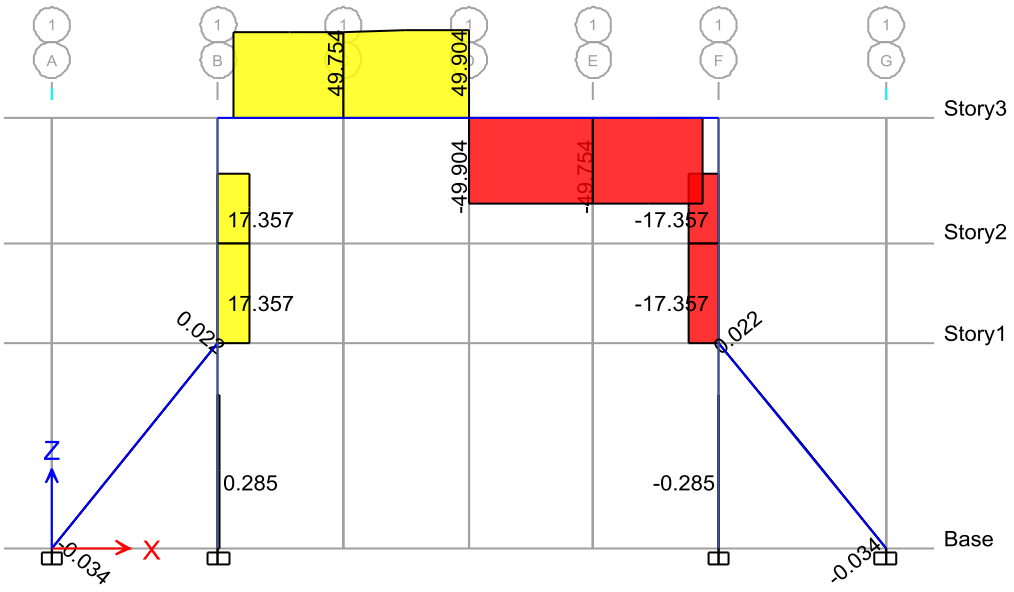

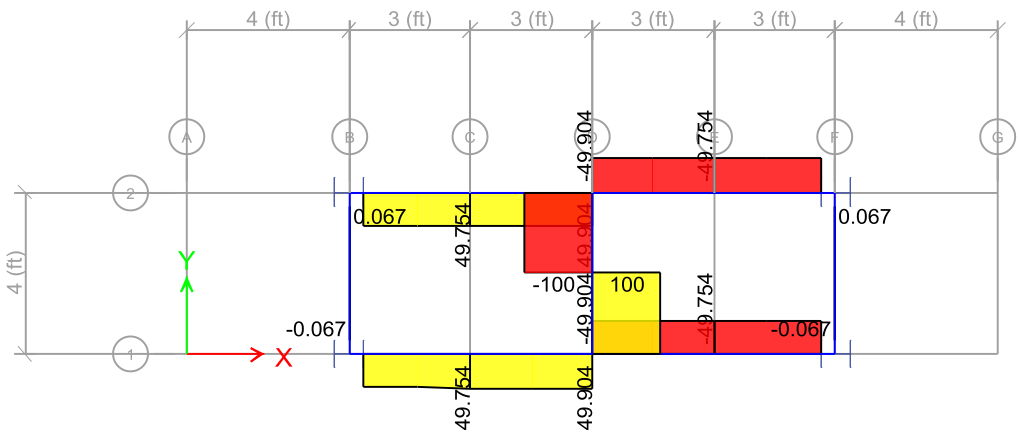

Figure A. 51. Shear diagrams, kip.

Axial Loads:

The critical axial loads are occurring in the columns and the braces. The tensile force in the columns is near 50 kips which their tensile capacity is about 720 kips, which is much higher than the applied force.

$$\phi_t P_n = 0.9 F_y A_g = 0.9 \times 50 \times 16 \simeq 720\,\text{kip} > P_u \qquad O.K$$

The tension in the braces is 27 kips while their capacity is about

$$\phi_t P_n = 0.9 F_y A_g = 0.9 \times 50 \times 5 \simeq 220\text{kip} > P_u \qquad O.K$$

Thus the braces provide enough tensile capacity for the frame.

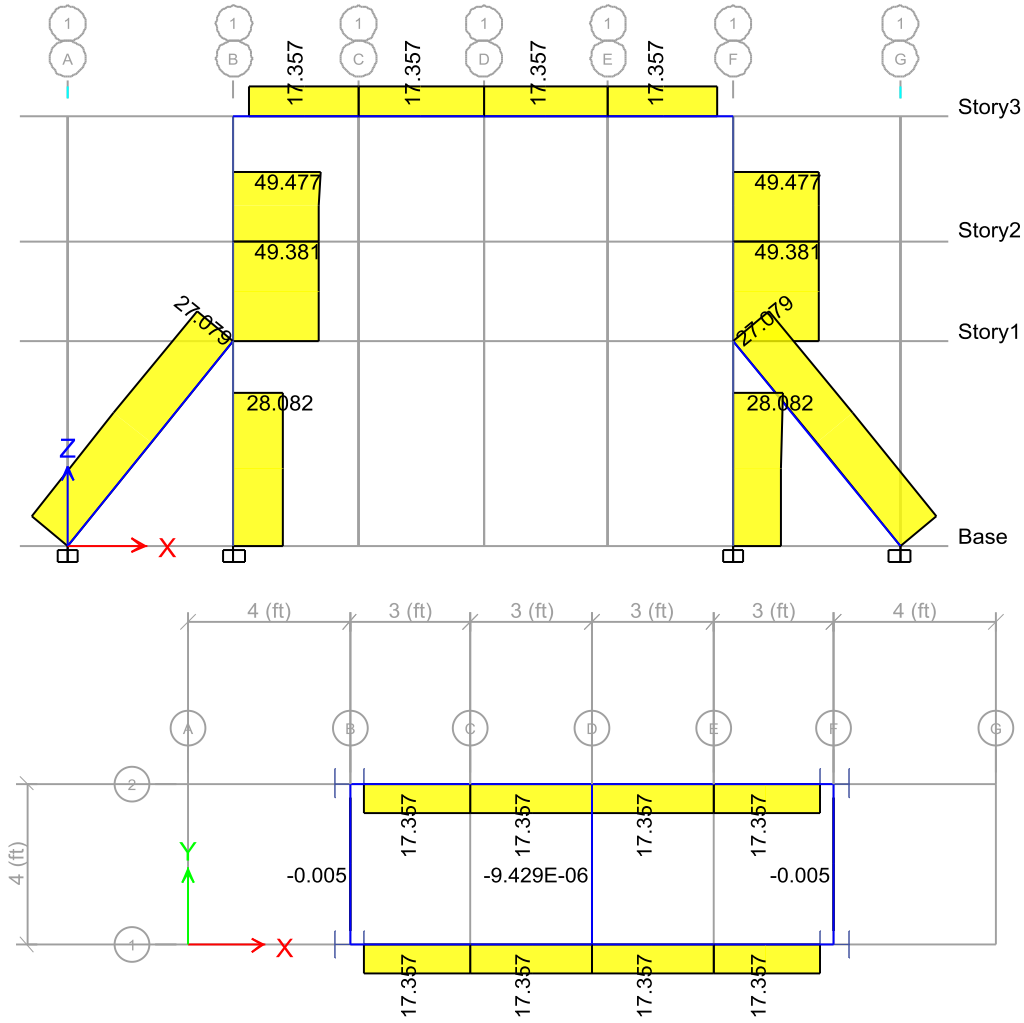

Figure A. 52. Axial forces, kip.

Design of the Joints:

The analysis and design process for the members showed that they are able to endure the applied forces and moments, however, the joints need to be controlled and redesigned, if required. For this purpose, FE analysis has been used to make sure an accurate analysis and design for the joints is achieved. The location of the joint is shown below, joint A. Due to the symmetry, the other three joints are similar to this joint and the results are applicable for all four joints in the frame.

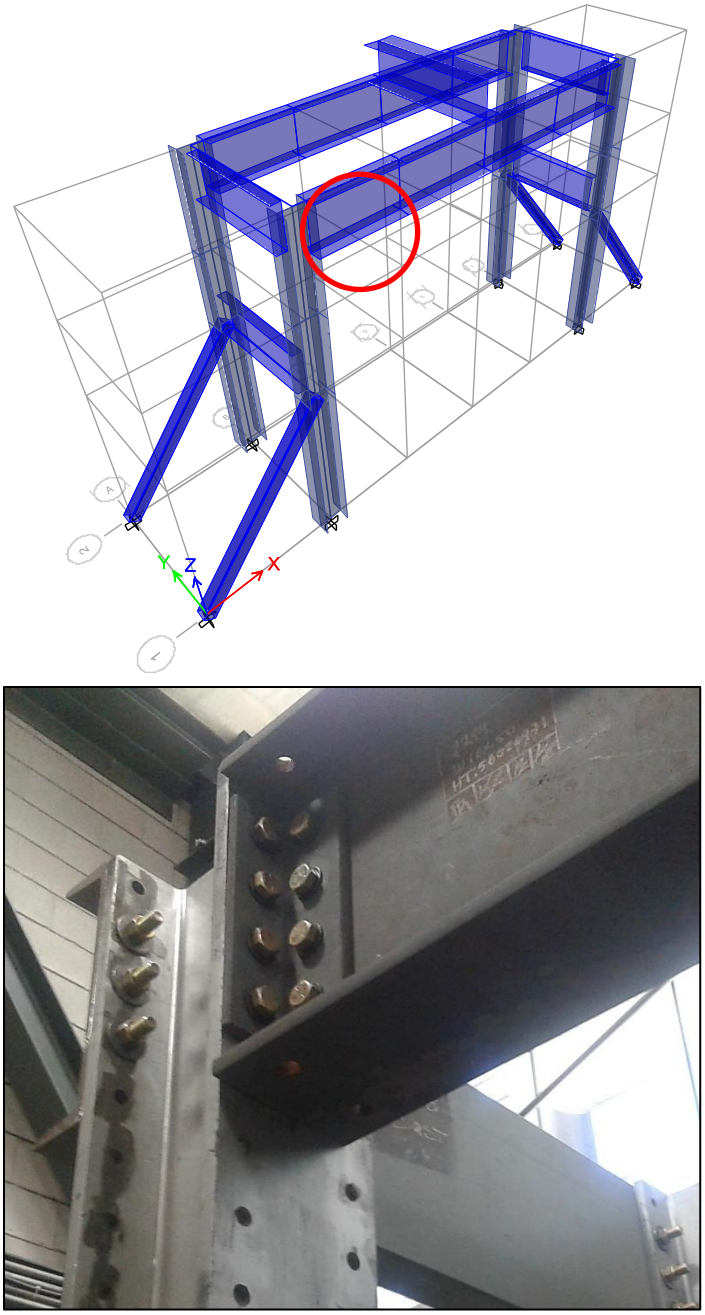

Figure A. 53. Location of joint A in the frame.

The FE Model is shown below.

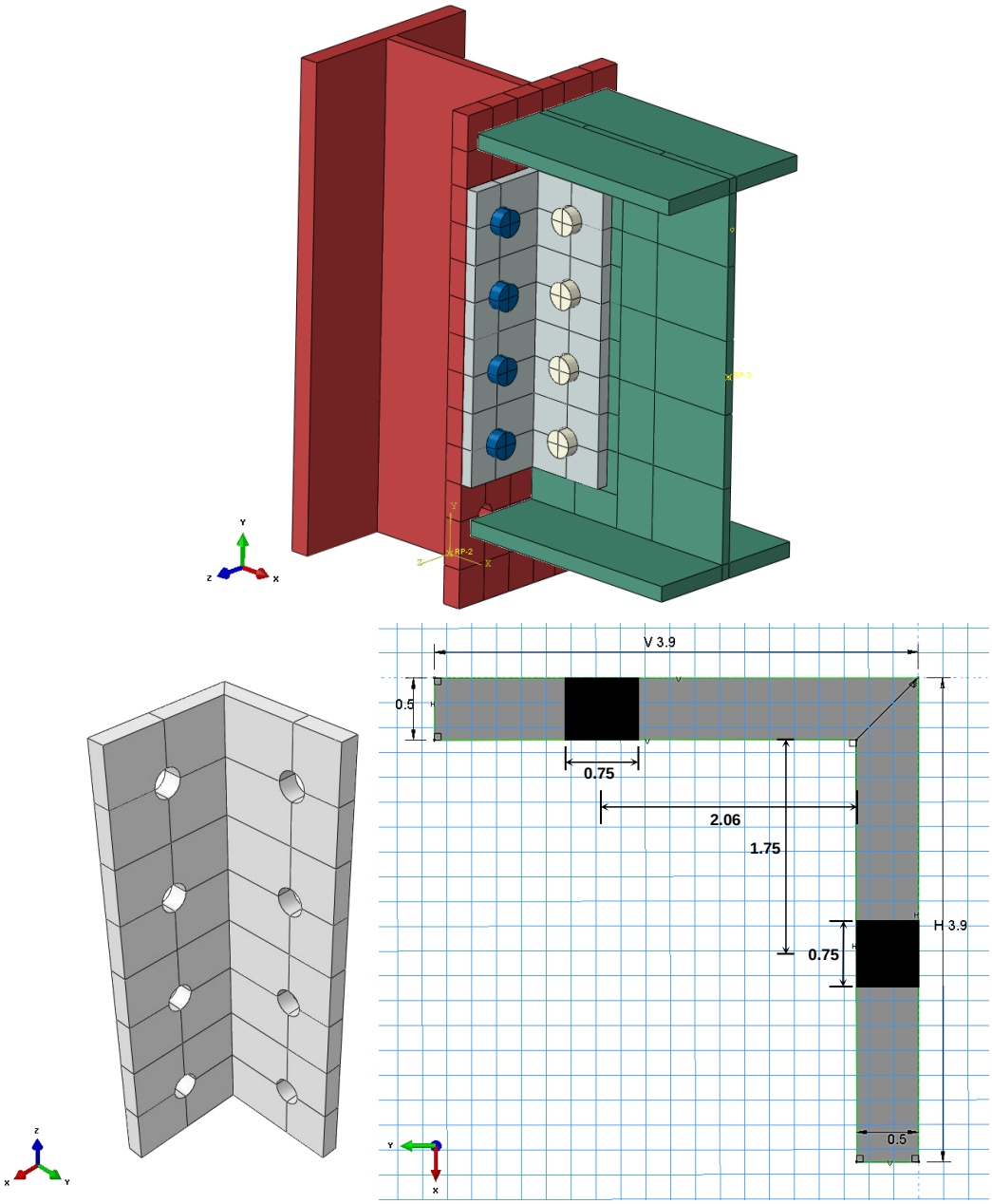

Figure A. 54. FE model of Joint A.

FE Analysis: Results (Units: in, lb, psi):

Elastic modulus and Poisson's ratios are assumed as **29e6 psi** and **0.3**, respectively. The analysis is performed in **one linear step**.

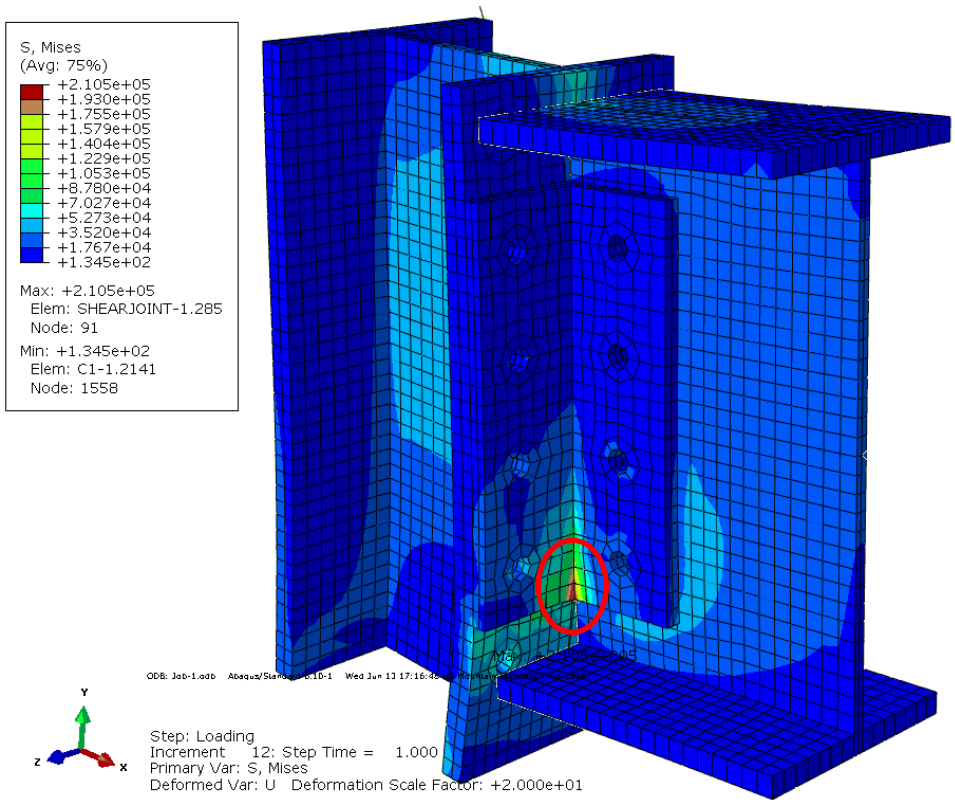

Figure A. 55. Analyzed joint using the FE method and the stress contours.

Analysis results show that the maximum Mises stress in the angle is 210 ksi. The location of the maximum stress is located in the figure. Based on the current analysis, it can be concluded that the stress in the bolts is not considerable, compared to the stress in the angle itself.

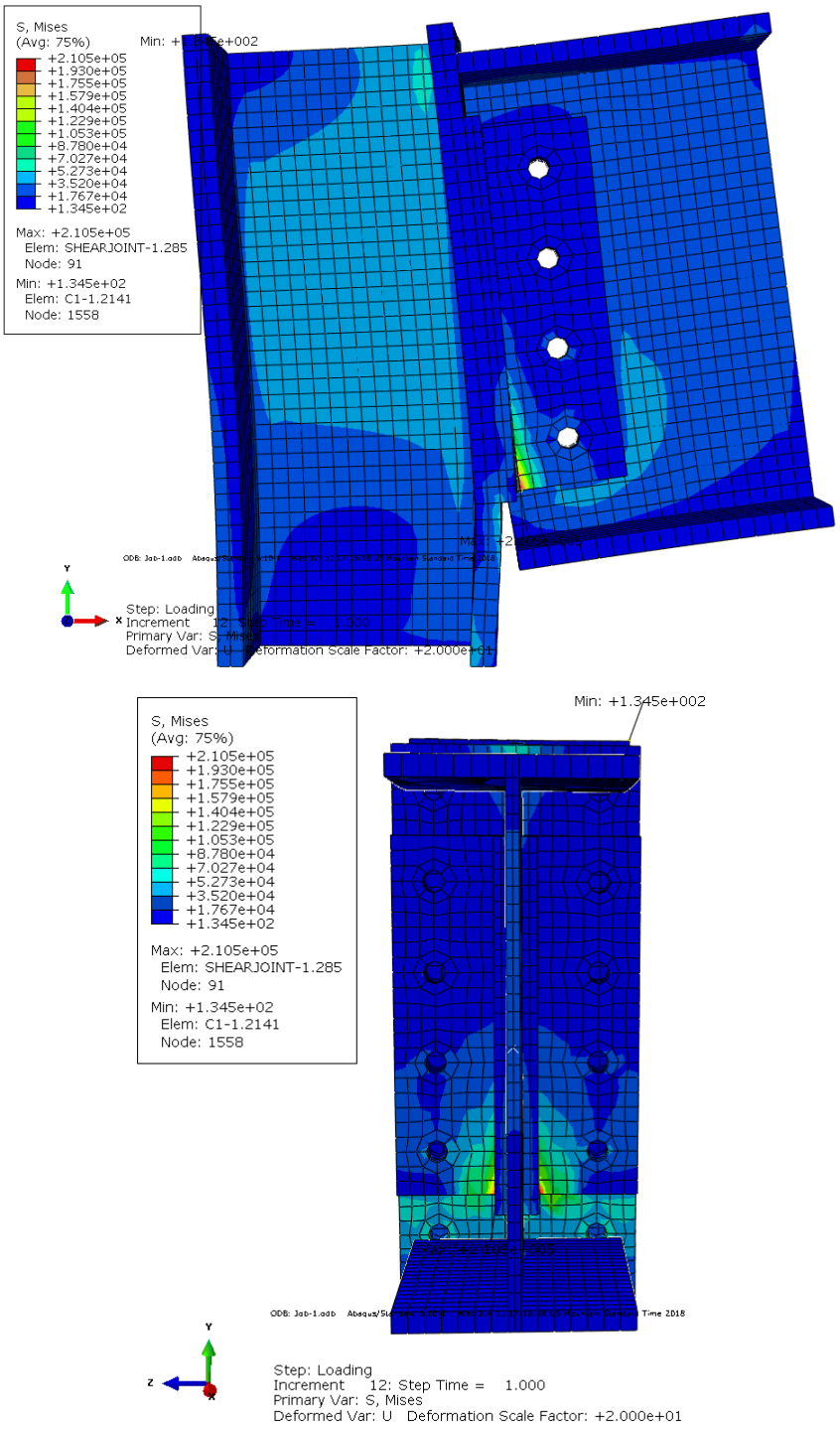

Based on the given analysis, the frame members are able to endure the applied moments and forces due to the loading. However, top joints need reinforcement. For this purpose, one brace will be designed for each joint, which is discussed in the next section.

Improved Frame:

In the previous section, it was demonstrated that the original frame is not able to endure the 200 kips point load. Although the members are all able to transfer the moments and forces, the top joints are the critical parts of the frame, which are vulnerable against the loading. To solve this issue, the top joints were decided to be strengthened with braces, similar to the braces that are connecting the columns to the ground. The upgraded frame is shown here.

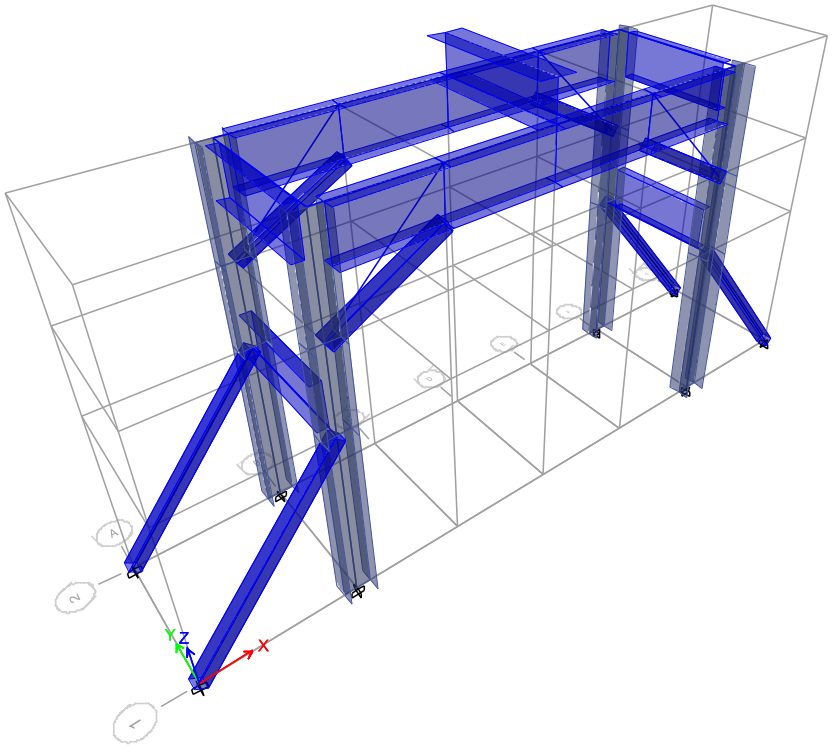

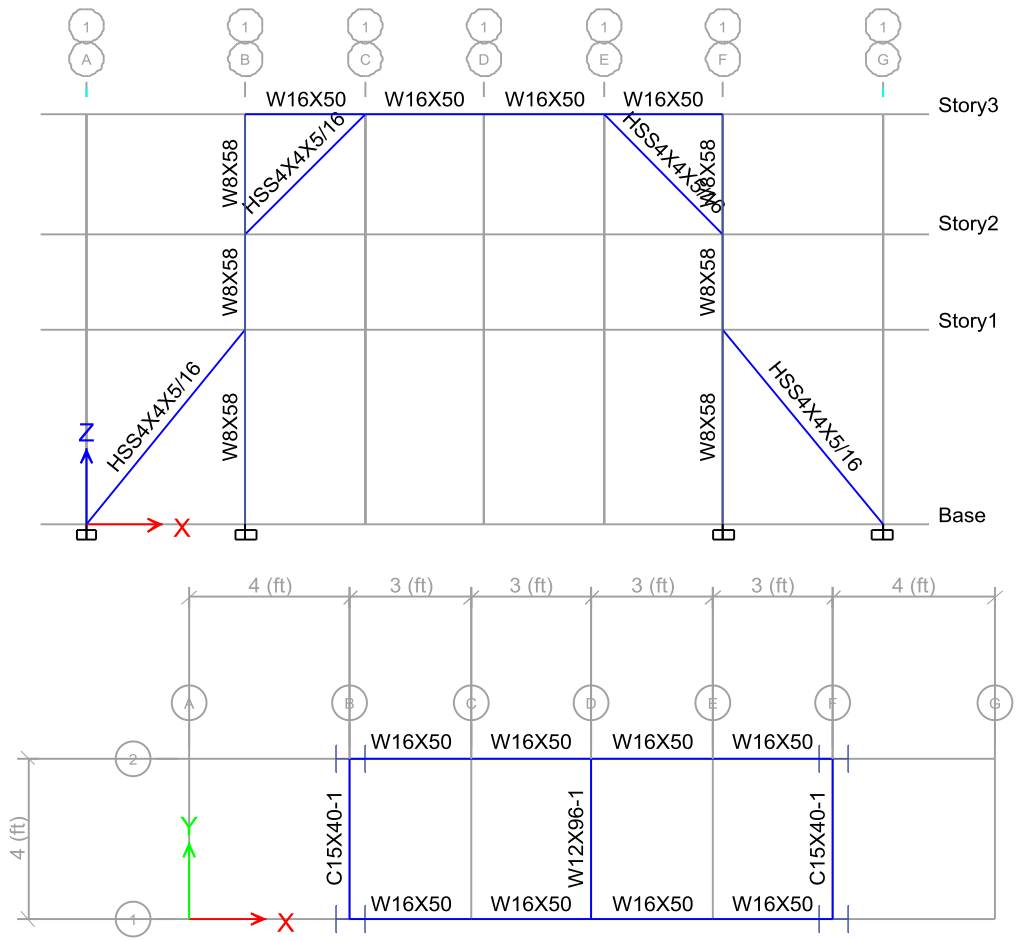

Figure A. 56. Dimensions and the cross-sections of the reinforced frame.

Moment Analysis, M33_Diagrams (kip-ft):

The moment diagrams are shown below. The results show that the bending moments are considerably reduced at the top joints. The original moment at the top joint was about 70 kip-ft while this value for the reinforced frame is about 16 kip-ft, which is 4.5 times lower than the original moment. Besides, the maximum bending moment in the top beams is reduced from 210 kip-ft to 175 kip-ft (i.e., about 17% reduction).

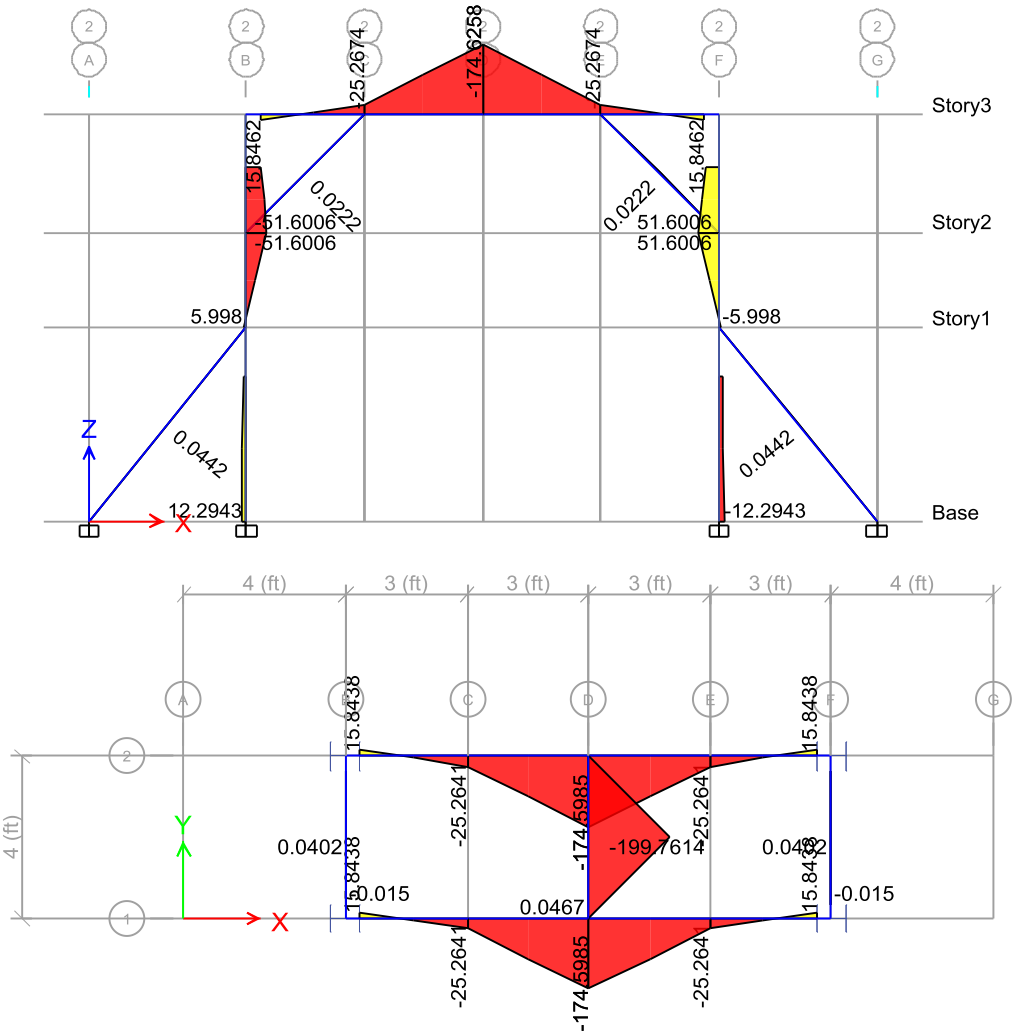

Figure A. 57. Moment diagrams in the reinforced frame, kip-ft.

Shear Diagram:

The shear diagrams for the reinforced frame are demonstrated here. The results show a reduction in the shear values at the joints around 70% (from 50 kips to 15 kips).

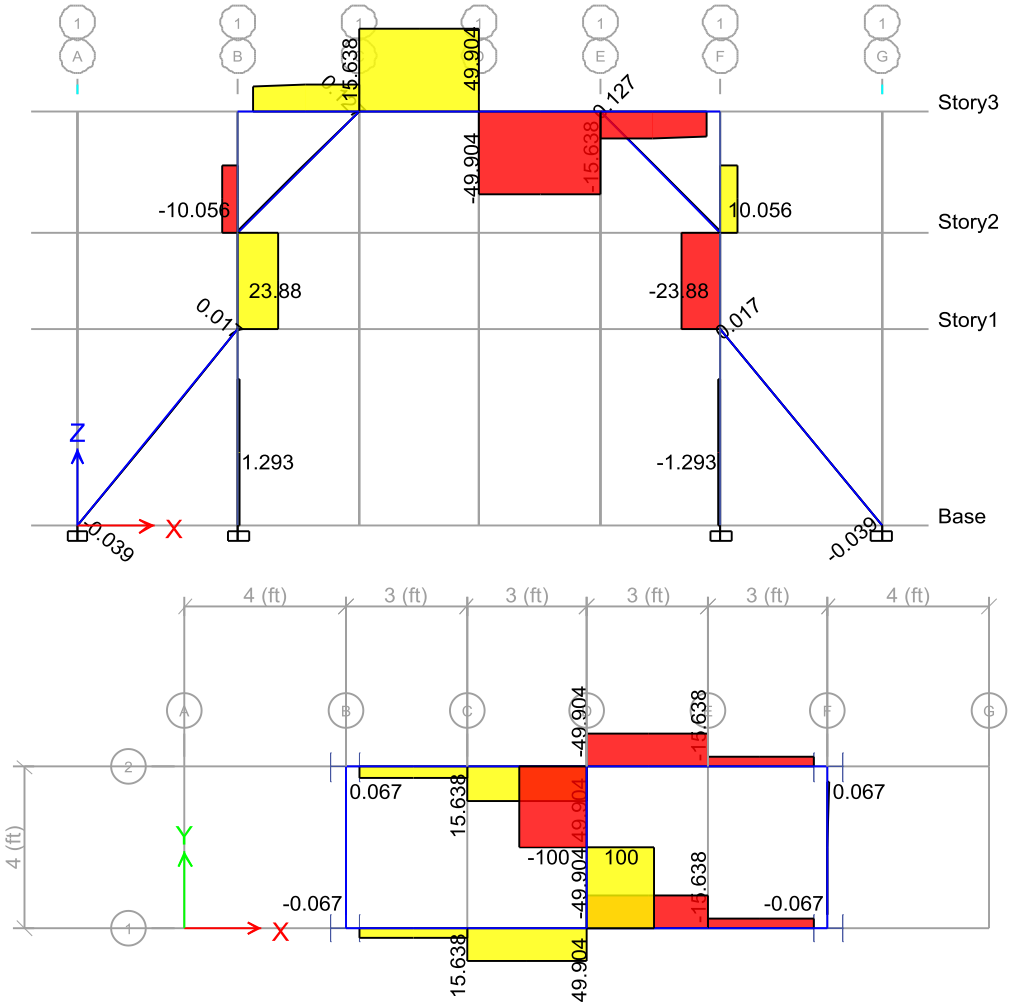

Figure A. 58. Shear diagram in the reinforced frame, kip.

Axial Forces:

The diagrams for the axial forces are shown here. The critical members under tensile forces are the top braces, which are under 48 kips tensile force. The cross-section of the top braces is similar to the bottom braces. Their tensile capacity was calculated in the previous section:

$$\phi_t P_n = 0.9 F_y A_g = 0.9 \times 50 \times 5 \simeq 220\,\text{kip} > P_u \qquad O.K$$

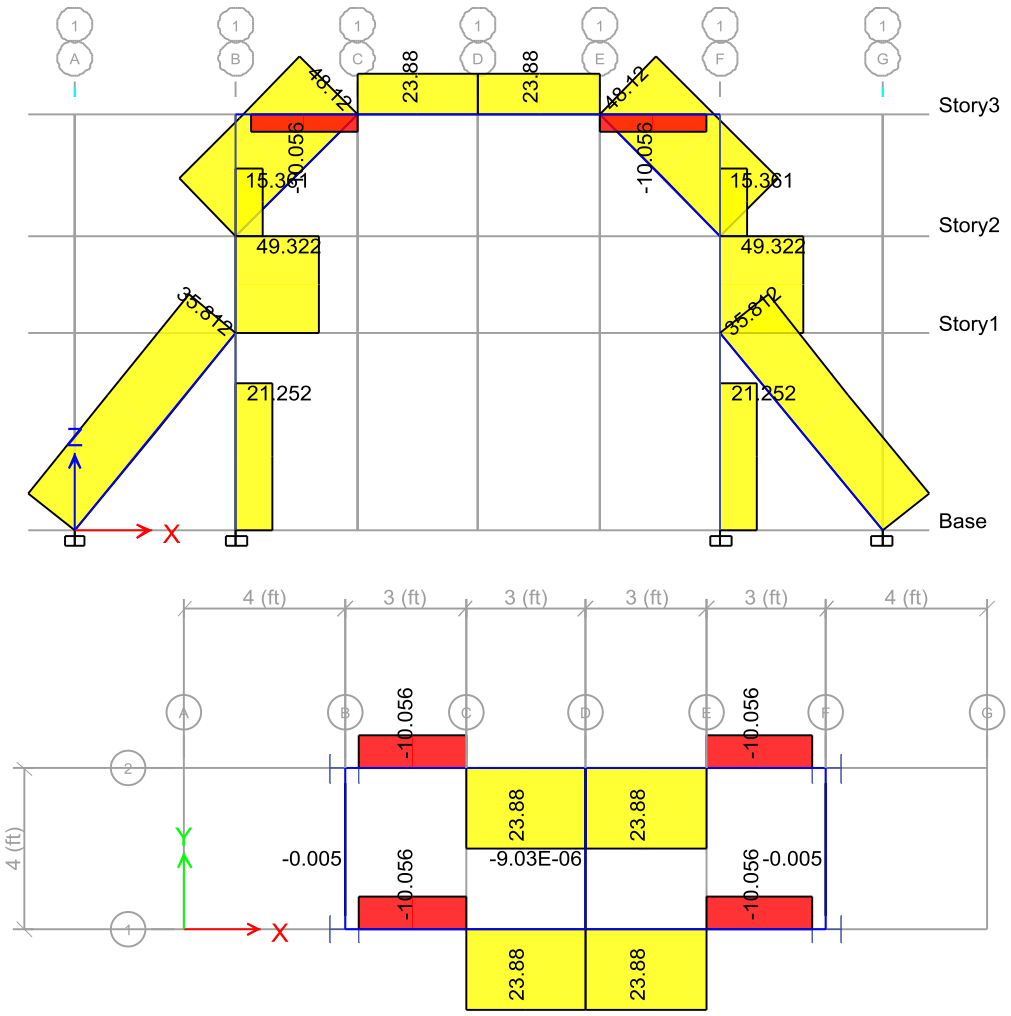

Connection of the Loading Beam (BI) to the Top Beams (BII):

The connection of the loading beam (BI) to the top beams (BII) is provided through four bolts which are passing through both top and bottom flanges (see Figure A. 59). However, to make sure that these bolts are able to endure the 200 kips loading at the center of the loading beam, an FE analysis has been performed.

Figure A. 59. Connection of the Loading Beam (BI) to the Top Beams (BII).

FE Model:

This section is itself divided into several sections that each section delivers the detailed modeling issues regarding the material properties, modeling, assembling, meshing, defining proper loading and boundary conditions, contacts and constraints, output requests and finally analyzing the model.

The top beam, B1, is symmetric around the center (loading point), therefore, only half of the beam is modeled, using solid 3D linear elements. The nodes are restrained, vertical to the symmetry plane. The initial model (bolts, stiffeners, and the beam) is shown in Figure A. 60. The units are reported in **in, lbf, and psi**.

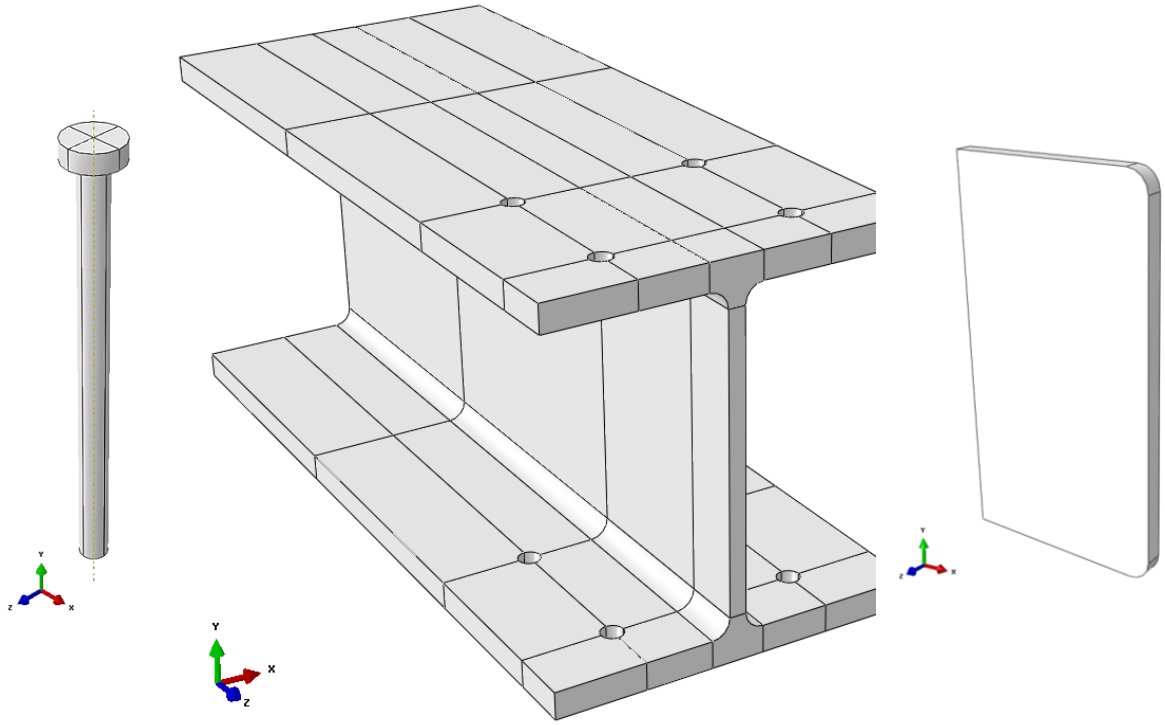

Figure A. 60. Top beam model, including bolts, stiffeners, and the beam.

The parameters for the steel material are listed in Table A. 3. Since the analysis is supposed to be in the linear range, there is no need to define the plastic parameters.

Table A. 3. Steel properties for the frame members.

Material	Young's modulus(psi)	Poisson's ratio
Steel	30×10^6	0.3

A Homogeneous solid section is defined for the Model. After assigning the defined section to the parts, it is time to import the parts into the assembly module as a dependent part, which means mesh only will be available in the part module and any change in the part module will affect all replicates in the Assembly module, see Figure A. 61. All parts are assembled using proper constraints and positioning tools.

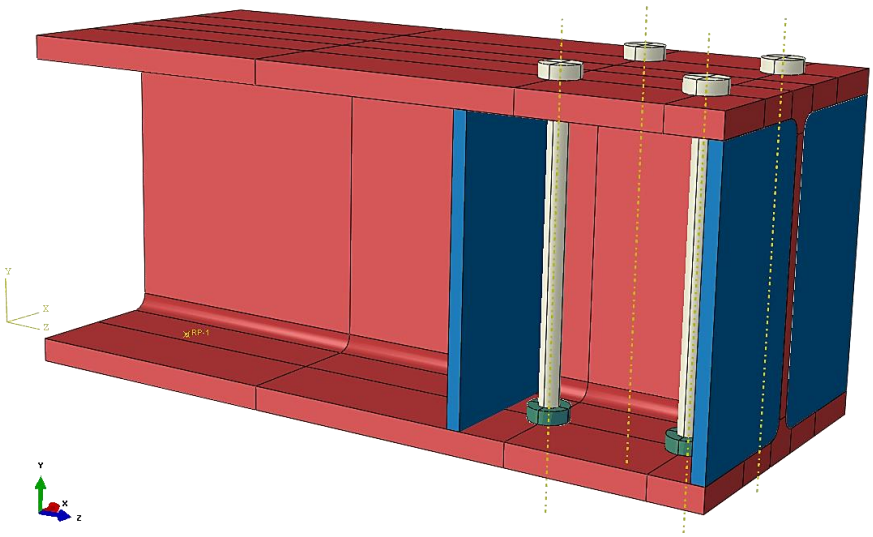

Figure A. 61. Assembled model.

For this type of analysis, **static and linear**, one Static-General step is defined. In this step, one step is defined with 1 second duration. Although we do not expect that the model experiences large deformations, and the analysis is also linear, but the large displacement has been activated to make sure its effect is considered, just in case if it happened.

In this model, the faces at the symmetry plan are restrained along the vertical direction (along the beam axis). The section of the bolts is also fully restrained (based on the assumption that there is not any deformation in the beam on the top of the frame, B2), which is an acceptable assumption given the fact that there is a small torsion in beam B2 (from structural analysis results). For the loading, half of the total loading value (i.e., 200 kips) is applied at the end of the beam B1.

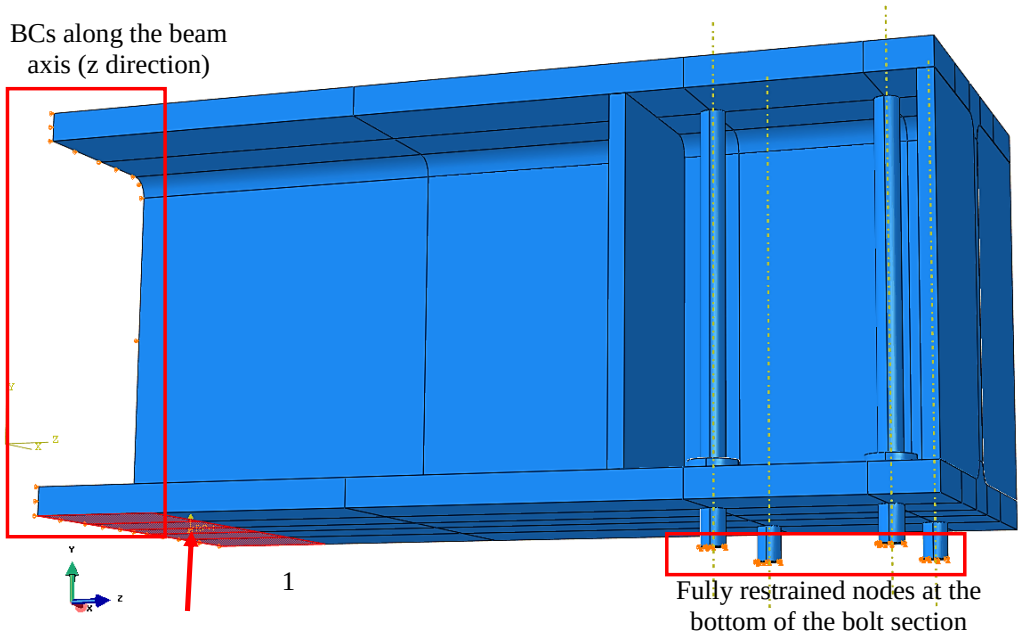

Figure A. 62. BCs and loading in the model.

Linear 3D Stress Elements (C3D8) are used for the analysis.

Analysis and Results:

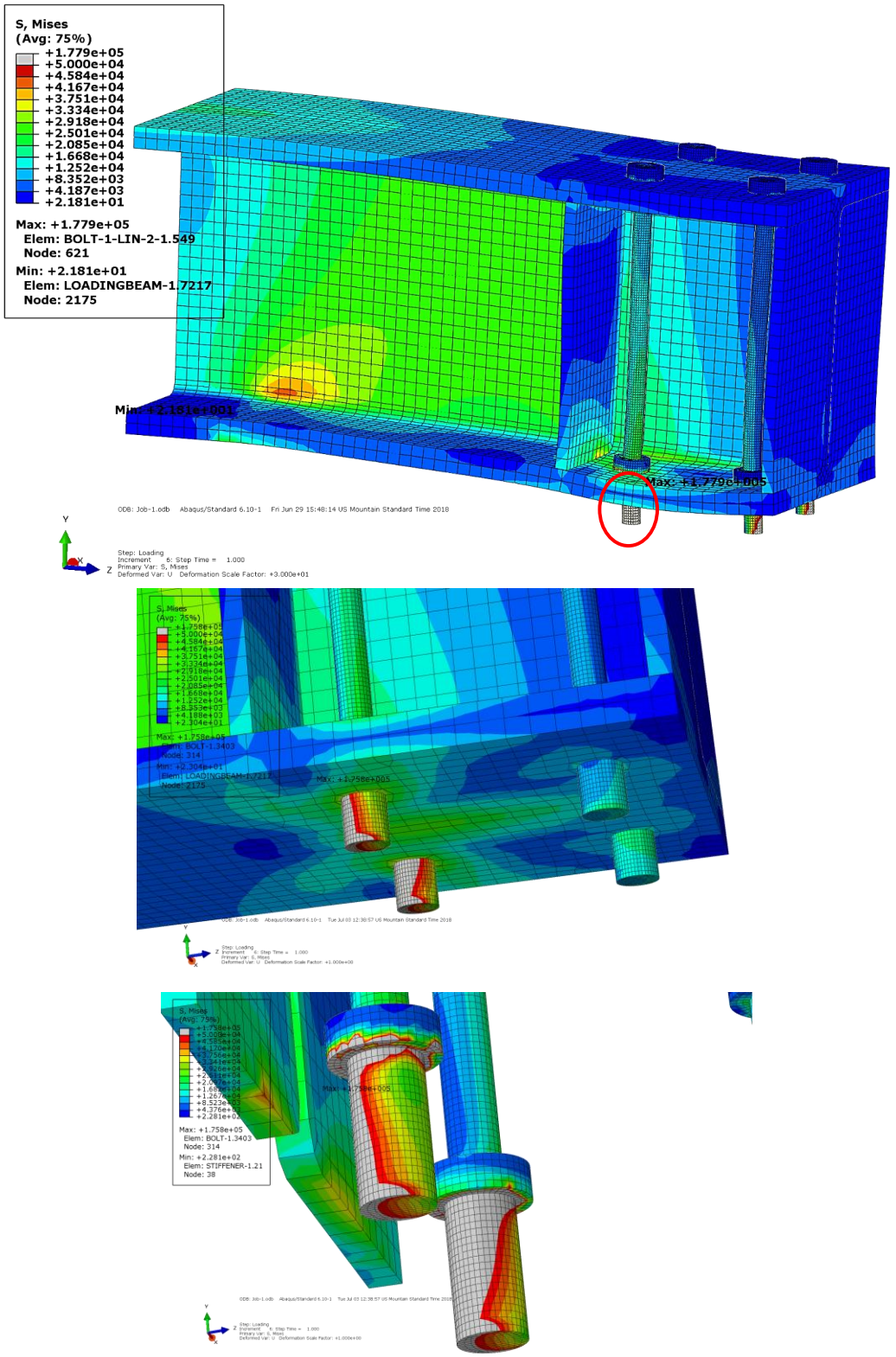

Figure A. 63. Analyzed model with 66982 nodes and 51204 elements, psi (the deformed shape is 20 times scaled up).

The analysis results show that there is a severe non-uniform stress distribution at the bolt sections so there is a stress concentration at the sections closer to the loading. Based on the FE analysis the bolts are not able to carry the applied loads. The maximum amount of the Misses stress is happening in the front bolts (depicted in the above figure), which is equal to 178 kips. This value is 2.4 times higher than the factored strength of the high strength bolts made of steel grade A325 (i.e., 78 kips). To overcome this problem, ultra-high strength rods, passing through the bottom and top flanges, were utilized instead of normal bolts.